UCRL 53868-98

FY 98

Engineering Research, Development and Technology

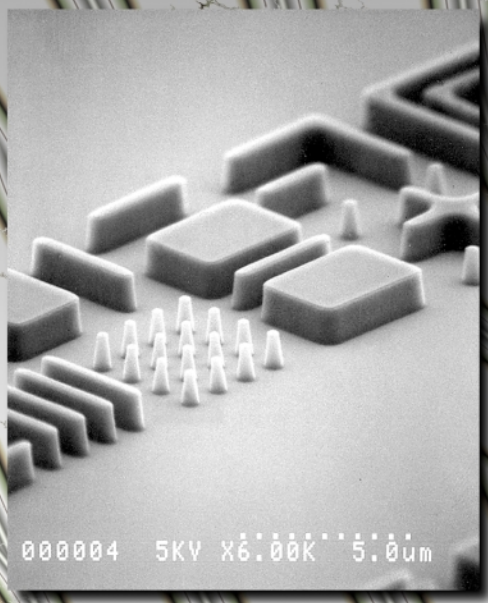

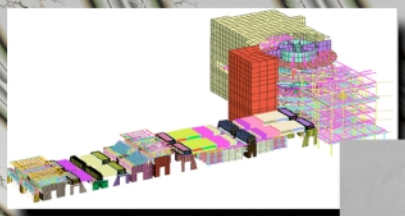

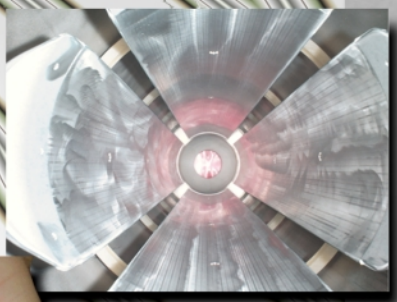

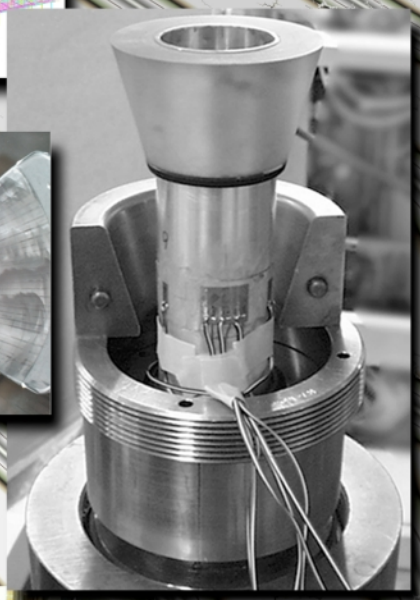

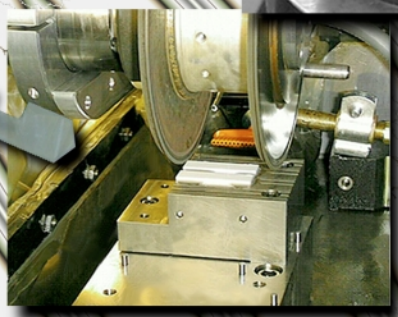

Disclaimer

This document was prepared as an account of work sponsored by an agency of the United States Government. Neither the United States Government nor the University of California nor any of their employees, makes any warranty, express or implied, or assumes any legal liability or responsibility for the accuracy, completeness, or usefulness of any information, apparatus, product, or process disclosed, or represents that its use would not infringe privately owned rights. Reference herein to any specific commercial products, process, or service by trade name, trademark, manufacturer, or otherwise does not necessarily constitute or imply its endorsement, recommendation, or favoring by the United States Government or the University of California. The views and opinions of authors expressed herein do not necessarily state or reflect those of the United States Government or the University of California, and shall not be used for advertising or product endorsement purposes.

This report has been reproduced
directly from the best available copy.

Available to DOE and DOE contractors from the
Office of Scientific and Technical Information
P.O. Box 62, Oak Ridge, TN 37831
Prices available from (615) 576-8401, FTS 626-8401

Available to the public from the
National Technical Information Service
U.S. Department of Commerce
5285 Port Royal Rd.,
Springfield, VA 22161

UCRL 53868-98

FY 98

Engineering Research, Development and Technology

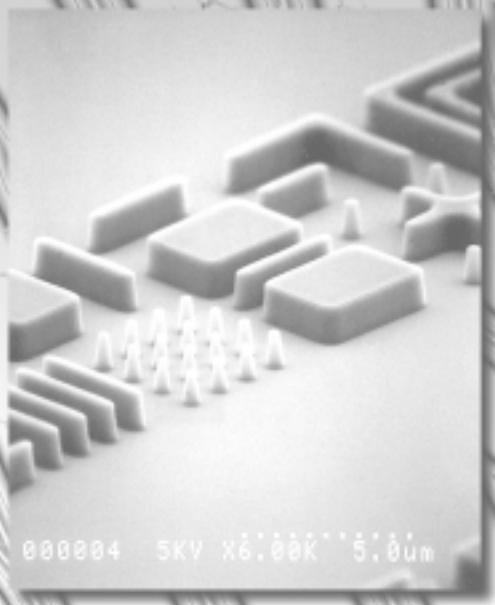

Manuscript Date February 1999
Distribution Category UC-706

Introduction

Spiros Dimolitsas, Associate Director for Engineering

1. Center for Complex Distributed Systems

Overview
Robert J. Deri, Center Leader

Accelerating the Development of Petaflop Applications and Systems
Anthony J. De Groot and Robert J. Deri *1-1*

Combined Sensing and Simulation for Enhanced Evaluation of Structures
David B. McCallen, Mathew Hoehler, Gregory A. Clark, and James V. Candy *1-3*

Modeling and Simulation of Wireless Sensor Networks
Rowland R. Johnson *1-11*

Information Warfare Analysis Capability
J. C. Smart *1-15*

2. Center for Microtechnology

Overview
Raymond P. Mariella, Jr., Center Leader

Disposable Microfluidic Biological Sample Preparation System
Robin R. Miles, Daniel L. Schumann, Kelye A. Allen, Jim A. Butler, and Kerry A. Bettencourt *2-1*

Sub-Micron Lithography with a 5X Stepper
Dino R. Ciarlo and Benjamin P. Law *2-5*

Advanced Packaging for Wireless Microsensor Modules
Abraham P. Lee, Charles F. McConaghy, Jimmy C. Trevino, Leslie M. Jones, and Jonathan Simon *2-7*

Radio Frequency Technology for Wireless Microsensor Modules
Charles F. McConaghy, Abraham P. Lee, Charles Chien, Chris Deng, and Igor Elgorria *2-11*

Ultra-High-Speed Analog-to-Digital Conversion Technology
Mark E. Lowry, Ronald E. Haigh, and Charles F. McConaghy *2-13*

HV Photovoltaics
Karla G. Hagans and Ronald E. Haigh *2-17*

Lattice Boltzmann Simulation of Complex Fluid Flows
David S. Clague *2-19*

Micro-Electromechanical Systems (MEMS) for Characterization of Plastic-Bonded Explosives
Jeffrey D. Morse, Dino R. Ciarlo, Scott E. Groves, Diane J. Chinn, Mehdi Balooch, and Mark J. LaChappel *2-23*

Micro-Electromechanical-Systems-(MEMS)-Based Fuel Cell Technology
Jeffrey D. Morse, Robert T. Graff, Alan F. Jankowski, and Jeffrey P. Hayes *2-27*

High-Power GaN Microwave Device Technology
Glenn A. Meyer, Gregory A. Cooper, Stacy L. Lehew, Thomas W. Sigmon, Daniel Toet, Steven DenBaars, and Umesh Mishra *2-31*

Glass Etching
Harold Ackler and Stefan P. Swierkowski *2-37*

Micro-Electromechanical Systems Foundry Interface
Michael D. Pocha *2-41*

A Hydrogel-Actuated Implantable Sensor
Amy W. Wang, Abraham P. Lee, Charles F. McConaghy, Christopher B. Darrow, Aleksandr Gilman, Stephen M. Lane, and Joe H. Satcher, Jr. *2-45*

Lambda Connect: Multi-Wavelength Technologies for Ultrascale Computing
Robert J. Deri, Michael C. Larson, Michael D. Pocha, and Mark E. Lowry *2-49*

3. Center for Precision Engineering

Overview
Kenneth L. Blaedel, Center Leader

Micro-Drilling of ICF Capsules
Steven A. Jensen and Brent C. Stuart *3-1*

A Spatial-Frequency-Domain Approach to Designing Precision Machine Tools
Debra A. Krulewich *3-3*

Precision Grinding of Brittle Materials
Mark A. Piscotty, Kenneth L. Blaedel, Pete J. Davis, and Pete C. Dupuy *3-9*

4. Center for Computational Engineering

Overview
Peter J. Raboin and Clfiford C. Shang, Center Leaders

Hybrid Ray/Wave Methods for Optical Propagation
Richard P. Ratowsky, Jeffrey S. Kallman, Michael D. Feit, and Bedros B. Afeyan.....4-1

Technologies for Advanced Induction Accelerators
Maurice A. Hernandez.....4-7

TIGER: An Object-Oriented Time-Domain Simulation Code
David J. Steich, Jeffrey S. Kallman, Gerald J. Burke, S Terry Brugger, and Daniel A. White.....4-9

OPUS: An Optically Parallel Ultrasound Sensor
Jeffrey S. Kallman, Dino R. Ciarlo, Elaine Ashby, and Graham H. Thomas.....4-13

Optical Transition Radiation Diagnosis for Electron Beams
Gregory P. Le Sage and Roger A. Richardson.....4-19

Characterization of Electromagnetic Scattering from Defects in the EUVL Process
Lisa Wang, Scott D. Nelson, Jeffrey E. Mast, and Abbie L. Warrick.....4-23

Nuclear and Electromagnetic Radiation Simulation Tools for Dual-Revalidation of the Stockpile
David J. Mayhall and Michael F. Bland.....4-29

Self-Effects in Expanding Electron Beam Plasmas
Manuel Garcia.....4-33

Pump-Induced Wavefront Distortion in Prototypical NIF and LMJ Amplifiers
Mark D. Rotter, Kenneth S. Jancaitis, Christopher D. Marshall, Luis E. Zapata,
Alvin C. Erlandson, Geoffroy LeTouze, and Stephane Seznec.....4-37

Parallel Algorithm Development for Computational Mechanics
Carol G. Hoover, Robert M. Ferencz, Anthony J. De Groot, Robert J. Sherwood,
Edward Zywicz, Yuen L. Lee, and Douglas E. Speck.....4-47

DYNA3D-TOPAZ3D Coupling and DYNA3D-NIKE3D Linkage
Jerry I. Lin.....4-55

A Physically Stabilized Eight-Node Hexahedral Element
Michael A. Puso.....4-59

A Cyclic Viscoplastic Constitutive Model
Phani Kumar V. V. Nukala.....4-65

Electromagnetic Cold-Test Characterization of the Quad-Driven Stripline Kicker
Scott D. Nelson and James E. Dunlap.....4-71

Photonic Doppler Velocimetry
Paul D. Sargis, Nicole E. Molau, and Daren Sweider.....4-77

Modeling Coupled Heat and Mass Diffusion
Arthur B. Shapiro and Philip M. Gresho.....4-81

Analysis and Modeling of a Stripline Beam Kicker and Septum
Brian R. Poole, Lisa Wang, Yu Ju (Judy) Chen, and George J. Caporaso.....4-85

5. Center for Nondestructive Characterization

Overview
Harry E. Martz, Center Leader

Techniques for Enhancing Laser Ultrasonic Nondestructive Evaluation
Graham H. Thomas, Robert D. Huber, Diane J. Chinn, James V. Candy, and James Spicer.....5-1

Nondestructive Evaluation of an Aluminum Alloy Using Hyperspectral Infrared Imaging
Randy S. Roberts.....5-9

***In-Situ* Identification of Anti-Personnel Mines Using Acoustic Resonant Spectroscopy**
Randy S. Roberts and Roger L. Perry.....5-13

An Acoustic Technique for the Non-Invasive *In-Situ* Measurement of Crystal Size and Solution Concentration
Diane J. Chinn, Paul R. Souza, and Harry F. Robey.....5-19

Micro X-Ray Computed Tomography for PBX Characterization
Diane J. Chinn, Jerry J. Haskins, Clinton M. Logan, Dave L. Haupt, Scott E. Groves, John Kinney, and Amy Waters.....5-23

Evaluation of an Amorphous Selenium Array for Industrial X-Ray Imaging
Clinton M. Logan, Jerry J. Haskins, Kenneth E. Morales, Earl O. Updike, James M. Fugina, Anthony D. Lavietes, Daniel J. Schneberk, Gregory J. Schmid, Keo Springer, Peter Soltani, and Kenneth Swartz.....5-27

LANDMARC Radar Mine Detection
Stephen G. Azevedo, Jeffery E. Mast. James M. Brase, and E. Tom Rosenbury.....5-39

IMAN-3D: A Software Tool-Kit for 3-D Image Analysis
Sailes K. Sengupta.....5-51

Image Recovery Techniques for X-Ray Computed Tomography in Limited-Data Environments
Dennis M. Goodman, Jessie A. Jackson, Maurice B. Aufderheide, and Erik M. Johansson.....5-61

6. Supporting Technologies

Overview
Robert T. Langland

Modeling of Anistropic Inelastic Behavior
Daniel J. Nikkel, Jr., Arthur A. Brown, and James Casey *6-1*

Modeling Large-Strain, High-Rate Deformation in Metals
Donald R. Lesuer, Mary M. LeBlanc, and Gregory J. Kay *6-7*

Uniform Etching of 85-Cm-Diameter Grating
Steven R. Bryan, Jr. and David L. Sanders *6-17*

Distributed Sensor Inertial Measurement Unit
Carlos A. Avalle and John I. Castor *6-23*

Fiber-Based Phase-Shifting Diffraction Interferometer for Measurement and Calibration of the Lick Adaptive Optics System
Eugene W. Campbell and Jong R. An *6-27*

Selected Engineering Publications

Selected Engineering Publications *PB-1*

Author Index

Author Index *AI-1*

Spiros Dimolitsas, Associate Director for Engineering

Cultivating our new research center organization

Nineteen ninety-eight has been a transition year for Engineering, as we have moved from our traditional focus on thrust areas to a more focused approach with research centers. These five new centers of excellence collectively comprise Engineering's Science and Technology program. This publication summarizes our formative year under this new structure.

Let me start by talking about the differences between a thrust area and a research center. The thrust area is more informal, combining an important technology with programmatic priorities. In contrast, a research center is directly linked to an Engineering core technology. It is the purer model, for it is more enduring yet has the scope to be able to adapt quickly to evolving programmatic priorities.

To put it another way, the mission of a thrust area was often to grow the programs in conjunction with a technology, whereas the task of a research center is to vigorously grow our core technologies. By cultivating each core technology, we in turn enable long-term growth of new programs.

Taking a longer view

The emphasis in the new research center structure is thus more long-term, building a research and development capability for the Laboratory for the five-year timeframe; a thrust area was often more short-term and narrower in technical scope, concentrating on the one- to two-year outlook of the technological needs of the programs. Our new research centers are positioned primarily not to solve today's problems but to pioneer innovative R&D work for emerging problems.

In a sense, we are internal venture capitalists for our Lab programs. It's in this way that we can help the Lab's programs attract funding for the long run.

Engineering must work to sustain the Laboratory's competitive advantage; we must create things that are technically one-of-a-kind. Within our organization, this means we are able to capitalize on our unique capabilities, specifically our comprehensive approach with dual disciplines. Many organizations have strong mechanical engineering programs; others offer solid electronics engineering. We have over a 40-year tradition of cross-pollinating both.

Our new centers are specifically designed to bring together the best of both disciplines, creating a synergy that most organizations can't. For example, as we model microscale systems, we advance a microtechnology that is unique in how it incorporates traditional electronic fabrication techniques with microminiature electromechanical designs.

For this reason, we have reorganized the Engineering Directorate to create a merged structure: the Engineering Science and Technology program, in addition to the Mechanical and Electronics Engineering programs.

The year ahead

Engineering is committed to the centers of excellence concept and will provide resources to seed bold new technologies. At the same time, because our new centers are closer to our core competencies, they will be easier to manage and offer more flexibility. Already we can see results. This year, Engineering competed much more successfully for the Laboratory's LDRD investment dollars that fund innovative projects.

In early 1999, we should complete the formation of our five centers and select their long-term leadership. Our second objective for the new year is synthesize our multiple visions for the centers so that we can write an updated version of our strategic plan.

Look through this report. It can be read as an overview of our new research centers, their enabling technologies, and supporting capabilities—and what we achieved this year.

Our future depends on how we find innovative but cost-effective engineering solutions to emerging technical problems. Through our partnerships with DOE and UC and a new center-based structure, we are planting new ideas and cultivating solutions that will grow value on a national scale.

Introduction

Robert J. Deri, Center Leader

The Center for Complex Distributed Systems is a focus for advanced technology development and applications involving ultrascale, spatially distributed systems. The Center seeks to develop an advanced suite of technical capabilities that enable the engineering of such systems, and to provide these capabilities in support of missions and programs at Lawrence Livermore National Laboratory (LLNL).

"Complex distributed systems" can be loosely defined as aggregations of large numbers of coupled, cooperating elements or subsystems, in which the system behavior cannot be described by simple hierarchical or nearest-neighbor interactions between elements. Examples include distributed sensor networks and beam diagnostics, large-scale distributed control and communication systems for optical and/or accelerator beams, and distributed information processing systems based on an underlying distributed sensor or control system.

Complex distributed systems play a critical role in several of LLNL's national security missions, with the potential to impact LLNL programs in other areas as well. This is illustrated by the four projects described in this report, all of which address applications of national importance and current interest:

1. "Accelerating the Development of Petaflop Applications and Systems" explores extremely large computational platforms, for application areas such as weapon simulations and climate modeling.
2. "Combined Sensing and Simulation for Enhanced Evaluation of Structures" describes the use of networked sensors to monitor the robustness of critical structural systems, such as bridges, dams, and buildings.
3. "Modeling and Simulation of Wireless Sensor Networks" investigates wireless sensor networks for applications such as early warning against attack by chemical agents. The networked sensor technology described in this work, and in the preceding article, will also impact environmental and industrial monitoring.
4. "Information Warfare Analysis Capability" discusses the challenges associated with, and techniques required for, defending information systems against attack.

A wide variety of technical disciplines are required for ultrascale system engineering. At this time, the Center is focussing on the areas of communications and control, system engineering, and simulation. These areas present fundamental challenges for most large-scale systems, as illustrated by all projects described in this report.

Communication and data flow issues are central to all four projects, as is the ability to simulate and design ultrascale systems. This underlying commonality of basic issues indicates that the technological capabilities developed by these investigators is generally applicable and transferable to other applications for complex distributed systems.

Center for Complex Distributed Systems

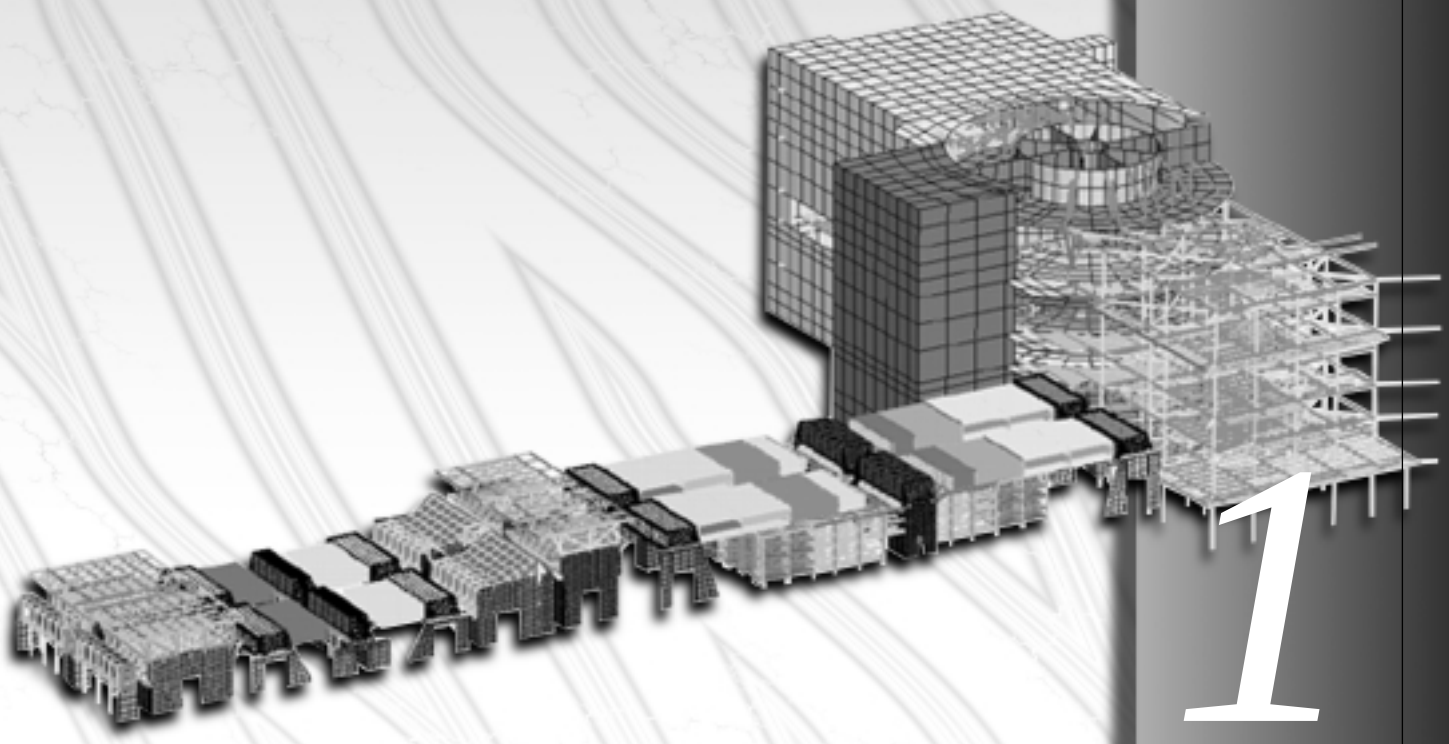

1

1. Center for Complex Distributed Systems

Overview
Robert J. Deri, Center Leader

Accelerating the Development of Petaflop Applications and Systems
Anthony J. De Groot and Robert J. Deri *1-1*

Combined Sensing and Simulation for Enhanced Evaluation of Structures
David B. McCallen, Mathew Hoehler, Gregory A. Clark, and James V. Candy *1-3*

Modeling and Simulation of Wireless Sensor Networks
Rowland R. Johnson *1-11*

Information Warfare Analysis Capability
J. C. Smart *1-15*

Accelerating the Development of Petaflop Applications and Systems

Anthony J. De Groot
Defense Sciences Engineering Division
Electronics Engineering

Robert J. Deri
Electronics Engineering Technologies Division
Electronics Engineering

We are creating a modeling and analysis framework to accelerate the development of petaflop applications and systems.

Introduction

The purpose of this project is to accelerate the development of technologies necessary to the creation of petaflop scientific applications and petaflop computing systems. This project brings together a multi-disciplinary team at Lawrence Livermore National Laboratory (LLNL) (computations, defense, engineering, physics, and lasers) to develop a modeling and analysis framework that will predict performance and identify bottlenecks for highly-relevant, unclassified Accelerated Strategic Computing Initiative (ASCI) applications (scaled to petaflop-class) running on proposed commodity-based architecture designs.

This will give LLNL a new capability that could assist in developing new high-performance applications, evaluating new hardware acquisitions, and creating a balanced computing environment.

Progress

One of the activities for this fiscal year was to begin development of a simulation capability to understand how interprocessor communication affects performance.

Simulation of the execution of large, complex applications on petaflop computing systems is a computationally intensive task. In the past, we have simulated the execution of an application at the instruction level. The computation required for this highly detailed simulation is approximately one hundred times more than the computation time to run the application on a real machine. We chose trace-based simulation to make this problem computationally tractable.

In our trace-based simulation, the application with its input problem are executed on a host machine, producing a trace of events. Events include all message passing operations, and optional user-defined events, including key subroutine entrances and exits. This trace, along with a description of the computer architecture to be simulated is used as input to a discrete-event simulator, that simulates the execution of the application on the simulated architecture.

Generation and visualization of traces and subsequent analysis have already improved performance of a complex application. We chose Parallel DYNA3D (ParaDyn) as the first application to study because it is one of the few parallel production codes far enough along in development for this project to make an immediate impact. We used the AIMS code from NASA Ames to generate and display the event traces from ParaDyn execution.

Figure 1 shows the execution of ParaDyn on eight processors. The problem simulated by ParaDyn is that of a buckling beam. In the figure, the horizontal direction represents the passage of time, and the vertical direction represents processor number. Line segments connecting bars represent message communication from the corresponding processors. The shading of a bar represents the execution of a set of subroutines by the corresponding processor. **Figure 1** shows that most of the time is used for computation and very little is used for

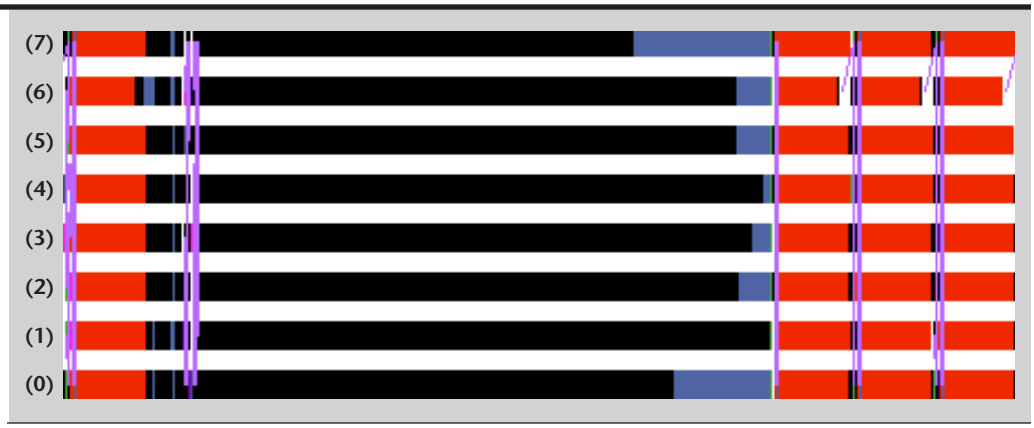

Figure 1. Visualization of ParaDyn execution trace, showing excessive time spent in the subroutine, represented by the black bars.

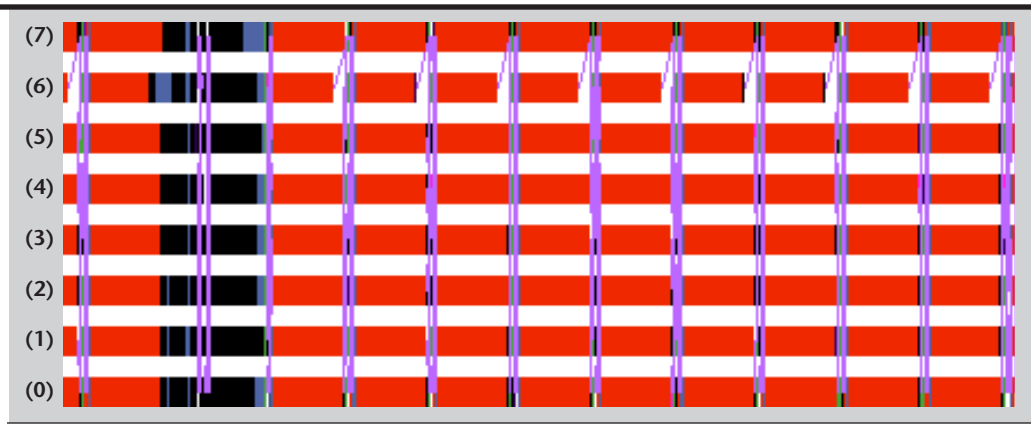

Figure 2. Visualization of ParaDyn execution trace after program optimization suggested by Figure 1.

communication. The figure also shows that the execution of the subroutine represented by the black bars is excessively long.

Further examination of the code showed that an optimization could be made to that subroutine to reduce execution time. **Figure 2** shows the result of that optimization, where the total execution time of that ParaDyn problem was reduced by a factor of about 1.5. Further optimizations may be possible with additional study.

Combined Sensing and Simulation for Enhanced Evaluation of Structures

David B. McCallen and Matthew Hoehler
New Technologies Engineering Division
Mechanical Engineering

Gregory A. Clark and James V. Candy
Electronics Engineering Technologies Division
Electronics Engineering

Large-scale computer simulation is an essential tool in the design and analysis of modern structures. With the enormous cost and construction effort associated with many large structures, it is imperative that computer simulations provide an accurate picture of structural performance spanning a multiplicity of loading environments such as bomb blasts, earthquakes, and ambient vibrations. In the current study, techniques are investigated that allow evaluation of simulation model accuracy and the possibility for subsequent enhancement. The multidisciplinary tools being used at Lawrence Livermore National Laboratory (LLNL) include finite-element-based structural simulation, model-based signal processing, and remote sensing and data communication. The overall objective of this research is to symbiotically couple numerical simulation with field measurement of structural behavior. The result will be enhanced accuracy and reliability of numerical simulation of structural response, and the ability to monitor fundamental changes in complex structural systems, a prerequisite to health monitoring and damage detection.

Introduction

With the proliferation and advancement of sophisticated numerical simulation software tools over the past twenty years, computational simulation of large structural systems has been a subject area experiencing rapid growth. Engineers now rely heavily on large-scale structural simulations to design and evaluate the performance of critical new structures, and to establish the performance of expensive retrofits on existing structures.

Despite the advances in computational methods, there remains a significant degree of uncertainty in predicting the field performance of many large-scale structural systems. These uncertainties are rooted in our inability to precisely quantify the phenomenological behavior of certain aspects of structural excitation and structural response—for example, uncertainties in the precise deformation characteristics of complex structural element interconnections or uncertainties in estimation of the actual loads a structure will be subjected to. To advance our ability to accurately and confidently simulate the response of structures, we must make use of measured structural response characteristics and measured excitation functions.

The notion of coupling simulation and measurement is emerging in the study and characterization of many complex systems found in the sciences and engineering. One of the tenets of a new National Science Foundation program on Knowledge and Distributed Intelligence is the recognition that: "Better understanding of complex phenomena now requires interplay between computations and data, often in real time." The work described in this report provides the foundation at LLNL for establishing an interplay between computations and measured data for the specific case of large structural systems.

The essential links between simulation and measurement are shown in **Fig. 1**. As indicated, information from a numerical structural model and data from field measurements of structural response are fed into a model-based signal processor. The signal processing toolbox is used to evaluate whether the model and as-built structure are in agreement, or if there is a discrepancy between the

dynamical behavior of the model and that of the actual structure.

In addition, research on the signal processing toolbox will attempt to discriminate the source of existing discrepancies between the simulation model and the as-built structure. Once discrepancies can be identified, the basis for damage detection in a structural system has been established. Experimental measurements before and after an event can be used to identify changes in the structural system, and identification of the source of the differences with a damage detector can be performed to investigate where damage has occurred in a large distributed structure.

Progress

In the first year of work, we have assembled a multidisciplinary team, the combined expertise of which spans the required technologies in mechanical and electronics engineering. Our accomplishments include the following:

1. An understanding of the relationship between the structural simulation models of mechanical engineering and the state space models of electronics engineering has been established for large structures.
2. The protocols and requirements for information exchange between second order equations of motion of a computational structural model, and first order equations of motion of state space, have been developed.
3. The software for a model-based signal processing state space model module has been completed for performance of structural simulations, and a state space filter has been developed for detection of differences between the simulation model and a measured structural response.
4. In the area of sensing and communication, a new data acquisition system has been developed which will allow on-demand wireless communication of data via cellular phone from an instrumented structure.

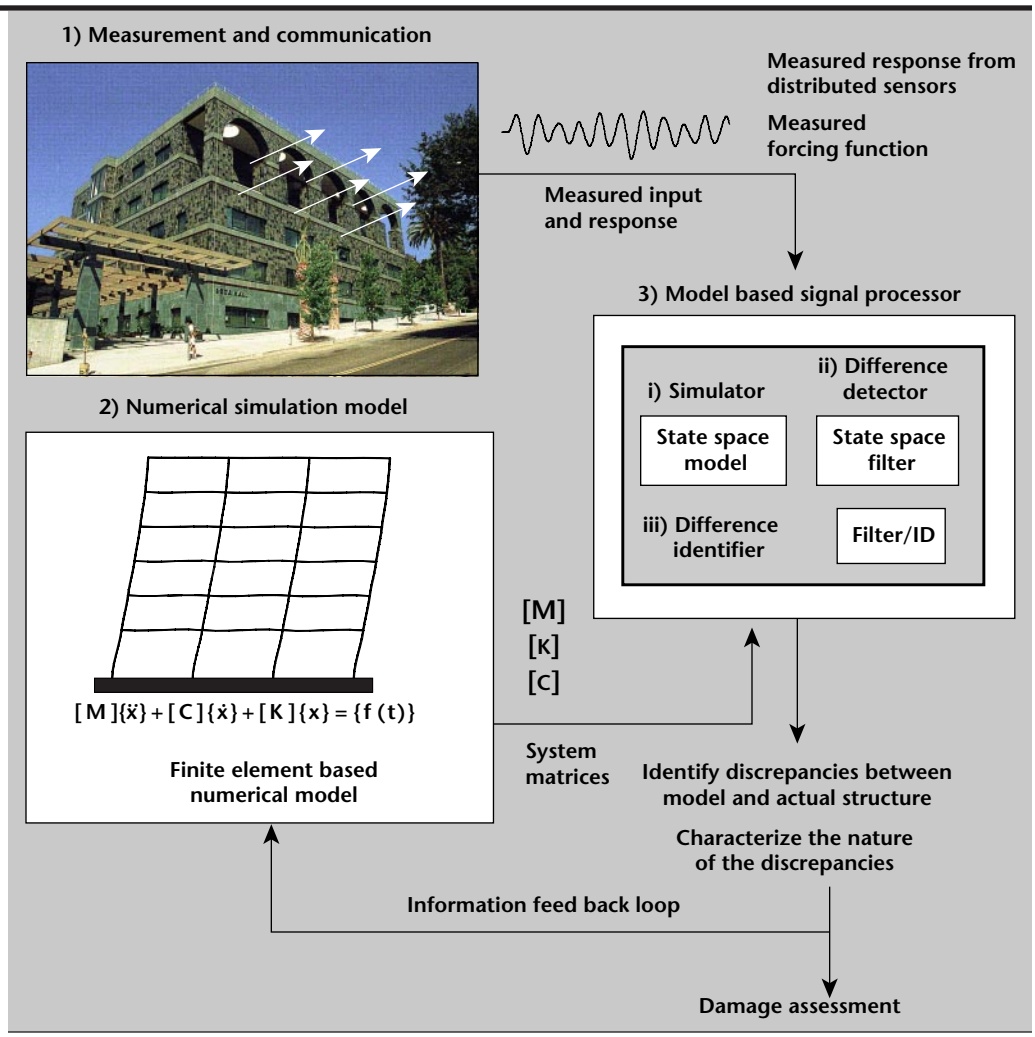

Figure 1. Model-based signal processing for linkage between numerical models and measured response.

5. A field experiment has been completed at the Nevada Test Site to evaluate the data acquisition system and to provide a real world data set for evaluation of the model-based signal processing algorithms in year two of this project.

Interfacing Numerical Simulation Models and Signal Processing

A capability for the model-based signal processing algorithms to detect discrepancies between a numerical structural model and the actual structure has been developed and coded in a MATLAB environment (**Fig. 2**).[1] The matrices constructed for the numerical simulation model are passed into the MATLAB-based state space model for process simulation (essentially a recast of the "N" second order equations of motion into a set of "2N" first order equations). Using the constructed state space model and measured data from a structure, a difference detector based on the whiteness test described by Candy[2] has been coded. This whiteness test, based on an autocorrelation check between measured structural response and the state space model,

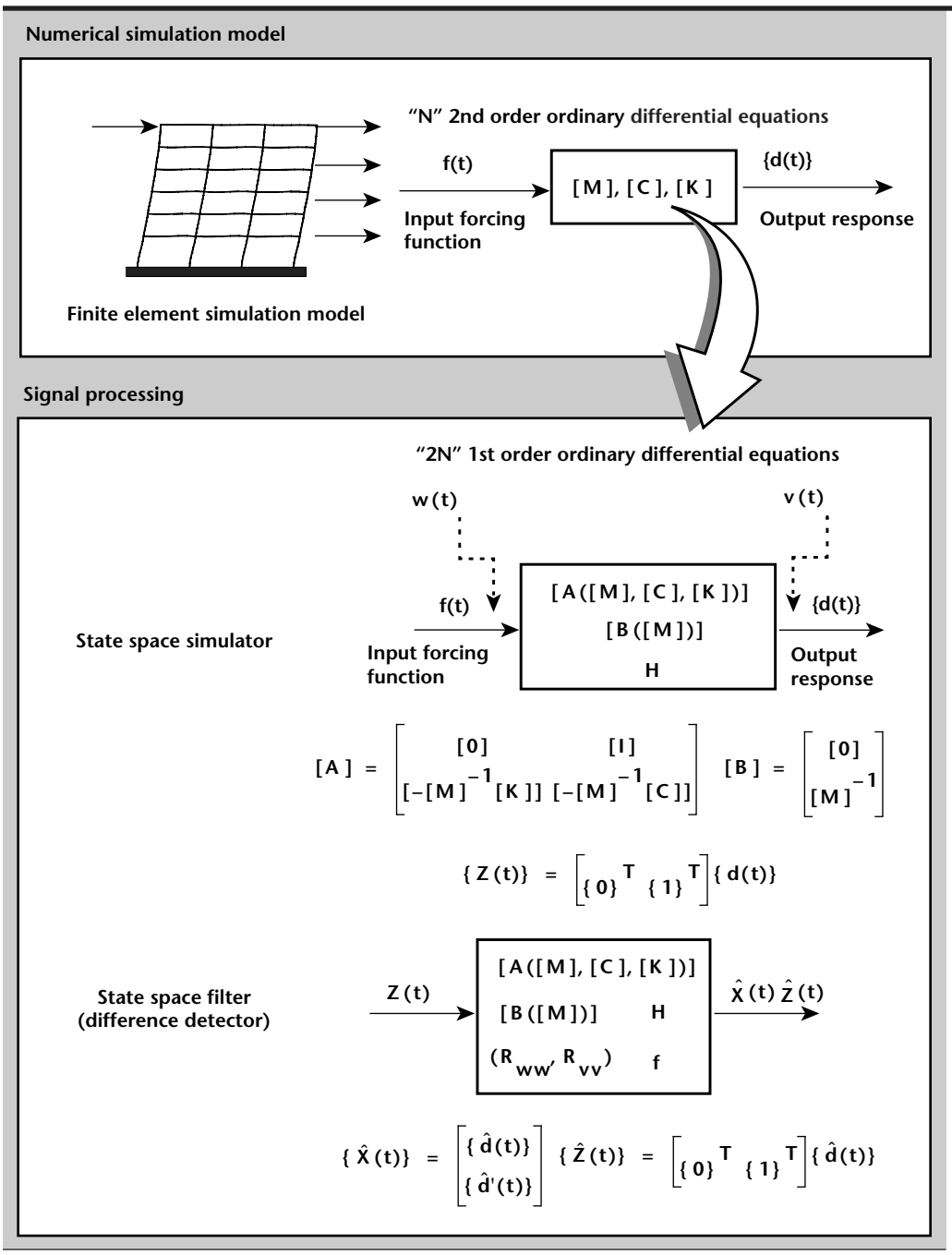

Figure 2. Numerical simulation model matrix hand-off to signal processing state space simulator and state space filter.

provides a rapid assessment of the validity of the numerical structural model.

An important feature of the model-based signal processor under development is the ability to work with full transient time history waveforms of the structural response. This is in contrast to most established model evaluation algorithms which are based on natural modeshape characteristics of the structure.[3] The ability to work directly with transient time histories will provide a powerful tool which can use any forcing function on the structure (that is, an impulsive load or sinusoidal load imposed on the structure by design). Furthermore, the signal processing methodology is not restricted to linear systems.

The ability of the signal processing algorithms to detect differences between the numerical structural model and the actual structure has been demonstrated with example problems. **Figure 3** illustrates an example for a five-story building, in which a simple five-degree-of-freedom "shear building" numerical simulation model of the structure has been constructed. In addition, a second model is constructed to be representative of the data from an actual "measured" structure. The second model is intended to provide the data which typically would be measured in the field.

To evaluate the ability of the signal processing algorithms to detect the difference between the model and the "measured" structure, transient response waveforms were determined for unit forcing functions applied to each floor level of the sample building. When the simulation model and "measured" structure are precisely the same structure, the whiteness test which discriminates differences between the model and actual structure is passed, indicating the model is in agreement with the actual structure (**Fig. 3a**). However, when the model representing the measured structure is perturbed by cutting the stiffness of the first floor level by one-half (**Fig. 3b**), the signal processing package immediately senses the difference between the numerical simulation model and the "measured" structure, providing the engineer with an immediate indicator of the deficiencies of the numerical structural model.

Sensing, Communication, and Field Experimentation

The signal processing linkage between the numerical structural model and the measured structure requires the ability to economically monitor the response of a large structural system. For many large, distributed structures this can be a difficult, and potentially prohibitive task if traditional wired sensor systems are used. In cooperation with the private firm of Jarpe Data Systems, a data acquisition system has been developed that will allow remote gathering of transient response data from a large structure. The capabilities of this data acquisition system have been tested in an experiment at the Nevada Test Site (**Fig. 4**). The data acquisition system records a data stream from a suite of structural sensors, typically accelerometers, and stores the time-stamped data on a disk storage system. The acquisition system has a cellular phone system on board and can be called up remotely with a laptop computer with a modem for on-demand download of data. This data acquisition system will provide an economical and practical means of remotely monitoring large distributed structures.

Future Work

The development of the model-based signal processing toolbox will continue with the construction of the Difference Identifier (the Filter/ID in **Fig. 1**). This will complete the basic signal processing package. Extensive sensitivity studies will be performed to assess the ability of the signal processing tools to detect and identify many different types of discrepancies between simulation models and measured structures. These studies will make use of computer simulation models (more sophisticated samples of the type shown in **Fig. 3**), existing full-scale structural tests performed at various universities, and the data obtained from the carefully controlled structural experiment performed at the Nevada Test Site in FY-98. In addition to identification of discrepancies, the research will determine the degree to which the precise cause of the discrepancies can be identified by the Difference Detector.

In parallel to the algorithmic developments, sensors and data acquisition systems will be placed on three large distributed structures to establish the ability to perform on-demand remote sensing over an extended time period. The target structures include the San Francisco-Oakland Bay Bridge[4,5] the National Ignition Facility laser bay structures, and the Bixby Creek Arch Bridge at Big Sur (**Fig. 5**).[6]

Each of these structures has been studied at LLNL as part of ongoing research and development projects or programmatic work, and numerical simulation models exist for each structure. These important structures present different sensing and communication challenges

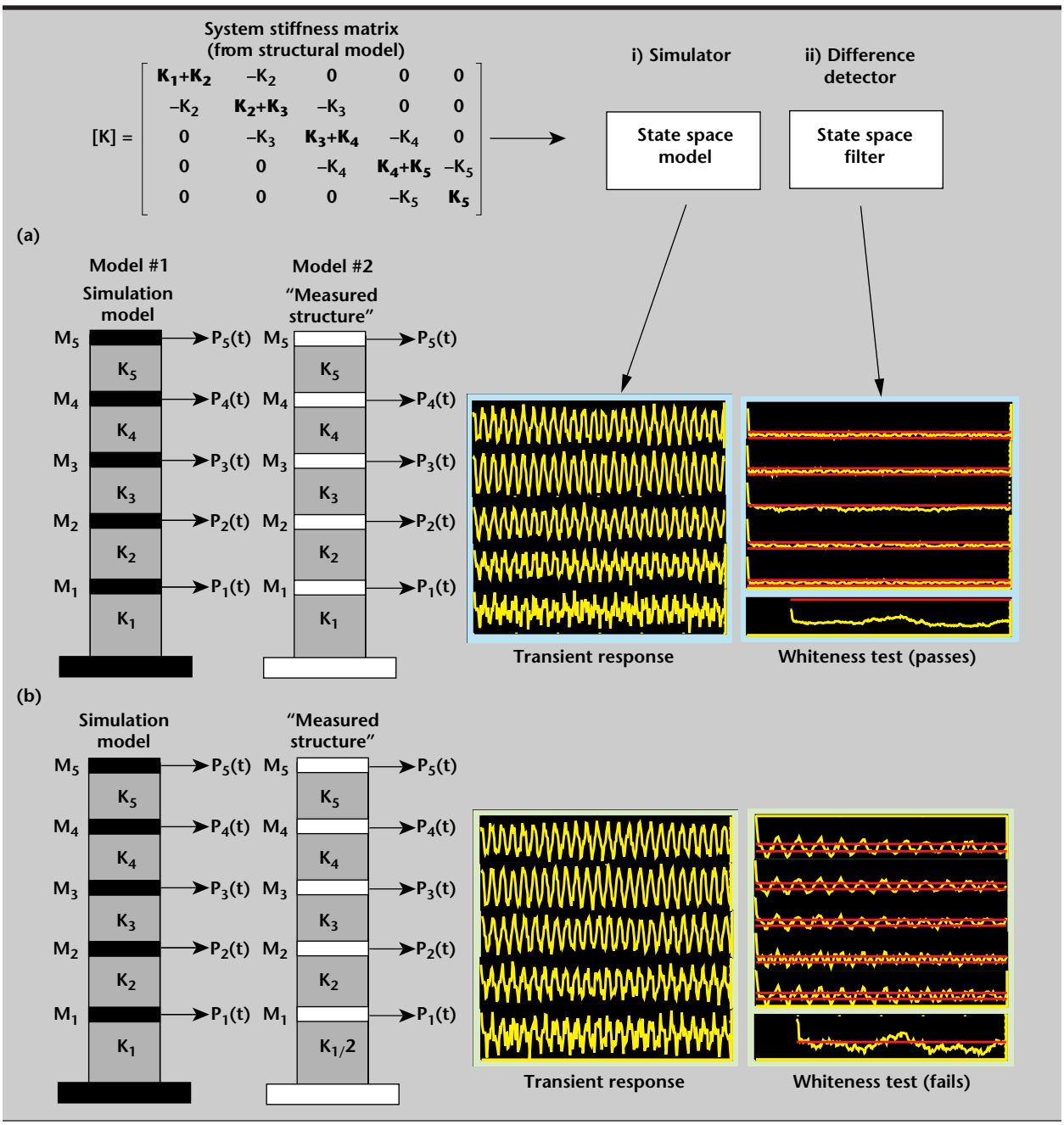

Figure 3. Development of model-based signal processing components—a model-based simulator for process simulation and a state space filter for difference detection. a) Application to a problem in which the computational model and measured structure agree (whiteness test is passed); b) application to a problem in which the computational model and measured structure disagree (whiteness test fails).

and will require structure-specific detailing of the sensors and data acquisition system. Previous study of these structures has provided the understanding of the frequency range of interest, and existing simulation models will be used to establish sensor placement locations. Successful monitoring of these structures will provide the hardware and methodology for deployment of dense instrumentation arrays on large distributed structures.

Large structural systems such as the National Ignition Facility or the Bay Bridge represent a tremendous capital investment and are critical structures for our society. The degree to which we analyze, design and monitor these structures should be commensurate with the cost and criticality of function which

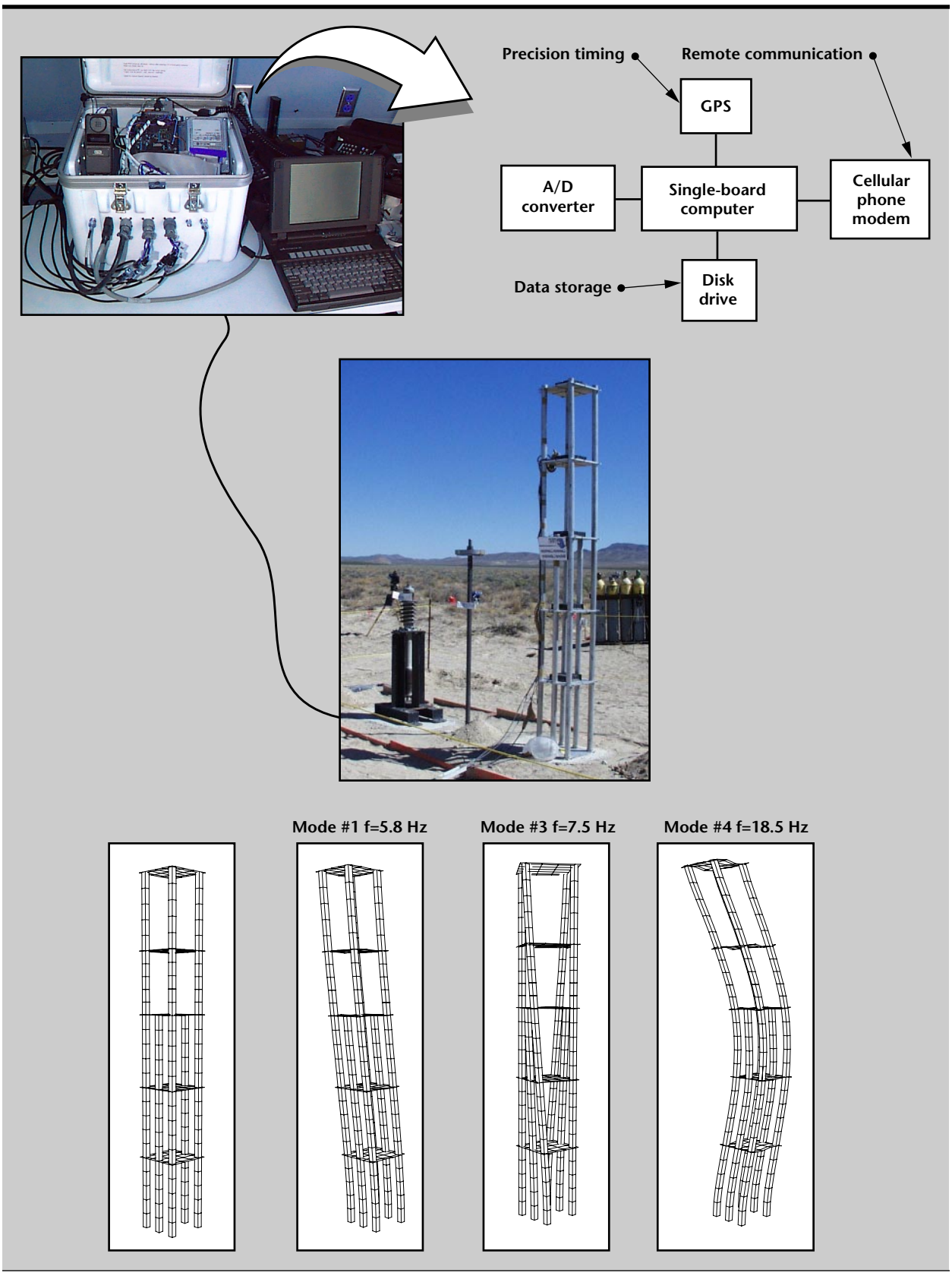

Figure 4. Data acquisition system for remote, wireless monitoring of a distributed structure. System includes GPS for precision time-stamping of data, and on-board cellular phone communications.

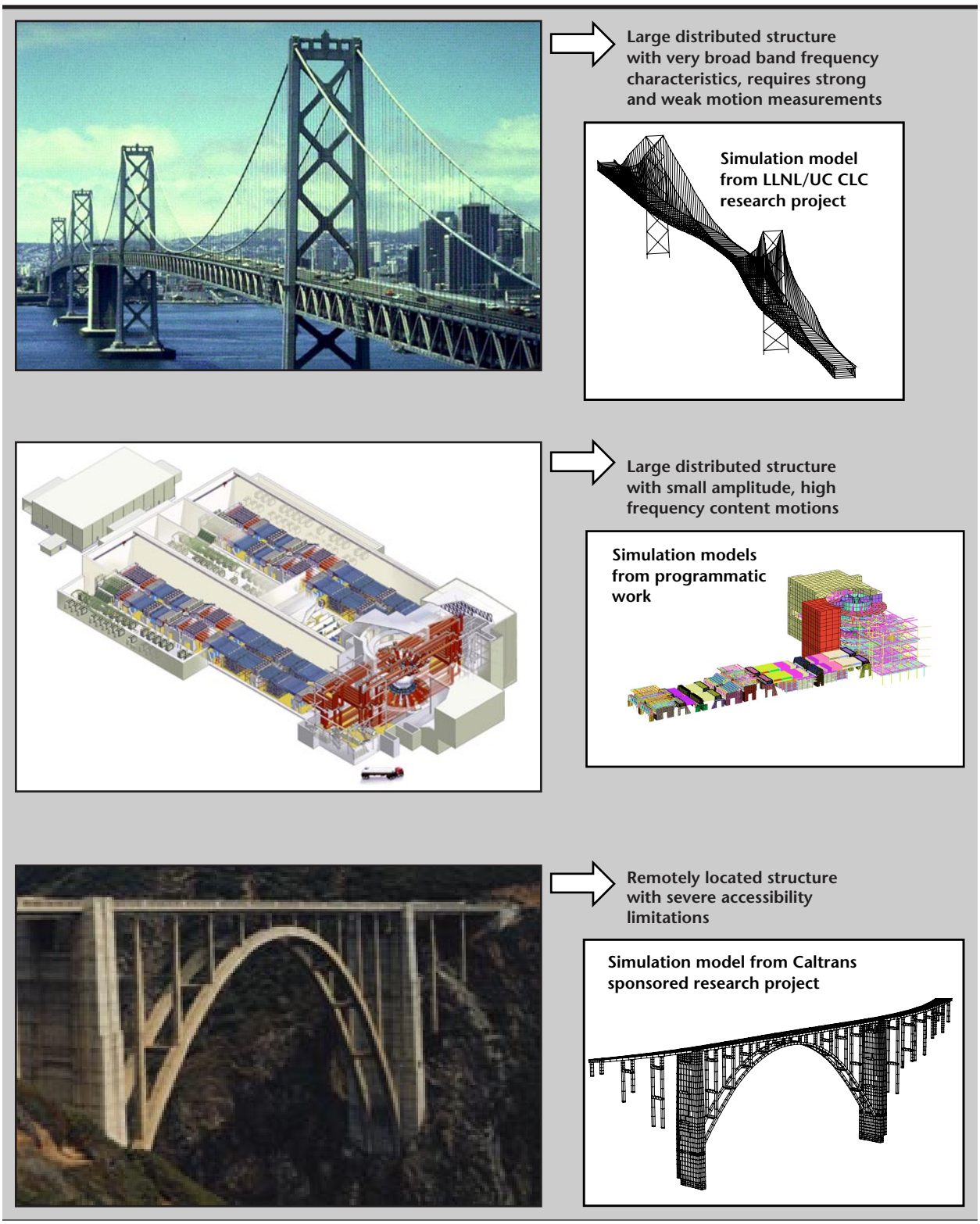

Figure 5. Large structural systems to be instrumented in FY-99.

they perform. The methodologies developed with this research will provide the tools necessary to significantly improve our understanding of how large distributed structures behave, will lead to increased reliability in numerical simulations, and will provide an entirely new capability for long term monitoring to ensure the integrity of important structures.

References

1. Clark, G. A., "Failure Detection for Mechanical Structures: A State-Space Model Base Approach," Lawrence Livermore National Laboratory Report, in preparation.

2. Candy, J. V., and D. L. Lager (1979), "Identification, Detection and Validation of Vibrating Structures: A Signal Processing Approach," Lawrence Livermore National Laboratory, Livermore, California (UCID-18720).

3. Berman, A., and E. J. Nagy (1983), "Improvement of a Large Analytical Model Using Test Data," *AIAA Journal*, Vol. **21**, No. 8, August.

4. McCallen, D. B., and A. Astaneh-Asl (1988), "Computational Simulation of the Nonlinear Response of Suspension Bridges," *Proceedings of the World Structures Congress*, Elsevier, San Francisco, California.

5. McCallen, D. B., and A. Astaneh-Asl, "Explicit Dynamic Analysis of Cable Supported Bridges," in preparation, to be submitted to *Computers and Structures*.

6. McCallen, D. B., C. R. Noble, M. S. Hoehler, and M. Gerhard, "The Seismic Response of Concrete Arch Bridges with Focus on the Bixby Creek Bridge, Carmel, California," Lawrence Livermore National Laboratory Report to the California Department of Transportation, in preparation.

Modeling and Simulation of Wireless Sensor Networks

Rowland R. Johnson
Computer and Communications Engineering Division
Electronics Engineering

Currently, Lawrence Livermore National Laboratory (LLNL) has several wireless sensor network (WSN) programs, and it is likely that the number will increase. In FY-98, LLNL researchers developed a core competency to model and simulate WSNs, which will give LLNL a competitive advantage in research and development. Contributions to existing programs are described, and the results of LLNL-funded academic research are presented.

Introduction

Recent advances in micro-electromechanical systems, low-powered circuit technologies, and computer networking have made possible a low-powered WSN involving thousands or millions of sensor nodes. Over the next ten to twenty years, LLNL will have the opportunity and obligation to participate in programs involving these networks. Just as the capability to model and simulate nuclear explosions was an R&D enhancer for nuclear devices, the capability to model and simulate WSNs will be an R&D enhancer for WSNs. A modeling and simulation capability 1) will dramatically reduce the effort required to develop a WSN; 2) can be used as a planning tool for a deployment; and 3) can be used to evaluate proposed network systems.

Current wireless network techniques do not meet node power consumption and total system throughput requirements. Academic researchers are beginning to consider non-hierarchical network topologies as a means to address power consumption and system bandwidth issues. Data packets are routed from node to node based on which RF channel offers the most efficiency at a particular time (usually, this results in a data packet being routed to a nearby node). Higher RF channel efficiency allows a lower RF power level to be used, which reduces the node power consumption. It also reduces RF interference by other nodes, thereby increasing total system throughput. It has been shown that, although latency usually increases (due to increased hop count), power consumption decreases and system throughput increases.

The disadvantage of non-hierarchical network topologies is that their behavior is only beginning to be understood. In addition, research has been focused mainly on applying these techniques to personal communication systems, such as cellular telephones and personal digital assistants. It is unknown how effective these existing techniques will be for the typical LLNL WSN application.

Progress

During FY-98 a core competency in modeling and simulation techniques for WSNs was developed. A team of LLNL researchers have attained expertise in analyzing WSNs via modeling and simulation techniques. Expertise has been developed in the use of state-of-the-art, commercially available simulation packages. In addition, researchers have developed key computer software components. Wireless sensor networks being considered are tightly coupled with a physical system that will affect their operation. Therefore, it is important to be able to integrate a simulator of such a physical system with the WSN simulation.

Consider, for example, a chemical attack warning system. Terrain and atmospheric conditions will affect both the movement and dispersion of a chemical release, and the ability of the wireless nodes to communicate with one another. An integrated simulation system makes it possible to investigate system issues such as the effect of terrain on battery life.

The development of the core competency has been guided by the requirements of two existing WSN programs at LLNL: the Joint Biological Remote

Early Warning System (JBREWS) and the Wireless Sensor project.

JBREWS will consist of 100 to 1000 biological sensor nodes, each capable of wireless communication with other sensor nodes or a central control node. The objective is to detect, track, and predict the movement of airborne biological agents. JBREWS is a multi-phase program, each phase based on newer, more sophisticated technology.

The performance of a JBREWS deployment will depend on sensor node placement, terrain, and atmospheric conditions. An overall system effectiveness is determined by obtaining performance criteria for widely varying deployment scenarios. Obtaining performance criteria for an actual deployment is expensive, and simulation offers a cost-effective alternative.

A primary concern of the JBREWS project is that the system be able to configure itself (**Fig. 1**) after sensor nodes have been randomly deployed, for example, by being air-dropped. In this case it is impossible to determine, *a priori*, what communication links between the nodes will be available. Once placed, each sensor node must be able to determine other sensor nodes that it can communicate with. Then, the sensor nodes, acting collectively, must configure themselves into a network. Several self-configuration algorithms were investigated.

JBREWS uses time-division multiple-access (TDMA) transport protocol as the basis for the communication channels. TDMA is characterized by a longer, though constant, latency when compared to other transport protocols. By eliminating the acknowledgment of successful data packet receipt, the latency will be reduced. The attendant reduction in reliability is dependent on the terrain and the exact placement of sensor nodes. Investigation of this issue by analytic means is not feasible.

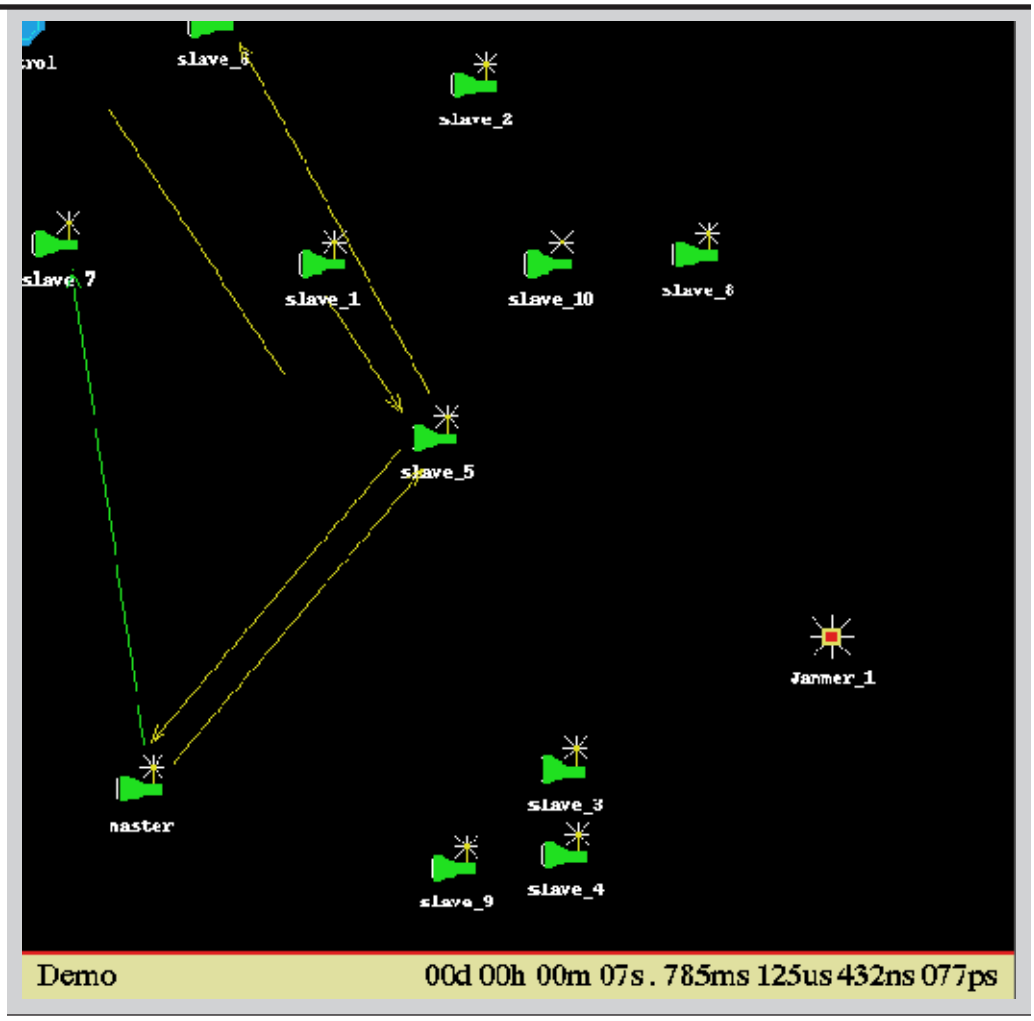

Figure 1. The JBREWS wireless sensor network configuring itself. The master node has determined that it cannot communicate with slave_1 and slave_6 (because of the obstruction). Therefore, it relies on slave_5 to relay data packets to slave_1 and slave_6.

However, simulation results have shown that the elimination of acknowledgment messages has had the unforeseen effect of reducing average latency, while increasing the variance in latency times.

The Wireless Sensor project is a joint project between LLNL's Microtechnology Center (MTC) and the University of California, Los Angeles (UCLA) to develop very low power wireless sensor nodes. The current focus of the project is on hardware development. In the next two or three years there will be opportunities to configure these nodes into systems for applications that are currently unknown. A simulation that accurately reflects current technology or technology being developed will provide the means to explore new applications.

The key issue that will drive the design of a system is the expected battery life (**Fig. 2**). This has a direct impact on system timing, because accurate clocks use more power than less accurate clocks. In turn, clock drift can degrade overall system performance by causing packet collisions and/or high latency times. The current simulation accurately reflects 1) the power cost of computing and communication operations, and 2) clock drift and system timing considerations.

In addition to work at LLNL, research at the University of California, Berkeley (UCB) on efficient multi-cast protocols was funded in FY-98. In many WSN applications there is a control node that will send directives to all sensor nodes. Typically, receipt of multi-cast packets is not acknowledged due to the network congestion that would occur when all sensor nodes acknowledge receipt at the same time. Without acknowledgment, totally reliable directive delivery is not possible, although it is possible to achieve some degree of reliability.

The research task undertaken by UCB was to develop methods to achieve high reliability with

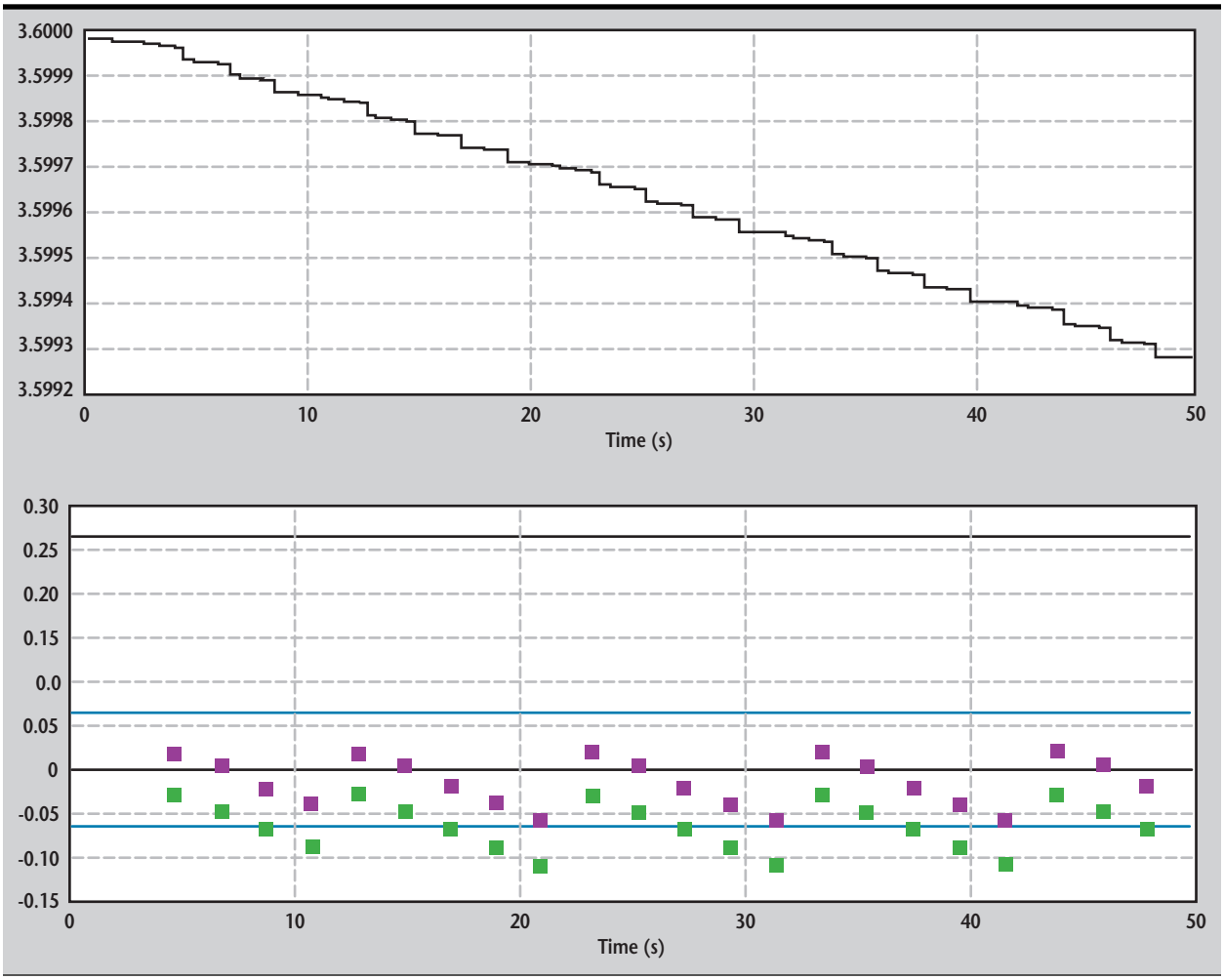

Figure 2. Battery level and packet arrival times. (a) The battery is being drained whenever the receiver is turned on or the transmitter is used to transmit a packet; (b) shows a window in time when the receiver is turned on, to acquire packets being sent to it. To save power the receiver is turned off outside this window. A clock drift is shown by the fact that packets arrive earlier and earlier until finally a packet arrival falls outside the window. At this point data packets are being lost until the system can re-sync itself.

non-acknowledged multi-cast protocols. Several multi-cast protocols were considered with the effectiveness of each being determined by modeling and simulation.

The result of this research is a "tunable" multi-cast protocol, that is, by specifying the degree of reliability, protocol parameters are selected that yield the desired reliability with the least overhead.[1,2]

Future Work

Thus far, we have used commercially available simulation systems for the basis of our work. The disadvantage of this approach is that the simulation kernel can not be modified for the purpose of 1) achieving tighter integration with existing simulations of physical systems; or 2) porting the simulation kernel to a massively parallel computer. In FY-99 we will develop the capability to construct simulation kernels that are specific to a particular application.

References

1. Wong, T., T. Henderson, S. Raman, and R. Katz (1998), "Exploiting Applications Level Framing in Reliable Multicast for Periodic Information Dissemination," Technical Final Report, University of California, Berkeley, August.

2. Wong, T., T. Henderson, S. Raman, A. Costello, and R. Katz (1998), "Policy-Based Tunable Reliable Multicast for Periodic Information Dissemination," Technical Final Report, University of California, Berkeley.

Information Warfare Analysis Capability

J. C. Smart
Electronics Engineering Technologies Division
Electronics Engineering

The Information Operations, Warfare, and Assurance initiative at Lawrence Livermore National Laboratory has advanced the enabling core technologies for information operations analysis. Special emphasis was placed on computer networks and telecommunications systems.

Introduction

With the rapid growth of global computing and communications, information security is a critical issue in all discussions of protection of the national infrastructure. The purpose of our project—the Information Operations, Warfare, and Assurance (IOWA) initiative—is to advance the enabling core technologies of this field.

Special emphasis was placed on computer networks and telecommunications systems.

Progress

During FY-98, we developed 1) techniques for identifying the topology of large, complex computer networks; 2) data representation models for these systems; 3) high-performance methods for visualizing the resulting complex models; 4) automated analysis methods for processing large-network representations; 5) specialized search techniques for isolating vulnerabilities; 6) a foundation for simulating network operation; and 7) an assessment methodology for determining the consequences of system component failure or disruption.

To automate information system protection, it is necessary to first identify the visible components that an intruder might attempt to access, and to determine the specific information that might be inferred about each component.

We began by developing a set of software modules for analyzing Internet-related protocols. This software examines the information that flows across a computer network and extracts network topology and details about the configuration of each component. At present, the tool suite processes over 20 popular Internet protocols, retrieving over 50 different system operating parameters.

Since modern computer networks have grown considerably in size (that is, more than 25,000 nodes), a special model was developed to capture the enormous amount of information that the tools process. The resulting model uses a unique blend of relational database technology integrated into a graphical theoretical framework, providing rapid information retrieval in an environment conducive to large-network mapping and analysis.

We demonstrated a platform-independent viewer for browsing the graphics model with integrated access to the relation database. To better manage the complexity of large networks, several powerful dependency constructs, graphics operations, and reduction functions were incorporated into the model. A diverse suite of generic graph-, fault-tree-, and Internet-specific processing algorithms was developed and demonstrated.

To better understand the nature of computer and network vulnerabilities, a taxonomy of known vulnerabilities was developed that forms the basis of our new vulnerability database. This database was subsequently populated with vulnerability facts from industry and private sources. The end result is a tool that can now be used to automate the search for weaknesses in our computer systems.

Working with the modeling tools, an environment was constructed to perform high-fidelity simulations of computer networks. The resulting tools can be used to simulate computer networks captured in the IOWA model. Arbitrary computer networks can also be constructed in the simulation environment and used to generate network traffic to test and calibrate the network mapping tools.

Raymond P. Mariella, Jr., Center Leader

The mission of the Microtechnology Center at Lawrence Livermore National Laboratory (LLNL) is to invent, develop, and apply microtechnologies in conjunction with programs in global security, global ecology, and bioscience.

Our capabilities cover materials, fabrication, devices, instruments, or systems that require microfabricated components, including micro-electromechanical systems (MEMS), electronics, photonics, microstructures, and microactuators. All of our microtechnology work revolves around our microfabrication facility, and is driven principally by the applications of our internal programs, and to a lesser extent, by external applications. For both of these we must have multidisciplinary teams to deliver complete solutions to the problems.

The Microtechnology Center continued to grow in FY-98. Its more than 60 people have training in electronics engineering, mechanical engineering, chemical engineering, chemistry, physics, and the biosciences. Our recent successes in analytical instrumentation reflect our broad, multidisciplinary base and the cross-fertilization that results from personnel sharing their capabilities and ideas with each other.

We continue to show a very high rate of return on investment. Over the last year, with a total budget of more than $15M, including approximately $0.6M of technology-base projects, we have successfully performed collaborations with industry, and have achieved considerable national recognition. We have had success in our on-going instrumentation project, developing both polymerase chain reaction (PCR) assays and instrumentation, supported by the Defense Intelligence Agency.

In January of 1998, we took our latest PCR instrument to the Joint Field Trials IV (JFT IV) in Dugway, Utah, for the open competition and demonstrated the highest sensitivity ever recorded there for detection of the plague simulant (*Erwinia herbicola*). Our microtechnology project on the fabrication of facets for GaN lasers has also shown excellent results.

As the applications for microtechnology grow, we continue to perform the technology-base activities that are needed to fulfill the needs of our LLNL and external partners and stay in a leadership position, both nationally and world-wide.

Overall, the numerous small investments in microtechnology have paid off this year in 1) outstanding results at JFT IV with the LLNL PCR instrument; 2) the highest performance hand-held gas chromatograph built, including microfabricated injector, column, and detector; 3) an LLNL electrophoresis system with etched/bonded plates containing 384 channels; 4) $1M in DARPA funding for dielectrophoresis technology; 5) a $1.7M CRADA: a medical catheter device to release embolic coils into cerebral aneurysms that uses laser light for release and detection; 6) projects for optical interconnects in partnership with the Photonics Program, resulting in significant demonstration of multiple-wavelengths carried per fiber; 7) highly visible multi-million-dollar CRADA with semiconductor businesses for EUV lithography; and 8) collaboration with the University of California, Santa Barbara, on high-performance laser facets for GaN and demonstration of an advanced process in laser-based doping of GaN.

Center for Microtechnology

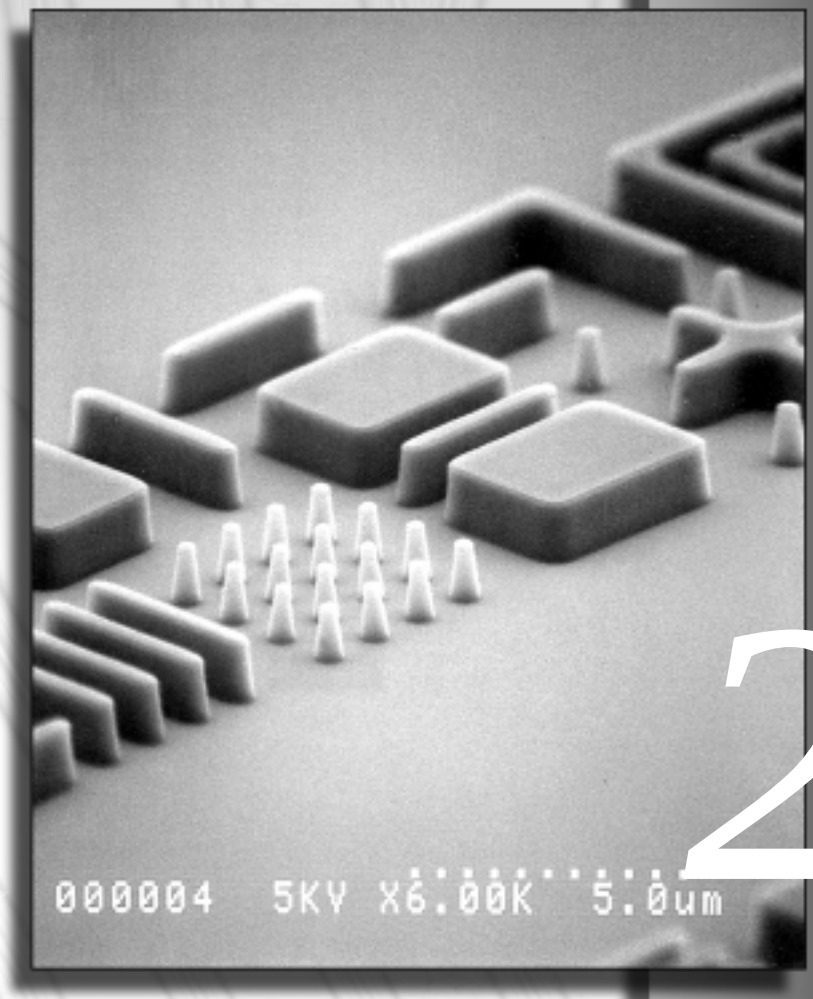

2

2. Center for Microtechnology

Overview
Raymond P. Mariella, Jr., Center Leader

Disposable Microfluidic Biological Sample Preparation System
Robin R. Miles, Daniel L. Schumann, Kelye A. Allen, Jim A. Butler, and Kerry A. Bettencourt 2-1

Sub-Micron Lithography with a 5X Stepper
Dino R. Ciarlo and Benjamin P. Law 2-5

Advanced Packaging for Wireless Microsensor Modules
Abraham P. Lee, Charles F. McConaghy, Jimmy C. Trevino, Leslie M. Jones, and Jonathan Simon.....2-7

Radio Frequency Technology for Wireless Microsensor Modules
Charles F. McConaghy, Abraham P. Lee, Charles Chien, Chris Deng, and Igor Elgorria 2-11

Ultra-High-Speed Analog-to-Digital Conversion Technology
Mark E. Lowry, Ronald E. Haigh, and Charles F. McConaghy 2-13

HV Photovoltaics
Karla G. Hagans and Ronald E. Haigh.....2-17

Lattice Boltzmann Simulation of Complex Fluid Flows
David S. Clague 2-19

Micro-Electromechanical Systems (MEMS) for Characterization of Plastic-Bonded Explosives
Jeffrey D. Morse, Dino R. Ciarlo, Scott E. Groves, Diane J. Chinn, Mehdi Balooch, and Mark J. LaChappel.....2-23

Micro-Electromechanical-Systems-(MEMS)-Based Fuel Cell Technology
Jeffrey D. Morse, Robert T. Graff, Alan F. Jankowski, and Jeffrey P. Hayes 2-27

High-Power GaN Microwave Device Technology
Glenn A. Meyer, Gregory A. Cooper, Stacy L. Lehew, Thomas W. Sigmon, Daniel Toet, Steven DenBaars, and Umesh Mishra 2-31

Glass Etching
Harold Ackler and Stefan P. Swierkowski.....2-37

Micro-Electromechanical Systems Foundry Interface
Michael D. Pocha 2-41

A Hydrogel-Actuated Implantable Sensor
Amy W. Wang, Abraham P. Lee, Charles F. McConaghy, Christopher B. Darrow, Aleksandr Gilman, Stephen M. Lane, and Joe H. Satcher, Jr. 2-45

Lambda Connect: Multi-Wavelength Technologies for Ultrascale Computing
Robert J. Deri, Michael C. Larson, Michael D. Pocha, and Mark E. Lowry.....2-49

Disposable Microfluidic Biological Sample Preparation System

Robin R. Miles
Electronics Engineering Technologies Division
Electronics Engineering

Daniel L. Schumann, Kelye A. Allen, and Jim A. Butler
Manufacturing and Materials Engineering Division
Mechanical Engineering

Kerry A. Bettencourt
Materials Science and Technology Division
Chemistry and Materials Science

We have fabricated plastic microfluidic devices to provide an inexpensive flow path for biological applications. External actuation was used for valving, pumping, and mixing functions. The advantages to this system over alternative microfluidic approaches are that it provides isolation of the biological material from actuators, reduces material compatibility concerns and system cost, and minimizes dead volume.

Introduction

The purpose of this project was to develop a microfluidic circuit based on thin film plastic. Fluidic channels and plenums were formed using thin film plastic such that they could be manipulated externally to provide valving, pumping, and mixing functions, as shown in **Fig. 1**. The device can be used in either a disposable or a semi-fixed system.

The chief advantage to such a system is that it provides isolation of the biological fluid from the actuation device. Low-power actuators, such as piezoelectric or electrostatic actuators, are generally incompatible with fluid environments. High-work actuators, such as thermal actuators, require significant increases in power when in contact with fluids.

Other advantages to this system over alternative microfluidic approaches include the use of a single material to reduce material compatibility concerns, reduce system cost, and minimize dead volume.

Progress

The primary focus of this effort was to develop a fabrication process for defining and sealing the plastic sheets. A second effort was to develop an external pneumatic actuator for the system to provide valving, pumping, and mixing operations.

Forming the Plastic Sheet

Forming and bonding the plastic sheets proved to be a difficult task. Our technique for manufacturing the plastic device was to first pre-form the cavities on each half of the structure, then bond the two halves together to make the final structure. We developed several techniques to form the plastic structure including heat-staking, laser welding, and molding. Stiff plastics such as polypropylene and polyethylene were first embossed to define the tubing and plenum areas of the structure, then laser welded to a second sheet of plastic to complete the structure. Elastomeric materials such as metallocene and silicone were molded or heat-staked.

Thermal Heat-Staking. Several outside vendors were contacted to provide heat-staking fixtures for fabricating the plastic structures. One vendor built a fixture for bonding pre-embossed polypropylene sheets. Unfortunately, their fabrication technique proved unsuccessful as they melted the entire plastic structure into one big lump. A second vendor successfully bonded two sheets of metallocene in

the desired configuration to provide for the desired internal tubes and plenums. The bonds were capable of withstanding 10 psi internal pressure.

Laser Welding. A CO_2 laser was used successfully to thermally weld the two halves of the plastic structure. **Figure 2** shows devices that were bonded together using this technique. Maintaining intimate contact between the plastic sheets was the primary challenge for laser welding these structures. For flat sheets, we used a vacuum platform to suction the work together and cut the top sheet larger than the bottom sheet. For embossed sections, we made nesting fixtures out of acrylic. We adjusted the height and spread of the beam to get reasonable welds. We were able to produce welds which held to internal pressures of 15 psi. However, we were not able to get within 0.02 in. of the edge of the raised embossed plastic because the two plastic films could not be reliably held together near that interface. Also, we could only weld a flat sheet with one embossed side, or two sheets that were embossed simultaneously and in the same direction. Later welds performed for a PCR sample preparation system were not leak-free due to the difficulty of controlling the very low energy density level of the available laser.

Silicone Molding. We turned to silicone for this application because of the increased manufacturability of the structures and the higher probability for obtaining good valve shut-off. We used etched silicon wafers to form molds into which we poured a two part, heat-cured silicone. We used both Sylgard 184 and Sylgard 186. We used two mirror-imaged molds

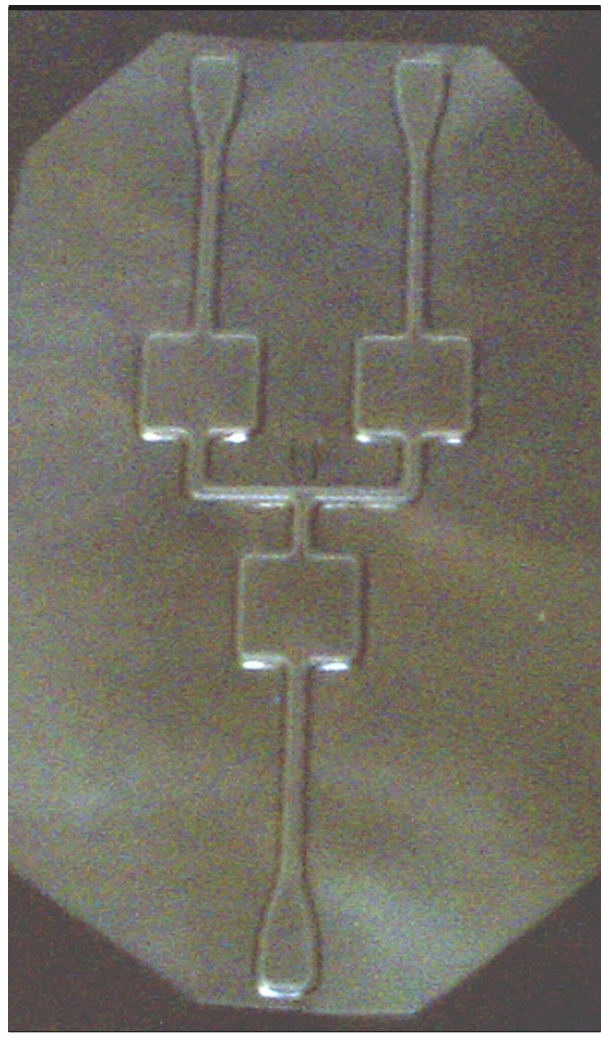

Figure 2. Embossed and laser-welded plastic sheet.

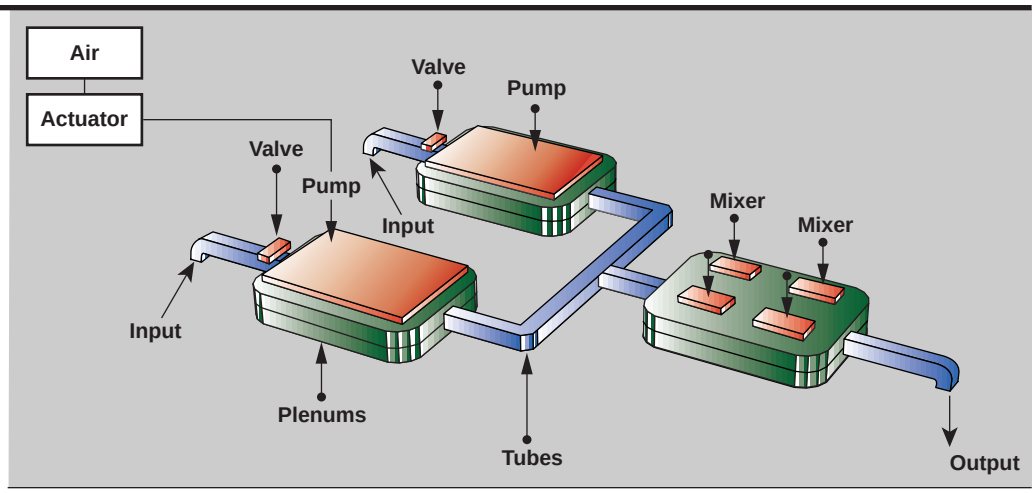

Figure 1. Formed plastic structure with external actuation.

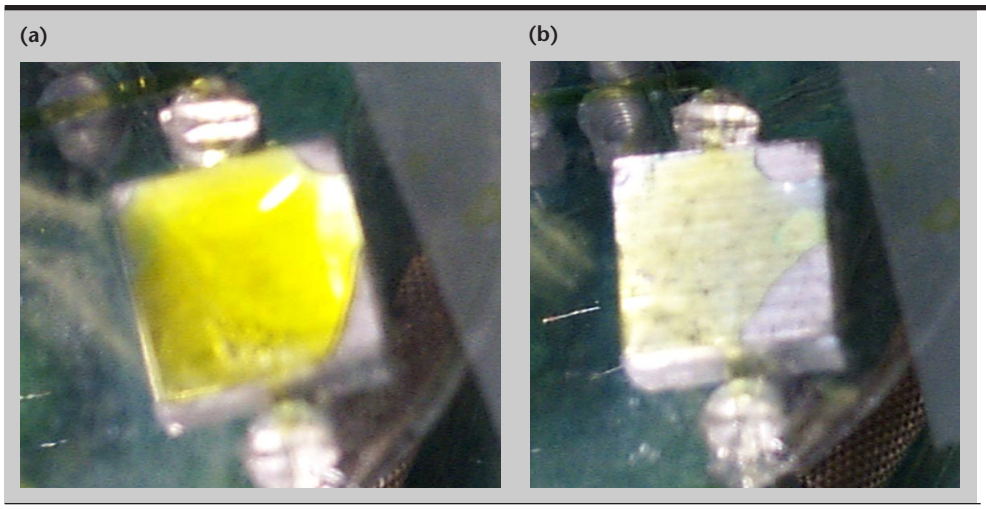

Figure 3. Pumping actuation on silicone chamber using pneumatic cylinder actuator.

to form two halves of the final structure. We cured these halves, removed them from the mold, then painted on an additional amount of the silicone to act as a glue between the two halves. Thus, the entire mold is made from just one material.

The Sylgard 186 is tougher, more tear-resistant, and has better adhesion than the Sylgard 184, but is much more viscous and sticks to the mold too well and is, therefore, difficult to use. However, we were able to make devices that could withstand a 35-psi internal pressure before delamination of the layers occurred.

Interconnects. Interconnecting the device to the outside world proved difficult. For the flat sheets, we designed a flared section that could be mated to a standard leur fitting. However, these leaked a little when used directly and needed sealant to hold. For the silicone structures, we used the silicone as the sealant for tubes that were inserted into the molded device. The best results were obtained using PEEK tubing, and acceptable results with silicone tubing. Tygon tubing tended to harden up and tear the molded device. Good surface preparation of the tubing was required for a good seal.

Pneumatic Actuation

Pneumatic actuation was used to provide the valving, pumping, and mixing functions of the fluidic circuit. One method of providing pneumatic actuation was to use silicone-molded buttons that were held in an aluminum clamped fixture, which created a silicone membrane that could be distended using air driven through standard pneumatic fittings. The silicone rubber was very flexible, and this method worked well, particularly for pumping.

The smaller buttons used for valving required a higher pressure. We found that complete shut-off of the flow required a channel depth on the order of 100 mm for the silicone molded devices, and zero gap for the welded plastic sheet. A second method for providing pneumatic actuation is to use off-the-shelf pneumatic cylinders attached to an aluminum plate for providing force against the plastic structure. Pumping and mixing can be accomplished using pneumatic cylinders. Additional force for valving was obtained by replacing the aluminum plate at the end of the pneumatic cylinder with a 0.010-in.-wide shim.

We found that we could also spin Sylgard 184 over silicon nitride windows formed by etching a silicon wafer to make silicone membrane actuators that may be more compatible with micromachined devices. The silicon nitride could be removed by a post-cure dry etch.

System Results

We were able to demonstrate the functions of pumping, valving, and mixing using these devices. Pumping is shown in **Fig. 3**. The fluid is forced from the silicone chamber using an external pneumatic plunger.

Future Work

We are using this technology in two other applications, a sample preparation system for the autonomous point detector program, and a hand-held PCR system. The heat-staked metallocene structures are the most cost-effective structures and will serve as the basis for the applications of this technology. We are working to replace the pneumatic actuators with low-power piezoelectric actuators and manually driven cam devices to make this device more attractive for portable applications.

Sub-Micron Lithography with a 5X Stepper

Dino R. Ciarlo and Benjamin P. Law
Electronics Engineering Technologies Division
Electronics Engineering

This year we installed a lithography system capable of printing sub-micron features onto silicon wafers. The system is a refurbished GCA DSW, Model 8500, which is an i-line system (365 nm), capable of printing 0.7-µm features anywhere within a 16-mm field of view. This system is now operational in the Microtechnology Center (MTC) at the Lawrence Livermore National Laboratory (LLNL).

Introduction

We continue to get requests for lithography with feature sizes <2 µm. From time to time, there are even requests for sub-micron images. The existing remote wireless sensors and adaptive optics projects are designing devices based on 2-µm rules, while the giant magneto-resistive (GMR) sensor project uses sub-micron features. In addition, we get requests for Fresnel zone plates and pinhole arrays with sub-micron feature sizes.

The contact printers in LLNL's MTC can be used down to 2 µm, with increasing difficulty because of diffraction effects. A new state-of-the-art projection lithography system with sub-micron printing capability can cost more than $5M. Fortunately, there is an industry dealing in used, refurbished equipment with adequate capability. We accepted delivery of a GCA DSW Model 8500 in January 1998. It is now operational in the MTC. The system is ten years old, cost $255K, and has been refurbished to perform to its original specifications, which allows the printing of 0.7-µm features.

Progress

We spent several months working with the vendor to install and learn to operate this system. It is a 5X reduction system, which means the photomasks need to be designed at five times the size of the features to be printed on the silicon wafer. The reduction lens is referred to as a T1635P, which means it has a 16-mm circular field of view with a numerical aperture of 0.35. This allows the printing of 0.7-µm features in 1-µm-thick resist, anywhere within the 16-mm field of view. The illumination source is a 1000-W mercury lamp which provides i-line illumination (365 nm). Typical exposure times for 1-µm-thick resist is 0.5 s. The system has its own environmental control chamber and atmospheric control system (ACS) to regulate temperature, pressure, and humidity.

This system has many automated features that are used to optimize its performance. For example:

1. RMS—Reticle Management System, used to select from 10 reticle stores in a rack. Each reticle is labeled with a bar code.
2. AWH—Automatic Wafer Handler, automatically loads and unloads 100-mm-diameter silicon wafers from cassette holders.
3. AFII—Autofocus System, automatically maintains best focus as the wafer is stepped from die to die.
4. AWA—Automatic Wafer Alignment, does the initial global alignment of the reticle to the wafer.
5. DFAS—Dark Field Alignment System, used for the final die-by-die alignment of the reticle to the wafer. Initial alignment is accomplished by a laser interferometer-controlled x-y stage. Final alignment is better than ±0.15 µm.

To properly use the automatic sub-systems, the main system must first be set up to be within their "capture" range. This is done during initialization of the system. The initialization parameters are stored in the MODE program for system operation.

Also, special targets need to be placed on the reticles for these automatic sub-systems to operate. For example, the AWA and DFAS sub-systems both need special targets to be placed on the reticles, in the proper position.

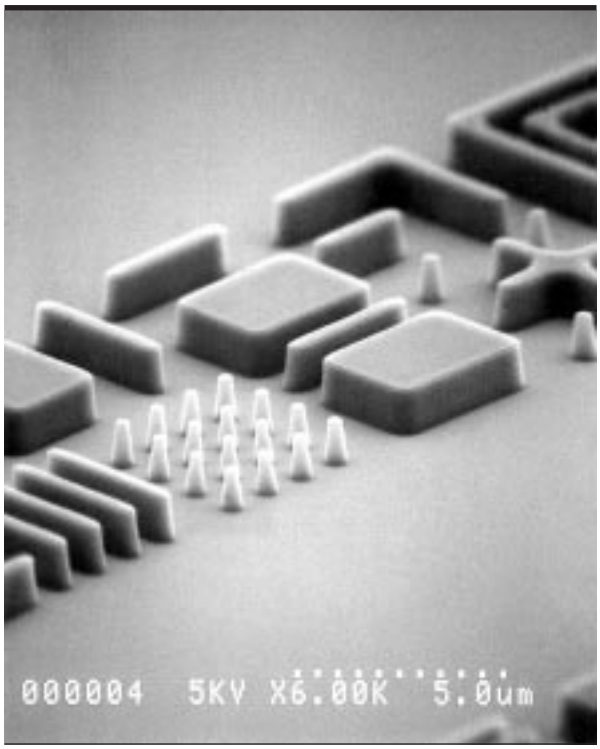

Figure 1. SEM image of features printed in 1-μm-thick positive resist. The small pedestals have a diameter of 0.5 μm.

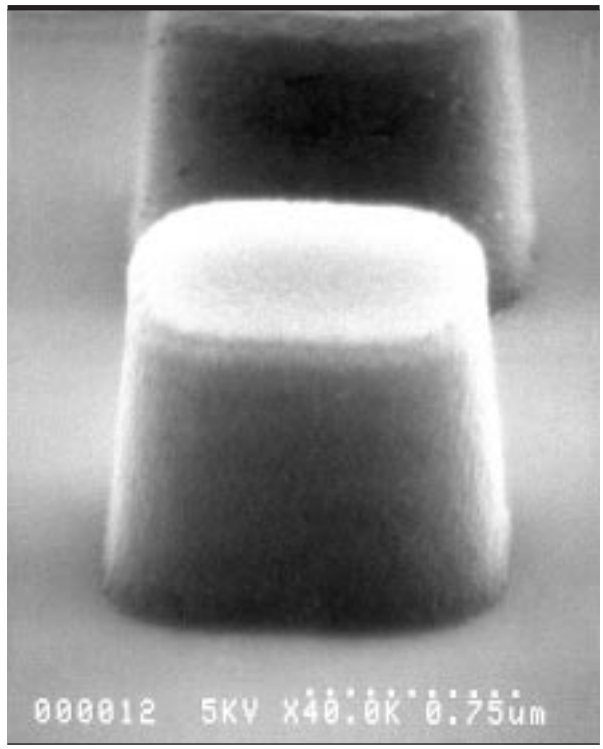

Figure 2. SEM image of a square resist pedestal. Resist thickness is 1 μm. Area of pedestal is 1.4 μm by 1.4 μm.

Figures 1 and **2** show SEMs of resist images printed in 1-μm-thick JSR 500 positive resist. The smallest pedestals in **Fig. 1** have a diameter of 0.5 μm. In **Fig. 2** are pedestals with lateral features of 1.4 μm by 1.4 μm. The sidewalls are nearly vertical.

Future Work

This 5X reduction system is now being used for several LLNL projects. We continue to learn how to operate the system and are becoming more comfortable with its capabilities. The system is optimized to use 100-mm-diameter silicon wafers that are 500 μm thick. We recently had a project that is using 100-mm-diameter wafers only 375 μm thick. This required a rather difficult manual adjustment of the optical column to focus onto the thinner wafers. Most likely, we will be getting other requests to print on "non-standard" substrates. The computer that controls the system is rather dated and is not very user-friendly, but we are learning.

Finally, there are now only three members of the MTC trained to operate this system, but we expect to add two to three more to this list of operators in the future.

Advanced Packaging for Wireless Microsensor Modules

Abraham P. Lee, Charles F. McConaghy, Jimmy C. Trevino, and Leslie M. Jones
Electronics Engineering Technologies Division
Electronics Engineering

Jonathan Simon
New Technologies Engineering Division
Mechanical Engineering

We have developed packaging technologies to integrate the components of wireless sensing modules such as MEMS microsensors, sensor electronics, modems, RF transceivers, and RF electronics, all of which may ultimately be on individual dies.

Introduction

A wireless microsensor module consists of four basic parts:

1. sensor—could be a low-g (µg) accelerometer. The sensor makes use of both bulk and surface micromachining.
2. interface electronics—to convert the signal from the sensor to a usable voltage. The interface electronics drive an A/D converter, which in turn interfaces to the modem.
3. modem electronics—the electronics that take care of some portion of the protocol, as well as producing the spread spectrum codes to drive (transmit data) or decode (receive data) the RF portion of the module.
4. RF section—the mixers, oscillators, amplifiers, and antenna switch. This section is the interface between the modem and the antenna.

To integrate these dissimilarly processed parts into a compact form factor, it is necessary to develop advanced packaging processes. We have chosen a microaccelerometer sensor to demonstrate a wireless module and establish the integration technologies.

The next generation of defense and intelligence activities requires covert large-area sensing networks for extended periods of time (one month to one year). Current micro-electromechanical systems (MEMS) technologies can enable only a point detection device without communications between multiple nodes. Wireless technologies are not self-sufficient without physical transduction capabilities through MEMS. The combination of the two is of limited use if it isn't covert, or close to covert. Although there are many microsensors being developed commercially and in academia, none are integrable with wireless communications platforms to enable network sensing.

The challenge lies in the integration of different chips in a compact form, which requires techniques to ensure compatibility of process and signal interfaces. The engineering capabilities supporting the Microtechnology Center (MTC) at Lawrence Livermore National Laboratory (LLNL) have interdisciplinary expertise in 1) MEMS-based microsensor design; 2) MEMS electronics packaging; 3) MEMS electronics sensing design, deep reactive ion etching (DRIE) capability (a key to integrating micromachining technologies in a compact form); and 4) programmatic applications requiring a systems approach and allowing the generation of a standard protocol.

Integration of the numerous parts of the module will be designed from the systems level to ensure miniaturization, compatibility in electronic interconnect and compatibility in different processing sequences.

Most other researchers are working on singular aspects of the problem, such as the wireless and MEMS technologies. Challenges to combine the state of the art in MEMS and wireless communications is a unique opportunity, bringing together expertise in electronics and mechanical engineering, chemistry and materials science, and nonproliferation control.

The technology developed by this project will directly enhance core competencies in the MTC since it will enable the integration of micromachining technologies for many applications.

While there are many researchers in the field, LLNL can distinguish itself as the leader in technology integration with advanced packaging of wireless components, large quantity sensor networks, and advanced MEMS electronics packaging. It also allows the opportunity for LLNL to set the standards and protocols for wireless microsensor modules and networks.

For the remote sensing needs that are increasingly important in this post-cold-war era, this project could have a significant effect on monitoring treaties and combatting urban warfare. It affects the capability to maintain world peace and national security. The State of California could benefit from border control technologies developed from this project. This project is in direct alignment with LLNL's mission of global security.

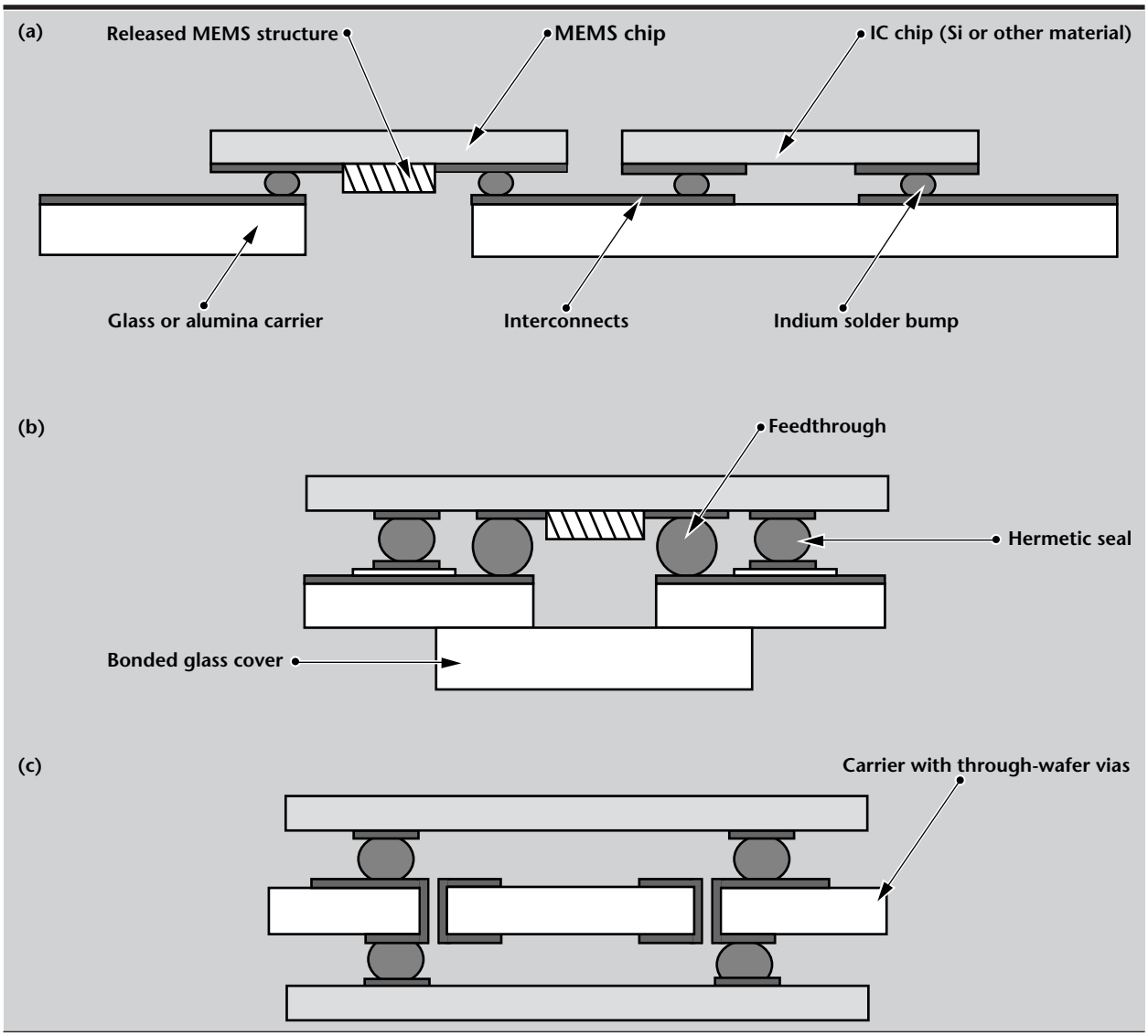

Figure 1. MEMS-integrated MCM packaging scheme.

Progress

Integration of Wireless Microsensor Module

We have developed packaging technologies to integrate the components of wireless sensing modules such as MEMS microsensors, sensor electronics, modems, RF transceivers, and RF electronics, all of which may ultimately be on individual dies.

There are several important constraints to the design:

1. Chips may be fabricated from different materials and processes, such as Si and GaAs.
2. Chips may be of largely varying size from 2 mm × 2 mm, to 1 cm × 1 cm.
3. MEMS sensors may require vacuum, fluid, or gas environments.
4. Post-processing of the chips should be minimal.
5. The approach is flexible.

We have opted for a Flip-Chip Multi-Chip Module (MCM) approach. In such a design, the individual chips are flipped over and bonded to a carrier, rather than interconnected using wire bonds. The hybrid package can then be further encapsulated or repackaged as necessary.

Figure 1a shows a glass (fused silica or Corning 7740) or alumina carrier with patterned interconnects and electro-deposited indium solder bumps. All the processing is done on the carrier wafer to ensure compatibility and minimize the handling of the various dies.

A variety of chips can then be flip-chip-bonded to the carrier. In this case, a recess for the MEMS device has been milled into the carrier. This recess can serve as an attachment point for fluid or gas interconnects, or as in **Fig. 1b**, the indium may also be used to seal the MEMS die into a vacuum reservoir or other filled reservoir.

In the case of extremely space-constrained systems, addition of through-wafer vias (**Fig. 1c**) to the carrier effectively doubles the packaging density.

A fabrication process flow for a carrier wafer with no vias is shown in **Fig. 2**. A carrier wafer of glass (fused silica or Corning 7740) is coated with a metal seed layer of 500 Å Ni/2000 Å Au/100 Å Ti. The gold acts as the primary conductor, while the titanium acts as an adhesion layer, and the nickel acts as a barrier to keep the plated indium from diffusing into the gold.

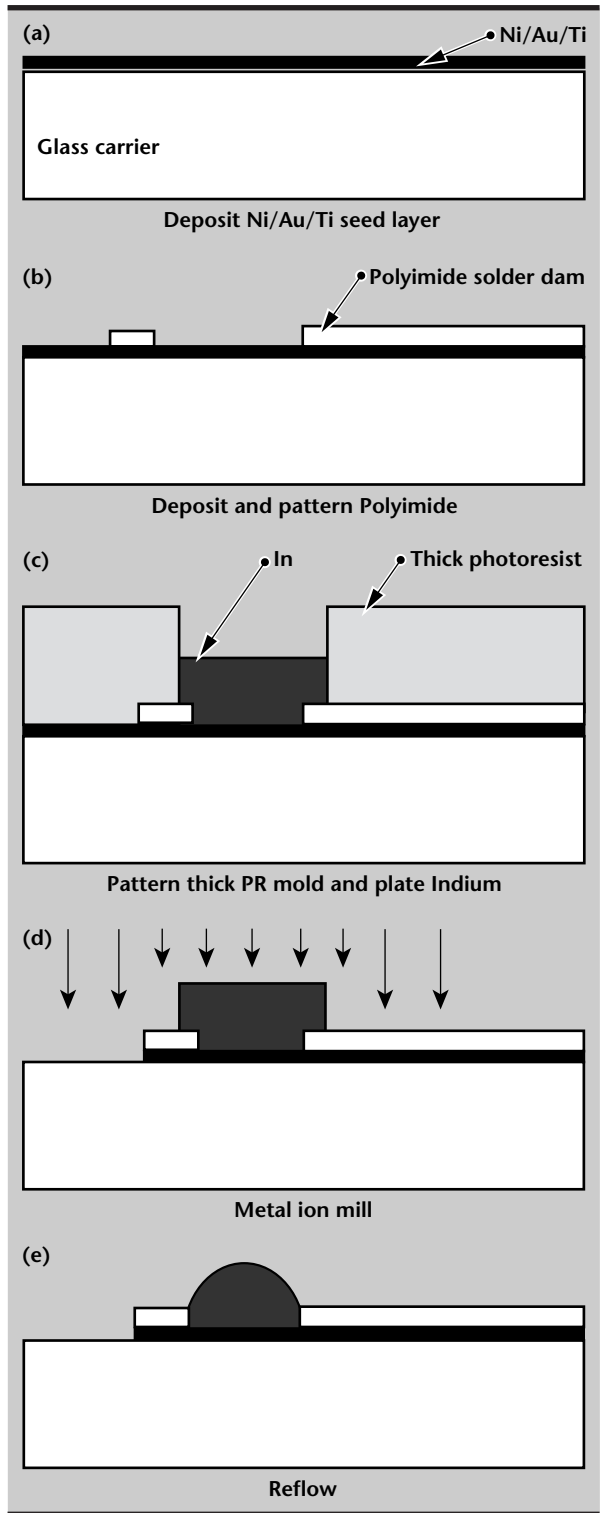

Figure 2. Process flow for carrier wafer traces and indium solder bumps.

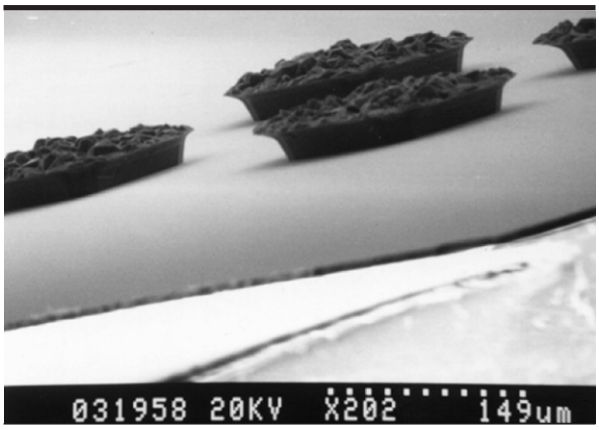

Figure 3. SEM of ~35-mm-tall electroplated indium bumps before reflow.

In the first mask step, a polyimide layer is patterned which will be used both as a solder dam for the indium and to define the traces. In the second mask step, a thick photoresist is spun onto the wafer and patterned to make a mold for indium plating.

After indium plating (~50 μm), the photoresist is stripped, and the parts are ion-milled to pattern the traces. The indium is then reflowed in an inert environment to form uniform bumps. **Figure 3** shows 35-μm-tall indium bumps before reflow.

Radio Frequency (RF) Technology for Wireless Microsensor Modules

Charles F. McConaghy and Abraham P. Lee
Electronics Engineering Technologies Division
Electronics Engineering

Charles Chien, Chris Deng, and Igor Elgorria
University of California, Los Angeles

We have developed a small, low-power RF link for connecting sensors to a central node. The link is in the 900-MHz ISM band and uses spread spectrum technology, as well as time division multiple access, to accommodate multiple sensor modules. This was a joint project with researchers at the University of California, Los Angeles (UCLA). The modem and RF technology developed at UCLA is being incorporated into a Lawrence Livermore National Laboratory wireless sensor package.

Introduction

Networks of low-power wireless sensors are envisioned to accommodate future sensor needs in the field. Such packages should not only include sensors, such as a seismic or bio-sensor, but also the means to transmit this information to some distant monitoring point. These sensors should be very low power and small in both size and weight to allow for ease in deployment. The communication distance of any module is about 30 to 100 m, and the RF power is 1 mW. However, networks of these modules can be assembled to cover much longer distances. The module being constructed this year is a cube 2 in. on a side. The RF components occupy about one third of the volume, the batteries and sensor occupy the remaining volume.

Progress

The RF section consists of a modem which is used to both modulate and demodulate the digital data onto and from a 900-MHz RF carrier that has been implemented with a field-programmable gate array (FPGA). In addition, on the sensor end of the RF link, the modem is also used to read the A/D converter that digitizes the sensor output. An additional operation of the FPGA is the superposition of a pseudo-random code on the data at transmit, and the removal of this code upon reception. Besides the modem, the necessary RF circuits, which either up-convert on transmission or down-convert on reception, the modem signals have been implemented on a pc board that is 2 in. square. These circuits were designed and built during FY-98.

A time division protocol has also been implemented which allows each sensor module to completely power its RF circuitry off except when needed. In low-power applications, even the receiver can cause a significant battery drain. The time division protocol allows each sensor module to power up its RF circuitry for 260 ms and then be off for about 2 s to save power. There is a sophisticated resynchronization process that occurs periodically to keep the clocks in the sensor module in sync with the base station that is interrogating the modules.

Future Work

Future work requires that we make even smaller and lower power RF circuitry, such that smaller batteries can be used for longer periods of deployment. In addition, the overall sensor module needs to fit a package that is about one cubic inch in volume, which means that the RF circuitry needs to be decreased in size. This will be achieved by using applications-specific integrated circuits (ASICs) rather than FPGAs, and RF chips with more functionality per unit of volume.

Ultra-High-Speed Analog-to-Digital Conversion Technology

Mark E. Lowry
Physics and Space Technology

Ronald E. Haigh
Defense Sciences Engineering Division
Electronics Engineering

Charles F. McConaghy
Electronics Engineering Technologies Division
Electronics Engineering

We have evaluated competing photonic approaches to the problem of high-speed analog-to-digital conversion (ADC). Our study of the existing literature has led to a novel technology that will enable extremely high-fidelity ADCs for a variety of national security missions. High-speed (>10 Gigasamples/s), high-precision (>10 bits) ADC technology requires extremely short aperture times (~1 ps) with very low jitter requirements (<10 fs). These fundamental requirements, along with other technological barriers, are difficult to realize with electronics.

We have conceived a multi-wavelength approach that uses a novel optoelectronic soliton. Our approach uses an optoelectronic feedback scheme with high optical Q to produce an optical pulse train with ultra-low jitter (<5 fs) and high amplitude stability ($<10^{-10}$). This approach requires low power and can be integrated into an optoelectronic integrated circuit to minimize the size.

Introduction

Many national security missions, particularly those that are intelligence community-related, involve the application of advanced communication, instrumentation, radar, sensor, and electronic warfare systems. These all rely on ADCs to digitize a large information bandwidth (GHz) with high dynamic range and precision. However, the performance of state-of-the-art ADCs has progressed rather slowly—about 1-bit improvement, or doubling in sampling speed every six to eight years. This can, to a large extent, be attributed to the limitations of the available semiconductor technologies in terms of device matching, device operating frequencies, and noise and nonlinearity in active devices.

To obtain a quantum leap in performance beyond that of current electronic ADCs, we propose to develop the enabling technology for a class of photonic ADC architectures based on advanced optoelectronic technology. With the unique ultra-high frequency capability of advanced optoelectronic components, the proposed class of photonic ADCs will simultaneously attain high sampling rates and large dynamic ranges. These photonic ADCs, along with advanced sensor technology, will allow measurement of physical phenomena of nearly every type with unmatched speed and accuracy. For applications that require high precision, but not necessarily fast sample rates, photonic ADCs will enable oversampling at unmatched sample rates to enable ultra-high precision sigma-delta ADC architectures which trade-off sample rate for precision.

Progress

Our conceived ADC photonic architecture (**Fig. 1**) uses a multi-wavelength ultra-short laser pulse train and a Mach-Zehnder modulator to sample a broadband signal of interest (**Fig. 1**, RF signal in). The sampled signal is temporally demultiplexed through a wavelength division multiplexer to an array of photodetectors where the outputs can then be digitized by a time interleaved array of slower-speed

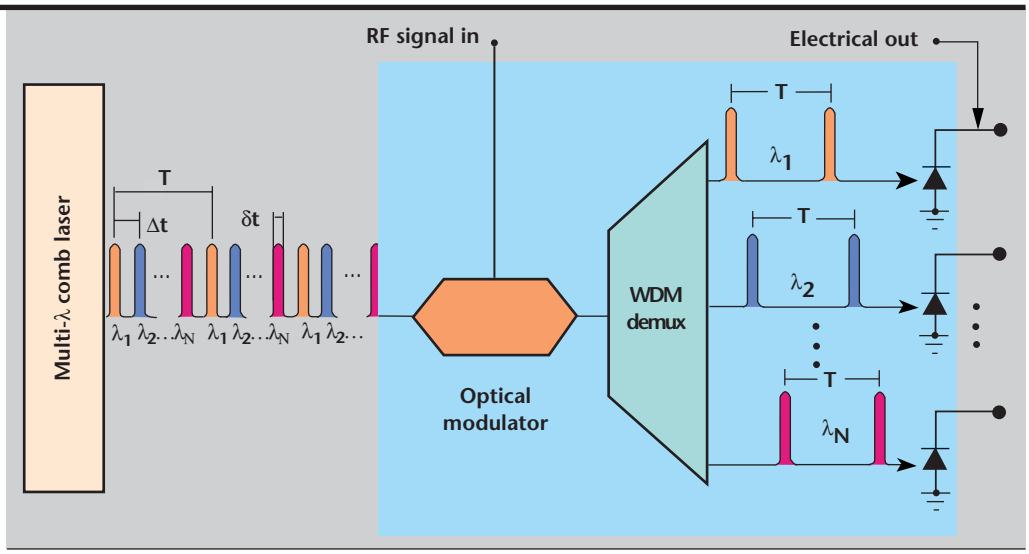

Figure 1. Optical Sampler/demultiplexer photonic front-end building block.

electronic ADCs. We have also envisaged more complex photonic ADC architectures. All require the proposed optical source to sample a signal of interest.

The multi-wavelength comb laser is realized with a novel externally modulated coupled-cavity Fabry-Perot interferometer with optoelectronic feedback (**Fig. 2**). Here the RF input driving the phase modulator will periodically sweep the optical pass-band through the cw wavelengths, simultaneously pulse modulating each wavelength and providing the appropriate temporal spacing for each wavelength in the resulting comb.

A portion of the optical output signal is routed through a fiber delay line back to the phase modulator input, thus, creating a high Q optical feedback circuit. The signal is then bandpass-filtered optically to select only one wavelength of the multi-spectral pulses for detection. The detected signal is band-pass-filtered electrically to eliminate harmonics, and amplified with a low-noise narrowband RF amplifier prior to driving the phase modulator.

The laser source will generate an optical pulse train with pulse widths between 1 and 10 ps and a jitter of 1 to 10 fs. We expect to realize a low-jitter optical pulse train with less than 5 fs of jitter over at least a 1-ms integration window using this approach. This jitter specification is at least an order magnitude improvement over state-of-the-art mode-locked feedback loop semiconductor and fiber lasers. These lasers have relatively large pulse jitter because of the amplified spontaneous emission (ASE) noise present in the lasers.

Because we modulate external to the gain medium, and in the absence of ASE, the timing jitter of our source will be governed exclusively by the effective Q of the optoelectronic circuit and the noise of the RF amplifier driving the external phase modulator. The long term stability will be governed by the mechanical and temperature stability of the electro-optic Fabry-Perot cavity and the fiber feedback loop.

The multi-wavelength nature of the optical pulse train is required to temporally demultiplex the optically sampled signal. The Fabry-Perot cavity can be simultaneously seeded with lasers of different wavelengths resulting in a multi-wavelength pulse train. Our approach synthesizes the generation of the required ultra-short pulses from an array of continuous wave lasers. Optical pulses with pulsewidths as short as 660 fs have been demonstrated using electro-optic synthesis.

Recent Accomplishments

Our accomplishments in FY-98 included the following:

1. Several classes of photonic ADC architectures have been conceived. These architectures have many common features including the notion of sampling a signal with a multi-wavelength optical pulse train to allow the signal to be demultiplexed spectrally.
2. A novel multi-wavelength optoelectronic sampling source has been envisioned. The source develops ultra-short optical pulses using external phase modulation in a Fabry-Perot cavity. This approach enables optical pulse trains to be generated with ultra-low jitter characteristics along with high amplitude stability.
3. A mid-year proposal was funded, based on these ideas. Some experimental results have been obtained.

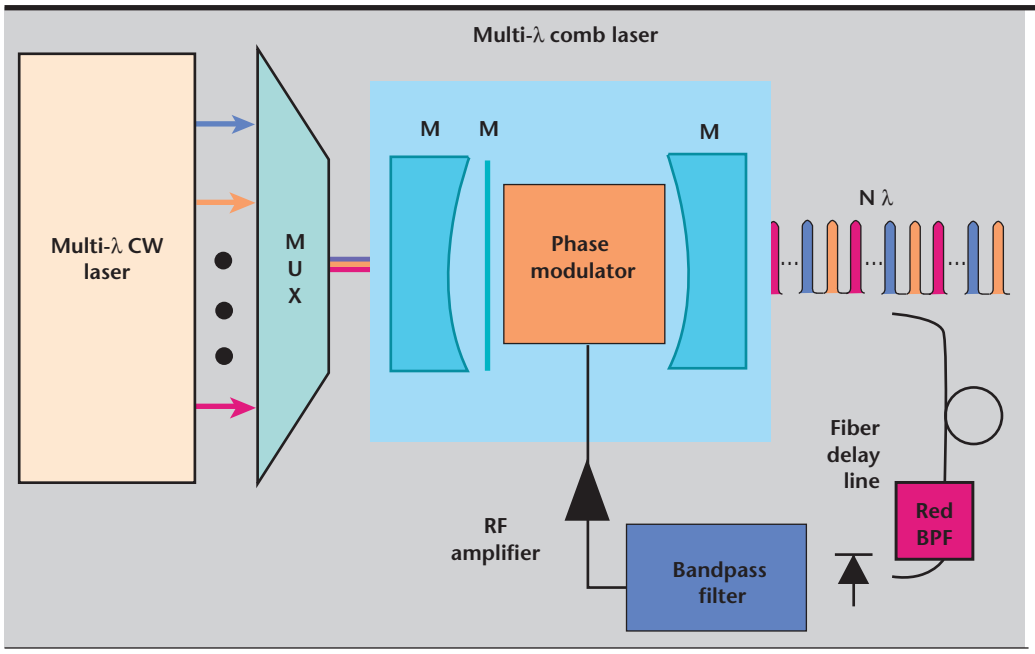

Figure 2. Coupled cavity multi-wavelength comb source with high-Q opto-electronic feedback.

4. A proposal to continue the development of this work with an external sponsor has been developed.

Finally, other applications for the proposed source have been considered, including 1) synthesis of optical sidebands with precise frequency separation for optical spectroscopy; and 2) wavelength encoding schemes for ultra-high (100 fs) temporal resolution of transient events.

Future Work

It is anticipated that this effort has a high probability of securing funding in FY-99 and is synergistic with other high-speed instrumentation projects at Lawrence Livermore National Laboratory including FemtoScope, RadSensor, and Photonic Doppler Velocimetry.

High-Voltage Photovoltaics

Karla G. Hagans and Ronald E. Haigh
Defense Sciences Engineering Division
Electronics Engineering

This technology-base project is a continuation of research to develop photovoltaic technology to generate voltages up to several kilovolts for powering electrically isolated systems with a fiber optic laser source.

Progress

This year, we undertook a development effort to successfully demonstrate kilovolt potentials in an electrically isolated manner using photovoltaics and a fiber optic laser source.

In FY-97, our research and development led us to investigate approaches to reducing the photons absorbed in the semi-insulating substrate between adjacent cells. These photons induce photoconductive current between the devices, which tends to shunt the cells. By depositing an absorptive or reflective material on the semi-insulating substrate regions of the device, we could successfully shield the substrate from photons and eliminate the photoconductive current in the substrate.

We designed prototype photovoltaic linear arrays, including the epitaxial structure of the devices, tested the functional, monolithically-integrated 90-V photocells, and evaluated techniques to stack these photocells to generate multiple kilovolts of potential in a compact area. We successfully demonstrated a 1260-V photocell by dicing the individual 90-V photocells and wirebonding fourteen of them in series on a glass substrate.

The photocell is shown in **Fig. 1**.

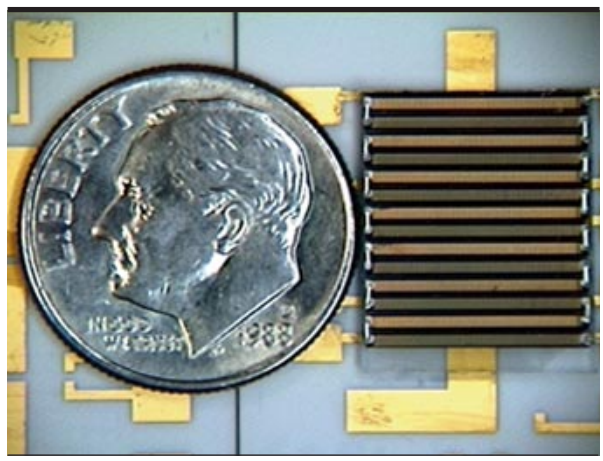

Figure 1. Photocell. We demonstrated 1260 V from this photovoltaic device.

Lattice Boltzmann Simulation of Complex Fluid Flows

David S. Clague
New Technologies Engineering Division
Mechanical Engineering

This report describes the lattice Boltzmann (LB) method for simulation of complex fluids. LB simulation results for a few flow configurations are considered; namely, results for flow between infinite parallel plates, the Hele-Shaw cell, and flow through a 3-D, ordered array of cylinders. The ability of the LB method to correctly predict the fluid velocity profile in the Hele-Shaw cell is examined, and the error as a function of lattice site density is discussed. The hydraulic permeability, which is a function of the hydrodynamic force acting on a stationary object due to fluid flow, for a 3-D, ordered configuration of cylinders is compared with the results of Higdon and Ford.

Introduction

Fluid flow has been a topic of engineering importance and research for many years. Traditional methods to solve such problems include exact theory, finite element methods, finite difference methods, finite volume methods and singularity methods. All of these approaches have their roots in the continuum approximation of fluid mechanics or the Navier-Stokes equations. When applied appropriately, these approaches provide a qualitative and quantitative description of flow systems. A relatively recent approach, the LB method, has been growing in utility and popularity in the fluids community.

The LB method has its roots in the kinetic theory of gases[1] or the Boltzmann transport equation. In the limit of small Mach number and small Knudsen number, the Boltzmann transport equation recovers the Navier-Stokes equations of motion. Because the Boltzmann transport equation describes the statistical average motion of fluid molecules, this is not surprising. In contrast, the continuum approaches cited above are macroscopic descriptions that assume that the properties of interest, for example, density, and fluid velocity, are continuous throughout space.

The LB equation can be thought of as the discrete form of the Boltzmann transport equation. Like the Boltzmann transport equation, the LB equation also recovers the Navier-Stokes equations of motion in the limit of small Mach and Knudsen numbers. The LB method provides great flexibility in the study of bounded, particulate media, or complex fluids.

Essentially, the study of complex systems using this approach is limited by the users' ability to describe the medium. For example, a core sample of sand stone was imaged and mapped onto a lattice, permitting the study of two-phase, oil/water, flow through the semi-permeable medium.[2] Additionally, the LB method has only recently found a niche in the engineering community, and therefore is still a novel approach to such problems.

For a detailed description of the theoretical considerations and breadth of application, the reader is encouraged to see the work of Chen and Doolen.[2]

Progress

Selected results from a recent article[3] and current research efforts are presented in this report to demonstrate the utility of the LB method. Specifically, results for the velocity profile in a Hele-Shaw cell are presented, and the hydraulic permeability calculations for the BCC lattice of cylinders as described by Higdon and Ford[4] using the LB method are compared with their Spectral Boundary Element results for the same system. In the conclusions a brief description of future work at Lawrence Livermore National Laboratory (LLNL) is discussed.

The Hele-Shaw Cell

Many flow systems of interest involve bounded flows. A well-known example of such a system is the Hele-Shaw flow cell. The Hele-Shaw cell was put

forth as a representation of a porous medium, as shown in **Fig. 1**.

The flow cell is periodic in both the x_1 and x_2 directions; hence, the unit cell gets replicated throughout space in the x_1-x_2 plane. The imposed flow is in the x_1 direction. Essentially, the vertical gap, *H*, between bounding walls represents the equivalent, average distance between fixed obstacles in a porous medium.

LB simulations were performed to study pressure-driven flow in this configuration and compared with the analytic solution. In lattice space, a pressure gradient is imposed by applying a constant body force on the fluid lattice sites between the walls. A representative fluid velocity profile is compared with exact theory in **Fig. 2**. The error between the LB result and the analytic solution is approximately 0.5%, on average.

Similar simulations were run for various node densities across the gap, *H*, and the spatial convergence is approximately second order.

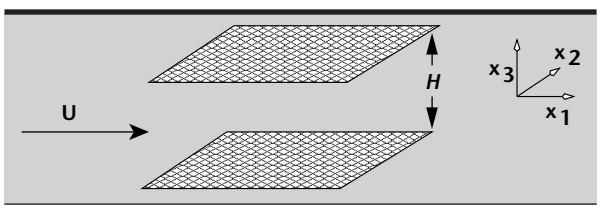

Figure 1. Hele-Shaw cell. The flow direction is in the x_1 direction, and the simulation cell is periodic in both the x_1 and x_2 directions. H is the vertical distance between the solid, infinite parallel planes.

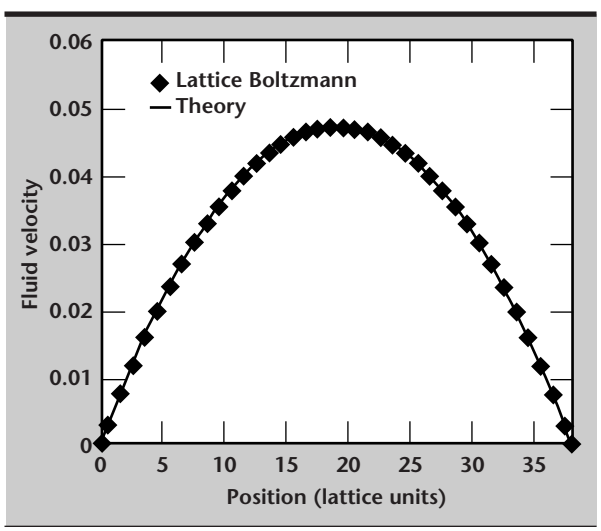

Figure 2. Fluid velocity profile. The LB result is compared with exact theory for pressure-driven flow in a Hele-Shaw cell. The separation, H, in lattice space is 38 lattice sites.

Three-Dimensional BCC Lattice of Cylinders

Flow through fibrous media is common in many filtration systems. Examples range from man-made air filters to blood filtration in the kidney; hence, the ability to predict flow behavior in such systems is of paramount importance. The BCC lattice[4] provides a rigorous test of the LB method for flow through 3-D fibrous media. An LB representation of a typical BCC simulation cell is shown in **Fig. 3**.

The solid lattice sites represent the solid phase, and the clear or unmarked lattice sites represent the fluid phase. For visual clarity, the cylinder radius is only three lattice sites, but for the actual simulation results, the cylinder radius was increased to increase the force resolution at higher fiber volume fractions, ϕ. Flow is imposed here, again, by applying a uniform body force on the fluid lattice sites. To enforce the no-slip condition in the LB method, the fluid is "bounced back" to originating lattice sites that are adjacent to the solid surfaces.[2,3] Therefore, knowing the pressure gradient, ∇P, the superficial average fluid velocity, $\langle \underline{u} \rangle$ and the fluid viscosity, μ, one can make use of Darcy's law,

$$\langle \underline{u} \rangle = -\frac{k}{\mu} \underline{\nabla} P \ , \qquad (1)$$

and calculate the hydraulic permeability, *k*, of the medium.

In the results shown in **Fig. 4,** the actual cylinder radii ranged from 5 to 30 lattice sites or lattice units.

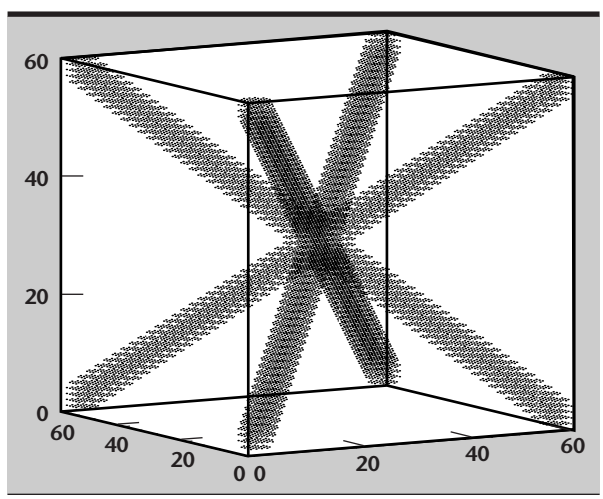

Figure 3. Three-dimensional, BCC lattice. The cylinders depicted have a radius of three lattice units. Cylinders emanate from the center of the cell and intersect the eight vertices of the cubic domain. The dimensions of the simulation cell are 60 x 60 x 60, which represents a fiber volume fraction that is approximately equal to 0.36.

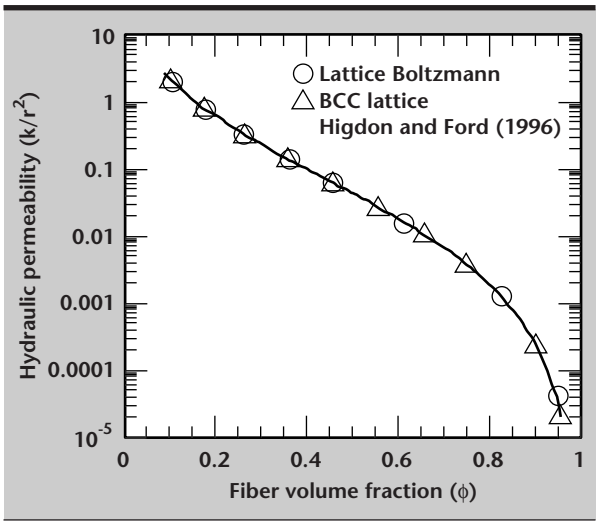

Figure 4. Hydraulic permeability for the BCC lattice of cylinders. LB results are compared directly with Spectral Boundary Integral results.

As shown, the hydraulic permeability, made dimensionless with the cylinder radius, $r,^2$ is plotted as a function of fiber volume fraction, ϕ. Here LB simulation results are compared with the result from the Spectral Boundary Element Methods of Higdon and Ford[4] for the BCC lattice configuration. Their approach is both rigorous and accurate for nearly all possible fiber volume fractions. As is clearly seen here, the LB results are nearly identical to that of Higdon and Ford[4] over the entire range of fiber volume fractions considered. This is remarkable since many methods fail when considering fiber volume fractions >0.5.

Future Work

The LB method is indeed a powerful tool for the study of fluid flow through complex media. The simulation results above confirm that it is as accurate as the best methods available, Spectral Boundary Integral Methods, for solving Stokes flow problems. The LB results represent building blocks for modeling and simulation of systems of greater complexity. Our research focuses on using LB methods to study transport phenomena issues relevant to current and future efforts in LLNL's Microtechnology Center.

References

1. Landau, L., and E. M. Lifshitz (1989), "A Course of Theoretical Physics, Volume 10," Pergamon Press.

2. Chen, S., and G. D. Doolen (1998), "Lattice Boltzmann method for fluid flows," *Ann. Rev. Fluid Mech.*, **30**, pp. 329-364.

3. Clague, D. S., B. D. Kandhai, R. Zhang, and P. M. A. Sloot (1998), "The hydraulic permeability of (un) bounded fibrous media," submitted to *J. Fluid Mech.*

4. Higdon, J. J. L., and G. D. Ford (1996) "Permeability of three-dimensional models of fibrous porous media," *J. Fluid Mech.*, **308**, p. 341.

Micro-Electromechanical Systems (MEMS) for Characterization of Plastic-Bonded Explosives

Jeffrey D. Morse
Electronics Engineering Technologies Division
Electronics Engineering

Dino R. Ciarlo
Engineering Research Division
Electronics Engineering

Scott E. Groves and Diane J. Chinn
Manufacturing and Materials Engineering Division
Mechanical Engineering

Mehdi Balooch
Defense and Nuclear Technologies

Mark J. LaChappel
Defense Sciences Engineering Division
Electronics Engineering

Nano-indentation using custom microprobes within an atomic force microscope (AFM) can be an extremely valuable tool for characterization of mechanical and viscoelastic properties of materials at the microscale level. We have used AFM nano-indentation to characterize the mechanical properties of mock plastic-bonded explosives (PBX). Characterization of the materials properties at the microscopic level enables better understanding of the aging mechanisms of these materials. Micromachining techniques have also been used to design calibrated experiments to assist in interpreting the nano-indentation results under various circumstances.

Introduction

One of the key problems in support of stockpile stewardship is the characterization of aging mechanisms for polymer binder materials used in PBX in various shapes and housings. Understanding the mechanical properties of PBX materials systems under accelerated aging conditions can provide valuable insight into the failure mechanisms of these materials, and subsequently, the lifetime of stockpile systems and devices.

Typical high-explosive (HE) crystallites in binder materials have dimensions on the order of 10 to 50 µm, with distances between crystallites as small as 5 µm. While mechanical properties of the binder material characterized at the macro-scale are important, it is critical to understand the micro-scale properties of the binder material, as well as the HE/binder interface.

Micromachined structures and devices provide characterization tools with these properties over µm scale dimensions. At present, micromachining technologies have focused on the fabrication of custom micro-probes for AFM nano-indentation measurements and custom templates to form reservoirs of binder materials for calibrated nano-indentation experiments. Nano-indentation enables the time-dependent mechanical properties of the binder material to be measured. With a fixed load applied to the AFM-nano-indenter, the micro-scale equivalent of a creep test is performed by monitoring how the nano-indenter plastically displaces with time. In this manner, the viscoelastic properties of the binder material can be characterized.

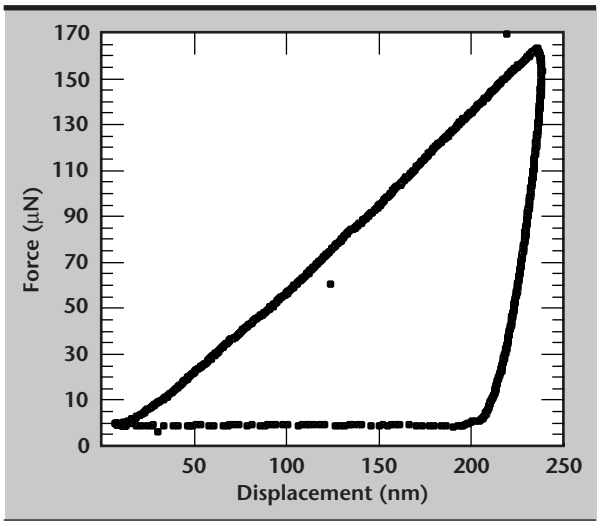

Figure 1. Force vs time information.

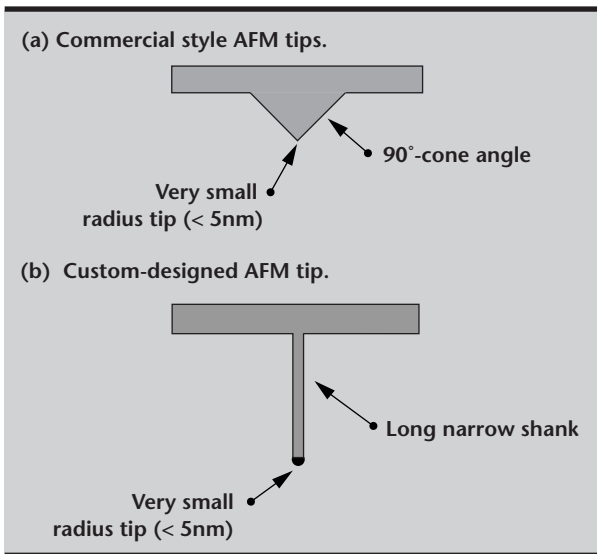

Figure 2. Sample nano-probe showing that (a) existing AFM tips cannot be used to probe surfaces with deep and narrow crevasses, and (b) tall thin probes can reach deep into crevasses.

Progress

Nano-indentation measurements were performed on mock PBX using an AFM system at Lawrence Livermore National Laboratory (LLNL). The AFM is modified with a transducer-indenter assembly called a Micromechanical Testing Instrument. Like its conventional counterpart, the instrument can image the topography of specimens by tracing the superficial contours of the sample with a constant sub-μN load.

In addition, the device is a force-generating and depth-sensing instrument capable of generating load-displacement curves at specified locations. The local mechanical properties such as stiffness,

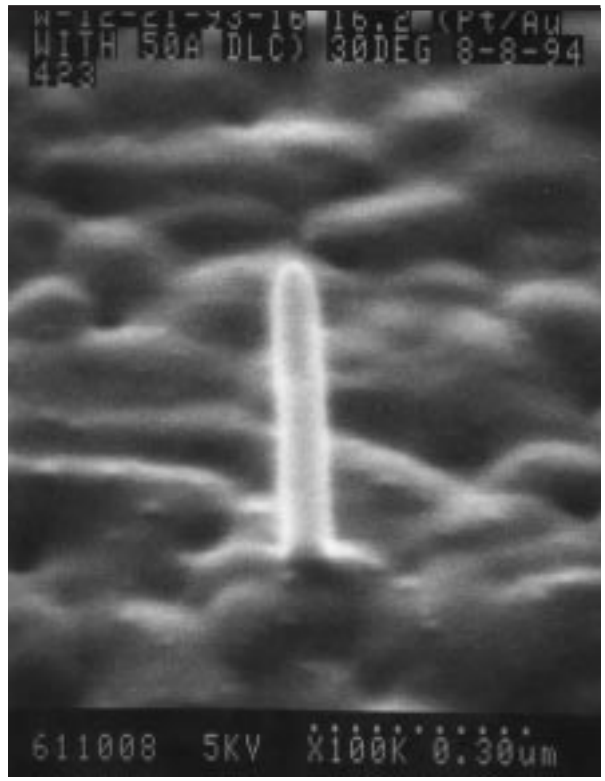

Figure 3. Structure formed by electroplating through a template patterned in a resist film.

hardness, and elastic modulus can be determined. The stiffness is defined as the slope of the force/displacement curve during unloading. The elastic modulus, E, and hardness, H, are defined as:

$$E = \pi^{1/2} \Big/ \left(2a^{1/2}\right) S \quad \text{and} \quad H = F_{\max}/a$$

where S is the contact stiffness, F_{max} is the maximum load and a is the projected contact area under the load. The resulting force vs time information is illustrated in **Fig. 1**.

While these results provide important information regarding the mechanical properties of moderately homogeneous binder material, the problem becomes much more complex with the addition of HE crystallites. For this case, custom microprobes of predetermined size and shapes must be used, typically with tip shank diameters <0.5 μm and aspect ratios >10:1. These can be designed and fabricated by micromachining techniques and mounted on the AFM fixture.

It would be desirable to be able to characterize the mechanical properties of the HE/binder interface, as well as regions between crystallites as narrow as 5 μm. This desire arises due to concerns that the interface becomes fatigued by aging, leading to delamination and eventual failure of the material.

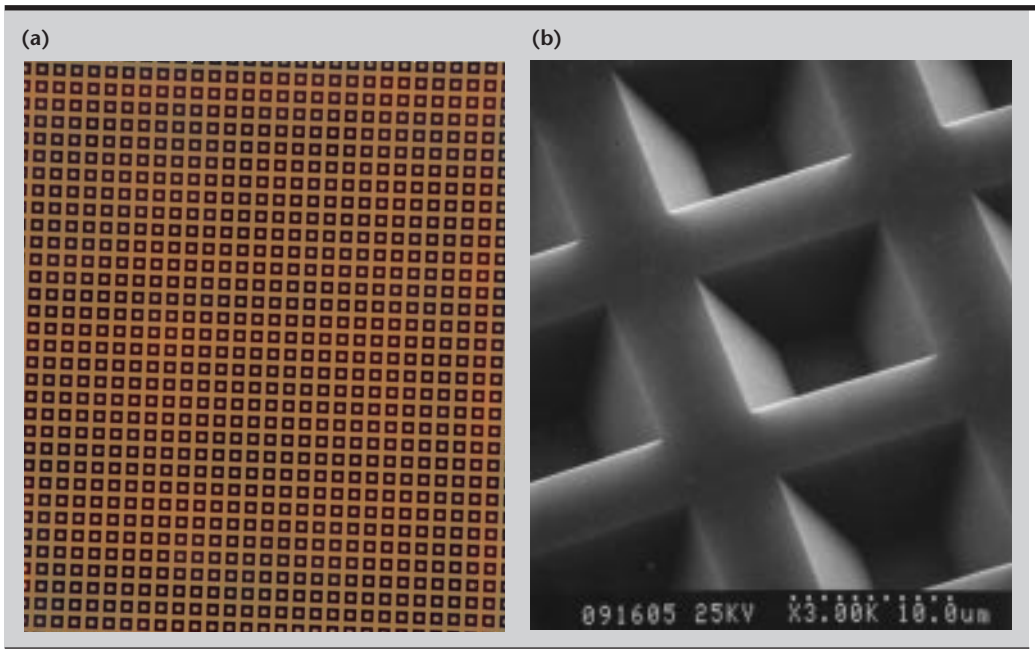

Figure 4. Custom template micro-machined in silicon substrate for calibration studies of nano-indentation techniques on mock PBX: (a) photograph; (b) SEM image.

To accurately characterize the mechanical properties of the interface and narrow regions, the AFM nano-indenter probe can be scanned across the HE/binder interface. Using this technique, a smaller diameter (<0.5 μm) probe is required which is cylindrical, with an aspect ratio on the order of 10:1. Thus, the probe exerts force on a constant surface area which can access extremely narrow areas.

An example of the required nano-probe is illustrated in **Fig. 2**, which compares this requirement to relatively standard AFM probes. A variety of microfabrication techniques can be used to realize this small-diameter, high-aspect-ratio structure.

Figure 3 shows a 1-μm-high, 0.1-μm-diameter structure formed by electroplating through a template patterned in a resist film. Similar structures can be formed through precision plasma etching techniques and are presently under development in a structure which can be retrofit onto the AFM system.

Finally, a custom template to form reservoirs was fabricated using photolithography to define patterns in a silicon nitride mask on a silicon substrate with areas ranging from 5 to 25 μm on a side. Wells were then etched in the silicon with various depths ranging from 5 to 25 μm. This is shown in **Fig. 4**. The wells are then filled with binder material, and AFM nano-indentation measurements are performed as means to calibrate the resulting mechanical response of the binder in proximity to the interface and as a function of depth to a hard surface beneath the probe region. This will provide important information regarding the three-dimensional nature of the samples being characterized.

Future Work

Custom reservoir templates have been fabricated in silicon and are presently being prepared for deposition of mock PBX. AFM nano-indentation measurements will be performed to provide a comparison between standard AFM probes and custom AFM probes, as described above. The custom AFM probes must be fabricated in a structure which is readily mounted in the AFM system for calibration and measurements.

Micro-Electromechanical-Systems-(MEMS)-Based Fuel Cell Technology

Jeffrey D. Morse and Robert T. Graff
Electronics Engineering Technologies Division
Electronics Engineering

Alan F. Jankowski and Jeffrey P. Hayes
Materials Science and Technology Division
Chemistry and Materials Science

We have fabricated a fuel cell stack which uses thin-film electrodes, catalysts, and ion-conducting layers deposited by physical vapor deposition techniques. The stack has been patterned with electrical connections using standard micro-fabrication techniques, and subsequently formed into free-standing membranes by micro-machining away the silicon substrate. Manifold structures have also been fabricated through silicon micro-machining techniques.

Introduction

A serious need exists for portable power sources with significantly higher power density, longer operating lifetime, and lower cost. Present rechargeable and primary portable power sources have excessive weight, size and cost, with limited mission duration. As an example, batteries covering a power range from 1 to 200 W have specific energies, ranging from 50 to 250 Wh/kg, which represents 2 to 3 h of operation for a variety of commercial and military applications.

An alternative power source is the fuel cell, which potentially provides higher performance power sources for portable power applications if the stack structure, packaging, and cell operation are made compatible with scaling down of size and weight.

Fuel cells typically consist of electrolyte materials, either polymer or solid oxide, which are sandwiched between electrodes. The fuel cell operates by delivering fuel (usually hydrogen) to one electrode, and oxygen to the other. By heating the electrode-electrolyte structure, the fuel and oxidant diffuse to the electrode interfaces, where an electrochemical reaction occurs, releasing free electrons and ions which conduct across the electrolyte.

Typical fuel cells are made from bulk electrode-electrolyte materials which are stacked and manifolded using stainless steel packaging. These systems are bulky and operate at high temperatures (>600 °C). If the electrode-electrolyte stack can be made very thin and deposited using thin-film deposition techniques, the temperature of operation will be significantly lower.

Previous efforts at Lawrence Livermore National Laboratory (LLNL) have demonstrated the synthesis of a thin-film solid-oxide-based electrolyte fuel cell (TFSOFC) stack.[1,2] The TFSOFC stack was formed using physical vapor deposition (PVD) techniques. The host substrate was a silicon wafer covered by a thin layer of silicon nitride. A layer of nickel was first deposited, followed by a layer of yttria-stabilized zirconia (YSZ).

The conditions during the deposition were adjusted to achieve smooth, dense, continuous films, thus avoiding pinhole formation which could result in electrical shorting through the electrolyte layer. This enables the electrolyte layer to be on the order of 1 μm thick, rather than typical thicknesses on the order of >10 μm for bulk solid-oxide fuel cells.

By thinning the electrolyte layer, resistive losses are significantly lower, and the fuel cell operates at much lower temperatures. A silver electrode layer is deposited on top of the YSZ layer. The deposition conditions of this film are adjusted to create a porous structure so that oxygen can readily diffuse to the electrolyte interface.

Progress

During the past year, this effort has focused on the utility of a TFSOFC, along with assessments for

other electrolyte materials systems. The incorporation of manifold structures within the host substrate through micro-machining techniques enables a complete fuel cell device to be realized which can be readily attached to fuel and oxidant sources. This concept is illustrated in **Fig. 1**.

In this approach, the fuel cell stack is created by thin-film deposition techniques. Integrated-circuit type micro-fabrication processes are used to pattern electrode contacts, as well as to form a resistive heater element within the stack structure.

The stack is subsequently formed into a free-standing membrane by selective etching of the substrate. Manifold channels are micro-machined in another substrate, which is subsequently bonded to the fuel cell substrate, as illustrated in **Fig. 1**.

This approach provides an effective means to form efficient fuel cell stack and electrode structures monolithically, and distribute fuel to the entire stack without the need for bulky complex manifolding. Furthermore, since the stack is now only a small percentage of the mass of the entire structure, appropriate thermal design of the fuel cell device, package, and resistive heating elements will allow efficient, low-power heating of the stack.

Figure 2a illustrates a completely fabricated fuel cell module with integrated heating element, with a view of the fuel cell stack free-standing membranes shown in **Fig. 2b**. To achieve this, the silicon substrate was selectively etched with potassium hydroxide, using patterned silicon nitride as the mask.

Manifold channels, shown in **Fig. 3**, were etched in a silicon substrate using similar techniques. These components will ultimately be bonded together to form a fuel cell module having inlet and outlet channels with approximately 50-µm-×-200-µm openings for fuel delivery.

The MEMS-based thin-film fuel cells are tested to measure the current output as a function of temperature as the voltage is incremented from nil through and above the open circuit voltage (OCV). The solid-oxide fuel-cell (SOFC)-layered combination of a Ni-YSZ anode, YSZ electrolyte, and Ag-YSZ cathode, allows

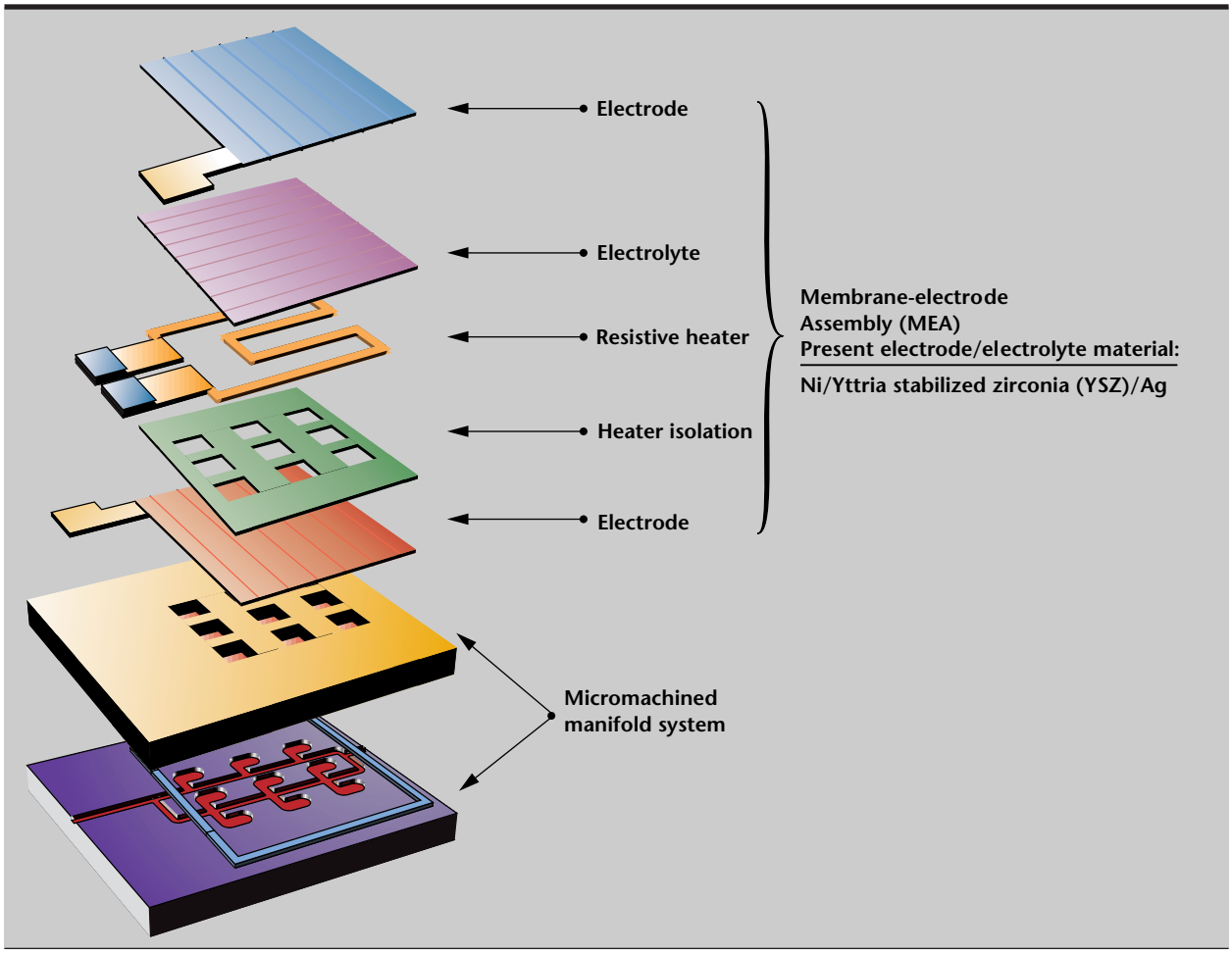

Figure 1. MEMS-based fuel cell concept using silicon micro-machined host structure and manifold system with fuel cell stack membranes.

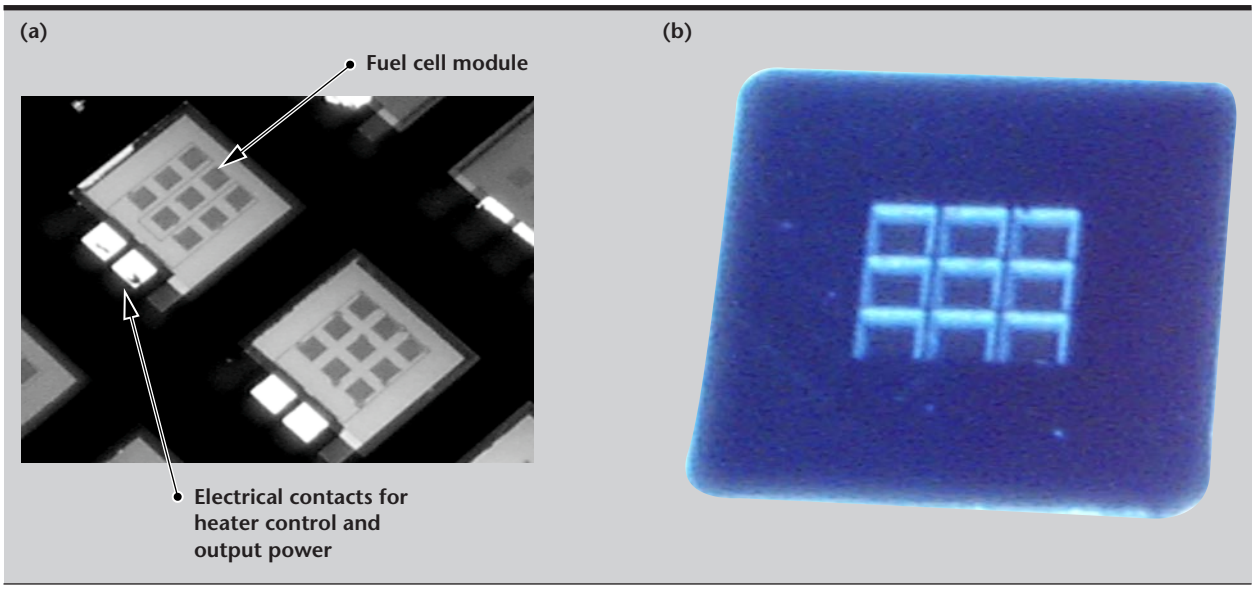

Figure 2. (a) Micro-fabricated fuel cell module, with (b) free-standing thin-film fuel cell stack membrane, formed by micro-machining silicon from backside.

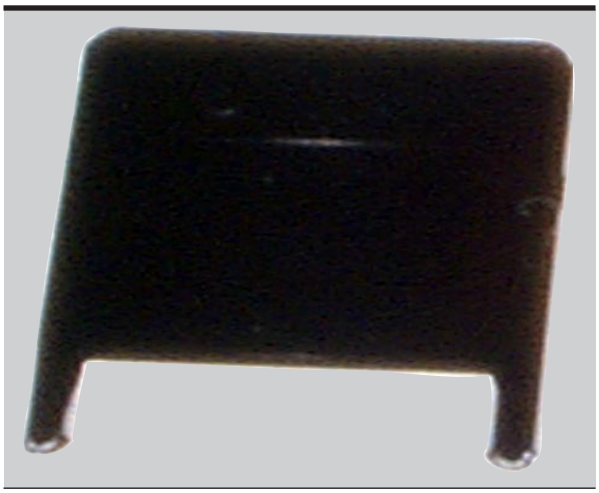

Figure 3. Fuel cell module with micro-machined manifold channels in bottom wafer.

for the transport of oxygen ions through the electrolyte via a diffusion-moderated process. The resistivity of the electrolyte is measured to typically exceed 1 MΩ-cm.

Once an oxygen ion diffuses through the electrolyte and combines with hydrogen, an (electron) current is generated. A maximum OCV of ~1.1 V exits for the combination of oxygen and hydrogen using this SOFC structure.

The TFSOFC sits atop a windowed silicon wafer that is bounded on the anode side to a quartz tube using a ceramic epoxy. The anode and cathode tabs on the silicon wafer are silver-epoxy bonded to silver wires. The wires are connected to a semiconductor parameter analyzer that controls the applied cell potential. The silicon-wafer-mounted tube is O-ring-sealed within a larger diameter quartz tube that is placed within a conventional (Lindbergh) clam-shell furnace.

Feedthroughs are provided at either end of the assembly, on both the anode and cathode sides, that allow the passage of the oxidant and fuel as gases. A fuel mixture of 3% hydrogen is flowed through the anode tube at a rate of 1 to 3 sccm. Air is flowed to the cathode surface at a rate of 1 to 3 sccm. The current-voltage output is measured as a function of temperature to 600 °C.

Initial results of this° testing are illustrated in **Fig. 4**. While not optimal, these results exhibit the expected overpotential for this electrolyte materials system with no output current, along with increasing current output as temperature increases.

While the output current densities are low, inherent limitations are present in fuel cell performance resulting from the high density of the nickel cathode layer. Thus, while fuel can readily diffuse through the nickel film to the electrolyte interface, water, the byproduct of the electrochemical reaction, is unable to diffuse away from the interface. Thus the reaction ions quench, resulting in limited efficiency of the fuel cell stack.

Future Work

The next iteration of fuel cell modules will include porous nickel electrode structures, thereby eliminating the effects of water vapor trapped at the electrolyte interface. Further efforts will focus on

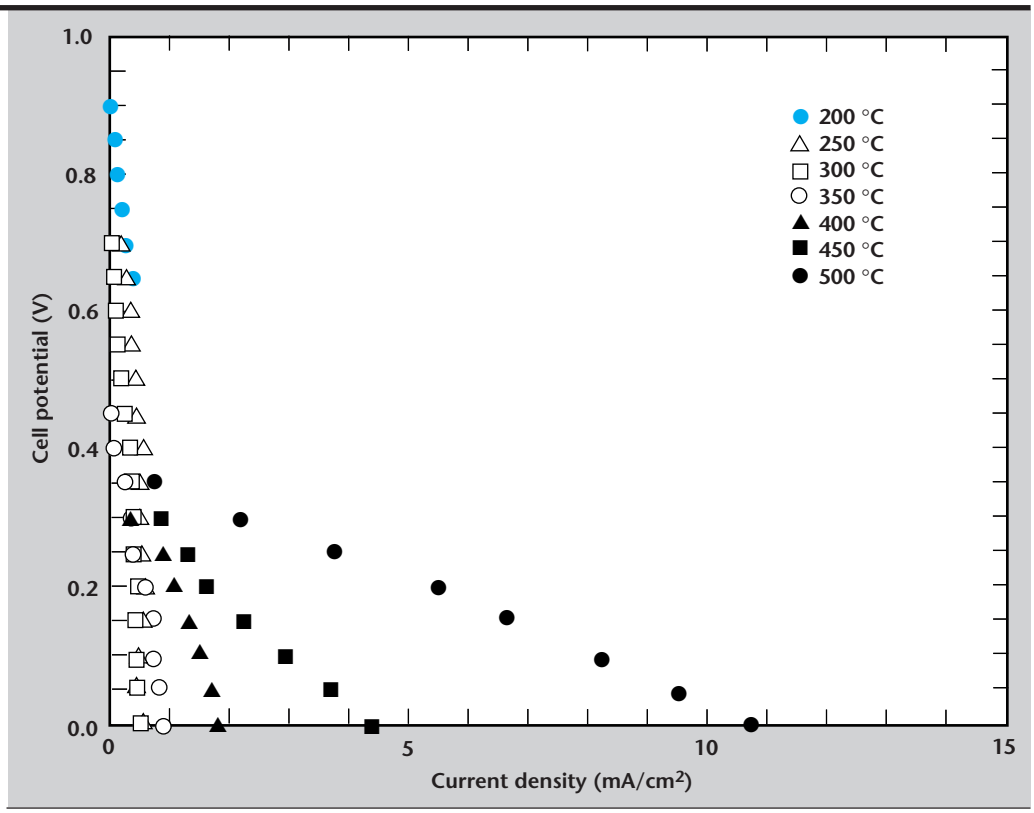

Figure 4. Current-voltage characteristics of thin-film solid-oxide fuel cell at various temperatures.

optimizing the design of the heating element and fuel cell stack, and packaging. This includes investigation of alternate electrolyte material, both solid-oxide and solid-polymer systems.

References

1. Jankowski, A. F., and J. D. Morse (1998), *Materials Research Society Symposium Proceedings* Vol. **496**, pp. 155–158.

2. Jankowski, A. F. (1998), U.S. Patent No. 5,753,385, May 19.

High-Power GaN Microwave Device Technology

Glenn A. Meyer
New Technologies Engineering Division
Mechanical Engineering

Gregory A. Cooper and Stacy L. Lehew
Electronics Engineering Technologies Division
Electronics Engineering

Thomas W. Sigmon and Daniel Toet
Information Science and Technology Program
Lasers

Steven DenBaars and Umesh Mishra
University of California
Santa Barbara, California

The purpose of this work was to develop more efficient doping processes for use in gallium-nitride (GaN)-based power microwave devices. We developed a pulsed laser processing technique aimed at activating n-type dopants for GaN field effect transistors. The laser processing is performed using a XeCl excimer laser with a 35-ns pulse length at a wavelength of 308 nm. This technology allows selective area doping of GaN, presently a major technology roadblock in the fabrication of devices in this material system.

Introduction

GaN is an ideal semiconductor material system for high-power microwave applications due to its unique properties: high thermal conductivity, high temperature stability, high breakdown field strength, and high carrier velocities. Researchers at the University of California, Santa Barbara recently demonstrated[1] GaN-based microwave devices operating at cw power densities greater than 3 W/mm gate width, at a frequency of 18 GHz. This performance is approximately three times higher than the best commercially available devices made from SiC or InP.

High-power microwave amplifiers presently used for communications and radar applications use bulky vacuum tube electron beam devices, such as traveling wave tubes, magnetrons and gyrotrons. Traveling wave tubes, for example, are typically tens of centimeters in size. An all-solid-state, high-power microwave amplifier would enable the development of much smaller and lighter microwave systems for use in satellite and ground based communications, and remote sensing. Compact devices and antennas enable the construction of phased-array radars with the ability to form steerable beams. Moreover, the DC to RF conversion efficiencies for solid-state transmitters is significantly higher than conventional, high-power RF electron beam devices.

Currently, the performance of GaN-based RF devices is limited by high operating temperatures. This is primarily due to resistive heating in two regions of the device, namely the resistance between the metal contact and the doped semiconductor contact layer (that is, the specific contact resistance) and the total resistance of the doped semiconductor layer. By increasing the number of electrical carriers in the semiconductor layer, the resistive heat generation in both of these regions can be reduced. However, one of the main obstacles to the full realization of the potential of GaN as a material for optoelectronic and microwave devices is the difficulty in reaching high enough doping levels in this material for fabricating low sheet resistance layers.

The most common technique used for doping GaN is incorporation of the dopant atoms into the material during crystal growth. Magnesium is the most common dopant used to create p-type material in metal-organic chemical vapor deposition (MOCVD) growth. The ionization energy of the Mg acceptor in GaN is 150 meV. This value is large enough to result in only a fraction of a percent of the Mg atoms being electrically active at room temperature.[2] This low ratio of electrical carriers to dopant atoms forces the growth to include a significantly higher level of Mg to achieve the desired carrier concentrations. Incorporation of high dopant concentrations causes the normally transparent GaN to become cloudy, indicating large concentrations of crystal defects. Presently, the p-type carrier concentrations achievable with magnesium are in the range of 2 to 3×10^{18} holes/cm^3, a value that is not high enough to achieve low sheet resistance layers or electrical contacts.

Ion implantation may offer a practical solution to the problems associated with achieving high p-type carrier concentrations in GaN. This technique is widely used in semiconductor device fabrication technology. Several researchers have investigated this technique for GaN but have encountered problems that do not appear for Si or GaAs. One of these problems is the high temperature required to incorporate the implanted dopant atoms into the crystal lattice. The effective incorporation of the dopants onto the correct crystal sites and removal of the implant damage requires annealing temperatures in excess of 1200 °C. Nitrogen, being a fundamental constituent of GaN, has a very high vapor pressure at the required annealing temperatures (>1000 bar). Therefore, annealing GaN material at these temperatures requires very robust capping layers to prevent the nitrogen from escaping.

Attempts to use rapid thermal annealing (RTA) have also resulted in thermal budgets well in excess of the levels tolerable for device fabrication. In addition, heterojunctions and quantum wells are particularly sensitive to annealing temperatures in excess of 900 °C. The time-temperature product must be limited to prevent serious degradation of the device layers.

A promising technique useful for reducing the time-temperature product is pulse laser annealing. Near-surface heating by absorption of a pulsed laser beam is expected to allow higher processing temperatures. This typically is a very fast, non-equilibrium process. For example, a 90 nm a-Si film on a low-temperature glass substrate can, following the absorption of a short laser pulse, fully melt and recrystallize within 150 ns, while the glass remains unaltered. A pulsed excimer laser can deposit large amounts of energy into a thin layer at the GaN surface in a very short time. Deeper layers, containing sensitive quantum structures, do not experience the high temperatures.

The objective of our project was to investigate a pulsed laser processing method for improving the doping activation process for n-type dopants in GaN field effect transistors. The laser annealing actually results in the melting of the implanted layer. During the recrystallization of the molten layer, the doping impurity assumes the appropriate lattice position, allowing realization of the desired low sheet resistance contact layer. This process technology has been demonstrated at Lawrence Livermore National Laboratory (LLNL) to provide very low electrical resistance contacts on Si, SiGe, and SiC semiconductor materials.

Progress

The initial phase of our research focused on the effects of the pulsed laser process on intrinsic GaN. Once the laser material interactions were understood, laser activation of ion implanted n-type and p-type dopants was investigated. The band gap of GaN semiconductor materials is approximately 3.4 eV, making it ideal for strong absorption of our 4 eV XeCl laser (λ = 308 nm) pulse. The laser absorption depth in the GaN is approximately 120 nm, using an absorption coefficient of 8.37×10^4/cm at λ = 308 nm.[3]

The GaN films used in the experiments were 2 µm thick, grown in a modified two-flow horizontal reactor on c-plane sapphire, using low-pressure MOCVD. The chemical precursors used were trimethylgallium (TMGa) and ammonia (NH_3). The samples were then ion-implanted at an energy of 150 keV with Si and Mg to doses of 8×10^{16} cm^{-2} and 5×10^{14} cm^{-2}, respectively.

Laser processing of GaN films is performed using a XeCl excimer laser (from Lambda Physik, Germany) with a 35-ns pulse length at a wavelength of 308 nm. The transformation induced in the GaN by this pulse is monitored *in situ* and in real time by measuring the time-resolved transmission (TRT) of an IR laser beam passing through the center of the spot irradiated by the XeCl laser. The samples are held in a vacuum cell with a quartz front window that is transparent to the excimer laser beam. Prior to laser processing, the sample chamber is evacuated to 1×10^{-3} Torr, using a Varian sorption pump. The chamber is then backfilled with flowing nitrogen.

Figure 1 shows the IR TRT profiles measured during the exposure of an undoped film to pulses at different energy fluences. As seen in this figure, the IR transmission drops dramatically upon laser exposure at fluences greater than threshold. This drop is associated with the heating and melting of the film following the absorption of the excimer laser light. The molten material blocks the IR beam due to its metal-like optical properties.

The transmission signals take more than 2 µs to return to their pre-pulse levels for the highest annealing fluence, indicating that the annealed material cools down slowly. This slow cooling rate is attributed to the fact that the thermal gradient across the film is very small, due to the relatively deep penetration (120 nm) of the 308-nm light in the GaN. Ultimately, we intend to confine the melting to a shallower region near the surface. Moreover, optical inspection of the films reveals that for laser exposures above threshold a roughening of the films resulted.

Figure 2 shows the results obtained during the exposure of a sample that was first implanted with Mg ions to a dose of 5×10^{14} cm^{-2}, and a depth of 100 nm. The most striking feature of this TRT plot is the fact that the melting duration is now much lower than that of the unimplanted sample. This implies that the implantation altered the optical absorption properties of the film, probably due to surface amorphization.

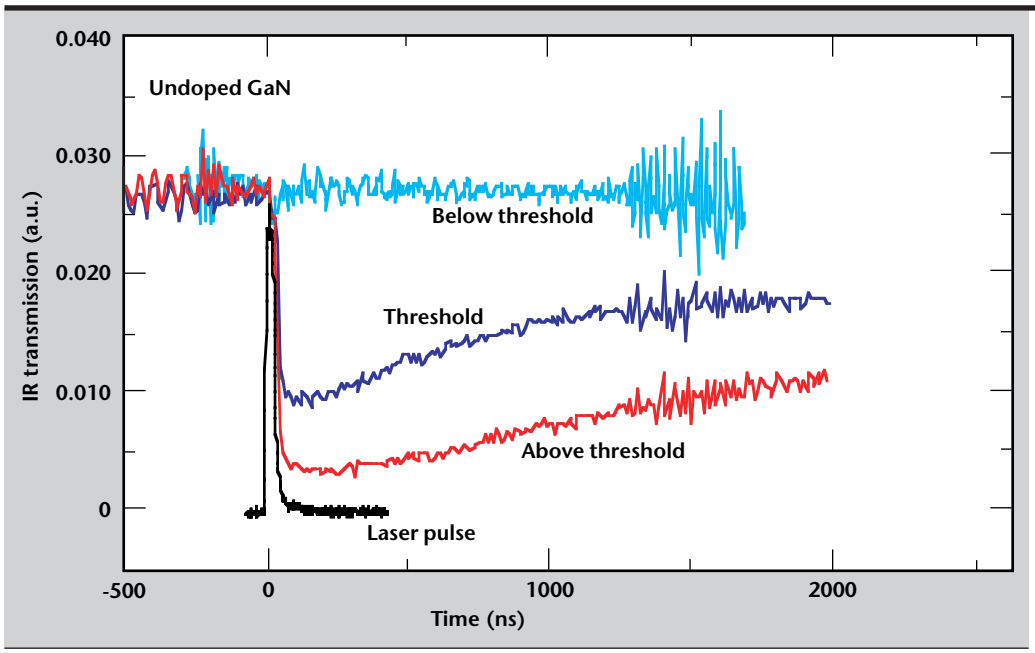

Figure 1. IR time-resolved transmission profiles obtained during laser exposure of undoped GaN film to various excimer laser fluences. The IR transmission drops dramatically upon laser exposure with threshold fluence indicating that surface melting occurred.

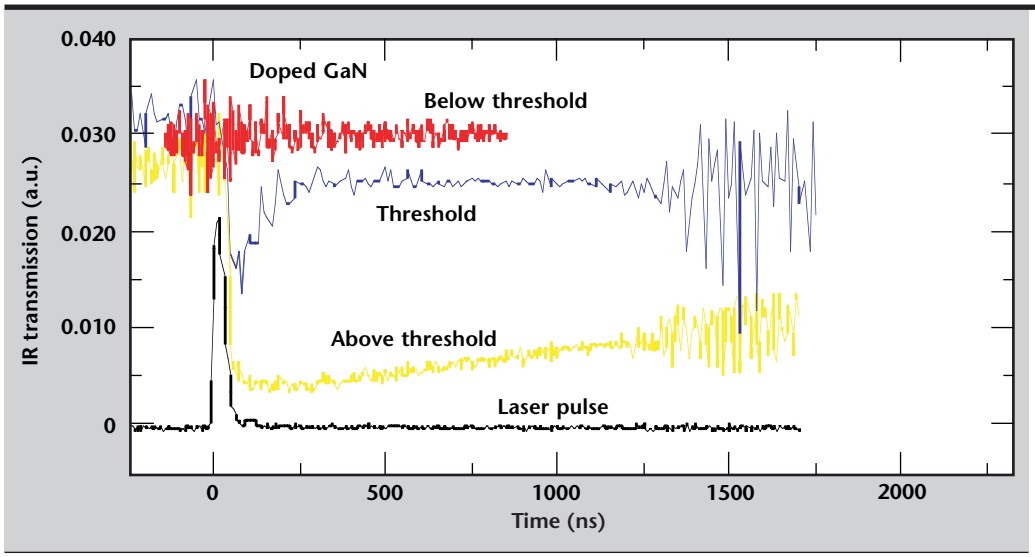

Figure 2. IR time-resolved transmission profiles resulting from laser exposure of Mg ion-implanted GaN film (Mg dose = 5 x 10^{14} cm^{-2}) to laser pulses with different energy fluences. The IR transmission drops dramatically upon laser exposure with threshold fluence indicating that surface melting occurred.

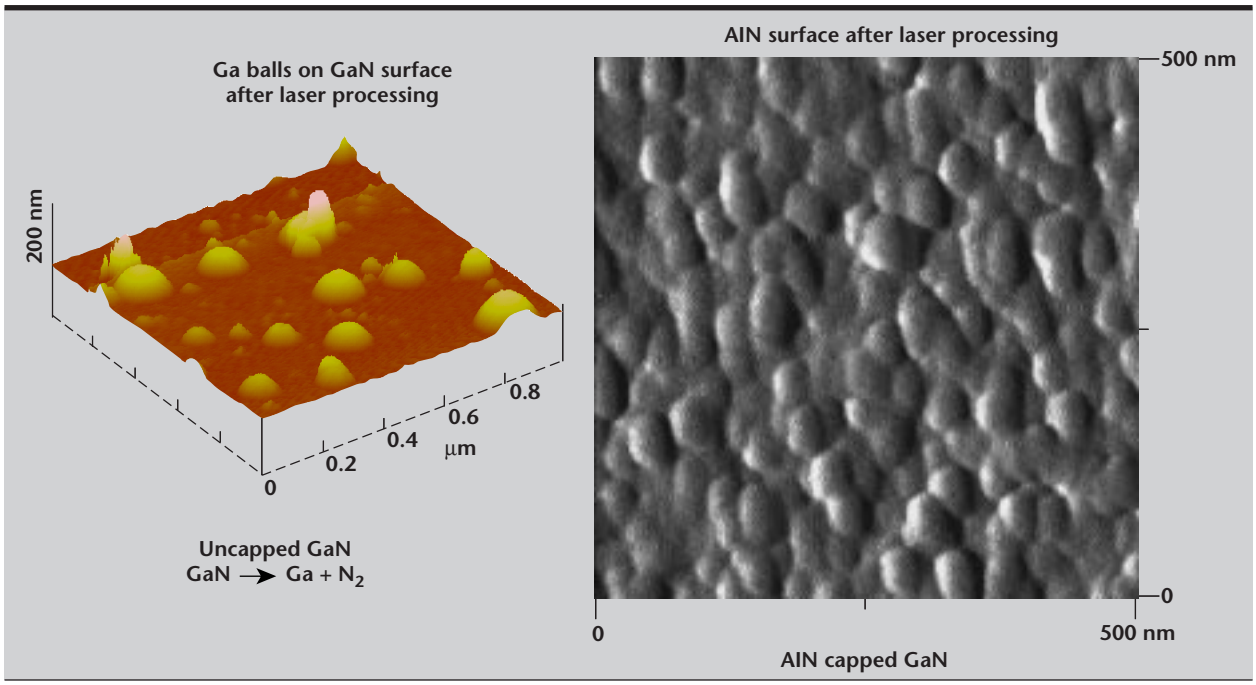

Figure 3. AFM images of GaN surfaces after laser processing. Use of an AlN cap layer prevents GaN decomposition and retains the original surface smoothness.

Figure 4. Secondary ion mass spectroscopy profile of ion-implanted Si in GaN (dose of 8 x 10^{16} cm^{-2} at 150 keV) laser processed at laser fluences above, at, and below threshold. Silicon redistribution is evident at a threshold laser fluence.

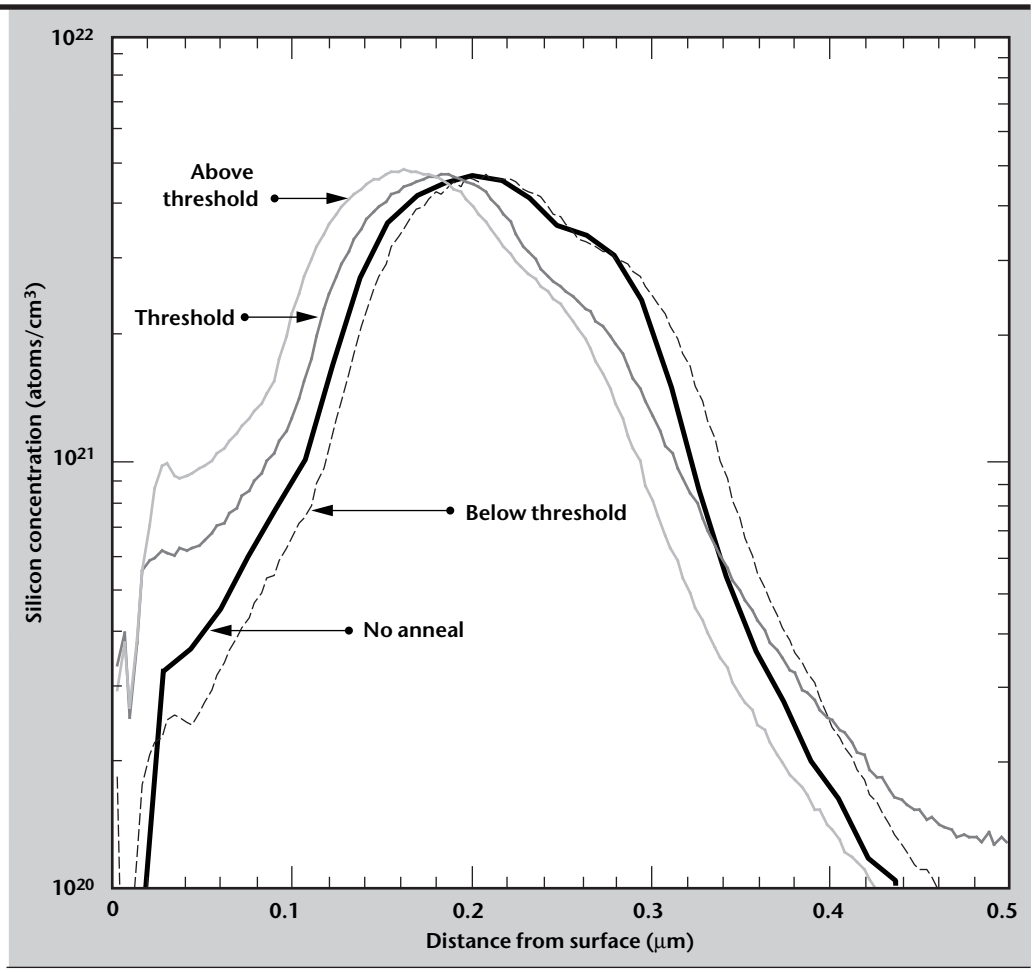

The curves obtained for higher fluence are similar to those observed for the undoped films. The TRT measured for the threshold laser pulse has a much shorter melt duration (~120 ns), that is, a shallower melt depth. (Heat flow simulations relating melt duration with melt depths are currently being developed for this material.) This corresponds exactly to what is required for dopant activation. In addition, the surface of the film annealed at threshold is not noticeably roughened. However, atomic force microscope (AFM) analysis indicates that the surface of this sample is covered with Ga droplets, suggesting that some surface decomposition has taken place (**Fig. 3**).

To prevent decomposition of the GaN during laser processing, the surfaces are encapsulated with an aluminum nitride (AlN) capping layer. The AlN was deposited by ion beam sputter deposition (IBS) using an AlN target in a 500-eV N_2/Ar ion beam. The IR TRT plots and melting thresholds for AlN coated samples were similar to those shown in **Fig 2**. However, a majority of the AlN cap layer was ablated during the laser exposure. AFM analysis of the surface of the AlN-capped sample after laser processing revealed that the surface was intact and that no GaN decomposition had occurred.

GaN films ion-implanted with Si to a dose of 8×10^{16} cm^{-2} were coated with a AlN cap layer and then exposed to laser fluences above, at, and below threshold. Secondary ion mass spectroscopy (SIMS) was used to measure the Si profiles of the Si-implanted samples before and after laser processing. The SIMS data was used to determine the threshold laser fluence at which Si redistribution occurs (**Fig. 4**). As can be seen in **Fig. 4**, the Si surface concentration increases with corresponding increased laser fluence.

Future Work

We have demonstrated that pulsed laser processing for the activation of dopants in GaN shows compelling promise. However, additional process development is required before this technology can be applied to actual devices. We will vigorously pursue outside funding for the continuation of this work. There are presently opportunities for funding available for GaN microwave power amplifiers through the Innovative Science and Technology Program of the Ballistic Missile Defense Organization.

References

1. Mishra, U. K., Y. -F. Wu, B. P. Keller, S. Keller, and S. P. Denbaars (1998), "GaN Based Microwave Power HEMTs," *Physics of Semiconductor Devices*, V. Kumar and S. K. Agarwal, Eds., Narosa Publishing House, New Delhi, India, pp. 878-883.

2. Akasaki, I., H. Amano, M. Kito, and K. Hiramatsu (1991), *J. of Luminescence*, **48/49**, p. 666.

3. J. H. Edgar (1994), *Properties of Group III Nitrides, INSPECT, Inst. Electrical Eng.*, London, UK ISBN 0 85296 818 3, p. 192.

Glass Etching

Harold Ackler and Stefan P. Swierkowski
Electronics Engineering Technologies Division
Electronics Engineering

A radically new type of glass, photostructurable glass, has been evaluated for the first time for suitability for micro-electromechanical (MEMS) structures. The final etch can have an anisotropy ratio of up to 10:1 (20:1 if etched from both sides), and etched features may have steep vertical wall angles of 1 to 4°. These initial results indicate that the glass may be very deeply etched, through the wafer if etched from both sides. However, the trench bottom and sidewall roughness of ±2 µm may preclude some applications with the current level of processing. We have done a multi-parameter etch study on conventional borosilicate glass, since this glass is commonly used in MEMS structures for silicon anodic bonding and glass-to-glass fusion bonding. These types of structures are currently used in major projects at Lawrence Livermore National Laboratory (LLNL). The results have greatly improved the process control to establish undercut ratios, and the control of etch defects, etch-depth uniformity, and etched surface roughness.

Introduction

Glasses come in many different types and compositions, with vastly different properties and uses. A relatively new photostructurable glass may be patterned into microstructures by exposing regions to be etched with deep UV light. When properly annealed, these regions crystallize into a phase of different composition that etches twenty times faster than the surrounding amorphous material in dilute HF.

The initial surface finish, hidden sub-surface damage, and thermal history of a glass may dramatically affect the formation of microstructures. Many projects at LLNL's Microtechnology Center (MTC) have been patterning borosilicate glass microstructures with varying degrees of success, but the quality of the patterned microstructures has often been severely impaired by the lack of suitable process infrastructure and understanding of the basic causes of defects.

Our recent work on the patterning of large microcapillary arrays (50 cm long, 100 µm wide and 10 to 100 µm deep) has demonstrated how important certain initial conditions are in determining the quality of the etched pattern. Our evidence shows that non-visible initial scratches and defects play a major role (sometimes disastrous) in the quality and shape of the etched features.

Three glass treatments were studied as a means of eliminating or reducing the effects of such defects. The variation of undercut ratios (side cut/depth) from 1.0 (isotropic) to 2 or greater (anisotropic—fast side etch) is commonly observed and poorly understood. This is attributed, in part, to initial glass conditions, but also to etching technique (for example, etch composition, orientation, convection, reaction rate, reactant diffusion, reaction product removal).

Systematic study of these process parameters is described below.

Progress

Foturan® Photostructurable Glass Processing

The recommended wavelength for exposure of Foturan® is 290 to 330 nm, where it absorbs moderately. Since it does not absorb at 405 nm (our standard flood/aligner source), the 235-nm lamp was used. Foturan® absorbs strongly at this wavelength, so the depth of the region that is adequately irradiated, and therefore crystallized, was strongly dose-dependent, whereas it is weakly so at the prescribed wavelengths.

Samples were irradiated with 2, 4, 8 and 16 J/cm^2 using a test pattern of lines with spacings

from 20 to 160 µm, with channel spacings equal to channel widths, and large rectangular features 200 to 1000 µm on a side. After annealing, the pieces were etched 10 min **(Fig. 1)**. Etch depths measured with a stylus profilometer are summarized in **Table 1**.

Similarly exposed samples were annealed, then cross-sectioned, polished, and etched ~5 min to reveal the depth of crystallized material. Crystallization depth vs dose is summarized for the 20- and 40-µm channels in **Table 2**. The large features were crystallized completely through the 0.5-mm wafer for a 16-J/cm^2 dose. Only the 16-J/cm^2 dose appears sufficient to produce crystallization deep enough to fully evaluate possible etch aspect ratios, which are approximately 3:1 with sidewall angles of approximately 6°.

The failure to meet figures specified by the manufacturer are due to the different wavelength used here, which alters the process. The surface roughness was ±2 µm. A means of smoothing the surface is yet to be developed. Finally, the CTE of this glass is approximately 8.5 ppm/°C, making it incompatible with Si and Pyrex. However, it is CTE-matched to Ti, Pt, Al_2O_3, and other glasses.

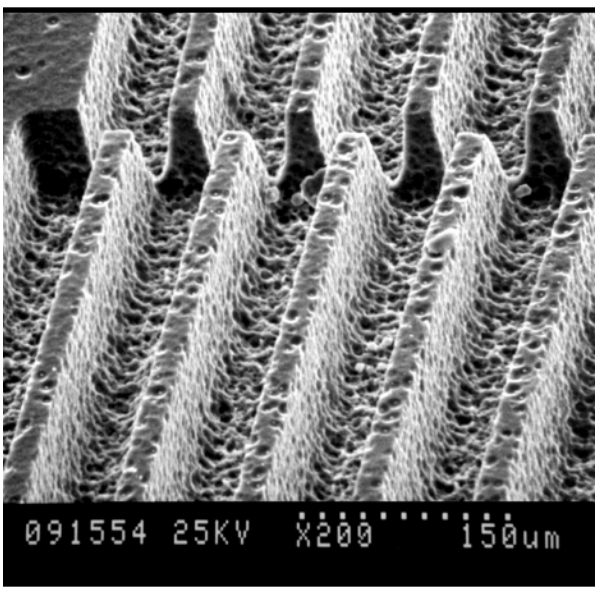

Figure 1. Foturan®, etched 10 min at 8 J/cm^2.

Process Control for Borosilicate Glasses and Initial Defects

The glass defects responsible for the generation of etch defects are believed to be due to either localized stress caused by mechanical damage, or chemical inhomogeneity. The former should be present only near the surface, and possibly relieved by thermal treatments. One group of Pyrex wafers was polished by a very gentle technique and another annealed. A final group was pre-etched in HF to remove defective material. These groups and another of as-received wafers were patterned and etched with 40-µm channels. The etch defects in channel walls were counted for known lengths of channels and are shown in **Table 3**.

Annealing was not effective in reducing defect rates. Polishing was very effective in that the defect rate was much lower and the defect size was much

Table 1. Etch depths (µm).

Dose (J/cm^2)	Feature width (µm) 40	80	120	160	1000
2	20	30			25
4	20		35		35
8		45		65	65
16		50		65	75

Table 2. Crystallization depths (µm).

Dose (J/cm^2)	Feature width (µm) 20	40
2	24.5	27.5
4	47.5	37.5
8	100	
16		164

Table 3. Defect rates in treated Pyrex wafers.

Wafer treatment	Average (defects/cm)	Standard deviation (defects/cm)	cm of 40-µm channel
As-received	47	26	~ 6
Annealed	35	18.6	~ 6.5
Polished	6.8	2.5	~ 6.5
Pre-etched	0.23	0.46	~ 4

smaller. However, this method costs approximately $200/wafer through a vendor. The pre-etch was remarkable at reducing defect rates to almost zero, with very small defects when observed. This process takes an extra 15 min; however, it leaves pits scattered over the entire surface, which are at most 250 nm deep. The effects of those pits that intersect channel edges on device performance have not been fully considered. They might be sealed up during bonding; however, this has not been completely evaluated.

A large set of parametric etch experiments were carried out on borosilicate (Pyrex) glass using Cr-Au as the etch mask with a varying grating pattern[1]. A few selected results are discussed. The quality of etching is strongly dependent on the etch composition, concentration, mask composition and definition, agitation, and prior history of the glass surface. Data from a frequently used (60 min duration/21 °C) etch is shown in **Fig. 2.**

These etch experiments show that the absolute roughness (vs normalized with depth) for **Fig. 2** is about 10 to 40 nm. This is true over a wide range of concentrations and depths, and to some extent, composition. Roughness can be dramatically worse if the surface of the glass is damaged, even with non-visible defects, especially scratches. For very high etch rates, the reaction products can't be removed quickly enough, resulting in very poor etch definition and roughness.

In **Fig. 2**, the absolute value of roughness remained approximately constant at ~30 nm as the HF concentration increased. However, the higher HF concentrations more rapidly remove the patterned field photoresist (6 µm thick), which is left over the Cr/Au etch mask (1 µm thick) as additional support. Since this etch is approximately isotropic, it undercuts the Cr/Au/photoresist mask significantly.

Uniform etch agitation is essential for uniform depths. The higher agitation needs a stronger mask and the higher the agitation, the more the mask is undercut. For etch times much longer than 60 min in the 22%-HF etch, the mask starts to seriously degrade with pinholes or cracking. The 22%-HF etch is a compromise between etch rate, roughness, and mask degradation.

A typical etch result is shown in **Fig. 3**. The total mask undercut is about the same as the depth, that is, 40 µm. The etch rate is reduced in the corner underneath the mask near the surface. The reaction rate and product removal is reduced here by limited convection, so the glass is locally etched anisotropically and yields a final glass undercut of 5 µm. The lateral definition of the glass edge appears to significantly replicate the roughness of the Cr pattern after it is etched. Care must be take to not over-etch the Cr, as it will undercut the Au and result in more jagged Cr edges.

Etch studies taken with small (7 cm) test pieces have yielded significant differences in uniformity compared with very large rectangular (15 cm × 58 cm) plates. The etch-volume to surface-area-being-etched ratio, combined with the detailed etch flow patterns during agitation, appears to be very important.

For etching small samples placed vertically along the wall of the etch beaker we have etch rates of about 0.75 µm/min—independent of zero, medium, or high-spin speeds. For etching small samples placed horizontally along the bottom of the etch beaker, we have etch rates of about 0.89 µm/min—

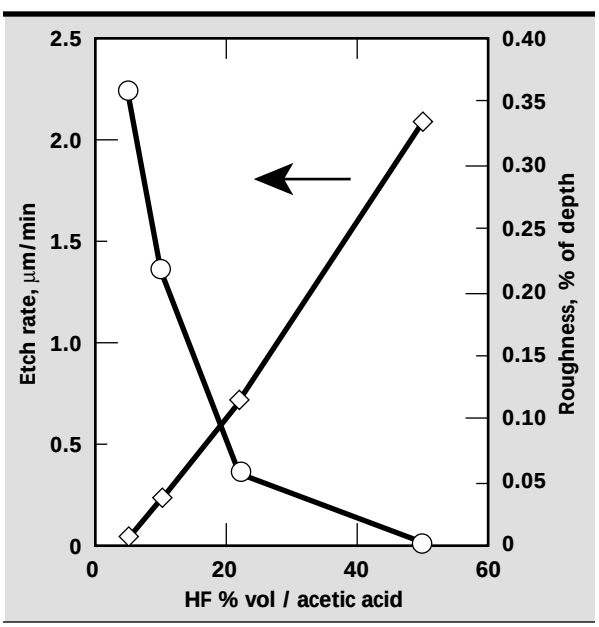

Figure 2. Etch parameters for borosilicate glass.

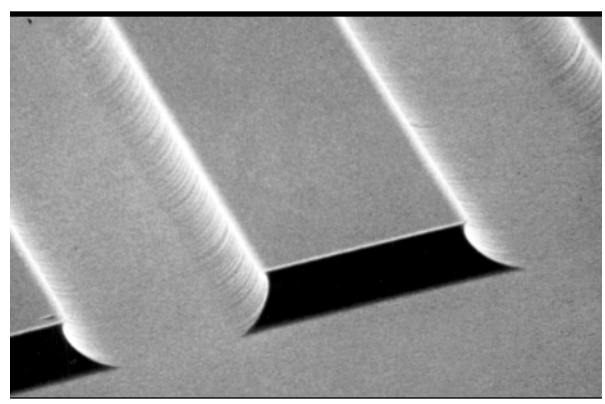

Figure 3. Etched channels in borosilicate glass, 40 µm deep, on a 250-µm pitch. The 5-µm undercut is key to forming a rounded channel.

independent of zero, medium, or high-spin speeds. The etch uniformity across these small samples is very good—less than 2%.

For large rectangular plates with a longitudinal etch agitation, the etch uniformity of the initial experiments could be higher, lower, or in the middle by 25%, depending on the agitation conditions. The lateral etch uniformity was very good—less than 2%. By optimizing the agitation conditions for large plates, overall longitudinal uniformity of etch depth of <4% has been achieved simultaneously with excellent lateral uniformity.

Using the baseline etch composition of HF 22% vol/acetic acid at 21 °C, the etch rate was reduced to 2/3 its value with a temperature of 5 °C, while the surface roughness may have been reduced slightly. The surface roughness measurements were highly variable since they were not averaged much at all. The exception is the roughness of the glass before processing, and on the unetched surface after processing, and this value was consistently between 0.8 and 1.3 nm.

Trying a few experiments with other HF-type etches including nitric acid, water, and acetic acid with small amount of surfactant did not yield any dramatic changes in etch rate or surface roughness, except that in some cases the etch mask was attacked more rapidly. Attempts to use sputtered Mo as an etch mask failed because of persistent pinholes and very high stresses in the film that made it crack during etching. Cr/Au/photoresist has worked very well as a mask material: e-beam Cr (30 nm) gives excellent adhesion to the glass and the subsequent Au. Au (1 μm) gives a thick, compliant, low-stress layer that is highly etch-resistant. The top layer of photoresist (6 μm) helps to mechanically support the Au as the etch proceeds to undercut the metal mask with significant etch convection taking place. This type of coating is amenable to low particulate defects and very large substrates. This masking layer can even be blown dry with nitrogen for intermediate depth inspection, followed by continued etching.

Future Work

Continued study of Foturan® processing will include increasing etch aspect ratios and etch uniformity, and reducing surface roughness. The effect of surface pits generated during pre-etching of Pyrex wafers on device performance and potentially sealing them during bonding will be studied. The etching of borosilicate glass seems to yield an initial surface roughness of about 20 nm that doesn't get rapidly worse with increasing etch depth. The factors controlling this roughness are not well understood.

The inhomogenities and impurities in the glass have not been characterized and should be studied further. For etch depths much more than about 75 μm, improved mask materials or etch compositions will be needed.

Acknowledgments

We gratefully acknowledge the assistance of D. Hilken and L. Tarte with the lithography and etching. Support for the microchannel array portion of the genome sequencing project at LLNL is appreciated.

Reference

1. Swierkowski, S. (1997), "Large Area Lithography," Engineering Research, Development and Technology, Lawrence Livermore National Laboratory, Livermore, California (UCRL-ID-125472), p. 3-23.

Micro-Electromechanical Systems Foundry Interface

Michael D. Pocha
Electronics Engineering Technologies Division
Electronics Engineering

The goal of this project was to establish a working interface between Lawrence Livermore National Laboratory (LLNL) and one or more micro-electromechanical systems (MEMS) foundries so that we could provide LLNL programs with a one-stop service for research and development of custom microstructures. Early in the project we found that traditional foundries make most of their money from volume manufacturing and are, therefore, not interested in the small-scale work that we need. Two small custom fabrication companies were identified, one for silicon MEMS and the other for glass/ceramic component fabrication. The silicon fabrication company proved excellent, and we are beginning to use their services for programmatic projects. The glass/ceramic fabrication company could not deliver the quality of components we need, however, and we are going elsewhere for those components. This project was extremely useful in that we were able to evaluate the capability of two companies, narrowed down from a much wider field. Also, we can now provide the components needed by our programmatic customers with confidence.

Introduction

The Microtechnology Center at LLNL is primarily a research facility for design and development of microstructures and microsystems. We typically perform the research needed to develop novel microstructures for a variety of programmatic and external customers. We generally build prototypes of the devices and systems we develop, but are not equipped to provide significant production quantities. We have several customers, however, who would like small-scale production quantities of devices. Recently, several commercial companies have advertised that they provide foundry service for MEMS, just as foundries have existed for custom integrated circuits for several years.

Most of the customers who would like production quantities are working on tight budgets and schedules, and cannot afford the cost and time delay for us to establish the interface and learn how to work with foundries. A small investment in establishing this interface and learning how to work with foundries will make it much more attractive and efficient for the programmatic customers to get the services they need.

Some foundries have low-cost multi-project fabrication services if one can use their standard process. These have a well-defined interface and are easy to use. They were not addressed by this project. We were interested in establishing a process for custom fabrication that is more general and able to satisfy a broader set of our needs. We began this project by contacting three possible foundries for custom silicon fabrication. They were identified from ads in trade journals, personal contacts, and internet searches.

All three foundries told us essentially that they can only provide large volume fabrication to be profitable. Microelectronics Center of North Carolina (MCNC) gave us a quote for a small run, but it was approximately five times higher than our costs to fabricate the same component in-house. We turned, then, to small custom fabrication companies who did not consider themselves as "foundries" *per se* but were more willing to consider the small production runs that we need. There were three in the San Francisco Bay Area whom we identified primarily from personal contacts established over the years. One of these, Nanostructures Inc., has proved to be able to provide the quality and quantities we need at

reasonable cost (comparable to fabricating in-house). We have already used their services for one programmatic customer with very favorable results and are beginning to perform another run for a second customer.

In a second technology area, we are increasingly interested in fabricating components in non-semiconductor materials like plastic, glass, and ceramic. Here we identified a company, Applied Ceramics in Fremont, California, that was willing to do glass and ceramic cutting more quickly and at less cost than others. Applied Ceramics had the potential not only to perform precision drilling and cutting of substrates, but also to provide substrates of many different materials. Unfortunately, they were not able to deliver the quality of material needed. But, we found that out without having committed any of our customers' funds. This project has been very beneficial to LLNL and will save the programs considerable cost and time in the future. We highly recommend other such projects for technology-base support.

Progress

As mentioned earlier, some foundries offer a multi-project chip where several different designs from several customers are all fabricated on a single silicon wafer, thus, lowering the cost to each customer. MCNC, for example, offers such a process for three-layer polysilicon-surface micromachined components. If you can make your design fit their standard process, you can purchase custom MEMS components for as low as $2,900 per run. They also have other standard processes to choose from. We have used this option. However, only about 10% of our structures can be designed within the constraints of the standard processes. We need a procedure for procuring components requiring a larger set of fabrication technologies.

An example we chose as representative of many of the components we need to fabricate is the silicon optical microbench. These chips need to have 1) pedestals or wells etched into the silicon surface several tens of micrometers deep; 2) polysilicon deposited and doped to obtain the correct resistivity for electrically activated heaters for melting solder; and 3) metal interconnects patterned on both levels of the steps in the silicon surface created during the pedestal/well etch. This set of steps encompasses the majority of silicon micromechanical components we design and build.

We are also often designing and building components out of materials other than silicon (glass, plastic, ceramic). Here, the primary new process step is the etching and drilling of holes in these materials. Patterning of plastic is a very broad and complex subject which was beyond the scope of this project.

Two companies that we know of provide custom patterning of glass and ceramic: Bullen Ultrasonics, Inc., in Eaton, Ohio and Applied Ceramics in Fremont, California. We have used Bullen Ultrasonics in the past, and so chose to try out Applied Ceramics, geographically closer to LLNL and offering lower cost service.

Table 1 below summarizes the results of our discussions and interactions with the companies we contacted.

In summary, after our extensive search, we found one company that was able and willing to fabricate the silicon microbenches and another company to evaluate for etching and drilling of glass and ceramic substrates. The silicon microbench fabrication was more successful than the glass and ceramic substrate fabrication.

Nanostructures Inc. delivered silicon microbenches, which we were able to deliver to an LLNL program. Our customer was happy to get free parts, but more importantly, pleased that he can now purchase microbenches, in quantity, at a fixed cost. We are in the process of making modifications to the design for the next generation of microbenches to be purchased from Nanostructures Inc.

We have also just placed an order for PCR Thermalcyclers, another component that requires the same silicon etching and polysilicon resistor formation process. We anticipate out-sourcing these well-defined and relatively simple designs, ultimately saving LLNL significantly more than the cost of this project.

Our experience with Applied Ceramics was not as successful. We contracted with them to deliver ten polished Al_2O_3 ceramic wafers with holes drilled in a prescribed pattern, and to drill a similar pattern of holes in Pyrex wafers that we supplied to them. The ceramic wafers were delivered with surfaces that were too rough for our applications and the holes, although placed correctly, had very rough and chipped edges. Also, the glass wafers had severely chipped holes which are unacceptable for our applications. We will, therefore, continue to get glass and ceramic substrates from the more expensive supplier, Bullen Ultrasonics, Inc.

Table 1. Summary of foundry research.

Silicon MEMS foundries	
Microelectronics Center of N. Carolina 3021 Cornwallis Road Research Triangle Pk., NC 27709 (919) 248-1800	(MUMPS) Multi-project run. Bid - $2900 for designs that use standard three-level polysilicon-surface micromachine processing. Full custom processing such as the silicon microbench; only interested if production lots are sufficiently large to be profitable to produce. Bid - $53,000.
Standard Microsystems Corp. 35 Marcus Boulevard Hauppauge, NY 11788 (516) 435-6961	Set up for volume production of silicon components; only interested at the 100 to 1000 parts per week level. No bid.
MEMStek Products, LLC 2111 SE Columbia Way Suite 120 Vancouver, WA 98661	Specialize in microfluidic delivery systems such as pumps and valves. Not interested in general MEMS. No bid.
Small custom fabrication	
MicroFlow Inc. 6701 Sierra Court Dublin, CA 94568 (925) 828-9650	Initially interested in bidding on our project, but were just acquired by a large custom house, Input/Output Inc., Houston, Texas. While we were in discussions, the new management made the decision that this project was too small to warrant further effort, so discussions ended. No bid.
TiNi Alloy Company 1621 Neptune Drive San Leandro, CA 94577 (510) 483-9676	Specialize in shape memory alloy actuated devices using Ti and Ni alloys. Had some initial interest in silicon fabrication to expand their capability, but while we were discussing our requirements, decided to concentrate on their core business. No bid.
Nanostuctures Inc. 3070 Lawrence Expressway Santa Clara, CA 95051 (408) 733-4345	Interested in our job. Bid $9500. Successfully fabricated microbenches.
Non-silicon fabrication	
Applied Ceramics 850 Corporate Way Fremont, CA 94539 (510) 249-9700	Delivered glass and ceramic substrates with holes in specified locations. Bid - $4150. Fabricated parts, but unacceptable quality.

Even this negative experience was useful because it confirmed that we were getting our glass and ceramic substrates from the most cost effective source.

Future Work

This was an excellent technology-base project. We recommend that each year a small amount of technology-base funding be set aside for the identification and evaluation of vendors to supply well-defined, non-research components. We can concentrate our more expensive resources (people and equipment) on the research we do best, but still supply our customers who need them a significant quantity of production components.

Acknowledgment

The author would like to thank H. Ackler at LLNL for conducting the non-silicon fabrication part of this project.

Hydrogel-Actuated Implantable Sensor

Amy W. Wang, Abraham P. Lee, and Charles F. McConaghy
Electronics Engineering Technologies Division
Electronics Engineering

Christopher B. Darrow, Stephen M. Lane, and Aleksandr Gilman
Medical Technologies Program

Joe H. Satcher, Jr.
Chemical Sciences Division
Chemistry and Materials Science

With this project we seek to demonstrate hydrogel-based transduction and telemetry technologies that could lead to a new class of implanted medical sensor devices. An implanted sensor is useful for any patient who must monitor a particular blood analyte and, thus, requires frequent extraction of blood samples. Examples include electrolyte and pH measurements (potassium, sodium, calcium) for many chronically ill patients, urea and potassium for dialysis patients, immuno-suppressant drugs for transplant and AIDS patients, anti-coagulants for many heart and stroke patients, and glucose for diabetic patients. We envision a wristwatch-sized, externally-powered component worn by the patient, which interrogates a passive, implantable element.

Introduction

Hydrogels are a class of polymers that have a high capacity for water absorption. Typical mass increases for the hydrated state of such polymers, for example, poly-hemas (PHEMAs), may be 10 to 100 times, and swelling volume ratios of up to 30% can be achieved. We are interested in suitably modified polymers that, in the hydrated state, exhibit reversible swelling in response to a change in pH, osmolarity, temperature, pressure, or the concentration of some analyte of interest. Enzymes can be embedded in the hydrogel to create specificity to a given analyte.

Currently, hydrogels are commercially used in absorbents, thickeners, dilators, and as osmotic pumps. However, few researchers have used hydrogels as an actuator for micromechanical structures. With the swelling volume achievable by these polymers, significant mechanical work may be accomplished.

Progress

We have demonstrated a micro-electromechanical system (MEMS) sensor that is sensitive to the concentration of an ionic solution, and a prototype passive resonant circuit that can be used for remote interrogation of the device. The sensor is actuated by a biocompatible PHEMA hydrogel that swells or shrinks in response to variations in concentration of an ionic solution. It consists of a silicon cell that encapsulates the hydrogel between a deformable membrane and a liquid-permeable mesh chip (**Fig. 1**).

As the hydrogel changes dimensionally in response to an analyte in solution, it flexes a deformable, conducting membrane that forms one plate of a parallel plate capacitor. The capacitive variation can be monitored by incorporating the hydrogel capacitor into a resonant LC circuit, such that a change in analyte concentration is reflected by a shift in resonant frequency of the circuit.

This design can be used in an implantable system in which a signal is sent transdermally, sweeping a range of frequencies to interrogate the implanted device and detect variations in resonant frequency. The signal can be transmitted or reflected back to the interrogating circuit, which is mounted at the skin surface in a readout package similar to a wristwatch.

Silicon Cell

The silicon cell encapsulating the hydrogel consists of two silicon chips bonded together. One wall of the cell is a deformable membrane formed from a 2-µm-thick biocompatible NiTi-based film sputtered on a 0.5-µm silicon nitride membrane. Nitride membranes are formed by silicon etching in potassium hydroxide (KOH). We found that NiTi-based membranes are preferable to gold-coated silicon nitride membranes in durability, since contraction of the polymer during drying results in breakage of the gold-nitride membranes. The NiTi-based membranes were used successfully and found to be quite robust.

The opposite wall of the cell consists of a rigid mesh made up of a 50-µm-thick silicon chip with 100- to 200-µm-size holes etched through its thickness. The mesh allows exposure of the hydrogel to the ambient analyte solution, while constraining the hydrogel. Fabrication of the mesh involves double-sided exposure of the mesh area and mesh holes on a silicon wafer, then simultaneous KOH silicon etching from both sides of the wafer, thinning it down to a thickness of 50 µm and etching through the holes.

Hydrogel Testing

Both uncross-linked and cross-linked PHEMA hydrogels were tested for swelling in response to the concentration of a calcium nitrate solution. Uncross-linked PHEMA gels were dissolved in methanol, pipetted into the silicon cell in liquid form, then dried before rehydration in water.

Cross-linked gels were dried in a nitrogen environment before rehydration. Gel swelling was observed for both types of gels, but cross-linked polymers exhibited more lateral swelling, rather than out-of-plane swelling that would displace the flexible membrane.

Uncross-linked PHEMA displayed good out-of-plane displacement, and increased swelling was observed with increasing salt concentration.

Optical membrane displacement measurements showed 4 µm, 20 µm, and 30 µm peak displacements for calcium nitrate concentrations of 0.5 M, 1 M, and 3 M, respectively. **Figure 2** shows an example of an optical measurement of membrane displacement (~30 µm) due to polymer swelling. At high salt concentration, the polymer began to extrude through the holes of the mesh chip due to "untangling" of the polymer strands. A thin layer of "stiffer" polymer used between the PHEMA and the mesh chip reduced the amount of extrusion. We have yet to determine hysteresis effects of the hydrogel.

Interrogation Circuitry

We have also built a resonant antenna circuit in which an inductor coil remotely probes a passive LC circuit. A network analyzer was used to sweep the interrogation frequency and measure the power reflected back through the inductor to indicate the resonant frequency (minimum reflected power) as shown in **Fig. 3**. We were able to interrogate the passive circuit with the inductor 5 mm away from the circuit, a distance that is sufficient for a sensor implanted directly beneath the skin. From optical displacement measurements, we predicted capacitive

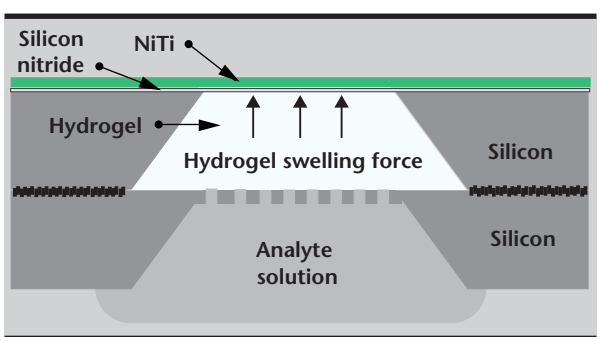

Figure 1. Diagram of hydrogel-actuated silicon MEMS cell. Hydrogel swelling in response to an analyte causes deflection of a conductive membrane and a resultant change in capacitance of a parallel plate capacitor.

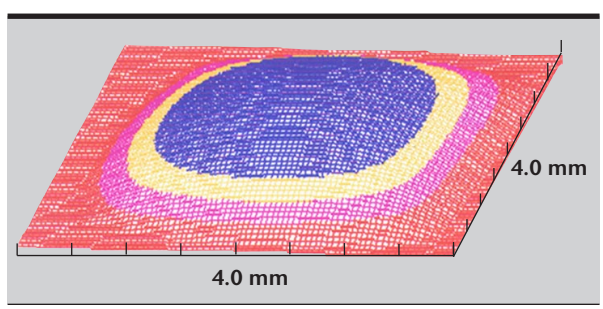

Figure 2. Optical measurement of membrane deflection due to hydrogel swelling.

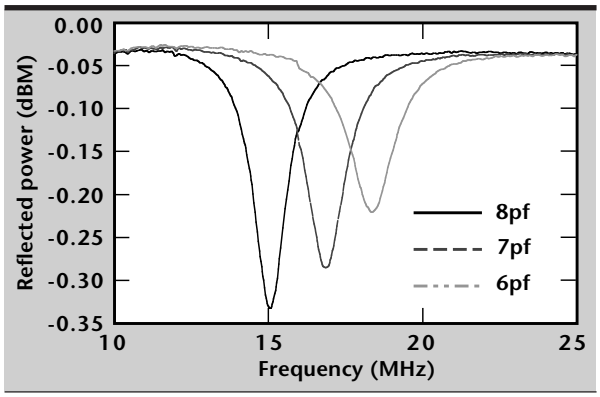

Figure 3. Reflected power from the resonant circuit. Resonance is indicated by minimum reflected power. Capacitive variations of 1 pF result in approximately a 1.5-MHz shift in an 18-MHz resonance frequency.

changes on the order of 1 pF due to polymer swelling. Using our antenna circuit, we were able to detect 1-MHz shifts in an 18-MHz resonant peak for incremental changes of 1 pF (**Fig. 3**).

In summary, we have demonstrated that significant shifts in resonant frequency can be observed as a result of hydrogel swelling, and that it is feasible to implant a passive circuit and use telemetry to interrogate the implanted element.

Acknowledgments

The authors gratefully acknowledge H. Ackler and P. Krulevitch for their ideas, discussion, and processing advice, and P. Ramsey for the deposition of the NiTi films.

Lambda Connect: Multi-Wavelength Technologies for Ultrascale Computing

Robert J. Deri, Michael C. Larson, and Michael D. Pocha
Electronics Engineering Technologies Division
Electronics Engineering

Mark E. Lowry
Defense and Nuclear Technologies

Byte-wide, multi-wavelength optical interconnects can substantially improve the performance of the system interconnects used in ultrascale computing platforms ("supercomputers"), leading to substantial improvements in overall system performance for applications that require global communications within the supercomputer. This year, we have developed the first generation of optical hardware required for such interconnects: byte-wide multi-wavelength transmitters and wavelength filters. The performance of these prototypes demonstrates the viability of our approach.

Introduction

Ultrascale computing—the integration of large numbers of processors into a single, highly capable multi-processor system—is currently of great interest in several government programs. These systems contain 100s to upwards of 1000 CPUs, to attain computing capabilities from 100 GFLOPS to 100 TFLOPS and beyond.

The provision of fast data communications within such systems poses a significant challenge. Effective communication is currently hampered by the bandwidth, latency, and congestion characteristics of the electronic fabric used to interconnect the many system-processing and memory elements. This communications bottleneck can substantially degrade computational performance, significantly complicate programmability, and cause inefficient use of costly memory resources.

The recent emergence of byte-wide optical interconnects, which use linear arrays of multi-mode optical fibers in a ribbon cable assembly, has substantially improved the cost and performance of Gbyte/s point-to-point communications. To fully leverage this technology, however, the latency and congestion issues with distributed electronic switching must be overcome.

We have recently proposed source-routed switching in the optical domain using a wavelength-switching mechanism. We have shown that this approach can yield highly capable switches that support 100s of Gbyte/s ports and yield minimal internal congestion and latency. Instruction-level simulation has demonstrated the advantages of this approach.[1]

To implement this multi-wavelength optical interconnect requires the addition of multi-wavelength capability to the existing byte-wide optical interconnect. The required components, which include optical transmitters capable of fast wavelength tuning, and fixed optical filters differ substantially from existing telecommunications fiber optics. All components must be compatible with existing multi-mode fiber ribbon cables, and provide compact form factors suitable for populating electronics boards.

This project aims at developing prototypes of these components, to investigate the feasibility of implementing byte-wide, multi-wavelength optical interconnects for ultrascale computers.

Progress

Multi-Wavelength Transmitters

We have developed prototype modules with the capability of transmitting on any of two or four selectable wavelengths. The module wavelength is selected by directing current into different lasers, each laser emitting at a different wavelength, so that current switching is used to provide fast wavelength switching on a timescale of the laser modulation bandwidth (1 to 2 ns switch time). Each module contains one linear array of 10 laser diodes for each

wavelength. Each array element can be independently addressed (modulated) by a current drive, so that the module can transmit 10 independent data streams comprising the 8 bits in an electronic data word of 1 byte capacity, plus clock and framing.

Our modules use arrays of vertical cavity, surface-emitting lasers (VCSELs), which we have fabricated from AlGaAs semiconductor layers grown by molecular beam epitaxy. Our VCSEL design uses an oxidized AlAs layer to control the "active region" of the laser which is pumped by the applied current drive, to achieve lasing threshholds of 2 mA for devices of 5 to15 µm oxide aperture.

The VCSELs are sized to emit in multiple transverse modes (1.5 nm spectral extent), to minimize speckle noise during multimode fiber transmission. These devices provide milliwatts of optical power when pumped with <10 mA at ≤3 V, conditions compatible with conventional CMOS electronic drive electronics. **Figure 1a** shows a typical VCSEL optical output characteristic as a function of drive current.

We use a separate VCSEL array chip for each selectable wavelength in our modules, with each chip originating from a separately processed AlGaAs wafer. This approach enables us to select an arbitrary spacing between system wavelengths, and enables the system wavelengths to span a very wide spectral range (many 10s of nanometers). This is attractive because it allows a moderate channel separation (8 to 10 nm) that minimizes issues associated with wavelength registration, uniformity, and drift between different photonic components within the interconnect.

This year, we demonstrated a dual-wavelength transmitter module that can launch light of either 815 or 830 nm into all 12 fibers in a ribbon cable. The optical signals are independently addressable, and originate from two VCSEL chips with approximately 6 µm oxide apertures.

Figure 1b shows our ceramic pin-grid-array (cPGA) module, which contains two laser chips. Each laser chip provides a different wavelength, and the emitters from both chips are coupled into a single fiber using passive optical alignment to a standard ribbon cable.

The dual-wavelength module exhibits good performance, as shown by the optical spectrum and 400 Mbit/s eye pattern of **Fig. 2**. The spectrum shows simultaneous emission into a single fiber from two wavelengths, with signal-to-noise ratios of 30 dB. All laser elements are functional, and deliver >2 mW of optical power into the fiber cable.

We have verified that the packaged lasers are suitable for high speed operation by observing their performance under high-speed modulation.

Our cPGA package exhibits resonance-free performance to 300 MHz when mounted with appropriate external impedance matching resistors. We anticipate that the module frequency response can be extended to the VCSEL device limit of several GHz by using suitable internal terminations and driver electronics, and possibly by transitioning to a higher-speed ceramic package.

We evaluated our module's transmission performance in a link using a commercial 400 Mbit/s receiver which performs some reshaping. The resulting eye pattern (**Fig. 2**) exhibits an open eye and measured bit error rates below 10^{-14} at 400 Mbit/s per fiber for a pseudo-random bit stream of sequence 2^{23}-1 bits.

We extended our optical packaging approach to a four-wavelength transmitter module by using a proprietary, optical superstrate assembly. This assembly combines optical signals from four VCSEL

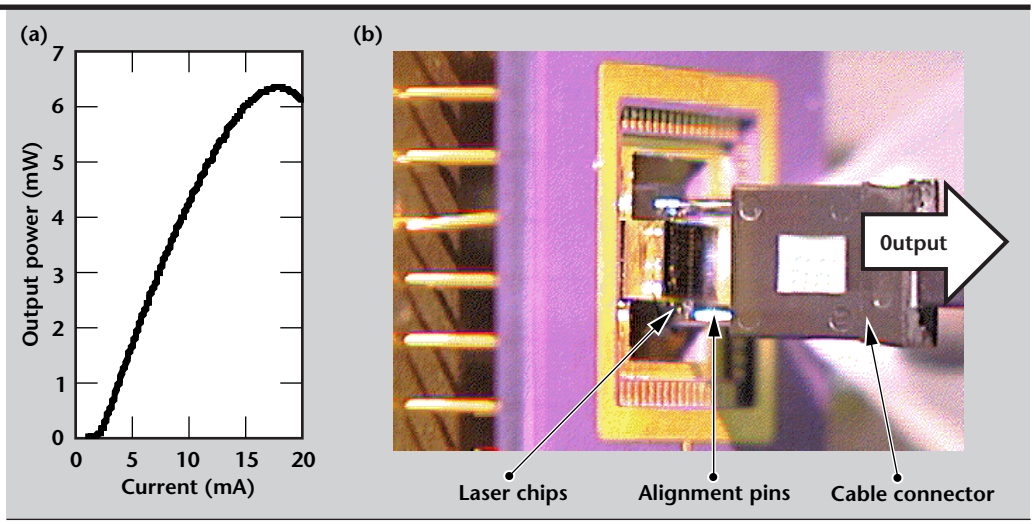

Figure 1. Dual-wavelength transmitter module: (a) light output vs drive current for VCSEL device (unpackaged); (b) overall ceramic PGA module, showing alignment to a fiber ribbon cable. The cable connector is 6.4 mm wide.

arrays, operating at wavelengths 823, 843, 971, and 986 nm. **Figure 3** shows the complete four-wavelength module in its cPGA package, and its output spectrum when all wavelengths are simultaneously activated. The module uses a similar guide pin approach for connecting to ribbon cable assemblies.

Byte-Wide Filter Modules

We have developed optical filter modules based on the packaging of thin-film interference filters within a housing comprised of ribbon cable connector ferrules.[2] The advantages of this approach are that 1) the module is assembled primarily by passive alignment using interlocking guide pins, and 2) the module automatically mates to ribbon cable connectors.

This year, we extended our filter approach to narrow band filters and to improved transmission characteristics for enhanced system channel spacing and wavelength tolerances.

Table 1 summarizes the performance of modules using single-cavity Fabry-Perot filters. The data show that acceptable insertion loss can be achieved for filter bandwidths as small as 4 nm. Modules with the broader (14 nm) passband have been cascaded in series to improve cross-talk suppression and to achieve somewhat narrower passbands. The modules exhibit a fiber-to-fiber wavelength uniformity (±1 nm) sufficient for channel spacings of several nanometers.

Filter modules with a flatter top and sharper skirts than are obtainable from the Lorentzian lineshape associated with single cavity designs are valuable, because they improve system tolerances to variations and drifts in the wavelengths of individual transmitter and filter modules, and enable tighter spacing of wavelength channels.

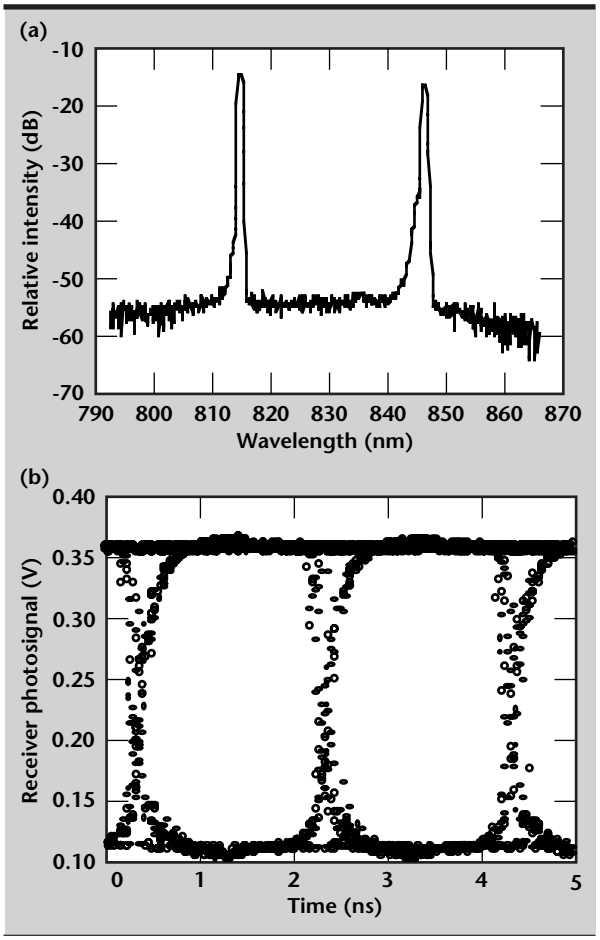

Figure 2. Dual-wavelength module spectrum (a), and high-speed signalling performance (eye diagram)(b). Note that the spectrum is displayed on a logarithmic (decibel) scale.

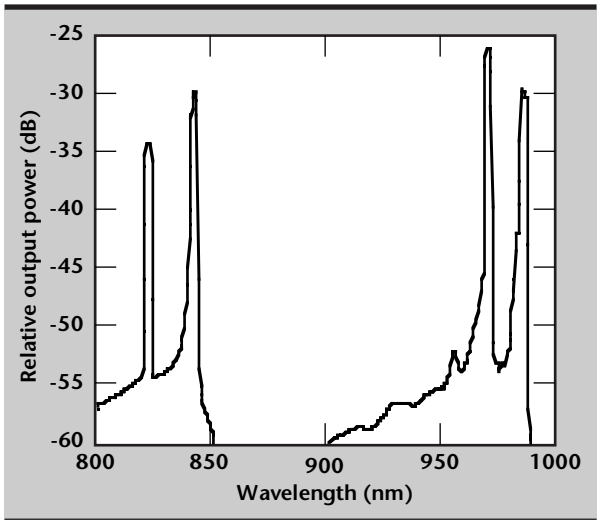

Figure 3. Output spectrum of four-wavelength module in cPGA. Note that the spectrum is displayed on a logarithmic (decibel) scale.

Table 1. Single cavity Fabry-Perot filter characteristics.

Filter bandwith	14 nm	4 nm
Number of layers in Bragg reflector	12	20
Packaged insertion loss (dB) average, <best>	1.5 <0.8>	2.7 <1.9>
Unpackaged insertion loss (dB) (collimated beam)	0.76	1.1
Cross-talk suppression (dB)	-11 (no cascade)	-19

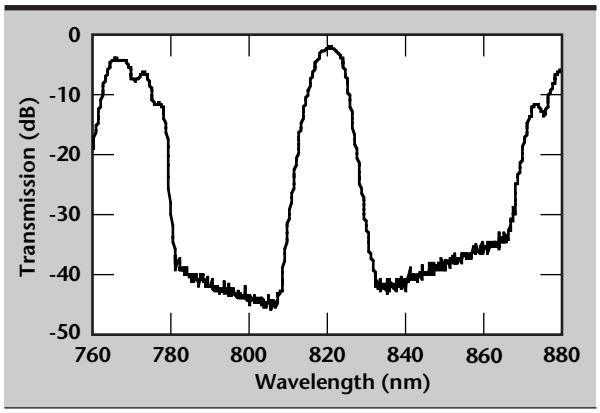

Figure 4. Transmission response of multi-cavity filter module.

We have demonstrated such a filter module, based on a multi-cavity interference filter design. Its reponse (**Fig. 4**) shows a flatter top and substantially sharper filter skirts than are achievable with single cavity devices, and exhibits cross-talk suppression better than 30 dB. Filter skirt sharpness can be quantified by the ratio of the filter's 3 dB bandwidth to 20 dB bandwidth. This ratio is 0.48 for the device of **Fig. 4**, three times sharper than our single cavity devices. This device is suitable for channels spaced 8 to 10 nm apart, and provides a 5-nm tolerance window for component wavelength variations (at 1 dB excess loss).

Future Work

These results demonstrate the feasibility of high-performance optical components for byte-wide, multi-wavelength optical interconnects, showing that compact, high-performance transmitter and filter modules can be realized for systems using four wavelength channels.

Our goal for next year is to demonstrate components enabling systems with higher wavelength count, since earlier simulations showed that eight system wavelengths are required for several interesting multiprocessing applications.[2] We also intend to develop additional passive routing devices for byte-wide interconnects, including N-to-N star broadcast components.

Acknowledgments

This project has benefited substantially from the efforts of M. Emanuel, H. Garrett, W. Goward, R. Patel, and H. Petersen of LLNL, and from contributions by Prof. C. Gu (University of California, Santa Cruz), and Prof. R. F. Drayton (University of Minnesota).

References

1. De Groot, A. J., and R. J. Deri (1996), *Proc. Third Intl. Conf. Massively Parallel Processing using Optical Interconnections*, IEEE, October.

2. Deri, R. J., and S. Gemelos (1998), "Simple fabrication of WDM filters for byte-wide, multimode cable interconnects," *Integrated Photonics Research Conf.*, Victoria, Canada, April.

Kenneth L. Blaedel, Center Leader

The mission of the Center for Precision Engineering at Lawrence Livermore National Laboratory (LLNL) is to ensure that programs have available an adequate base of high-precision design and manufacturing technology, not necessarily resident at LLNL, to help solve their critical future problems.

Our specific goals are 1) to develop an understanding of fundamental fabrication processes and the models that reflect that understanding; 2) to advance methods of the design of machinery that incorporate those fabrication processes; and 3) to maintain continuing relationships among our colleagues in industry, government and academia that promote our collective capabilities in precision engineering.

In support of these goals, three projects are reported here that bring either higher precision or lower cost-of-precision to the manufacturing challenges that we face over the next few years.

The first project, "Micro-Drilling of Beryllium Capsules," has seen significant advance. Last year's conclusion was that the evolutionary changes in commercial capability could not be expected to laser-drill holes small enough and precise enough for future National Ignition Facility (NIF) capsules. This year's result, which included holes made with a femtosecond laser, holds promise for being able to do so.

The second report, "A Spatial-Frequency-Domain Approach to Designing Precision Machine Tools," presents a new view of how we can design machine tools and instruments to make or measure parts that are specified in terms of the spatial frequency content of the residual errors of the part surface. This represents an improvement in our ability and a reduction in cost to design manufacturing machines in comparison to using an "error budget," a design tool that saw significant development in the early 1980s, and has been in active use since then.

The third project, "Precision Grinding of Microfeatures in Brittle Materials," demonstrates our ability to develop high-precision manufacturing processes and then convey them to commercial industry, which can then supply that technology for high production.

In addition to conducting the three projects above, the Center for Precision Engineering holds membership in two academic consortia, allowing us insight into broader areas of precision engineering that we cannot pursue ourselves.

Looking to the future of precision engineering at LLNL, we have drawn two conclusions. First, conducting the business of LLNL will require machinery capable of material removal, deposition, and metrology to produce components and assemblies to atomic-level dimensional tolerances. Second, significantly reducing the cost of precision for component manufacture and for assembly of precision products will actually enable many LLNL projects. It is in projects such as NIF that the expenses of precision manufacturing can defeat big physics.

With the focus of this year's projects on creating high-precision processes and instruments at acceptable cost, we think the Center for Precision Engineering has materially contributed to LLNL's ability to field small- and large-scale science.

Center for Precision Engineering

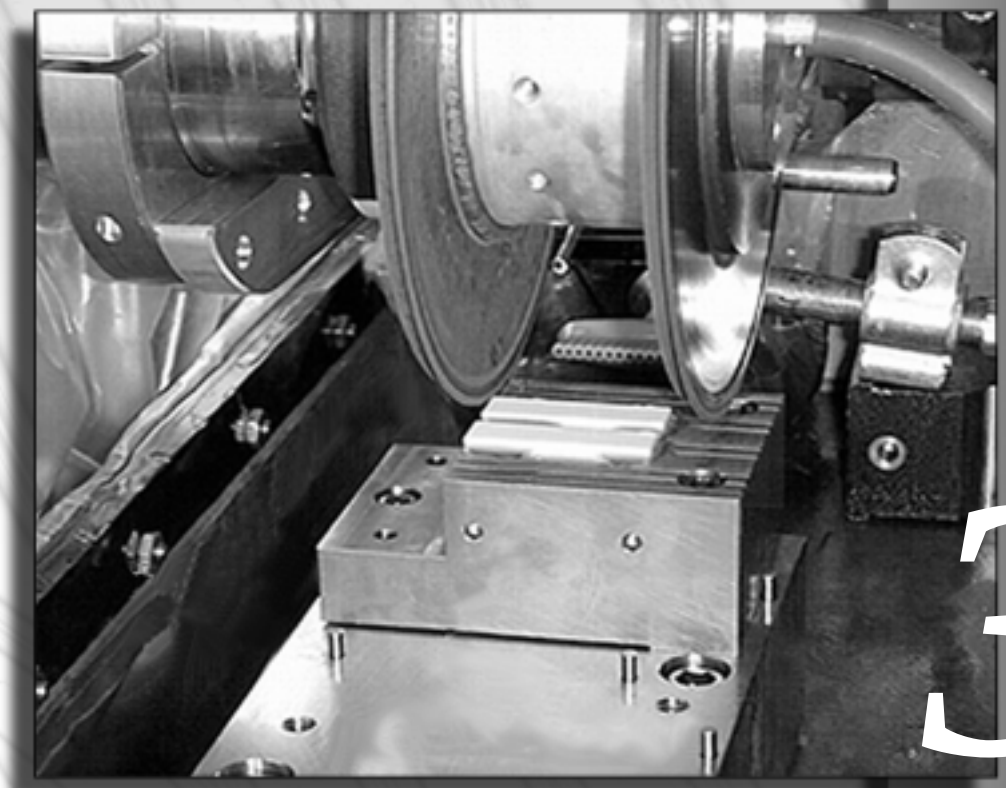

3

3. Center for Precision Engineering

Overview
Kenneth L. Blaedel, Center Leader

Micro-Drilling of ICF Capsules
Steven A. Jensen and Brent C. Stuart *3-1*

A Spatial-Frequency-Domain Approach to Designing Precision Machine Tools
Debra A. Krulewich *3-3*

Precision Grinding of Brittle Materials
Mark A. Piscotty, Kenneth L. Blaedel, Pete J. Davis, and Pete C. Dupuy *3-9*

Micro-Drilling of ICF Capsules

Steven A. Jensen
Manufacturing and Materials Engineering Division
Mechanical Engineering

Brent C. Stuart
Laser Science and Technology
Laser Programs

Further studies are reported on micro-drilling of holes in fusion capsules. This update outlines the preliminary efforts using short-pulse (≈100 fs) lasers to potentially drill holes in the ICF capsules.

Introduction

This report serves as an update to "Micro-Drilling of ICF Capsules."[1] In that report the commercial capabilities of micro-drilling small holes were investigated for limits of precision, quality, and attainable aspect ratios. The motivation behind the investigation was to determine the feasibility of drilling small holes in the National Ignition Facility (NIF) fusion capsules, suitable for filling with the intended fuel mixture.

The report concluded that although the micro-drilling of holes in the fusion capsules is feasible, the commercial sector currently cannot produce these holes. SEM photos of commercially drilled holes showed an excessive amount of thermal damage (that is, dross, re-melt, and thermal cracking) due to laser pulse lengths of relatively long durations (nanosecond and longer). Melt-expulsion, and not evaporative ablation, largely dominates the mechanism behind commercially drilled holes.

Furthermore, most commercial companies are not equipped with the appropriate lenses and laser set-up to drill holes smaller than 5 µm because current demand is limited. It was speculated in the FY-97 report,[1] based solely on published data, that lasers with pulse lengths in the femtosecond to 0.1 ps range could eliminate much of the thermal damage and potentially produce small enough holes to meet stringent NIF requirements.

This update outlines the preliminary efforts using short-pulse (≈100 fs) lasers to potentially drill holes in the ICF capsules.

Progress

The ICF capsules will be made of doped beryllium (Be) having an ablator shell thickness between 100 and 150 µm. Therefore, the goal of the preliminary studies was to drill 5-µm or smaller holes through 125-µm-thick Be foil. In our experiments the Be foil was mounted on a xyz-translation stage in a vacuum chamber pumped down to 25 mTorr. The experiments were performed using a 1-kHz, 120-fs, Ti:Sapphire short-pulse laser system. Numerous combinations of spatial filtering, focus lens, f-number, and wavelength were tried and the best focal spot obtained was 5-µm $1/e^2$ diameter (where spot size is defined as the distance at which the Gaussian beam intensity has dropped to $1/e^2$ = 0.135 times its peak value).

To achieve this, the laser output was spatially filtered, frequency doubled to 413-nm, spatially filtered again, and then focused with a 25-mm focal length GRIN lens (LightPath) at approximately f-number = 5. Both the quality of the BBO doubling crystal ($\lambda/2$ surface) and the choice of focusing lens leave room for reducing the focal spot size.

SEM images, after ultra-sonic cleaning, of one of the smallest holes obtained are shown in **Fig. 1**. The entrance diameter is approximately 6.5 µm, while the exit diameter is approximately 3 µm. This gives a taper angle of approximately 1.6° which is significantly better than the 4 to 12° that was seen in commercially drilled holes. This hole was drilled with approximately 1.8-µJ pulses (18J/cm^2) at 1 kHz in 12 s.

These preliminary studies are encouraging. The diameter of the heat-affected zone is much smaller than commercially drilled holes. There were no visible signs of thermal cracking and the re-melt around the walls was minimal. Furthermore, the taper angle associated with the hole is much smaller than has been seen in commercially drilled holes. It is speculated that the focal spot size can be further reduced to approximately 2 μm in diameter by using a smaller f-number and possibly third harmonics. With some fine-tuning of parameter settings these holes could potentially meet NIF standards.

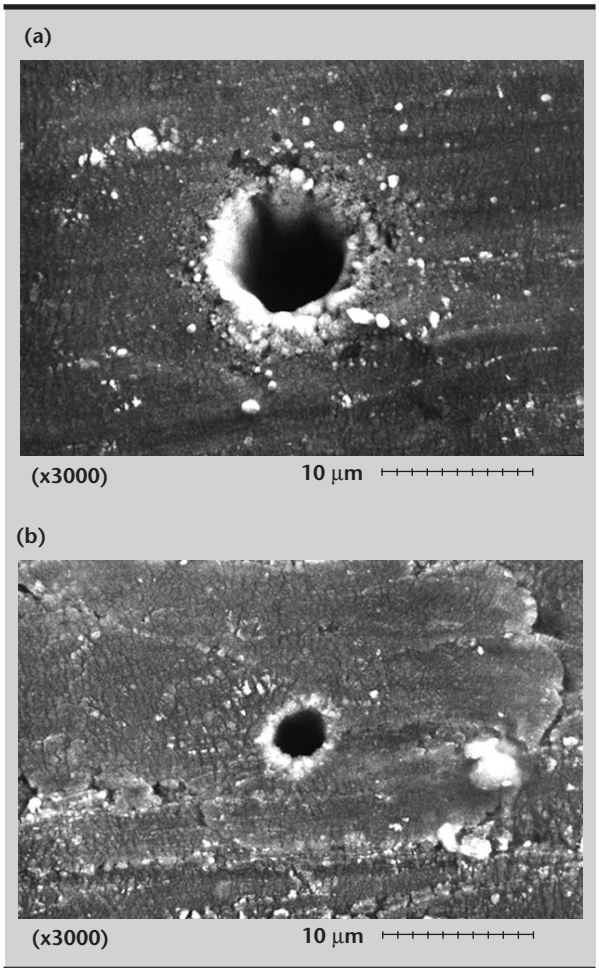

Figure 1. SEM images of smallest holes obtained: a) entrance hole; and b) exit hole.

Having performed these preliminary studies and prior to further studies, the question of "how small is small enough" remains to be answered. Initial indications suggested that entrance hole diameters on the order of 1 to 2 μm in diameter would be small enough. However, studies need to be performed which ultimately back up these initial estimates and quantify the largest allowable capsule perturbation that would affect the hydrodynamic stability and hinder a symmetrical implosion. Whether this work is done experimentally or through simulation, it is necessary to validate the continued efforts of reducing and refining the micro-drilled hole.

Assuming that a 1- to 2-μm hole would be sufficiently small, there are still issues that must be resolved if this approach to capsule filling is to succeed. The hole will need to be sealed shut once the capsule is filled with the intended fuel mixture of deuterium-tritium (DT). The sealing process, like the drilling process, will have to minimally affect the integrity and surface quality of the capsule. Work needs to be done to determine the extent and size of the area around the hole affected by the sealing process. Ideally it would be desirable to use the same laser set-up to seal the holes as was used to drill them. This might be accomplished by reducing the intensity of the beam and/or using longer pulse durations to sinter the hole shut. The feasibility of this approach also remains to be studied.

In addition to the sealing process, a micro-polishing process may be necessary to smooth over ablator shell perturbations due to the sealing process. This would also help to ensure a surface roughness that meets specifications. Currently, the specification for surface roughness is on the order of 10 nm rms or less, and efforts thus far have not produced capsules with a surface roughness less than 50 nm rms. Micro-polishing of the capsules needs to be studied, since this process may be needed even if diffusion filling is adopted as the approach to capsule filling.

Reference

1. Jensen, S. A., "Micro-Drilling of ICF Capsules," *Engineering Research, Development and Technology*, Lawrence Livermore National Laboratory, Livermore, California (UCRL-ID-129204).

A Spatial-Frequency-Domain Approach to Designing Precision Machine Tools

Debra A. Krulewich
Manufacturing and Materials Engineering Division
Mechanical Engineering

The aim of this project is to develop a methodology to design machines used to manufacture parts with spatial-frequency-based specifications, thus reducing risk while maintaining accuracy. Using in error budget, we are able to minimize risk during the design stage by ensuring that the machine will produce components that meet specifications before the machine is actually built. Minimizing the risk while maintaining accuracy is a key manufacturing goal for programs that cannot tolerate yield factors less than 100%, such as the nuclear weapons program. Current error budgeting procedure provides no formal mechanism for designing machines that can produce parts with spatial-frequency-based specifications. However, recent specifications for advanced optical and weapons systems are being posed in terms of the continuous spatial frequency spectrum of the surface errors on the machined part. Based on these requirements, it is no longer acceptable to specify tolerances in terms of a single number that spans all temporal and spatial frequencies. During this project, we will develop a new error budgeting methodology to aid in the design of new machines used to manufacture parts with spatial-frequency-based specifications.

Introduction

Increased precision in manufacturing is being demanded by Lawrence Livermore National Laboratory (LLNL) Programs in areas ranging from NIF optics manufacturing and ICF target positioning, to the production and alignment of optics for EUV lithography. Other LLNL areas that drive unique requirements for precision include the machining of diffractive optical systems, the fabrication of ICF targets, and the assembly/packaging of fiber optical systems.

The precision-to-cost ratio is another metric that relates to a wide variety of industrial mechanical systems, such as automotive engine components, but has a special significance at LLNL where an increased interest in tighter tolerances is matched by the need to lower program costs. Minimizing technical risk while maintaining precision is a complementary issue that defines manufacturing goals for programs that cannot tolerate yield factors less than 100%, such as in fabricating components for the nuclear weapons program.

This project presents an opportunity to significantly improve the foundation that underlies our precision engineering expertise: the process of formulating an error budget for a manufacturing, positioning, or measurement system. Error budgets provide the formalism whereby we account for all sources of uncertainty in a process, and sum them to arrive at a net prediction of how "precisely" a manufactured component can meet a target specification. The error budgeting process drives decisions regarding the conceptual design of the system and choice of components and subsystems, and enables a rationale for balancing precision (performance), cost, and risk.

The principles of designing precision instruments for meeting challenging tolerance requirements have a rich history.[1] Likewise, the methodologies for analyzing the errors in experimental data and performing differential sensitivity analyses are well-documented.[2,3] Yet the first clear formalization of error budgeting applied to precision engineering appears to originate in the analysis by R. Donaldson during the design of the Large Optics Diamond Turning Machine at Lawrence Livermore National Laboratory (LLNL).[4] Donaldson's formalism is referenced in current textbooks[5] and is the basis for subsequent machine designs at LLNL.[6]

Figure 1 shows flowcharts for both the conventional and the new error budget procedure and how they differ. The upper portion of **Fig. 1** shows Donaldson's flowchart illustrating the mapping of error sources onto part geometry.

The first step of the conventional error budget is to identify the physical influences that generate the dimensional errors that propagate through the machine tool. These include effects such as thermal gradients and temperature variability, bearing noise, fluid turbulence in cooling passages, and way non-straightness.

The second step is to determine how this source couples to the machine. A coupling mechanism converts these physical influences into a displacement that has a direct influence on machine performance. An example of a coupling mechanism is the thermal expansion that may transform a time-varying heat source in the vicinity of the machine into a machine way distortion. These displacements represent dimensional changes in the system. A single peak-to-valley number is usually used to quantify the dimensional changes, not differentiating between the spatial frequency content of the error.

The next step is to sum all the contributing errors using an appropriate combinatorial algorithm. Literature suggests a variety of combinatorial algorithms.[7]

The last step in the error budgeting procedure is to transform these errors into the workpiece coordinate system. To convert these machine displacements into the errors that would reside on the workpiece surface in the directions of interest, we must consider the tool path (feed rates and spindle speeds, for example).

The output from this procedure is a single number predicting the net error that would result on a machined workpiece. We would then compare this number to the part specifications. If the prediction meets target specifications, we would accept the machine design under evaluation. If the prediction does not meet specifications, we would evaluate methods to improve this design by observing which sources are the dominating contributing errors. In this way we can evaluate the cost vs accuracy of different candidate designs.

If improvements could be made to an existing design, we would make those changes to the error budget and reevaluate the net error. If the modifications were not practical, we would then consider an entirely new design, or possibly reevaluate the specifications.

Progress

The lower portion of **Fig. 1** shows the new error budget approach. The first two steps, identifying the sources and how they couple to the machine, are identical and are explained in the previous section. However, the new approach differs in the next step, where the elemental errors are converted into the frequency domain. The next step is to combine the errors in the frequency domain. The combinatorial rule is a completely new algorithm with a statistical foundation. These steps are explained below.

Figure 2 displays a block diagram of the machining process. During cutting, an instantaneous amount of material is removed, which creates forces. The ratio between the cutting force and amount of material removed is the material removal transfer function. These cutting forces combine with forces induced by the machine errors. The machine structure responds with displacements that ultimately result in errors on the machined part.

The conventional error budgeting approach does not consider the dynamics of the material removal transfer function. In other words, the conventional approach assumes that the forces are directly proportional to the amount of material removed, so the cutting process doesn't damp or amplify the error sources at certain frequencies. Our proposed

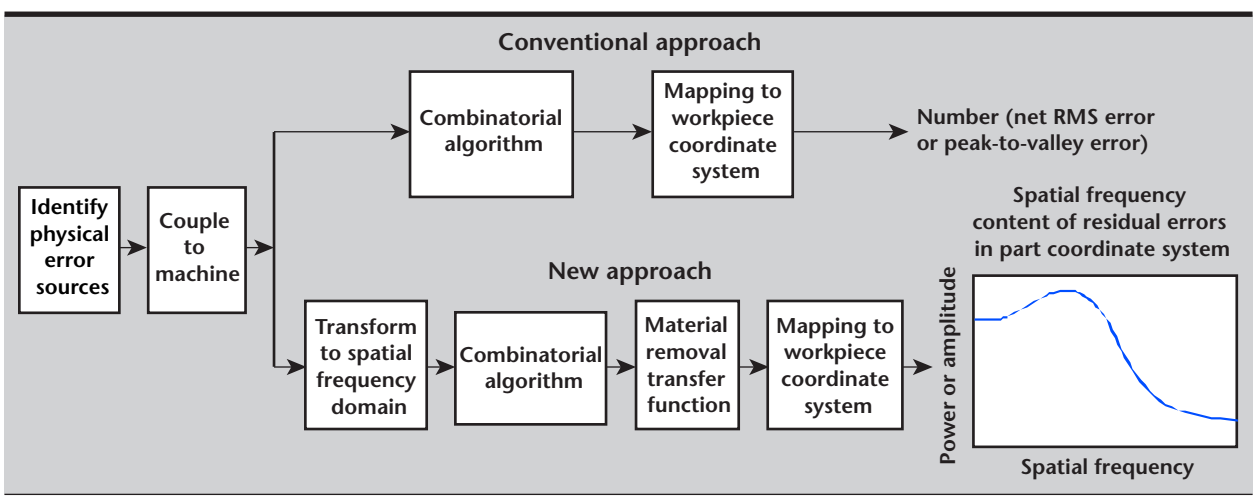

Figure 1. Flowcharts for both the conventional and the new error budget.

approach considers the dynamics of the material removal transfer function. The last step is to transform the errors into the part coordinate system. The output from this process is the continuous spectrum of errors at all spatial frequencies on the part. Each component in this block diagram is described below.

We are performing experimentation and validation of each step in the error budgeting procedure on a T-based lathe. Test results are also discussed in the following sections.

Transforming Errors into Spatial-Frequency Domain

Conventionally, a single peak-to-valley number is used to quantify the dimensional changes, not identifying the spatial frequency content of the error. This new approach requires us to determine the full frequency spectrum of the errors. To do this, we must relate the error characteristics to physical properties of the system. Forces generate the dimensional errors. The machine structure responds to these forces due to the compliance of the machine, as shown in the block diagram of **Fig. 2**.

Often the forces are related to physical properties of the machine, such as the cycling of the rolling elements in bearing systems or the number of poles in a motor. However, when these forces are at or near the machine resonances, the displacements caused by these forces are amplified.

While the frequency content of the error forces is often fixed in the spatial-frequency domain, the machine resonance is fixed in the temporal-frequency domain. The spatial frequency is converted to the temporal frequency by multiplying the spatial frequency by the velocity. While the spatial frequency content of the force error may be independent of velocity, the spatial frequency content of the displacement error is dependent on velocity.

For example, consider a machine with a resonance at 100 Hz. If the axis velocity is 10 in./min, then 600 cycles/in. is equal to 100 Hz in the temporal-frequency domain and is amplified by the machine resonance. However, if the axis velocity is 100 in./min, then 60 cycles/in. is equal to 100 Hz and is amplified by the machine resonance. Therefore, the spatial-frequency content of the displacement error is dependent on the velocity of the moving components.

We observed this effect when we measured axial and radial error motions of the spindle on our test machine. As expected, the air-bearing spindle is very repeatable with sub-micrometer levels of asynchronous motion. However, the error characteristics drastically change at different spindle speeds. For example, the axial motion at 840 RPM spindle speed has a synchronous error with a dominant lobing of 17, 18 and 19 cycles/revolution, as shown in **Fig. 3**. If the errors were associated with a physical property of the motor such as the number of commutations, we would expect the spatial frequency of the lobing to remain fixed. However, at a spindle speed of 300 RPM, we observed a much higher spatial frequency lobing pattern, as seen in **Fig. 4**.

In general, the spatial frequency of the lobing increases with decreasing spindle speed. However, the temporal frequency of the dominant errors remain in the same region for all spindle speeds, as shown in the plots on the right sides of **Figs. 3** and **4**.

We are investigating the source of the forcing function. It is curious that the forcing function remains almost completely synchronous. Our hypothesis is that the forcing function is due the spindle speed variations about the set point. This will be investigated further during the next fiscal year.

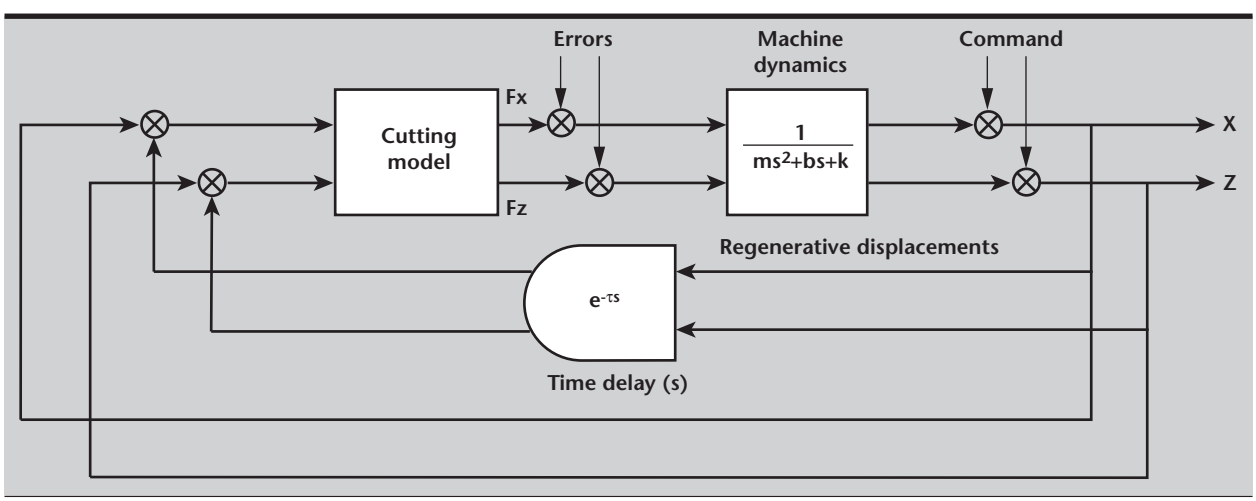

Figure 2. Block diagram of the machining process.

We also observed a similar effect with the straightness errors. The cycling of the balls in the bearing system causes the lower frequency displacement errors. This component is fixed in the spatial-frequency domain and remains constant at different feed rates of the axis. However, the higher frequency displacement errors fell at the machine resonances, which are fixed in the temporal-frequency domain. Therefore, the spatial-frequency spectrum of the displacement errors is dependent on the axis feed rate.

Combinatorial Rule

We have developed a combinatorial rule for the addition of the frequency content of each elemental error. The key to the combinatorial algorithm is to consider the spectrum of each elemental error as the sum of sinusoidal errors at specific frequencies. The addition of two sinusoidal signals at a given frequency results in a sinusoidal signal with the same frequency, but the amplitude can vary anywhere from the direct difference to the sum of the two amplitudes, depending on the phase shift between the two signals.

We first identify all elemental errors that are correlated, and appropriately sum the amplitudes of these errors. We then consider the phase shift between the remaining elemental errors to be uniformly distributed variables between 0 and 2π. We have analytically shown that the expected value of the square of the net amplitude is equal to the sum of the squares of the amplitudes of each elemental error. This is equivalent to saying that the expected net power spectral density (PSD) is the sum of the elemental PSDs.

Furthermore, we can now determine the probability distribution function of the net error with the use of a Monte Carlo simulation. The 95% confidence limit of the net PSD is approximately three times the mean, and the 99% confidence limit is approximately 4.6 times the mean. This is significantly less than the worst case error. For example, if 25 errors of equal amplitude were summed, the worst case net PSD would be over eight times larger than the 95% confidence

Figure 3. Axial errors at 840 RPM.

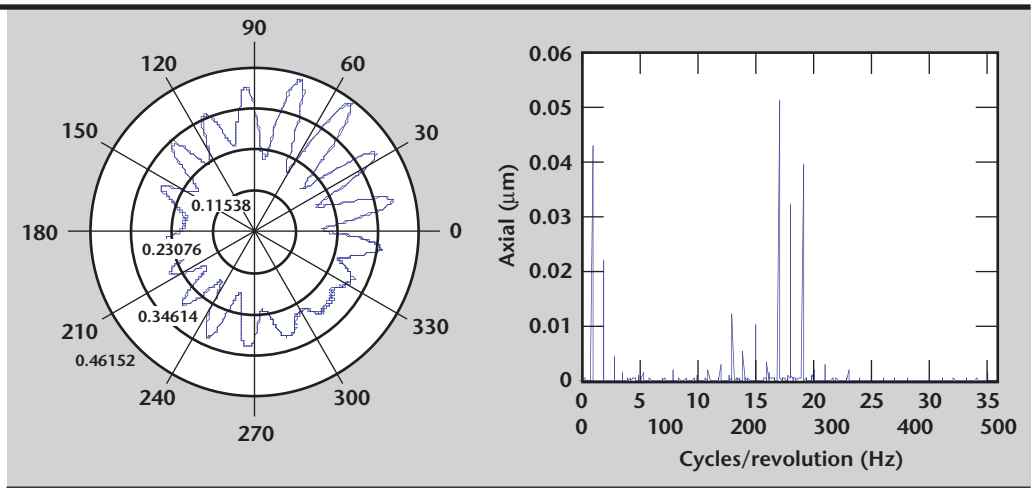

Figure 4. Axial errors at 300 RPM.

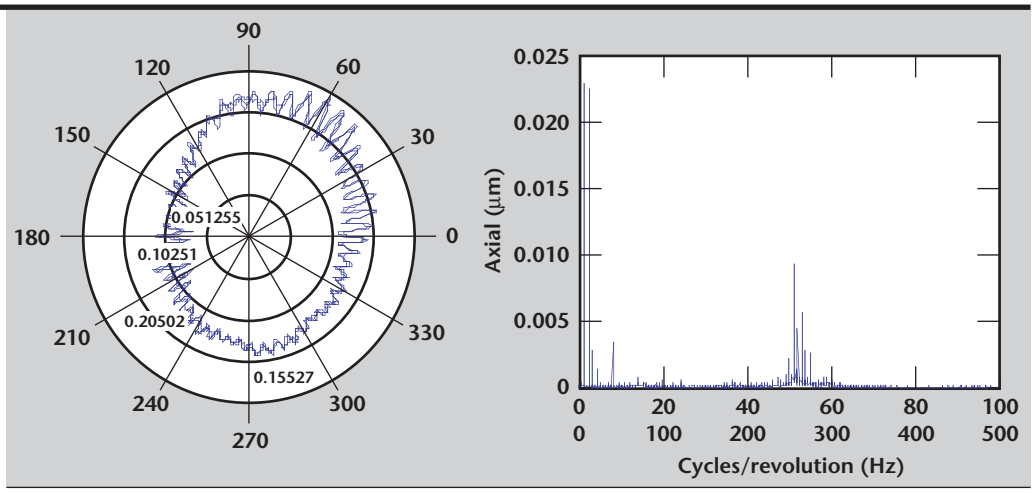

limit, and over five times larger than the 99% confidence limit.

Material Removal Transfer Function

The purpose of the material removal transfer function is to convert the motion of the tool in free space to the motion of the tool in the part during the cutting process. This step is necessary because current error characterization procedures measure the error motion of the tool in an open loop sense. The loop is closed when tool is in contact with the part during the cutting process. Differences occur when the loop is closed due to static and dynamic stiffness of the machining process.

The conventional error budgeting procedure assumed that the measured motion of the tool in free space is the same as the motion of the tool in the part during cutting. In other words, it assumes that the transfer function equals one. We have analytically shown that the material removal transfer function equals one under the following assumptions: 1) we have made multiple cutting passes on the part; 2) the material removal transfer function is linear; and 3) the errors can be adequately represented in the frequency domain with negligible random components.

While the first assumption is valid, the second and third assumptions are invalid. However, to a first order approximation, we have experimentally determined that the material removal transfer function is approximately linear around small deviations in the operating point. Furthermore, precision machines often have very repeatable error characteristics, so the third assumption is valid to first order.

Mapping the Errors into the Workpiece Coordinate System

Given the frequency content of the error motion of the tool during cutting, we must take into consideration that the path of the tool and the tool geometry determine the frequency content of the residual surface errors on the workpiece. Typical tools with a round cutting edge impart a nominal surface finish, or scalloping, during turning, even for a process with no errors. Next, we consider the exact path of the tool during the entire cutting procedure to map these errors onto the relevant workpiece coordinate system.

For example, during a facing operation on a diamond turning machine, the part turns while the tool remains stationary. Consider the spatial frequency content of a radial trace across the workpiece. The turning process can be considered a sampling mechanism. The radial trace is composed of the time domain sampling of the tool motion once every revolution of the part. Once every revolution, the tool falls on the radial trace of interest, leaving behind the signature of the tool as well as any error motions.

The description of the process so far has been in the time domain. However, we are interested in the frequency domain. Sampling in the time domain can be decomposed into a multiplication procedure of the original time-domain signal by a series of impulses. Since multiplication in the frequency domain is equivalent to convolution in the frequency domain, the sampling procedure is converted to the frequency domain by a convolution process. Note that unavoidable aliasing occurs for errors with higher frequency content than the rotational speed of the spindle. Note also that errors at frequencies that are an even multiple of the spindle speed (such as ‘synchronous’ spindle errors) do not appear on the radial trace due to this aliasing.

The imparting of the tool geometry onto the workpiece can be considered a convolution in the time domain. Conveniently, convolution in the time domain is equivalent to multiplication in the frequency domain. Therefore, the imparting of the tool geometry onto the workpiece in the frequency domain can be considered a filter.

Future Work

Transformation of Errors into Spatial-Frequency Domain

During experimentation and validation, we have been able to measure the contributing errors. However, during the design process, we will not have this luxury. Therefore, we must relate the physical properties of the machine to the general types of errors that are created. For example we discussed the error motions of the spindle. We believe that these errors arise from the fact that the spindle speed is varying, due to the spindle/motor/controller system. During FY-99 we will relate the physical properties of general machine components to the frequency content of errors that are associated with these types of systems.

Material Removal Transfer Function

For simplification we assumed that the material removal transfer function was linear. This is known to be false. During FY-99 we will study the nonlinearities associated with the cutting process and

develop strategies to deal with these nonlinearities in the frequency domain.

Error Budget Procedure

At the end of FY-99 we will deliver an error budgeting procedure to predict the spatial-frequency content of errors on a machined part for a variety of machining conditions. The user will input specifics about the machine components, structure, and control systems along with machining parameters such as spindle speed and axis velocity. Software will perform the appropriate combinatorial algorithm and processing to predict the spatial-frequency content of the errors on the machined surface of the part. With this tool, the user can study the effect of changing machining parameters or system components on the spatial-frequency content of the errors on the machined part. For example, the user will be able to replace the spindle type or axis velocity and observe the effects on the spatial-frequency content of the errors on the machined part.

References

1. Evans, C. (1989), *Precision Engineering: An Evolutionary View*, Cranfield Press, Bedford, UK.

2. Bendat, J. S., and A. G. Piersol (1986), *Random Data: Analysis and Measurement Procedures*, 2nd ed., Wiley-Interscience, New York, New York.

3. Sokolnikoff, I. S., and R. M. Redheffer (1966), *Mathematics of Physics and Modern Engineering*, 2nd ed., McGraw-Hill, San Francisco, California, p. 319.

4. Donaldson, R. R. (1980), "Error Budgets," in *Machine Tool Accuracy*, Vol. **5** of *Technology of Machine Tools: A Survey of the State of the Art by the Machine Tool Task Force*, R. Hocken, ed., Ch. 9.

5. Slocum, A. H. (1992), *Precision Machine Design*, Prentice Hall, Princeton, New Jersey.

6. Thompson, D. C. (1989), "The design of an ultra-precision CNC measuring machine," *39th CIRP General Assembly*, Trondheim, Norway, August 20–26.

7. Shen, Y. L., and N. A. Duffie (1993), "Comparison of Combinatorial Rules for Machine Error Budgets," *Annals of the CIRP*, Vol. **42** (1), pp. 619–621.

Precision Grinding of Brittle Materials

Mark A. Piscotty, Kenneth L. Blaedel, Pete J. Davis, and Pete C. Dupuy
Manufacturing and Materials Engineering Division
Mechanical Engineering

High performance brittle materials, such as silicon, beryllium-oxide (BeO) and glasses, offer high-performance properties for demanding engineering applications. Similar to the need that motivated the development of diamond turning capabilities at Lawrence Livermore National Laboratory (LLNL), the demand for precision-machined brittle material components is driving the development of precision grinding. Precision grinding is often the only viable process to fabricate precision components in a cost-effective manner. The goal of our development project is to meet the needs of LLNL's programs for brittle material components that are difficult to manufacture. We focus on the process development and associated activities, such as process modeling, metrology and commercialization for medium- to high-volume production.

Introduction

For LLNL to meet the increasing demands of its programs, it is crucial that we extend our expertise in precision grinding.

The need for the development of cost-effective precision fabrication of brittle material components is driven by the increasing demand for high-performance components from LLNL's large programs, such as Weapons and Lasers. High-performance brittle materials such as silicon, glasses and a wide variety of ceramics will play an ever-increasing role in many of LLNL's and DOE's major programs. This project focuses on the precision grinding of BeO ceramic components to be used as heatsinks for mounted electrical components (**Fig. 1**). BeO is the preferred material for this application and others because of its rare combination of high thermal conductivity (~56% that of copper) and its low electrical conductivity. The challenge is developing a process to machine necessary heatsink features in BeO substrates while meeting optically-driven tolerance specifications.

Along with the need to develop precision fabrication and process techniques, computer modeling and other analytical capabilities are instrumental as tools to predict grinding wheel wear rates, material grindability and resultant characteristics of the workpiece. In addition, metrology processes are required to provide process information feedback and to ensure the workpieces meet specifications.

LLNL's precision grinding core technology development effort encompasses a number of related tasks, all of which play key roles in advancing precision machining of brittle materials for programmatic applications and give it great potential for successful commercialization with outside vendors.

Progress

Precision grinding of brittle materials encompasses a variety of processes, including profile

Figure 1. BeO ceramic heatsink component.

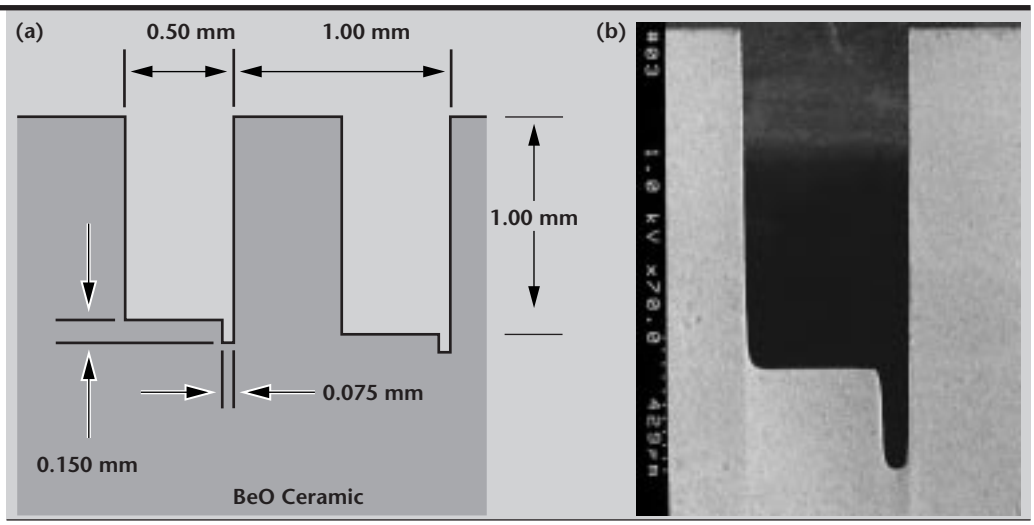

Figure 2. (a) Typical heatsink dimensions; and (b) heatsink groove end view.

grinding, cylindrical grinding, and surface grinding.[1] In this project, the focus is profile grinding of intricate geometries in 2-mm-thick ceramic substrates. **Figure 2a** shows a schematic and dimensions of the experimental components used in this study.[2] Typical tolerances required for this component range from ±1 µm to ±5 µm. An SEM end view of a precision ground sample feature is shown in **Fig. 2b**. Note that the internal corners display finite radii, which is an indication of corner wheel wear. Wheel wear is a major complicating factor in grinding small features such as these, since a small amount of wheel wear can result in out-of-specification workpieces.

In addition to the dimensions shown in **Fig. 2a**, other characteristics of the ground specimen also have stringent requirements. **Figures 3a** and **3b** show additional SEMs of a typical precision ground workpiece. The long vertical wall shown in **Fig. 3a** has both flatness and straightness tolerances of ±1 µm along the groove length. Meeting these requirements entails stringent control of the side wheel wear and the ability to maintain the wheel in a free-cutting state. These two conditions are often adversarial because free-cutting wheels typically shed used diamond abrasives to expose sharp, fresh abrasives, which itself is a form of wheel wear. Excessive side wheel wear can produce canted vertical walls, resulting in unusable workpieces.

Brittle materials are highly susceptible to edge chipping during processes such as precision grinding. Zero-tolerance edge chipping is typically required as it can degrade the strength and performance of the component. **Figure 3b** shows an SEM used to examine the edges of a feature bottom for

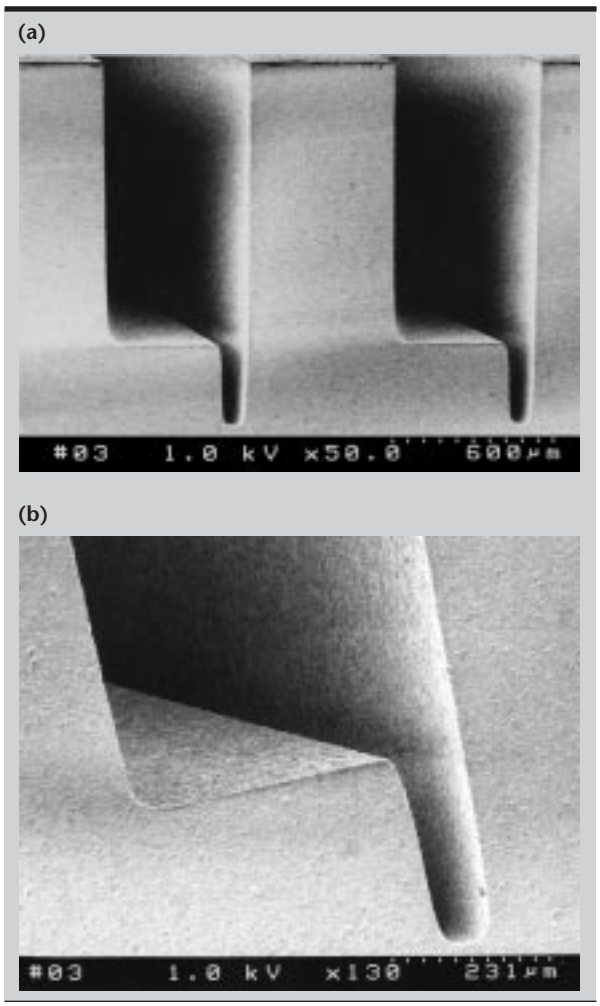

Figure 3. (a) SEM of heatsink features; and (b) SEM of feature bottom notch.

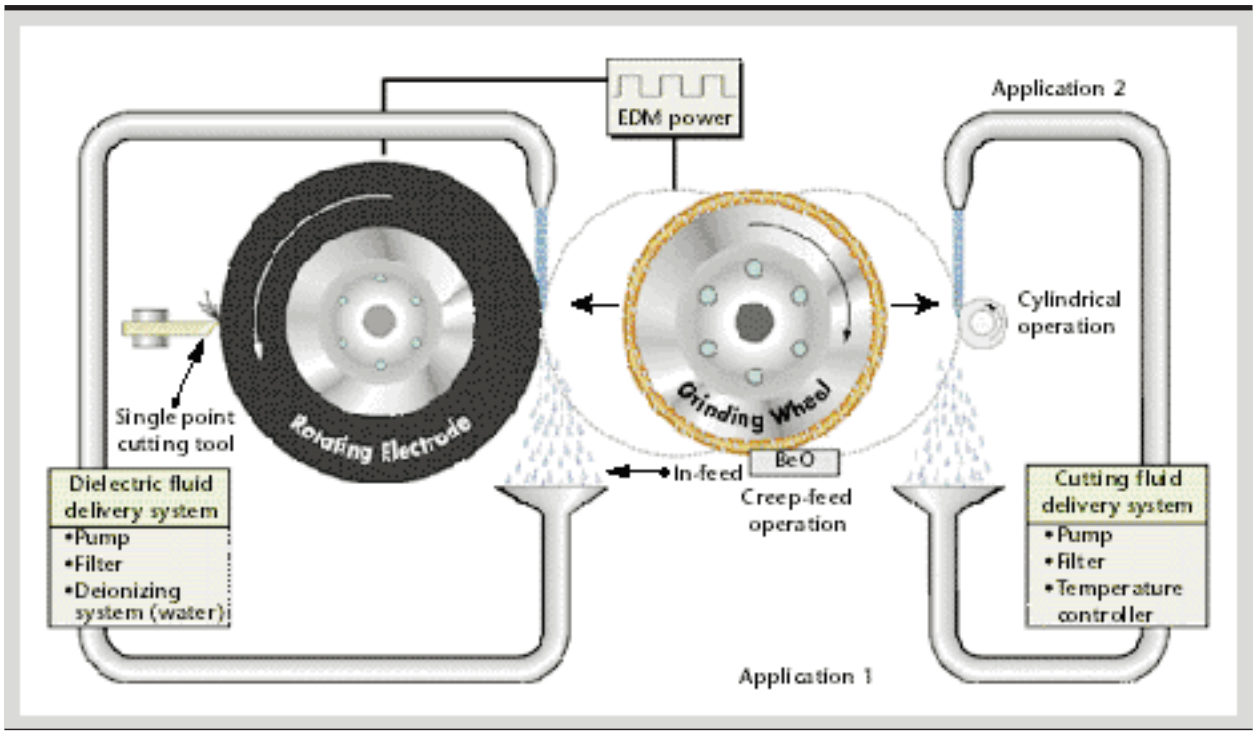

Figure 4. Schematic of machine tool set-up.

edge chipping. The nominal grain size of the BeO used in this study is 15 to 25 µm. To generate sharp corner surfaces without edge chipping requires that intragranular grinding take place. This requires that the grinding wheel maintain a well-dressed condition throughout the grinding cycle, ensured by intermittent dressing of the wheel during the grinding process.

A number of viable processes, each with its advantages and disadvantages, were possible candidates for machining these components. The process used at LLNL was selected because of its flexibility, robustness, and potential to be commercialized. Shown in the schematic in **Fig. 4** are two separate applications using the same basic process, one for creep feed grinding of flat substrates (BeO heatsinks) and the other cylindrical grinding (ceramic engine components).

An on-line electrical discharge machining (EDM) system is used to impart precision profiles on a metal bond, diamond abrasive grinding wheel. Features on the rotating graphite EDM electrode are turned on its outside diameter surface using a single point carbide tool and are used in the process to machine the profiles on the grinding wheel. In this case, a grinding wheel with two profiles is optimal, since two grinding passes are required to complete a groove. However, this process can be extended to generate additional profiles on a single grinding wheel or to fabricate several profiled grinding wheels on a multiple wheel arbor. The ceramic workpieces are held in a chucking fixture below the profiled grinding wheel (**Fig. 5**).

Metrology

The unique heatsink configuration used in this project has several critical dimensions and requires geometric verification using off-line inspection procedures. These procedures involve a combination of both visual and contact metrology. Visual inspection is used for specific profile portions, such as the

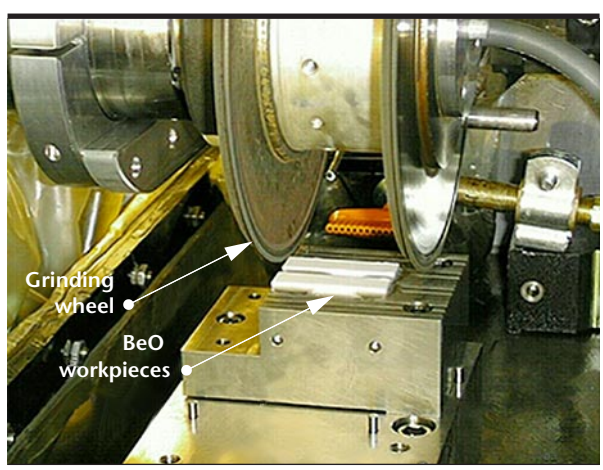

Figure 5. BeO heatsinks in grinding position.

flatness of the groove bottoms, the widths and depths of the relief notch at the bottom, and the flatness of the groove walls. Contact metrology is performed using a delicate stylus probe to allow interrogation of the grooves' inner geometries (walls and bottom).

Figures 6a and **6b** show inspection photographs of the process using a precision coordinate measuring machine (CMM) located at Sandia National Laboratory in California. The touch probe is held in a low force sensor head, and axes-positioning feedback is provided from distance measuring laser interferometers. This inspection procedure enables each part to undergo 100% inspection, which is a valuable diagnostic during process development. As processes become more robust and proven, inspection procedures may be streamlined to increase throughput.

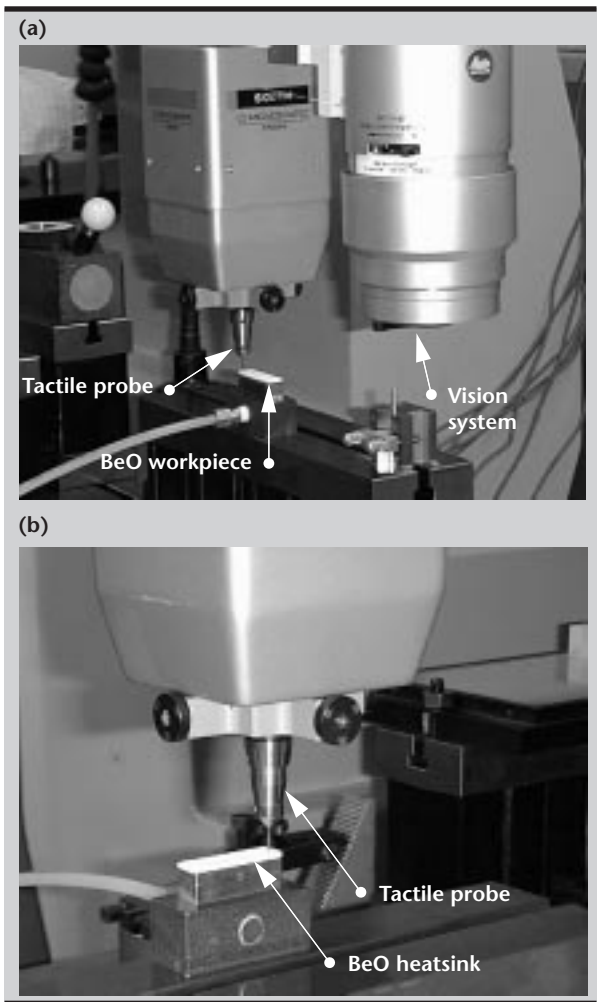

Figure 6. (a) Moore M48 CMM for heatsink metrology; and (b) set-up for tactile probe metrology.

Commercialization

While the primary goal of this project is to develop precision grinding, a secondary goal is to enable this technology to be commercialized with at least one outside vendor for higher volume and lower cost production for LLNL's programs.

A number of challenges were encountered during the effort to commercialize this technology. Among these challenges were determining technically competent vendors with the necessary machine tools for precision fabrication of ceramic components. In addition, the vendors must be willing and qualified to machine BeO, which is considered toxic in its powdered state. This narrowed the selection down to one vendor, Brush Wellman in Tucson, AZ. Brush Wellman is the sole supplier of BeO in the U.S. and has significant experience machining BeO for customers.

However, the precision needed to fabricate these heatsink components was beyond their experience and we therefore are working closely with them to transfer our process technology to them. Because Brush Wellman's machine tools and machining capabilities vary significantly from those at LLNL, we tailor the technology transfer to accommodate this.

Brush Wellman owns two machine tools that can meet the stringent performance criteria to fabricate BeO heatsinks in medium lot sizes (about 100 pieces per lot). The first is a surface grinder that has been used as a workhorse for other precision-ground BeO components. The second machine tool, which we feel has the most promise for delivering these heatsinks at the lowest cost, is an MTI612 precision slicing machine. This machine is capable of using a ganged wheel arbor (multiple wheels mounted on one precision arbor) and has three-axes-positioning accuracy of better than 1 µm. Collaborations between LLNL and Brush Wellman are establishing processes on both these machine tools at Brush Wellman, now the vendor of choice for these heatsinks.

Modeling

The modeling development of this project centers on understanding the mechanisms for generating and propagating sub-surface damage (SSD) during the precision grinding of brittle materials. This has been studied by a number of researchers using a variety of models and techniques.[3,4,5] The modeling technique investigated involves a continuum damage mechanics (CDM) model developed at the University of Connecticut under Professor B. Zhang and Ph.D.

candidate R. Monahan. The current CDM model investigates the resulting SSD generated by a single grit material removal.

While this model has interesting implications and information, a new model will include material removal interaction among several grits in a grinding wheel, which is more characteristic of a real grinding process. The CDM model introduces inelasticity and damage to accommodate the non-linear responses of brittle materials. The current states of effective stress and damage and hydrostatic stress are used to simulate the cumulative anisotropic damage of the brittle material. The next generation of this model will be developed at the University of Connecticut with input and review from LLNL.

Conclusions

Precision fabrication of programmatically important brittle material components is a vital capability that is being maintained and extended at LLNL. Precision grinding of brittle materials is often the procedure of choice for this type of fabrication, since it offers many advantages over other possible methods. This project leveraged a number of these advantages including process flexibility, readily available precision grinding machine tools and components, beneficial ties to industrial processes and vendors, and the ability to transfer a precision process to a vendor for large volume commercialization.

Future Work

Clearly, grinding has a long history and recent developments in the area of precision grinding are producing remarkable results. However, precision grinding of brittle materials remains a relatively young technology area compared to other techniques such as diamond turning, and thus cries out for more research.

Future work should be focused on understanding the fundamentals of the material removal mechanisms, wheel wear phenomenon, the dynamics of the precision grinding process, and the propagation of surface and subsurface damage in the workpieces. Understanding the implications of how these mechanisms affect the precision of ground brittle material components is key to realizing the full potential of this fabrication process.

Semiconductor materials, thin films and optical systems are in the forefront of advanced materials that play a critical role in many LLNL programs. New coating and fabrication techniques are producing materials to meet the ever-increasingly stringent dimensional, defect and SSD requirements. To use these materials to their maximum potential, their dimensions and defect state must be measured with heretofore-unattainable precision.

Conventional SSD measurement techniques typically focus on destructive methods, including taper polishing and tunneling electron microscopy.[6,7] X-ray diffraction has been used with little success since it works best with well-defined crystalline substrates.

It became obvious during the course of this project that the technology to quantitatively evaluate SSD in a nondestructive manner demands substantial research and development. An *in-situ*, nondestructive evaluation technique would be an extremely valuable and unique tool for interrogating SSD as a result of grinding, lapping and polishing.

Current methods to quantitatively evaluate SSD are labor- and time-intensive, and destroy the surface of the workpiece being evaluated. Drs. S. Soares (California Institute of Technology) and B. Zhang have developed a proposal for a nondestructive method to evaluate SSD in brittle materials.

References

1. Komanduri, R., D. A. Lucca, and Y. Tani (1997), "Technological Advances in Fine Abrasive Processes," *Annals of CIRP*, **46**, pp. 1-52.

2. Drawing No. AAA98-107146-OA, Lawrence Livermore National Laboratory, Livermore, California.

3. Fahrenthold, E. P. (1991), "A Continuum Damage Model for Fracture of Brittle Solids Under Dynamic Loading," *Journal of Applied Mechanics*, **58**(4), pp. 904-909.

4. Hu, K. X., and A. Chandra (1993), "A Fracture Mechanics Approach to Modeling Strength Degradation in Ceramic Grinding Process," *Journal of Engineering for Industry*, **115**(1), pp. 73-84.

5. Ju, J. W., and X. Lee (1991), "Micromechanical Damage Models for Brittle Solids, I: Tensile Loadings," *Journal of Engineering Mechanics*, **117**(7), pp. 1495-1536.

6. Zhang, B. (1995), "Subsurface Evaluation of Ground Ceramics," *Annals of CIRP*, **44**, pp. 263-266.

7. Xu, H. K. (1996), "Material Removal and Damage Formation Mechanisms in Grinding Silicon Nitride," *Journal of Material Research*, **11**(7).

Peter J. Raboin and Clifford C. Shang, Center Leaders

The Computational Engineering Center is a vital and growing component of the Engineering Directorate of Lawrence Livermore National Laboratory (LLNL). This new center is the result of combining the Computational Electronics and Electromagnetics Thrust Area with the Computational Mechanics Thrust Area.

The combined entity fuses the computational expertise of two organizations and represents a consolidation of capabilities and activities. The number of engineering analysts at LLNL has grown this past year, as has the demand for sophisticated scientific numerical simulations. The purpose of the Computational Engineering Center is to anticipate and provide for the future analytic needs of the Engineering Directorate at LLNL.

Activities and code development work in LLNL's Accelerated Strategic Computing Initiative (ASCI) began this year with new efforts to parallelize implicit finite element methods. This long range effort will bring the advantages of scaleable computing on massively parallel supercomputers to the entire suite of computational mechanics codes (NIKE, TOPAZ, and DYNA) for important programmatic applications.

Interactions with the Department of Defense (DoD) High-Performance Computing and Modernization Program and the Defense Special Weapons Agency are of special importance as they support our ParaDyn project in its development of new parallel capabilities for DYNA3D. Working with DoD customers has been invaluable in driving this technology in directions mutually beneficial to the Department of Energy.

The research and development activities within the computational electronics and electromagnetics area have yielded a set of simulation and design codes that have contributed to three LLNL "R&D 100" awards in the past two years: theory and design support for high-gradient insulator development, and antenna synthesis for microwave-based bridge deck inspection, were 1997 and 1998 R&D 100 application award winners; work in high-frequency electromagnetics modeling and optical propagation codes resulted in a 1997 R&D 100 award for the code MELD. This work was continued in the optical-full-wave algorithms being evaluated and developed for use in target design codes.

In this report for FY-98, the computational mechanics articles cover five code development activities that have expanded our ability to handle large problem sizes on parallel computers and problems that deal with greater physical complexity than before. The parallel code work is summarized in a single article covering all of computational mechanics.

Two articles describe how the explicit DYNA3D code and the implicit codes NIKE3D and TOPAZ3D have been linked and coupled together.

For the code linkage, special element formulations were created to enhance the compatibility of the differing finite-element methods. Another article presents a substantial new cyclic viscoplastic constitutive model added to our codes. The final mechanics article talks about coupling mass diffusion and heat transfer.

The computational electronics and electromagnetics articles describe on-going code development, parallel implementation, design, and validation activities for time-dependent and multi-length scale electromagnetics.

Articles summarizing physics modeling and control of charged-particle beam devices for inertial fusion energy, microwave structure analysis, and accelerator design for LLNL's advanced radiography mission are also in this section. Another article highlights this year's development of new diagnostics which have been developed for novel laser-electron interaction experiments aimed at developing the next generation of light sources. A family of intercepting high-current electron beam diagnostics was also developed. A final article highlights progress in various facets of computational electronics, including electromagnetic and nuclear effects modeling.

Center for Computational Engineering

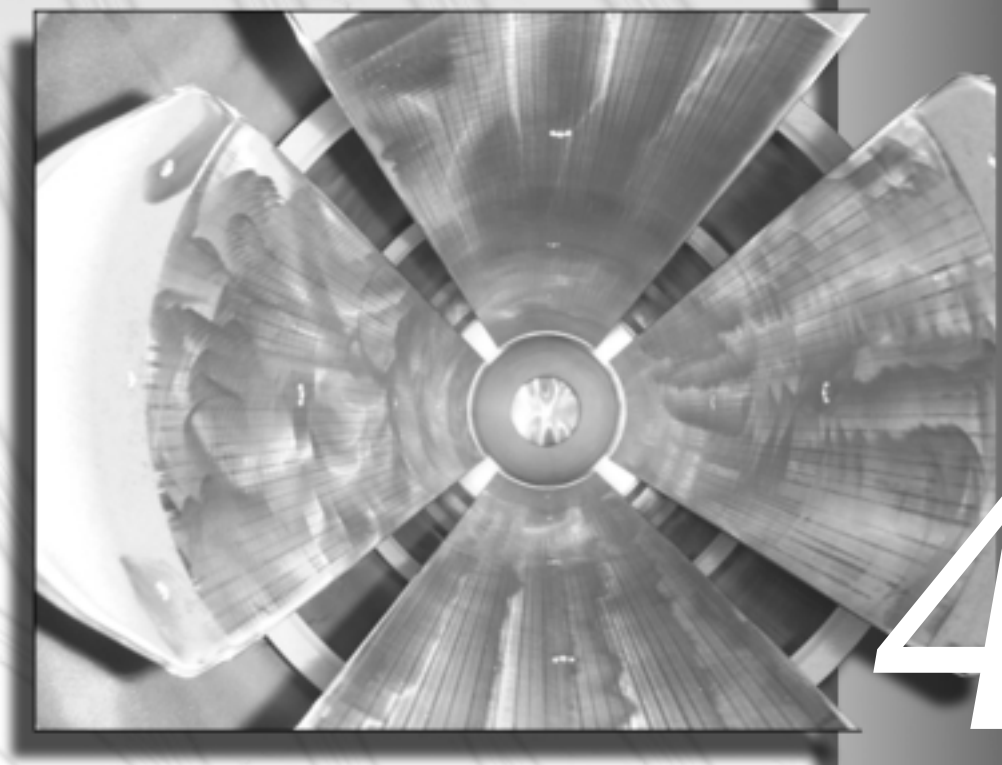

4

4. Center for Computational Engineering

Overview
Peter J. Raboin and Clfiford C. Shang, Center Leaders

Hybrid Ray/Wave Methods for Optical Propagation
Richard P. Ratowsky, Jeffrey S. Kallman, Michael D. Feit, and Bedros B. Afeyan.....4-1

Technologies for Advanced Induction Accelerators
Maurice A. Hernandez.....4-7

TIGER: An Object-Oriented Time-Domain Simulation Code
David J. Steich, Jeffrey S. Kallman, Gerald J. Burke, S Terry Brugger, and Daniel A. White.....4-9

OPUS: An Optically Parallel Ultrasound Sensor
Jeffrey S. Kallman, Dino R. Ciarlo, Elaine Ashby, and Graham H. Thomas.....4-13

Optical Transition Radiation Diagnosis for Electron Beams
Gregory P. Le Sage and Roger A. Richardson.....4-19

Characterization of Electromagnetic Scattering from Defects in the EUVL Process
Lisa Wang, Scott D. Nelson, Jeffrey E. Mast, and Abbie L. Warrick.....4-23

Nuclear and Electromagnetic Radiation Simulation Tools for Dual-Revalidation of the Stockpile
David J. Mayhall and Michael F. Bland.....4-29

Self-Effects in Expanding Electron Beam Plasmas
Manuel Garcia.....4-33

Pump-Induced Wavefront Distortion in Prototypical NIF and LMJ Amplifiers
Mark D. Rotter, Kenneth S. Jancaitis, Christopher D. Marshall, Luis E. Zapata,
Alvin C. Erlandson, Geoffroy LeTouze, and Stephane Seznec.....4-37

Parallel Algorithm Development for Computational Mechanics
Carol G. Hoover, Robert M. Ferencz, Anthony J. De Groot, Robert J. Sherwood,
Edward Zywicz, Yuen L. Lee, and Douglas E. Speck.....4-47

DYNA3D-TOPAZ3D Coupling and DYNA3D-NIKE3D Linkage
Jerry I. Lin.....4-55

A Physically Stabilized Eight-Node Hexahedral Element
Michael A. Puso.....4-59

A Cyclic Viscoplastic Constitutive Model
Phani Kumar V. V. Nukala.....4-65

Electromagnetic Cold-Test Characterization of the Quad-Driven Stripline Kicker
Scott D. Nelson and James E. Dunlap.....4-71

Photonic Doppler Velocimetry
Paul D. Sargis, Nicole E. Molau, and Daren Sweider.....4-77

Modeling Coupled Heat and Mass Diffusion
Arthur B. Shapiro and Philip M. Gresho.....4-81

Analysis and Modeling of a Stripline Beam Kicker and Septum
Brian R. Poole, Lisa Wang, Yu Ju (Judy) Chen, and George J. Caporaso.....4-85

Hybrid Ray/Wave Methods for Optical Propagation

Richard P. Ratowsky and Jeffrey S. Kallman
Defense Sciences Engineering Division
Electronics Engineering

Michael D. Feit
Laser Science and Technology
Laser Programs

Bedros B. Afeyan
Polymath Associates
Pleasanton, California

This aim of this project was to create a computational tool that bridges the gap between the wave and ray optical regimes, important for applications such as laser propagation in plasma and multi-mode photonics. We used phase space methods, where a set of rays distributed in a particular way in position and angle retain many essential features of wave optics. To characterize and enhance our understanding of the method, we developed a GUI-based photonics tool that can analyze light propagation in systems with a variety of axial and transverse refractive index distributions.

Introduction

Until the mid-19th century, natural philosophers argued vigorously over whether light was in reality a wave or a particle. Compelling reasons existed for both points of view: light seemed to travel mostly in straight lines like a particle, but showed diffraction and interference like a wave. In the early 20th century, the same issues surfaced again in the context of the quantum theory, where both light and matter exhibited both wave-like and particle-like behavior, depending on the observational setting.

The ability of light to act like a wave or a particle has practical consequences for the calculation of its propagation. For systems large compared to a wavelength, such as conventional bulk optics, particle-like geometrical optics is usually a good approximation. On the other hand, if the scale of features is on the order of a wavelength, such as at a focal point, solving a wave equation is necessary to capture the physics of diffraction. Often, as in the bulk optics example, both circumstances arise in sub-domains of the same problem.

Many practical situations important to Lawrence Livermore National Laboratory (LLNL) programs share this dual length-scale property. One important application is laser propagation in fusion plasmas. Traditional modeling uses ray tracing to transport the laser intensity, and this is usually a good approximation. But when plasma gradients are wavelength scale, as may occur in regions of NIF targets, a wave optical treatment is essential.

Another relevant area is multi-mode photonics. A multi-mode optical fiber may be optically large, but calculating the effects of interference—speckle—between the modes is of critical importance.

The purpose of our proposal was to create a computational tool which would move easily between the wave and ray optical regimes. We accomplished this by using phase space methods, where a set of rays distributed in a particular way in position and angle retain many essential features of wave propagation, including diffraction.[1,2]

By launching the right set of rays, diffraction can be calculated directly from the ray distribution without explicitly solving a wave equation. In this way, a problem domain can easily use both ray and wave optics in the regions where the descriptions are most appropriate. To characterize and enhance our understanding of the method, we developed a GUI-based photonics tool that can analyze light

propagation in systems with a variety of axial and transverse refractive index distributions.

This report gives an overview of our work in FY-98. First, we convey the principles of the phase space method and give some simple examples. Then, we describe the software tool we developed to study the propagation of fields through the Wigner method. This tool allows us to study the important issue of the appropriate sampling of rays in phase space to achieve desired accuracy.

Further examples of light propagation in systems with a variety of axial and transverse refractive index distributions are given.

Finally, we describe some of the limitations of our current scheme and the path we envision for further development and applications.

Progress

Methodology

We usually think of an electric field as a vector quantity that varies in space and time according to Maxwell's electromagnetic field equations. We can also describe the field in terms of the wavenumbers or spatial frequencies which comprise it ("Fourier representation"). However, it is sometimes most natural to think in terms of a mixed representation, whereby the field is thought of as a set of spatial frequencies, the spectrum of which changes with position. This is analogous to the way music, which is a pressure oscillation changing in time, can be represented by a musical score which shows a set of pitches (frequencies) changing in time. For the electric field, a wavenumber defines a direction in space; the coordinates of the direction are a set of angles. Thus, the field can be represented by a function of position and angle, which defines the ray phase space.

One such function is known as the Wigner distribution.[3] Originally invented for quantum mechanics, the Wigner distribution allows us to calculate wave optical properties on the position-angle ray phase space.

Mathematically, the Wigner transform can be thought of as a Fourier transform not of the field, but of its correlation function relating the field at two points in space. An example of a Wigner distribution is shown in **Fig. 1** for a Gaussian field and for a uniformly illuminated aperture. Qualitatively, the reason diffraction is included in the ray description is that, at each point in space, one

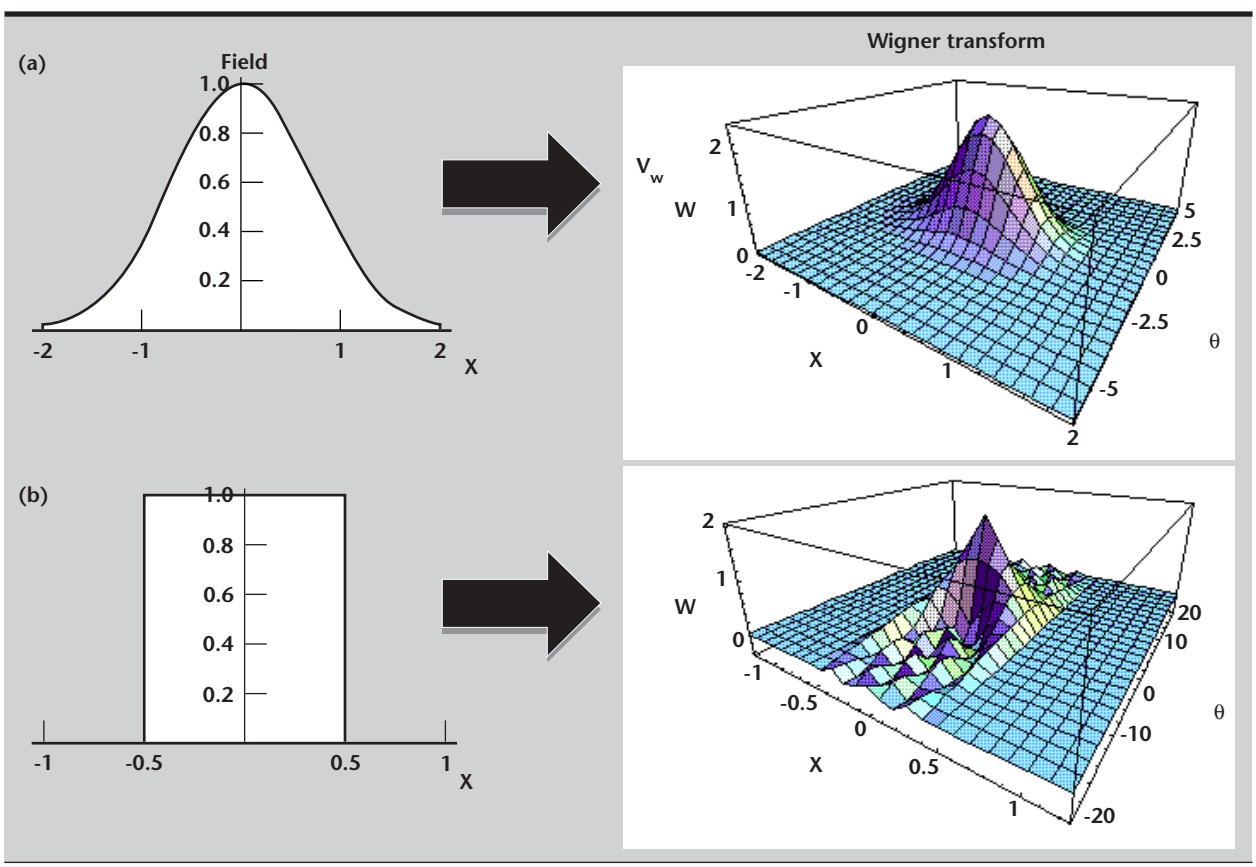

Figure 1. Wigner phase-space distributions for (a) Gaussian and (b) uniformly illuminated apertures.

has a fan of ray angles: this is just a manifestation of the Fourier uncertainty principle. The Wigner distribution is not strictly a phase-space density, however, since it is not always positive.

The Wigner propagation algorithm works as follows. From an initial complex electric field distribution, we calculate the Wigner transform. This distribution is then evolved in space by simply transporting it along rays, that is, assuming conservation along a ray. This will be an excellent approximation if the index is not too rapidly varying on a wavelength scale. If at every position in the ray phase space for the new (evolved) distribution, we integrate over all ray angles, we obtain the intensity distribution ("near field") as a function of spatial position.

Conversely, if at each angle in phase space we integrate over position, we obtain the intensity distribution as a function of ray angle ("far field"). Since in wave optics the near-field and far-field amplitudes are related by Fourier transform, the complex electric field can be reconstructed (up to a constant phase factor) from the ray intensity distributions in position and angle.

As an example of a calculation using the Wigner propagation algorithm, we calculated the diffraction pattern from a double slit (**Fig. 2**). The Wigner function is calculated in the plane of the slits, then propagated along rays to the plane of the screen. The calculated result and the exact solution are overlaid, and agreement is excellent. In fact, for free propagation, the Wigner method is formally exact, and the only errors are due to sampling. This illustration shows strikingly that diffraction and interference, usually considered outside the domain of ray optics, can be obtained through ray tracing the Wigner distribution.

PHASTER

To study the Wigner method we developed a GUI-based code which allows us to propagate beams in a variety of media in two spatial dimensions. We call the code "PHASTER": Phase Space Techniques for Electromagnetics Research.

PHASTER allows us to set up an arbitrary initial beam consisting of a sum of Gaussians with selected widths and amplitudes. After computing and displaying the Wigner distribution for the beam, it will solve the ray equations for a set of points in the ray phase space which sample the Wigner distribution in a prescribed manner. The rays are traced using an adaptive Runge-Kutta method through a variety of refractive index distributions having both transverse and axial variation.

After propagating the prescribed set of rays to the exit plane, it will display the phase-space distribution at the exit plane, as well as the x-space and angle-space intensities (near field and far field). PHASTER gives useful insight into the dynamics of the rays in phase space and their effect on the wave optical distribution.

Our first example of a PHASTER calculation is shown in **Fig. 3**. A Gaussian beam is shown propagating through three "soft slabs," that is, small regions where the refractive index rises and falls, depicted in

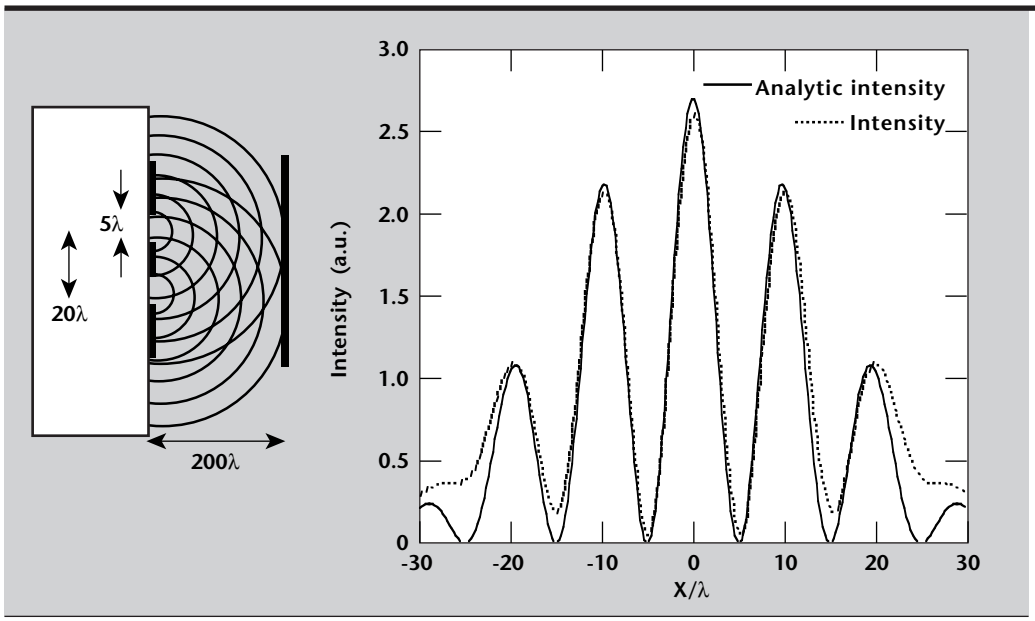

Figure 2. Wigner phase-space method calculation of double-slit diffraction by ray tracing.

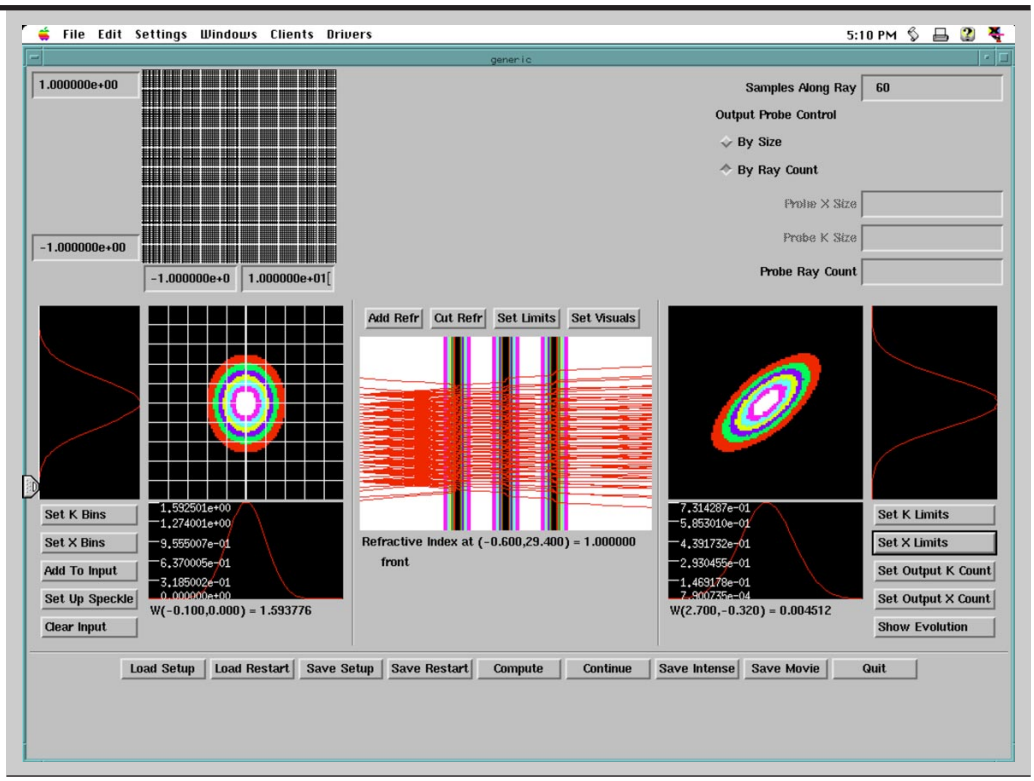

Figure 3. PHASTER calculation of propagation through three slabs. The tilted distribution on the right is the manifestation of diffraction in the ray phase space.

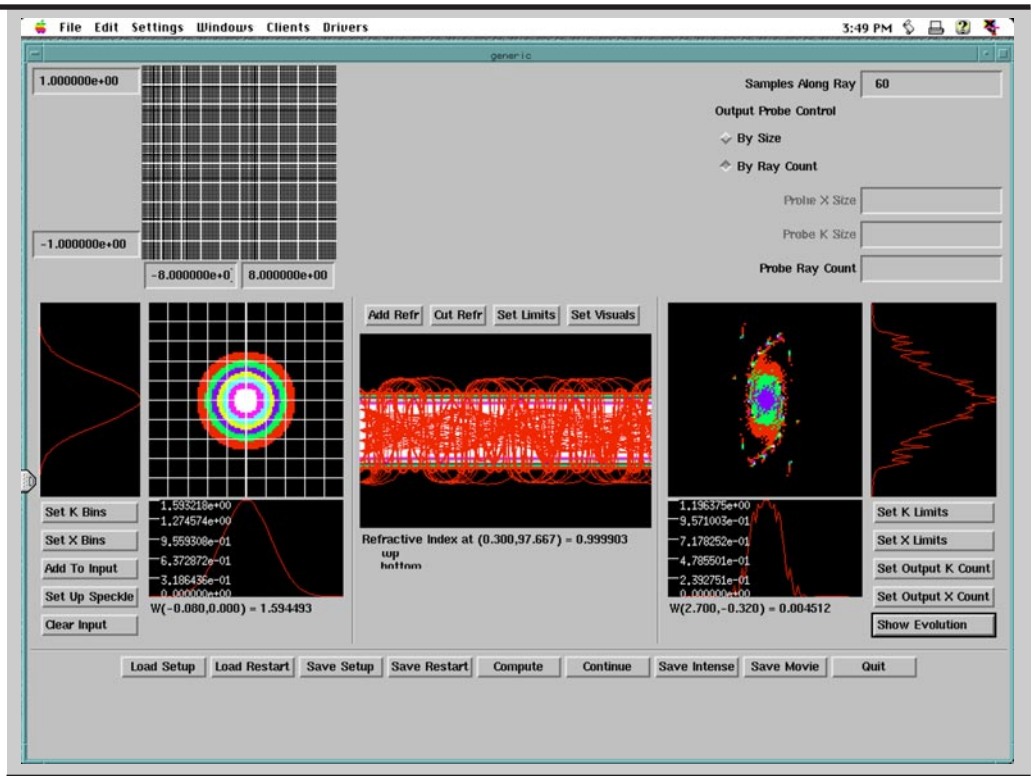

Figure 4. PHASTER calculation of waveguide propagation, showing rays with transverse turning points.

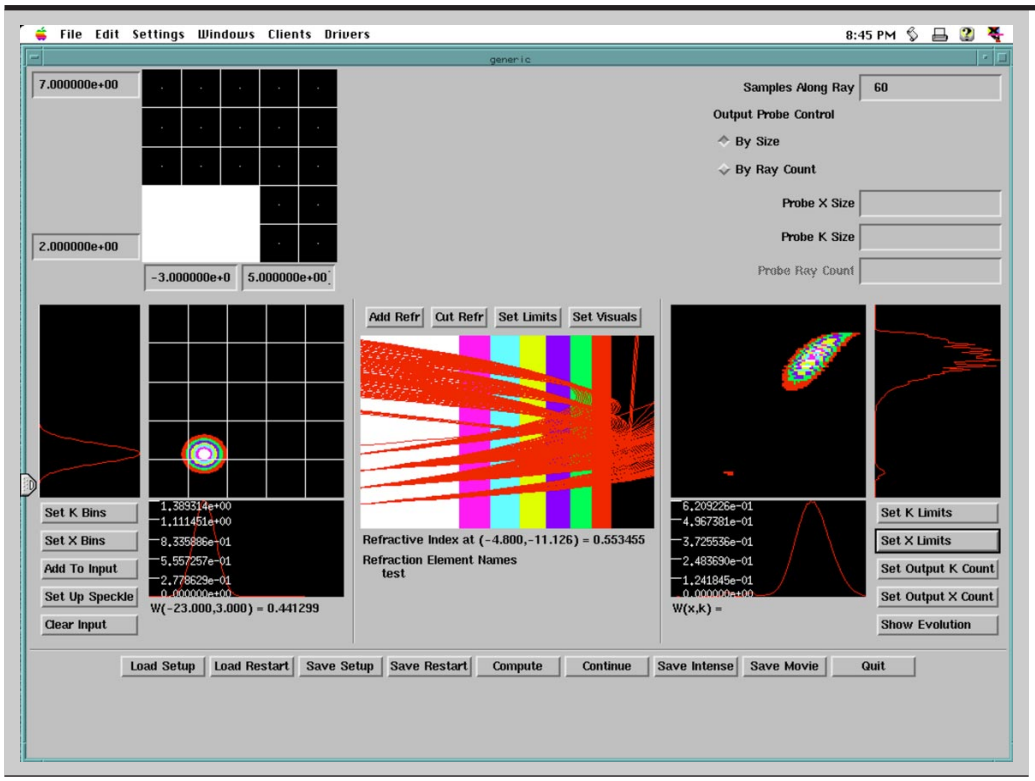

Figure 5. PHASTER calculation for oblique incidence on inhomogeneous plasma with linear density gradient.

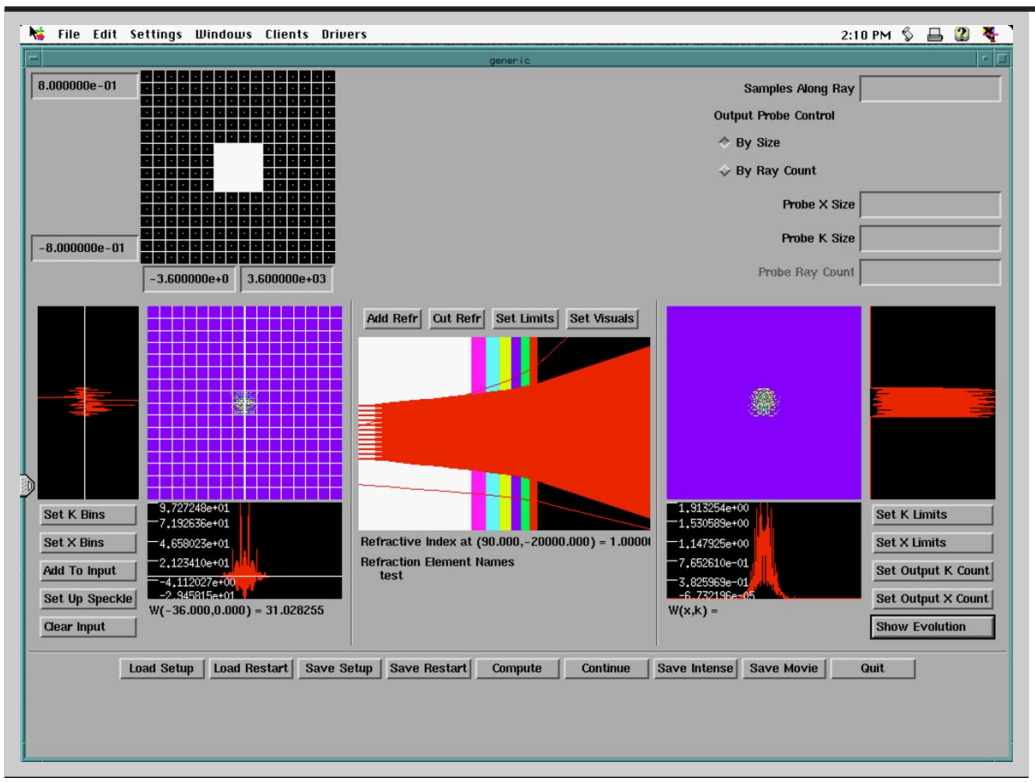

Figure 6. PHASTER calculation for speckled beam at normal incidence on inhomogeneous plasma.

the central window of the GUI. The contour plot on the left shows the initial Wigner distribution of the Gaussian. Below it we see the x-space intensity, and to the left the angle-space intensity (far field). The windows on the far right show the analogous data for the propagated distribution. Note that the phase-space distribution has become elongated and tilted: this is simply a graphic depiction of diffraction.

Rays at large-magnitude angles (top and bottom of distribution) move fastest in x, while small-angle rays (near center of distribution) move little. The result is a spreading of the x-space distribution while the angular distribution does not change, exactly what we would expect from simple free-space diffraction. Due to the plates, additional spreading occurs in x-space but not in angle, because rays receive no transverse impulse from the axially varying index.

Figure 4 shows propagation in a waveguiding structure. The rays are obviously confined to the waveguide, and at the exit have formed a "galaxy-shaped" distribution. A given ray will encircle the origin as it traces out a periodic path, but the frequency of the rotation decreases as the angle increases, causing the spiraling.

A third example is shown in **Fig. 5**. Here a beam is incident at an oblique angle on a linear index gradient, a model for a laser propagating in a plasma. A subset of the rays is reflected by the plasma index gradient, while the rays getting through form the distorted distribution on the right. This example is of particular interest because the problem admits an exact solution in terms of Airy functions,[4] and thus will allow direct evaluation of accuracy.

Our final example (**Fig. 6**) shows the propagation of a speckled beam through the inhomogeneous plasma. By speckled we mean that we are launching a set of Gaussians with a distribution of transverse tilt angles and random phases. Propagation of speckle is important for laser-plasma interaction physics and also for propagation in multi-mode fiber. Again, an exact solution to this problem is available.

An important feature of the code is its flexibility in sampling the phase space at the entrance plane so as to put a higher density of rays where the Wigner distribution has larger values. Sampling is critical for the method, because if we do not sample wisely we suffer in computational efficiency for a given accuracy. PHASTER allows us to divide the phase space into rectangular bins and vary the size of the subdivisions of the bins.

Future Work

The Wigner method shows great promise as a wave propagation algorithm, and much remains to be done to fully exploit its capabilities. To treat reflections accurately, for example, requires extending the calculation to the time domain.

The method will be most effective when it is relatively inexpensive to trace rays, as in bulk optics where all that is required is Snell's law of refraction (and reflections if wanted) at boundaries. We are in the process of developing a 3-D bulk optics solver. Up to now, we have ignored polarization, which can also be included. More subtle effects, such as accurately calculating tunneling, will require propagating complex rays.

We recognize that using rays is only a first step for the method to come to fruition. Because rays are 1-D, it is difficult to sample a 2- or 3-D space effectively. One extension is to use "fat rays," or Gaussian basis functions, whose centers propagate along a ray.

Ultimately, we envision using a wavelet basis, which can optimally sample a system that has disparate length scales. Resolution can be applied only where needed, and crude representations retained where they cause minimal harm. This way, from rays to full wave optics in phase space, can be simulated by retaining a hierarchy of successively more accurate approximations.

In FY-99 we are focusing on applications of the Wigner method to multi-mode photonics, where effective simulation tools are in demand but full wave optics solvers are computationally difficult.[5]

References

1. Wolf, E. (1978), "Coherence and Radiometry," *J. Opt. Soc. Am.* **68**, pp. 6–17.

2. Bastiaans, M. (1997), "Application of the Wigner distribution function in optics," *in The Wigner Distribution: Theory and Applications to Signal Processing*, W. F. G. Mecklenbräuker, ed., North-Holland, Amsterdam.

3. Wigner, E. (1979), "On the quantum correction for thermodynamic equilibrium," *Phys. Rev.* **40**, pp. 749–752.

4. Afeyan, B. B. (1996), *Bull. Am. Phys. Soc.* **41**, No. 7, paper 9Q2, p. 1598.

5. Ratowsky, R. P., B. B. Afeyan, J. S. Kallman, and M. D. Feit (1998), "Propagation modeling for multimode photonics," Lawrence Livermore National Laboratory, Livermore, California (UCRL-JC-131253-ABS).

Technologies for Advanced Induction Accelerators

Maurice A. Hernandez
Defense Sciences Engineering Division
Electronics Engineering

The Technologies for Advanced Induction Accelerators project is aimed at developing the technologies necessary for a commercial fusion energy source. In FY-98, we developed components for tailored beam acceleration and bending, continued our modeling efforts, and conducted beam dynamics experiments.

Introduction

The Technologies for Advanced Induction Accelerators Project has just completed the second year of a three-year effort. This project is one component of the Inertial Fusion Energy (IFE) research at Lawrence Livermore National Laboratory, aimed at developing the technologies necessary for a commercial fusion energy source. We have focused on the concept of indirect drive targets using a heavy ion accelerator. A 1991 study showed that a recirculating accelerator (or recirculator) is a promising candidate for a cost-effective IFE driver. A recirculator is exactly what its name implies—an accelerator in which the beam travels around a ring-shaped configuration, repeatedly passing through each accelerating element.

Progress

We have used the HIF Small Recirculator (which presently has one-quarter of the full ring completed) as a test bed. Our work in FY-98 concentrated on 1) developing the components necessary for tailored beam acceleration and bending; 2) continued modeling efforts aimed at constructing efficient beam steering correction algorithms; and 3) conducting beam dynamics experiments to further our understanding of the beam control parameters.

Acceleration of the recirculating beam requires high-efficiency induction core materials driven by high-repetition-rate, programmable, pulse waveforms. As the beam is accelerated, it gains both kinetic and electrical energy. In addition, our acceleration scheme calls for compressing the beam to help reduce emittance effects. The induction core modulators must thus be able to produce precise, fast-rise-time waveforms with varying shapes, amplitudes, and widths.

During FY-98, we designed and built two prototype versions of the required modulator. One version is based on four parallel MOSFETs and associated drivers configured as switching circuits, while the other version uses the MOSFETs as linear control elements, complete with feedback and proportional drive circuitry.

The linear version has demonstrated acceptable voltage regulation at average currents in excess of 200 A, and peak currents in excess of 800 A. This performance level is consistent with that required for the recirculator. We expect to build and install modulator boards (based on the linear prototype) to drive the induction cells on the existing 90º recirculator early in FY-99.

The dynamic beam parameters also require that we drive the beam-bending dipoles with varying voltage levels. As the beam becomes more energetic, the dipole voltage necessary to provide the proper bending increases. During FY-98, we installed and tested a prototype bending dipole pulser on the small recirculator. Pulser performance was mixed. Its power stages performed as expected, but we experienced unexplained failures in some of the output transformers. In addition, we worked to modify the pulser's waveform generation and control feedback elements, to integrate the pulser into the existing recirculator timing, control, and diagnostics sub-systems, and to compensate for the effects of output loading and filtering.

We conducted beam dynamics experiments using the modified pulser, which determined the relative effects of timing, voltage level, and output ripple on

beam bending. We will conduct further bending experiments once the induction core modulators have been brought online.

We have used beam modeling throughout this project to develop steering control algorithms and to identify critical beam control issues. During FY-98, we studied the relative merits of two fundamental steering methods, which will help determine the best configuration for steering modules on the small recirculator.

The first method applies steering corrections based on measured values of beam position, velocity, and momentum. This method tends to impart larger "kicks" to the beam, using relatively fewer steering modules. The second method is based on solving simultaneous equations designed to minimize functions based on measured beam displacements and steering module voltages. This method tends to apply smaller "kicks" using steering modules in more locations. We will carry out experiments in this area during FY-99.

TIGER: An Object-Oriented Time-Domain Simulation Code

David J. Steich, Jeffrey S. Kallman, and Gerald J. Burke
Defense Sciences Engineering Division
Electronics Engineering

S Terry Brugger
Computer Applications Sciences and Engineering
Computation

Daniel A. White
Center for Applied Scientific Computing
Computation

This report discusses our progress to date and our future plans for the Time-Domain Generalized Excitation and Response (TIGER) code. TIGER is an object-oriented computational electromagnetics (CEM) field solver. A prototype version of TIGER was built last year. This year we extended the code to model more realistic structures, and began building the next version. We also studied the incorporation of thin-wire algorithms. Our FY-99 plans include the continued development of the parallel-hybridized version of TIGER and the building of a powerful GUI for the code.

Introduction

There is a significant need to advance our time-domain simulation capabilities. Projects desiring more advanced CEM include antenna applications, vulnerability and susceptibility assessments, field/radiation effects due to outside stimulus, full-wave field behavior of kickers, splitters, induction cells, broadband phased arrays, Eigenvalues/Eigenvectors of lossy cavities, and lightning assessments, to name a few.

Time-domain CEM techniques have been in existence for more than 30 years and have grown in popularity. There are now hundreds of publications each year in the area as the techniques have matured. With so much previous work, it remains a challenge to keep up with the latest approaches. Often today it does not suffice to apply a single method to a complex application. Although we are living in an age where simplicity is preferred over complexity, the advantages of hybridized solutions cannot be ignored. However, the management of this complexity comes at a price. This price is usually delayed technology advances and increased effort to solve the problem.

The TIGER project endeavors to circumvent much of the complexity involved in judiciously applying multiple algorithms to a given geometry to improve accuracy and lower computational overhead. TIGER accomplishes this management of complexity by using object-oriented techniques.

This report describes our continuing progress in modeling components for the Advanced Hydrotest Facility (AHF) at Lawrence Livermore National Laboratory (LLNL), our parallelization progress, and our current efforts to model thin wires in the time domain.

Progress

Last year we built a prototype version of TIGER and modeled a Beam Position Monitor (BPM), which is essentially a 1/10-scale version (1/100 volume) of a simplified kicker. We achieved a greater than 100-fold reduction in the number of cells required to simulate the BPM with comparable or improved accuracy. We also performed extensive testing and validation of the code.

Testing and validation included comparisons with analytic solutions, convergence studies, and careful study of known error sources often found in these simulations, such as absorbing boundary conditions and accurate modeling of sources and feeds.

Last year's results were limited to monopole and dipole wakefield calculations of a BPM. This year we chose to model a full scale 3-D kicker structure built as a prototype design for LLNL's AHF programs, and obtained wakefield results for modes m = 0 through m = 4. Previous modeling was limited to m = 0 and m = 1 for a scaled BMP geometry only.

Figure 1 is a photograph of a prototype accelerator kicker for LLNL's Experimental Test Accelerator (ETA-II). Shown in **Fig. 2** is a view of a section of a CAD kicker model. **Figures 3** and **4** depict the real and imaginary transverse quadrupole wake impedances of the kicker, respectively. **Figures 5** and **6** depict normalized sextupole (m = 3), and dipole (m = 1) transverse wake potentials for an m = 3 source, respectively.

Results show that the dipole wakes caused by a sextupole excitation are not insignificant and must be taken into account. This is in agreement with experimental evidence of the kicker. Preliminary testing of the kicker shows a triangular-shaped beam hitting a foil for large input beam radius (**Fig. 7**), suggesting a large sextupole wakefield. Research into understanding this phenomenon is ongoing.

Figure 1. Photograph of prototype ETA-II accelerator kicker.

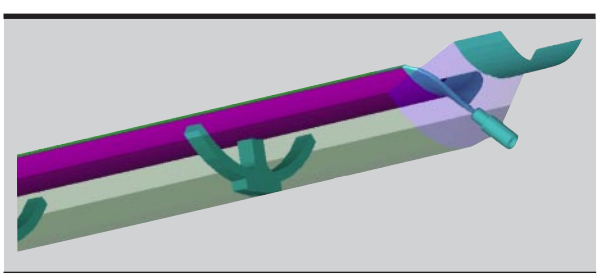

Figure 2. CAD enlargement of feed transition region for prototype ETA-II accelerator kicker.

Also in FY-98, we focused on building the next major parallel version of TIGER. This next version will be even more capable, flexible, and extensible. Shown in **Fig. 8** is a plot of speed-up versus number of processors for TIGER's preprocessor on the ASCI Blue machine. The geometry is a 234,000-cell mesh that is partitioned on 1, 2, 4, 8, 16, and 32 processors. We are getting excellent speed-ups up to 32 processors.

The slight decrease in speedup performance for the 16- and 32-processor runs is due to the extra communication that is involved. Since we are splitting up the same geometry on successively more and more processors, the surface to volume ratio is increasing. This means there is less relative work to do for a given amount of required communication. In general, we must communicate the entire outer surface cell layer(s) of the geometry to adjacent processors. For 32 processors, there are only roughly 7312 cells per processor.

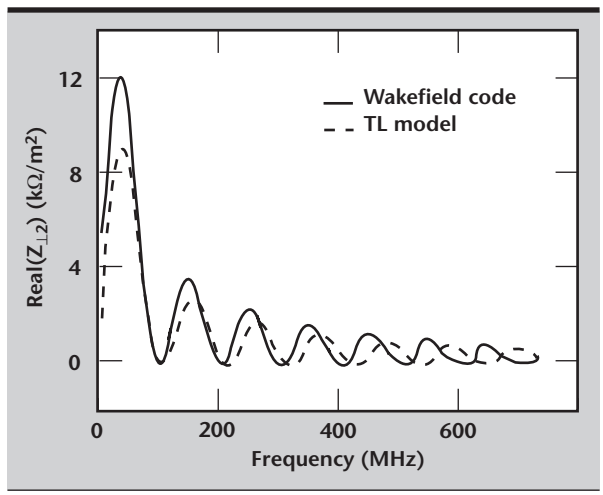

Figure 3. Real transverse quadrupole wakefield impedance for prototype ETA-II accelerator kicker.

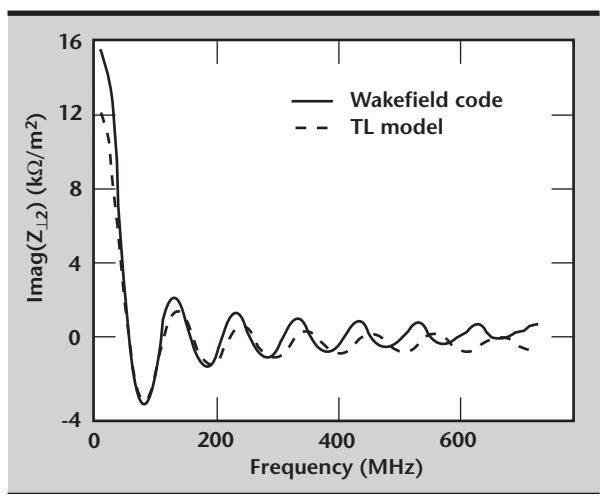

Figure 4. Imaginary transverse quadrupole wakefield impedance for prototype ETA-II accelerator kicker.

If we would instead increase the geometry so that the number of cells per processor remained a constant, our speed-up would again start to approach perfect speed-up performance. For real production runs we would keep at least several hundred thousand cells per processor. It is our intent to eventually run problems with tens to hundreds of millions of cells.

Time-Domain Thin-Wire Capabilities

Adding thin-wire capabilities to TIGER would greatly extend its usefulness to LLNL programs. There are applications in micro-impulse radar, nonproliferation, defense technologies, and the Department of Defense that could utilize thin-wire simulation capabilities. While finite-difference and finite-volume techniques are very powerful and have found widespread use in electromagnetics, modeling thin wires in such algorithms presents several challenges. The wires are usually much thinner than the desired cell size. Several methods, which use either contour path integration, integral equations for wire currents, or transmission line equations have been used. Each of these methods has different advantages and disadvantages. However, each of the above mentioned techniques requires the wires to lie along electric or magnetic mesh edges, which restricts the wire geometry when cells are orthogonal. Furthermore, with more general meshes, generation of a new mesh is required when a wire is moved.

Our goals for FY-98 were to implement a thin-wire algorithm and see if we could generalize the algorithm to move the wire laterally along the grid. This would be the first step toward having an arbitrary wire within the grid without having to mesh the wire.

We successfully implemented thin-wire algorithms by Holland[1], Riley[2], and Taflove[3]. We also improved the accuracy of Holland's method and generalized the algorithm to allow for wires moved laterally within a mesh. Results for our new scheme are shown in **Fig. 9** for the real part of a dipole impedance for a thin wire of 0.001-m radius with a cell size of 0.035 m for various wire locations within an FDTD cell.

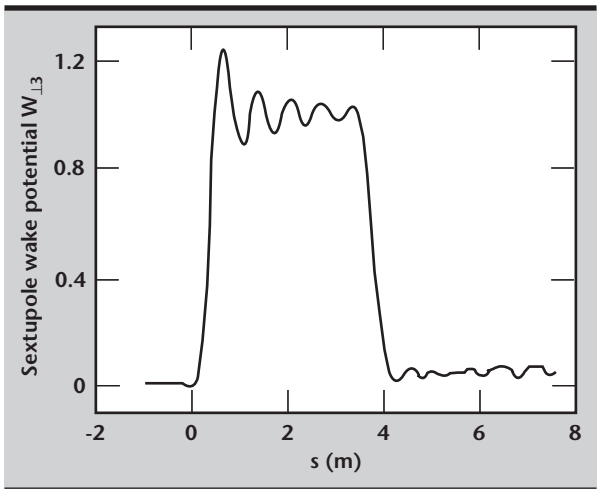

Figure 5. Normalized sextupole (m = 3) transverse wake potential for an m = 3 source.

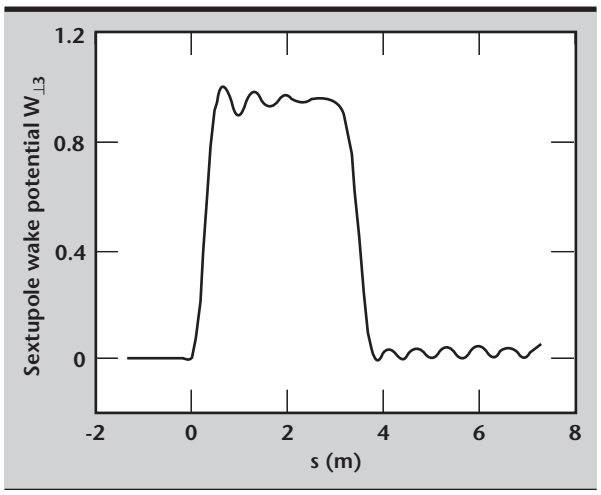

Figure 6. Normalized dipole (m = 1) transverse wake potential for an m = 3 source.

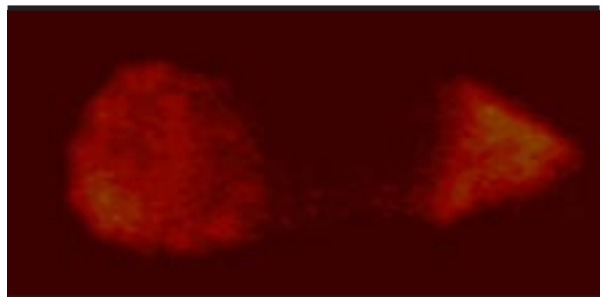

Figure 7. Experimental results for triangular-shaped beam hitting foil, for large input beam radius in the prototype ETA-II accelerator kicker.

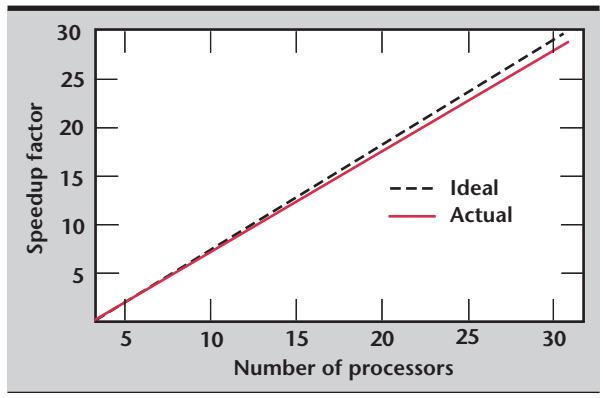

Figure 8. TIGER preprocessor speed-up factor vs number of processors on ASCI-blue.

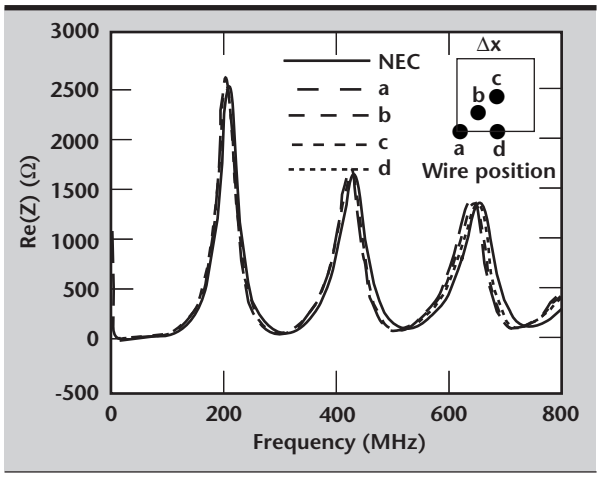

Figure 9. Thin-wire results for dipole moved to various locations within a cell.

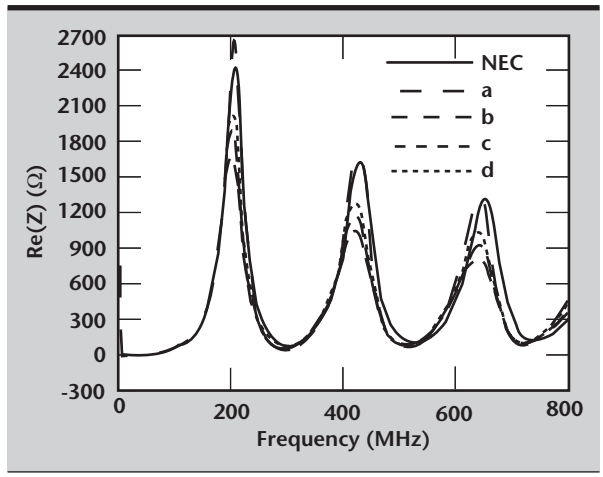

Figure 10. Holland's thin-wire results for dipole moved to various locations within a cell.

Shown in **Fig. 10** is Holland's scheme for the same dipole impedance. Note the large variation in the real part of the dipole impedance of Holland's scheme for various wire locations.

Future Work

Next year, our technology-base focus will be to provide a powerful graphical user interface (GUI) for TIGER. This GUI will be object-oriented and allow many of TIGER's capabilities to be used in a user-friendly environment. We will continue to extend the parallel version of TIGER. Extensions will include the parallelization of the solver and the simultaneous hybridization of mesh types and physics algorithms.

References

1. Holland, R. (1981), "Finite-Difference Analysis of EMP Coupling to Thin Struts and Wires," *IEEE Trans. Electromag. Compat.,* Vol. EMC-**23**, No. 2, May.

2. Riley, D. J., and C. D. Turner (1998), "The VOLMAX Transient Electromagnetic Modeling System, Including Sub-Cell Slots and Wires on Random Non-Orthogonal Cells," *Fourteenth Annual Review of Progress in Applied Computational Electromagnetics,* March.

3. Umashanker, K. R., A. Taflove, and B. Beker (1987), "Calculation and Experimental Validation of Induced Currents on Coupled Wires in an Arbitrary Shaped Cavity," *IEEE Trans. Antennas and Propagation,* Vol. **35**, pp. 1248–1257.

OPUS: An Optically Parallel Ultrasound Sensor

Jeffrey S. Kallman
Defense Sciences Engineering Division
Electronics Engineering

Dino R. Ciarlo
Engineering Research Division
Electronics Engineering

Elaine Ashby and Graham H. Thomas
Manufacturing and Materials Engineering Division
Mechanical Engineering

This development project addresses the need for a faster, less expensive method of transmission ultrasound. It uses the principle of frustrated total internal reflection to transduce acoustic pressure into optical modulation. An entire 2-D plane of data at a time can be acquired. We describe the modeling and verification of a final sensor design.

Introduction

Ultrasound imaging is used to inspect parts, monitor processes, and diagnose problems in human patients. Soon after x-ray CT was invented, attempts were made to do the same kind of imaging with ultrasound. One of the many problems encountered was the difficulty of acquiring the necessary data in a timely fashion. Other problems included the tendency of ultrasound not to travel in straight lines, and to require a couplant between source, object, and sensor.

The existence of these problems is unfortunate, considering that 3-D volumetric imaging by ultrasound would be quite useful for screening for breast cancer. Consider the advantages: no ionizing radiation, no compression, and no toxic developing solutions or film. At present the only way to get the information necessary to do this kind of imaging is to use arrays of piezoelectric sensors, and either multiplex them in time or have multiple copies of the necessary electronics to read them, which is expensive. The sensor we are developing addresses these problems.

Our new sensor uses the classical optical phenomenon, frustrated total internal reflection (FTIR), to make the incident ultrasonic wave modulate a beam of light, which is then acquired by a camera and computer. A sequence of images, each taken at a different source acoustic phase, enables us to reconstruct the ultrasonic phase and amplitude over an entire 2-D surface.

In this report we detail the development and design of our optically parallel ultrasound sensor.

Optics

FTIR is a consequence of the wave nature of light.[1] When light moves from a slow medium to a fast one, there is a critical angle, $\theta_c = \sin^{-1}(n_2/n_1)$ (where n_1 is the index of refraction of the slow medium and n_2 is the index of the fast medium), beyond which the light is totally reflected. However, an evanescent wave extends a short distance (approximately one wavelength) into the fast medium, and if another piece of slow medium intercepts this evanescent wave, some of the light tunnels across the gap (**Fig. 1**). How much light tunnels is a function of the angle of incidence, the indices of the media, and, most importantly from our point of view, the size of the gap.

We can exploit this effect to build an array of acoustic pixels. Each acoustic pixel is composed of a thin silicon nitride membrane suspended on short gold walls over an optical substrate. The gap

between the membrane and the optical substrate is filled with air (**Fig. 2**). The entire assembly is immersed in the ultrasonic couplant. When an ultrasonic pressure wave impinges on the acoustic pixel, the membrane deflects, causing a change in the amount of light reflected from the total internal reflection surface of the acoustic pixel. An entire array of acoustic pixels can be used to modulate a beam of light.

The information we desire from this sensor is the phase and amplitude at each acoustic pixel. To obtain this information we illuminate the sensor with ten sequences of optical pulses, each sequence timed to act as a strobe light at a specific acoustic phase (**Fig. 3**). We extract the phase and amplitude at each pixel by fitting the intensity at that pixel through the sequence to the form $I = B + A \sin(2\pi i/10 + \phi)$, where I is the intensity, B is the background, A is the amplitude of the sinusoidal variation, i is the index of the image in the sequence, and ϕ is the phase of the variation.

The optical train of this device is as follows: we illuminate the sensor using an LED, the light from which is homogenized, polarized, and collimated. We acquire the reflection from the sensor using a CCD still camera.

Acoustics

The inspection technique we are interested in is transmission ultrasound. In this modality, an acoustic source sends out pressure waves through a couplant, such as water, oil, or medical ultrasound gel, to the object of interest. The pressure waves are transmitted through the object, being changed in amplitude and phase along the way. The pressure wave emerges from the object of interest and travels, via the couplant, to an acoustic sensor. The sensor determines the acoustic phase and amplitude, either at a point, on a line, or in a plane. The sensor we are developing will measure the acoustic phase and amplitude of an entire plane at a time.

Our sensor works because the pressure wave causes the flexing of a membrane, causing it to vibrate with a phase and amplitude that are functions of that wave.

In designing our sensor, we needed to have a membrane with a frequency response high enough to vibrate at the frequencies of interest to us (approximately 1 MHz).

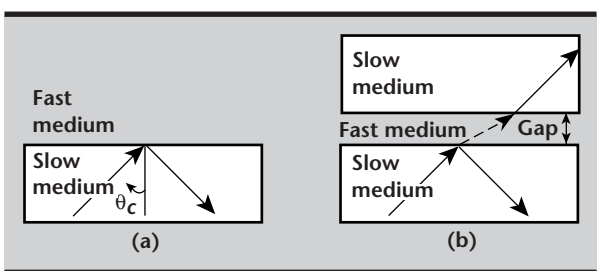

Figure 1. (a) Illustration of total internal reflection. Light trying to exit the slow medium at an angle higher than the critical angle will be completely reflected. (b) Frustrated total internal reflection. The evanescent wave that extends into the fast medium overlaps another piece of slow medium, and some of the light tunnels across the gap. The amount of light that tunnels through the gap is sensitively dependent on the size of the gap.

Progress

Modeling

We began our work on this project by modeling as many of the systems and processes as possible. We used TSARLITE to model the optical elements of the sensor (FTIR), DYNA3D to model the acoustic responses of the membranes and their supports, and

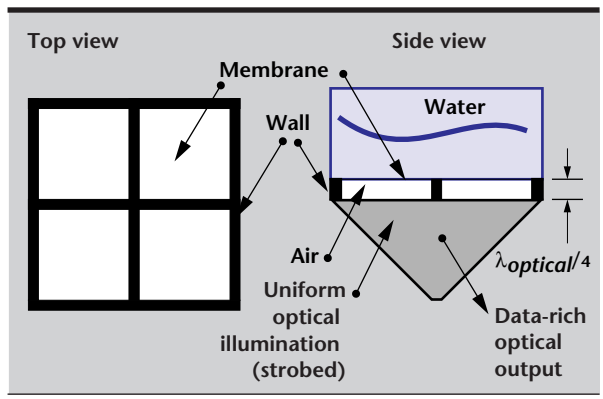

Figure 2. Illustration of an acoustic pixel, a thin membrane suspended over an optical substrate by gold walls. There is an air gap between the membrane and the optical substrate, and the acoustic pixel is exposed to water. An ultrasonic pressure wave moving through the water will cause the membrane to vibrate, changing the air gap enough to modulate a beam of light reflected from the total internal reflection surface of the optical substrate.

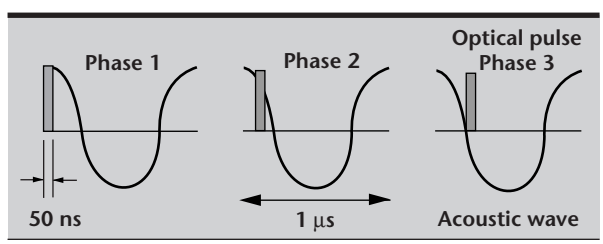

Figure 3. Illustration of the illumination of the optical substrate at particular times during the acoustic wave. This causes the optical beam to act as a strobe light. A sequence of ten images allows us to deduce the motion of each acoustic pixel through the acoustic wave, and thus the pressure and phase of the acoustic pixel excitation.

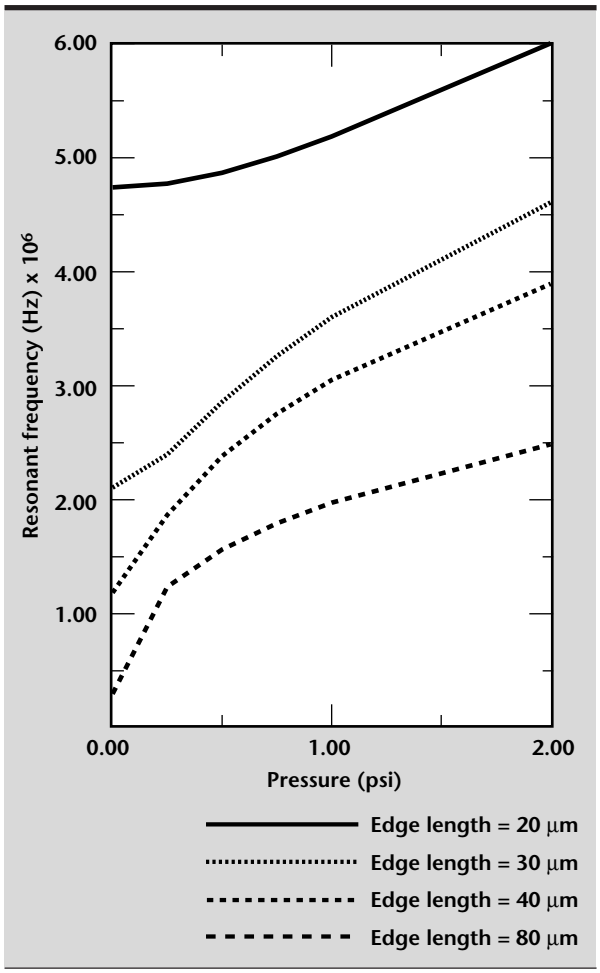

Figure 4. Graph showing how the resonant frequency of a set of simulated acoustic resonators varies with the hydrostatic pressure load.

a modification of BEEMER to model the imaging system as a whole.

Using TSARLITE, we were able to determine the ranges where we could expect FTIR to be useful, and bounded the permissible thickness of the membrane and the heights of the supports it would stand upon. This aspect of the modeling was performed to make certain that we would be able to engineer to the physical phenomenon we were using.

The modified BEEMER program was used to examine the issues that will arise when we use the sensor for diffraction tomographic imaging. It was used to model the tomographic data acquisition processes, as well as a variety of reconstruction algorithms.

The simulation program we used most was DYNA3D. We used this program to model our first sensor design, a membrane suspended on an array of posts. DYNA3D showed us that this design had neither the sensitivity nor the frequency response necessary to allow us to acquire the data we needed. Guided by our simulations, we developed a more responsive design, a set of resonant membranes suspended on walls (**Fig. 2**). Simulation showed this design was responsive and sensitive, but had problems with cross-talk and drift of the resonant frequency as a function of hydrostatic pressure (**Fig. 4**). Further simulation allowed us to modify the design so as to greatly reduce cross-talk (**Fig. 5**).

Simulation eliminated the need to experiment blindly, but we still needed to do experiments to verify that the simulations were correct, and get proof of principle results. To do these experiments we built a test system.

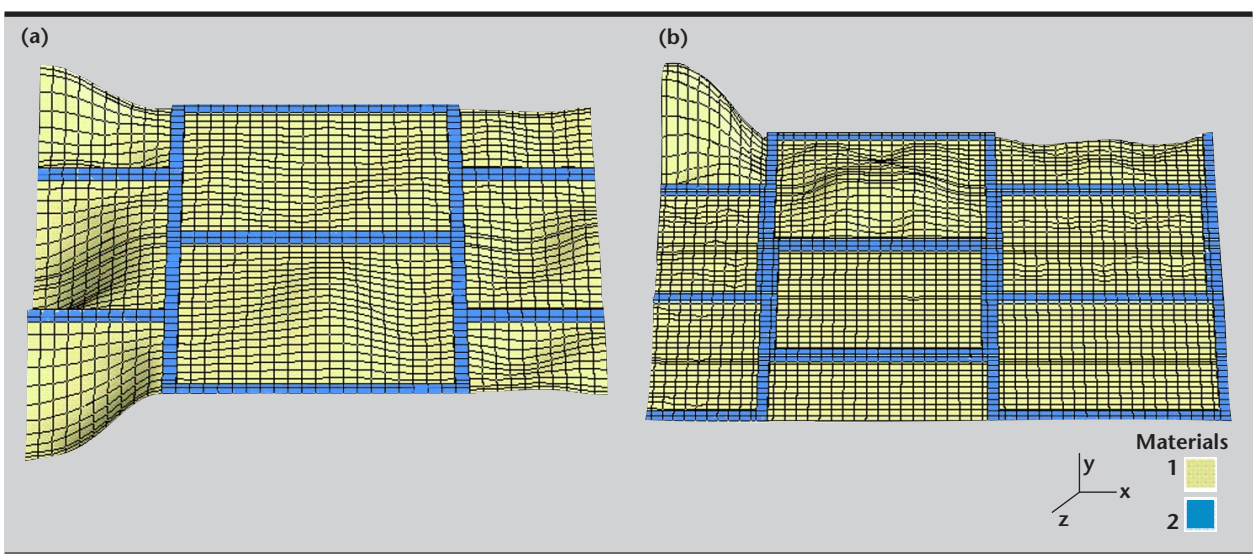

Figure 5. Simulation Results. (a) All of the acoustic pixels in this simulation have the same resonant frequency. An excitation of the rear left pixel spreads to all the surrounding acoustic pixels. (b) Staggering the sizes of the acoustic pixels greatly reduces the spreading of energy (cross-talk).

Verification

The test system we built consisted of the test membrane, a tank with an acoustic source, and the optics. The test membrane was designed to allow us to examine the responses of a wide range of membrane resonator sizes to variations in hydrostatic pressure. The rest of the system was designed to make all of the parameters of interest easily available for manipulation.

The test membrane consists of a 1-cm-by-1-cm membrane of silicon nitride, supported by gold walls, held in a silicon frame. The gold walls are patterned as shown in **Fig. 6**. On the left hand side of the test membrane are alternating rows of 60 acoustic pixels ranging in size from 20 μm to 80 μm on a side. On the right hand side of the test membrane only half of the rows are populated with acoustic pixels. The reason for the wide range in size is evident from **Fig. 4**.

We suspected that only acoustic pixels that were at the exact resonant frequency would be sensitive enough to modulate the optical input, and so attempted to include all pertinent sizes. In addition to the wide range in resonator sizes available we had membrane fabrication parameters available for modification as well, that is, membrane thickness and gold wall height.

The remainder of the system is illustrated in schematic form in **Fig. 7**. The oscillator provides a 1-MHz signal, which is amplified and fed through the power meter to the acoustic source in the water tank. The same signal goes to the pulse generator, which in turn excites the optical source as a strobe light. The pulse generator output and the oscillator output are both fed to an oscilloscope to allow the user to place the optical pulse at any point in the acoustic phase. The optical pulses are homogenized, polarized, collimated, and fed through the prism to the sensing surface, and the reflected light is captured by the camera and saved in the computer. The user has control over the oscillator frequency, the amplifier gain, the camera exposure time, the optical pulse width, amplitude, and placement in the acoustic phase, and the depth of the water in the tank.

This is the procedure followed during a typical experimental run: the water tank is filled to the desired depth, and the acoustic power level, camera exposure time, optical pulse width, and optical pulse amplitude are set. Four sequences of ten images are acquired, each with the optical pulse occurring at a different acoustic phase.

We learned a great deal using the test system, most importantly that: 1) we can engineer to the sizes and tolerances necessary to use the physical phenomenon; 2) we can extract phase and amplitude data at each acoustic pixel from sequences of images; 3) the resonances are so broad as to make acoustic pixel size non-critical; and 4) hydrostatic pressure causes little change in membrane response.

After performing numerous experimental runs we were able to arrive at an optimal set of design parameters for the final sensor.

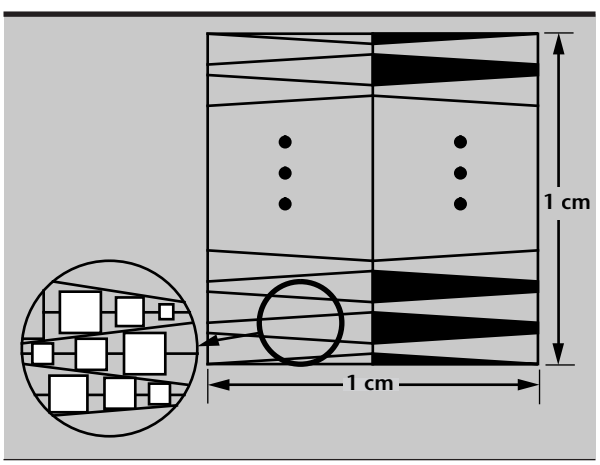

Figure 6. Schematic of the pattern of acoustic pixels in the test membrane. On the left are alternating rows of 60 acoustic pixels ranging in size from 20 μm to 80 μm on a side. On the right only half of the rows are populated with acoustic pixels.

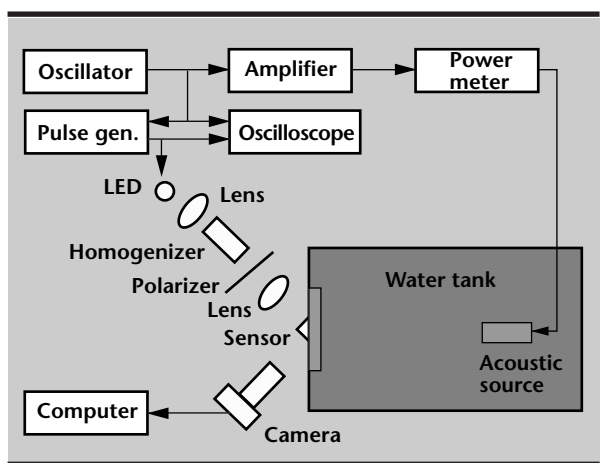

Figure 7. The test system. The oscillator drives the amplifier and pulse generator with a 1-MHz sinusoid. The acoustic source insonifies the test membrane which is illuminated with 50-ns optical pulses strobing at a user-specified acoustic phase. Images of the membrane are acquired by the camera and stored and processed in the computer.

Future Work

We have completed the design for the final sensor. The final sensor is currently in the process of fabrication. Since we have funding to continue this work in the next fiscal year, we will complete the construction of our final sensor, calibrate it, and use it to collect phase and amplitude data through a variety of test subjects. Initially we will only make 2-D transmission ultrasound images, but ultimately we will generate volumetric images of 3-D objects using data from this sensor to feed a diffraction tomography code.

References

1. Yeh, P. (1988), *Optical Waves in Layered Media*, John Wiley and Sons, New York, New York.

Optical Transition Radiation Diagnosis for Electron Beams

Gregory P. Le Sage and Roger A. Richardson
Defense Sciences Engineering Division
Electronics Engineering

We describe the accomplishments of two technology-base projects dealing with the development of electron beam diagnostics using optical transition radiation (OTR). Diagnostic experiments using OTR were performed at the Lawrence Livermore National Laboratory (LLNL) flash x-ray facility (FXR), and at the LLNL 100-MeV RF linac facility. The original charter for the RF linac was the development of diagnostics appropriate for a high-peak-brightness electron beam. OTR appeared to be a suitable candidate for measuring micron-scale beam spots, and milliradian divergences. Transition radiation diagnostics were evaluated using the thermionic electron beam produced by the LLNL RF linac facility. The diagnostics are intended for use with the high-brightness electron beam that will be produced by a photocathode injector currently under development. The FXR effort concentrated on the use of OTR for transverse beam profile imaging at viewing angles away from the OTR radiation peaks, at time scales short compared to the bunch length. The effects of surface roughness on the radiation pattern of OTR were examined theoretically.

Introduction

Transition radiation is produced when a charged particle traverses a barrier between two media with different dielectric characteristics. This radiation emerges with a distinct angular distribution, which can be exploited to reveal electron beam characteristics that are otherwise difficult or cumbersome to measure. The basic configurations for these measurements include a single or multiple samples of dielectric or metallic material inserted into the electron beam. Using appropriate materials and optical measurement techniques, the spatial profile and the divergence of the electron beam can be measured at a single point, in a single shot.

Though the divergence of the beam is degraded by the thin (few micron) dielectric foils, it is not completely disrupted, as in the case of traditional slit projection techniques used to measure the same information. These seemingly delicate foil samples have in fact proven to be quite robust in some cases, accepting long macropulse lengths, high-average currents, high-energy beams, and relatively tight focal spots.

The equations describing this radiation are well known, but are somewhat cumbersome to use for real materials, particularly for relativistic particles. Typically, approximations are made so the equations can be used analytically. The materials used to produce transition radiation are described by dielectric constants in the desired frequency range, both real and imaginary parts. Simplified forms of the transition radiation formulae were programmed for comparison to measured data, and for estimation of flux levels at angles away from the peaks of the OTR pattern.

A characteristic of the radiation pattern at high energies is the directivity of the back-scattered radiation. For a relativistic factor γ of 100, OTR is confined to tens of milliradians of the reflection angle. The reflection angle is equal to the incident angle, so that for a foil angled at 45° with respect to an electron beam, the radiation pattern will be centered at 90°.

This is convenient for most applications, but for the confined space available in the FXR experiment, it was not possible to view transition radiation at the proper angle of maximum intensity. To broaden the radiation pattern, the surface of an OTR foil was roughened so that a more random incident angle is presented to the electron beam.

The effects of surface roughness on an OTR radiation pattern were modeled using MATHEMATICA. The surface roughness was modeled as a random Gaussian function, centered at the foil angle. An OTR distribution was integrated over this Gaussian

function to observe the effects of this roughness model. When the foil surface roughness was increased in the model, the radiation lobes were broadened. Light produced by OTR was successfully measured at the FXR using a roughed KAPTON foil far from the optimum specular angle.

Progress

The efforts and accomplishments for the RF linac facility for FY-98 are described in this section. We have expanded the scope of the effort to include preparation of the photocathode electron accelerator.

A single foil OTR measurement in FY-98 provided the first emittance data ever collected on the high-energy S-Band RF linac beam at LLNL. The technique was proven for our beam parameters, and the diagnostic will certainly be used as the machine is improved.

A theoretical study of the angular distribution of transition radiation was performed to evaluate the measured data under our particular conditions. One can imagine that while a single electron produces a perfect angular distribution of transition radiation light, a broad thermal distribution of electrons with a large spot size produces a blurred pattern with characteristics that are not readily tractable. A simulated distribution of electrons with imposed spatial and angular distribution (MATHCAD-script developed) was used to generate characteristic OTR patterns that could be compared to measured data. Added complication results from the large spot size, which affects the optical collection of the data, and depends on the distance to the point of measurement (a CCD).

Taking all relevant effects into account, a multiple-parameter fit was performed to compare the theoretical and measured distributions (C++-code developed). Error bars were thus established between the measured data and the theoretical fit over a range of measured angles, and an emittance with specified tolerance was measured.

When two or more foils are used for a transition radiation measurement, an interference pattern is produced by the forward-projected OTR light from the first foil, and the specularly reflected light from the adjoining foils. This technique is useful since multiple peaks and nulls allow more precise evaluation of the beam divergence.

From a practical perspective, the angular pattern of light coming from a multi-foil arrangement is much less ambiguous than that from a single foil, since the interference fringes appear to sharpen considerably as the beam and optical system parameters are properly adjusted.

Just such an effect was measured this year, again using the LLNL linac beam, and a pair of aluminized mylar foils. This measurement also provided another significant milestone in the life of the linac beam. For the first time, we had visual feedback for tuning the divergence of the linac beam at a given point. Starting with a beam spot optimized for small size and regular (round) appearance, we noticed that the OTR interference pattern was quite poor. As the fringe sharpness was optimized by tuning the linac optics, we found that the spot image became much more irregular, indicating that the beam transport system was astigmatic (horizontal and vertical focal lengths were not equal). With a remotely rotatable polarizer, the collimation in orthogonal directions can be investigated. These capabilities will provide essential information for interaction experiments between the linac beam and a short laser pulse.

In addition, the prompt light produced by transition radiation can be used to characterize the temporal characteristics of an electron beam. The FXR effort described previously included the use of a gated intensifier to measure the beam evolution. Short pulse beams can be similarly characterized using a streak camera.

Measurement of the OTR light produced by the two-foil setup using a fast-risetime PMT was performed at the RF linac facility, confirming the RF signals produced by low bandwidth beam current monitors. With the bandwidth of the PMT (3 GHz), we were able to detect changes in the macropulse as a function of time.

Future Work

In FY-99 an experiment is planned to relay-image OTR light to an optical test bench, where the image can be masked to allow precise measurement of divergence characteristics across the beam profile. If a mask with multiple apertures is used, an “optical pepper-pot” measurement will be possible, allowing reconstruction of the beam phase space. This technique would be extremely useful for the high-energy linac beam, since a collimator for a 100- to 150-MeV electron beam would be many centimeters thick. The imaging arrangement is near completion, with relay optics and wall penetrations in place. Though the concept for this technique is patented, this diagnostic has never been implemented before. We are

currently discussing this and other collaborative experiments with the two authors of the optical pepper pot diagnostic patent.

OTR has been successfully demonstrated as a useful diagnostic for two very different classes of relativistic electron beams. Closer ties are being forged between the RF linac group, FXR, and ETA II. Further development of these diagnostics is expected.

Characterization of Electromagnetic Scattering from Defects in the EUVL Process

Lisa Wang and Scott D. Nelson
Defense Sciences Engineering Division
Electronics Engineering

Jeffrey E. Mast and Abbie L. Warrick
Laser Engineering Division
Electronics Engineering

Extreme ultraviolet lithography (EUVL) is a promising technology for producing high-resolution semiconductor features in next generation lithography. For EUVL, even small defects can pose a significant problem. Scattering models of defects, both for the substrate and the mask blank, are needed to understand the critical issues associated with mask defects. In FY-98, we have applied both asymptotic/analytical methods and numerical techniques to model the electromagnetic scattering from substrate defects to study how electromagnetic waves at optical or EUV wavelengths interact with anomalies on the substrate.

Introduction

In recent years, there has been an increasing interest in extreme ultraviolet lithography (EUVL), which is a promising technology for producing semiconductor features with resolutions <0.07 μm. The use of EUV technology would permit the development of computer chips with faster speed and more memory storage. At EUV wavelengths, all materials become very absorptive. Therefore, unlike transmissive masks used in traditional optical lithography, this technology uses multi-layer coated reflective masks.

Currently, the mask blanks are constructed by depositing 81 alternating layers of molybdenum (Mo) and silicon (Si) on an Si substrate. Each layer pair is 7 nm thick (3 nm of Mo and 4 nm of Si), producing a 284-nm high multi-layer coating. The masks are then made by depositing absorber patterns on top of the Mo/Si multi-layer mask blanks.

Figure 1a shows the complete EUV lithographic process. The EUV light, created using a laser plasma source, is directed toward the mask using reflective Mo/Si multi-layer coated condenser optics. After the EUV light passes through the mask containing the circuit patterns, it then passes through the multi-layer imaging optics to reduce the image size to allow very small circuits to be printed.

The multi-layers are deposited using a newly developed ion beam deposition system, IBD-350, shown in **Fig. 1b**. This system is capable of producing uniform low-defect-density multi-layer-coated reflective mask blanks (**Fig. 2**).[1,2] In depositing different layers of material for a reflective mask, ions collide with the target of Mo or Si, and are then precisely deposited on the substrate.

For EUVL, even small defects on the substrate or in the multi-layer mask blank may pose a significant problem. It is not only because of the small feature size, but also because very small defects may introduce compound errors from the multi-layer deposition process, which can then cause problems when the circuit patterns are printed. Preliminary printability models suggest that defects >30 nm in diameter may print in the EUVL lithographic process.[3]

There is considerable concern about the effect of defects in the EUVL mask blanks caused by contaminating particles, substrate scratches, and other imperfections that may result in printable defects. The identification of printable defects is essential to the development of projection EUVL. This is the subject of an ongoing experimental program at Lawrence Livermore National Laboratory.

The development of a realistic scattering model to predict how electromagnetic waves interact with anomalies in the multi-layer coating of the mask

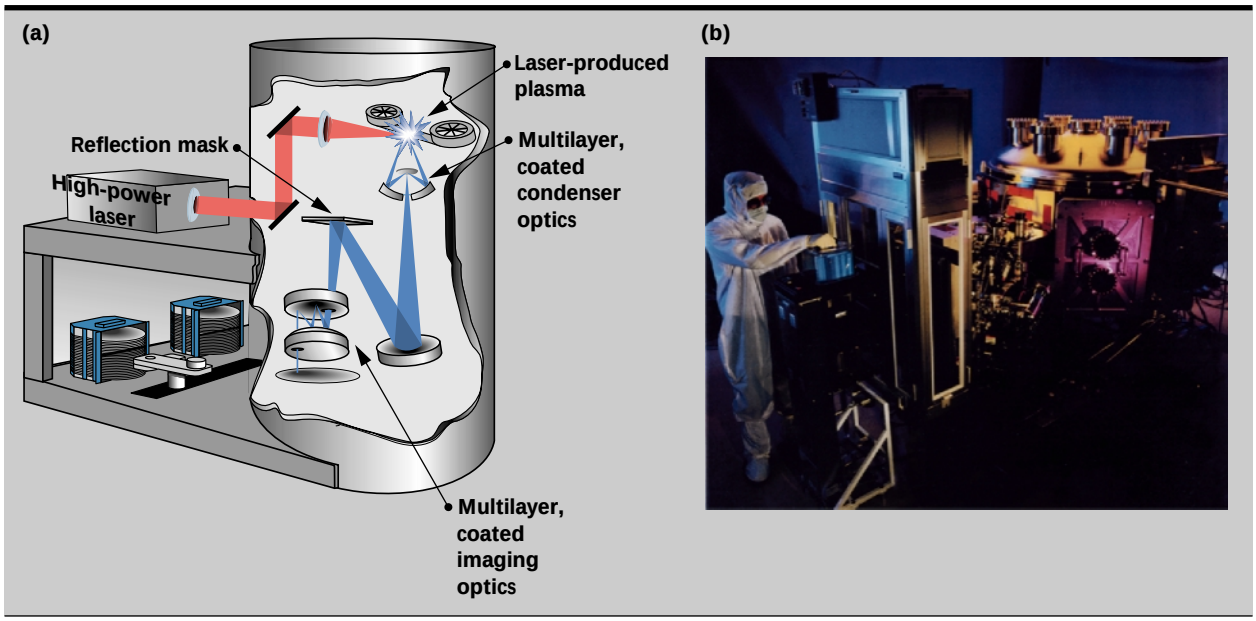

Figure 1. The EUV lithographic process. (a) EUV light is guided toward the mask using multi-layer-coated reflective optics. After the light passes through the mask and the multi-layer imaging optics, the circuit patterns on the mask are transferred onto Si wafers with reduced image size. The ion beam deposition system (b) is used to produce these uniform low-defect-density multi-layer-coated reflective mask blanks. The system includes the substrate loader and the deposition chamber where the multi-layer coatings are applied.

blank is needed for the identification of printable defects. In addition, the scattering cross-section of printable EUVL defects is needed for the development of inspection tools and effective diagnostic algorithms at both optical and EUV wavelengths.

Progress

Both asymptotic/analytical methods and numerical techniques were applied to model the electromagnetic scattering from defects on the substrate. The applicability of asymptotic/analytical methods as a function of defect size and shape was first evaluated.

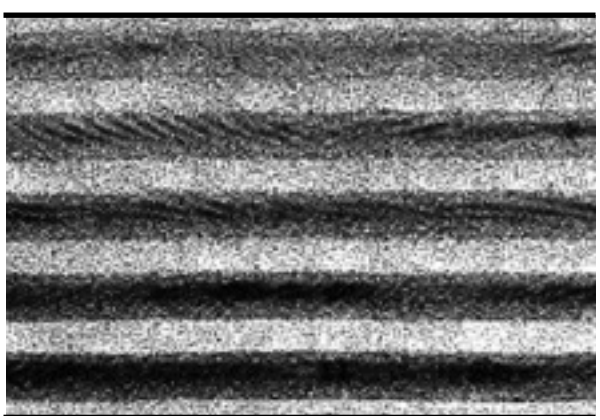

Figure 2. Magnified image of multi-layer coating, showing alternating layers of Mo and Si. The dark and light bands are Mo and Si, respectively.

Within their range of validity, asymptotic methods increase the computational efficiency at least tenfold, compared to current numerical methods, helping us gain physical insights into scattering mechanisms, and facilitating the interpretation of numerical solutions. Several asymptotic/analytical methods were examined, among which are the physical optics approximation (which is applicable when the defect is large compared to a wavelength);[4-7] the physical theory of diffraction (which takes into account the diffracted rays due to edges, corners, and curved surfaces);[6,8] the shooting and bouncing ray technique;[8] and radiative transfer theory.[7]

Electromagnetic models were developed to simulate the scattering from substrate defects and particles including spheres, cylinders, disks, ellipsoids, and hemispheres. Given an incident wave E_i in the direction θ_i, ϕ_i, the first-order solution of the back-scattered electric field from a substrate defect can be expressed as

$$E_q^s(\bar{r}) = \frac{e^{ikr}}{r}\Big[f_{qp}(\pi-\theta_i, \pi+\phi_i; \theta_i, \phi_i)$$

$$\times\ e^{i[\bar{k}_p^i(\theta_i,\phi_i)-\bar{k}_q^s(\pi-\theta_i,\pi+\phi_i)]\cdot\bar{r}}$$

$$+\ R_q(\theta_i) f_{qp}(\theta_i, \pi+\phi_i; \theta_i, \phi_i)$$

$$\times\ e^{i[\bar{k}_p^i(\theta_i,\phi_i)-\bar{k}_q^s(\theta_i,\pi+\phi_i)]\cdot\bar{r}}$$

$$+\ f_{qp}(\pi-\theta_i, \pi+\phi_i; \pi-\theta_i, \phi_i) R_p(\theta_i)$$

$$\times\ e^{i[\bar{k}_p^i(\pi-\theta_i,\phi_i)-\bar{k}_q^s(\pi-\theta_i,\pi+\phi_i)]\cdot\bar{r}}$$

$$+\ R_q(\theta_i) f_{qp}(\theta_i, \pi+\phi_i; \pi-\theta_i, \phi_i) R_p(\theta_i)$$

$$\times\ e^{i[\bar{k}_p^i(\pi-\theta_i,\phi_i)-\bar{k}_q^s(\theta_i,\pi+\phi_i)]\cdot\bar{r}} \Bigg] E_p^i,$$

where q and p are the polarization components ($\{q, p\}$ = horizontal or vertical) of the scattered and incident waves, respectively; f_{qp} is the scattering matrix element; $\bar{k}_p^i$ is the propagation vector of the incident wave; $\bar{k}_q^s$ is the propagation vector of the back-scattered wave; $\bar{r}$ is the location of the scatterer; $R_p(\theta_i)$ and $R_q(\theta_i)$ are the Fresnel reflection coefficients.

The first-order solution in the above equation describes four major scattering mechanisms (**Fig. 3**). The first term in the equation is the direct scattering from a particle (**Fig. 3a**). The second term is a single scattering from the scatterer, followed by a reflection off the boundary between air and the substrate (**Fig. 3b**). The third term is the opposite of the second term (**Fig. 3c**), and the fourth term describes a reflection by the boundary followed by a single scattering from the particle and further followed by a reflection off the boundary (**Fig. 3d**).

The scattering matrix element f_{qp} in the equation is calculated using the analytic method for different defect shapes. For example, Rayleigh and Mie scattering methods were applied to calculate the scattering returns from spheres.[4] Scattering from cylindrical defects (**Fig. 4a**) was calculated using the finite cylinder approximation[9] in which the induced current in the dielectric cylinder was assumed to be the same as that of the infinitely long cylinder of the same radius. This is a good approximation when the cylinder is long and thin compared to the wavelength. The scattered field is obtained by evaluating the field radiated from this approximate induced current source.

For disk-shaped defects (**Fig. 4b**), the returns were calculated using the physical optics approximation for elliptic disks,[10] which assumes the internal field inside the disc to be the same as that of the infinitely extended dielectric layer of the same thickness. Numerical full-wave techniques in both the time and the frequency domain, including ANSOFT™ and TSARLITE,[11] were used to validate scattering returns calculated with asymptotic/-analytical methods.

The scattering result from a cylindrical dielectric defect is shown in **Figs. 5** to **7** as an example

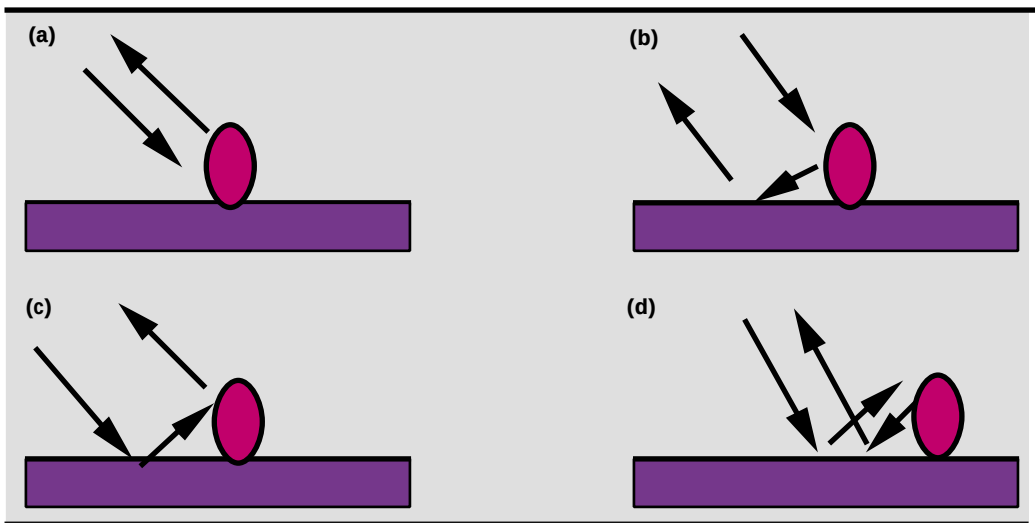

Figure 3. Four major scattering mechanisms considered part of the characterization of EUVL defects: (a) direct scattering from a scatterer; (b) single scattering from the scatterer followed by reflection off the boundary; (c) surface reflection followed by single scattering; and (d) direct reflection from the boundary, direct scattering from the scatterer, secondary reflection off the boundary.

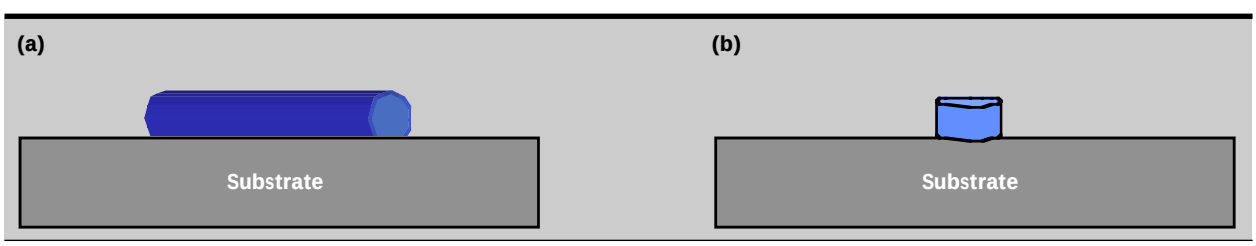

Figure 4. (a) Scattering from a cylindrical dielectric defect, calculated using the finite cylinder approximation; (b) scattering from a dielectric disk-shaped defect, obtained using the physical optics approximation.

of the results we have obtained. Before the scattering from a cylindrical defect on top of the substrate was calculated, analytic scattering results from a vertical dielectric cylinder (without considering the ground effect) was first compared with the result obtained from TSARLITE, a 2-D finite-difference time-domain code.

The 2-D problem is equivalent to taking a cut-plane at some length along the cylinder. A TSARLITE simulation of scattering from a cylinder is shown in **Fig. 5**.

In **Fig. 6**, scattering cross-sections of a vertical dielectric cylinder for HH and VV polarizations are plotted as a function of the scattering angle on the cut-plane. Scattering in the forward direction is at 0°, while back-scattering is at 180°. The vertical axis is the scattering cross-section of the cylinder in units of μm^2, plotted in dB.

The scattering cross-section, σ_{qp}, is defined in terms of the incident field and the scattered electric field described in the previous equation, as follows:

$$\sigma_{qp} = 4\pi \lim_{r\to\infty} r^2 \frac{|E_q^s|^2}{|E_p^i|^2}.$$

For the 2-D problem, instead of scattering area, the scattering width (obtained for the infinite structure) is defined:

$$\sigma_{2Dqp} = 2\pi \lim_{r\to\infty} r \frac{|E_q^s|^2}{|E_p^i|^2}.$$

The 3-D scattering cross-section of a truncated 2-D structure can then be calculated from the approximate relationship[12]

$$\sigma_{3Dqp} = \frac{2\ell^2 \sigma_{2Dqp}}{\lambda} \left| \frac{\sin(k\ell \sin\tau)}{k\ell \sin\tau} \right|^2,$$

where ℓ is the length of the structure, λ is the wavelength, and τ is the tilt angle of the structure measured from broadside incidence.

The comparison between σ_{HH}, σ_{VV} calculated from analytic approximation and σ_{3DHH}, σ_{3DVV} obtained from TSARLITE is shown in **Fig. 6**. The length and radius of the cylinder are 5λ and 0.1λ, respectively. The dielectric constant of the cylinder is 19 + i0.7. The comparison shows good agreement between the analytic and TSARLITE results.

Figure 7 shows the HH and VV back-scattering radar cross-section of a cylindrical dielectric defect lying on top of the substrate as a function of the incident angle (measured from the vertical direction). The scattering returns include the direct scattering from the cylinder, and the phase interactions between the substrate and the cylinder. The length and radius of the cylinder are the same as in **Fig. 6**. The dielectric constant of the cylinder and substrate is 19 + i0.7.

This analytic solution is indicative of the size/structure of the defect and will allow the experimental inspection to determine characteristics of the substrate anomalies.

Future Work

For the coming year, we will extend the models to include scattering from defects under multi-layer coatings. A combination of asymptotic/analytical

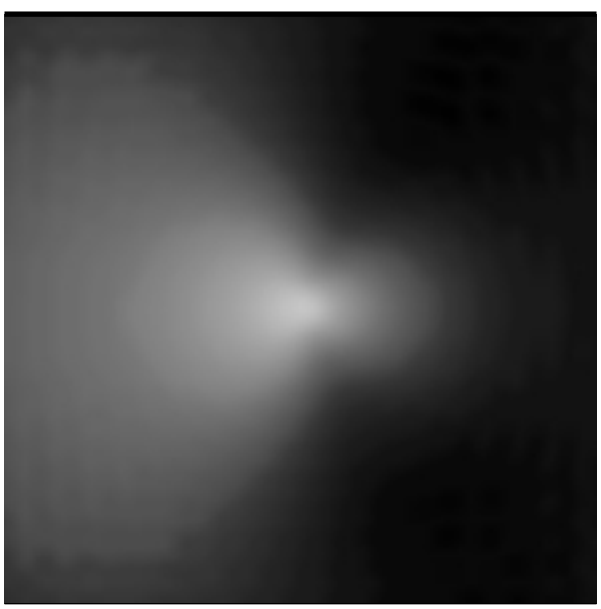

Figure 5. TSARLITE simulation of scattering from a dielectric cylinder, performed to validate the analytical approximation.

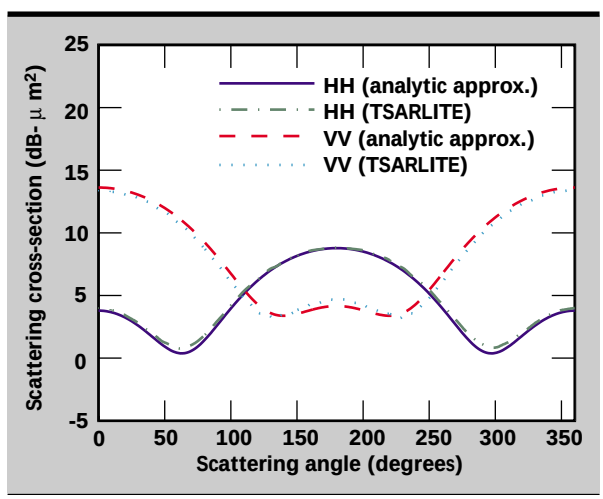

Figure 6. Scattering from a vertical dielectric cylinder as a function of the scattering angle on a cut-plane at some length along the cylinder. The length and radius of the cylinder are 5λ and 0.1λ, respectively. The dielectric constant of the cylinder is 19 + i0.7.

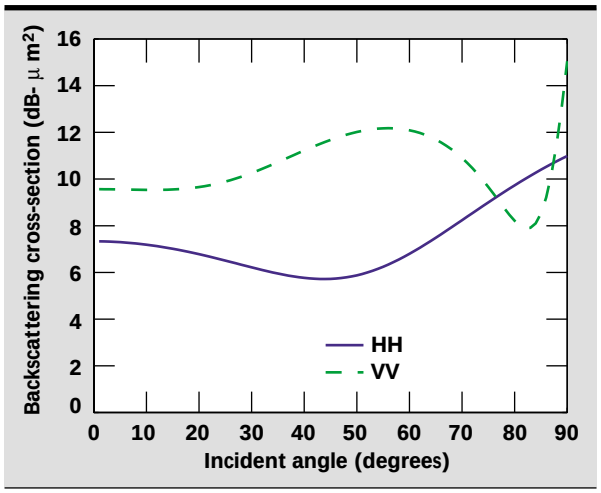

Figure 7. Back-scattering radar cross-section from a cylindrical dielectric defect lying on top of the substrate, as a function of the incident angle. The result takes into consideration the phase interactions between the cylinder and the substrate. The length and radius of the cylinder are 5λ and 0.1λ, respectively. The dielectric constant of the cylinder is 19 + i0.7 .

methods and numerical techniques will be used to calculate scattering from those defects. Numerical techniques will be used to validate scattering returns calculated with asymptotic/analytical methods. They will also be used in calculating scattering from defects with more complex shapes, and in those cases where the asymptotic/analytical methods are no longer valid.

At the end of the year, the scattering model will be extended to include scattering from defects under multi-layer coatings. The simulation results include scattering cross-section for detection of defects, as well as the scattered field. The latter couples into lithography printing simulation codes. Simulation programs will be benchmarked with experimental data.

Acknowledgment

The authors wish to thank M. Bujak for assistance with the TSARLITE results.

References

1. Vernon, S. P. , D. R. Kania, P. A. Kearney, R. A. Levesque, A. V. Hayes, B. Druz, E. Osten, R. Rajan, and H. Hedge (1996), "Reticle Blanks for Extreme Ultraviolet Lithography: Ion Beam Sputter Deposition of Low Defect Density Mo/Si Multilayers," *OSA Topical Meeting on Extreme Ultraviolet Lithography*, Vol. **4**, G. Kubiak and D. Kania, eds, pp. 44-48.

2. Kearney, P. A. , C. E. Moore, S. I. Tan, S. P. Vernon, and R. A. Levesque (1997), "Mask Blanks for Extreme Ultraviolet Lithography: Ion Beam Sputter Deposition of Low Defect Density Mo/Si Multilayers," *Journal of Vacuum Science and Technology B*, Vol. **15,** (6), pp. 2452–2454.

3. Lin, Y., and J. Bokor (1997), "Minimum Critical Defects in Extreme-Ultraviolet Lithography Masks," *Journal of Vacuum Science and Technology B*, Vol. **15,** (6), pp. 2467–2470.

4. Ishimaru, A. (1991), *Electromagnetic Wave Propagation, Radiation, and Scattering*, Prentice Hall, Englewood Cliffs, New Jersey.

5. Kong, J. A. (1990), *Electromagnetic Wave Theory, 2nd ed.*, John Wiley and Sons, New York, New York.

6. Ruck, G. T., D. E. Barrick, W. D. Stuart, and C. K. Krichbaum (1970), *Radar Cross Section Handbook*, Vol. **1**, **2**, Plenum Press, New York, New York.

7. Tsang, L., J. A. Kong, and R. T. Shin (1985), *Theory of Microwave Remote Sensing*, John Wiley and Sons, New York, New York.

8. Bouche, D., F. Molinet, and R. Mittra (1997), *Asymptotic Methods in Electromagnetics*, Springer-Verlag, New York, New York.

9. Karam, M. A. , A. K. Fung, and Y. M. M. Antar (1988), "Electromagnetic Wave Scattering from Some Vegetation Samples," *IEEE Transactions on Geoscience and Remote Sensing*, November, Vol. **26**, (6), pp. 799–808.

10. Le Vine, D. M., A. Schneider, R. H. Lang, and H. G. Carter (1985), "Scattering from Thin Dielectric Disks," *IEEE Transactions on Antennas and Propagation*, December, Vol. **33**, (12), pp. 1410–1413.

11. Kallman, J. S. , and R. J. Hawkins (1992), *TSARLITE and BEEMER: Tools for Integrated Optic Design*, Lawrence Livermore National Laboratory, Livermore, California (UCRL-JC-110403).

12. Skolnik, M. (1990), *Radar Handbook, 2nd ed.*, Chapter 11, McGraw-Hill, New York, New York.

Nuclear and Electromagnetic Radiation Simulation Tools for Dual-Revalidation of the Stockpile

David J. Mayhall and Michael F. Bland
Defense Sciences Engineering Division
Electronics Engineering

We have obtained and installed three codes for the assessment of system-generated electromagnetic pulse effects for dual-revalidation of the stockpile. We have run these codes and have begun validation of them. The good agreement between results from the MEEC vacuum regime code and the MAFIA code for the case of low-emitted charge gives us confidence that the MEEC provides accurate results for non-space-charge-limited emission for simple internal geometries. Documents we have obtained show good agreement between MEEC simulations and experiments for low- and high-pressure cases using simple geometries.

Introduction

The goal of this project is to obtain, install, validate, use, and improve simulation software tools for predicting system-generated electromagnetic pulse (SGEMP) effects in the stockpile dual-revalidation program. SGEMP is the transient electromagnetic pulse created by electrons emitted by a system exposed to incident photons from large gamma fluences.

SGEMP can be external or internal. In the external case, the electromagnetic fields are produced on the outer surfaces of the system. In the internal case, the fields are produced within the system. SGEMP can cause upset, damage, and system failure due to large currents burning out components. The presence of trapped or evolved gasses around the system or inside cavities significantly modifies SGEMP. Experiments indicate that breakdown of the space charge layer occurs at low pressures, significantly increasing current flow. For this reason vacuum simulations are not sufficient to evaluate worst case threats.

Approach

Our approach to this project has been to obtain, install, run, and test the codes MEEC, MCNP, and CEPXS. We have also obtained a dedicated Pentium-class PC with a removable hard drive and a state-of-the-art FORTRAN compiler and development studio to run these codes. We have contracted to have the presently script-based MEEC code upgraded with a GUI to make it much more user-friendly. In addition, we have compared results from the MEEC vacuum regime code with those from the TS3 electromagnetic particle-in-the-cell (EM-PIC) module of the MAFIA code.

MEEC is a set of 2- and 3-D EM-PIC codes for SGEMP in the vacuum, low-pressure, and atmospheric regimes. MCNP (Monte Carlo Neutron Photon) is a 3-D, time-dependent code for electron generation due to photon and neutron incidence and transport in materials. CEPXS solves the 1-D transport equation for coupled photon-electron cascades for energies greater than 1 keV. Since CEPXS is a deterministic, finite-difference code, it is less computationally intensive than a Monte Carlo code and will allow more efficient calculation of generated electron fluences for input to the MEEC code.

Validation

As a validation of the MEEC vacuum regime code, we have run a test problem consisting of an electrically perfectly conducting right rectangular solid within an electrically perfectly conducting right rectangular container. Two values of electron charge emission from the top of the internal solid, 6.33×10^{-8} C and 6.33×10^{-6} C have been simulated. We have also run the same problem with a similar, but slightly different, computational grid with MAFIA TS3.

The MAFIA geometry is shown in **Fig. 1**. Since symmetry is assumed about the z-axis, the MAFIA calculation is confined to the first quadrant of the

z-projected xy plane (positive x and positive y). The xz and yz planes are symmetry planes. The domain of the inner solid is $0 \le x \le 0.5$ m, $0 \le y \le 0.5$ m, -0.5 m $\le z \le 0.5$ m. The domain of the computational space within the outer solid is $0 \le x \le 2$ m, $0 \le y \le 2$ m, -2 m $\le z \le 2$ m. Part of the spatially uniform MAFIA grid is shown on the surfaces of the inner solid.

The time history of the emission is triangular, with a linear rise from 0 to 10 ns, followed by a linear fall from 10 ns to 20 ns to a null value. The angular distribution of emitted particles about the z-axis in the plane parallel to the xy plane is uniform. The angular distribution of emitted particles, as measured from 0 to 90° from the positive z-axis, is parabolic, with minima at 0 and 90° and a maximum at 45°. The spatial distributions of emitted particles are uniform in the x and y directions. The distribution of emitted particles with kinetic energy is half-parabolic with the maximum at 1 keV, the minimum at 24 keV, and a maximum to minimum ratio of 10. The spatial state of the electron macroparticles emitted from the top surface of the inner solid at 21.6 ns, for 6.33×10^{-8} C of emitted negative charge, is shown in **Fig. 1**.

The MAFIA calculation uses one randomly emitting area. The MEEC calculation uses five emitting areas of extent, 0.1 m × 0.5 m, in the x and y directions. Each calculation uses 4000 macroparticles. The MEEC grid is nonuniform, with finer spacings near the interfaces of the inner solid with the surrounding vacuum space. In both calculations, the electrons incident on the inner surfaces of the outer container and inner solid are totally absorbed. Because of restrictions on image plane locations, the MEEC calculation is performed in the third quadrant of the z-projected xy plane (negative x and negative y).

Figure 2 shows the spatial state of the particles for the MAFIA calculation at 21.6 ns for 6.33×10^{-6} C of emitted charge. For this case, fewer particles are

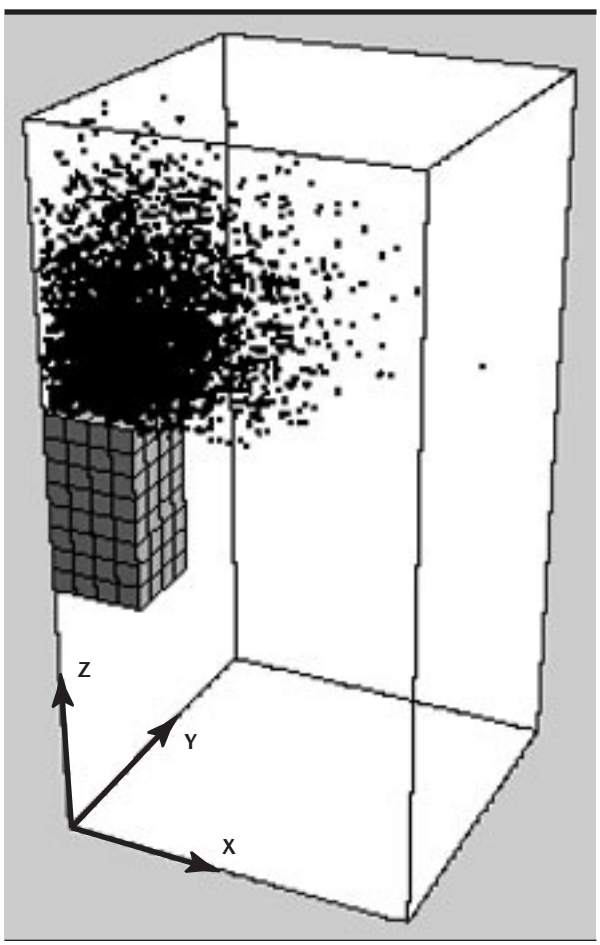

Figure 1. MAFIA problem geometry and the electron macroparticles at 21.6 ns for 6.33 x 10^{-8} C of emitted charge.

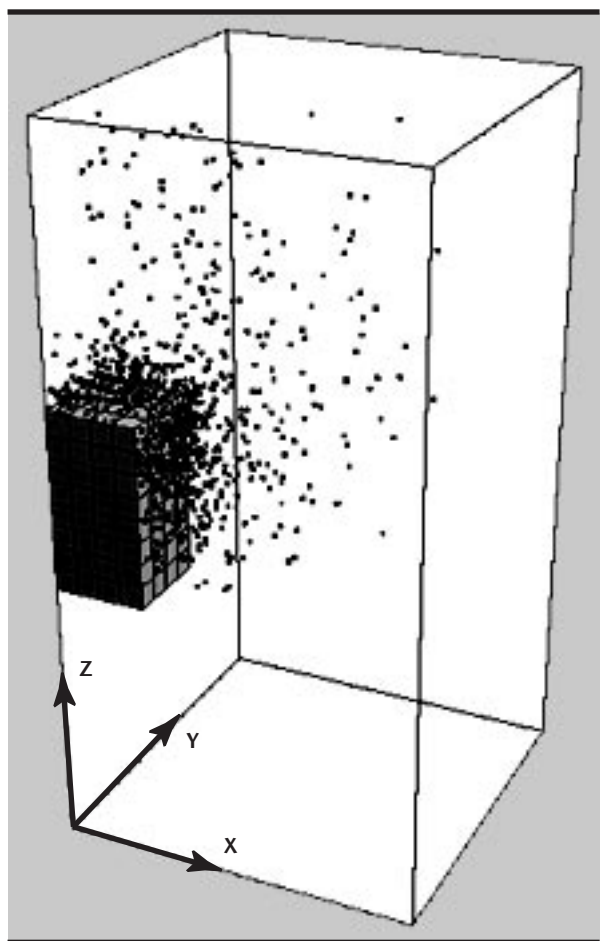

Figure 2. The MAFIA electron macroparticles at 21.6 ns for 6.33 x 10^{-6} C of emitted charge.

situated within the bulk of the space between the two solids. More are confined near the surface of the inner solid. Space-charge-limited emission is thus evident in this second calculation. For this amount of emitted charge, many of the emitted particles remain close to the inner solid, move down its sides, and then move across its bottom at z = –0.5 m.

Figure 3 shows a comparison of MEEC and MAFIA E_z-field waveforms at two nearby points above the emitting top of the solid on the positive z-axis. The MEEC electric field point is at (0, 0, 0.81 m); the MAFIA point is at (0, 0, 0.8125 m). The MAFIA result is noisier and rises to a higher corresponding positive value than does the MEEC result. Some of the MAFIA noise may be due to the single emitter used, as opposed to the five emitters used in the MEEC calculation. The discrepancy in the values after the negative peaks may be due to differences in the two grids.

Figure 4 shows a comparison of MEEC and MAFIA H_x waveforms at two more nearby points. The MEEC field component is calculated at (0, –0.425 m, 0.525 m); the MAFIA component at (0, 0.4375 m, 0.5625 m). These points lie on the x = 0 symmetry plane, slightly above the emitting surface near the outer edges of the inner solid. Because the initial axial current density in the space above the inner solid is in the negative z direction, the right-hand rule gives a negative H_x component for the MEEC simulation in the third quadrant and a positive one for the MAFIA simulation in the first quadrant.

For ease of comparison, we have inverted the MAFIA result in **Fig. 4**. The MAFIA point is slightly closer to a top edge of the inner solid (1.25 cm) and somewhat higher above the emitting surface (3.75 cm) in the positive z direction. The MAFIA waveform is thus expected to be delayed with respect to the MEEC waveform and to be somewhat lower in amplitude. **Figure 4** shows the MAFIA result to be delayed by about 1 ns during the fall toward the negative peaks. An apparent smoothed value of the MAFIA negative peak is ~–2.5 A/m, which is slightly lower in magnitude than the MEEC negative peak of ~–2.55 A/m. The MAFIA result is once again more noisy than the MEEC result.

Greater differences between the results of the two codes occur for 6×10^{-6} C of emitted charge. Although the shapes of the waveforms are generally similar, the MAFIA peaks are usually greater and delayed. Some of the MAFIA E_z waveforms show strong late time (>29 ns) discrepancies. The MAFIA waveforms, especially for the magnetic field and current density components, are also noisier. The reasons for these discrepancies are not yet known. Some possibilities include computational differences and object description differences. However, because a run with a more refined MEEC grid produced results for the high-charge-emission case similar to those for the initial MEEC grid, we believe that MEEC results are good for space-charge-limited emission in simple geometries.

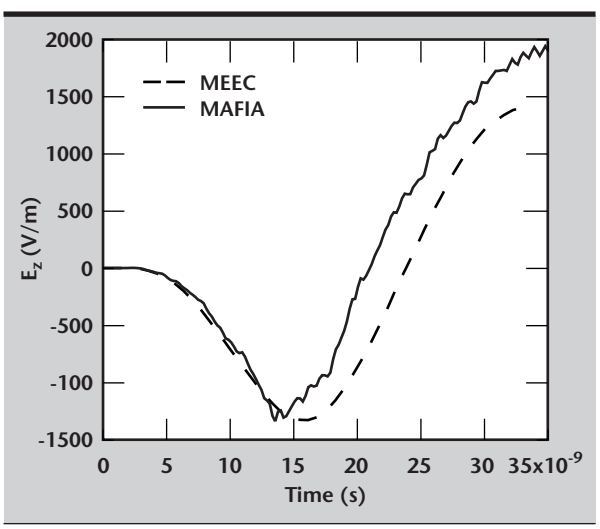

Figure 3. Comparison of MEEC and MAFIA E_z components for 6.33×10^{-8} C of emitted charge.

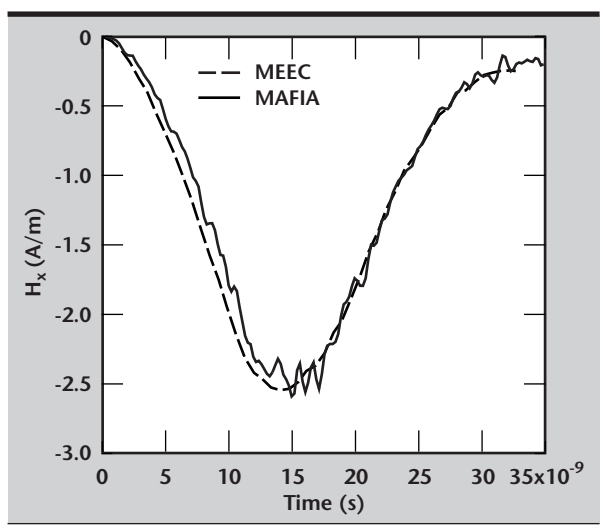

Figure 4. Comparison of MEEC and MAFIA H_x components for 6.33×10^{-8} C of emitted charge.

Future Work

We plan to further investigate the accuracy of the MEEC vacuum and the MAFIA codes for cases of space-charge-limited emission. Benchmarking against standard test problems or accepted analytical solutions is desired. We plan to validate the MEEC low- and atmospheric-pressure codes in simple geometries. When available, we plan to test MEEC with the new GUI capability. To support the W76 revalidation we plan to model the W76 weapon electronic and radiation case geometry. Simulations of cable-induced SGEMP currents will be calculated and compared to test data.

Self-Effects in Expanding Electron Beam Plasmas

Manuel Garcia
Laser Engineering Division
Electronics Engineering

An analytical model of plasma flow from metal plates hit by intense, pulsed, electron beams aims to bridge the gap between radiation-hydrodynamics simulations and experiments in the Advanced Hydrotest Facility at Lawrence Livermore National Laboratory (LLNL). This model also helps quantify the self-effect of the electron beam penetrating the target material, which is not addressed by simulations.

Introduction

When a pulsed electron beam hits a metal plate with sufficient energy, a volume of the metal becomes ionized fluid that subsequently sprays out of the plate. Does this counterflow disrupt the tight focus of the initial electron bunch, or later pulses in a train? This work aims to model the spatial distribution of plasma speed, density, degree of ionization, and magnetization to address this question.

Progress

Numerical simulations of target flows are very accurate for the initial 2 μs. Beyond this point, the relative density is quite low, precision drops, and calculation times are long. The initial solid-density, several-eV plasma expands to 1 cm and 10^{-4} relative density by 2 μs. Yet, a Faraday cup detector located 25 cm from the target at LLNL's experimental test accelerator (ETA-II) facility, observes the flow after an expansion of 50 μs. In addition, the Faraday cups at ETA-II are immersed in the focusing magnetic field of the accelerator. There is a wide gap between what the Faraday cups see and what the simulations provide. An analytical model of the plasma flow helps to connect the experimental observations with the simulations of early times.

The expansion of the target plasma into the vacuum of the accelerator is so rapid that the ionized portion of the flow departs from local thermodynamic equilibrium downstream. In fact, we found that when the temperature (in eV) in a parcel of fluid drops below $V_I \times [(2\gamma - 2)/(9\gamma + 15)]$, where V_I is the ionization potential of the target metal (for example, 7.8 eV for tantalum), and γ is the ratio of specific heats, then the fractional ionization and electron temperature in that parcel remain fixed during its subsequent expansion. This effect is called freezing. For atoms, $\gamma = 5/3$ and the freezing temperature as defined here is $V_I/22.5$.[1,2]

An electron beam penetrating the target and its plasma will experience a radical change in the balance it had in vacuum, between the pinching force of its own azimuthal magnetic field and the disruptive electric field of its negative space charge.

The effects are as follows: 1) the target plasma cancels the electric field of the beam by an overwhelming charge density; 2) the plasma conductivity creates an internal eddy current to counter the magnetization introduced by the transit of relativistic electrons; and 3) the plasma magnetization changes as electron beam heating alters the density gradient and the magnitude of the conductivity.

This combination of effects could cause either pinching or expansion of a penetrating beam (aside from scattering) at different times during its transit. References 3 and 4 initiate the exploration of thermally-generated magnetization, while References 5, 6 and 7 are guides to a deeper analysis.

Figures 1, **2**, and **3** show a tantalum flow generated by depositing an impulse of 5 J within a diameter of 0.8 mm and depth of 50 μm. The initial temperature of this plasma was 9 eV.

Figures 1, **2,** and **3** also show profiles of the heavy particle density, fluid and electron temperatures, and electron density, respectively, outside the plate at 300 ns. The leading edge of the flow has reached 1.2 mm, the source volume within the plate has cooled to less than 1 eV, and the source plasma has 2% of its original density.

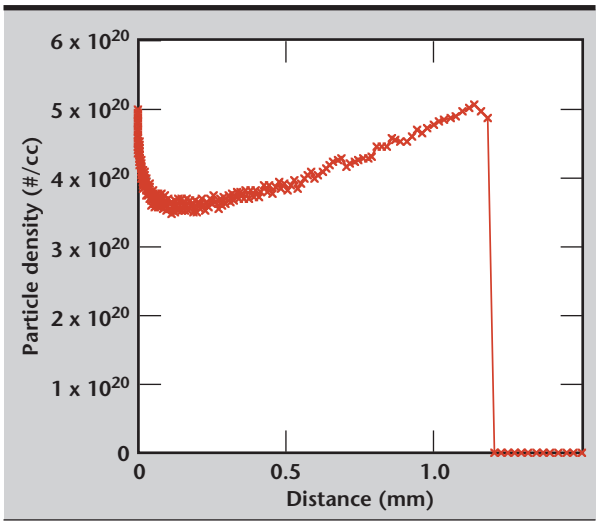

Figure 1. Particle density at 300 ns.

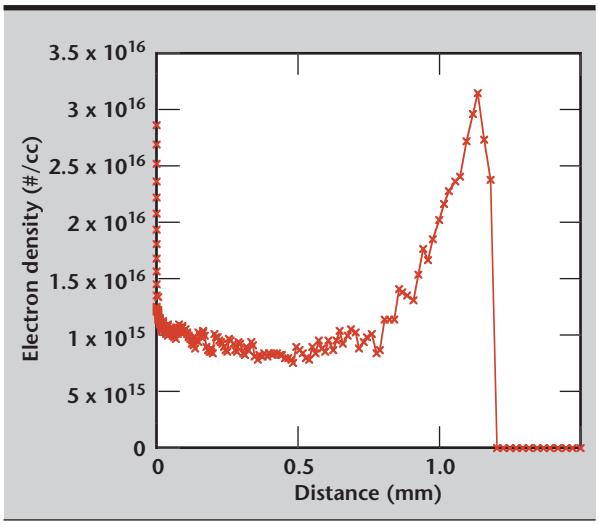

Figure 3. Electron density after 300 ns.

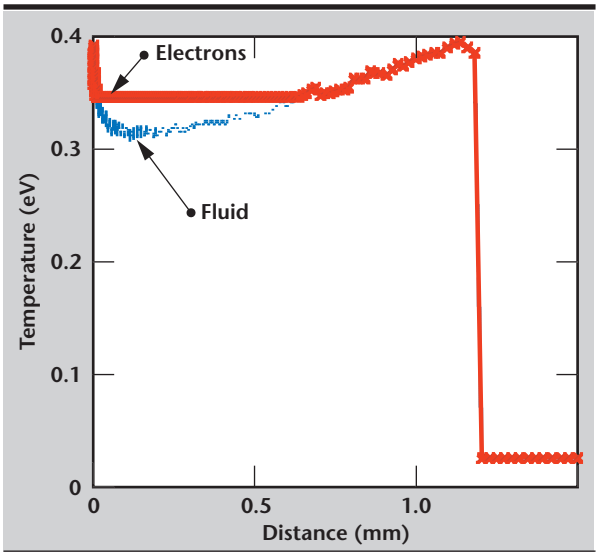

Figure 2. Electron and fluid temperatures after 300 ns.

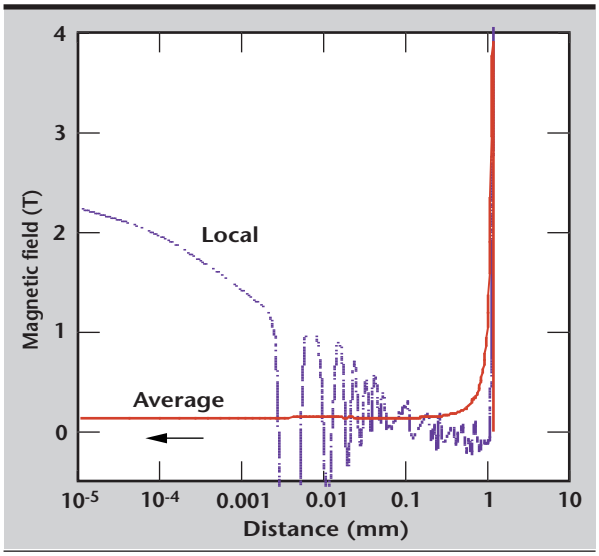

Figure 4. Local and average magnetic field along the flow.

The freezing effect is just visible in **Fig. 2**. Flow later in time and downstream of this point will have a frozen ionization fraction (2×10^{-5}) and electron temperature (0.35 eV). An ideal probe at 25 cm from the plate would observe the arrival of plasma at 51 µs, with an atom density of 2×10^{16} cm^{-3}, an electron density of 4×10^{11} cm^{-3}, and a decrease to one quarter of these peak values by 140 µs.

Figure 4 shows profiles of the azimuthal magnetic field (tesla) that arises within the tantalum cloud, just described, on being penetrated and heated by an electron beam pulse of 1000 A within a 0.8-mm diameter for 30 ns. One profile in **Fig. 4** is of local magnetic field values, the other is a running average from the leading edge of the flow.

The magnetic field is generated thermally by the nonalignment of the gradients of electron temperature and density.[5,6] This thermally-generated magnetic field has the opposite polarity to the self-field of the electron beam (which is – 0.5 T in this example). Large local values arise where the density gradients are large: at the leading edge, and at the exit of the plate. In this example, the average thermally-generated field does not cause the electron beam to diverge because high local fields occur only in narrow zones.

Future Work

Current work aims to improve the estimates of thermally-generated magnetic fields by refining the many approximations required to describe such intricate physics in an analytical model. In particular, a realistic conductivity model $\sigma\ (T, N)$[8] and a more accurate dynamic heating model for improved density gradients are the focus of effort. Also, comparison to the Faraday cup and interferometer data from ETA-II can help improve both model and experiment.

References

1. Garcia, M. (1997), "Splash flow from a metal plate hit by an electron beam pulse," Lawrence Livermore National Laboratory, Livermore, California (UCRL-ID-128660).

2. Garcia, M. (1997), "Frozen plasma within the flow from a metal plate hit by an electron beam pulse," Lawrence Livermore National Laboratory, Livermore, California (UCRL-ID-126296).

3. Garcia, M. (1998), "On electromagnetic acceleration of material from a plate hit by a pulsed electron beam," Lawrence Livermore National Laboratory, Livermore, California (UCRL-JC-130448).

4. Garcia, M. (1998), "Electron beam expansion by target heating," Lawrence Livermore National Laboratory, Livermore, California (UCRL-ID-131291).

5. Haase, R. (1969), *Thermodynamics of Irreversible Processes,* Addision-Wesley Publishing Company, London.

6. Haines, M. G. (1997), "Saturation mechanisms for the generated magnetic field in a nonuniform laser-matter irradiation," *Phys. Rev. Lett.* **78** (2), p. 254.

7. Craxton, R. S., and M. G. Haines (1978), "$\mathbf{j} \times \mathbf{B}$ acceleration of fast ions in laser-target interactions," *Plasma Physics,* Vol. **20**, Pergamon Press Ltd., Northern Ireland, pp. 487–502.

8. Redmer, R. (1998), "Electrical conductivity of dense metal plasmas," submitted to *Phys. Rev. E*, **6**.

Pump-Induced Wavefront Distortion in Prototypical NIF and LMJ Amplifiers

Mark D. Rotter
Laser Engineering Division
Electronics Engineering

Kenneth S. Jancaitis, Christopher D. Marshall, Luis E. Zapata, and Alvin C. Erlandson
Laser Science and Technology
Laser Programs

Geoffroy LeTouze′ and Stephane Seznec
Commissariat à l′Energie Atomique
Villeneuve, St. Georges, France

In large-aperture laser amplifiers such as those envisioned for the National Ignition Facility (NIF) and Laser Megajoules (LMJ) lasers, the geometry is such that the front and back faces of the laser slab are heated unevenly by the pump process. This uneven heating results in a mechanical deformation of the laser slab and consequent internal stresses. The deformation and stresses, along with a temperature-dependent refractive index variation, result in phase variations across the laser beam, so-called pump-induced wavefront distortions. These phase variations lead to beam steering which may affect frequency conversion as well as energy-on-target. We have developed a model that allows us to estimate the pump-induced wavefront distortion for a given amplifier configuration as well as the spatially-resolved depolarization. The model is compared with experiments taken in our amplifier development laboratory (AMPLAB).

Introduction

We are currently developing large-aperture amplifiers for the National Ignition Facility (NIF) and Laser Megajoules (LMJ) lasers at Lawrence Livermore National Laboratory (LLNL). These multi-segment amplifiers are the flashlamp-pumped, Nd:Glass type, and are designed to propagate a nominally 36-cm-square beam. The apertures within a particular amplifier bundle are arranged in a four-high-by-two-wide configuration and use two side flashlamp arrays and a central flashlamp array for pumping (**Fig. 1**).

As shown in **Fig. 1**, the slabs are oriented at Brewster's angle and are pumped on both sides by arrays of flashlamps, denoted as central arrays (lamps that pump both slabs) and side arrays. The geometry of the amplifier results in one end of the slab being situated closer to the lamps than the other. Consequently, the amount of heat deposited in the slab (primarily from the quantum defect of the broad-band pump light) is uneven front-to-back as well as side-to-side.

This uneven pumping results in a warping of the laser slab, indicated by the dashed lines in **Fig. 1**. An initially plane wavefront incident on such a slab will not remain planar upon exit. Ultimately, wavefront distortion is due to differences in the optical path (defined as the refractive index times the physical path length) at one point in the aperture vs that at another. We have seen one source of these optical path differences (OPDs), namely, the mechanical distortion of the laser slab. There is another source of OPD: the spatially-varying refractive index to which temperature and stress contribute.

We have developed a model that takes all of the above effects into account, and that allows us to predict the pump-induced wavefront distortion for these large-aperture amplifiers. In this report, we describe various aspects of the model and present comparisons between the model and experimental data taken on AMPLAB, our amplifier test laboratory.

Progress

Pump-Induced Wavefront-Distortion Model

Description of Model. As mentioned in the introduction, the non-uniform deposition of heat in the laser slab is responsible for slab distortions and aberrations of any plane wavefront incident on it. Thus, the fundamental ideas may be summarized as follows: the non-uniform heat deposition results in a distortion of the laser slab and accompanying stresses. The distortion of the laser slab, in conjunction with the temperature and stress-induced refractive index variations result in the OPDs and consequent wavefront distortion.

To calculate the various effects listed above, we use a suite of computer codes: TOPAZ3D[1] to calculate the temperature distribution within the laser slab, NIKE3D[2] to calculate the displacements and stresses from the temperature field given by TOPAZ3D, and OPL, which calculates the OPDs, given the results from NIKE3D. The codes NIKE3D and TOPAZ3D are 3-D finite element analysis codes which have been in use at LLNL for more than ten years. The optics code OPL is an in-house code based on the BREW code.[3]

Determination of Temperature. The first step in calculating the wavefront distortion is to determine the temperature distribution within the laser slab. To do this, we need to specify the thermal source function as a function of position and time. In general, this thermal source function is an arbitrary function of position and time. For purposes of this model, however, we have assumed a separable source function, that is:

$$Q(x,y,z,t) = As(x)\left[g_0(y)\ f(z) + g_h(y)\ f(h-z)\right]\ u(t) + Q_{ec}\ , \qquad (1)$$

where $s(x)$ denotes the vertical variation of the pump profile; $g_{0,h}(y)$ denotes the horizontal variation of the pump profile at $z = 0,\ h$; $f(z)$ denotes the pump profile through the thickness of the slab; and Q_{ec} is the thermal source term for the edge cladding. The units for this source function are W/cm.[3] In **Eq. 1**, h is the thickness of the slab and A is a constant multiplier. Each of these terms will now be described.

In the multi-segment amplifiers envisioned for use in the NIF, there is strong vertical symmetry. The flashlamps are oriented vertically, and there are silver-coated metal reflectors at the top and bottom of the pump cavity. As a result, we have taken the function $s(x)$ to be a constant. In reality, the reflectors are not perfect, and so there is a slight roll-off in pump light at the extreme top and bottom of the pump cavity. We have found that this is a small effect insofar as calculating the pump-induced wavefront distortion is concerned, and so have elected to keep $s(x)$ a constant.

As mentioned above, the geometry of the pump cavity results in a roll-off of the pump radiation from one side of the aperture to the other. We used our 2-D+ ray-trace code[4] to calculate the distribution of pump light across the laser slab. An example of the functions so obtained is shown in **Fig. 2**. Because these functions can be rather convoluted, no curve fitting is done. Instead, TOPAZ3D uses $g(y)$ as is, and interpolates to return values for Q for any y.

The thermal energy deposition through the thickness of the slab is given by the function $f(z)$. This function is calculated using our Lamp Model code,[5] which calculates the energy deposition profile as a

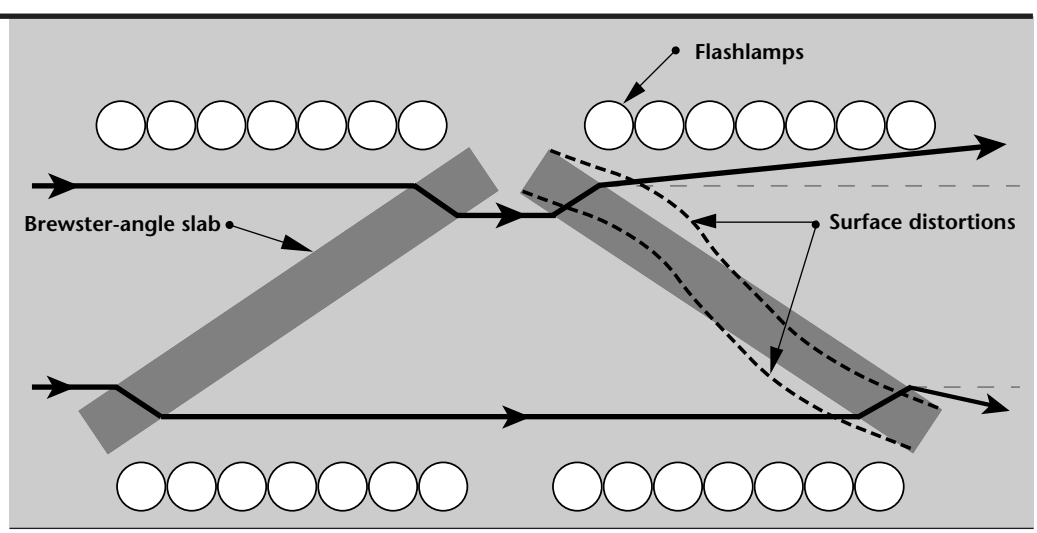

Figure 1. Plan view of multi-segment amplifier showing geometry of Brewster-angle laser slabs. Surface distortions (greatly exaggerated) are caused by uneven pumping.

function of slab geometry, doping density, and lamp operating level. The profile so obtained is a spectrally-integrated thermal energy deposition profile, which we then fit to a double exponential:

$$f(z) \propto e^{-\mu 1 z} + c\, e^{-\mu 2 z} \quad , \tag{2}$$

where μ_1, μ_2, and c are the fit coefficients. A plot of the energy deposition profile and the corresponding fit is shown in **Fig. 3**.

To describe the temporal behavior of the pump pulse, we use an analytic expression for $u(t)$. We first need to describe the temporal behavior of the electrical input power to the lamp. Since the flashlamp is a nonlinear circuit element, the acutal pulse shape is described by a nonlinear differential equation.[6] We have found, however, that an excellent approximation to the shape is given by the function:

$$p(t) \propto t \exp\left[-(t - a)^2 / \tau^2\right] \quad , \tag{3}$$

where a and τ are fit parameters. A plot of the electrical input power as determined from a numerical integration of the circuit equation and the approximation given by **Eq. 3** is shown in **Fig. 4**. With the electrical input power so determined, we then calculate the optical output power from the flashlamp. The output power, $u(t)$, may be calculated from the following equation:[7]

$$du/dt = \left[\eta(u)\, p(t) - u(t)\right] / \tau_R \quad , \tag{4}$$

where $\eta(u)$ is the instantaneous radiant efficiency of the flashlamp (corrected for arc-expansion effects), and τ_R is radiative recombination time of the plasma (~30 µs). Since $\eta(u)$ is a nonlinear function of u, **Eq. 4** is likewise nonlinear.[7] We have found, however, that an excellent approximation is to take $\eta(u)$ to be a constant, parametric in the pulsewidth:

$$\eta(u) = .653 + 2.33 \times 10^{-4}\ \tau_{10}$$

$$200 < \tau_{10} < 500\ \mu s \quad , \tag{5}$$

where τ_{10} is the full-width tenth-maximum time of the electrical input power pulse. In **Fig. 5** we show the comparison between the numerical solution to **Eq. 4** and the solution using the approximation given by **Eq. 5**. We see that over the time range specified, the agreement is quite good. Using **Eqs. 3** to **5**, an analytic expression for $u(t)$ may be obtained.

At this point, we do not have a good *ab initio* calculation for the heat deposited in the laser slab. Present calculations disagree with measurements by

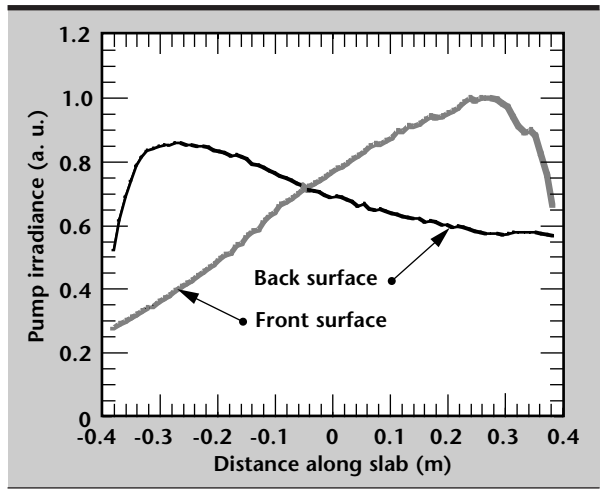

Figure 2. Pump irradiance profiles—AMPLAB diamond configuration.

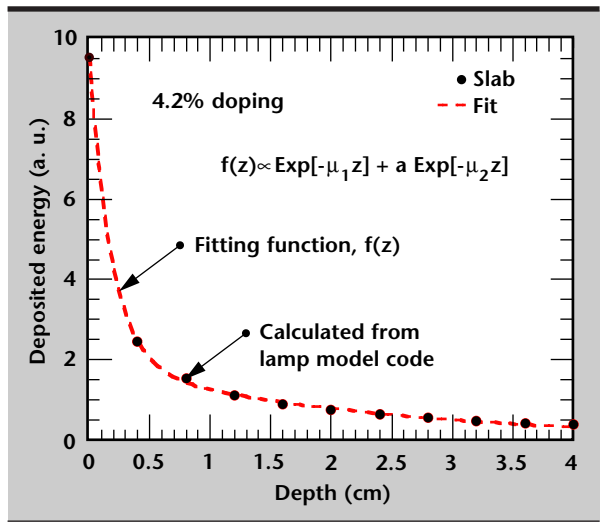

Figure 3. Energy deposition profile through slab and fit.

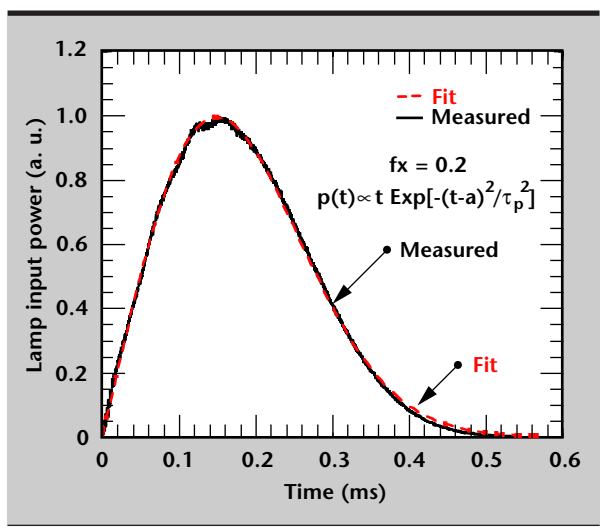

Figure 4. Measured electrical input power to lamp and fit.

about a factor of two. The cause of this discrepancy is currently not known. Thus, we have included a scale factor, A in **Eq. 1**, to scale our results to experimental measurements. It should be pointed out that once this factor is determined (for example, from AMPLAB measurements), then that factor is held constant for all succeeding calculations.

The last term in **Eq. 1** represents the heat deposited into the edge claddings that surround the laser glass. This term, Q_{ec}, is composed of two parts:

$$Q_{ec} = Q_{ec,pump} + Q_{ec,ASE} , \tag{6}$$

where $Q_{ec,pump}$ and $Q_{ec,ASE}$ represent the heat deposited into the edge claddings by the pump and by amplified spontaneous emission (ASE), respectively. The source term is broken up in such a manner because the time dependence of the two parts is different. For $Q_{ec,pump}$ the time dependence is just $u(t)$, described above. For $Q_{ec,ASE}$ the time dependence is different due to the fact that the peak of the ASE pulse occurs at the time of peak gain, not at the time of peak pump power. The relationship between the output power from the flashlamp and the stored energy density, $\rho(t)$, is given in Reference 7. Once $\rho(t)$ is determined, it may be shown that the time dependence of the ASE, $\phi(t)$, may be written as:[8]

$$\phi(t) \propto \rho(t)\left[a + b\left\{\exp\left[\rho(t)\right] - 1\right\}\right] , \tag{7}$$

where a and b are constants. With **Eq. 7** describing the time dependence of the ASE, we then have, for example, for the edge cladding at x = constant:

$$Q_{ec,ASE} \propto \phi(t)\beta\Gamma e^{-\beta x} , \tag{8}$$

where β is the edge-cladding absorption coefficient, and Γ is the incident fluence. At present, we do not have an accurate *ab initio* calculation of the ASE fluence on the edge cladding. However, based on measurements with the Beamlet laser, we estimate a fluence of 4 J/cm^2 for ASE and another 2.5 J/cm^2 due to the pump light.

Equations 1 to **8** are used in TOPAZ3D to determine the temperature distribution in the laser slab. Due to the shortness of the pump pulse (a few hundred μs), adiabatic boundary conditions are used on all faces of the slab. The result of this calculation is used in the code NIKE3D to calculate the displacements and stresses, as described in the next section.

Determination of Displacements and Stresses. As mentioned above, we use the temperature distribution in the slab to calculate the displacements and stresses. Since the displacements are very small (on the order of 1 μm), we are in the linear elastic regime and the problem is a standard one in thermo-elasticity. Consequently, we use a thermo-elastic material model and specify Poisson's Ratio, Young's Modulus and the thermal expansion coefficient.[9] These parameters are taken to be constants, independent of temperature, insofar as the maximum temperature rise is on the order of 1 °C.

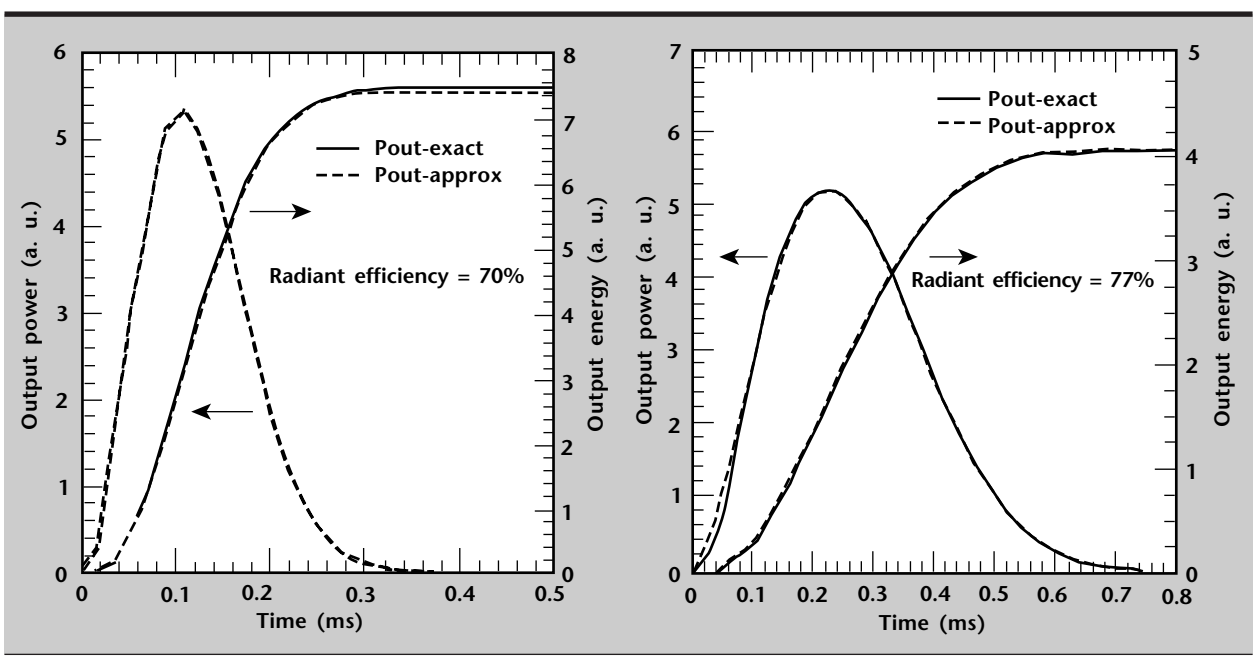

Figure 5. Comparison of exact and approximate solutions to flashlamp output equation.

At this point in the calculation, the mechanical boundary conditions for the slab are specified. In reality, the slab sits on a Marcel spring—a sinusoidally varying metal strip. While the capability exists to model the spring as it actually exists, we have found that a satisfactory substitution is to have the slab sit on a region of metal one element thick. The nodes in the glass material are joined to the nodes in the metal so no slipping can occur. The bottom of the metal region is simply supported, and we also fix the displacements at two additional corners to eliminate rigid-body motion. The rest of the slab surfaces are assumed to be free.

NIKE3D calculates the displacements and stresses as a function of time during the course of the pump pulse. Typically, the code is run up to the time of peak gain as the wavefront distortion at that time is what is usually requested. However, it is a simple matter to run the code for times longer than the time of peak gain to compare with experiments.

Determination of OPDs. The last part of the calculation involves computing the OPDs through the laser slab. For this, we use our in-house code OPL. The optical path length of a ray through the slab may be written as:

$$\text{OPL} = \int n(x,y,z)\,ds \quad , \tag{9}$$

where n is the (spatially-varying) refractive index and s is the distance along the ray path. There are two main sources of OPD in the laser slab: 1) variations in path length caused by mechanical motion of the slab, and 2) variations in path length caused by refractive index changes.

The variations in path length caused by mechanical motion of the slab are due to the spatially-varying displacements calculated in NIKE3D; that is, a point x, y, z on the slab is translated to:

$$\begin{aligned} x &\rightarrow x + u(x,y,z,t) \\ y &\rightarrow y + v(x,y,z,t) \\ z &\rightarrow z + w(x,y,z,t) \quad . \end{aligned} \tag{10}$$

We take two effects into account to calculate the spatially-varying refractive index: 1) the variation of refractive index with temperature, and 2) the variation of refractive index with stress (stress-optic effect), that is:

$$\begin{aligned} n(x,y,z) = n_0 &+ (dn/dT)\,\Delta T(x,y,z) \\ &+ (dn/d\sigma)\,\Delta\sigma(x,y,z) \quad , \end{aligned} \tag{11}$$

where n_0 is the isotropic refractive index, dn/dT denotes the change of refractive index with temperature, and we have symbolically written the change in refractive index due to stress as $dn/d\sigma$.

Note that in general, ΔT and $\Delta\sigma$ are functions of time. However, for the purposes of calculating the OPD, we select one point in time for the calculation. This is permissible since the time duration of the laser pulse is at most 20 ns. On this time scale, all thermal and mechanical motion is frozen.

The sequence of events in calculating the OPD is as follows. The OPL code reads in the finite-element geometry from the NIKE3D plot file. We then go through the mesh and break up each finite-element "brick" into six four-node tetrahedra and generate a connectivity matrix for these tetrahedra. We then use **Eq. 11** to calculate the refractive index at each node in the mesh. Within each tetrahedra, we linearize the refractive index:

$$n(x,y,z) = a + bx + cy + dz \quad . \tag{12}$$

The four unknowns in **Eq. 12** are uniquely determined by the values of the refractive index at the four nodes of a given tetrahedron. With the refractive index linearized as in **Eq. 12**, we can then analytically solve the Eikonal equation[10] for the ray path within a tetrahedron:

$$\frac{d}{ds}\left(n\frac{d\mathbf{r}}{ds}\right) = \nabla n \quad , \tag{13}$$

where s is the distance along the ray path and $\mathbf{r}$ is the position vector of the ray. The connectivity matrix helps us determine which tetrahedron the ray will enter, and consequently at which nodes to evaluate the refractive index to calculate the unknowns in **Eq. 12**. We then track the ray as it propagates through all the tetrahedra, all the while accumulating the distance that the ray propagates.

In addition to calculating the OPD for the ray, we can also calculate the depolarization a ray experiences as it propagates through the optic. We do this by assuming each tetrahedron acts as a linear retarder, and calculate the Jones matrix[11] for each tetrahedron. The final amount of retardation (and hence depolarization) is given by the product of all the individual Jones matrices for a given ray path.

A typical result from this calculation is shown in **Fig. 6**. The calculation was performed for the AMPLAB amplifer in the diamond configuration. In **Fig. 6a** we show the OPD for all effects (displacement, temperature, and stress) combined. It is often

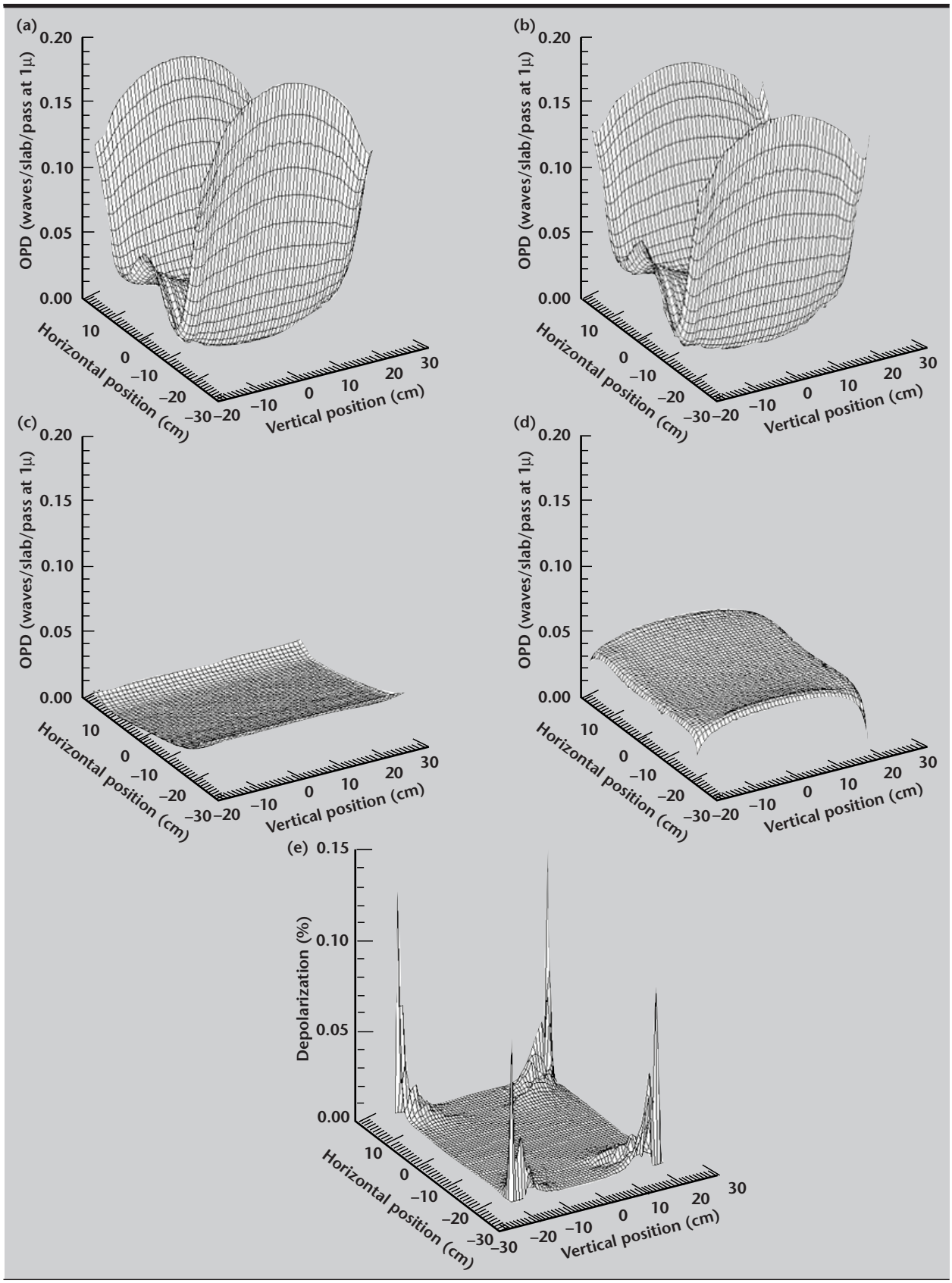

Figure 6. OPD calculated for the AMPLAB diamond configuration, f_x = 0.2: (a) all effects; (b) displacement effects only; (c) dn/dT effects only; (d) stress effects only; and (e) depolarization.

useful to examine each component indivudually, and this is done in **Figs. 6b**, **c**, and **d**. In **Fig. 6b** we show the contribution to the OPD due solely to mechanical deformation.

Comparison with **Fig. 6a** shows that for AMPLAB, the wavefront distortion is due mainly to the mechanical deformation of the slab. In **Figs. 6c** and **d** we show the contriubtion to the OPD from temperature and stress effects on the refractive index. As may be seen, these effects play a relatively minor role in determining the overall OPD. Finally, in **Fig. 6e** we show the P-to-S depolarization.

As expected, the greatest amount of depolarization occurs in the corners, where the two pieces of edge cladding meet. It is there where the greatest amount of stress occurs. Nevertheless, the overall amount of depolarization is small, well within its specification of 0.05% averaged over the aperture.

Error Analysis. In this section, we estimate the error in our calculation of the OPD. For the amplifier conditions considered in this report, the dominant contribution to the OPD is the mechanical deformation of the laser slab (see **Figs. 6a** and **b**). Consequently, it makes sense to closely analyze the uncertainties associated with mechanical motion.

For simplicity, assume the laser slab is a simply-supported thin plate, with the thin dimension along the z-axis. We will neglect any time dependence in this analysis. It may be shown that the equation for w, the displacement in the z-direction, is given by:[12]

$$\nabla^2 w(x,y) = -\left(\frac{M_T(x,y)}{1-\nu}\right), \tag{14}$$

where the thermal moment, defined as:[12]

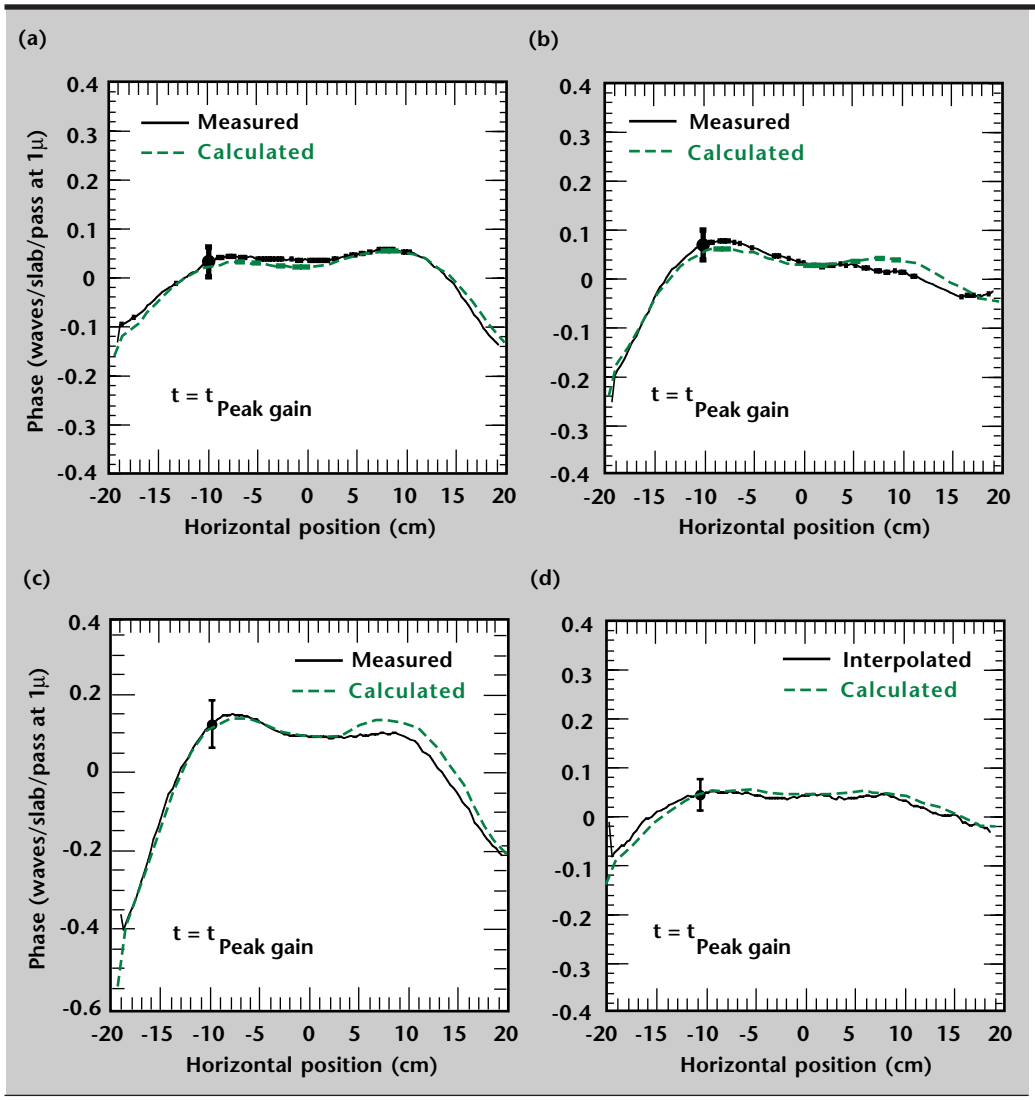

Figure 7. Measured and calculated wavefront, horizontal component—AMPLAB: (a) diamond configuration; (b) X configuration. Error bar shows typical error for measurements. (c) Three-slab-long configuration; (d) interior configuration—interpolated from 3-slab-long, diamond, and X results.

$$M_T(x,y) = \alpha E \int_0^h (z - h/2)\ T(x,y,z)dz \qquad (15)$$

is the source function for the displacement. In **Eqs. 14** and **15**, ν is Poisson's Ratio, α is the thermal expansion coefficient, and E is Young's modulus.

On the time scales of interest, one may neglect diffusion. Consequently, $T(x, y, z) \propto Q(x, y, z)$. If one substitutes **Eq. 1** into **Eq. 15** using **Eq. 2**, one finds that the thermal moment is proportional to the difference in pump profiles, that is, $M_T \propto g_0(y) - g_h(y)$. Consequently, small uncertainties in the values of g_0 and g_h can lead to large uncertainties in the thermal moment, and hence the amount of deformation. Since the steering of the laser beam is driven by the curvature of the laser slab, it follows that the phase front, which is the integral of the beam-steering, is proportional to the gradient of the displacement, or the integral of the thermal moment.

With our 2-D ray-trace code, we can match the gain profile across the aperture to within 1%. Because of ASE within the laser slab, we can vary the pump profile by 2% and still be within 1% in the gain coefficient. Consequently, if we take the pump profiles shown in **Fig. 1**, and assume a worst-case uncertainty of 2%, it can be shown that the variation in the peak-to-valley value for the phase front can be as much as ±15%.

Comparison with AMPLAB Experiments

In this section, we present comparisons of experiments performed in AMPLAB with the model described in the previous section. Unless otherwise mentioned, all comparisons are done at the time of peak gain at an explosion fraction of 0.2. As shown in **Fig. 6**, the OPD is calculated over the entire aperture. However to facilitate making comparison with the data, we shall show horizontal lineouts of calculations and experiments. These lineouts were taken at the vertical midplane of the aperture.

In **Figs. 7a** and **b**, we show the comparison between the calculated and measured phase front (essentially the negative of the OPD) for the diamond and X configurations in AMPLAB. Also indicated on the experimental curve is a typical value for the error in the measurement. As may be seen, there is excellent agreement in both configurations over the entire aperture.

In **Figs. 7c** and **d**, we show the calculated and measured phase front for the 3-slab-long and interior configurations, respectively. As indicated on the graph, the data for the interior configuration was interpolated from the measured diamond, X, and 3-slab-long data using the following algorithm:

$$\phi_i = \phi_3/2 - \phi_d - \phi_x\ , \qquad (16)$$

where ϕ_3 is the measured 3-slab-long phase in waves and all other phases are in waves/slab/pass. As can be seen from the figure, there is excellent agreement between calculation and measurement over the entire aperture.

Another check on the model is to calculate the wavefront distortion at times other than the time of peak gain. The results of these calculations, and comparison with the measurement, are shown in **Figs. 8a** to **f** (**Fig. 8b** is repeated for ease of comparison).

In these experiments, we measured the prompt wavefront distortion at 100, 200, 300, and 500 µs after the time of peak gain. As may be seen, the amount of wavefront distortion continues to increase after the time of peak gain up to 500 µs. In fact, the peak-to-valley value of the wavefront distortion is about three times greater at $t_{peak\ gain}$ + 500 µs than at $t_{peak\ gain}$. The agreement of the model with the measurement is excellent, matching both the magnitude and the shape of the wavefront at all times.

Summary and Conclusions

We have presented the results of detailed analysis and modeling of the AMPLAB data, summarized in **Table 1**.

We have also presented a description of our prompt pump-induced wavefront model. This model calculates the wavefront distortion due to mechanical deformation, and refractive index changes due to temperature and stress. We have benchmarked the code against AMPLAB measurements and will be using it to predict the wavefront distortion for the NIF amplifiers.

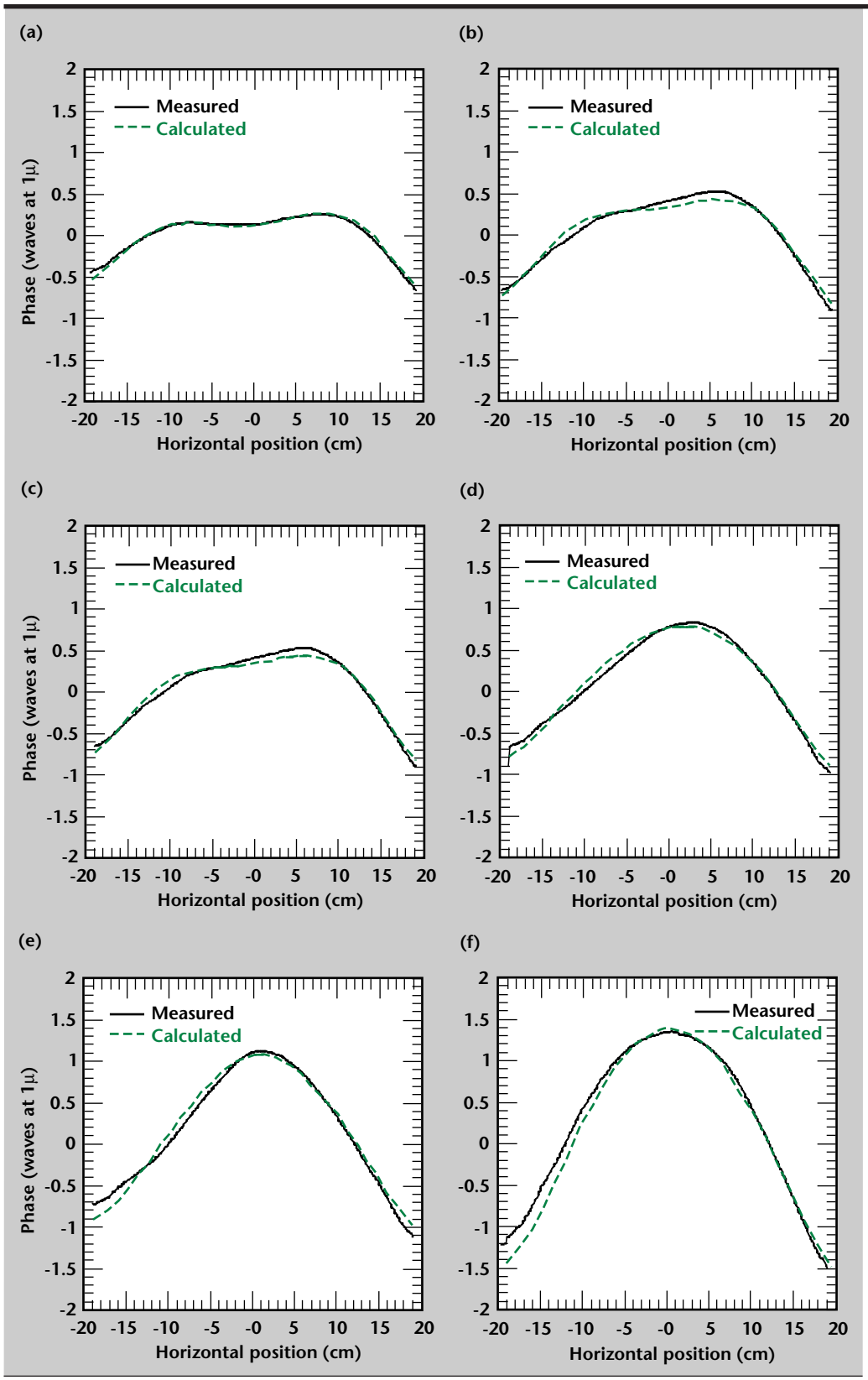

Figure 8. Measured and calculated wavefront, horizontal component—AMPLAB, diamond configuration: measurements taken at (a) $t = t_{peak\ gain}$; (b) $t = t_{peak\ gain} + 0.1$ ms for $f_x = 0.2$; (c) $t = t_{peak\ gain} + 0.1$ ms; (d) $t = t_{peak\ gain} + 0.2$ ms; (e) $t = t_{peak\ gain} + 0.3$ ms; and (d) $t = t_{peak\ gain} + 0.5$ ms.

Table 1. AMPLAB data analysis.

Configuration	Measured $\phi_{horiz.}$ (waves/slab/pass)	Calculated $\phi_{horiz.}$ (wave/slab/pass - LG-770)
Diamond	0.22 ± .03	0.21 ± .03
X	0.29 ± .03	0.27 ± .04
Interior	0.18 ± .03	0.16 ± .02

References

1. Shapiro, A. (1985), "TOPAZ3D—A 3-D Finite Element Heat Transfer Code," Lawrence Livermore National Laboratory, Livermore, California (UCID-20484), August.

2. Maker, B. N. (1995), "NIKE3D—A Nonlinear, Implicit 3-D Finite Element Code for Solid and Structural Mechanics," Lawrence Livermore National Laboratory, Livermore, California (UCRL-MA-105268, Rev. 1), April.

3. Doss, S., and R. Gelinas (1986), "Mathematics and Physics of the BREW Code," Lawrence Livermore National Laboratory, Livermore, California (UCRL-50021-86), pp. 7-132.

4. LeTouze′, G., O. Cabourdin, J. F. Mengue, M. Rotter, and K. Jancaitis (1996), "Shaped Reflectors for Pump Cavities," *2nd Annual Conf. Solid State Lasers for Application to ICF*, Limeil, France.

5. Jancaitis, K. (1986), "Flashlamp Modeling,"Lawrence Livermore National Laboratory, Livermore, California (UCRL 50021-86), p. 6-3.

6. Markiewicz, J. P., and J. L. Emmett (1966), "Design of Flashlamp Driving Circuits," *IEEE J.Q.E.*, **QE-2**, p. 707.

7. Powell, H. T., A. C. Erlandson, K. S. Jancaitis, and J. E. Murray (1990), "Flashlamp Pumping of Nd:Glass Disk Amplifiers," *SPIE* **1277**, p. 103.

8. Jancaitis, K. S. (1993), "Disk Amplifier Performance Model," Lawrence Livermore National Laboratory, Livermore, California (UCRL-LR-105820-88/89), p. 6-12.

9. Stokowski, S. E., R. A. Saroyan, and M. J. Weber (1981), "Laser Glass - Nd-doped Glass Spectroscopic and Physical Properties, V**1**," M-095, Rev. 2, V. **1**, Lawrence Livermore National Laboratory, Livermore, California.

10. Born, M., and E. Wolf (1980), "Principles of Optics, 6th ed.," p. 122, Pergamon Press, New York, New York.

11. Azzam, R. M. A., and N. M. Bashara (1987), "Ellipsometry and Polarized Light," North-Holland, Amsterdam, p. 488.

12. Boley, B., and J. Weiner (1960), "Theory of Thermal Stresses," Ch. 12, John Wiley and Sons, New York, New York.

Parallel Algorithm Development for Computational Mechanics

Carol G. Hoover and Robert M. Ferencz
Defense Technologies Engineering Division
Mechanical Engineering

Anthony J. De Groot and Robert J. Sherwood
Defense Sciences Engineering Division
Electronics Engineering

Edward Zywicz
New Technologies Engineering Division
Mechanical Engineering

Yuen L. Lee and Douglas E. Speck
Computer Applications Division
Computations

We have successfully implemented dynamic load balancing algorithms in the automatic contact and material erosion algorithms in the ParaDyn program. These algorithms provide an efficient method for treating arbitrary interface motion and extend the applicability and scalability of ParaDyn simulations to large problems of interest. ParaDyn algorithms for partitioning, parallel contact, and load balancing can be applied to parallel implicit methods. The most challenging algorithm research foreseen for future parallel models is the development of an efficient linear solver for both implicit solid mechanics and fluid models. New areas of development in particle continuum methods and parallel visualization are also described.

Introduction

This report features five parallel algorithm development projects that are part of our plan for implementing a full structural mechanics capability on our Accelerated Strategic Computing Initiative (ASCI) parallel computers.

Progress

Parallel Contact Algorithm with Load Balancing

Partitioning methods are the key to developing efficient algorithms for parallel computers. Generally, in designing parallel algorithms for a finite element method, the mesh is divided up by assigning elements to processors so that the calculation of the internal forces is balanced across the processors. However, some applications in nonlinear mechanics involve calculating contact at material interfaces that may represent as much as fifty to eighty percent of the total computation time.

For example, timing results for a benchmark crashworthiness simulation show that nearly eighty percent of the total time is used for the contact calculation. In the algorithm described below two partitions are used. The first is a partitioning of the mesh and the second is a method for localizing and partitioning the contact surfaces.

In our previous work[1] we described a parallel technique for treating contact interfaces when the surface motion remained in a localized region of the mesh throughout the dynamics of the calculation. In the more general case it is not possible to define *a priori* which surfaces will come into contact. This more general form of contact, referred to here as arbitrary contact, will occur if material surfaces undergo folding or large deformation, or if objects on the grid are in motion.

Hence, a localization technique must be used. The arbitrary contact algorithm currently implemented in DYNA3D[2,3] uses a localization technique that is conveniently extended into a parallel implementation. This algorithm is a node-on-patch method. The steps are as follows:

1. For each surface node, find a second surface node which is the nearest node in the remaining set of surface nodes;
2. Construct the facets connected to the second surface node; and
3. Determine whether the first surface node penetrates a facet connected to the second node. If so apply a contact force to prevent penetration.

The first step uses a grid of cubes, also referred to as buckets, to localize the search for nearest surface nodes. Surface nodes are sorted into the buckets and the search for the closest node is carried out over 27 buckets in three dimensions. The side length of the buckets is set to the maximum diagonal length of a face, plus an incremental length based on the velocity of the nodes forming the diagonal (**Fig. 1a**). This characteristic length is used so that at least one of the surface nodes associated with a penetrated patch is always contained in one of the 27 buckets in the set over which the search is conducted.

The parallel implementation of the arbitrary contact algorithm partitions the contact surfaces by allocating the buckets to processors. The buckets are added to the processors so as to approximately equalize the total number of surface nodes in each processor. One overlap bucket is needed across processors so that surface nodes in the center bucket of a strip of three buckets will find its connected patches in either the adjacent left or right bucket (**Fig. 1b**).

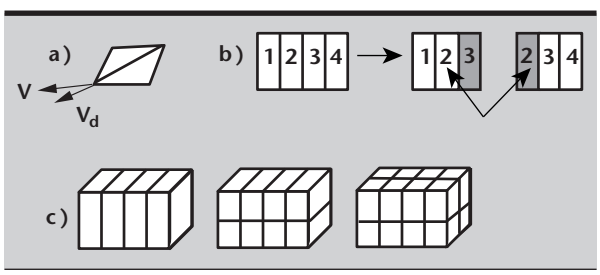

Figure 1. Illustration of the three steps in the load balancing of arbitrary contact surfaces. a) The bucket length is set to the maximum diagonal length of a face, plus a predicted incremental length based on the velocity along the diagonal; b) a set of buckets, in this case 4 1-D strips, is divided among two processors with one overlapping strip at the processor boundary; c) the grid of buckets is divided among processors by dividing the grid into 1-D slices, 2-D pipes, or 3-D cubes. The examples above show 4-, 8-, and 16-processor allocations of the same grid using slices, pipes, and cubes, respectively.

The allocation of buckets to processors is carried out by using 1-, 2-, or 3-dimensional geometric layout of processors (**Fig. 1c**). This corresponds to allocating buckets which are slices of the grid in one dimension, rectangular pipes in two dimensions, and cubes in three dimensions. The algorithm is currently implemented based on a fixed maximum number of buckets, N_{max}, for the full problem. The processor geometry is selected based on whether the number of buckets for a particular processor geometry is less than N_{max}. If more than one processor geometry satisfies this condition, then the processor geometry with the highest dimensionality is selected.

The use of two partitions (one for the full mesh and a second for contact surfaces) requires communication of the contact force values from the contact partition to the mesh partition. After this communication step, the total nodal forces are computed in processors associated with the mesh partition. Similarly, the time integration to compute the velocities and coordinates are calculated for nodal points in the mesh partition. After the time integration step, the updated nodal coordinates and velocities are communicated back to the processors containing the nodes in the contact partition.

The load balancing of the contact calculations occurs at time intervals corresponding to the time interval over which rebucketing occurs in the case of a single processor computer. This interval corresponds to the time required to move a surface node across the length of a bucket. The load balancing is carried out in parallel using parallel reduction operations which provide each processor with the global minimum and maximum for the geometry, the bucket structure, and the number of nodes in each bucket.

All processors then compute the rebucketing on the full grid. This is followed by a communication step in which each processor sends and receives surface nodes and patches corresponding to the buckets in the new contact partition.

Reliably detecting contact is a difficult task. **Figure 2** illustrates the deformation of a sheet of shell elements enclosed by moving stonewalls forming the faces of a cube. Contact detection for this problem uses the new method for treating contact which accounts for the thickness of shell elements. This problem runs correctly using 64 processors.

The material erosion algorithm in DYNA3D uses an algorithm formulation similar to the arbitrary contact described above and consequently was merged into the arbitrary contact algorithm. The erosion algorithm has been implemented in parallel during this last year. **Figure 3** illustrates the erosion algorithm for a small benchmark similar to the

model in large production calculations of a hypervelocity impact on a reentry vehicle.

Linear Solvers for Implicit Methods

Essentially all the parallel algorithmic strategies implemented within ParaDyn will be directly applicable to our implicit mechanics code, NIKE3D. However, NIKE3D's requirement for the solution of coupled systems of linear equations creates a new and significant challenge. Traditionally, linear equation solvers are divided into two classes: direct and iterative.

Direct methods are known for their robustness and predictable number of operations. However, they require a global data structure that grows rapidly with problem size and that presents challenges for large-scale parallelism.

Iterative methods typically use a much smaller data structure that can be readily distributed for large-scale parallelism. Unfortunately, the operation counts for iterative solvers grow enormously in the presence of ill-conditioning, that is, the existence of widely-spaced natural frequencies in the system. Sources of ill-conditioning are most often part of the simulations we seek to perform: material softening and damage, material anisotropy, mesh refinement to capture local effects, combined bending and membrane response of shells, and near-singularities as buckling behavior is approached.

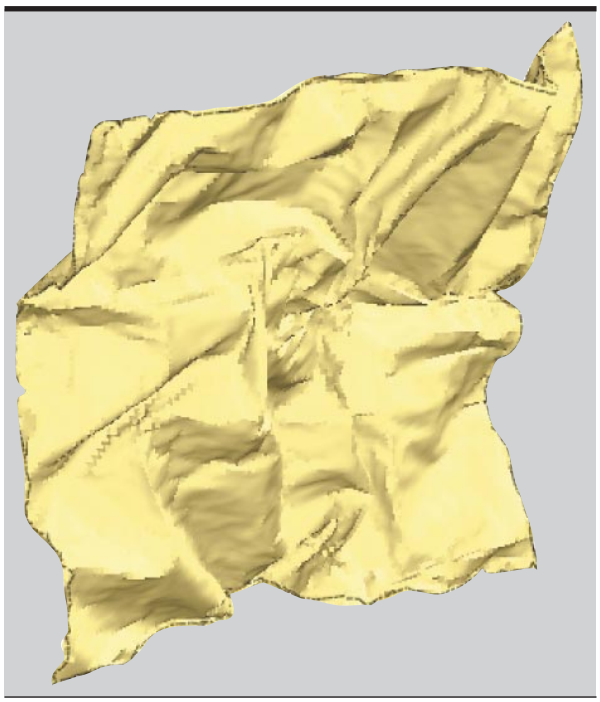

Figure 2. Arbitrary contact algorithm, used when a sheet of shell elements is deformed by moving stonewall boundaries that are the faces of a cube enclosing the sheet

These tradeoffs between direct and iterative methods mean there is no one technology presently available that totally meet our needs for parallel linear equation solving. Fortunately, this topic is a broad area of inquiry in the academic community and one that is well supported by multiple efforts within the ASCI program.

We are monitoring and interacting with these activities as we assess current capabilities. As an example, we completed an interface within NIKE3D to a parallel direct linear equation solver named PSPASES from the University of Minnesota.[4] This was a prototype effort used to evaluate the linear solver technology.

The first processor acts as "master": it performs all I/O, computes the finite element matrices, and then works in cooperation with the remaining "slave" processors to perform the linear equation solving. This NIKE3D prototype is running in message-passing mode on our DEC cluster and IBM SP (ASCI Blue Pacific).

The test problem examined is the so-called Boussinesq problem: a concentrated force on the surface of an elastic half space. In this case the domain is represented by a mesh of $24 \times 24 \times 24$ hex elements, resulting in a system of 45,000 equations. This highly coupled system of equations is representative of those arising from true 3-D geometries.

The CPU data plotted in **Fig. 4** immediately illustrate one limitation of this particular solver: it only permits the use of 2^N processors. Comparing the "linear algebra" and "total" CPU times for the uniprocessor run confirms that this simulation is dominated by the cost of linear equation solving.

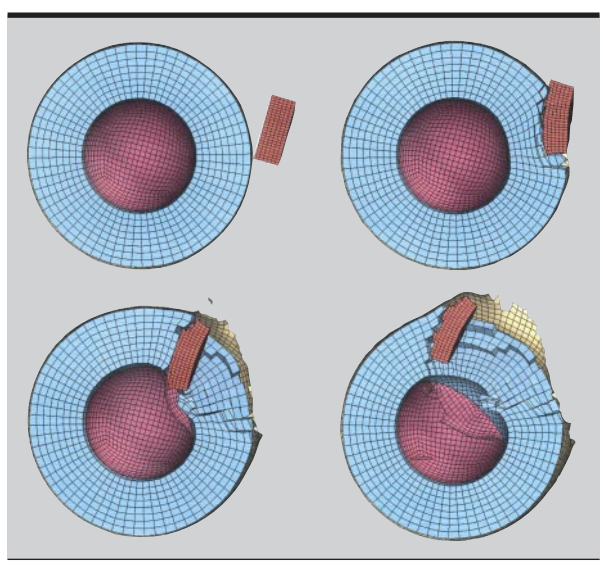

Figure 3. Benchmark test, illustrating the material erosion algorithm.

The trends for the parallel runs show reasonable scalability. Given the fixed problem size, the timing curve will flatten as the number of processors increases. The quite mild growth in the gap between the linear algebra CPU time for Processor 0 and the wall time for the factorization seems to indicate that communication latency is not a major penalty even for the case of 32 processors.

Finally, for the parallel runs, one sees a larger, though relatively constant offset between the linear algebra and total CPU time for Processor 0. This contrast from the uniprocessor case reflects the cost of mapping from NIKE's internal representation of the global system of equations to that required by this parallel solver. This cost could be readily eliminated by having NIKE assemble into the desired data structures from the outset.

When assessing the performance of a particular software library, it is important to characterize the effect of the available algorithmic features and run-time environment.

For example, the data in **Fig. 5** illustrate the impact of two different ordering strategies available in this package. Sparse direct solvers use a reordering of the equations to reduce the number of non-zero coefficients created during the factorization process. In one case, the "parallel" ordering option uses multiple processors to collectively perform this operation. The "serial" ordering restricts the operation to a single processor.

The latter approach has the advantage that the entire equation structure is simultaneously optimized, and thus a better overall ordering is attained. The developers note that typically the serial option results in twenty to thirty percent fewer non-zero terms in the factorized representation of the matrix, leading to possibly a factor of two reduction in arithmetic operations. These savings are reflected in **Fig. 5**.

Additional performance improvements will be available when we are able to use the SP's "User Space" high-speed communication sub-system. We are currently restricted to the slower "IP" communication sub-system, due to a combination of limitations in this prototype "master-slave" implementation, as well as the vendor's operating system.

The total memory graph in **Fig. 6** illustrates how memory for this benchmark grows with the number of processors when using the parallel reordering option in PSPASES. To provide a basis for comparison, note that a uniprocessor execution of NIKE3D using a sparse direct solver requires less than 600 Mb of total memory.

As mentioned previously, the parallel reordering cannot reduce factorization fill-in as effectively as serial reordering, thus more memory and floating-point arithmetic operations will be required. However, for sufficiently large problems, the serial reordering will require more memory than is available on a single node of the IBM SP system. In such instances the parallel option will be the only viable choice and we can anticipate the behavior shown in this graph.

Iterative methods for linear equation solving are not out of the running, and we look forward to additional improvements through ASCI-related efforts.

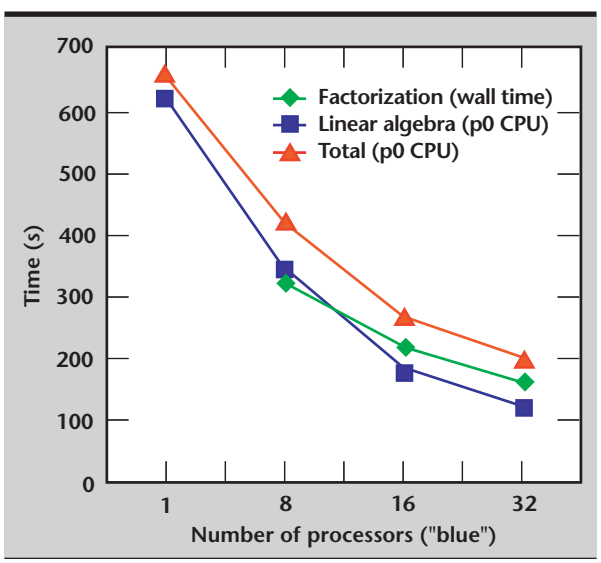

Figure 4. Timing comparison for the 24 x 24 x 24 Boussinesq problem of uniprocessor NIKE3D with trials on the IBM R/S6000 SP (ASCI Blue-Pacific), using the PSPASES sparse direct parallel linear equation solver.

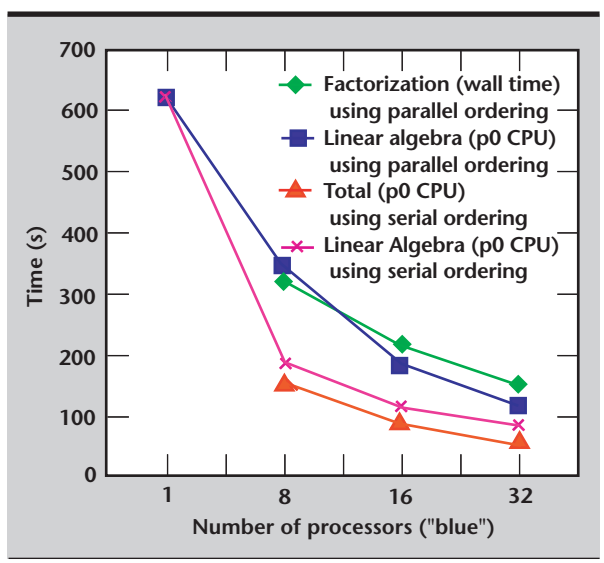

Figure 5. Timing comparison for the 24 x 24 x 24 Boussinesq problem, using the two reordering strategies available within the PSPASES package.

For example, algorithms such as algebraic multigrid have proved quite powerful for computational fluid dynamics and may prove equally useful for solid mechanics. And, looking at the relative strengths of direct and iterative methods, it is plausible that the ultimate solution will be the blending of the two technologies into so-called "hybrid methods."

One example of this approach is the FETI algorithm developed for large-scale aerospace structure by C. Farhat (University of Colorado).[5] We are currently creating a prototype implementation of FETI which will be used to evaluate the methodology on problem classes of interest to Lawrence Livermore National Laboratory (LLNL).

Shared Memory Parallelism

We have been motivated to evaluate shared memory parallelism for our finite element programs for two reasons. Computer companies developing multiprocessor workstations and workstation clusters with up to 32 processors in a box are providing fast, efficiently-coded shared-memory parallel linear solvers. A second reason is that the target computer architecture for the ASCI Blue Mountain and Blue Pacific computers will consist of multiple processors on shared memory nodes connected with a very high speed interconnect network.

The ASCI architectures will support hybrid parallel models combining shared memory and message passing. Although the computer operating system and compiler software is very immature at this point, we have experimented with shared memory parallel syntax in the DYNA3D program using the new OpenMP standard.

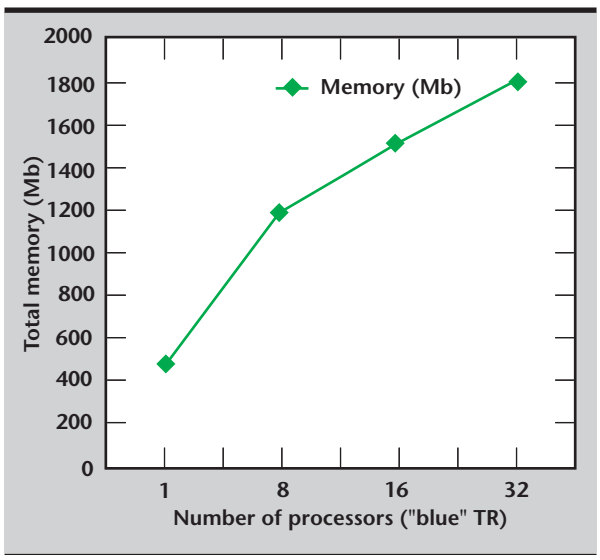

Figure 6. Memory comparison for the 24 x 24 x 24 Boussinesq problem of uniprocessor NIKE3D with trials, using the PSPASES sparse direct parallel linear equation solver with parallel reordering.

We had determined in earlier tests with NIKE3D that the automated compiler parallelism generated on a loop level provided parallel granularity that was too small to overcome the latency associated with allocating the threads to a processor. The DYNA3D shared memory implementation uses a large granularity for parallel tasks by defining OpenMp parallel regions in the upper level integration routine.

For example, the threads are initialized over the stress divergence calculation by element type. Threads are also distributed across the materials for each element type. Shared nodal data for the scatter step in the nodal force update are treated as a critical data region so that the nodal force update remains sequential. The contact algorithms are treated by spreading the loops which include large amounts of computational work over the processors.

The most tedious aspect of this implementation was the identification of shared and processor-local variables when parallel threads are initialized. Some modifications to the COMMON blocks storing element and material data were required in this step. Further modifications would be needed in the future for a hybrid model to identify shared and processor-local variables which are used in message passing data structures. This step would be taken only if the performance of the shared memory parallelism provides large speed gains over message passing models with multiple domains on a computer node.

Our performance results for shared memory parallelism are still quite preliminary. We find good performance for a two-processor SGI Octane workstation and also for some problems on a four-processor SGI Origin 200. On the other hand we have found it difficult to achieve good performance with some of our test cases using more than four processors on an SGI Origin 2000. By using performance analysis tools we were able to identify cache misses as the most significant limitation on the performance. Nodal reordering techniques may provide a remedy for these performance problems and may be investigated in the future.

Parallel Smooth-Particle Applied Mechanics

The use of particle techniques to solve the equations of continuum mechanics has become of increasing interest over the last decade. This interest in particle methods is motivated by the fact that they can be used to recast the partial differential

equations describing continuum mechanics into a set of ordinary differential equations which may be easier or more efficient to solve numerically.

Perhaps a more compelling reason for using particle methods is that there is no underlying grid in the calculation. Thus, models for fracture, fragmentation, penetration mechanics, and plastic flow can be developed without resorting to adaptive grid methods.

The smooth-particle applied mechanics (SPAM) method, often referred to as smooth-particle hydrodynamics (SPH), is one of several particle methods.

SPAM has been applied to both solids as well as fluid mechanics problems.[6,7] This method describes the continuum as a set of particles with each particle associated with a position and a weighting function. The weighting function has a range that smears out the particle over a region around its position. The density at any point in space is calculated by the summed contribution of all particles within the range of the point.

Similarly, other physical quantities such as velocity, strain, stress, and energy are calculated by the weighted averages of the same physical variables ascribed to the particles. Details of this method for converting the partial differential equations of continuum mechanics into an equivalent set of ordinary differential equations are described in the above references.

Work is in progress to develop a SPAM model for anisotropic granular solid-melt systems generated during mold filling and other manufacturing processes. Two-dimensional atomistic simulations of this system have been completed and will be compared to SPAM calculations for an equivalent continuum model.[8] A parallel implementation of a two-dimensional SPAM algorithm is under development and will be used for simulating solid-melt systems on ASCI parallel computers.

Parallel Visualization

In anticipation of problem sizes in the range of 15 million elements and larger, we are developing a prototype parallel visualization tool based on the GRIZ program. Our initial implementation assumes the domain decomposition from the finite element analysis and uses a master/slave parallel model which splits GRIZ functionality over one master processor and multiple slave processors. The master processor is responsible for all interactive functions including full frame display and interactive menu and mouse commands. The slave processors compute results and render frames associated with their subdomain from the full mesh.

Frame generation proceeds as follows. The master processor receives user input to generate a frame displaying a result (primal or derived). The master broadcasts this command to slave processors that process the command, calculate results, and render their portion of the frame into a local offscreen frame buffer. The slave processors perform a global reduction of the pixel color values, based on their associated z-buffer (depth) values to arrive at a composite mesh image across all subdomains. The composite mesh image is sent to the master, which loads it into the user's frame buffer and renders foreground information such as text, labels, and colormap over it.

We use two MPI (Message Passing Interface) communicator groups to implement this model. The first contains the master and all of the slave nodes. The second contains slave nodes only.

This parallel prototype is implemented in the Mili version of GRIZ. Mili (Mesh I/O Library) provides code developers with a flexible tool for creating self-defining binary data bases for the visualization of complex grids. The self-defining feature is particularly useful for parallel simulations where it is important to limit the size of the resulting data sets.

Future Work

The ParaDyn program has matured to a full production status. New algorithms or extensions to existing DYNA3D algorithms are now being designed with a plan that includes the parallel implementation. Three projects scheduled for next year are: 1) to write a users' manual for the ParaDyn program; 2) to add message-passing communication to the Lagrange contact algorithm; and 3) to complete the programming for the few remaining DYNA3D options not implemented in parallel.

Future development projects will include parallel algorithm development for NIKE3D and a collaborative effort with LLNL's Thermal Fluids Group to develop parallel versions of TOPAZ3D and fluid codes used in coupled thermomechanical analysis.

Investigations will continue in grid-free methods such as SPAM. These methods may prove to be useful in capturing highly localized physical phenomena when used in combination with finite element methods which describe a large-scale engineering analysis on a parallel computer.

Acknowledgments

We gratefully acknowledge support for ParaDyn code development from the Weapons Program at LLNL and from the Department of Defense High-

Performance Computing and Modernization Program. We especially thank M. Giltrud from the Defense Threat Reduction Agency (formerly the Defense Special Weapons Agency) for funding both serial and parallel contact algorithm development. Professor W. Hoover (University of California, Davis) inspired the model for the crumpled material benchmark for ParaDyn. He has also conducted extensive research on the SPAM algorithm and has developed many physical applications using the method. We appreciate the feedback and helpful comments from analysts running the ParaDyn program, especially D. Badders, T. Lee, and D. Faux from LLNL, and R. Namburu and P. Papados from the U. S. Army Corps of Engineers Waterways Experiment Station.

References

1. Hoover, C. G., A. J. De Groot, and R. J. Sherwood (1998), "Parallel Contact Algorithms for Explicit Finite Element Analysis," *Modeling and Simulation Based Engineering*, S. N. Atluri and P. E. O'Donoghue, eds., Tech Science Press, Palmdale, California.

2. Whirley, R. G., and B. E. Engelmann (1993), "DYNA3D: A Nonlinear, Explicit, Three-Dimensional Finite Element Code for Solid and Structural Mechanics—User Manual," Lawrence Livermore National Laboratory, Livermore, California (UCRL-MA-107254, Rev. 1).

3. Benson, D. J., and J. O. Hallquist (1990), "A Single Surface Contact Algorithm for the Post-Buckling Analysis of Shell Structures," *Computer Methods in Applied Mechanics and Engineering*, Vol. **78**, pp. 141-163.

4. Gupta, A., F. Gustavson, M. Joshi, G. Karypis, and V. Kumar (1997), "Design and Implementation of a Scalable Parallel Direct Solver for Sparse Symmetric Positive Definite Systems," *Proceedings, Eighth SIAM Conference on Parallel Processing*.

5. Farhat, C., and F.-X. Roux (1991), "A Method of Finite Element Tearing and Interconnecting and its Parallel Solution Algorithm," *International Journal for Numerical Methods in Engineering*, Vol. **32**, pp. 1205-1227.

6. Posch, H. A., W. G. Hoover, and O. Kum (1995), "Steady-state shear flows via nonequilibrium molecular dynamics and smooth-particle applied mechanics," *Physcial Review E*, Vol. **52**, No. 2, pp. 1711-1720.

7. Hoover, W. G., T. G. Pierce, C. G. Hoover, J. O. Shugart, C. M. Stein, and A. L. Edwards (1994), "Molecular Dynamics, Smoothed-Particle Applied Mechanics, and Irreversibility," *Computers Math. Applic.*, Vol. **28**, No. 10-12, pp. 155-174.

8. Hoover, W. G., and S. Hess (1998,) "Anisotropic Plasticity with Embedded-Atom Potentials," *Physica A*, in preparation.

DYNA3D-TOPAZ3D Coupling and DYNA3D-NIKE3D Linkage

Jerry I. Lin
Defense Technologies Engineering Division
Mechanical Engineering

This report describes the coupling of DYNA3D and TOPAZ3D and the linkage between DYNA3D and NIKE3D. The combined DYNA3D-TOPAZ3D code provides a tool for coupled thermal-mechanical analyses, and the DYNA3D-NIKE3D link enables the multi-staged simulations for structural/continuum mechanics problems. For a coupled thermal-mechanical analysis, DYNA3D and TOPAZ3D run in parallel and exchange structure/continuum deformation and temperature as the analysis progresses. For structural/continuum mechanics problems involving different regimes of loading, deformation, or frequency characteristics, the DYNA3D-NIKE3D link is designed to run in series. It aims to fully use the explicit/implicit advantages of the individual codes at the proper stages.

Introduction

Over the years, coupled thermal-mechanical engineering problems had been solved by a "weak coupling" approach of mechanics codes and heat transfer codes. The analyst first runs a thermal analysis for the model by TOPAZ3D,[1] a 3-D, implicit heat transfer finite-element (FE) code, and writes the temperatures at selected times to a file. These temperatures are then read from the file at their corresponding times in the subsequent mechanical analysis, usually by the 3-D, explicit structural/continuum FE code DYNA3D.[2] The coupling is achieved through the use of temperature-dependent material properties or temperature change-induced thermal stresses. From the structural analysis standpoint, this procedure does reflect the temperature-sensitive nature of the problem, but does not quite capture the essence of thermal-mechanical interaction.

With the evolution of the weapon systems and the expanding scope of laser-related applications at Lawrence Livermore National Laboratory, the importance of detailed thermal-mechanical stress analysis has become evident. The integration of DYNA3D and TOPAZ3D is intended to accomplish this goal. When requested by a user, TOPAZ3D would be compiled as a program module in DYNA3D. For a thermal-mechanical analysis, the coupling is then achieved by the continuous exchange of deformation and temperature data between these codes on a real-time basis.

The link between DYNA3D and NIKE3D,[3] an implicit, structural/continuum FE code, is arranged in a serial mode and intended to solve certain classes of structural/continuum mechanics problem. This combined explicit-implicit method is particularly effective for simulations involving initial stress, such as failure analysis of rotating fan blades, or residual stress, such as sheet metal forming process with spring-back.

Due to its explicit nature, DYNA3D would have difficulty attaining an equilibrium state for the rotation-induced initial stresses in the fan blades or sustaining a long duration simulation of spring-back phenomena, whereas the implicit NIKE3D is perfectly suited for these purposes. However, the impulsive loading, high nonlinearities and complicated contact conditions in the transient phase of these problems usually render NIKE3D ineffective and necessitate the use of DYNA3D.

The capability of reading a file generated by its opposite code, and writing a file for its opposite code is implemented in both DYNA3D and NIKE3D. This binary file contains the nodal kinematic variables and element stresses, strains, and other state variables. Series of DYNA3D and NIKE3D analyses, with essential data transmitted through this file, can be strung along to solve complicated multi-phase problems. Different element formulations are preferred in DYNA3D and NIKE3D because of their explicit/implicit natures. Change of element formulation is permitted during the transition from one code to the other to accommodate this fact.

Progress

DYNA3D-TOPAZ3D Coupling

In DYNA3D, temperature dependency can be established through the use of material type 4 (thermal-elastic-plastic), type 15 (Johnson/Cook elastic-plastic), type 21 (thermal-orthotropic-elastic) or type 23 (thermal-orthotropic-elastic with variable properties). They have either the material temperature as part of the constitutive equations, or temperature-dependent material properties. Because of different time increments used in time integration in these codes—usually a greater time step in the implicit TOPAZ3D, and a smaller one in the explicit DYNA3D—the coupling can be executed only when the simulation times in both codes are synchronized. The temperatures at the intermediate DYNA3D steps are obtained by linear interpolation.

The coupling procedure, depicted in **Fig. 1**, can be described as follows:

1. DYNA3D feeds current nodal coordinates to TOPAZ3D when simulation clocks in both codes are synchronized.
2. TOPAZ3D does a thermal analysis and returns the updated current temperature to DYNA3D at the end of this thermal step. TOPAZ3D advances its clock.
3. DYNA3D executes the mechanical analysis based on the current temperatures provided by TOPAZ3D and advances its clock incrementally until the clock catches the TOPAZ3D clock.

This process repeats itself until it reaches the designated simulation time.

A TOPAZ3D compilation flag is set in DYNA3D. Only if the flag is activated will TOPAZ3D be integrated into DYNA3D. A special arrangement is also made to have the temperatures written into the DYNA3D plot database for post-processing purposes.

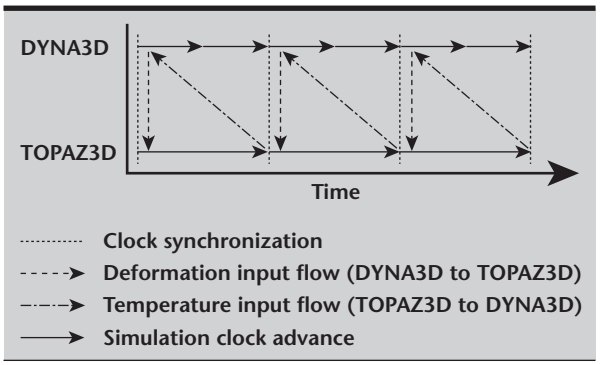

Figure 1. Illustration of DYNA3D-TOPAZ3D coupling procedure.

DYNA3D-NIKE3D Link

Due to the explicit nature of DYNA3D, the Belytschko-Lin-Tsay shell element[4] and the uniformly under-integrated hexahedral elements (URI)[5] are the preferred elements in DYNA3D. On the other hand, the Hughes-Liu shell element and the Selective-Reduced Integrated (SRI)[6] hexahedral element are favored by NIKE3D because of its implicit integration approach.

To take full advantage of the codes' characteristics, different elements can be used in these codes. A transformation of the shell element stresses to the global coordinate system is performed before DYNA3D writes them into the link file. It ensures the stresses NIKE3D reads are as expected by the code. A reverse stress transformation is also done right after DYNA3D reads the link file generated by NIKE3D. For hexahedral continuum elements, NIKE3D averages the stresses at element integration points to give DYNA3D elements a uniform stress state, and imposes uniform stresses on element integration points while reading the stresses from the DYNA3D-generated link file.

The SRI hexahedral elements as well as a fully integrated shell element[7] have been implemented into DYNA3D, whereas the URI and shell elements have been added to NIKE3D, to give both codes a complete element library. In the event that high fidelity transfer from one code to the other is necessary, users have the choice to use unified element formulations, albeit it may come with a high price on DYNA3D analysis.

Figure 2 depicts the sequence for a typical multi-phase mechanical analysis. A Pokel Cell example (**Fig. 3**) is used to demonstrate the advantages of the combined analysis. In this problem, an O-ring is being pressed into the seal groove by a piece of laser glass. Because of the O-ring's viscous elastic material behavior, the response includes a sharp rise of stress in the loading phase and a prolonged relaxation in the unloading phase. DYNA3D can handle the transient loading phase with ease, but would have difficulty bringing the stress to a relaxed steady state. The use of NIKE3D during the unloading phase results in a satisfactory solution, as shown in the stress-time plot in **Fig. 3**.

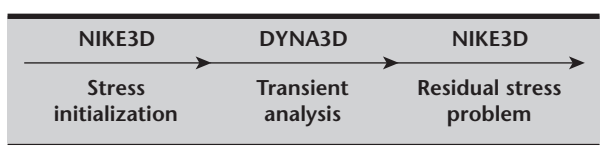

Figure 2. Illustration of DYNA3D-NIKE3D link sequence for typical multi-phase mechanical analysis.

In large scale models, especially with complicated contact conditions or a long simulation time, DYNA3D users sometimes encounter spatial instability that cannot be controlled by the existing anti-hourglass algorithms. With the multi-point integrated elements now available in DYNA3D, users have the option to deploy them at critical parts of the mesh that are particularly susceptible to hourglass modes.

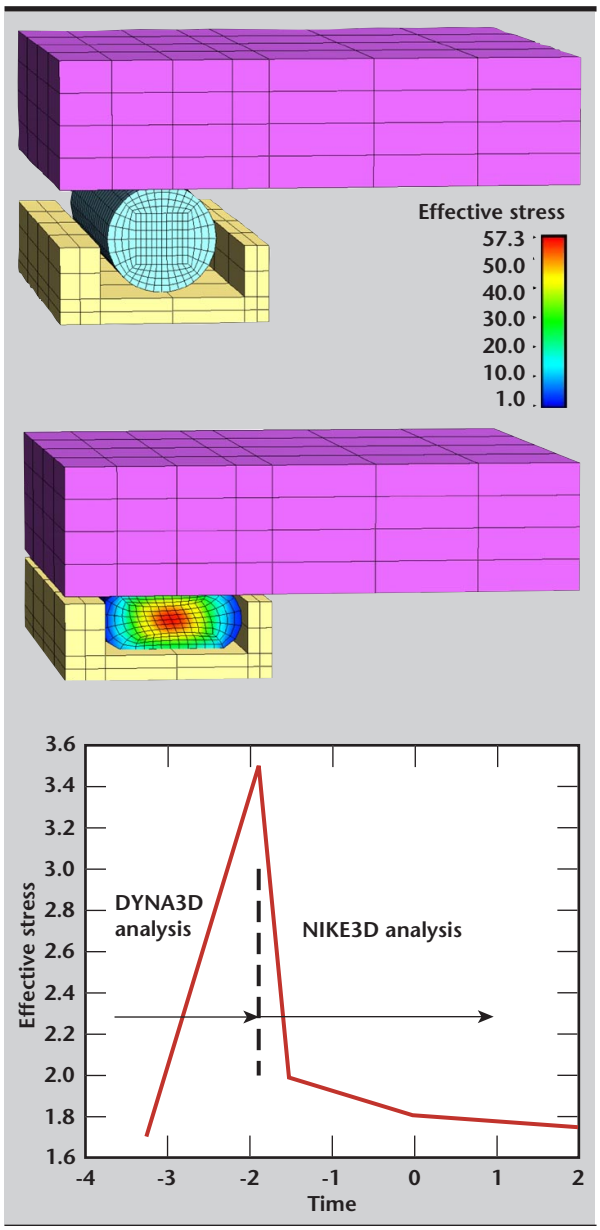

Figure 3. DYNA3D-NIKE3D example: stress-time plot, showing use of NIKE3D during the unloading phase.

Future Work

For coupled thermal-mechanical analyses, the possible temperature change due to the dissipation of element plastic strain energy still needs to be accounted for. This plastic strain energy must be computed by DYNA3D and transferred along with the deformation to TOPAZ3D.

On the DYNA3D-NIKE3D link, we are looking into the implementation of global stress interpolation schemes in DYNA3D. It would enable DYNA3D to provide non-uniform element stresses, without the high cost of multi-point integrated elements, to NIKE3D.

Acknowledgments

The DYNA3D-TOPAZ3D coupling is a joint effort by A. Shapiro and the author. The DYNA3D-NIKE3D link and the implementation of new elements are a team effort by M. Puso, E. Zywicz, and the author.

References

1. Shapiro, A. B. (1985), *TOPAZ3D—A Three-Dimensional Finite Element Heat Transfer Code*, University of California, Lawrence Livermore National Laboratory, Livermore, California UCID-20484.

2. Whirley, R. G., and B. E. Engelmann (1993), *DYNA3D: A Nonlinear, Explicit, Three-Dimensional Finite Element Code for Solid and Structural Mechanics—User Manual*, University of California, Lawrence Livermore National Laboratory, Livermore, California UCRL-MA-107254.

3. Maker, B. N. (1995), *NIKE3D: A Nonlinear, Implicit, Three-Dimensional Finite Element Code for Solid and Structural Mechanics—User's Manual*, University of California, Lawrence Livermore National Laboratory, Livermore, California UCRL-MA-105268.

4. Belytschko, T., J. I. Lin, and C. S. Tsay (1984), "Explicit Algorithms for the Nonlinear Dynamics of Shells," *Computer Methods in Applied Mechanics and Engineering*, **42**, pp. 225-251.

5. Goudreau, G. L., and J. O. Hallquist (1982), "Recent Developments in Large Scale Finite Element Lagrangian Hydrocode Technology," *Computer Methods in Applied Mechanics and Engineering*, **30**.

6. Hughes, T. J. R. (1987), *The Finite Element Method: Linear Static and Dynamic Finite Element Analysis*, Prentice-Hall, Princeton, New Jersey, pp. 232-237.

7. Bathe, K., and E. N. Dvorkin (1985), "A Four-Node Plate Bending Element Based On Mindlin/Reissner Plate Theory and a Mixed Interpolation," *International Journal for Numerical Methods in Engineering*, **21**, *pp. 367-383.*

A Physically-Stabilized Eight-Node Hexahedral Element

Michael A. Puso
Defense Technologies Engineering Division
Mechanical Engineering

We have developed a novel single-point integration scheme that performs as well as the fully integrated element for many problems, but is much more efficient computationally. We used the physical stabilization method to compute the hourglass forces by a Taylor series expansion of the stresses and strains about the center of the element.

Introduction

The explicit and implicit finite-element methods have spawned two different element types to maximize their efficiencies. The bottleneck for the explicit method is the strain and constitutive evaluations. Consequently, we have used a single-point integration method, where these evaluations are made only at the center of the element. To make up for the loss of resolution from the single-point integration, more elements are used in the calculation.

On the other hand, the bottleneck for the implicit method is the inversion of a system of linear equations. Consequently, it is desirable to reduce the number of equations/elements in the analysis by using a higher-order integration rule over the spatial domain of the element, to gain resolution and stability. However, the increased use of mixed implicit/explicit analysis necessitates a new element strategy that combines the austerity of the single-point integration with the robustness of the multiple-point integration. In this work, a novel single-point integration scheme is developed that performs as well as the fully integrated element for many problems but is much more efficient computationally.

Progress

The single-point integration method requires hourglass control to eliminate zero-energy modes, to remain stable. The perturbation method currently used in explicit finite-element codes requires *ad hoc* parameters to calculate the hourglass forces and, consequently, can give poor results particularly for coarse meshes.

In this work, we use the physical stabilization method to compute the hourglass forces by a Taylor series expansion of the stresses and strains about the center of the element. This allows the element to be integrated in closed form, providing the exact hourglass forces for initially parallelepiped elements. Consequently, no artificial parameters are required to preclude hourglassing.

As many analysts know, some problems require calibration of hourglass parameters to eliminate hourglassing in a mesh while avoiding spurious stiffening of the structure. This new method should eliminate this time-consuming procedure and provide better coarse mesh accuracy, particularly for bending-dominated problems.

After contact, the hourglass control forces are typically the most expensive calculation in the explicit method. For an all brick element problem with no contact and a simple elastic material, stiffness-based hourglass forces comprise twenty percent of the total CPU time. With the new physical stabilization method, the hourglass forces will comprise about thirty percent of the total CPU time. Overall, this amounts to a ten percent increase in total CPU time for the worst case.

With problems including contact and more expensive material models, the extra time for the physical stabilization will be further amortized. Compare this to a fully integrated element, which takes between four and six times more CPU time in the element calculation than the perturbation method.

This physical stabilization method is implemented into DYNA3D and NIKE3D for general use and can be exploited in mixed explicit/implicit analysis via the DYNA3D/NIKE3D link, or the NIKE3D implicit/explicit analysis mode.

Theory

The perturbation hourglass control method can apply either elastic or damping forces to resist the hourglass modes. Although slightly more efficient, the damping-based method is entirely non-physical and is not applicable to static problems, since motion is required to resist the modes. Furthermore, with the damping method, hourglass modes will always eventually become evident in problems where boundary conditions allow them to propagate. Only the stiffness-based hourglass control methods are considered here.

Flanagan and Belytschko[1] were the first to use the orthogonal hourglass control method for 3-D nonlinear transient analysis. This method uses the so called γ stabilization vectors, which are orthogonal to the homogenous strain states, and consequently satisfy the patch test, providing a convergent formulation for hourglass control. In the first appearance of physical stabilization,[2] this method was applied to shells and four-node quadrilateral elements (2-D).

The first physical stabilization method applied to eight-node hexahedral elements (3-D) was by Belytschko and Bindeman.[3] This method alleviated the problems of locking due to incompressibility, and avoided the parasitic shear locking in bending-dominated problems for undistorted elements. But the element required a co-rotational coordinate system, which is only well-posed for parallelepiped elements and in general is not indifferent to element node number.[4]

Furthermore, hourglass forces are not convected with the deformation in a consistent fashion. Zhu and Cescotto[5] proposed a general method for physical stabilization of the eight-node hexahedral but required the storage of 36 hourglass stresses, as opposed to the twelve hourglass forces quantities usually needed. Also, no valid solution to parasitic shear locking was offered.

In this work we formulate a physical stabilization method that uses the convected frame in lieu of a co-rotational frame.[3] This allows us to use an assumed strain field for the hourglass forces, which can avoid shear lock yet be frame-indifferent. Furthermore, only twelve hourglass forces are needed, and hourglass forces are correctly convected for material models using the so-called convected or Truesdale rate (for example hyperelasticity, F_e/F_p plasticity model).

For ordinary general hypoelastic models the hourglass forces are valid for small strain/large rotation, but should still be effective.

In the finite-element method, the internal forces for an element with domain Ω_e is given by

$$\boldsymbol{F}_{int} = \int_{\Omega_e} \boldsymbol{B}^T \sigma \, dV \,, \tag{1}$$

where $\boldsymbol{B}$ is the strain displacement matrix and σ is the stress. In single-point integration, only the values of the stress and strain displacement at the element center (σ_0 and $\boldsymbol{B}_0$) are used in **Eq. 1** so that the internal force is calculated at time *n+1* by

$$\boldsymbol{F}_{int}^{n+1} = \int_{\Omega_e} \boldsymbol{B}_o^T\left(t_{n+1}\right)\sigma_o\left(t_{n+1}\right) dV \,. \tag{2}$$

The additional forces used to preclude the zero-energy modes are given by the update:

$$\boldsymbol{F}_{hg}^{n+1} = \sum_{i=1}^{4} \Gamma_i \boldsymbol{f}_i^{n+1} \,,$$

$$\boldsymbol{f}_i^{n+1} = \boldsymbol{k}_{ij}\Gamma_j^T \Delta\boldsymbol{u} + \boldsymbol{Q}\boldsymbol{f}_i^n \tag{3}$$

where

$$\boldsymbol{k}_{ij} = \alpha\,\delta_{ij}\,\boldsymbol{I}_{3\times 3} \,,$$

$$\Gamma_i = \begin{bmatrix} \gamma_i & 0 & 0 \\ 0 & \gamma_i & 0 \\ 0 & 0 & \gamma_i \end{bmatrix}, \tag{4}$$

γ_i is the ith 8 x 1 stabilization vector, $\Delta\boldsymbol{u}$ is the incremental displacement, $\boldsymbol{Q}$ is the incremental rotation given by the spin at the element center, $\boldsymbol{f}_i$ is the ith 3×1 hourglass force, and α is the artificial hourglass control parameter.

In the physical stabilization method, it is recognized that the strain matrix has a constant and bilinear (or hourglass) portion, such that $\boldsymbol{B} = \boldsymbol{B}_o + \boldsymbol{B}_{hg}$. Furthermore, by using the following approximation:

$$\frac{\partial(\cdot)}{\partial x} \approx \frac{\partial\xi}{\partial x_{\xi=0}} \frac{\partial(\cdot)}{\partial\xi} \,, \tag{5}$$

to calculate the hourglass portion of the strain displacement matrix, certain orthogonality conditions can be exploited such that **Eq. 1** can be integrated in closed form.

In this work the Truesdale rate is used as the objective rate in the constitutive law, such that the volume integration can precede the constitutive time integration in **Eq. 1**, and the 36 hourglass stresses per element needed (that is, stored) are condensed to just 4 3×1 hourglass forces needed in the update.

An assumed strain field is used for the contravariant strain tensor so that parasitic shear lock is avoided for bending-dominated problems. The following form is used to calculate the hourglass forces:

$$\boldsymbol{F}_{hg}^{n+1} = \sum_{i=1}^{4} \Gamma_i \boldsymbol{f}_i^{n+1} ,$$

$$\boldsymbol{f}_i^{n+1} = \boldsymbol{k}_{ij} \Gamma_j^T \Delta \boldsymbol{u} + \boldsymbol{J}_o \boldsymbol{f}_i^n \tag{6}$$

where

$$\boldsymbol{k}_{ij} = \sum_{l=1}^{6} \boldsymbol{J}_o \boldsymbol{B}_{il}^T \mathbf{J}^{-T} \mathbf{C} \mathbf{J}^{-1} \boldsymbol{B}_{jl} \boldsymbol{J}_o^T , \tag{7}$$

$\boldsymbol{J}_o$ is the 3-x-3-element Jacobian at the element center, **C** is the 6-x-6 material stiffness, **J** is the 6-x-6 matrix that transforms the incremental strain vector onto the covariant coordinate system form by the columns in $\boldsymbol{J}_o$, and $\boldsymbol{B}_{ij}$ is a 6-x-3 matrix that accounts for the individual contravariant strains.

Although **Eq. 7** looks ominous, about half the $\boldsymbol{B}_{ij}$s are zero matrices. The other half are sparse, in that they include at most two ones. The remaining terms are zeros. Furthermore, some redundancies can be exploited in the implementation. The bottom line is that **Eq. 7**, when implemented appropriately, is not exorbitantly expensive. As mentioned, the new method takes about 50% longer than the perturbation method, resulting in at most a ten percent increase in total CPU time.

Examples

Many problems work quite well with the perturbation method hourglass control, depending on the boundary conditions and material properties involved. In problems with highly anisotropic material properties or point loads that occur due to boundary conditions or contact, the perturbation method may not eliminate all hourglassing and give poor results in coarse meshes. Furthermore, hourglass parameters that are too big cause the problem to be overly stiff.

The following plate problem illustrates the penalty sensitivity that can sometimes occur. A square plate with the following material properties:

Ex = 50000 ksi,	Ey = 100 ksi,	Ez = 100 ksi
G_x = 10000 ksi,	G_x = 10000 ksi,	G_x = 10000 ksi
V_{yx} = 0.00075,	v_{zx} = 0.3,	v_{zy} = 0.3

is loaded at the center, as shown in **Fig. 1**. The hourglass parameter α from **Eq. 3** is chosen to be some percentage of the maximum Eigenvalue in the stiffness matrix. In DYNA3D and NIKE3D this amounts to the following equation for the orthotropic material models:

$$\alpha = \kappa \cdot 0.05 \cdot E_{\max} \cdot \left(\boldsymbol{B}_o\right)_{ij} \left(\boldsymbol{B}_o\right)_{ij} , \tag{8}$$

where $\boldsymbol{B}_o$ is the strain displacement matrix and κ = 0.1 by default. This value of κ proves overly stiff, and three other values for κ are tried: κ = 0.00002, 0.0002, and 0.002. The value κ = 0.1 (100/50000) = 0.0002 replaces E_{max} with E_{min} in **Eq. 8** and uses the default 0.1, which seems to work well with isotropic materials.

Two different loadings shown in **Figs. 1** and **2** are analyzed with the five different meshes (**Table 1**).

Figures 3 and **4** show results for the different meshes using the different κs, the physical stabilization method (denoted by ps) and full integration (using the incompatible modes element). For the load case in **Fig. 1**, from **Fig. 3** it is seen that the physical stabilization method converges at about the same rate as the fully integrated element. With κ = 0.0002, the perturbation method performs well, whereas with 0.00002 it is too soft, and with 0.002 it is too stiff for the mesh densities used.

Table 1. Matrix parameters.

n_z x n_x x n_y	No. of elements
1 × 6 × 6	36
3 × 6 × 6	54
3 × 13 × 13	507
6 × 26 × 26	4056
7 × 38 × 38	10108

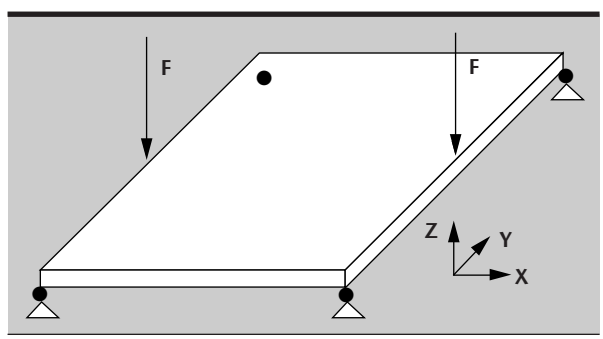

Figure 1. Loading case 1: 20-in.-x-20-in.-x-1-in. plate with 8-lb edge loads and simple supports.

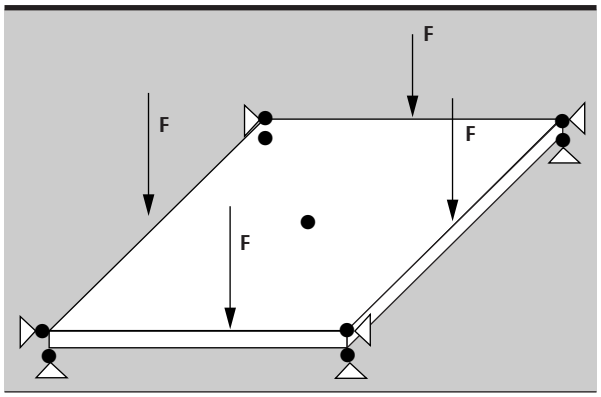

Figure 2. Loading case 2: 20-in.-x-20-in.-x-1-in. plate with 32000-lb edge loads and clamped supports.

For the load case in **Fig. 2**, we get some hourglassing for κ = 0.00002 and 0.0002, as seen in **Fig. 5**. For κ = 0.002, we get no hour glassing, but as seen in **Fig. 4**, the perturbation method gave results that were too soft. The physical stabilization method gives no hourglassing (**Fig. 6**), and again converges at the same rate as the fully integrated element.

The conclusion to be drawn from these examples is that the perturbation method does not perform well under certain types of loadings and the results are highly sensitive to the values of the stiffness parameter, κ. The new physical stabilization method is very reliable since its hourglass forces are derived from the fully integrated element.

Figure 3. Convergence plot for loading case 1.

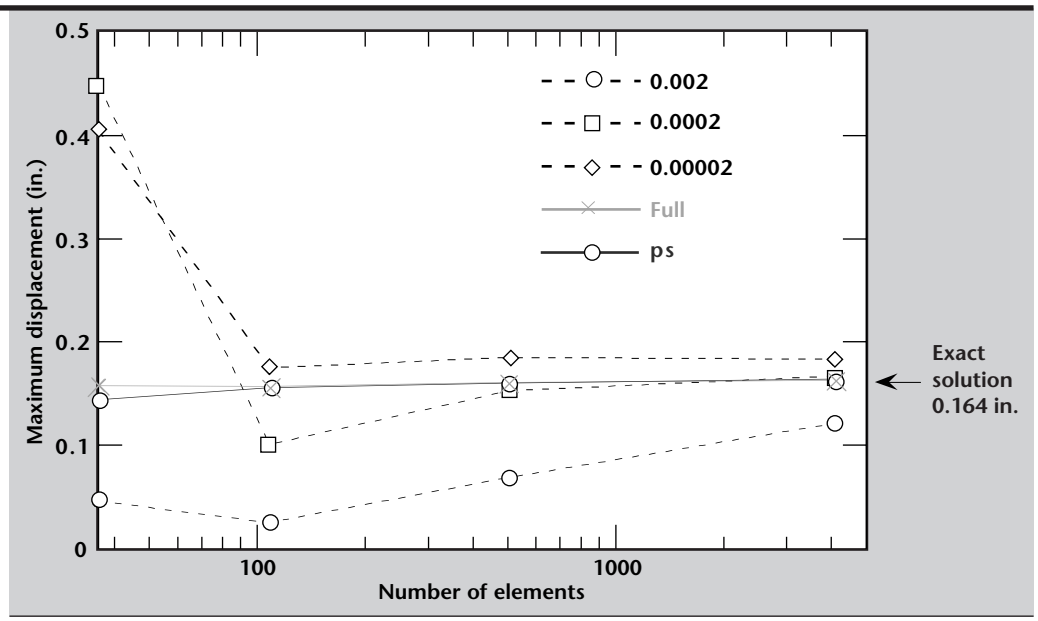

Figure 4. Convergence plot for loading case 2.

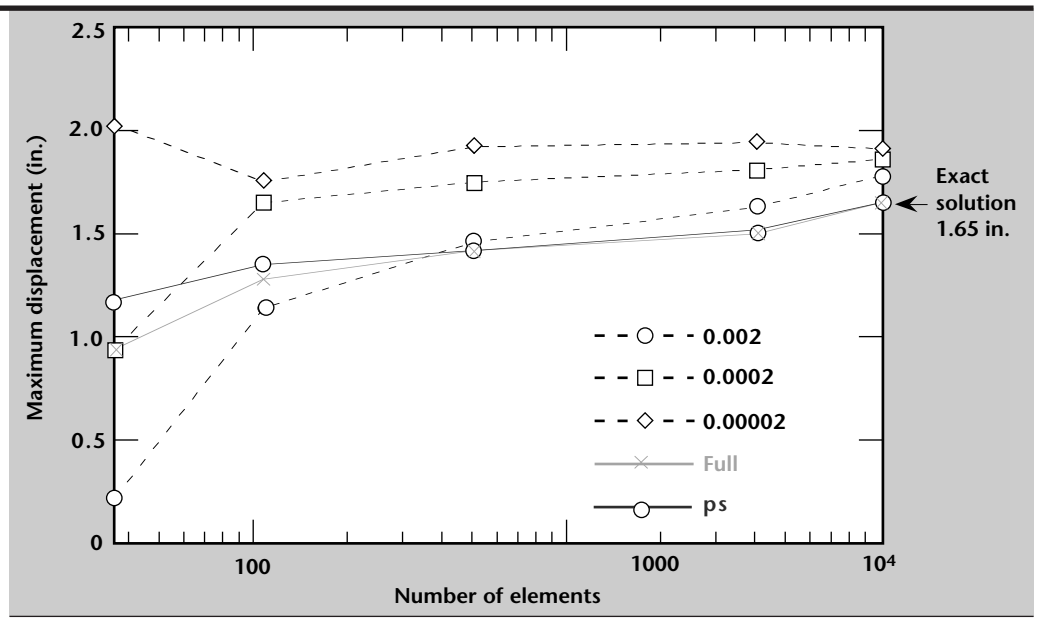

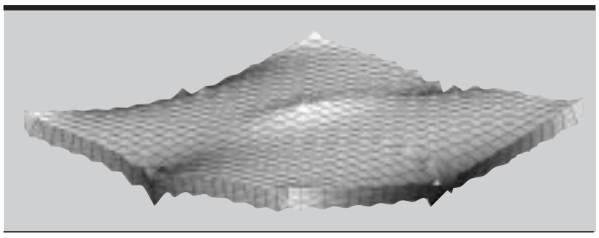

Figure 5. Loading case 2 with κ = 0.00002.

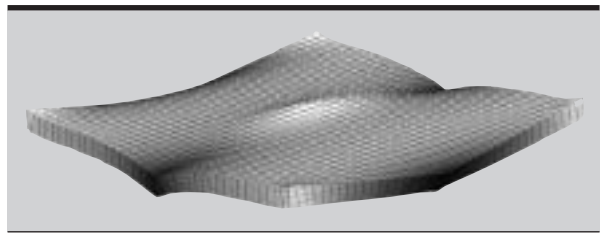

Figure 6. Loading case 2 with physical stabilization.

Future Work

The physically-stabilized element works well, particularly for elasticity. Even with plasticity, the physical stabilization method offers a consistent method, capturing plasticity in the hourglass modes. Nevertheless, with plasticity the element is either all plastic or elastic because of the single-point integration. The fully integrated element, on the other hand, can resolve the plastic front more accurately in coarse meshes. This partial plasticity could potentially be incorporated into the hourglass force calculation by monitoring the hourglass strains and modifying the hourglass stiffness appropriately.

Although the assumed strain field used in the physically-stabilized element works well for many problems, like all assumed-strain methods where some portion of the strain field is projected out, the results can sometimes be diffusive. Higher-order enhanced strain methods could be used in a physical stabilization setting to give better resolution.

References

1. Flanagan, D. T., and T. Belytschko (1981), "A Uniform Strain Hexahedron and Quadrilateral with Orthogonal Hourglass Control," *IJNME*, **17**.

2. Liu, W. K., J. S. Ong, and R. A. Uras (1985) "Finite Element Stabilzation Matrices—A Unification Approach," *CMAME*, **53**.

3. Belyschko, T., and L. P. Bindeman (1993), "Assumed Strain Stabilization of the Eight-Node Hexadral Element," *CMAME*, **105**.

4. Crisfield, M. A., and G. F. Moita (1996), "A Co-Rotational Formulation for 2-D Continua Including Incompatible Modes," *IJNME*, **39**.

5. Zhu, Y. Y., and Cescotto, S. (1996), "Unified and Mixed Formulation of the Eight-Node Hexahedral Elements by Assumed Strain Method," *CMAME*, **129**.

Cyclic Viscoplastic Constitutive Model

Phani Kumar V. V. Nukala
New Technologies Engineering Division
Mechanical Engineering

We have implemented a cyclic viscoplastic constitutive model that includes material memory effects into NIKE3D. The constitutive model is based on multi-component forms of kinematic and isotropic hardening variables in conjunction with von Mises yield criteria. In addition, a memory surface (non-hardening surface) is used to capture the strain-range-dependent material memory effects. This work addresses the issues involved in the complete algorithmic treatment of the rate-dependent constitutive model for any desired stress- or strain-constrained configuration subspace. That is, beam, shell, plane stress, plane strain and other stress- and strain-based kinematic constraints can be handled within a single framework. The constitutive model is capable of representing the cyclic hardening and softening behavior, transient and stabilized hysteresis behavior, and the non-fading memory effects of the material.

Introduction

The life prediction of structures and structural components subjected to complex loading histories, which include repeated loading and unloading, requires an accurate representation of the material behavior. Typically, at the very least, this includes an accurate representation of monotonic and cyclic hardening and softening behavior, transient and stabilized hysteresis behavior, and the non-fading memory effects of the material. However, the material models that are currently available in NIKE3D do not have the capability to represent the above-mentioned material behavior.

Furthermore, the implementation of many of these material models into NIKE3D is intrinsically linked to the element technology. That is, the same material model is implemented separately for elements such as bricks, shells, and beams. This inconvenience is quite apparent when the user is forced to use a certain type of element not because of the geometry and loading conditions of the problem, but because of the availability of the required material model to that certain element type.

In this work, a unified cyclic viscoplastic constitutive model along with the multi-component forms of nonlinear kinematic and isotropic hardening rules, is implemented for an accurate prediction of the complex cyclic structural response.[1–3]

Armstrong-Frederick type rules are used to describe the nonlinear evolution of each of the multi-component kinematic hardening variables. A saturation type (exponential) rule is used to describe the evolution of each of the isotropic hardening variables. The concept of memory surface is used to describe the strain-range-dependent material memory effects that are induced by the prior strain histories.[1,4]

In addition, the algorithmic treatment of the above constitutive model is such that it allows a single implementation for any desired stress- or strain-constrained subspace. Hence, the cyclic viscoplastic model can be used with any of the elements currently available in NIKE3D.

Progress

A cyclic viscoplastic constitutive model that includes material memory effects has been implemented into NIKE3D. In the following, a brief description of the constitutive model is presented in the standard generalized materials framework.[1–3,5] For the sake of simplicity of notation in the constrained subspaces (such as plane stress, and beam and shell kinematics), we represent the tensorial variables in terms of their corresponding matrix and vector forms.

In the standard generalized materials framework, the cyclic viscoplastic constitutive equations are expressed as:

- additive decomposition of total strain, ε, into elastic (ε^e) and plastic (ε^p) parts:

$$\varepsilon = \varepsilon^e + \varepsilon^p \tag{1}$$

- state laws based on the form of Helmholtz energy Ψ:

$$\sigma = \frac{\partial \Psi}{\partial \varepsilon^e} = C : \varepsilon^e \tag{2}$$

$$X_i = \frac{\partial \Psi}{\partial \alpha_i} = \frac{2}{3} C_i R : \alpha_i \tag{3}$$

$$R_i = \frac{\partial \Psi}{\partial r_i} = b_i Q_i r_i \tag{4}$$

- evolution laws of internal variables (based on plastic flow potential):

$$\dot{\varepsilon}^p = \dot{\lambda} P \eta \tag{5}$$

$$\dot{\alpha}_i = \dot{\lambda} P \left(\eta - \frac{2}{3} \kappa a_i X_i \right) \tag{6}$$

$$\dot{r}_i = \frac{2}{3} \kappa \dot{\lambda} \left(1 - \frac{R_1}{Q_i} \right) \tag{7}$$

- yield function $f(\sigma, X, R)$:

$$f = \frac{1}{2} \eta^T P \eta - \frac{1}{3} \kappa^2 \leq 0 \ , \tag{8}$$

where

$$\eta = \left(\sigma - X \right) \tag{9}$$

$$\kappa = \sigma_0 + R \tag{10}$$

$$X = \sum_i X_i$$

$$R = \sum_i R_i$$

- loading/unloading and consistency conditions (rate-independent plasticity):

$$f \leq 0; \ \dot{\lambda} \geq 0; \ \dot{\lambda} f \equiv 0; \ \dot{\lambda} \dot{f} = 0 \tag{11}$$

- viscoplasticity (Perzyna rule):

$$\dot{\lambda} = \left\langle \frac{f}{K} \right\rangle^n \ , \tag{12}$$

where C denotes the elastic constitutive matrix in the constrained subspace, α_i denotes the vector form of the tensor variable associated with the kinematic hardening, and r_i denotes a scalar variable associated with the isotropic hardening.

In addition, σ represents the Cauchy stress tensor and X_i and R_i represent the thermodynamic forces associated with α_i and r_i, respectively. The mapping, P, maps the symmetric rank-two stress tensors in the constrained-stress subspace onto symmetric rank-two strain tensors in the deviatoric subspace.

In the following, a non-hardening memory surface is introduced to model the non-fading memory effects of the material.

Let g represent the memory surface, defined as

$$g = \left(\frac{2}{3} \zeta^T R \zeta \right) - q^2 = 0 \ , \tag{13}$$

where the reduced plastic strain, ζ, is defined as $\zeta = \varepsilon^p - \beta$. The evolution of the memory surface is defined through the following relations:

$$\dot{\beta} = \dot{\mu} \zeta \tag{14}$$

$$\dot{q} = \left(\frac{2}{3} \dot{\beta}^T R \dot{\beta} \right)^{\frac{1}{2}} = \dot{\mu} \left(\frac{2}{3} \zeta^T R \zeta \right)^{\frac{1}{2}} = \dot{\mu} \bar{g} \ . \tag{15}$$

The Kuhn-Tucker optimality conditions along with the consistency requirement can be stated as

$$g \leq 0; \ \dot{\mu} \geq 0; \ \dot{\mu} g \equiv 0; \ \dot{\mu} \dot{g} = 0 \ . \tag{16}$$

The main difference between the rate-dependent and rate-independent cases is in the evaluation of the plastic multiplier, $\dot{\lambda}$. The other conceptual difference is that, in the case of rate-independent plasticity, $f \leq 0$, whereas in the case of viscoplasticity, $f > 0$. However, the numerical treatment for rate-independent and rate-dependent cases is similar.[5,6]

A generalized midpoint algorithm is used to integrate the rate-constitutive equations. Furthermore, the consistent tangent operator is obtained through an exact linearization of the return mapping algorithm.[5]

Numerical Examples

The return mapping algorithm and the corresponding consistent tangent operator are implemented into NIKE3D.[7] In the following, several

numerical examples representing the cyclic hardening and softening behavior, transient hysteresis loops, the non-fading memory effects and rate-dependent effects of the material are presented. These examples demonstrate the accuracy and robustness of the present algorithmic framework.

Uniaxial Stress Response for Aluminum Alloy AA6060: Multiple-Step Test. In the following, numerical simulation of a multiple-step test[8] with eight steps of increasing strain amplitude is performed. This example demonstrates plastic strain-range-dependent hardening (memory) effects on the cyclic stress response. Ten cycles are performed during each step. The material model consists of two independent kinematic hardening variables and two independent isotropic hardening variables. Memory effects include both plastic strain-range-dependent isotropic and kinematic hardening variables. The material parameters for aluminum alloy AA6060 (temper T4) are given in **Table 1**.

Figures 1a and **1b** show the stress response and the hysteresis loops obtained for the multiple-step test during increasing and decreasing strain

Table 1. Material parameters for aluminum alloy AA6060.

E	=	66240 MPa	ν	=	0.3	σ	=	42 MPa			
Q_{x1}	=	28 MPa	D_{M1}	=	800	D_{01}	=	4800	δ_1	=	400
Q_{x2}	=	38 MPa	D_{M2}	=	12	D_{02}	=	72	δ_2	=	400
b_1	=	25	Q_{M1}	=	75 MPa	Q_{01}	=	22.5 MPa	ω_1	=	80
b_2	=	0.5	Q_{M1}	=	65 MPa	Q_{02}	=	19.5 MPa	ω_2	=	80

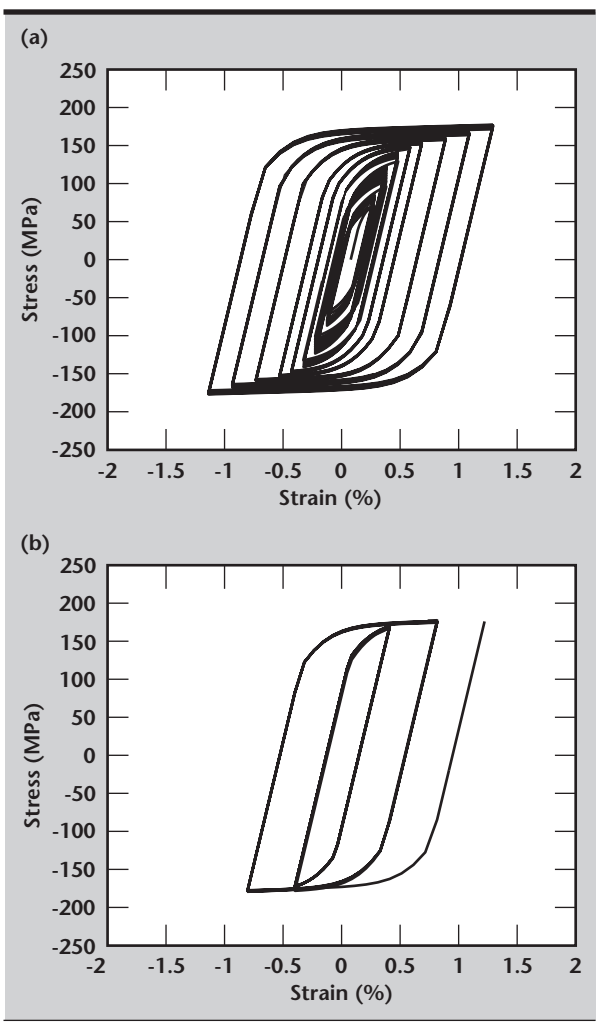

Figure 1. Symmetric multiple step test: (a) increasing strain amplitudes; (b) decreasing strain amplitudes.

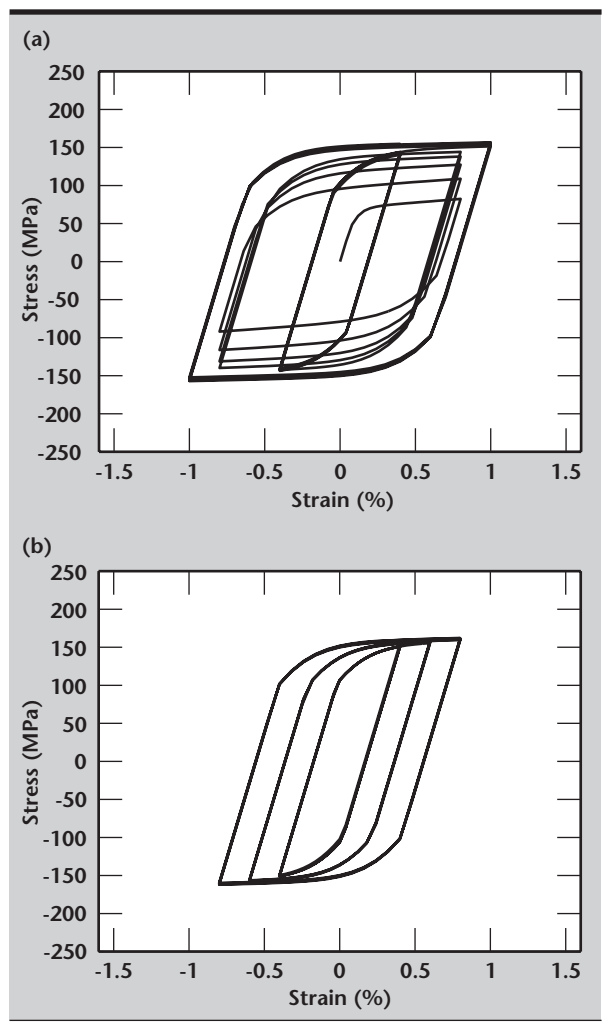

Figure 2. Variable amplitude test: (a) type 1; (b) type 2.

amplitudes, respectively. From the numerical simulation response, it should be noted that cyclic hardening occurs not only during the progressive cycles within a step but also during the increase in step (plastic strain range) size.

Uniaxial Stress Response for Aluminum Alloy AA6060: Variable Amplitude Test. This test[8] demonstrates the influence of increasing and decreasing strain amplitudes on the cyclic stress response. The first test is conducted in three steps with strain amplitudes 0.8, 0.4 and 1.0%. In the second test, three steps with strain amplitudes 0.4, 0.6 and 0.8% are used. Five cycles are performed during each step. The material parameters used in the numerical simulation are identical to those used in the multiple-step test. The stress response

Table 2. Material parameters for rate-dependent effects.

E	=	185000 MPa	v	=	0.3	σ_0	=	82 MPa
K	=	151 MPa	n	=	24			
D_1	=	4200	Q_{x1}	=	38.667 MPa			
D_2	=	37.5	Q_{x2}	=	180 MPa			
b_1	=	8	Q_1	=	60 MPa			

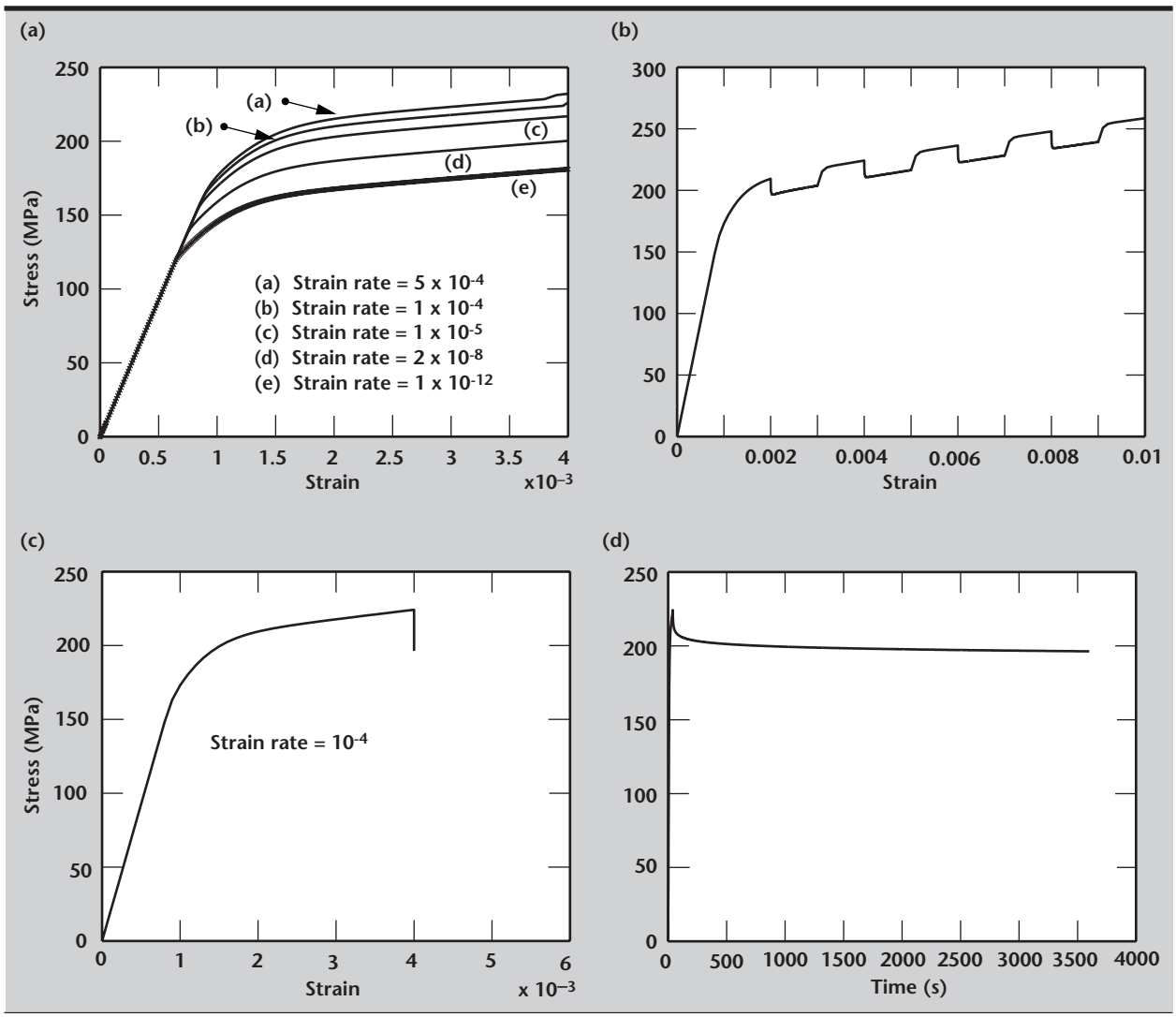

Figure 3. Uniaxial tensile stress-strain behavior: (a) effect of strain rate; (b) effect of strain rate jumps; (c) harding-relaxation stress-strain curve; (d) harding-relaxation stress versus time.

obtained for the first and second tests are shown in **Figs. 2a** and **2b**, respectively. For both sequences of variable strain amplitudes, the stress response obtained from the numerical simulations is in good agreement with the physical behavior of the material.

Rate-Dependent Effects. In the following, the effect of strain rate on the stress response is illustrated through three examples. The material model consists of two independent kinematic hardening variables and an isotropic hardening variable to describe the material behavior. A power law is used to describe the rate-dependent effects. The material parameters used for the problems concerning rate-dependent effects are given in **Table 2**.

Figure 3a shows the effect of strain rate on the monotonic tensile behavior of 316L stainless steel. The influence of change in rate of strain during the test on the monotonic stress-strain curve is shown in **Fig. 3b**. From **Fig. 3b**, it can be seen clearly that a change in the rate of strain during the test results in an immediate change in the stress-strain curve, and tends to rejoin the monotonic stress-strain curve corresponding to the new strain rate. **Figures 3c** and **3d** represent the numerical simulation of hardening-relaxation behavior of the material.

Future Work

Modeling of ratcheting effect, static recovery effects, and the effect of temperature on the material behavior is the scope of the future work. Formulation and a complete algorithmic treatment of the above cyclic viscoplastic constitutive model in the finite strain hyper-elastic-plastic constitutive framework are also planned.

References

1. Lemaitre, J., and J. L. Chaboche (1990), *Mechanics of Solid Materials*, Cambridge University Press, Cambridge, UK.

2. Chaboche, J. L. (1989), "Constitutive equations for cyclic plasticity and cyclic viscoplasticity," *International Journal of Plasticity*, **5**, pp. 247–302.

3. Ohno, N. (1990), "Recent topics in constitutive modeling of cyclic plasticity and viscoplasticity," *Applied Mechanics Review*, **43**, p. 283.

4. Ohno, N. (1982), "A constitutive model of cyclic plasticity with a non-hardening strain region," *Journal of Applied Mechanics*, **49**, p. 721.

5. Nukala, P. K. V. V., "A Cyclic Viscoplastic Constitutive Model," submitted to *Computer Methods in Applied Mechanics and Engineering.*

6. Simo, J. C., and S. Govindjee (1991), "Non-linear B-stability and symmetry preserving return mapping algorithms for plasticity and viscoplasticity," *International Journal of Numerical Methods in Engineering*, **31**, pp. 151–176.

7. Maker, B. N. (1995), "NIKE3D: A nonlinear implicit three-dimensional finite element code for solid and structural mechanics," Lawrence Livermore National Laboratory, Livermore, California (UCRL-MA-105268, Rev. 1).

8. Langseth, M., O. S. Hopperstad, and S. Remseth (1995), "Cyclic stress-strain behavior of alloy AA6060, Part I: Uniaxial experiments and modeling," *International Journal of Plasticity*, **11**, pp. 725–739.

Electromagnetic Cold-Test Characterization of the Quad-Driven Stripline Kicker

Scott D. Nelson and James E. Dunlap
Defense Sciences Engineering Division
Electronics Engineering

The first kicker concept design for beam deflection was constructed to allow stripline plates to be driven—thus directing, or kicking, the electron beam into two subsequent beamlines. This quad-driven stripline kicker is an eight-port electromagnetic network consisting of two actively driven plates and two terminated plates. Electromagnetic measurements performed on the bi-kicker and quad-kicker were designed to determine: 1) the quality of the fabrication of the kicker, including component alignments; 2) quantification of the input feed transition regions from the input coax to the driven kicker plates; 3) identification of properties of the kicker itself without involving the effects of the electron beam; 4) coupling between a line current source and the plates of the kicker; and 5) effects on the driven current to simulate an electron beam through the body of the kicker. Included are the angular variations inside the kicker to examine modal distributions. The goal of the simulated beam was to allow curved path and changing radius studies to be performed electromagnetically. The cold-test results were then incorporated into beam models.

Introduction

The original kicker design[1-3] was conceived to allow for the diversion of the electron beam dynamically during a long pulse, thus acting like a beam-splitter (**Figs. 1 and 2**). Experiments performed on the kicker[4] detail the operating parameters of the system. This report outlines the electromagnetic cold-test measurements performed on the kicker as part of the analysis, and concepts for the kicker pulser requirements.

Due to beamline use and the motivations for the cold-test measurements, the kicker was tested in the Lawrence Livermore National Laboratory (LLNL) Electromagnetics Laboratory using a variety of vector network analyzers to sweep the frequency band, and time-domain impulse generators and scopes.

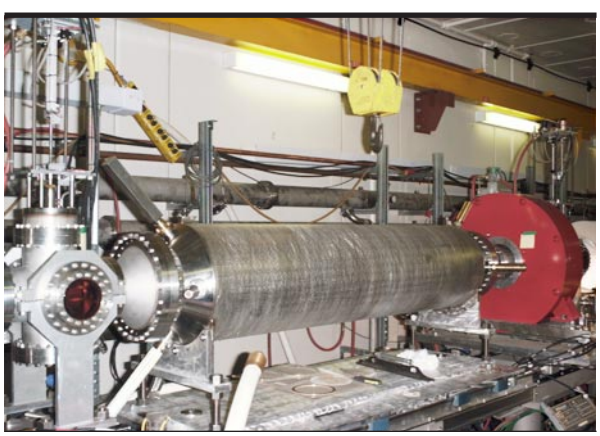

Figure 1. The quad-kicker in the Experimental Test Accelerator beamline as part of the verification experiments. Note the four ports on each end, which connect directly to the deflection plates. Two of the white pulser cables are visible in the foreground.

Figure 2. The quad-kicker, tested using frequency- and time-domain scopes to cover the band for the swept frequency tests and instantaneous impulse tests.

Progress

Kicker Port Testing

Each of the eight input ports of the kicker was tested over a frequency band from 45 to 500 MHz. Two ports connected to the input and output of each of the four plates through a tapered transition region, through a coaxial connector (**Fig. 3**). The pin on the plate connected directly to the center pin of the coax. The results of the measurements, shown in **Fig. 4**, indicate a broadband match, with the exception of resonances caused by the feed regions. The comparison in **Fig. 5** illustrates the feed region effects based on experience from the bi-kicker and quad-kicker development activities. **Figure 6** shows the complex input impedance of the kicker for one of the ports.

Cross-Coupling Terms

The cross-plate coupling terms of the kicker corresponded to the coupling between adjacent and opposite ends of the various plates to each other. These terms represent energy that couples from the kicker pulser-driven plate to those plates that are terminated, thus inducing fields onto plates that are not directly driven. These cross-coupling terms are appreciable (8% and 20%) even at the lower frequencies. **Figure 7** shows the magnitude of the coupling between adjacent plates vs frequency. **Figure 8** is a photograph of the quad-kicker plates.

Figure 3. Photograph showing four striplines of the kicker, each forming impedance-matched transmission lines. The center pin that connects to the coaxial cable is visible at the end of each plate. The configuration at the other end is identical.

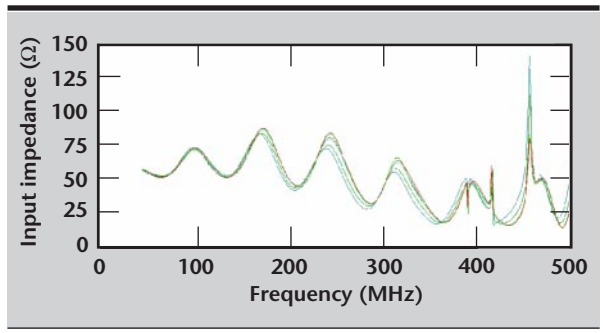

Figure 4. Input impedance of each of the ports shown vs frequency (margin of error ±0.3 Ω). The spikes at 388.75, 414.0, and 460 MHz are higher-order mode resonances and correspond to Qs of 310 (quadrupole mode), 61 (dipole mode), and 29 (dipole mode), respectively.

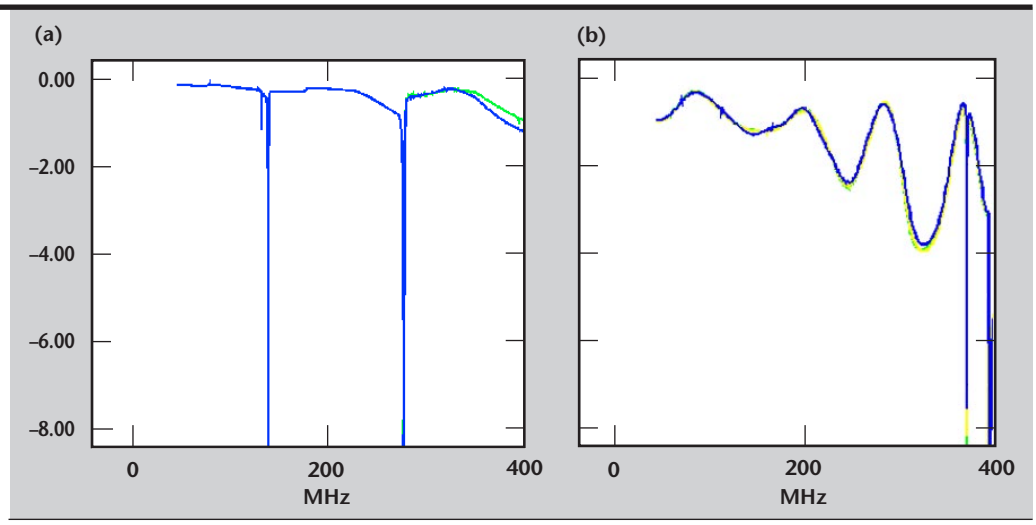

Figure 5. Kicker port testing. The input reflection coefficient vs frequency of the bi-kicker (a) was much more uniform due to the more gradual transition region after the coaxial feeds. The quad-kicker (b) had a more abrupt transition after the coax and has a larger input reflection coefficient. The spikes in the bi-kicker response curve are due to the grounded plate resonances and were eliminated in the quad-kicker.

Forward-Coupling Terms

The kicker pulsers drive one end of the plates and the other end is mated to reduce reflections on the plate structure. The loss along the plates is less than 1 dB. The transfer function from one end of the plate to the other is shown in **Fig. 9**.

Kicker Response

For identification of the transient properties of the kicker and the association between a simulated beam and the kicker ports, a ramp pulse (0.95 V/300 ns) was used to excite the wire current. The resulting waveform that was induced on the downstream output port is shown in **Fig. 10**.

When the central wire representing an electron beam was excited through the main body of the kicker, the "pump-up" time of the kicker was observed as an equivalent time constant of 70 ns. This corresponds to the cavity fill time between the simulated beam pulse and the ports.

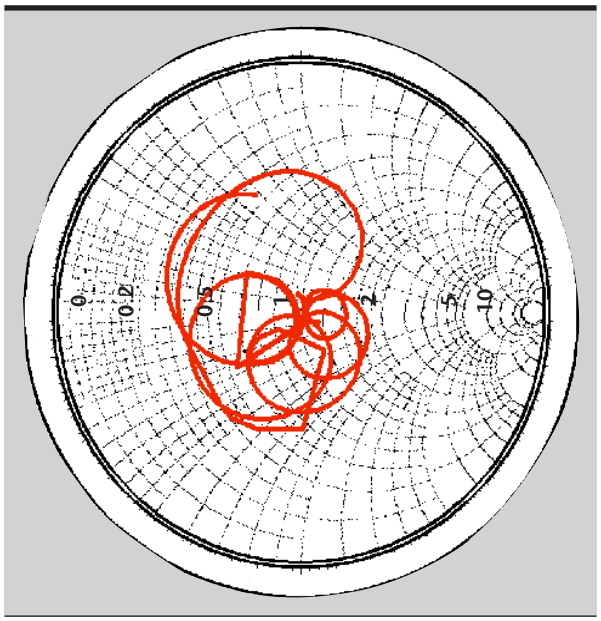

Figure 6. Complex input impedance of the kicker for one of the ports (the variance between the ports is ±7 Ω due to fabrication differences). The three straight lines in the curve represent under-sampling.

Azimuthal Variations

During the course of the measurements, the azimuthal variation caused by the offset-rotations of the current wire was measured and compared against the theoretical solution for an offset wire in an ideal kicker. A comparison between the theoretical solution (dashed line) for an electrostatic coupling case and that for the experimental cases at the peak coupling points of 68.4, 139.2, and 209.4 MHz is shown in **Fig. 11**. The angular frequency spectrum of the plots was taken to determine the relationships between the various modes (dipole, quadrupole, and sextupole) in the kicker. The modal ratios are shown in **Table 1**.

The ratios are in a range similar to that determined by integrating the simple analytic representation[5] along the plate boundaries shown in **Eq. 1**.

$$\frac{V_s}{V_D} = \frac{4q\dfrac{a^3}{b^4}\displaystyle\int_{-\phi}^{\phi}\cos 3\theta d\theta}{4q\dfrac{a}{b^2}\displaystyle\int_{-\phi}^{\phi}\cos\theta d\theta} = \frac{1}{3}\frac{a^2}{b^2}\frac{\sin 3\phi}{\sin\phi};$$

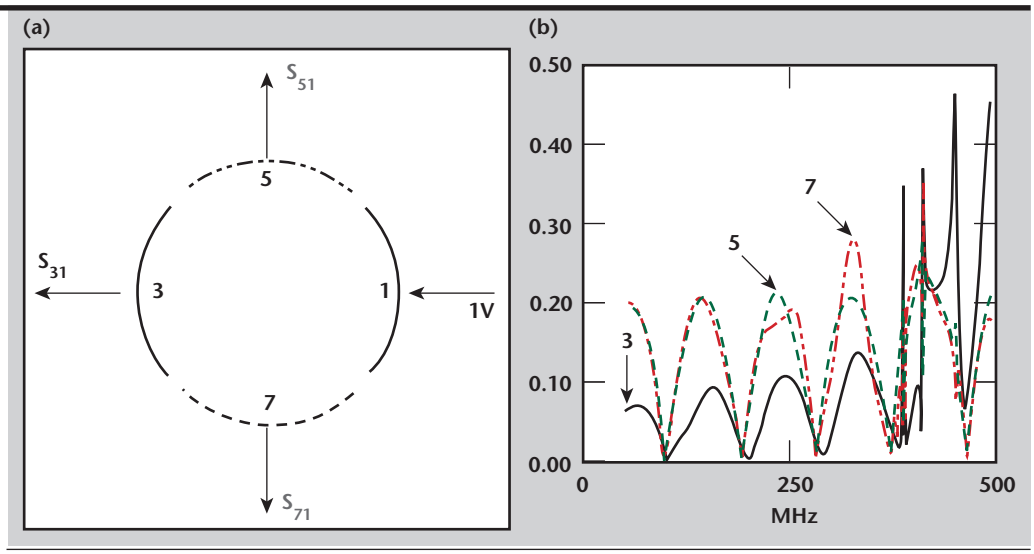

Figure 7. Magnitude of coupling between adjacent plates vs frequency, showing significant cross-coupling at multiples of 80 MHz. The adjacent plate coupling is 20%; the cross plate coupling is 8%.

$$\frac{V_Q}{V_D} = \frac{1}{2}\frac{a}{b}\frac{\sin 2\phi}{\sin \phi} \qquad (1)$$

where ϕ is the plate half-angle (39°), but 45° was used, to be consistent with the theory, since **Eq. 1** assumes no gaps, b is the plate radius (12.87 cm), and a is the radius to the wire position (3.175 cm). Differences can be attributed to gap effects between plates, end effects near the feeds, and simplifications of the analytic representation.

Conclusions

Although the frequency range of interest for kicker applications is in the low hundreds of megahertz and is based on the bandwidth of the kicker pulser, there were initial concerns about

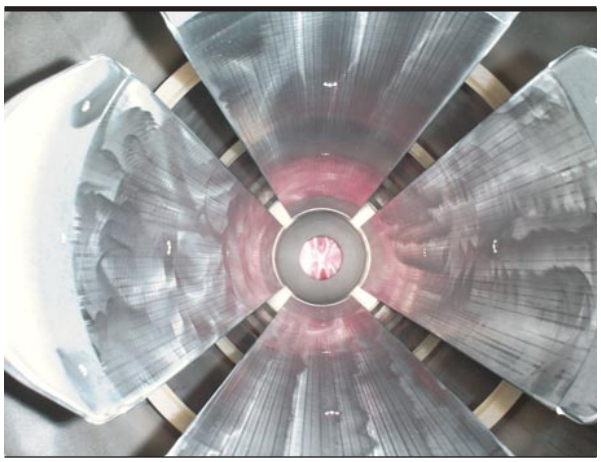

Figure 8. Identical quad-kicker plates connected to a 50-Ω coaxial port. For experiments using the existing kicker pulsers, two of the plates were driven and two were terminated in matched loads. Each plate is 78° wide (12.87 cm radius) and is supported by rexolite.

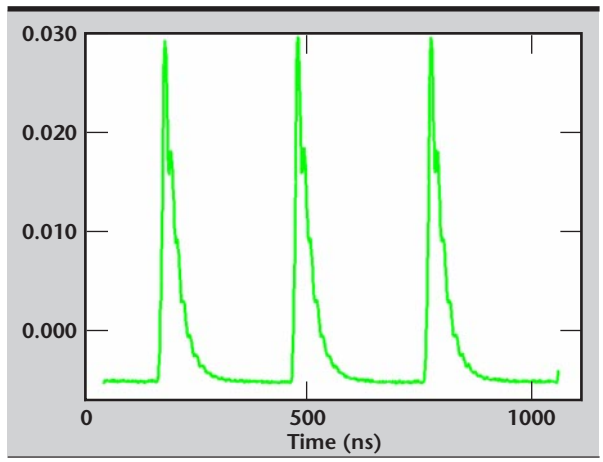

Figure 10. Effect of the 300-ns ramp pulse coupling from the wire current to one of the kicker plates monitored at a downstream port. Notice that after about 70 ns, the coupling stabilizes to -0.005 V (-0.53%). The spikes occur at the transition of each 300-ns excitation ramp waveform.

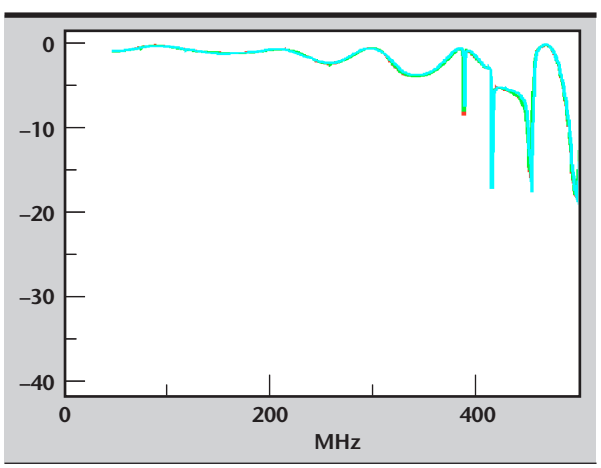

Figure 9. Transfer function vs frequency from one end of the plates to the other. In the low frequency part of the spectrum, the curves for the various plates overlap to within 0.025 dB.

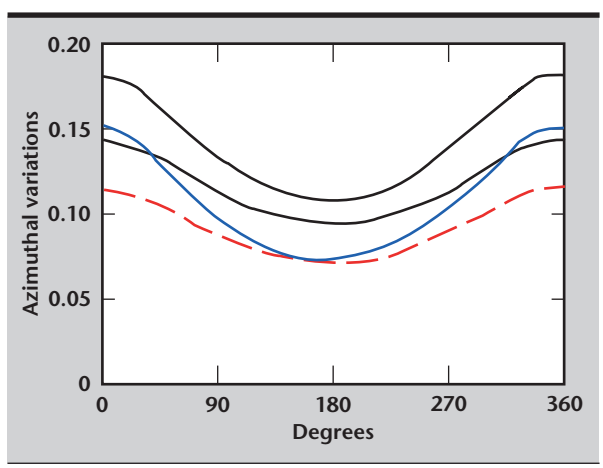

Figure 11. Comparison between theoretical coupling curve (dashed) based on electrostatic modeling of an ideal kicker structure and experimental data.

Table 1. Angular frequency spectrum.

	Static	68.4	139.2	209.4	Eq. 1
V_Q/V_D	0.136	0.134	0.140	0.169	0.174
V_S/V_D	0.0252	0.0315	0.0327	0.0351	0.0203

beam-induced effects. For this frequency range: the cross-coupling between adjacent ports is <14 dB; the input impedance for each port is between 50 and 90 Ω; transmission along the plates experiences less than 1 dB of loss; cavity measurements show a cavity pump-up time, and a dI/dt coupling between the current wire and the cavity.

The input reflection coefficient for some higher frequencies can approach 30%; but these frequencies are expected to be outside of the normal operating range of the kicker. However, in making the modifications from the bi-kicker design to the quad-kicker design, the frequency band where these effects make a pronounced difference was lowered and is closer to the operating band. Thus, subsequent changes in the kicker design would need to be made with this limit in mind. It should be emphasized however that the elimination of the shorted plates from the bi-kicker design substantially improved the operation of the quad-kicker.[4]

Acknowledgments

Thanks to B. Poole for numerous conversations about kicker development and to J. Chen and J. Weir for their experimental activities.

References

1. Caporaso, G. J., Y. J. Chen, and B. R. Poole (1997), "Transmission Line Analysis of Beam Deflection in a BPM Stripline Kicker," *1997 Particle Accelerator Conference*, Vancouver, B.C., Canada, May, Lawrence Livermore National Laboratory, Livermore, California (UCRL-JC-126073).

2. Nelson, S. D. (1998), "Electromagnetic (Cold Test) Characterization of the Bi-Driven Kicker," Lawrence Livermore National Laboratory, Livermore, California (UCRL-ID-129997), January, http://www-dsed.llnl.gov/documents/em/sdnkick98/.

3. Poole, B. R., G. J. Caporaso, and Y. J. Chen (1998), "Analysis and Modeling of a Stripline Beam Kicker and Septum," *1998 Linear Induction Accelerator Conference*, Chicago, Illinois, August 24-28.

4. Chen, Y. J., G. J. Caporaso, and J. Weir (1998), "Experimental Results of the Active Deflection of a Beam from a Kicker System," *1998 Linear Induction Accelerator Conference*, Chicago, Illinois, August 24-28.

5. Chao, A. W. (1993), "Physics of Collective Beam Instabilities in High Energy Physics," John Wiley and Sons, New York, New York, p. 6.

Photonic Doppler Velocimetry

Paul D. Sargis, Nicole E. Molau, and Daren Sweider
Defense Sciences Engineering Division
Electronics Engineering

We are developing a novel fiber-optic approach to laser Doppler velocimetry as a diagnostic for high-explosives tests. Using hardware that was originally developed for the telecommunications industry, we are able to measure surface velocities ranging from centimeters per second to kilometers per second. Laboratory measurements and field trials have shown excellent agreement with other diagnostics.

Introduction

Laser Doppler velocimetry is a powerful diagnostic for the high-explosives physics community. The frequency of the Doppler-shifted light provides a direct measure of the instantaneous velocity of a rapidly moving target illuminated by a laser. Light from a multi-mode optical fiber illuminates the target and another multi-mode fiber collects the Doppler-shifted light, allowing spatially-resolved velocimetry information to be obtained.

Currently, physicists perform surface velocity measurements using a technique called Fabry-Perot Velocimetry. This system uses free-space Fabry-Perot interferometers and streak cameras for each data channel. These components are costly, complex, require maintenance and operator set-up, require a custom-built optical table and occupy a considerable volume. The Fabry-Perot system also uses a large YAG laser whose output is doubled to 532 nm because the streak camera photocathode is insensitive in the infrared region of the spectrum. Although the Fabry-Perot velocimeter yields excellent data, overall channel count will always remain low due to its size, cost, and complexity. As new NTS high-explosives facilities become available to experimenters, it will be highly desirable to have many velocimetry data channels available without the cost, complexity, and manpower-intensive set-up required for the current diagnostic system.

Our technique uses multi-mode fiber optics, an optical PIN detector, RF electronics, and moderate sample-rate A/D converter technology. All of the components fit into a small chassis. The advantage of using multi-mode fiber is the significant increase in optical light collection from the target, compared to that from a single-mode fiber. This advance in laser Doppler velocimetry will enable the fielding of significantly more data channels, greatly improving the spatial-temporal information obtained from this diagnostic at reduced cost, complexity, and experimental footprint.

A simplified version of this diagnostic will permit nanosecond-resolution shock arrival-time measurements by detecting the first incidence of Doppler-shifted light. Such a diagnostic will be very useful on high-fidelity flight tests in the weapons program at Lawrence Livermore National Laboratory (LLNL). Future versions of this diagnostic could be made sufficiently compact and rugged to be practical for the flight test application.

Figure 1 illustrates the basics of the photonic Doppler velocimetry system. A laser-generated optical carrier propagates through a multi-mode fiber to a probe lens. The probe illuminates the target with the optical carrier. As the target moves towards the lens, the reflected light is Doppler-shifted. The probe lens collects a portion of the Doppler-shifted light, and the light propagates back through the multi-mode fiber. The Doppler-shifted light is mixed with a fraction of the original optical carrier in a fiber-optic coupler and is detected by a “square-law” optical detector. Under the appropriate polarization and modal conditions, the square-law detector generates an electrical current proportional to the square of the optical fields. For the Doppler-shifted light, this corresponds to a beat frequency proportional to the instantaneous velocity of the target.

At high velocities, the beat frequency is too high to record directly on a transient digitizer. To overcome this limitation, we use a microwave phase discriminator to measure the frequency-dependent phase shift induced by the Doppler signal. Recording of the phase discriminator data is accomplished using a digitizer having a modest sampling rate.

Progress

In the past year, our efforts have focused on laboratory experiments and field trials.

The target for our first refereed test was a shock-driven copper foil, with the Fabry-Perot velocimeter acting as the referee. As illustrated in **Fig. 2**, the copper foil was in close proximity to a bridge wire, which was driven by a capacitive discharge unit (CDU). Green light from a frequency-doubled YAG laser was focused onto the copper target through a probe lens. The Doppler-shifted light was reflected back through the probe lens and was simultaneously processed by both the Fabry-Perot velocimeter and the photonic Doppler velocimeter.

The raw transient digitizer data from the photonic Doppler system is plotted in **Fig. 3a**, and the raw streak camera data from the Fabry-Perot system is shown in **Fig. 3b**. The Doppler beat frequency signal in **Fig. 3a** was converted into frequency versus time,

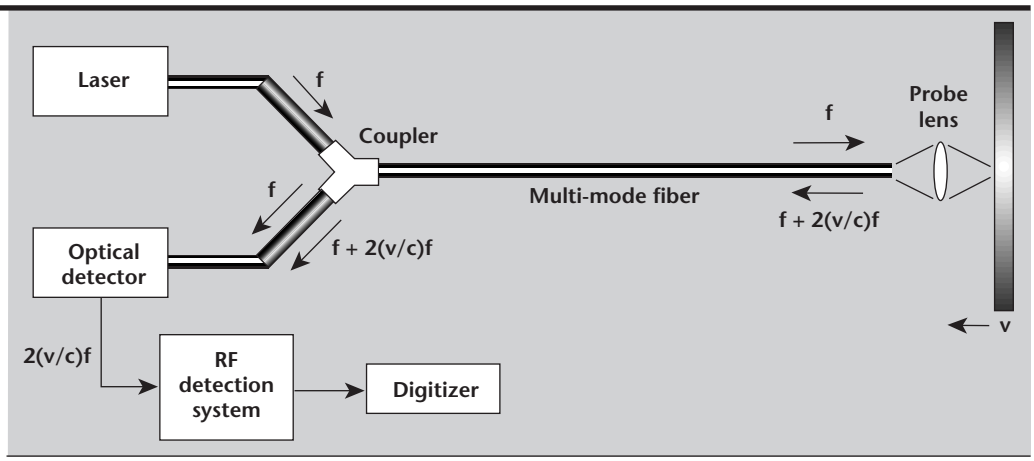

Figure 1. Basic block diagram of the photonic Doppler velocimetry system.

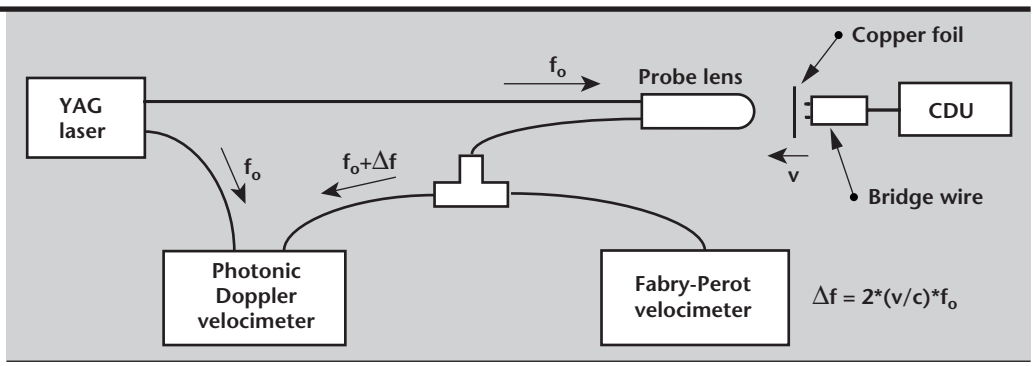

Figure 2. Block diagram of the copper foil velocity experiment.

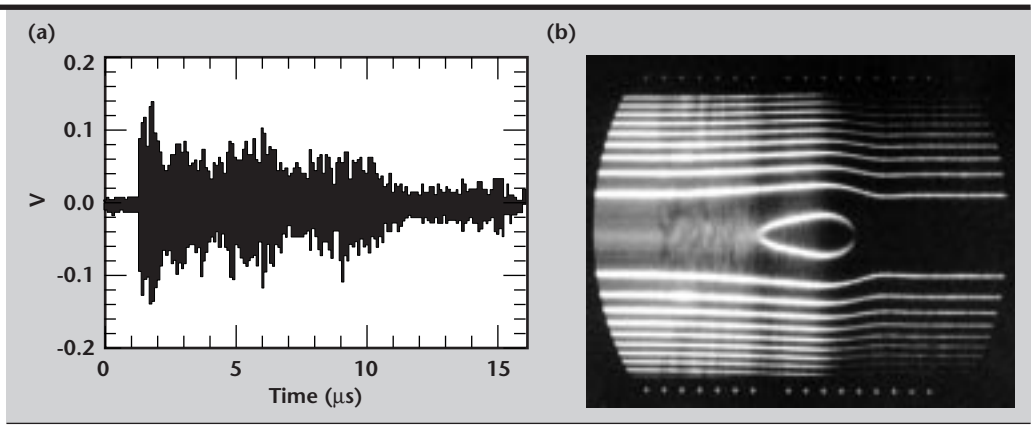

Figure 3. Raw data from the copper foil experiment: a) photonic Doppler velocimeter; b) Fabry-Perot velocimeter.

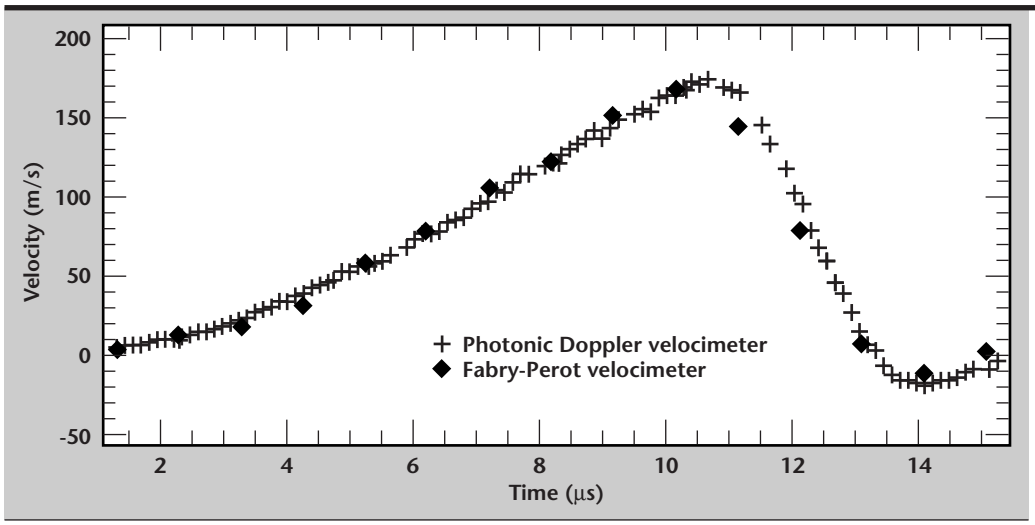

Figure 4. Processed data from the copper foil experiment.

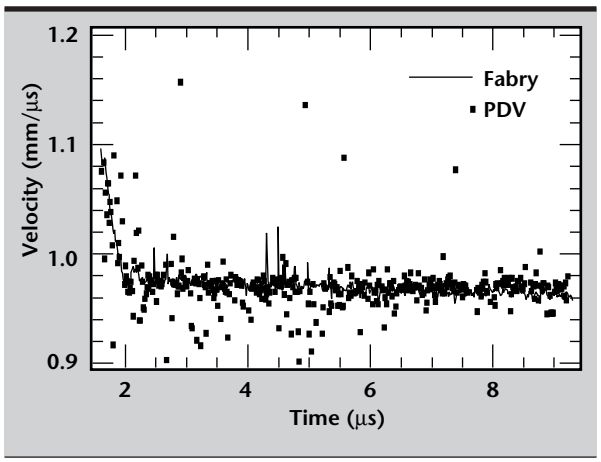

Figure 5. Processed data from the Site 300 aluminum plate experiment.

and then into velocity versus time, as shown in **Fig. 4**. Velocity values were hand-digitized from the Fabry-Perot data and then plotted on the same graph in **Fig. 4**. The negative velocity at the end of the data record is consistent with the rebounding of the copper foil after the shock event.

In a later experiment conducted at LLNL's Site 300, the copper foil target was replaced with an aluminum plate that was driven by high explosives. The remainder of the experimental set-up was the same as that illustrated in **Fig. 2**. This time, however, the Doppler beat frequency was too high to be recorded directly on a transient digitizer. We used a microwave phase discriminator to measure the frequency-dependent phase shift of the incoming signal. The processed result is plotted with the Fabry-Perot result in **Fig. 5**.

We also conducted a series of measurements in the laboratory using a continuously moving target, which consisted of a speaker driven by an audio oscillator. This set-up provided the framework for evaluating system stability and reliability. We discovered that the signal-to-noise ratio varies with time and is adversely affected by physically moving the multi-mode fiber. The likely causes of this phenomenon include: instability of the optical state on the polarization optical detector, mode selective loss, and de-phasing of the optical signals caused by the surface reflection and optical fiber propagation.

Future Work

We plan to conduct further research into system stability and reliability issues, including making detailed measurements of the changes induced in the optical polarization state, the mode populations, and their relative phases by the moving surface and the optical elements in the system. Once we have gained a better understanding of these issues, we will design and build an optimized system. Finally, we will demonstrate the optimized system on an Asay foil experiment.

Modeling Coupled Heat and Mass Diffusion

Arthur B. Shapiro
New Technologies Engineering Division
Mechanical Engineering

Philip M. Gresho
Atmospheric Science Division
Environmental Programs

We have developed a model that includes thermally-driven mass diffusion to predict the evaporation rate of bound water in a porous material in a vacuum. All water in the porous material is in the "sorptive" or "bound" state and the main mechanisms of moisture transfer are bound water and vapor diffusion. This differs from the state in which free water exists in the pores and moisture transfer is by capillary flow.

Introduction

Drying is the removal of water from a solid by evaporation. In the evaporation process, heat has to be supplied to the material, so that simultaneous transfer of heat and mass occurs. Several drying periods are defined:

1. First Drying Period (constant rate drying). The surface of the solid is covered with a continuous layer of free water, and evaporation takes place mainly at the surface. The rate of drying depends entirely on parameters external to the solid, such as the air velocity, temperature, and humidity. If the external conditions are constant, then the drying rate is constant. The temperature of the solid will equilibrate to the wet bulb temperature of the air.
2. First Falling Rate Period. As drying proceeds, the fraction of wet area decreases with decreasing surface moisture content. The surface will form discontinuous wet patches and the mass transfer from the surface will decrease with a slowly rising surface temperature. Free water still exists at the surface, the "dry" patches still contain bound water, and the vapor pressure at the surface is determined by the Clausius-Clapeyron equation.
3. Second Falling Rate Period. No free water exists at the surface. The surface temperature will rise rapidly, during which a receding evaporation front appears, dividing the solid into a wet region and the sorption (bound water) region. Inside the evaporation front, the material is wet (that is, the voids contain free water), and the main mechanism of moisture transfer is capillary flow. Outside the front, all water is in the sorptive or bound state and the main mechanisms of moisture transfer are bound water and vapor diffusion. Evaporation takes place at the front as well as in the whole sorption region, while vapor flows through the sorption region to the surface.

In our application all the water is in the "sorptive" or "bound" state, and the main mechanisms of moisture transfer are bound water and vapor diffusion.

Progress

The most appropriate and applicable model for mass transfer that seems to describe well the relevant physics over the entire range of pressure—from atmospheric pressure where continuum dynamics prevails, on down to hard vacuum conditions at

which free-molecule flow prevails—is a model that was first envisaged by James Clerk Maxwell about 140 years ago, during the early development of the kinetic theory of gases. It was later rediscovered several times by others. Called (in recent times) the dusty gas model[1] (DGM), it treats the porous medium (the "dust") as a collection of fixed spheres around which "n" ideal gases flow. The DGM is most succinctly described for isothermal conditions as follows:

$$\frac{\underline{N}_i}{D_i^e} + \sum_{j \neq i}^{n} \frac{X_j \underline{N}_i - X_i \underline{N}_j}{D_{ij}^e} = -\frac{1}{RT}\nabla\left(x_i P\right) - \frac{x_i D_v}{RTD_i^e}\nabla P \tag{1}$$

where $\underline{N}_i$ is the molar flux ($c_i \underline{u}_i$) of component i (g-moles/cm^2 s), x_j is the mole fraction of component j, P is pressure (dyne/cm^2), T is temperature (K), R is the gas constant (~8.3 x 10^7 gm cm^2/g-mole s^2 K), and the diffusivities are as follows:

1. $D_i^e = K_o \upsilon_i$ is the effective Knudsen (free-molecule) diffusivity, K_o is an effective diffusion length ($K_o = 2a/3$ for a tube of radius a), in cm, and

   $$\upsilon_i \equiv \sqrt{8RT/\pi M_i} \tag{2}$$

   is the mean molecular speed (M_i is the molecular weight);
2. $D_{ij}^e = K_1 D_{ij}$ is the effective ordinary (bulk) binary diffusivity associated with continuum (Stefan-Maxwell) diffusion, where K_1 is a dimensionless constant ($K_1 \leq 1$) and D_{ij} is the (known) binary molecular diffusivity;
3. $D_v = B_o P/\mu$ is the viscous/Darcy diffusivity, where μ is the gas viscosity (gm/cm s) and B_o is the effective "area" of the medium (cm^2; $B_o = a^2/8$ for a tube of radius a—Poiseuille flow).

For a porous medium, the DGM is a three-parameter model, in which the three parameters that "characterize" the porous medium (K_o, K_1, B_o) are best determined experimentally. Note that the DGM successfully combines three physical phenomena in one model: 1) free-molecule flow (Knudsen flow/diffusion) that prevails at very low pressure (where $D_{ij} \to \infty$ and $D_v \to 0$); 2) ordinary (Stefan-Maxwell) diffusion that is important at higher pressures ($D_i^e / D_{ij}^e \to \infty$); and 3) viscous flow, which carries all species at the same rate (non-separative) and is most simply "described" by the first term in the left-hand side and the last term in the right-hand side of **Eq. 1**, via $\underline{N}_i^v \cong -x_i D_v \nabla P / RT$, which basically describes Poiseuille flow.

In addition to the transport of water in the porous media defined by **Eq. 1**, an expression is needed for the evaporation rate of liquid water to gas in a vacuum.[2] Kinetic theory applies to systems in vacuum. Equilibrium requires that the rate of evaporation equals the rate of condensation. Therefore, we can determine the evaporation rate by equating it to the mass of molecules striking the surface.

From kinetic theory, the number of molecules of a gas that strike a surface is

$$\nu = \frac{1}{4} n \upsilon_a \quad \text{(molecules/cm}^2\text{ s)},$$

where the average gas velocity is given by **Eq. 2**, and the number of molecules per volume is determined by the ideal gas law

$$n = \frac{N_A P_{mm}}{RT} \quad \text{(molecules/cm}^3\text{)},$$

where N_A is Avogadro's number (6.0228×10^{23} molecules/gmole), R is the universal gas constant (6.236×10^4 cm^3 mm/g gmole K), P_{mm} is the water vapor pressure in mm of Hg, and T is the temperature in K.

The mass of gas striking (or leaving) a surface per unit area per unit time is then

$$G = m\nu = m\left(\frac{1}{4} n \upsilon_i\right)$$

$$= \frac{M}{N_A}\left[\frac{1}{4}\left(\frac{N_A P_{mm}}{RT}\right)\left(\frac{8RT}{\pi M}\right)^{1/2}\right] = \left(\frac{P_{mm}^2 M}{2\pi RT}\right)^{1/2}.$$

Using the molecular weight of water as M = 18.02 g/gmole, the expression for the mass of water vapor leaving a surface, G, can then be evaluated to be

$$G = 0.247\frac{P_{mm}}{T^{1/2}} \quad \text{(g/cm}^2\text{ s)}.$$

Over a small temperature range, the vapor pressure of water may be represented by the Clausius-Clapeyron equation

$$P_{mm} = \exp\left(A - \frac{B}{T}\right),$$

where A and B are constants determined from experimental data such as shown in **Table 1**.

Using the end points in **Table 1**, A and B are determined to be A = 17.765 and B = 5314.8. Then, the final expression to calculate the evaporation rate is

Table 1. Pressure of aqueous vapor over water.[3]

T (K)	P (in. of Hg)
288.6	0.5218
294.1	0.7392
299.7	1.0321

$$G = 6.27 \frac{\exp\left(17.765 - \frac{5314.8}{T}\right)}{T^{1/2}} (\text{g/cm}^2\ \text{s}). \qquad (3)$$

Equation 3 applies to a completely wet liquid surface. This expression must be multiplied by the fraction of surface area that is wet to give the evaporation rate for a partially wetted surface.

Future Work

Experiments are planned that will determine the three parameters of the DGM for one or more particular cases of current interest. Also, the restriction to isothermal flow will be removed. This is most easily introduced at the low pressure end (vacuum conditions, where it is most important) by adding the following term to the right-hand side of **Eq. 1**:

$$+\frac{x_i P}{2RT^2} \nabla T ,$$

which accounts for thermal transpiration (bulk flow owing to temperature gradients) and, interestingly, is perhaps somewhat counter-intuitive in that thermally-induced flow is *up* the temperature gradient.

Our ultimate goal is to include these developments in the TOPAZ heat transfer code to extend the code's capability into the arena of low-speed flow and heat transfer of ideal gaseous mixtures in porous media, especially at low pressure.

References

1. Mason, E., and A. Malinauskas (1983), *Gas Transport in Porous Media: The Dusty Gas Model*, Elsevier, Amsterdam.

2. Dushman, S. (1966), *Of Scientific Foundations of Vacuum Techniques*, 4th ed., John Wiley and Sons, New York, New York.

3. Hougen, O. (1959), *Chemical Process Principles*, 2nd ed., John Wiley and Sons, New York, New York, p. 82.

Analysis and Modeling of a Stripline Beam Kicker and Septum

Brian R. Poole, Lisa Wang, and Yu Ju (Judy) Chen
Defense Sciences Engineering Division
Electronics Engineering

George J. Caporaso
Laser Programs

A fast stripline beam kicker and septum are used to dynamically switch a high-current electron beam between two beamlines. The transport of the beam through these structures is determined by the quality of the applied electromagnetic fields as well as temporal effects due to the wakefields produced by the beam. In addition, nonlinear forces in the structure will lead to emittance growth. The effect of these issues is investigated analytically and by using particle transport codes. Due to the distributed nature of the beam-induced effects, multiple macro-particles (slices) are used in the particle transport code, where each slice consists of an ensemble of particles with an initial distribution in phase space. Changes in the multipole moments of an individual slice establish electromagnetic wakes in the structure, and are allowed to interact with subsequent beam macro-particles to determine the variation of the steering, focusing, and emittance growth during the beam pulse.

Introduction

The stripline kicker is designed to spatially separate a high-current electron beam for transport into two separate beamlines. However, to provide a significant angular kick to the beam, a magnetic dipole septum is required. This system is shown schematically in **Fig. 1**.

The operation of the system is as follows: a high-voltage pulse is applied to the downstream ports of the kicker, and the beam is spatially separated (kicked) by a combination of the transverse electric and magnetic dipole forces associated with the transverse electromagnetic (TEM) waves propagating on the strip transmission lines.

The beam is then directed into a septum magnet with opposite polarity dipole fields on either side of the plane separating the two downstream beamlines. All the upstream ports and the two downstream ports in the non-kick plane are terminated in a matched load impedance for the dipole transmission mode on the structure. It should be noted that steering in both planes can be accomplished by also driving the other pair of plates.

Kicker TEM Fields and Beam Deflection

To steer the beam in x, opposite polarity high-voltage pulses are applied to the downstream ports in the $y = 0$ plane. The potential within the kicker plates ($r < b$) is given by

$$V = \frac{4V_p}{\pi} \times \sum_{m=odd} \left(\frac{1}{m}\right) \sin\left(\frac{m\phi_0}{2}\right) \cos(m\phi) \left(\frac{r}{b}\right)^m , \quad (1)$$

where b is the interior radius of the kicker plates, and ϕ_0 is the angle subtended by the kicker plates.

The voltage applied to the plate is V_p, giving a total steering voltage of $2V_p$. The solution is determined by solving for the potential in the region $r < b$, and using the boundary conditions that 1) the potential at $r = b$ is given by the appropriate applied plate voltages, and 2) the potential in the gaps between the plates is zero. The TEM fields can be easily derived from this scalar potential.

The $m = 1$ term in **Eq. 1** represents a transverse dipole force which provides the beam steering, while the higher order terms will contribute to emittance growth in the beam. The beam deflection due to the combined electric and magnetic dipole forces is given by

$$\Delta x = \frac{\pi b V_p}{I_c Z_k \sin\left(\phi_0/2\right)} , \qquad (2)$$

where the critical current, I_c, is defined by

$$I_c = \frac{\pi}{16} \frac{\gamma \beta^2 I_0}{\sin^2\left(\frac{\phi_0}{2}\right)} \frac{Z_0}{Z_k}\left(\frac{b}{L}\right)^2 , \qquad (3)$$

and I_0 = 17 kA, Z_0 = 377 Ω, L is the length of the kicker, b is the inner radius of the kicker plates, Z_k is the kicker impedance, and γ is the usual relativistic factor.

Progress

Dipole Wake Impedance and Beam-Induced Steering

In our application, the beam current is sufficiently large to induce substantial voltages and currents on the strip transmission lines. These voltages and currents are introduced on the transmission lines as the beam traverses the upstream and downstream gaps, and from changes in the dipole return current as the beam is deflected. A detailed model has been described previously.[1,2]

The $m = 1$ transverse dipole wake impedance for this structure[3] is given by

$$Z_\perp(\omega) = \frac{8cZ_k}{\pi^2 b^2} \sin^2\left(\frac{\phi_0}{2}\right)\left(\frac{1}{\omega}\right) \times \left[\sin^2\left(\frac{\omega L}{c}\right) + j\sin\left(\frac{\omega L}{c}\right)\cos\left(\frac{\omega L}{c}\right)\right] . \qquad (4)$$

The imaginary part of the dipole impedance, $Z_{\perp 0} = \mathrm{Im}[Z_\perp(\omega = 0)]$, is a measure of the asymptotic beam deflection due to the beam-induced fields. It has been shown that the asymptotic beam deflection for an initially offset beam with current I_B injected into the kicker has the form[1]

$$x_\infty = x_0 \cosh\left(\sqrt{\frac{2I_B}{I_c}}\right) , \qquad (5)$$

where x_0 is the injection offset of the beam. It is easily shown for sufficiently small beam currents that

$$x_\infty \approx x_0 \left[1 + \left(\frac{2\pi L}{\gamma \beta^2 I_0 Z_0}\right) I_B Z_{\perp 0}\right] . \qquad (6)$$

To examine the relevant physics issues, a kicker has been designed and installed on Lawrence Livermore National Laboratory's Experimental Test Accelerator (ETA-II). The ETA-II kicker has the following set of parameters: b = 12.87 cm, ϕ_0 = 78°, Z_k = 50 Ω, L = 164 cm, and I_c = 3.9 kA. The outer enclosure has a radius of 19 cm. To verify the validity of the transmission line model, the structure was modeled using LLNL's TIGER 3-D time-domain electromagnetic code to determine the dipole impedance spectrum.

Figure 2 shows a comparison of the dipole impedance as calculated from **Eq. 4** with numerical results from the TIGER code for the ETA-II kicker. As can be seen, there is good agreement between the transmission line model and the 3-D code results. The differences can be attributed to end cavity effects associated with the feeds to the external ports and effects due to higher order modes in the structure.

The effect of the wake impedance on the deflection of the beam can be quite dramatic. For example, for a 6-MeV, 2-kA beam initially offset by 2 cm going into the kicker, the tail of the emerging beam will be offset by 3.1 cm at the exit of the structure. These effects have been observed experimentally[4] and are consistent with theory.

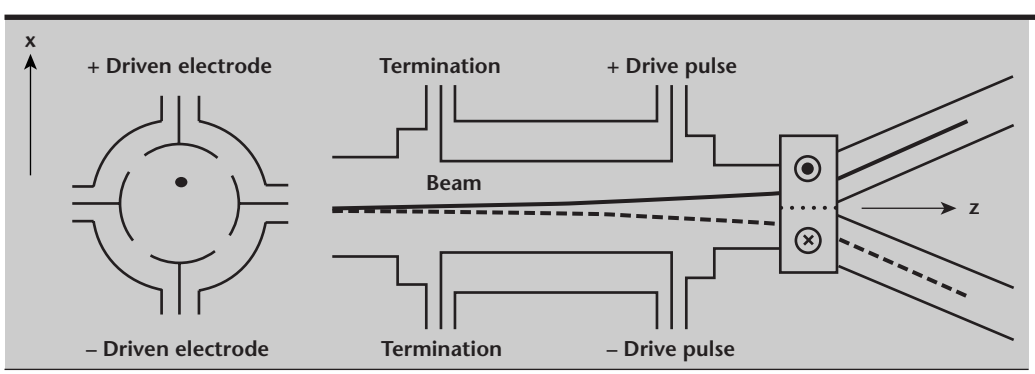

Figure 1. Kicker and septum configuration for dynamic beam-steering in one plane.

Nonlinear Forces and Emittance Growth

From **Eq. 1** it is seen that for a dipole excitation of the kicker, all higher order odd multipoles will be excited in the structure. Although the higher order multipoles reduce in strength as $(r/b)^m$, it is possible under certain conditions that the beam will experience these fields, especially the $m = 3$ sextupole component.

For example, with ETA-II parameters the space-charge fields due to the beam may require that the beam entering the kicker have a large radius to enable the downstream beam to be at or near a waist when entering the dipole septum. This is important to minimize any emittance growth due to the nonlinear fields associated with the septum magnet.

To estimate the effect of the higher order multipoles due to the kicker on the beam emittance, a simple particle transport code was developed. The code includes the external fields in the kicker region as defined by **Eq. 1**, and is being expanded to include the beam-induced effects and space-charge effects self-consistently.

Presently, the particles respond only to the external fields. However, we can estimate the emittance growth in the structure by using the external fields only. As an example, using the ETA-II kicker previously described, a 6-MeV beam is injected into the kicker with an unnormalized edge emittance of 13 cm-mrad and a convergence angle of 0.03 rad. The injected beam radius is 4 cm, which allows the beam to experience the higher order multipoles. **Figure 3** shows a configuration-space image of the emerging beam from the kicker showing a centroid location of 2.7 cm, consistent with **Eq. 2**. The triangular image has been observed experimentally.[4]

Despite the strong deformation of the beam image, the emittance growth is predicted to be about 53% for this beam. However, transport calculations have also shown that it is possible to transport a smaller radius high-current beam, ~2 kA, through the kicker giving an estimated emittance growth on the order of 2%.

Magnetic Dipole Septum

The septum magnet provides an additional angular kick to the beam as it emerges from the kicker. The kick is in opposite directions on either side of $x = 0$. The septum is shown schematically in **Fig. 4**.

The dipole magnetic field required to produce a beam exit angle of ~15° is determined from

$$B\ell = \frac{mc}{e}\sqrt{\left(\frac{E_b}{mc^2}\right)^2 + 2\left(\frac{E_b}{mc^2}\right)} \times \left[\sin\left(\theta_i + \Delta\theta\right) - \sin\left(\theta_i\right)\right] , \qquad (7)$$

where ℓ is the axial length of the magnet, θ_i is the incident beam angle, $\theta_i + \Delta\theta$ is the desired exit beam angle, and E_b is the beam energy.

A preliminary design for a dipole septum magnet to be used with the ETA-II kicker is being developed. The parameters for the design are an axial length of 20 cm, and a magnetic field of about 276 G for a beam energy of 6.3 MeV. The dimensions of the aperture are about h=6 cm high and w=31 cm wide. Careful optimization of the design is required to minimize possible emittance growth in the transition region where the field changes sign.

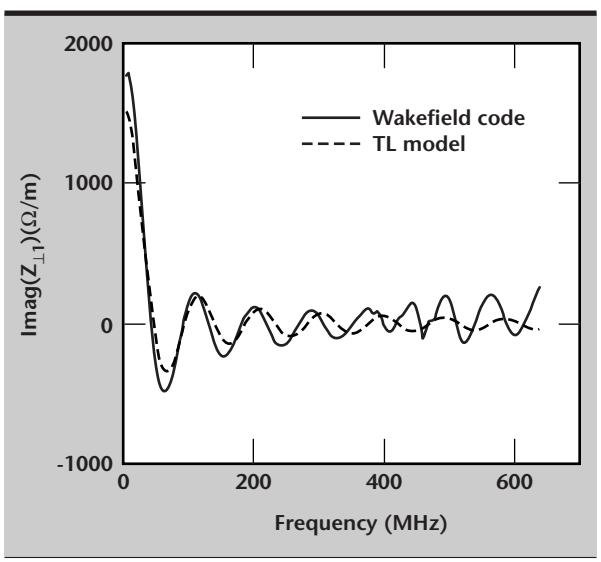

Figure 2. Dipole wake impedance.

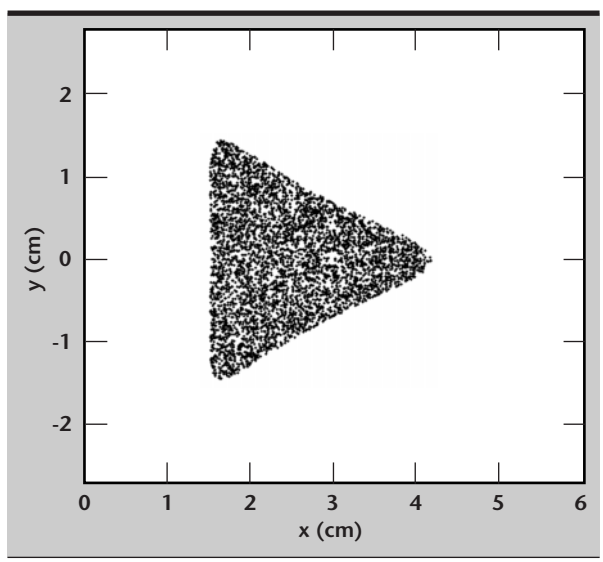

Figure 3. Configuration-space image of beam emerging from kicker experiencing a large sextupole field.

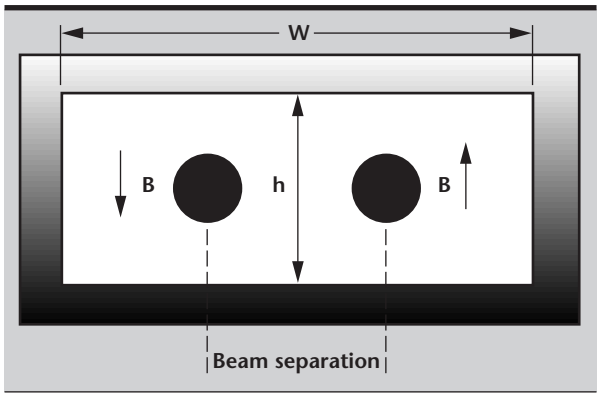

Figure 4. Magnetic dipole septum magnet.

Magnetic modules are being developed for particle transport codes to estimate the emittance growth through the septum magnet. With careful design, including shims, preliminary estimates show an emittance growth on the order of 4% through the septum magnet.

Conclusions

Self-consistent models are being developed for modeling the transport of high-current, space-charge-dominated beams through fast beam kickers and dipole septum magnets. The effect of beam-induced forces due to the wakefields of the beam are included in the analysis.

In addition, emittance growth due to nonlinear forces associated with higher order multipoles in both the kicker and septum have been estimated. Preliminary estimates of beam-induced steering are consistent with the experimental program.[4] The effect of space charge, image forces, and fringe fields in the structures have yet to be included.

Acknowledgments

Discussions on the electromagnetic characterization of the kicker with S. Nelson are greatly appreciated. Thanks also go to D. Steich for running the 3-D electromagnetic simulations of the kicker.

References

1. Caporaso, G. J., Y. J. Chen, and B. R. Poole (1997), "Transmission Line Analysis of Beam Deflection in a BPM Stripline Kicker," *1997 Particle Accelerator Conference*, Vancouver, B.C., Canada, May 12–16, Lawrence Livermore National Laboratory, California (UCRL-JC-126073).

2. Poole, B. R., G. J. Caporaso, and W. C. Ng (1997), "Wake Properties of a Stripline Beam Kicker," *1997 Particle Accelerator Conference*, Vancouver, B.C., Canada, May 12–16, Lawrence Livermore National Laboratory, California (UCRL-JC-126075).

3. Ng, K.-Y. (1988), "Impedances of Stripline Beam-Position Monitors," *Particle Accelerators* **23**, pp. 93–102.

4. Chen, Y. J., G. J. Caporaso, and J. Weir (1998), "Experimental Results on the Active Deflection of a Beam from a Kicker System," *XIX International Linac Conference (Linac98)*, Chicago, Illinois, August 23–28.

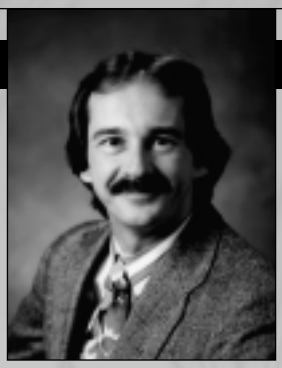

Harry E. Martz, Center Leader

The Nondestructive Characterization (NDC) Center (formerly the Nondestructive Evaluation Thrust Area) at Lawrence Livermore National Laboratory (LLNL) supports initiatives that advance inspection science and technology. Our goal is to provide cutting-edge technologies that show promise for quantitative inspection, and characterization tools three to five years into the future.

The NDC Center strategic objectives involve quantitative NDC, and fast nanometer-scale imaging. This past year the NDC Center portfolio of projects focused on quantitative NDC in support of weapons system performance and laser systems.

The NDC Center supports a multidisciplinary team, consisting of mechanical and electrical engineers, physicists, material and computer scientists, chemists, technicians, and radiographers. These team members include personnel that cross departments within LLNL. Some are from academia and industry, within the United States and abroad. This collaboration brings together the necessary and diverse disciplines to provide the key scientific and technological advancements required to meet LLNL programmatic and industrial NDC challenges.

NDC provides materials characterization inspections of finished parts and complex objects, to find flaws and fabrication defects and to determine their physical and chemical characteristics. In addition, applying NDC throughout the life cycle of a part saves time and money and improves quality. For example, NDC is being applied at the beginning of a part to develop new materials and to aid in process design and development. NDC encompasses process monitoring and control sensors and the monitoring of in-service damage. NDC is also being applied at the end of a part's life for proper reuse or safe and proper disposal. Therefore, NDC is becoming both a front-line and an end-of-line technology that strongly impacts issues of certification, life prediction, life extension, reuse, and disposal.

To meet today's programmatic demands, it is important to increase collaboration among LLNL engineering centers, departments, and programs. This year, collaborators included the Microtechnology Center, Defense Systems, Materials Science and Technology, Physics, the Life Extension Program, the National Ignition Facility Project, Computations, and Nonproliferation. Such collaborations enable us to stay at the leading edge of NDC technology, research, development, and application in support of LLNL programs.

Center for Nondestructive Characterization

5

5. Center for Nondestructive Characterization

Overview
Harry E. Martz, Center Leader

Techniques for Enhancing Laser Ultrasonic Nondestructive Evaluation
Graham H. Thomas, Robert D. Huber, Diane J. Chinn, James V. Candy, and James Spicer 5-1

Nondestructive Evaluation of an Aluminum Alloy Using Hyperspectral Infrared Imaging
Randy S. Roberts 5-9

***In-Situ* Identification of Anti-Personnel Mines Using Acoustic Resonant Spectroscopy**
Randy S. Roberts and Roger L. Perry.....5-13

An Acoustic Technique for the Non-Invasive *In-Situ* Measurement of Crystal Size and Solution Concentration
Diane J. Chinn, Paul R. Souza, and Harry F. Robey.....5-19

Micro X-Ray Computed Tomography for PBX Characterization
Diane J. Chinn, Jerry J. Haskins, Clinton M. Logan, Dave L. Haupt, Scott E. Groves, John Kinney, and Amy Waters 5-23

Evaluation of an Amorphous Selenium Array for Industrial X-Ray Imaging
Clinton M. Logan, Jerry J. Haskins, Kenneth E. Morales, Earl O. Updike, James M. Fugina, Anthony D. Lavietes, Daniel J. Schneberk, Gregory J. Schmid, Keo Springer, Peter Soltani, and Kenneth Swartz.....5-27

LANDMARC Radar Mine Detection
Stephen G. Azevedo, Jeffery E. Mast. James M. Brase, and E. Tom Rosenbury 5-39

IMAN-3D: A Software Tool-Kit for 3-D Image Analysis
Sailes K. Sengupta.....5-51

Image Recovery Techniques for X-Ray Computed Tomography in Limited-Data Environments
Dennis M. Goodman, Jessie A. Jackson, Maurice B. Aufderheide, and Erik M. Johansson.....5-61

Techniques for Enhancing Laser Ultrasonic Nondestructive Evaluation

Graham H. Thomas, Robert D. Huber, and Diane J. Chinn
Manufacturing and Materials Engineering Division
Mechanical Engineering

James V. Candy
Electronics Engineering Technologies Division
Electronics Engineering

Professor James Spicer
Johns Hopkins University
Baltimore, Maryland

Ultrasonic nondestructive evaluation has been an extremely powerful tool for characterizing materials and detecting defects for many years. Piezoelectric transducers, traditionally used to generate and detect high-frequency acoustic energy, usually require a liquid medium to couple the ultrasound into the material being characterized. This need for a couplant restricts the applicability of ultrasonics since many materials can be damaged by the use of couplants. We are developing a technology that generates and detects the ultrasonic pulses with lasers and thus there is no requirement for couplants. The ultrasound is generated and detected in a remote, non-contact manner since only the laser light is in contact with the material. Laser-based ultrasound has wide application in many Lawrence Livermore National Laboratory (LLNL) programs, especially when remote and/or non-contact sensing is necessary.

Introduction

Although the use of ultrasound for nondestructive evaluation is a mature technology, there continue to be many advances that expand its role in material characterization, manufacturing process control, defect detection, and life cycle management. Ultrasonics is evolving with improvements such as higher frequencies to sense smaller defects, modern signal processing methods to increase sensitivity, classification algorithms for defect characterization and the most recent imaging techniques to display defects.

Despite these advances, a universal limitation of traditional piezoelectrically generated and detected ultrasound is the need to transmit the acoustic energy from the transducer into the part through a fluid, most often water. For many parts and materials, particularly those of interest to LLNL and the Department of Energy (DOE), it is extremely desirable to eliminate this couplant.

Laser generation and detection of ultrasonic energy provides a method to perform remote, non-contact ultrasonics.[1] It allows ultrasonic evaluations in high-temperature and radioactive environments, in applications where access is restricted, such as in a vacuum, and on materials that would be damaged by couplant contamination. For ultrasonic inspections on radioactive materials, any couplant used becomes hazardous waste, and thus laser ultrasonics reduces hazardous waste since no couplant is required.

Applications for laser-based ultrasound continue to be implemented as breakthroughs in the technology occur, but there is still much to be understood before its full potential can be realized. A significant limitation of laser-based ultrasound is its poor sensitivity as compared to the sensitivity of traditional piezoelectric-based ultrasonics. To improve the sensitivity, research is being pursued in the areas of improved ultrasonic generation, better detectors, and signal processing to make

laser ultrasonics viable. Also beam-forming and other signal processing techniques have been developed to improve the defect detection levels of laser acoustics. Significant improvements in both the generation and detection aspects of LLNL's laser-based ultrasound capability were realized during this project. Laser-based ultrasound will continue to have an increased role in nondestructive evaluation as the sensitivity limitation is solved through research.

Progress

This project is exploring the science of generating acoustic energy with a laser pulse, and the methodology of detecting ultrasonic signals with laser interferometers. The goal is not to replace existing piezoelectric-based ultrasonics with laser generation and detection, but to supplement the technology to expand its role in LLNL programs. The following text describes the equipment and software algorithms for laser-based ultrasonics developed by this project.

Signal and Image Processing and Beam-Forming

A large portion of our effort has been in the area of signal and image processing, an approach to improve the sensitivity of laser-based ultrasonics. It helps extract more information from the experimentally obtained data. In the past we have demonstrated the benefits of several signal processing approaches that greatly improve laser-based ultrasonic sensitivity to finding defects.

A model-based signal processing technique has been developed and tested.[2,3] This technique predicts the acoustic signals that are generated by a specific laser. A code (WAVER) developed at the Johns Hopkins University[4] has been modified to handle materials and laser configurations that are of interest to LLNL programs. The model-based signal processing was implemented on ultrasonic signals generated with a Nd:YAG laser and detected with a Michelson interferometer.[5] This demonstrated technology is significant to the implementation of laser-based ultrasound for many nondestructive evaluation applications since it allows the application of laser-based ultrasonics for materials where acoustic attenuation is large.

Another signal processing approach that we have demonstrated is beam-forming. Beam-forming improves defect detection sensitivity by viewing the defect from several directions and combining the information from each direction in a manner to accentuate the defect's image. Previous work modeled the acoustic beam from an array of senders and receivers. This year the predicted defect sensitivity was confirmed with beam-forming algorithms processing experimental data. This method enhances the detection and display of defects by combining the information from an array of sensors.[5,6] We have modeled the array and its response to a flaw.

Based on these results, we configured a synthetic laser ultrasonic array and confirmed the model. This new technology is one of our methods for processing ultrasonic data.

This past year we have developed matched-field imaging of the laser-based ultrasound signals. This signal processing technique uses a novel correlation-canceling approach to eliminate noise, thereby increasing the signal-to-noise ratio of the experimentally obtained data. Eleven linear scans of Nd:YAG pulsed-laser-generated, laser-based Michelson-interferometer-detected data were obtained on a 9.5-mm-thick aluminum plate. Each scan consists of 21 amplitude vs time waveforms.

Figure 1 shows the source and detection locations for these scans. There were 11 source locations spaced 2 mm apart, and 21 detection locations spaced 1 mm apart. The source position was held fixed for a scan (21 different detection locations), and then moved 2 mm for the next scan. A 1/16-in. (1.6 mm)-diameter hole was then drilled into the aluminum plate to simulate a defect, and the plate was scanned over the same region that was scanned prior to the hole being drilled.

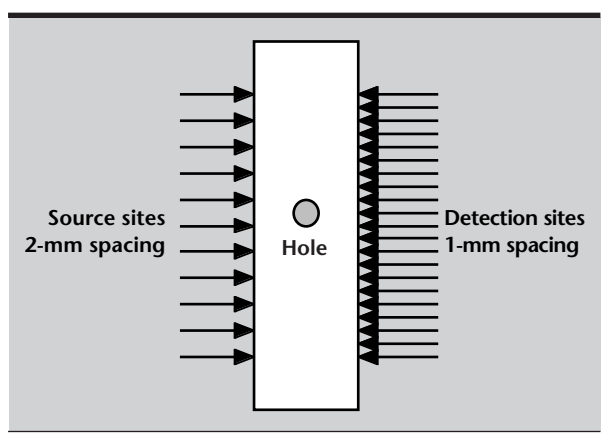

Figure 1. Source and detection sites for laser ultrasonic generation and detection on an aluminum plate with hole. Data obtained before and after the hole was drilled were used to obtain data in Figure 2.

The waveforms obtained after the hole was drilled, shown in **Fig. 2a**, were used along with the reference waveforms obtained before the hole was drilled (**Fig. 2b**). An optimal correlation-canceling scheme was developed to extract just the hole information, as shown in **Fig. 2c**, with a single channel result shown in **Fig. 2d**.

Processing yielded the canceled signal from the pre-hole and post-hole data. These signals were used to generate images, which show the effects of the presence of the hole on the ultrasound for different source and detector locations (**Fig. 3**). This demonstrates how laser-based ultrasound with signal processing can be used for defect detection and location.

Facility

Significant improvements in our laboratory have been realized over the duration of the project. At the start, LLNL had a Michelson interferometer and a small Nd:YAG laser for laser-based ultrasound work. These items had only limited application, and there was only a small area devoted to laser-based ultrasound. Once the project began, improvements to the correction circuit of the Michelson interferometer were made that greatly increased its stability. Modifications to both the electronic and mechanical components were made.

We have added a LISOR (Light In, Signal Out Receiver) interferometer to expand our detection

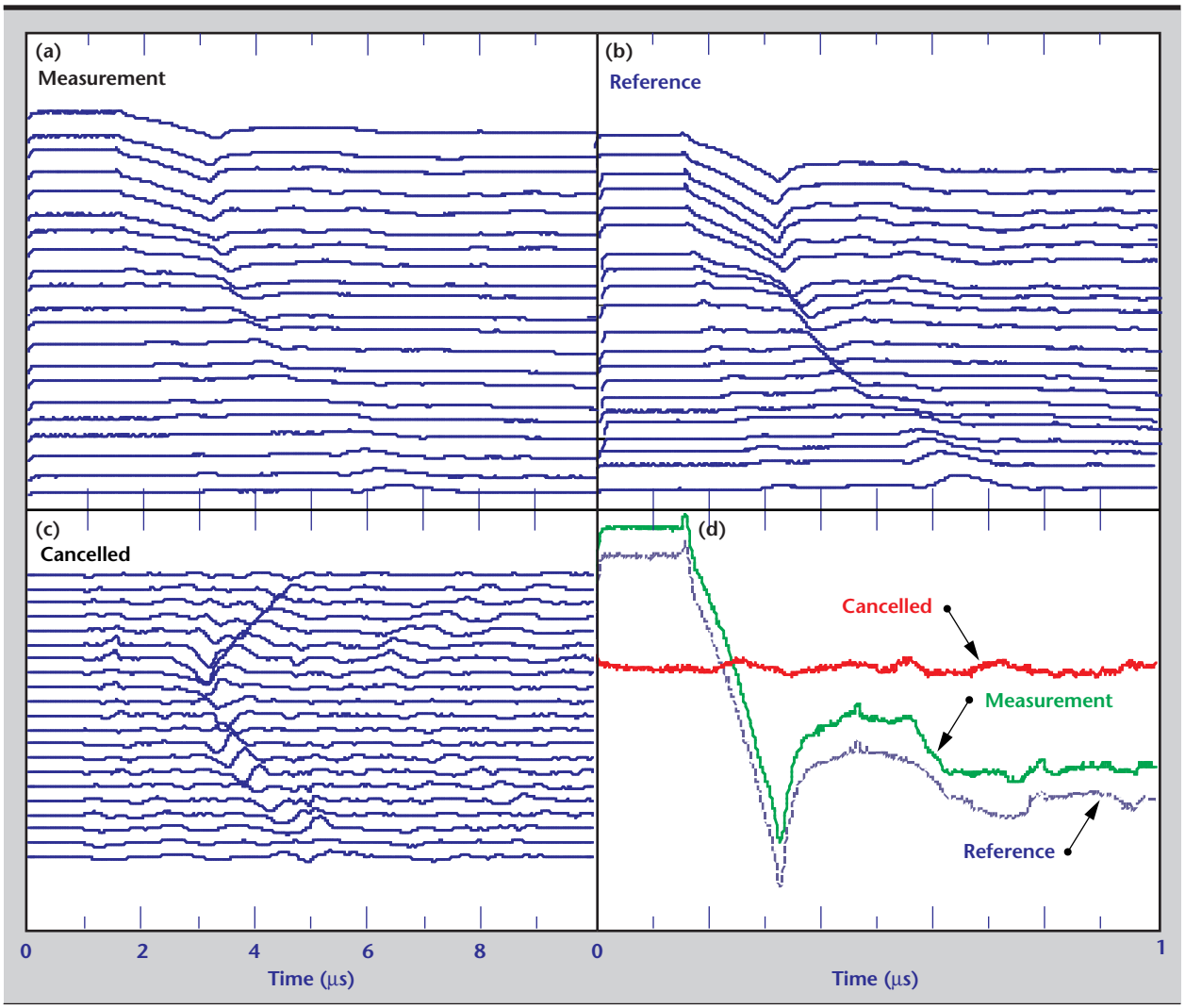

Figure 2. Laser ultrasonic correlation cancelation for enhanced flaw detection. Top left plot (a) shows the waveforms obtained after the hole was drilled (Measurement) for one source location. Top right signals (b) were obtained prior to drilling of the hole (Reference). Bottom left plot (c) displays the cancelled signals. Bottom right display (d) shows an individual wave for the pre- and post-drilled cases with the corresponding cancelled signal.

capabilities. This instrument is a Fabry-Perot-based system that complements the earlier path-stabilized Michelson interferometer. The Michelson requires highly reflective surfaces to sense the ultrasonic signal, whereas the Fabry-Perot works on less reflective surfaces.

This system includes an interferometer and a laser. The laser is a frequency doubled Nd:YAG, which has an output power of 200 mW at a wavelength of 532 nm. Fabry-Perot interferometers can use light scattered from rough surfaces since they can work with multiple speckles. Michelson interferometers work with a single speckle only, which limits their use to polished surfaces.

The LISOR system has been used successfully in the laboratory to detect ultrasound propagating through various materials and specimens. To increase the flexibility of the ultrasonic detection system, an optical fiber cable 20 m long transmits the laser light from the interferometer's laser to the specimen, allowing the testing of items up to that distance away from the laser and interferometer.

Fiber optics have the advantages of allowing large distances between equipment and test location, providing access to hostile or hard to reach environments, changing test configuration easily, and eliminating the need for line of sight between laser and part. The Michelson interferometer has a frequency range of DC to 40 MHz, while the Fabry-Perot has a frequency range of 3 to 100 MHz. Together, these interferometers provide a full range of detection capabilities for most ultrasonic evaluation needs.

Another addition to the laser ultrasonic facility is a much improved source laser that provides more

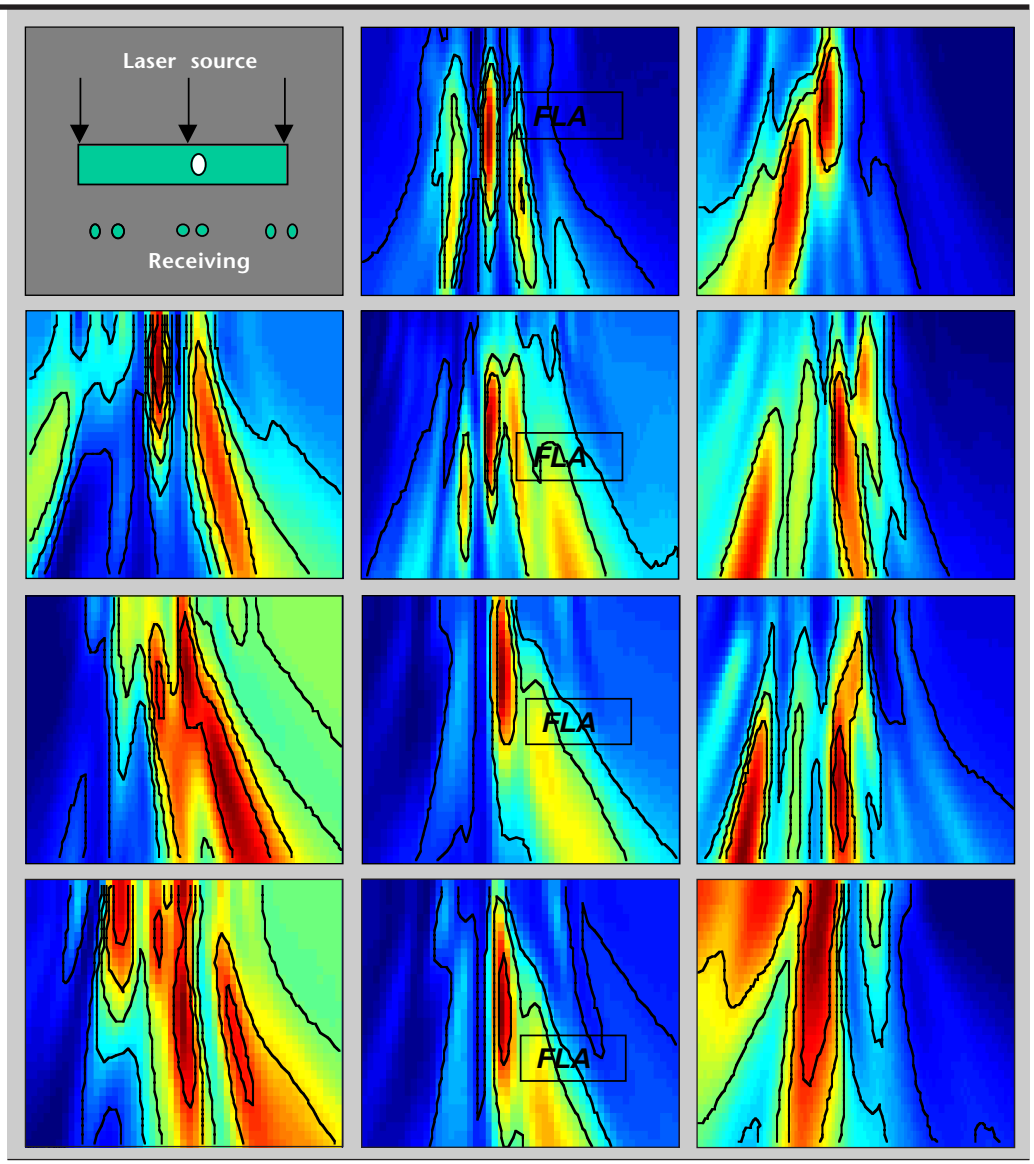

Figure 3. Images obtained from correlation cancellation. The 11 images correspond to 11 different source locations for linear scans on the aluminum plate. The hole appears sharpest when the source is directly over the hole.

light energy, a higher repetition rate and a uniform spot. This Nd:YAG source laser can operate at two wavelengths and has much better beam quality than the smaller Nd:YAG laser. This laser has made a tremendous difference in the signals obtained, and is aiding greatly in the model-based processing work being performed at LLNL.

As part of the data acquisition and imaging effort, we acquired computer-controlled motion stages. These stages include two translation stages and one rotation stage that allow the movement of specimens for scanning. Data acquisition and motion control programs have been written to control the stages and capture the ultrasonic signals. The signal processing and beam-forming algorithms are combined with this software to render images of defects from the data obtained when specimens are scanned. Most nondestructive evaluation tasks require the results to be an image of the defects. Scanning capability is needed to generate ultrasonic images.

Fiber Optics

Fiber optics are a significant development for laser-based ultrasonic implementation since they allow lasers and other equipment to be located in one place, with the object under test located in another place. The laser light can then be transmitted from one location to the other, completely contained in the fibers, thus eliminating the hazards of transmitting beams through the air. Fiber optics have been developed and implemented in several applications. The first such activity involved placing the probe arm of the Michelson interferometer in a single mode optical fiber.

Figure 4 is a comparison of signals obtained using the Michelson interferometer for the two cases of 1) optical fiber probe path, and 2) no optical fiber. The two waveforms show the ultrasound detected in an aluminum plate for a through transmission case for a laser-generated thermoelastic source. The thermoelastic source causes no damage to the sample and is therefore useful for nondestructive evaluation and characterization.

The waveforms are quite similar, with only a slight decrease in the signal-to-noise for the case of the fiber, because there is some loss of light associated with the use of the optical fiber. Although there is a slight decrease in the signal-to-noise ratio for the case of optical fiber in the interferometer, there may be situations where the benefits of fiber outweigh the decrease in signal-to-noise.

Fiber optics are also used with the Fabry-Perot interferometer. Initially the illuminating laser was transmitted through air and only the light reflecting off the specimen was transferred to the Fabry-Perot interferometer in a multi-mode fiber. Then we demonstrated that the light from the part-illuminating source laser could be transmitted through a multi-mode fiber. Thus all of the travel path of the laser light can be contained in optical fiber.

Fiber optic transmission of the laser beam provides a means to place the laser away from the part and still minimize the hazard to people. Also fiber optic light transmission allows for ultrasonic evaluations inside components with access provided by a small hole.

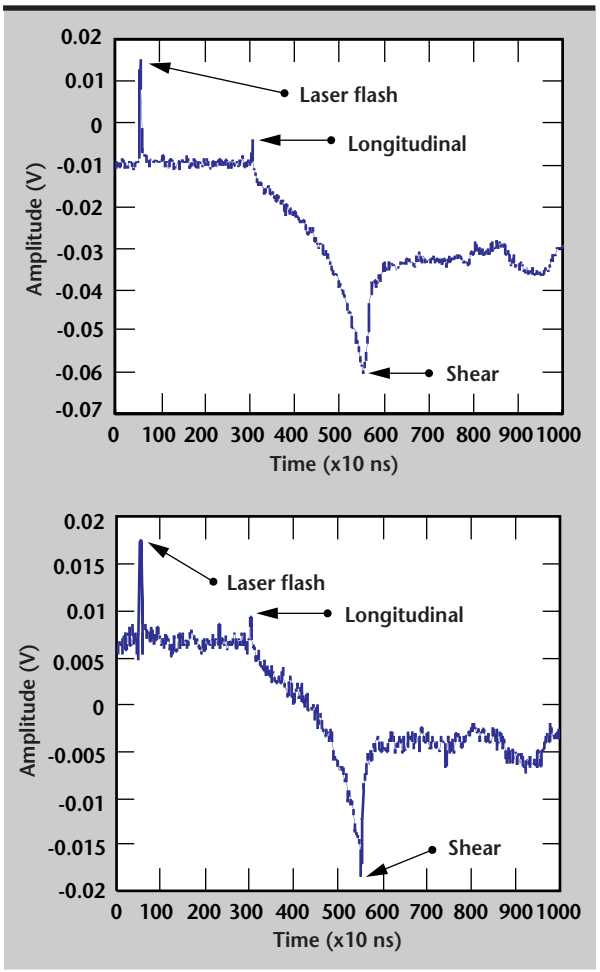

Figure 4. Comparison of signals. The upper waveform was captured using the Michelson interferometer with no fiber, while the lower was captured using fiber in the probe arm. Only a slight decrease in signal-to-noise ratio is seen. The above are through-transmission on epicenter.

Applications

The laser-based ultrasound laboratory has the capability to evaluate a wide variety of materials, and has looked at materials including aluminum, stainless steel, uranium and paper. Thus we have demonstrated the applicability of laser-based ultrasound on a variety of important, program-critical materials. This capability will allow us to support programs at LLNL such as those for weapons, lasers, nonproliferation, and energy. The following section briefly describes programmatic applications that resulted from this research.

Process Control. As a sensor for process control, ultrasonics is extremely valuable. The speed at which ultrasonic testing can acquire measurements facilitates feedback control for machining operations. We selected a process control problem as a vehicle to direct our research. The process was a cutting application with a state-of-the-art laser that produces very short pulses. The pulses from the cutting laser generate acoustic signals that contain information about the cutting process.

Our first challenge was to understand the phenomenon and the types of ultrasonic waves that are generated. We modeled the system with a computer code that calculates the expected ultrasonic signal, based on laser input parameters and the material properties and geometry. Initial tests were run on thin stainless steel plates.[7] The cutting laser beam was directed at the plates, and the Michelson interferometer was used to detect the ultrasound generated by the cutting beam.

The Michelson interferometer was able to detect both bulk and surface waves, depending on the test set-up. In one set-up, detection was performed on the side of the plate opposite that on which the cutting beam was incident, for the capture of bulk waves. In the other set-up, the cutting beam and the interferometer beam were both incident on the same side, for the capture of the surface waves. This configuration represented the process monitoring set-up.

Next, the Michelson interferometer was used to detect the ultrasound generated by the cutting laser in a real part.[5] At the start of the cut, a clear signal was seen, and this signal disappeared by the time cut-through occurred. This loss of acoustic signal at cut-through is the parameter selected for sensing when the laser had cut through the part. After successfully detecting the signals generated by the cutting laser with the Michelson interferometer, we switched to a Fabry-Perot interferometer for ultrasound detection. Whereas a strip of reflective tape was required at the detection site when using the Michelson interferometer, no tape is needed for the Fabry-Perot, and thus detection on non-specularly reflecting surfaces is possible.

The case for the process monitoring application involves non-specularly reflecting components. The Fabry-Perot interferometer is designed to operate with minimal operator intervention. Light for the interferometer is transmitted to and from the cutting chamber by optical fibers 20 m in length. To test the sensitivity, a laser-based ultrasonic through-transmission test on an aluminum plate was run using a Nd:YAG laser to generate ultrasound in the thermoelastic regime and the Fabry-Perot interferometer for detection. The waveform for this case is shown in **Fig. 5**.

The Fabry-Perot interferometer was also used to detect laser-generated ultrasound on a stainless steel surrogate part, to more nearly mimic the testing on actual parts. **Figure 6** shows a waveform signal-averaged from 10 laser pulses. The stainless steel part was a thin shell, and the waveform shows a dispersive plate wave. Over the course of the laser cutting project, various parameters of the cutting pulses such as energy and repetition rate were changed. A piezoelectric transducer was used to verify that the pulses were still generating ultrasound once the Fabry-Perot interferometer was obtained. Once the feasibility was demonstrated, the program funded this feedback control sensor as a standby option that can be implemented if needed.

Laser-based Ultrasound Sensor for Paper Manufacturing. The DOE has an initiative to reduce energy consumption in the largest industries in the

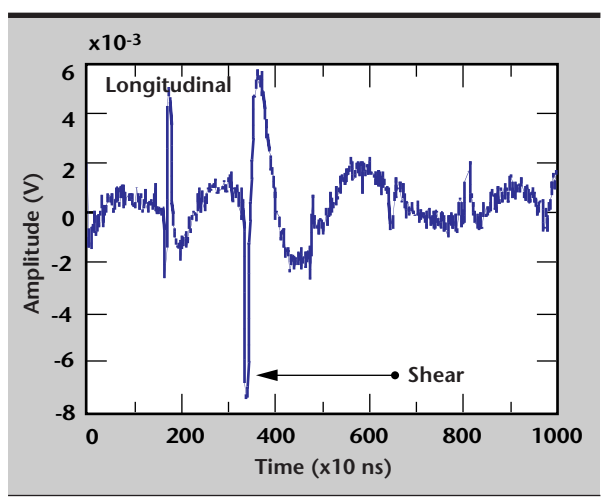

Figure 5. Fabry-Perot-interferometer-detected signal of laser-generated ultrasound. This is a through-transmission on epicenter case in aluminum for a thermoelastic source.

United States. Paper manufacturing is one such industry. We are collaborating with Lawrence Berkeley Laboratory (LBL) on developing a laser ultrasonic sensor. Real time process control afforded by this sensor will increase the quality of the product and reduce the energy consumption.

The researchers from LBL and LLNL are working to demonstrate ultrasonic characterization of paper as it is being processed. Plate waves are generated in the paper with a laser, and a Fabry-Perot interferometer detects the ultrasonic signals. Changes in acoustic velocity and attenuation signify variations in the paper processing. This project is on-going and may result in a demonstration at a factory.

Work on Aluminum at Elevated Temperatures. One task of a cooperative research and development agreement (CRADA) between the DOE and the "Big Three" automobile manufacturers is to explore nondestructive evaluation techniques to improve the casting of aluminum. Nondestructive evaluation could play a crucial role in improving cast parts by determining the condition of the molten materials prior to casting. Impurities in the molten metal cause defective castings. These defective castings increase manufacturing costs as well as energy consumption.

For example, if it can be determined that a particular melt contains an excessive amount of oxide, then that melt would not be used to cast parts. Laser-based ultrasound offers a means of testing metallic materials at elevated temperatures since it is a non-contact technique, whereas contact techniques, such as piezoelectric transducer ultrasound, have an upper limit on temperature, above which they will not work.

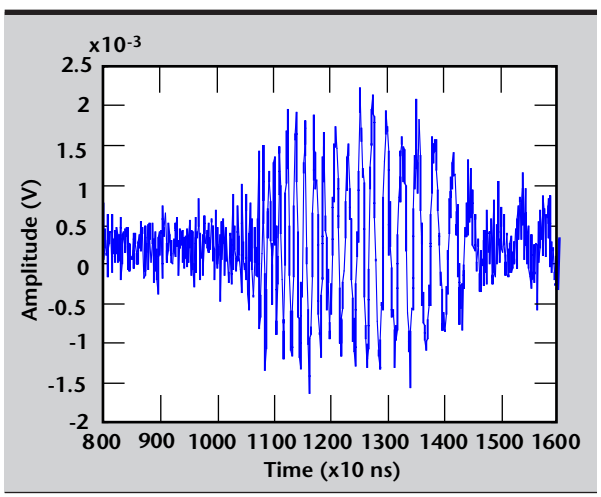

Figure 6. Fabry-Perot-interferometer-detected signal of laser-generated ultrasound in a stainless steel shell. The waveform shows the dispersion of the plate waves, that is, the high frequencies travel faster than the low frequencies.

We are funded to demonstrate laser generation and detection of ultrasound in molten metal. A furnace that has a port to pass the laser beam has been installed in the laser-based ultrasonic laboratory. Impurities in the liquid aluminum will reflect the acoustic energy that was generated by a laser. The acoustic energy reflected by impurities in the molten material is detected by an interferometer. This system will remotely monitor the quality of raw material feeding the casting process and sense problems before defective parts are produced.

Future Work

Although LLNL funding of laser-based ultrasound has produced a working facility for nondestructive characterization and evaluation of materials, there is still much work to be done in this area. Refinement of the computer code that calculates the ultrasound generated in materials from laser pulses will allow model-based processing on more complex parts, such as parts containing defects. Continued advances in the signal and image processing aspect of the work will lead to increases in the signal-to-noise ratios of experimentally obtained data, and will thus allow laser-based ultrasonic testing on a wider variety of materials and parts.

Recently, a fair amount of research has been performed in the area of higher frequency laser-based ultrasound. An interferometric technique for detection has been reported,[8] with a number of references in laser-generated high-frequency ultrasound. This includes acoustic frequencies >100 MHz and well into the GHz range. These high frequencies are required when working with materials whose characteristic dimension or defect size is <1 µm. This relatively new area of research has the potential for meeting the high spatial resolution demands emerging in LLNL program applications.

References

1. Scruby, C. B., and L. E. Drain (1990), "Laser Ultrasonics, Techniques and Applications," Adam Hilger, New York, New York.

2. Candy, J. V., G. H. Thomas, D. J. Chinn, and J. B. Spicer (1996), "Laser Ultrasonic Signal Processing: A Model-Reference Approach," *J. Acous. Soc. Am.*, **100** (1).

3. Huber, R. D., D. J. Chinn, G. H. Thomas, J. V. Candy, and J. Spicer (1997), "Model-Based Signal Processing for Laser Ultrasonic Signal Enhancement," *Review of Progress in Quantitative Nondestructive Evaluation*, **16**, pp. 757–764, Plenum Press, New York, New York.

4. Spicer, J. (1991), "Laser Ultrasonics in Finite Structures: Comprehensive Modeling with Supporting Experiment," Ph.D. Thesis, Johns Hopkins University, Baltimore, Maryland.

5. Thomas, G. H., D. J. Chinn, R. D. Huber, J. V. Candy, and J. B. Spicer (1998), "Techniques for Enhancing Laser Ultrasonic Nondestructive Evaluation," Lawrence Livermore National Laboratory, Livermore, California (UCRL-ID-129207).

6. Johnson, D., and D. Dudgeon (1993), "Array Signal Processing: Concepts and Techniques," Prentice-Hall, Princeton, New Jersey.

7. Chinn, D. J., R. D. Huber, D. D. Scott, G. H. Thomas, J. V. Candy, and J. B. Spicer (1997), "New Techniques in Laser Ultrasonic Testing," Lawrence Livermore National Laboratory, Livermore, California (UCRL-ID-125476).

8. Fiedler, C. J. (1996), "The Interferometric Detection of Ultrafast Pulses of Laser Generated Ultrasound," Wright Laboratory (WL-TR-96-4057).

Nondestructive Evaluation of an Aluminum Alloy Using Hyperspectral Infrared Imaging

Randy S. Roberts
Defense Sciences Engineering Division
Electronics Engineering

Fourier transform spectroscopy has found application in many areas, including atmospheric chemistry and material characterization. This report describes an investigation into the application of the Lawrence Livermore National Laboratory (LLNL) Hyperspectral Infrared Imaging Spectrometer (HIRIS) to the nondestructive evaluation of blocks of aluminum alloy. We describe the HIRIS system and the aluminum alloys used in the investigation, and the technique used to collect the hyperspectral imagery. We discuss the processing required to transform the data into usable form and a technique to analyze the data. We also provide some preliminary results.

Introduction

The HIRIS is a second-generation Fourier transform spectrometer developed at LLNL (see Reference 1 for an excellent discussion of HIRIS's predecessor). While it has been used primarily in remote sensing applications, the focus of this project is to assess its usefulness in nondestructive evaluation applications.[2] The HIRIS consists of a Michelson interferometer, a cryogenically cooled silicon arsenide (Si:AsBIB) focal plane array, and associated optics.

Figure 1 is a block diagram of a hyperspectral imaging spectrometer.[3] Infrared light enters the interferometer and is split into two paths by the beam-splitter. Along one path, a fixed mirror reflects the light back through the beam-splitter and onto the focal plane array. Along the second path, a movable mirror reflects the light back through the beam-splitter which in turn reflects it onto the focal

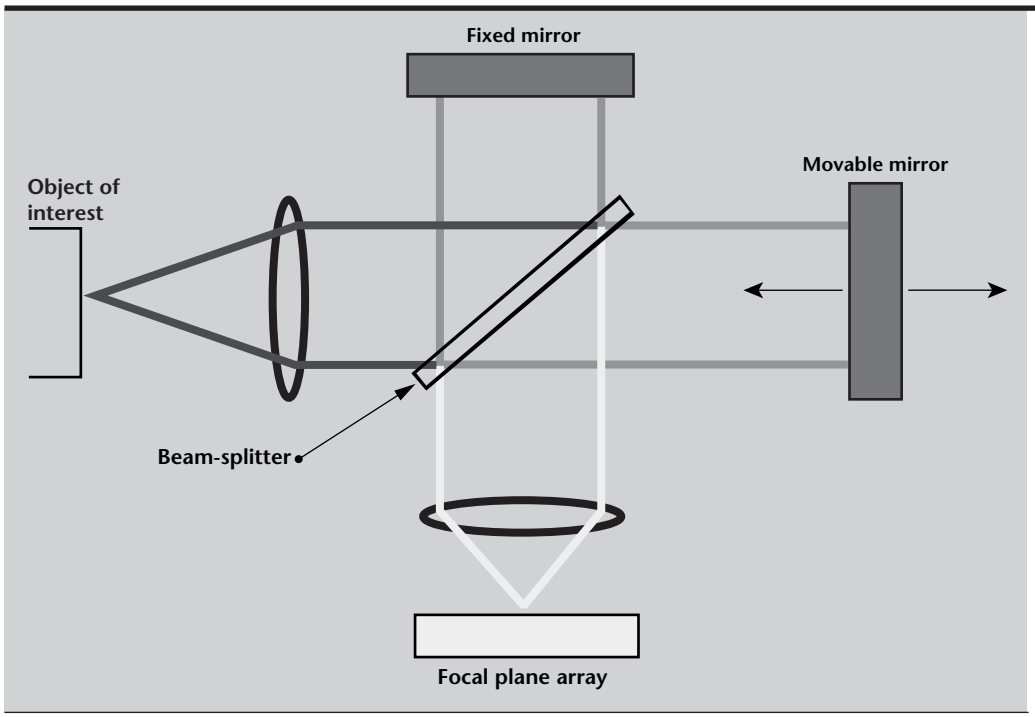

Figure 1. Schematic diagram of the HIRIS imaging system. Light enters the interferometer from the left, and is split into two paths by the beam-splitter: towards a fixed-position mirror, and towards a movable-position mirror. The mirrors reflect the light back to the beam-splitter, which directs the light onto the focal plane array. Translation of the movable mirror results in a time-varying interference pattern on the focal plane array.

plane array. Note that the optical length for the first path is fixed, while the length of the second path can be adjusted by moving the mirror.

If the light impinging on the focal plane array is in phase, constructive interference results. If the light is out of phase, destructive interference results. If the movable mirror translates with a fixed velocity, a time-varying interference pattern is formed on the focal plane array. Since HIRIS uses a focal plane array, a time-series of interference data, called an interferogram, evolves in each pixel. Fourier transformation of all interferograms results in the desired hyperspectral image data.

The objects of our interest are several aluminum blocks provided to LLNL by General Motors Corporation (GM). The blocks are made of an aluminum alloy denoted A356.[4] This alloy consists primarily of aluminum (~92%), silicon (~7%) and trace amounts of copper, magnesium, manganese, iron, and zinc. The alloy has excellent corrosion resistance and casting properties, good machinability and weldability, and high strength. It is most often used in the automotive and aircraft industries where high strength and low corrosion are required.

The blocks we received from GM were subjected to compression-tension cycles until they fractured. Typically, A356 reliably fails after approximately 500,000 cycles, but these samples failed after approximately 5000 cycles. It is conjectured that the premature failure was due to the addition of salts, such as potassium chloride and sodium chloride, during processing.

The objective of our investigation is to study the fracture sites in the A356 samples using hyperspectral infrared imagery, and if possible, determine the validity of this conjecture.

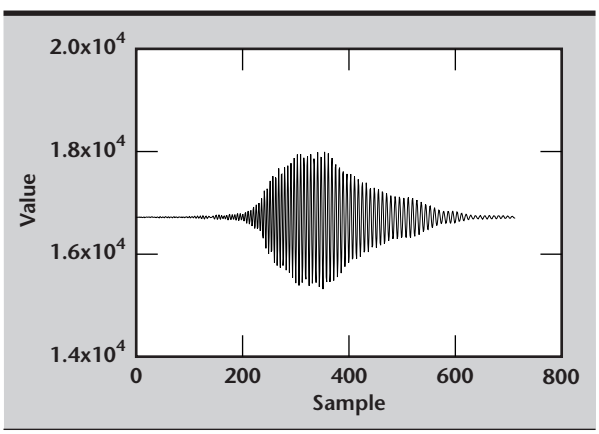

Figure 2. Plot of an exemplar interferogram from an A356 sample. This interferogram was formed in pixel (64, 64), and its range has been limited to reveal the most interesting structure.

Progress

For these experiments, the HIRIS was reconfigured from a remote sensor to a laboratory instrument. Reconfiguration essentially consisted of installing a collimator lens at the input point of the interferometer. The focal length of the collimator lens was 100 mm, and the focal length of the condenser lens was 226 mm, thereby yielding a system magnification of 2.26. The focal plane array in the HIRIS is a 128 × 128-pixel array with a pixel size of 75 μm/pixel. The resulting resolution of the system is thus on the order of 33 μm/pixel.

To collect the data, the aluminum blocks were heated with a hot air gun until they reached a temperature in excess of 50 ºC. The blocks were then held at this temperature for the duration of the data collection. In addition to the A356 blocks, calibration data was collected from a blackbody source. The source was set to 55 ºC for a hot reference, and 45 ºC for a cold reference.

A scan in the HIRIS consists of translating the movable mirror at a constant velocity through a fixed distance. As a point of terminology, the resulting sequence of images produced by a scan is referred to as a raw data cube. The scan time and sampling rate of the interferograms determine the spectral resolution of the hyperspectral data. For these experiments, the resulting resolution of the system was set to 16 cm^{-1}.

To increase the signal-to-noise ratio of features in the spectral data, an ensemble of data cubes were collected from each object of interest. In our case, 32 data cubes were collected from each A356 sample, and 16 data cubes each were collected from the hot and cold body sources for each A356 sample.

A portion of one of the interferograms associated with pixel (64, 64) of an A356 sample is shown in **Fig. 2**. Note the structure of the interferogram between frames 220 and 580. An image associated with this part of the data cube, frame 278, reveals a ring-like interference pattern, as illustrated in **Fig. 3**.

Interferograms, while illuminating some signal structure in the data cube, are difficult to interpret. However, the spectral information contained in interferograms can be quite revealing. To begin the processing, the data cubes were first averaged to increase the signal-to-noise ratio. As a result of the averaging, three data cubes were produced for each collection: an A356 data cube, a hot calibration data cube, and a cold calibration data cube.

The spectral content of a data cube is found by Fourier transforming each interferogram in the data cube. To reduce spectral sidelobes, each interferogram is multiplied by a triangular data-tapering window prior to Fourier transformation. To ease the computational burden of subsequent analysis, the fringe portions of the spectra are discarded. Finally, the A356 data is calibrated using the hot and cold references.[1] The calibrated data cube was then analyzed as described below.

Spectral data in a data cube is analyzed using a technique called Principle Component Analysis,[5,6] a powerful analytical tool for analyzing complex data sets. In essence, data is rotated into a coordinate system with some highly desirable properties such as orthogonality and minimum basis restriction error. The technique begins by estimating the correlation matrix of the data. The eigenvalues and eigenvectors of the correlation matrix are then computed. By themselves, the eigenvectors form an orthogonal coordinate system in which to represent the data. However, the eigenvectors associated with the largest eigenvalues correspond to the axes that most efficiently represent the data. By representing the data in the new coordinate system, that is, a coordinate system using the eigenvectors associated with the largest eigenvalues, the most important features of the data are more readily determined.

The distribution of eigenvalues can reveal a great amount of information about the structure of the data. A plot of the logarithm of the eigenvalues of one of the A356 samples is shown in **Fig. 4**. As illustrated in the figure, the magnitude of the eigenvalues decreases rapidly over the first four or five. From approximately the fifth to perhaps the twentieth eigenvalue, the decrease is more gentle, but the eigenvalues still have a large magnitude.

The modes associated with these twenty eigenvalues comprise the main structure of the data. If the data were reconstructed from these modes, the residual error would be minimal. The modes associated with the remaining eigenvalues are not important to the analysis. In particular, the modes from twenty to approximately eight-five are associated with system noise. The remaining eigenvalues belong to degenerate modes. They are artifacts of the processing, and are not useful in the analysis. Once the important features of the data set have been determined using eigenanalysis, they can be interpreted for physical meaning. Indeed, this technique has been used to identify constituent components of mineral specimens.[1]

Summary

The HIRIS developed at LLNL has found many uses in remote sensing. This project assessed its use in the nondestructive evaluation of several blocks of aluminum A356. Hyperspectral data was collected on the blocks after a slight modification to the HIRIS input optics. Several data sets were collected on the specimens and calibration sources. The data sets were averaged to increase the signal-to-noise ratio, processed, and Fourier transformed to produce data

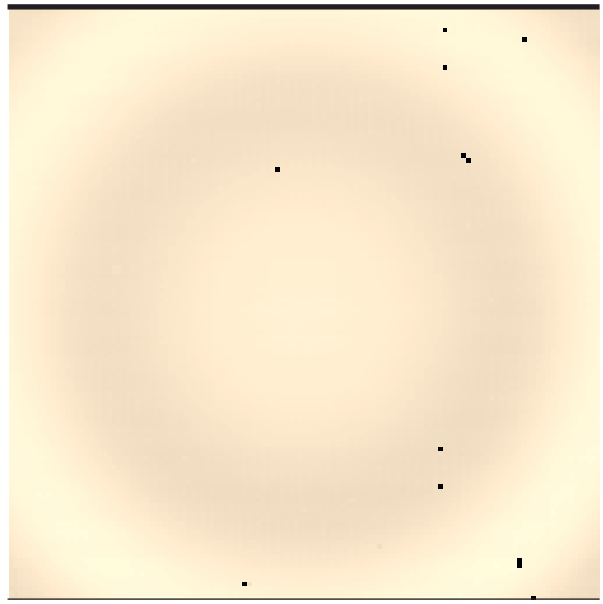

Figure 3. Frame 278 from the raw data cube of the A356 sample used in Figure 2. Note the concentric ring structure of the image formed by the interferograms. The black dots result from pixel imperfections in the focal plane array.

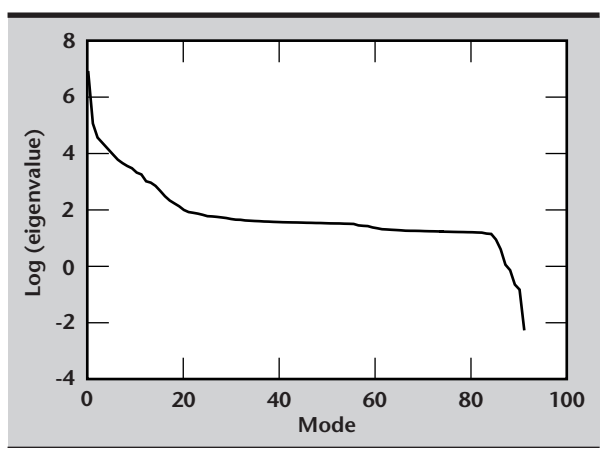

Figure 4. Plot of the logarithm of the magnitude of the eigenvalues of an A356 imagery. There are three types of modes associated with the eigenvalues: modes related to structure of the data (0 to 20); modes associated with system noise (21 to 85); and degenerate modes produced by the processing. (86 to 92).

cubes of spectral data. Preliminary analysis of the spectral data using Principle Component Analysis reveals interesting structure in the data, but additional analysis is required to fully assess the potential of this technique.

Acknowledgments

The author would like to thank J. Bixler for collecting the data, W. Aimonetti for help with the analysis, and C. Bennett for interesting discussions on hyperspectral infrared imagery.

References

1. Bennett, C. L. (1988), "LIFTERS, The Livermore Imaging FTIR Spectrometer," *Fourier Transform Spectroscopy: 11th International Conference*, J. A. de Haseth, ed., American Institute of Physics.

2. Roberts, R. S., W. D. Aimonetti, and J. V. Bixler (1998), "Material Characterization Using a Hyperspectral Infrared Imaging Spectrometer," *Proceedings of the IEE Thirty-Second Conference on Signals, Systems, and Computers,* Pacific Grove, California, November.

3. Beer, R. (1992), *Remote Sensing by Fourier Transform Spectrometry,* John Wiley and Sons, New York, New York.

4. American Society for Metals Reference Book, 2nd ed., 1983.

5. Malinowski, E. (1991), *Factor Analysis in Chemistry*, 2nd ed., John Wiley and Sons, New York, New York.

6. Fukunaga, K. (1990), *Introduction to Statistical Pattern Recognition*, Academic Press, New York, New York.

In-Situ Identification of Anti-Personnel Mines Using Acoustic Resonant Spectroscopy

Randy S. Roberts and Roger L. Perry
Defense Sciences Engineering Division
Electronics Engineering

We have presented a novel technique for discriminating between anti-personnel (AP) mines and other buried objects. The technique is based on measuring the acoustic resonant spectrum of a buried object, using a probe to provide an excitation signal and a stand-off radar to detect the object's response. Several experiments were performed on mine-like objects to assess the potential of the identification technique. One set of experiments found spectral features that might be used as the basis for discrimination algorithms. The second set of experiments indicate that the spectra of the objects have a tolerable degree of variability. Taken together, we conclude that it is highly likely that AP mines can be distinguished from other buried objects using acoustic resonant spectra acquired by a stand-off radar.

Introduction

The detection of buried anti-personnel (AP) mines is a problem of tremendous importance in many parts of the world. The International Committee of the Red Cross and Red Crescent Societies estimates that approximately 110 million AP mines have been placed in 64 countries world wide.[1] The disruption to daily life caused by AP mines in these countries is enormous. For example, over the last fifteen years, land mines in Afghanistan have caused 600,000 casualties (one out of fifty Afghans).

In addition to causing direct injuries, land mines often contribute to malnutrition and promote disease in a population. For example, safe drinking water can be denied to a village where there is a mere suspicion of a land mine field. The village might therefore use unsafe supplies, increasing the risk of dysentery. Similarly, land mines can easily remove farmland from production, increasing the risk of malnutrition.

Modern AP mines are surprisingly simple, effective, and insidious devices. They tend to be cylindrical in shape, with diameters ranging from 6 to 15 cm, and heights from 3 to 6 cm.[2] They often have simple pressure-sensitive triggers, requiring a mass of 3 to 25 kg for detonation. The explosive charge is typically 50 to 200 gm of TNT. This amount of explosive can cause serious injury to an adult, such as the destruction of a foot or leg, and it can kill small children.

Modern mines contain very little metal, and thus are very difficult to locate with conventional metal detection instruments. Operationally, they are buried in soil to a depth of 1 to 4 cm, and laid out in a variety of patterns, depending on the application. They are very robust devices, and can remain operational for decades after planting.

Conventional demining techniques are time-consuming, labor-intensive and dangerous.[2] Due to its thoroughness and effectiveness against minimum-metal mines, manual probing is the most widely used demining technique in the world.

For clarification, we note that we draw a distinction between humanitarian demining and mine field clearing. Mine field clearing refers to a military unit breaching a mine field. Often, this is accomplished by a simple linear path through the field. Speed is of the essence. Safety and thoroughness of mine removal are secondary. In contrast, humanitarian demining calls for clearing large areas of terrain, and thoroughness of mine removal is paramount (as is the safety of the demining crew). Speed is a secondary concern.

In manual probing, a deminer pushes a probe into the ground at a shallow angle. The probe is lifted slightly and extracted. A deminer trained in this technique can feel a mine above the probe as it is lifted and extracted. To ensure that all AP mines in an area are detected, probing is performed over a 3-cm-×-3-cm grid. With this type of search pattern, one deminer can clear approximately one square meter of land per day.

Emerging mine detection techniques include infrared sensing for wide area detection, olfactory and chemical sensors for explosive detection, and ground-penetrating radar for detecting buried objects. Of these techniques, ground-penetrating radar has shown the most promise.

A current project at Lawrence Livermore National Laboratory (LLNL) seeks to image buried objects using micropower impulse radar (MIR) as an imaging sensor. The idea is to rapidly survey the top layer of soil for objects that have geometric properties similar to AP mines. When such an object is detected, it is marked for probing. The application of such a ground-imaging system would no doubt increase the efficiency of deminers. However, deminers could easily be inundated by the large number of false alarms produced by shrapnel, debris and other objects that produce images similar to AP mines.

In Situ Identification Technique

The technique described here allows a deminer to discriminate between mines and other buried objects *in situ*. It thus provides a means to distinguish AP mines from other buried objects detected by ground-imaging systems. The technique is based on acoustic resonance spectroscopy (ARS), a technology that has been successfully applied to the identification of chemical munitions.[3–5]

The ARS technique is based on the premise that objects of interest, such as AP mines, have characteristic resonant frequencies that we can excite and detect and that are nominally reproducible. Since the resonant frequencies of an object are functions of its geometry and construction materials, it follows that objects of a similar nature will have similar patterns of resonant frequencies. Thus, the frequency response pattern of an object can be used to identify it.

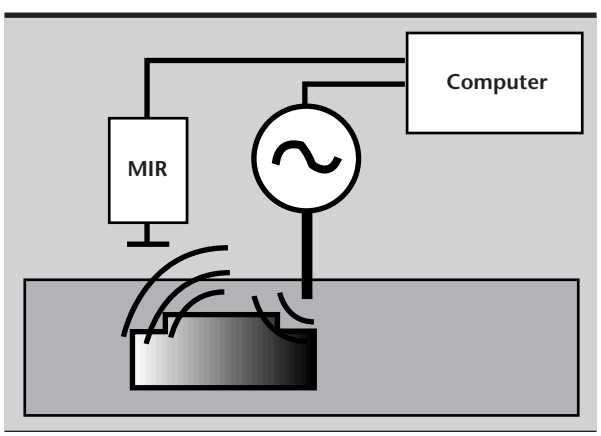

Figure 1. Schematic of the in-situ anti-personnel mine identification technique. A probe excites the buried object with a stepped-frequency sinusoidal signal. The response of the object is received by an MIR system, analyzed, and classified by the computer.

As mentioned, this technique was used with great success in the ARS Munition Classification System (MCS) developed at Los Alamos National Laboratory. An instrument based on this concept was developed, tested, and accepted for use as a verification tool for the 1997 Chemical Weapons Convention.

There are several ways to estimate the acoustic resonance spectrum of an object. In the case of an AP mine, the objective is to obtain the spectrum in the most non-invasive manner possible. **Figure 1** is a schematic diagram of the technique.

To begin with, an excitation force spanning the frequency band containing the resonances is applied to (or near) the object. The magnitude of the excitation force does not need to be large to obtain a useful spectrum. In the case of the ARS-MCS, the excitation force is provided by a piezoelectric transducer. The induced vibrations on the munition have amplitudes on the order of 10 nm.

For AP mines, a simple approach is to touch the object with a probe that produces low amplitude vibrations over the frequency band of interest. Although this requires contact with the object, it is perhaps the best way to excite the object's resonant frequencies. And as previously noted, touching mines with a probe is accepted practice with deminers.

With regard to the form of excitation signal, a narrow-band sinusoid stepped over the frequency range of interest has a major benefit: the tone provides a coherent reference for processing the received signal. A coherent reference can be used to increase the signal-to-noise ratio of the returned signal, and can also be used to extract phase information.

To collect the frequency response of the object, a sensor is required to detect the object's vibrations. In general, radar is well suited for the non-invasive sensing of vibrations. In particular, the MIR technology invented at LLNL provides a unique means of non-contact, stand-off vibration sensing.[6]

Even though the objects of interest are buried, the burial depths are shallow enough that a low power radar should have little problem sensing the vibrations. By using localization information provided by the LLNL MIR ground-imaging radar, the range gate and other parameters on the vibration

sensing radar can be adjusted to maximize the signal-to-noise ratio of the returned signal.

Progress

We have conducted several experiments to assess the feasibility of the identification technique. The experiments consisted of measuring the acoustic resonant spectrum of several objects over a limited frequency range. The measurements were collected with unburied objects to maximize the signal-to-noise ratio.

Four objects of similar geometry were used in the experiments (**Fig. 2**). The first object was an inert M14 mine; the second a nondescript mine detection target (MDT); and the third object, serving as debris, was a galvanized pipe covered with duct tape. A fourth object, not pictured, which also served as debris, was a plastic can containing PlayDough.®

The M14 surrogate is made of a hard plastic, roughly cylindrical in shape and approximately 4.3 cm in height, and 5.2 cm in diameter. The MDT is also made of hard plastic, and is approximately 3.5 cm in height, and has a diameter of 7.5 cm. The pipe is 8 cm in height and has a diameter of 6 cm., and the PlayDough® a cylindrical plastic can approximately 6.1 cm in diameter and 8 cm in height.

The objects were secured in a wooden cradle for the experiments. The excitation signal was provided by an HP35670A signal generator. That signal was amplified and applied to a Wilcoxan F4 vibrator. A probe approximately 1 ft in length was attached to the vibrator, and touched to the sides of the objects. (See **Figs. 3** and **4** for photographs of the experimental arrangement.)

Object vibrations were sensed by a low-power MIR. The radar was placed 60 mm from the surfaces of the objects, in an orientation perpendicular to the surface. Both the drive signal from the HP generator and the return signal from the MIR were digitized at a 40-kHz sampling rate.

Spectra from the objects were collected over the frequency ranges 50 to 100 Hz, 100 to 200 Hz, and 200 to 400 Hz. In each band, the frequency of the drive signal was stepped over approximately thirty tones, each with a duration of 1.5 s. The response signals from the radar were re-sampled to 10 kHz, normalized to the maximum amplitude of the excitation signal, and Fourier transformed.

Magnitude plots of the frequency responses in the 200 to 400 Hz excitation band are shown in **Fig. 5**. The upper plot is the response of the M14 AP mine, the middle plot the response of the MDT, and the lower plot the response of the pipe. Notice that the three objects produce distinguishable spectra over this frequency range.

The M14 produces a large response in the 325 to 400 Hz region, whereas the responses of the other

Figure 2. Objects used in the preliminary experiments (PlayDough® not shown). On the left is an inert M14 mine; in the center is a nondescript mine detection target; and on the right is a pipe covered in duct tape.

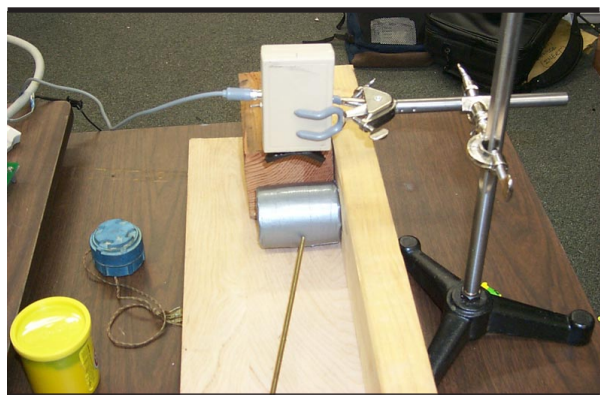

Figure 3. Experimental apparatus used to measure the acoustic resonant spectrum of surrogate mines and debris. The object under inspection is a small pipe covered with duct tape. The MIR system (above the pipe) is typically used for speech analysis.

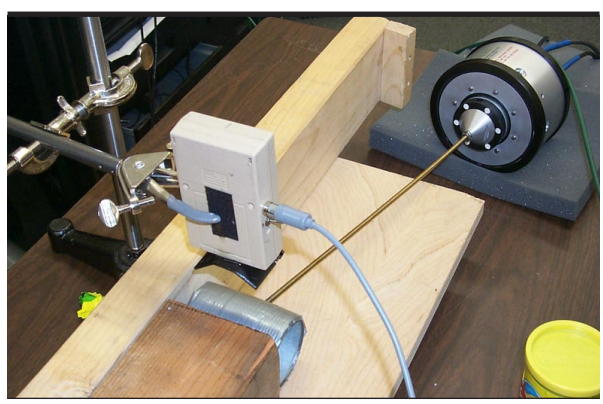

Figure 4. Another view of the experimental apparatus. The probe is attached to a vibrator that provides an excitation signal to the object.

two objects are much more subdued. In contrast, the 275 to 325 Hz band of the M14 is slightly depressed compared to the same band in the other objects. The responses in the 200 to 275 Hz band are somewhat similar in that they all tend to increase as the frequency increases from 200 to 250 Hz. The mine surrogate and the pipe have similar responses in the 275 to 400 Hz bands with a noticeable spike in the pipe's response at 275 Hz, and null at the same frequency as the mine surrogate.

The other frequency ranges contained similar spectral features. As an aside, spectra from the can of PlayDough® are uninteresting, containing few features. Lack of features in the PlayDough® spectra is not unusual since PlayDough® and its plastic container are non-rigid. Most of the excitation energy is absorbed by the PlayDough®, leaving little response signal.

In addition to the experiments described above, several experiments were performed to assess the variability of the spectral measurements. The experiments consisted of multiple measurements of the spectra of the objects over a 200 to 500 Hz band. The multiple measurements were graphed on a raster plot for comparison. The spectra showed some degree of variability, but overall the measurements appeared repeatable.

Future Work

Although our preliminary experiments indicated the feasibility of this approach to AP mine identification, several critical issues remain. These issues include the structure of the resonant spectra of AP mines and similar objects in the frequency range above 1 kHz, the variability of the resonant spectra, and collecting spectra from buried objects.

We estimate that the resonant frequencies of the M14 mine and MDT occur at approximately 1.2, 4.8, 10.8, … , kHz.[7] (A similar set of resonant frequencies occurs for the pipe and PlayDough.®)

The radar that we used in the first set of experiments had an upper frequency range of approximately 1 kHz. As a result, we were unable to investigate the region above 1 kHz, where potentially unique information about AP mines (that is, their resonant peaks) is located. Concerning spectral variability, robust discrimination algorithms depend

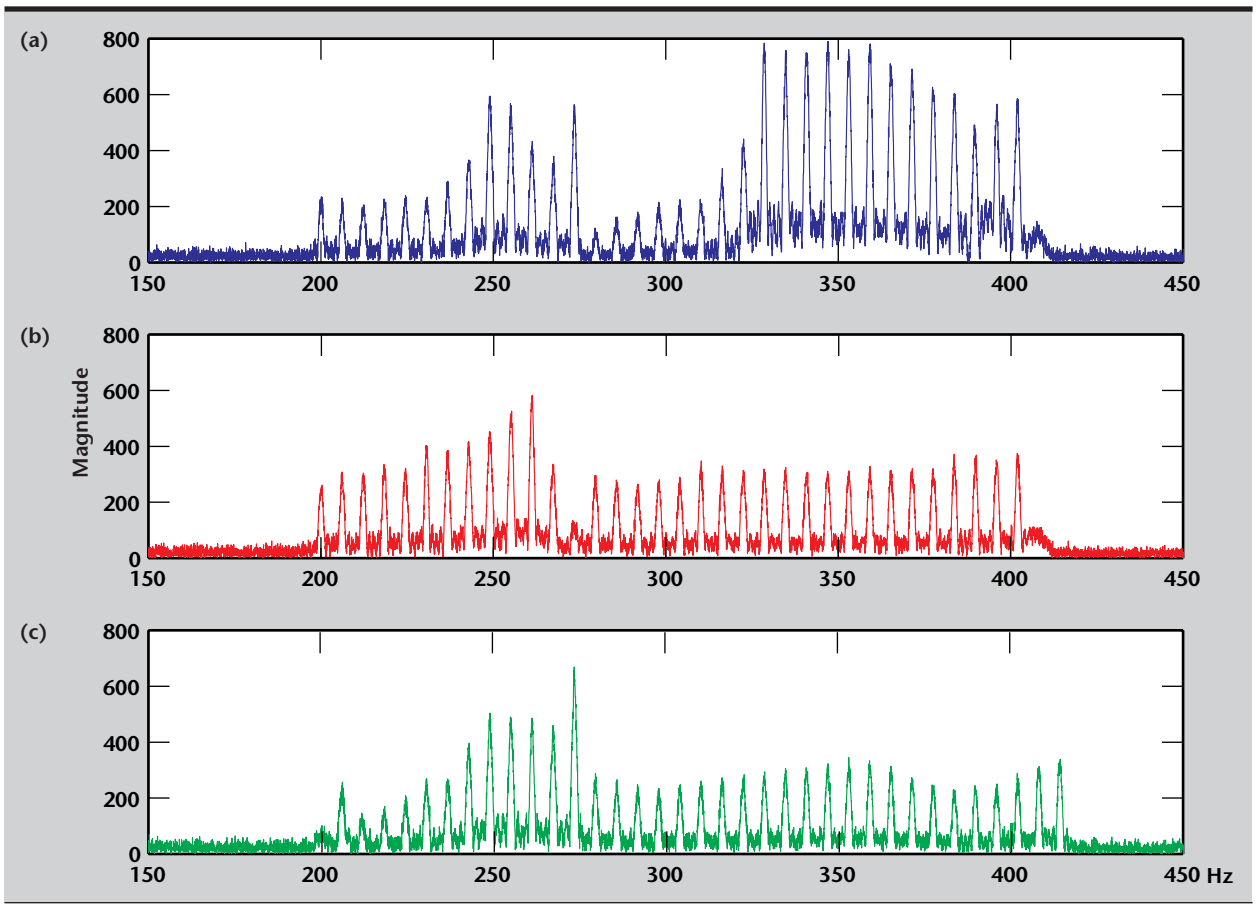

Figure 5. Magnitude vs frequency plots of the three objects in Figure 1: (a) the M14 AP mine, (b) the mine detection target, and (c) the pipe.

on spectral features that can be reliably extracted from resonant spectra. The greater the variability of the resonant spectra, the less reliable the spectral features, resulting in poor discrimination. We collected some data to assess spectral variability, but a large ensemble of spectral data is required for a full assessment.

Finally, although our experiments have laid the groundwork for this identification technique, the measurement of spectra from buried objects remains to be performed. This set of experiments would collect spectra from objects similar to the ones used here, but buried in a variety of soils, such as sand, rock, and clay, and under a variety of conditions, dry to very wet.

We conclude this section with thoughts on the automated pattern classification of spectra and the future of algorithm development.

Automated pattern classification is necessary to provide deminers with confidence in the technique. From the deminer's point of view, the processing should produce a binary decision ("yes, the object is a mine," or "no, the object is not a mine"), along with a numerical measure of confidence.

The key to providing such a decision to the deminer resides in the object's spectral features. If invariant spectral features can be found, clustering techniques can be used for classification. Such was the case in the ARS-MCS liquid-solid discrimination algorithm, where features extracted from the spectra of liquid- and solid-filled munitions grouped into two clusters, one for solids, and one for liquids.

If the spectral features tend to be variable (due to factors such as soil conditions and the age of the mine), a comparative approach can be used. Such was the case in the ARS-MCS munition classification algorithm, where spectral features of different chemical munitions (in this case, the frequencies of resonant peaks) tended to vary. The munition classification algorithm compared spectral features from the unknown munition to templates of spectral features built from known munitions. (The templates quantified the variability of the spectral features.)

While the algorithms developed for the ARS-MCS may not be directly applicable to the proposed project, they form a strong foundation for future algorithm development.

Acknowledgments

The authors would like to thank J. Holzrichter and G. Burnett for the use of their MIR and data acquisition systems, and T. Woehrle for the use of equipment in LLNL's Modal Analysis Laboratory.

References

1. U.S. Army Communications Electronics Command, Night Vision and Electronic Sensors Directorate, Countermine Division, *Humanitarian Demining* (1998). http://www.demining.brtrc.com. Also see *Direct and Indirect Consequences of Land Mines on Public Health*, http://www.demining.brtrc.com/contents.htm.

2. *Jane's Mines and Mine Clearing* (1997), C. King, ed., Jane's Information Group Inc., Alexandria, Virginia.

3. Roberts, R. S., J. T. Chen, O. A. Vela, and P. S. Lewis (1993), "Munition Classification Using an Acoustic Resonance Spectroscopic Technique," *Proceedings of the Twenty-Seventh Annual Asilomar Conference on Signals, Systems, and Computers*, Pacific Grove, California, November 1–3.

4. Roberts, R. S., P. S. Lewis, J. T. Chen, and O. A. Vela (1994), "Techniques for Classifying Acoustic Resonant Spectra," *Proceedings of the Twenty-Eighth Annual Asilomar Conference on Signals, Systems, and Computers*, Pacific Grove, California, October 30–November 2.

5. Roberts, R. S., P. S. Lewis, and O. A. Vela (1995), "A Pattern Recognition Algorithm for the Blind Discrimination of Liquid- and Solid-Filled Munitions," *Proceedings of the Twenty-Ninth Annual Asilomar Conference on Signals, Systems, and Computers*, Pacific Grove, California, October 29–November 1.

6. Holzrichter, J. F., G. S. Burnett, L. C. Ng, and W. A. Lea (1998), "Speech Articulator Measurements using Low Power EM-wave Sensors," *J. Acous. Soc. Am.* **103** (1) p. 622, January.

7. Skudrzyk, E. (1966), *Simple and Complex Vibratory Systems*, Pennsylvania State University Press, University Park, Pennsylvania.

An Acoustic Technique for the Non-Invasive *In-Situ* Measurement of Crystal Size and Solution Concentration

Diane J. Chinn and Paul R. Souza
Manufacturing and Materials Engineering Division
Mechanical Engineering

Harry F. Robey
Laser Programs

We demonstrated the use of acoustic measurements for tracking potassium dihydrogen phosphate (KDP) crystal growth. Both KDP solution concentration and KDP crystal size can be found by using information derived from acoustic wave propagation in the solution. Acoustic measurements show good correlation to conductivity measurements for KDP solution concentration.

Introduction

The National Ignition Facility (NIF) at Lawrence Livermore National Laboratory (LLNL) is currently developing rapid growth techniques for potassium dihydrogen phosphate (KDP) single crystals. NIF requires over six hundred KDP optical components, sized about 0.4 m^2, for optical switching and frequency conversion of the beam line. Rapid boule growth rates of approximately 10 to 15 mm/day are necessary to produce the large number of KDP optical components at a reasonable cost. While conventional growth methods would take more than one year to grow a KDP crystal of the size required, NIF scientists are developing a technique to grow the crystal in approximately eight to ten weeks.

Crystals are grown from a point seed in a highly supersaturated solution of KDP. The supersaturation level of the solution is the primary operational parameter used to determine the growth rate of the crystal.[1] Thermal control of KDP solution is used to keep supersaturation at desired levels. Fast growth rates of such large crystals requires stringent controls on the KDP solution concentration.

Several techniques are commonly used to determine solution concentration in crystal growth. The current method uses visual measurement of the KDP crystal size. Given the known solid density of the KDP crystal, the mass of salt in the crystal, removed from solution is estimated. Subtraction of this estimated value from the initial starting salt gives the solution concentration as a function of time.

This method is rather inaccurate because visual crystal sizing is accurate to only 1 to 2 mm. Other methods using density (from buoyancy), refractive index, and electrical conductivity are also commonly used commercially by crystal growers to determine solution concentration. Generally, solution concentration is determined from empirical relationships of the measured properties. These commercial techniques all require access to the solution. Acoustic measurements offer the possibility of a non-invasive technique for monitoring crystal growth. High-frequency acoustic measurements have the advantage of non-invasively obtaining information about the solution concentration and crystal size during the growth process.

This work assessed acoustic velocity as a diagnostic for KDP crystal growth. Electrical conductivity measurements for solution concentration are used as a comparison. Acoustic velocity measurements are also tested as a means of sizing the crystal during growth.

Progress

We designed a probe to empirically determine the relationship between acoustic velocity and temperature and concentration of KDP solution. Used for determining the empirical relationship, this probe is

designed to operate invasively in the solution. After determining the empirical relationships, acoustic measurements can be made non-invasively from outside the solution.

Figure 1 shows a sketch and a photograph of the probe and the measured acoustic waveform. A 15-MHz ultrasonic transducer mounted on top of the probe sends a wideband pulse (bandwidth = 55 %) propagating into the probe. Fabricated from fused silica, the probe has threaded sides to disperse diffracted waves incident on the sides.

Notched into the probe is a 10-mm gage length. The low coefficient of thermal expansion of fused silica ensures that the gage length remains constant through the temperature range of KDP supersaturation. A pulsed acoustic wave travels roundtrip from the transducer, into the probe, through the solution within the gage length and back to the transducer through the probe. Travel time of the pulse through the KDP solution gives the acoustic velocity. The wideband 15-MHz ultrasonic pulse permits high temporal resolution of the acoustic velocity in the KDP solution. The probe can discern changes as small as 0.25% in acoustic velocity.

In fluids, acoustic velocity is directly related to density. For example, empirical relationships in sea water show that acoustic velocity increases linearly with salinity and as a second-order polynomial with temperature.[2] KDP solution should follow acoustical relationships similar to those found in sea water.

Figure 2 shows acoustic velocity and conductivity data for different concentrations of KDP solution. Curve fitting indicates that acoustic velocity is related to temperature through a second-order polynomial. At a given temperature, velocity increases with solution concentration. The data show that acoustic velocity peaks between 60 °C and 65 °C for all concentrations. From linear regression at T = 60 °C,

$$v(C_0) = 0.6414C_0 + 1.534, \quad (1)$$

where C_0 = solution concentration and $v(C_0)$ = acoustic velocity.

For a fixed concentration, conductivity increases linearly with temperature, as expected. At T = 65 °C,

$$c(C_0) = 379.7C_0 + 82.9, \quad (2)$$

where $c(C_0)$ = conductivity.

Empirical equations derived from curve fitting for normalized velocity and concentration are shown in

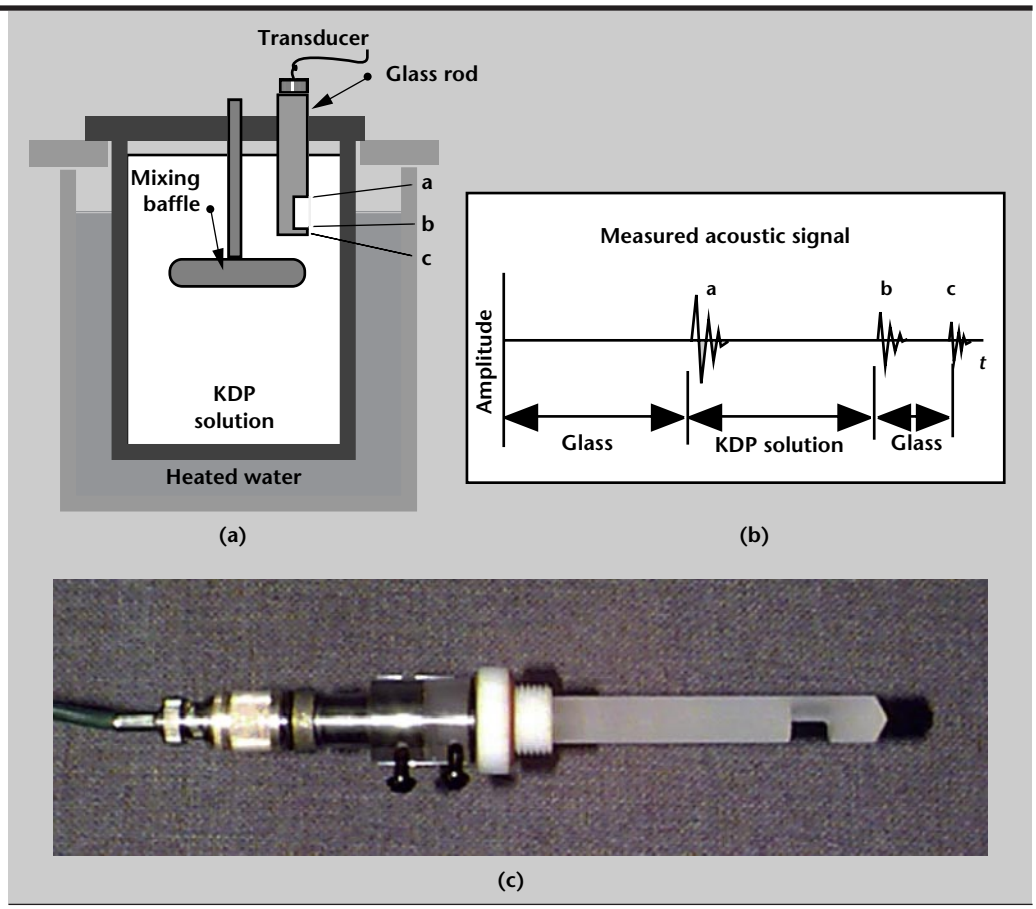

Figure 1. Probe and waveform. Attached to a 15-MHz transducer, the fused silica probe with 10-mm gage length is placed in the KDP solution to measure acoustic velocity: (a) measurement configuration; (b) measured acoustic signal; and (c) photograph of the probe. Three reflections from the probe are measured in the signal. Velocity is found from the travel time in the KDP solution.

Fig. 3. In **Fig. 3a**, measured velocity, $v_{measured}$, is normalized to $v(C_0)$ by the equation

$$v^*(T) = \frac{v_{measured}}{v(C_0)}, \quad (3)$$

where $v^*(T)$ is normalized velocity. In **Fig. 3b**, conductivity is normalized to $c(C_0)$ by the equation

$$c^*(T) = \frac{c_{measured}}{c(C_0)}, \quad (4)$$

where $c^*(T)$ is normalized conductivity.

Conductivity shows better correlation to concentration (R = 0.99976) than velocity (R = 0.9106), though for some applications, the non-intrusive nature of the acoustic technique may be of more importance than the small loss in accuracy of the measurement. Also, the conductivity probe is very sensitive to the presence of bubbles on its measurement surface, which strongly affect the conductivity reading.

The empirical equations shown in **Fig. 3** are useful for *in-situ* continuous monitoring of the solution concentration. Given a temperature, these equations allow us to relate measured values of velocity and conductivity to concentration.

Crystal size in solution is currently measured visually with a telescope and a scale mounted to the side of the tank. The resolution currently obtainable is approximately 1 to 2 mm. Acoustic measurements of crystal size were performed with the configuration sketched in **Fig. 4**. In this configuration, transducers are mounted on the outside of the KDP solution tank. The arrival time of the reflected wave

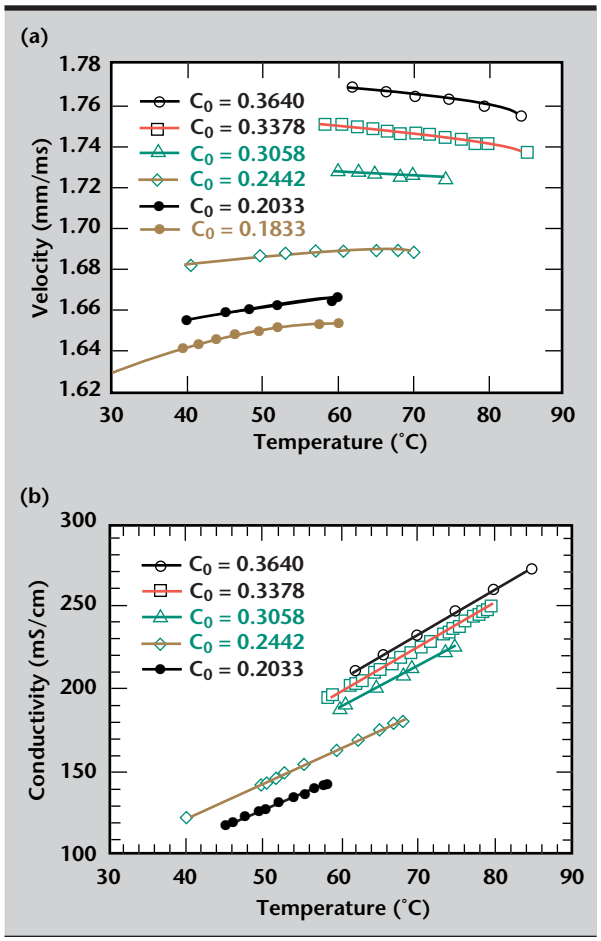

Figure 2. Acoustic velocity (a) and conductivity (b), measured at different temperatures and concentrations. For a given concentration, velocity follows a second-order polynomial fit, while conductivity increases linearly with temperature.

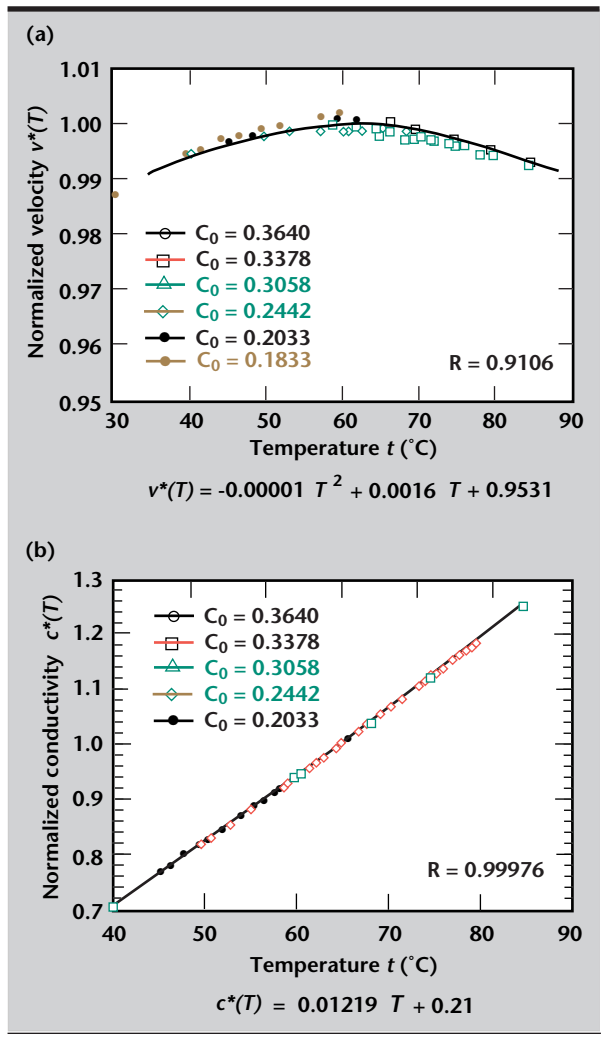

Figure 3. Normalized velocity (a) and normalized conductivity (b) derived from empirical equations. Velocity and concentration are normalized for concentration according to Eqs. 1 and 2. Velocity follows a second-order polynomial fit with temperature with the maximum velocity occurring at 60 °C. Conductivity fits its empirical equation (R = 0.99976) better than velocity (R = 0.9106).

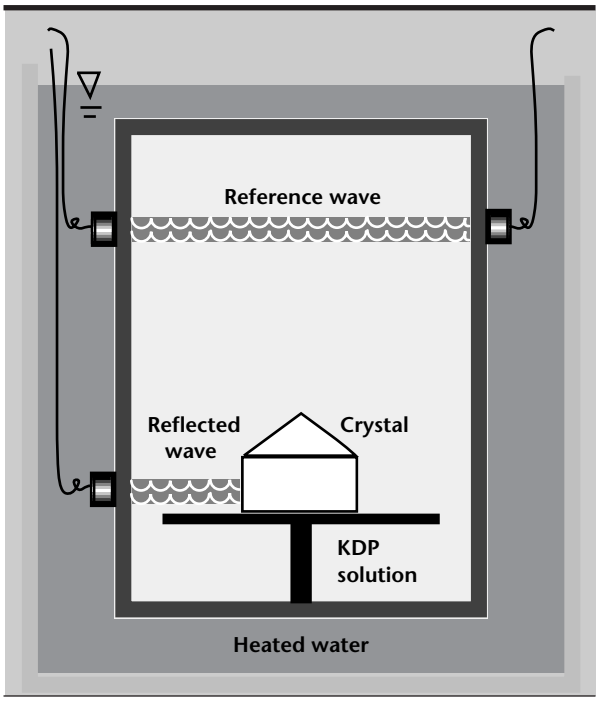

Figure 4. Illustration of acoustic techniques as a non-invasive diagnostic for crystal growth. Solution concentration is found from a reference wave propagating through the solution. Crystal size is derived from the travel time of the reflected wave from the crystal.

from the crystal face is calibrated to the arrival time of the reference wave. This technique is sensitive to approximately 0.1-mm changes in crystal size, resulting in a factor of 10 improvement.

The configuration in **Fig. 4** shows a non-invasive method of measuring solution concentration in addition to crystal size. Acoustic velocity is obtained from the reference signal. Given the temperature and acoustic velocity, the solution concentration can be determined using the empirical relations in **Fig. 3**.

Summary

Acoustic measurements have proven to be a viable, continuous, in-process diagnostic technique for crystal growth. The technique has no adverse effect on the solution. Acoustic velocity measurements for solution concentration correlate well with electrical conductivity measurements. This work developed a supplemental tool for the continuous measurement of both KDP solution concentration and crystal size.

Future Work

Because of its ultimate simplicity and minimal cost, visual observation is currently the method being used to determine crystal size during growth. Solution concentration, however, is being measured only before and after the crystal growth run. It would be very desirable to have continuous measurement capability to obtain this quantity throughout the growth run.

This work demonstrated the feasibility of using acoustic measurements for determination of the solution concentration. Additional work is needed, however, to minimize the cost of a fielded acoustic measurement system and to provide a more convenient operator interface for converting the raw acoustic signals to a direct reading of solution concentration.

References

1. Cooper, J. F., and M. F. Singleton (1985), "Rapid Growth of Potassium Dihydrogen Phosphate Crystals," Lawrence Livermore National Laboratory, Livermore, California (UCRL-91795).

2. Birks, A. S., and R. E. Green (1991), "Nondestructive Testing Handbook, Ultrasonic Testing," Vol. **7**.

Micro-X-Ray Computed Tomography for PBX Characterization

Diane J. Chinn, Jerry J. Haskins, Clinton M. Logan, Dave L. Haupt, and Scott E. Groves
Manufacturing and Materials Engineering Division
Mechanical Engineering

John Kinney
Materials Science and Technology Division
Chemistry and Materials Science

Amy Waters
Department of Material Science
Johns Hopkins University
Baltimore, Maryland

We compared two micro x-ray computed tomography systems for use in the characterization of plastic-bonded explosive microstructure. This comparison will help guide the development of a technique to generate an accurate structural model of plastic-bonded explosive from nondestructive x-ray tomographic scans.

Introduction

Current efforts to characterize the weapons stockpile have produced heightened interest in the aging mechanisms of plastic-bonded explosives (PBX). Structural modeling offers one method of understanding the aging process. Accurate modeling of PBX crystal and binder components requires a realistic 3-D characterization of the microstructure.

X-ray computed tomography (CT) is an advanced imaging technique that provides 3-D characterization of materials for nondestructive evaluation. *In-situ* characterization of structures and components makes CT an attractive method for analyzing existing parts and components. Recent developments in hardware have permitted CT imaging with micron spatial resolution.

In addition to geometric characterization, CT offers quantitative information on the linear x-ray attenuation of component materials. Related to source energy, material density, and chemical composition, x-ray attenuation can be used to identify and characterize different phases in materials.

Progress

We investigated the use of CT for microstructural characterization of PBX. Two CT systems, KCAT and XTM, were used to quantify the structure of a 2-mm-diameter sample of mock PBX. Component materials of mock PBX do not have the same x-ray attenuation as PBX. However, the microstructure of mock-PBX approximates PBX.

The x-ray tomographic microscope (XTM) at Lawrence Livermore National Laboratory (LLNL) uses beam line 10-2 at the Stanford Synchrotron Radiation Laboratory (SSRL). Located at the Stanford Linear Accelerator Laboratory (SLAC), the XTM facility contains a 15-keV monochromatic synchrotron radiation source tomography system.[1,2] The XTM system scanned the mock-PBX sample at 5 μm full-width half-maximum (FWHM) of the point spread function spatial resolution.

Recently developed by the Nondestructive Evaluation (NDE) Section at LLNL, the high-resolution KCAT x-ray tomographic system uses a polychromatic source.[3] The mock-PBX sample was scanned at an energy of 60 keV peak at 10 μm FWHM spatial resolution.

Figure 1 shows CT slices of the 2-mm-diameter sample from each of the systems. KCAT data is shown in **Fig. 1a**, XTM data is shown in **Fig. 1b**. The slices are representative slices taken at different locations on the sample. Because of higher spatial resolution and higher contrast sensitivity, the XTMslice in **Fig. 1b** provides sharper edges and better contrast of the component structures than the KCAT slice.

Histograms of linear attenuation values for each of the systems are shown in **Figs. 1c** and **1d**. Attenuation values in the XTM data show four distinct phases in the sample. The KCAT data does not distinguish separate phases in the attenuation histogram.

Mock PBX consists of four phases: talc, Kel-F, cyanuric acid, and voids. Expected attenuation values for these component materials at discrete energies ranging from 10 to 100 keV are calculated and presented in **Fig. 2**. For the monochromatic XTM energy of 15 keV, expected attenuation values are 14 cm^{-1} for talc, 12 cm^{-1} for Kel-F, 3.4 cm^{-1} for cyanuric acid, and 0 cm^{-1} for void space. These values are based on 100% density. It should be noted that *in-situ* density of the component materials can deviate substantially from 100% density. Consequently, *in-situ* attenuation values can be different from the expected attenuation values.

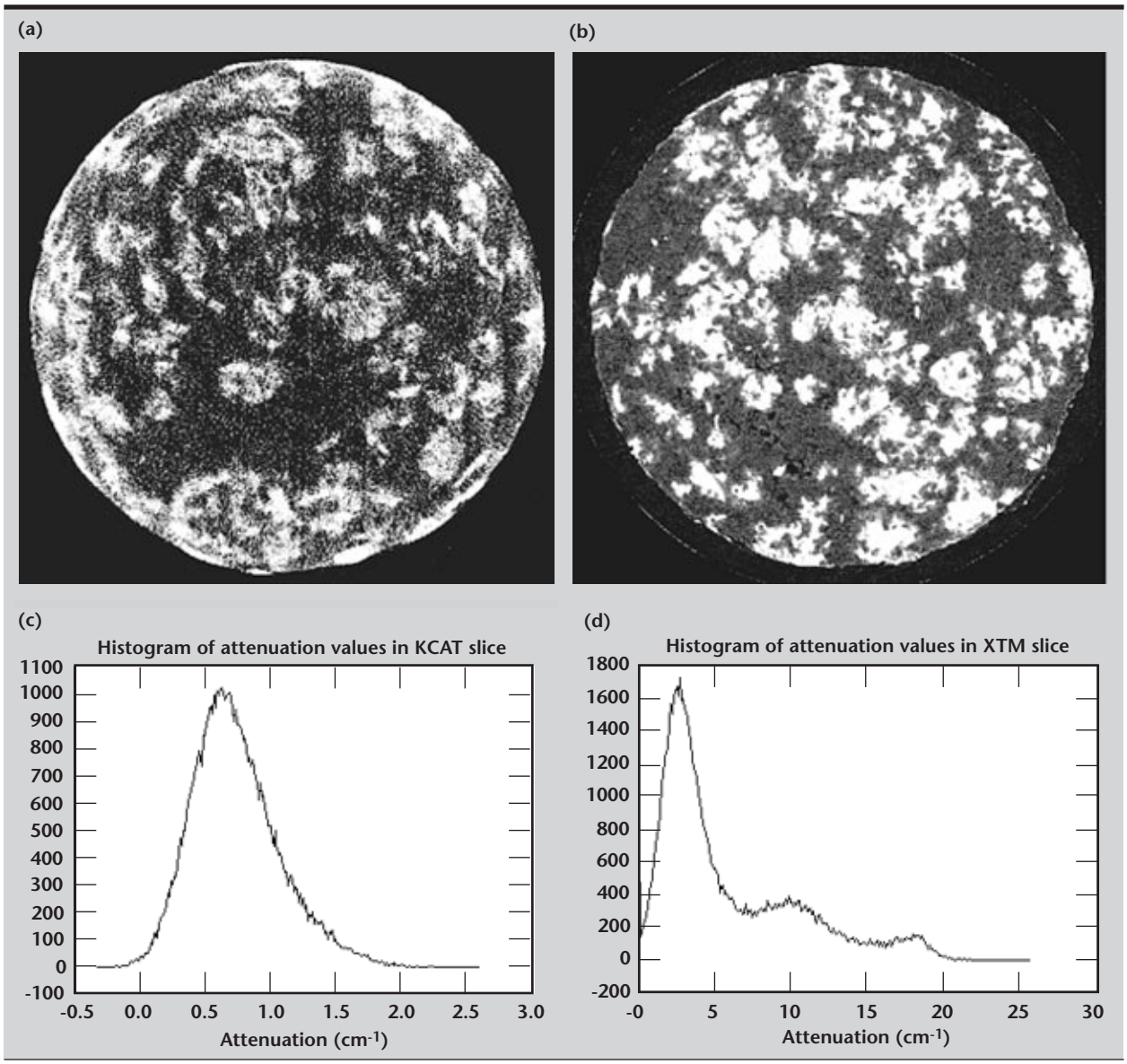

Figure 1. KCAT (a) and XTM (b) representative slices, showing the difference in the systems. Histograms of attenuation values in KCAT slice (c) and XTM slice (d) show the difference in contrast sensitivity from the two systems.

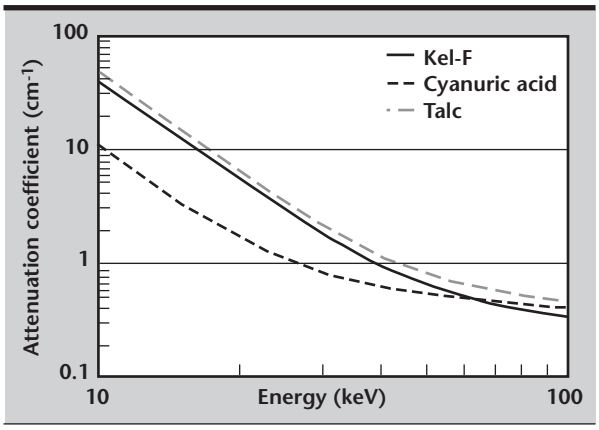

Figure 2. Calculated linear attenuation coefficient vs energy for three of the four components of PBX, plotted for comparison to the experimental results. Attenuation is calculated from chemical compositions and density, where Kel-F = $H_2C_8F_{11}C_{13}$ at 2.02, cyanuric acid = $H_{10}C_3N_3O_2$ at 2.50, and talc = $H_2O_{12}Si_4Mg_3$ at 2.78.

In **Fig. 3**, the four phases of the sample from the XTM scan are segmented from a region of interest (ROI) according to attenuation values. Segmentation reveals the morphology of each of the components. **Table 1** shows the range of attenuation values for each of the phases in the ROI. The range of the measured attenuation values in the scan in **Table 1** fits well within the range of the expected attenuation values for each of the component materials and allows the identification of each of the phases.

Although the KCAT slice in **Fig. 1b** shows some features of the microstructure, distinct phases are not readily identifiable in the histogram in **Fig. 1c**. Unlike the monochromatic XTM source, the polychromatic KCAT source energy ranges from 0 to 60 keV. **Figure 2** shows the range of attenuation values for each of the component materials. Contrast sensitivity between the phases is diminished by using a polychromatic source. As a result,

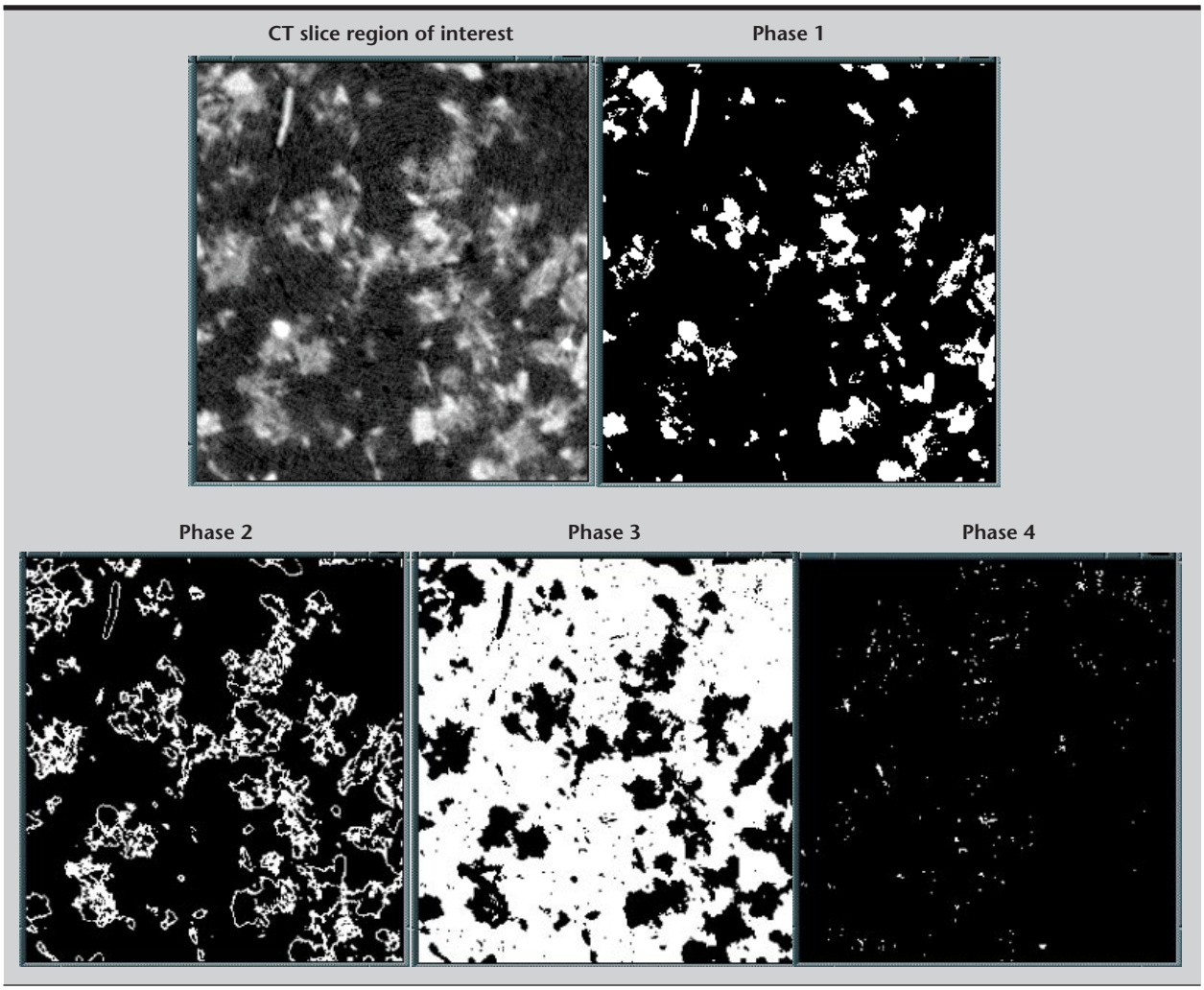

Figure 3. Segmentation of the XTM slice, showing morphological information of the phases. This segmentation is based on one feature, linear attenuation. The original XTM data and all segmented phases (indicated by white areas) are as labeled.

Table 1. Attenuation values in the XTM data.

Phase	Attenuation (cm^{-1})	Slice area (%)	Size (μm)
1. Talc	12.4–22	11.7	7.5–35
2. Kel-F	7–12.4	15.6	10.5–128
3. Cyanuric acid	0.1–7	71.2	—
4. Void	0–0.1	0.7	3.5–30

the phases in the sample are difficult to identify based on their measured attenuation values.

Summary

Micro-CT was assessed for use in the 3-D characterization of PBX microstructure. Comparison of two micro-CT systems indicates that a monochromatic source with 5-μm FWHM spatial resolution provides sufficient spatial resolution and contrast sensitivity to characterize and identify mock-PBX microstructure. Our initial attempt to use a polychromatic source at 10 μm spatial resolution allows imaging of the microstructure but does not easily permit identification of phases in mock-PBX.

Future Work

The XTM micro-CT system is not readily available to LLNL's NDE Section and as such is not an easy option in PBX characterization. This project sought to determine the viability of the KCAT system, a system readily available, for PBX characterization.

Several modifications and processing techniques can be used to improve the sensitivity of the KCAT system to PBX microstructure. The KCAT source spectrum can be modified to a spectrum more appropriate for distinguishing the materials in PBX. This can be accomplished by reducing the peak energy and filtering the source. Spatial resolution can also be improved. A plan for improving spatial resolution of KCAT has been developed and awaits funding.

In addition, image processing techniques can be used to identify phases. Preliminary processing indicates that curve-fitting the attenuation histogram, thereby forcing attenuation values into four phases, may help segment different phases of PBX. Edge enhancement routines can help sharpen the image, improving characterization of the microstructure.

Acknowledgments

Some of this work was performed at SSRL, which is funded in part by the U.S. DOE/ Chemical Sciences.

References

1. Kinney, J. H., and M. C. Nichols (1992), "X-ray tomographic microscopy using synchrotron radiation," *Annual Reviews of Materials Science*, **22**, pp. 121–152.

2. Kinney, J. H., D. L. Haupt, M. C. Nichols, T. M. Breunig, G. W. Marshall, and S. J. Marshall (1994), "The x-ray tomographic microscope: 3-D perspectives of evolving microstructure," *Nuclear Instruments and Methods in Physics Research A*, **347**, pp. 480–486.

3. Martz, H., J. Haskins, C. Logan, D. Perkins, D. Rikard, R. Roberts, D. Schneberk, S. Sengupta, and E. Updike (1998), "CT characterization of CVIT-II/III (U)," Lawrence Livermore National Laboratory, Livermore, California (UCRL-ID-130261), June.

Evaluation of an Amorphous Selenium Array for Industrial X-Ray Imaging

Clinton M. Logan, Jerry J. Haskins, Kenneth E. Morales, and Earl O. Updike
Manufacturing and Materials Engineering Division
Mechanical Engineering

James M. Fugina and Anthony D. Lavietes
Defense Sciences Engineering Division
Electronics Engineering

Daniel J. Schneberk
Computer Applications Science and Engineering Division
Computations

Gregory J. Schmid
Isotope Science Division
Chemistry and Materials Science

Keo Springer
Applied Research Engineering Division
Mechanical Engineering

Peter Soltani
Liberty Technologies, Inc.
Conshohocken, Pennsylvania

Kenneth Swartz
Sterling Diagnostic Imaging
Newark, Delaware

The large market for digital x-ray imaging in medicine has driven the development of flat panel imaging devices. We evaluated one such device using the higher energy x rays typical of industrial applications. This imager is a 360-mm-×-430-mm array using amorphous selenium (amSe). The defining characteristic of this technology is that electrons produced by radiation interaction in the Se are directly collected and processed with no intermediate scintillation or other conversion process. Comparing performance to existing technology, we found 1) the modulation transfer function (MTF) remains high as spatial frequencies approach the limit imposed by the 139-µm pixel size; 2) increasing x-ray energy degrades spatial resolution performance somewhat, but the amSe imager performs well in spectra as energetic as 450-kV applied potential; 3) the MTF of this amSe imager drops rapidly with frequency between 0.0 and 0.1 mm^{-1} for the heavily-filtered spectra used in this study. Secondary radiation transport in material behind the Se is a significant contributor to this attribute; 4) required exposure for the spectra tested ranges from 10 to 100 mR. This is 15 to 100 times less than Lawrence Livermore National Laboratory (LLNL)'s home-built system using scintillating glass and a charge-coupled device (CCD) camera. Cycle time for CT applications will be dominated by read and refresh times of nearly 1 min. This will allow for great flexibility in using microfocus (low power) sources or large source-to-detector distances. Finally, we found 5) except for issues of peripheral electronics, which we did not address, Monte Carlo simulations suggest that this amSe imager could offer attractive performance at x-ray energies of 3 MeV or more.

Introduction

Sterling Diagnostic Imaging (Newark, Delaware) is introducing a new type of x-ray imager for medical imaging. It is designed for use with medical x-ray spectra of about 80-keV average energy. It has an active area (360 mm × 430 mm) equal to standard chest film, with superior speed and spatial resolution. It is packaged into a box not much larger than a film cassette, and packs an impressive 7.5×10^6 pixels with 14-bit data depth.

This new imager uses manufacturing technology similar to that used for flat panel displays. There is a very thin coating of electrical conductor on the radiation side of the panel, followed by 500 μm of amorphous selenium (amSe). Beneath each pixel is a capacitor to store charge and a thin-film transistor for read-out. A voltage of a few kV is applied across the amSe so that when x rays produce ionization in the amSe, the resulting charge moves directly along electric field lines and is collected in the pixel in which the radiation interaction occurs. This is shown schematically in **Fig. 1**.

This direct collection of radiation-induced charge is the most important attribute of this new imager. It converts x rays to electrons, which are then collected and integrated without intermediate conversion to visible light. This eliminates the blurring that inevitably occurs in scintillator-based imagers. The technology is scalable to still higher spatial resolution.

The workhorse system configuration for digital x-ray imaging and computed tomography at LLNL is a scintillating glass that is mirror/lens coupled to a CCD camera. Compared to this technology, we expect amSe to be more portable and to have 1) higher x-ray sensitivity, 2) larger detector area, 3) more pixels, 4) higher spatial resolution (expressed relative to the field of view), and 5) fewer alignment issues.

There are several unknowns with respect to the application of amSe to nondestructive evaluation (NDE) applications. AmSe has only been demonstrated at relatively low x-ray energy used for medical imaging. Most NDE applications use higher-energy x-ray spectra. More energetic x rays will penetrate deeper into and through the panel substrate to the electronic components behind the substrate with unknown effects. Also, resolution may degrade at higher x-ray energy as a result of secondary radiation (x rays and Compton electrons) transport.

In addition, dark current in the imager may be an issue with the longer integration times required for industrial imaging. Finally, x rays must be turned off during read-out. We need to understand the issues associated with computer control of on/off with respect to our x-ray sources.

Progress

We evaluated 1) spatial resolution, 2) dark current, 3) reproducibility, 4) latent image effects, and 5) dynamic range. In addition, we used the Monte Carlo code GEANT to model radiation transport in the detector up to MeV x-ray energies relevant to imaging high opacity objects such as turbine blades, nuclear weapons, and engine components. This work is intended to suggest what the spatial resolution performance might be at MeV energies and indicate possible solutions to shielding the electronics.

We evaluated possible methods for turning x rays on and off for our 450-kV Philips tube and for the 9-MV electron linac.

X-ray Spectra

We acquired data using three different x-ray spectra (**Fig. 2**), filtering to narrow the energy range. The softest x-ray spectrum tested used a tube potential of 120 kV and 76 μm of W filtration; the intermediate a tube potential of 250 kV and 3.2 mm of Cu filtration; the hardest a tube potential of 450 kV and 6.5 mm of Cu filtration.

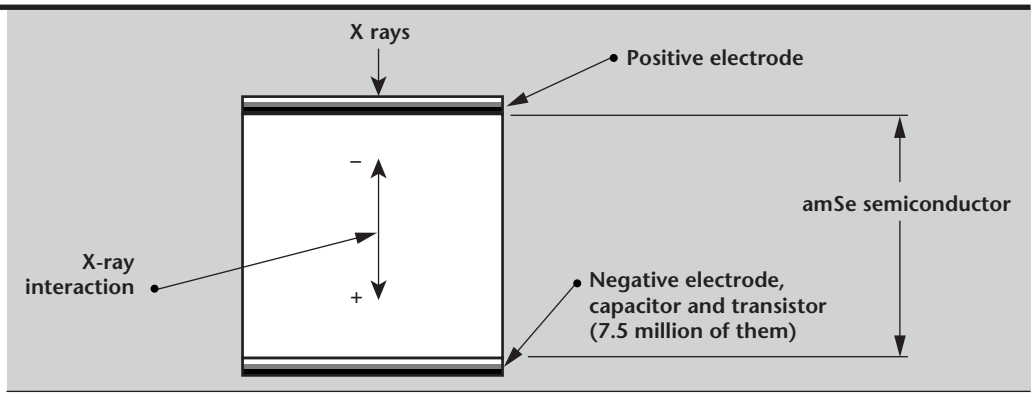

Figure 1. Schematic representation of the layer structure and detection method of an amSe imager.

Source Stability

The amSe imager requires that x rays be absent except during the manufacturer-set interval during which the image is acquired. The only method available to us for these tests was to use the preset exposure-time-mode of the LLNL Philips model 451 x-ray source controller. This method of control causes the high voltage to be ramped up and down to turn x rays on and off. To observe drift or change in x-ray sensitivity of the amSe imager, it was necessary to establish that exposure controlled in this way is sufficiently reproducible. Details of this evaluation are given in Reference 1.

To evaluate the reproducibility of exposure controlled from the tube controller, we ran a series of exposures for both the lowest and the highest kV spectra used for the amSe detector tests. The data indicated sufficient source stability to do the detector characterization without an independent measurement of source output for each image.

Monte Carlo Modeling Results

We used the Monte Carlo code GEANT[2] to model radiation transport in the detector. We chose to model monoenergetic x rays at energies of 70, 120, 170, 450, 3000 and 9000 keV. The first three energies were selected to approximate the effective energies of the polyenergetic spectra that we tested experimentally; 450 keV is the maximum x-ray energy produced in the hardest spectrum we tested (**Fig. 2**); we chose 3000 keV because it is a technologically important energy for large dense objects; and 9000 keV is the end-point of the spectrum produced by our 9-MV linac.

We calculated several configurations to help us understand how the imager might be improved for more energetic x-rays. Results from two configurations are presented here. The first configuration is the array as it exists, while the second explores the effect of adding a Au layer in front of the Se.

The calculated interaction probability for 0.5 mm of Se as a function of photon energy is given in **Fig. 3**. By putting material in front of the Se, it is possible to suppress the response to low energy x rays while possibly increasing the response to high energy x rays. The potential increase at high energy comes from transport of secondary radiation (primarily electrons) out of the Au and into the Se. To have the desired effect, the material should be dense and high-Z. We used computational Au since it is free.

For these calculations, a monoenergetic x-ray source was made incident normal to the detector surface along a line. The structure of the amSe imager was represented by 12 layers of various materials. The Se is 0.5 mm thick in the Sterling Diagnostic Imaging design. GEANT transports secondary photons and electrons. We present here the results of energy deposition in the Se. The problem was zoned so that we could tally energy deposition as a function of distance from the source. We used 10-µm-thick lateral spacing and extended the calculation to a distance of 10 mm from the source. To avoid edge effects, we tallied energy deposition in a central 3-mm band within a 1-cm-wide panel. A schematic of the calculation geometry is shown in **Fig. 4**.

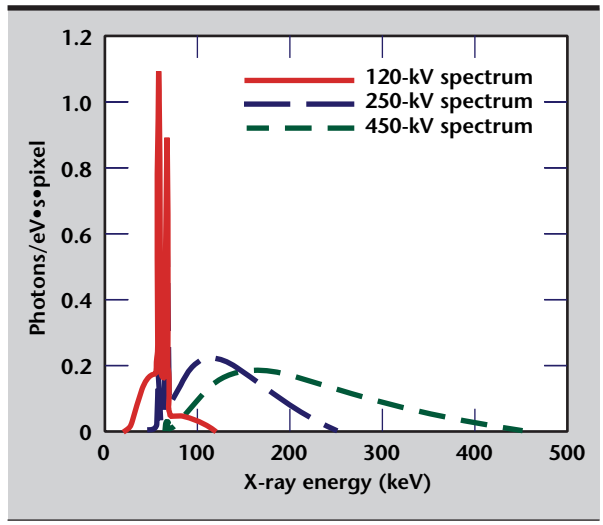

Figure 2. Calculated x-ray spectra used to evaluate and compare imaging systems. Spectra are in units of photons/eV·s into each pixel for the source-to-detector distance and tube current used with the amSe imager. The 120kV, 250kV, and 450kV spectra are integrated over 11, 25, and 37 d photons/s. pixel, respectively.

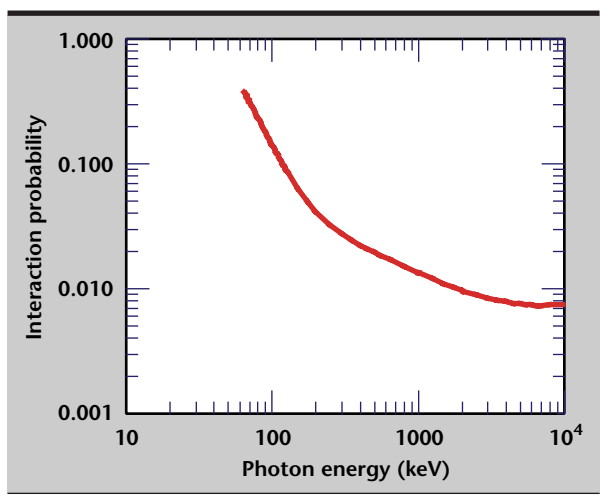

Figure 3. Calculated probability of x ray interacting in a layer of Se 0.5 mm thick.

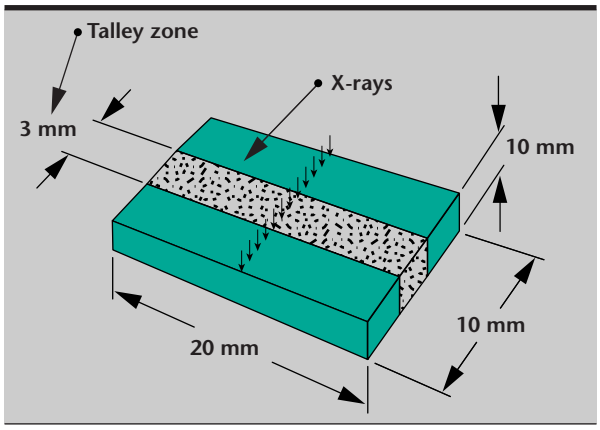

Figure 4. Schematic of configuration used for Monte Carlo calculations. Tally zones are within a 3-mm band centered in a 10-mm band.

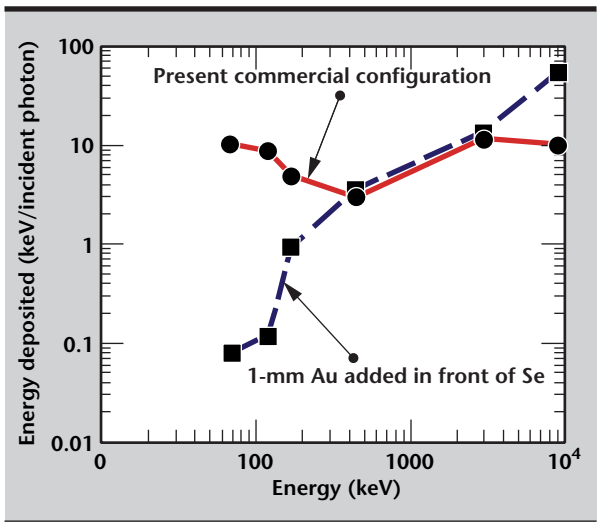

Figure 5. Calculated energy deposition in Se layer of amSe imager as a function of incident x-ray energy.

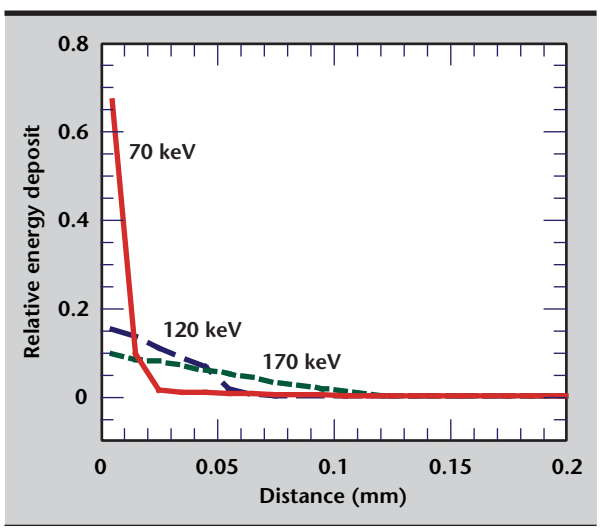

Figure 6. Calculated energy deposition in Se layer of amSe imager as a function of distance from line source. Zones in the calculation are 0.01 mm wide.

Figure 5 presents the calculated energy deposition for the two configurations reported and the six different x-ray energies. Energy deposition by primary and secondary radiation produces electrons in the Se that are then collected by the applied voltage. There may be some variation in recombination with the ionization density of the secondary radiation, but, to first order, the signal in the detector should be proportional to the energy deposited by the incident radiation. The calculations indicate that in the present configuration, the amSe panel should have a decreasing response (per incident x ray) over the energy range that we tested experimentally.

The location of the minimum at 450-keV x-ray energy is highly approximate since we calculated a sparse energy set.

Addition of the Au gives part of the desired effect on energy deposit. It suppresses the amSe imager response at 70 keV by two orders of magnitude. The response at 450 and 3000 keV is nearly unchanged. For imaging high-Z objects with the LLNL 9-MV linac, this may result in substantially better imaging performance. Most of the important imaging photons are between 1 and 4 MeV. Most of the scatter is below 450 keV. It is disappointing that the response at 3 MeV is not improved, but we tried only one material and thickness. The important conclusion is that a tool exists to alter the energy response of this imager.

There is, however, a potential advantage of the altered configuration for imaging 3-MeV x rays. For the amSe imager in the present configuration, it is possible that the energy deposit comes from a small number of high-energy events. This could make the image quantum-noise limited. The configuration with the Au has much higher interaction probability, possibly leading to more interaction events being recorded and therefore to lessened quantum noise. Insight into these effects is available in the Monte Carlo calculations already performed. Time and budget did not permit this evaluation.

The shape of the energy deposition as distance from the (line) source increases is given in **Fig. 6** for the lower energies computed. The zone width in the Monte Carlo calculation was 0.01 mm.

Figure 7 shows the shapes of the energy deposition binned into pixels the size of the amSe imager. The data have been normalized so that each energy has the same integral. These data suggest that there should be an experimentally observable effect on the line-spread function from secondary radiation transport as x-ray energy is increased up to a tube voltage of 450 kV. They also show that the line-spread function will be further broadened by secondary

radiation transport at energies produced by LLNL's 9-MV linac.

Figures 6 and **7** do not reveal one very important aspect of the computational results. A significant portion of the total energy deposited is contained within the long tails of the line-spread functions.

Figure 8 presents the computational results for the configuration of the commercial amSe imager as running integrals. The ordinate is the fraction of the total deposited energy that is contained within a distance, x, of the line source. We have normalized these curves to a value of 1.0 at 10 mm from the source.

In the type of display given in the figure, the desired response is an immediate rise to 1.0 at a very small distance, and then no additional energy deposited at larger distances from the incident radiation. This spread represents only the effects of secondary radiation transport in the amSe imager. It does not include object scatter, air scatter, electronic crosstalk, source unsharpness, digital pixel sampling and many other things.

We see from **Fig. 8** that significant energy is deposited many pixels from the location of the incident radiation. For example, 10% to 30% of the energy is deposited more than 1 mm from the incident radiation, even at medically relevant energies. The importance of this can most easily be appreciated if one imagines imaging a small, high-opacity, object within an otherwise empty field of view.

Even if no source photons reach the amSe imager in the shadow of the object, the aggregate effect of inscatter from the other 7.5 million pixels will cause significant detector response in the shadow. This can severely limit the useful dynamic range and contrast sensitivity in NDE applications. This same characteristic exists to some extent in every technology available for quantitative digital x-ray imaging.

Results for the configuration with 1 mm of Au inserted before the Se are shown in **Fig. 9**. The curves for lower energies are degraded from the commercial amSe configuration. This is of only intellectual interest since the response is so strongly suppressed. The two most technologically important cases are 450 keV and 3 MeV. These are compared in **Fig. 10**. Clearly the presence of a Au converter layer in front of the Se will have negligible effect on spatial resolution at 450-keV and 3-MeV x-ray energy.

These Monte Carlo calculations show that secondary radiation transport in the imager itself creates long tails on the line-spread function of the amSe imager in its commercial configuration for all energies simulated, 70 keV to 9 MeV.

For imaging with the LLNL 9-MV linac, spatial resolution will be degraded compared to lower energies, but potentially better than any other available technology for area imaging at these energies. Adding a high-Z converter in front of the Se is a potentially viable method of adjusting the imager x-ray energy response with negligible impact on spatial performance.

amSe Image Acquisition Procedure

Initially we had intended to collimate the x-ray beam to approximately one quadrant of the amSe imager. In the event that our tests did irreparable damage, this strategy would have retained some

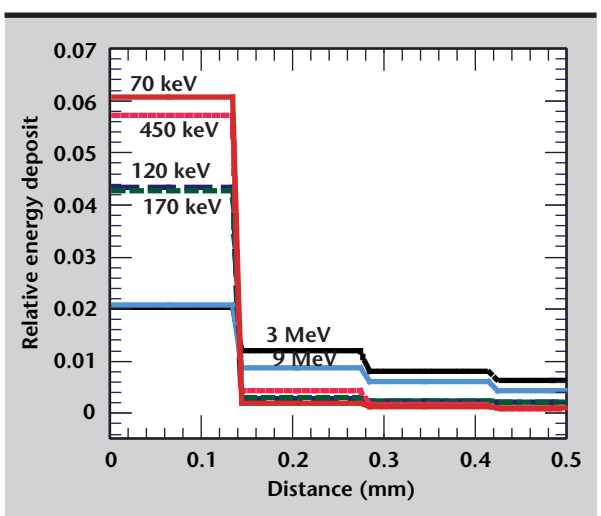

Figure 7. Calculated energy deposition in Se layer of amSe imager as a function of distance from line source. Data presented here are binned to the pixel pitch of the amSe imager.

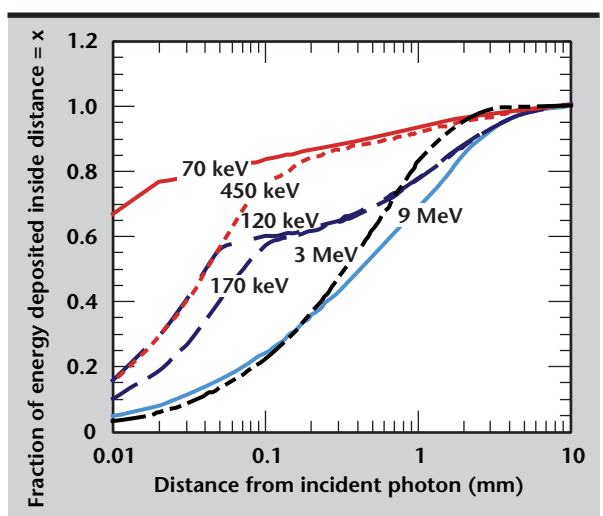

Figure 8. Calculated shapes of the integrated energy deposition as a function of distance from the line source for the amSe imager in the commercial configuration.

functionality. However, the imager has an internal calibration procedure that must be run for each x-ray spectrum. To complete this calibration it is necessary to fully illuminate the entire panel. We removed all collimation from the source and allowed the x rays to fill the entire panel and surroundings.

To provide shielding for peripheral electronics within the imager, we applied a 0.25-in. Pb shielding in front of the wide "borders" of the imager. We have insufficient knowledge of internal construction to know whether this shielding protected the vulnerable components. This Pb was installed after the data set at 120 kV had been acquired, but this is of no consequence, since 120 kV is within the normal operating envelop of the amSe imager.

Spectral and exposure data is presented in **Table 1**. Prior to acquiring the set of images for each spectrum, we performed the "calibration" procedure as outlined by the manufacturer.

We see from **Table 1** that exposure times are quite short. If we were to cut the distance to 1.5 m and run at maximum current, exposure times would be well under 1.0 s. If we operated without source filtration, it would approach 0.1 s. To make full use of this amSe imager in the

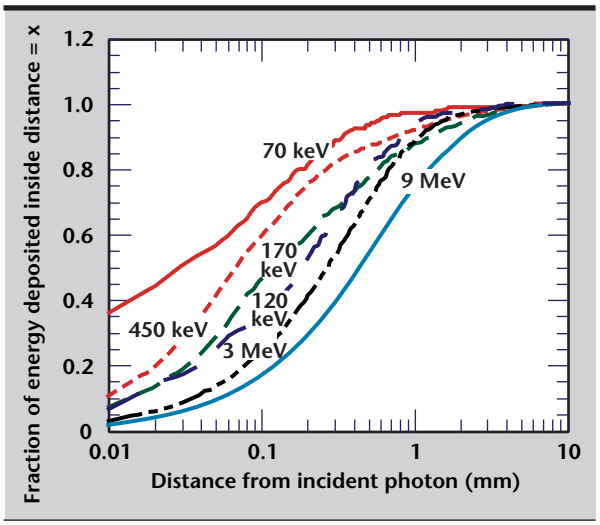

Figure 9. Calculated shapes of the integrated energy deposition as a function of distance from the line source for the amSe imager with 1 mm of Au inserted in front of the Se layer.

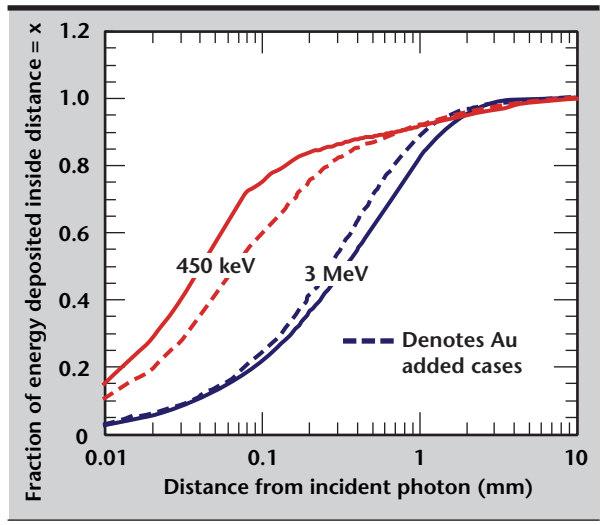

Figure 10. Effect on energy deposit shape from adding 1 mm of Au in front of the Se.

Table 1. Spectral and exposure data for amSe imager.

Tube voltage (kV)	Filter material and thickness (mm)	Tube current (mA)	Exposure time (s)	Source-to-detector distance (m)	Exposure (mR)
120	W: 0.076	1.75	10.0	3.00	10.2
250	Cu: 3.2	3.00	10.0	3.00	40.8
450	Cu: 6.5	2.00	12.0	3.00	102

Table 2. Spectral and exposure data for PCAT system.

Tube voltage (kV)	Filter material and thickness (mm)	Tube current (mA)	Exposure time (s)	Source-to-detector distance (m)	Exposure (mR)
120	W: 0.076	7.50	110	1.52	1873
250	Cu: 3.2	3.50	100	1.52	1854
450	Cu: 6.5	2.00	85	1.52	2814

future, it is imperative to have some type of shutter control over exposure. These exposure times are less than the time required for the tube to reach operating voltage if we use the tube controller as the on/off switch.

Glass CCD Test Procedure

For the comparative images acquired with the PCAT system, we set up PCAT so that the pixel size was 103 µm, slightly smaller than the pixels in the amSe imager. This resulted in a 105-mm field of view. We used the fiber optic scintillator that is 140-mm square and 12-mm thick. Parameters are given in **Table 2**.

The objects we imaged are 1) a line-pair gage; 2) a Ta cylinder; 3) a Ta edge; and 4) a 3/8-in. socket head screw with nut (amSe imager only).

The overall configuration of the set-up for data acquisition is shown in **Fig. 11**. The amSe imager with objects in place is shown in **Fig. 12**.

With PCAT we omitted the bolt. We imaged a Pb ruler to establish the pixel size and field of view. The Ta edge and the cylinder were imaged together. The line-pair gage was imaged separately.

Experimental Results

Exposure Results. We see from the exposure conditions in **Tables 1** and **2** that the amSe imager reaches the desired digital signal level with considerably less exposure than the scintillating glass/CCD system of PCAT. We can correct the PCAT exposure values to account for the difference in pixel size between the two systems. For optically coupled systems such as PCAT, the exposure required is inversely proportional to the pixel area (constant number of x rays per pixel). The exposure advantage derived from **Tables 1** and **2**, corrected for pixel area, is given in **Table 3**.

Dark Image Results. To evaluate the magnitude and stability of the dark image from the amSe imager, we manually selected a region 300 × 600 pixels that contained few bad pixels. These images were acquired with the same integration time used for x-ray images. The mean and standard deviation for the selected region are given in **Table 4**. The last two digits of the image indicate the minute of image acquisition.

Two of the dark images, 1607 and 1609, have significant counts, about 1% and 2% of the usable dynamic range of the imager. We don't understand

Figure 11. The overall arrangement used for data acquisition with the amSe imager. The Philips tube head with high-voltage cables is on the left. Three meters away on the table is the imager.

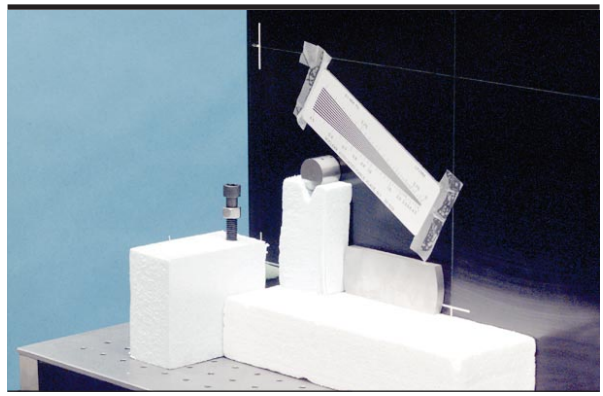

Figure 12. Close up of the amSe imager with objects in place. The white foam was used to support some objects. The white marks on the imager face denote the active imaging area of the device.

Table 3. Exposure advantage, corrected for pixel area.

Tube voltage (kV)	Filter material and thickness (mm)	AmSe exposure advantage (X)
120	W: 0.076	100
250	Cu: 3.2	25
450	Cu: 6.5	15

Table 4. Dark image results.

Image	Mean	Standard deviation
1605	0.00374	1.38
1607	70.5	11.6
1609	171	17.4
1612	0	0
1614	0.0001	.042
1615	0.0003	0.011

this behavior. We believe that the images written to disk have been dark-corrected by the Sterling software, so we expect an average of zero, with a variance caused by noise in the dark images.

The images appear to have been clipped so that no negative values appear. We also cannot rule out the remote possibility that images 1607 and 1609 may have been affected by external interference. Four of these images are effectively dead zero with no significant standard deviation. This needs more work.

Temporal/Radiation Stability. One of the problems in our scintillator-based systems is complex temporal behavior. The particular glass formulation that we use has both a long-lived "afterglow" and light output that increases with recent radiation exposure. We checked the amSe imager for a residual image within a dark image after a series of five object images. Some residual image is observable. This is shown in **Fig. 13**.

The object image at the top left is the fifth in a series of five acquired using the 120-kV spectrum. A portion of the line-pair gage is shown along with a line-out in units of digital levels. The lower image is a dark image acquired as soon as our manual procedure allowed (~2 min) after the fifth in the object-image sequence. The two images are shown with different gray scales to reveal the residual image. The magnitude of the residual image is quite small, within the variation in overall dark image variation in **Table 4**. This effect disappears entirely in a second dark image.

Another form of temporal bad behavior is for the imager signal to exhibit dependence on prior exposure. To evaluate this, we acquired five blank images for each x-ray spectrum tested. These were acquired as rapidly as our clunky manual method and the amSe imager control software would allow, typically one exposure every 2 min. We examined a 300-×-600-pixel patch from each image and determined mean, standard deviation, median and number of "bad" pixels, where "bad" is defined as having a digital level >15,700 or <2000.

Mean digital values are plotted in **Fig. 14** for three sequences of five blank images, one sequence for each x-ray spectrum. These variations are very large, greater than 10% for the

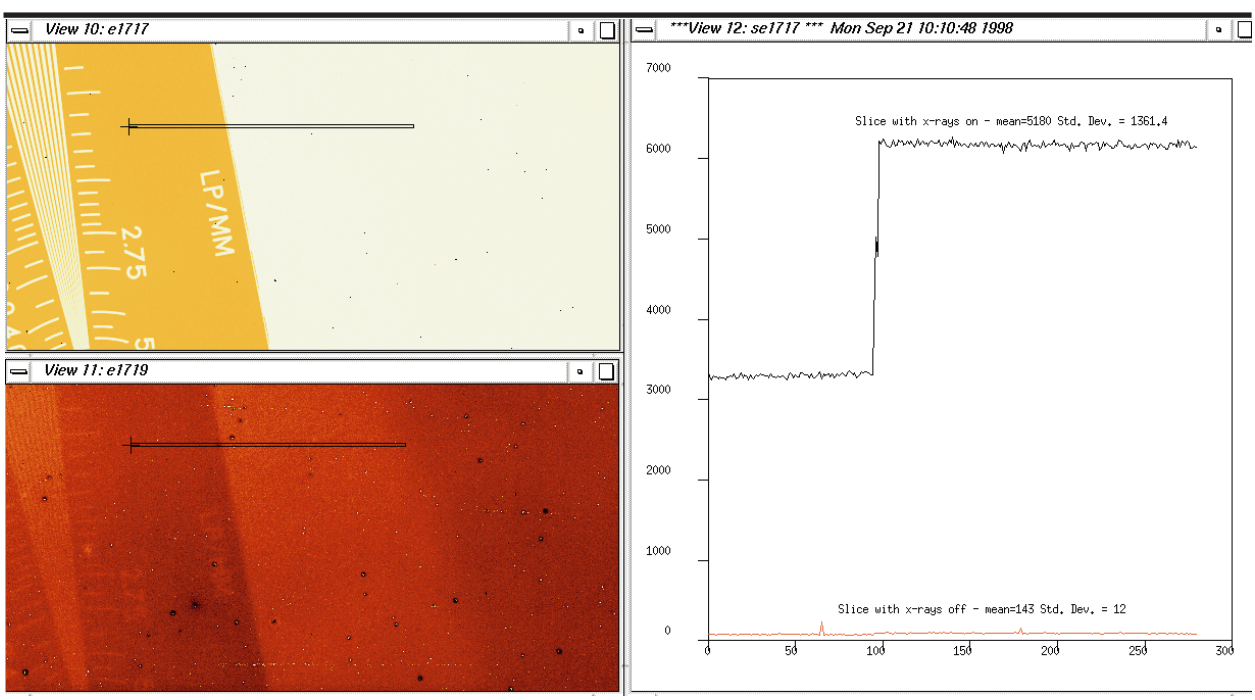

Figure 13. Upper left image is the fifth in a series of five images acquired at 120 kV. The object is a 0.1-mm-thick Pb line-pair gage. Just after acquiring image 5, the dark image, lower left, shows a slight residual image. Line-outs are shown on the right for both images. Line outs were taken at exactly the same pixels in the two images.

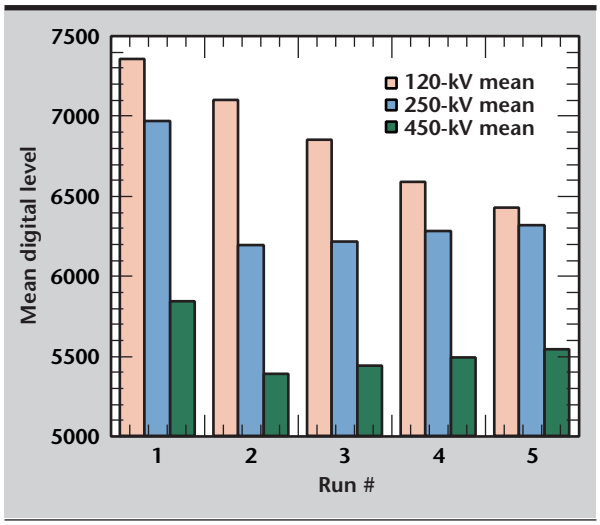

Figure 14. Mean digital value for a series of five blank images taken for each of the three x-ray spectra used in these experiments. Note the plot has non-zero origin.

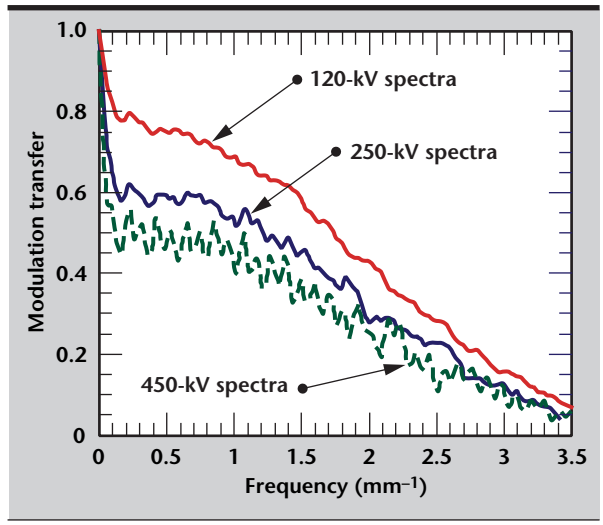

Figure 15. MTFs for three x-ray spectra for the amSe imager. These MTFs were derived from the images of a Ta edge.

120-kV spectrum. Nothing about the time or sequence behavior makes sense to the authors. The sequence at 120 kV starts high and drops throughout the sequence. The others drop, then climb. The number of bad pixels is very small, 0.03% in the worst case. No trends with continued exposure are evident. The source output is reproducible to about 1%, so the variation of **Fig. 14** must arise in the amSe imager. If this is a change in sensitivity that is spatially invariant, then correction is a simple matter. LLNL software routinely renormalizes CT data. Further work is needed to assess whether this variation has any spatial dependence, which would be a serious problem for CT.

Modulation Transfer Function. The MTF is a frequency-domain description of the spatial resolution of an imaging system or component.[3]

One derives MTF from the image of an edge. First, a line-out is taken. The derivative of the line-out is the line-spread function. The Fourier transform of the line-spread function is the MTF. One consequence of the digital spatial sampling in a digital system is that aliasing can occur if the image contains frequencies that exceed one-half the sampling frequency. For the amSe imager with 139 μm pixels, this limiting frequency is 3.6 mm^{-1}, called the Nyquist limit.

Experimentally determined MTFs for the amSe imager are given in **Fig. 15** for all three spectra. They drop very rapidly at low spatial frequency, then hold up well as the Nyquist limit is approached. The MTFs decrease with increasing x-ray spectral energy.

Our Monte Carlo modeling simulates secondary radiation transport, one of the components of the experimental MTF of **Fig. 15**. Recall that we modeled monoenergetic x rays of 70, 120 and 170 keV as representative of the three polychromatic spectra. On the basis of relative energy deposition at large distances from the incident x ray, the Monte Carlo results indicate that MTF for the 120-kV spectrum will drop less rapidly at low spatial frequency than will the MTFs for the two harder spectra. We see this behavior in **Fig. 15**.

Experimental MTFs for the glass/CCD imager at the three x-ray spectra are given in **Fig. 16**. The effect of harder x-ray spectra is in the same direction as for the amSe imager, though of smaller magnitude. Comparing **Figs. 15** and **16,** we see that amSe is inferior at low spatial frequencies and superior at high spatial frequen-

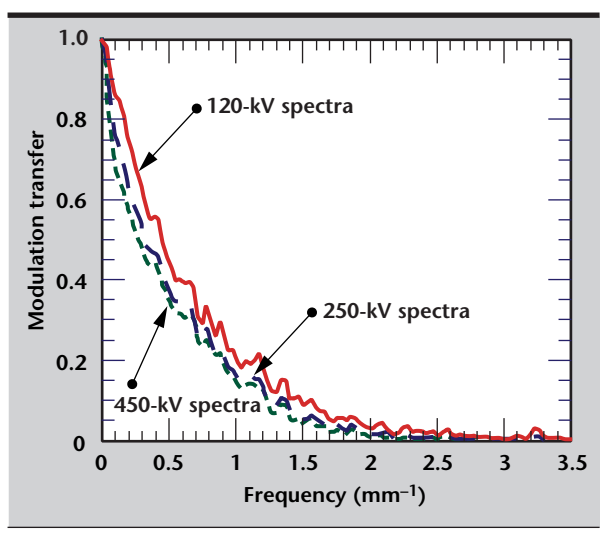

Figure 16. MTFs for three x-ray spectra for the glass/CCD imager. These MTFs were derived from the images of a Ta edge.

cies. This comparison is shown in **Fig. 17** for the 120-kV spectrum.

The MTF from digital spatial sampling is given by the expression:[4] $MTF_x = \sin x/x$. In this expression x = spatial frequency (mm^{-1}) · pixel size (mm) · π. We calculate this quantity for 139-µm pixel size and present it along with the measured amSe MTF in **Fig. 18**.

MTF at Low Spatial Frequency. The MTF of the amSe imager at low spatial frequency generally decreases contrast and messes up quantitative measurement. This is made clear by our measurements of signal level in the shadow of an opaque cylinder. The signal at the center of the cylinder arises when the MTF of the imager at low spatial frequencies is not quite unity. This

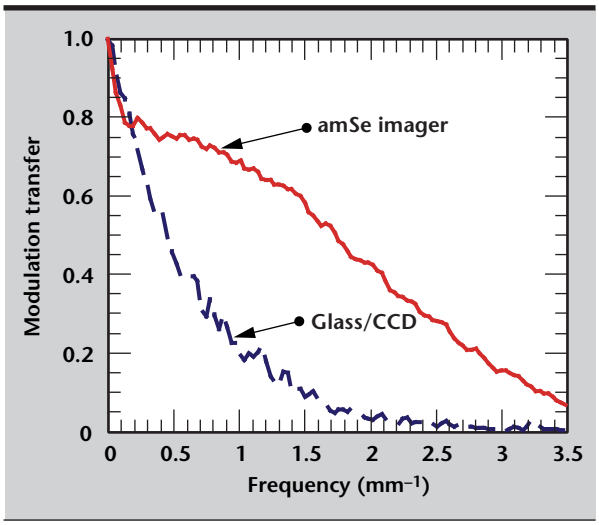

Figure 17. Comparison of MTFs for the two imaging systems using the 120-kV spectra.

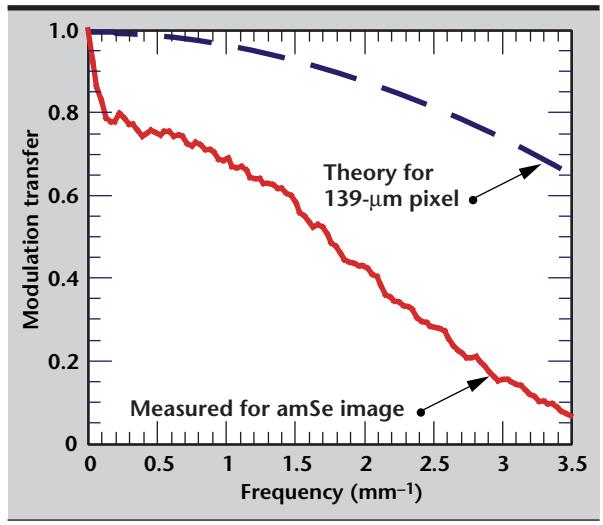

Figure 18. Comparison of measured amSe imager MTF at 120-kV spectrum and theory, for a digital sample size of 139 µm.

Figure 19. Normalized line-outs of the image of the thick Ta cylinder, with both amSe imager and the LLNL PCAT system using a fiber optic scintillating glass lens-coupled to a CCD. The data is split at 15 mm with the amSe imager on the left and the glass/CCD on the right. The digital counts have been normalized so that the maximum level is the same in each signal. Counts for glass/CCD system have had the dark image subtracted. Counts for the amSe imager have internal dark image subtraction.

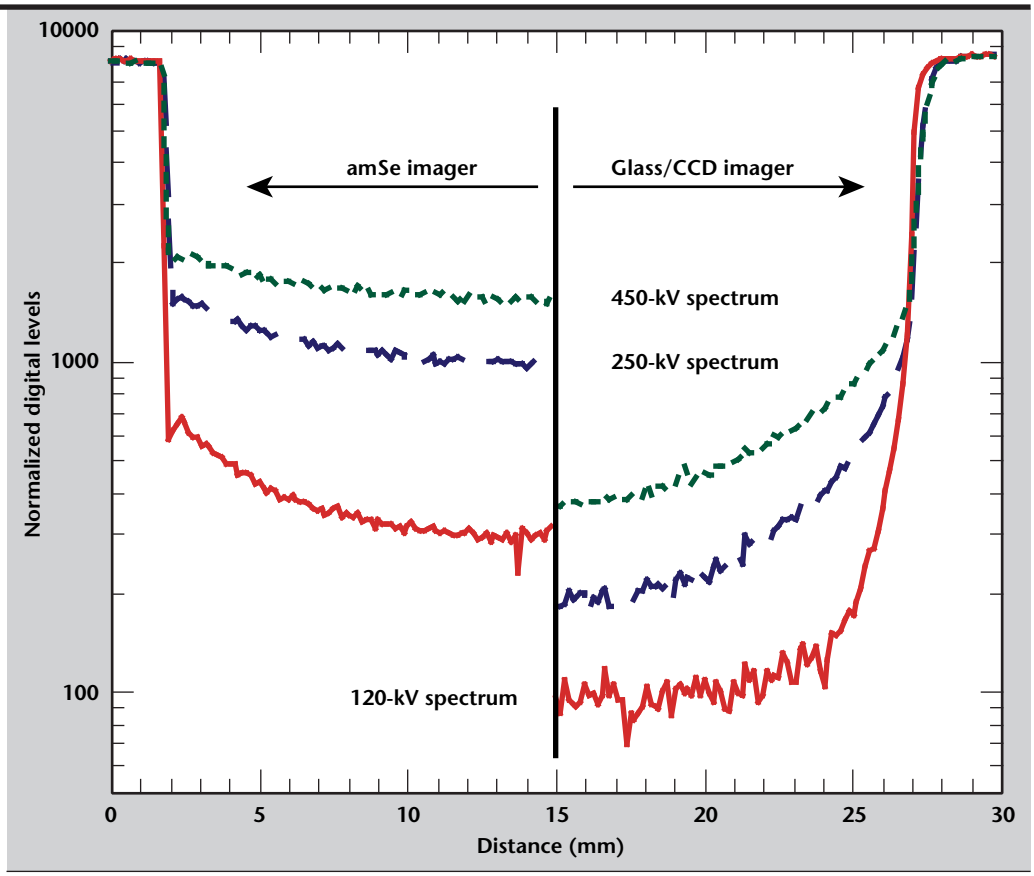

attribute is important to NDE applications, especially to CT.

The results of these images for the amSe imager are compared to the LLNL glass/CCD system in **Fig. 19** containing portions of line outs from six images (two imagers and three spectra) of the thick cylinder. Each signal has been normalized so that they all have the same maximum value. The trend with increasing spectral energy for the amSe imager is consistent with the Monte Carlo results presented earlier.

Example Images. Images of the Pb line-pair gage taken with the two imaging systems are presented in **Fig. 20**. These images were acquired at 450-kV applied potential. Since the Pb thickness in the gage is only 0.1 mm, this is a modest-contrast object.

Source Control

The amSe imager is continuously active and therefore will not operate as a snapshot camera device in a constant x-ray field. X-Ray exposure time must be controlled with the source or a shutter, and x rays must remain off during read out, image transfer, and preparation of the imager for the next exposure. To imagine future use of this imager for CT, this whole process must be controlled from the computer used for data acquisition and motion control.

One component of this project was to understand issues regarding source control so that we could lay out a reasonable plan for future use of the amSe imager as the data acquisition component of an NDE CT system.

Though our experiments were not extensive, it appears that the LLNL linacs can be operated in a mode amenable to computer control of relatively short bursts. The ramp-up and ramp-down times appear to be immediate, though a closer examination may find subtle differences.

We performed these tests using a pulse burst that produced about 1 R. At the time these tests were performed, we did not have amSe exposure results for softer x-ray spectra nor the Monte Carlo calculations. These combined results suggest that a 2-s linac burst at 100 Hz may be too long. More detailed testing will be required to pin this down and to evaluate operation at lower

(a)

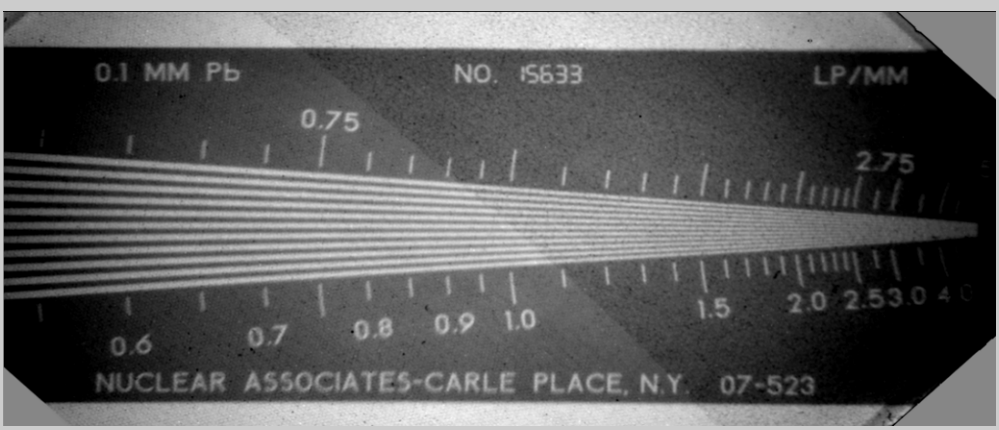

(b)

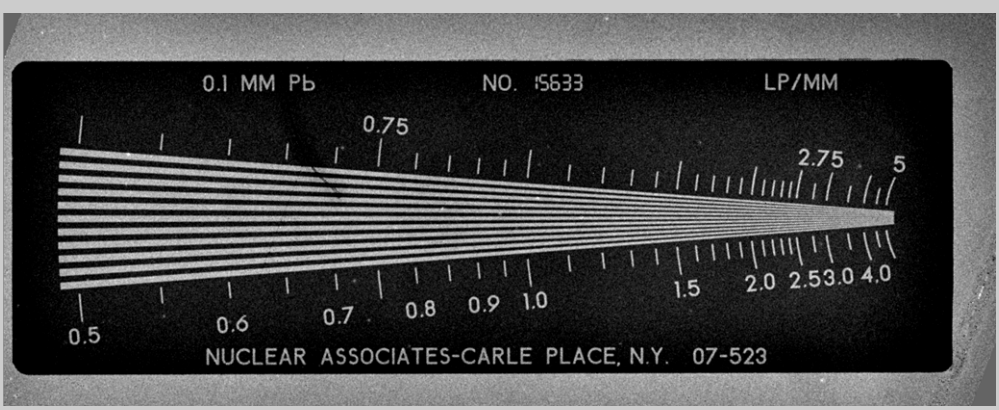

Figure 20. Images of the Pb line-pair gage in the region of 2.0 lp/mm. (a) Acquired with the LLNL PCAT system, using a fiber optic scintillator that is mirror/lens-coupled to a CCD. The only correction applied to this image is dark image subtraction. The brightness gradient from left to right, and the pattern noise are of no consequence because they will disappear once the image is ratioed to the blank image. (b) The same region of the line-pair gage, acquired with the amSe imager. The two images are different size because they were acquired with different pixel size and we chose to print them with constant pixel dimensions.

Table 5. Summary of performance of CCD-based configuration.

Feature	amSe	CCD	Comment
Spatial resolution (MTF at 1.0 mm^{-1})	0.40	0.15	
Maximum field of view (cm)	43	30	a
1.5-m image cycle time (s)	46	120	b
3.0-m image cycle time (s)	64	375	c
24.7-mm contrast ratio	27	80	d

a) amSe provides spatial resolution and field of view simultaneously. CCD systems can achieve 30 cm field of view, but not simultaneously, with 0.15 MTF at 1 mm^{-1}. LLNL maximum field of view for CCD system is 15 cm.
b) Sum of exposure and read/refresh time. For Philips 451 source operated at 2.0 mA, 450 kV, with 6.5 mm Cu filtration. Source-to-detector distance = 1.5 m.
c) Same as (c), except source-to-detector distance = 3.0 m.
d) Contrast ratio = (digital level in open field ÷ digital level at center of 24.7-mm-diameter opaque disk).

frequency and/or shorter pulse burst, but it looks promising.

Conclusion

This amSe imager shows great promise for digital radiography and CT. We encountered no problems in operating it in x-ray spectra up to 450-kV applied voltage. **Table 5** provides a highly simplified summary of performance relative to one LLNL CCD-based configuration at the 450-kV spectrum tested in this work.

Future Work

The next steps toward routine use of the amSe imager for LLNL Programs are:

1. Write LLNL software to control the imager.
2. Understand the dark image anomalies that we observed.
3. Determine whether the variation we see in blank images is spatially dependent.
4. Test the 450-kV shutter we designed for reproducibility of x-ray illumination.
5. Understand the impact of the poor MTF at low spatial frequency and what mitigation measures can be applied.
6. Perform the same suite of characterization measurements at the 9-MV linac.
7. Evaluate other LLNL CCD-based configurations and commercial detectors based on amorphous Si.

Acknowledgments

J. Mahler (LLNL) made this project possible by catching a bit of our enthusiasm for this technology.

References

1. Logan, C. M., "Evaluation of an Amorphous Selenium Array for Industrial X-Ray Imaging," in press.

2. Brun, R., F. Bruyan, and M. Maire (1987), "GEANT3 Users Guide," DD/EE/84-1, CERN.

3. Bushberg, J. T., J. A. Seibert, E. M. Leidholdt, Jr., and J. M. Boone (1994), "The Essential Physics of Medical Imaging," Williams and Wilkins.

4. Barrett, H. H., and W. Swindell (1981), "Radiological Imaging," Academic Press, New York, New York.

LANDMARC Radar Mine Detection

Stephen G. Azevedo, Jeffrey E. Mast, and James M. Brase
Laser Engineering Division
Electronics Engineering

E. Tom Rosenbury
Defense Sciences Engineering Division
Electronics Engineering

This report describes work done in the second year of a three-year project, LANDMARC, for detection of land mines using advanced radar technology. The primary objective of the overall project is to study the use of small radar sensors, such as Micropower Impulse Radar (MIR), and complementary sensors, with optimized detection efficiency. Besides detector design and experimental tests, other aspects of radar mine detection are under study, including electromagnetic modeling, signal processing, assisted detection, and parallel processing methodologies. Both military and humanitarian demining goals were set as standards of operation so that, in the end, a feasible mine detection system could be designed that would meet the goals and constraints of deminers. A first-prototype system was also used to measure detector performance in blind tests. The MIR mine detector has been shown to effectively detect and locate small plastic anti-personnel land mines (with explosive simulant and no detonators) in three different soil types and under adverse conditions. It achieved an 85% overall probability of detection in 18 blind tests, compared with 44% with an Army-standard metal detector, and roughly half the false alarm rate.

Introduction

Land-mine detection is important for soldiers facing an unknown threat, as well as for civilians returning to their land after a conflict. Besides the military threat for our troops overseas, land mines throughout the world pose an enormous hindrance to economic and environmental stability, and indirectly to national security. Policy decisions regarding the development, stockpiling, use, and clean-up by warring nations are being carried out through high-level international negotiations, but there are many problems that still remain—particularly the millions of mines left in the ground. As a national laboratory developing science and technologies in the national interest, Lawrence Livermore National Laboratory (LLNL) has undertaken several efforts over the years to address the land-mine problem. [1-10]

The main problem is that roughly one billion mines are still in place, killing large numbers of civilians and children daily. They will continue to be a problem until they can be easily found and removed. Detection and clearance technologies are under investigation by several agencies, but none are adequate for all situations, particularly for humanitarian demining scenarios. This report describes internal research and development for a new mine detection strategy that takes advantage of the Micropower Impulse Radar (MIR) developed at LLNL.

We describe the second year of this project and the plans to continue toward its deployment for use around the world. We begin with an introduction to the mine detection problem and alternate approaches.

Mine Detection Problem

The mine detection problem being addressed in this project is repeatedly listed “number one” by people who clear minefields: finding the small plastic mines near the surface to be removed after a regional conflict. Other problems are difficult as well (for example, locating a field containing mines, education and care of locals, clearing vegetation, disposing of the mine once found, and verification that a field is cleared), but detecting individual mines is paramount.

This problem represents one of the major difficulties facing humanitarian demining operations, whose goals are to clear land and save lives. It is also a problem for U. S. forces conducting peacekeeping operations (PKO) in troubled areas around the world. The current methods to find these mines are unreliable and slow.

Some facts about this problem are given below.

1. *Anti-personnel (AP) mines are small, have low metal content (a few grams), and are the most numerous*. These mines operate indiscriminately, killing or maiming 2000 civilians and children per month worldwide—draining the resources not only of their own countries, but also of relief efforts and eventually the global economy. One of the most important needs of "deminers" (people who remove post-conflict land mines around the world) is for improved detection of individual minimum-metal AP mines. These mines are numerous, small, effective, and nearly invisible to most current technology. Large anti-tank mines are detectable, and therefore not a problem.
2. *Metal detectors and mine probes are used in 100% of clearance operations.* These tools are primitive, and cause numerous false detections, thereby slowing the operation. In one instance in Cambodia, deminers detected 70 mines in one acre of land, but they also found 500,000 metal fragments in the same field. This false alarm rate slows operations and causes fatigue that can lead to accidents.
3. *Radar technology has never been used by deminers.* Even though many disjointed efforts have tried to develop radar-based mine detection systems in the last 20 years, none are in use. This is because radar has been large, heavy, expensive, requires power, and has been susceptible to clutter. The wavelengths used have been much larger than the AP mines, thus mines have been below the diffraction limit.
4. *Clutter is the limiting factor in all mine detection technologies*. The sources of this clutter are many – surface effects, mine-like targets, electronic or thermal noise, and natural features such as roots, rocks, and holes. The clear need is for improved methods of reducing the effects of clutter for the technologies of interest.

Approaches

Many people in the international humanitarian demining field agree that the most expedient way to address the mine detection problem is to develop a hand-held, cheap, rugged, and easy-to-use subsurface mine detector. To do this involves development of better detection strategies.

Current technologies are either incomplete and dangerous (for example, metal detectors miss plastic mines), indiscriminate and slow (for example, dogs are prone to fatigue), or expensive and hence not available to those who need them. All sensors look for some distinguishing feature that differentiates the mines from their natural surrounding either by emissions, geometrical form, internal voids, size, depth, distance from each other, material, conductivity or thermal signature.

A list of detection technologies was compiled by H. Ehlers and H. G. Kruessen of Stiftung Menschen gegen Minen (MgM, The Humanitarian Foundation of People against Land Mines), a Germany-based non-government humanitarian relief organization (web page: http://www.mgm.com) with help from numerous organizations including the U. S. Army. They divide the sensor systems into two general types: substance-analyzing sensors and imaging sensors.

The substance-analyzing sensors are as follows: passive/active metal detection, chemical detectors, bio-sensors (animals or animal tissue reacting to explosive vapors), and nuclear detection (by various backscatter principles such as x-ray analysis, thermal neutron analysis, fast neutron activation and quadrupole resonance). Some of the most common ones that have been tested are shown in **Table 1** in roughly increasing order of cost for the sensor. There are many reference materials for these sensors and none is a clear choice for all situations; that is, a detector that works well in the desert may not be good for snowy forested mountains.

Because of their relatively lower cost, only the first two sensor systems are in common use. False positives are due to clutter in the environment causing the sensor to alarm, so one might imagine a suite of different types of sensors for each possible scenario that would allow for cross-checking. This approach clearly drives the cost up for complete systems, making it even less accessible to the people who need it. What **Table 1** does not show is the reliability of each system measured in terms of probability of detection (PD) and false alarm for every possible situation.

To assess their performance, receiver operating characteristic (ROC) curves are measured for each detector. Schematic plots of ROC curves for AP mines are shown in **Fig. 1** for metal detectors and ground-penetrating radars (GPRs). PD is plotted relative to the number of false alarms per square meter. The clear goal is to reach nearly 100% detection with no false alarms (marked as "Desired" on the plot).

Current systems are nearing this number for anti-tank mines, but published results show that AP mine detection is far from that goal. The U. S. Army counter-mines and the U. N. humanitarian mine detection goals for PD are noted on the graph (90% and 99.6%, respectively).

The LANDMARC goal, as noted on the graph, is to approach the Army and U. N. goals in incremental steps. The clear objective is to continue to move the curves farther toward the desired sensor goal. Measures of ROC values for various terrain, environment, and mine conditions will help to track progress and determine the success of an MIR mine detector. Success of this project will be defined as having made fair and accurate measures of the ROCs for MIR, to determine if radar-based mine detection is feasible for military or humanitarian mine-clearance goals.

Imaging sensors are used with computer equipment to enhance the user's vision to reduce the clutter problem. They can be designed for surface mines (passive video, active/passive millimeter-wave

Table 1. Tested mine detection technologies and their capabilities.

Type	Detection method	Advantages	Disadvantages
Probes or sticks	Carefully probe into the ground and search for hard materials to remove	Inexpensive	Very dangerous and slow
Metal detectors	Induction coil measures weak fields caused by metal content	Sensitive to metal mines & firing pin	Clutter, cannot find non-metallic mines
Dogs	Measure trace amounts of HE in air	Very sensitive to HE and trip-wires	Subject to fatigue and masking
Ground-penetrating radar	Microwave reflectance from dielectric interfaces	50-70% PD for non-metallic AP	Clutter, resolution, expensive
Infrared	Finds thermal differences between soil and mine (or disturbed soil)	Stand-off to 10 m	Contrast difference low, expensive
Thermal neutron activation	Analyze energy distribution of neutron backscatter using 10-MeV gammas	Very sensitive to trace HE	Large, expensive, slow, hazardous

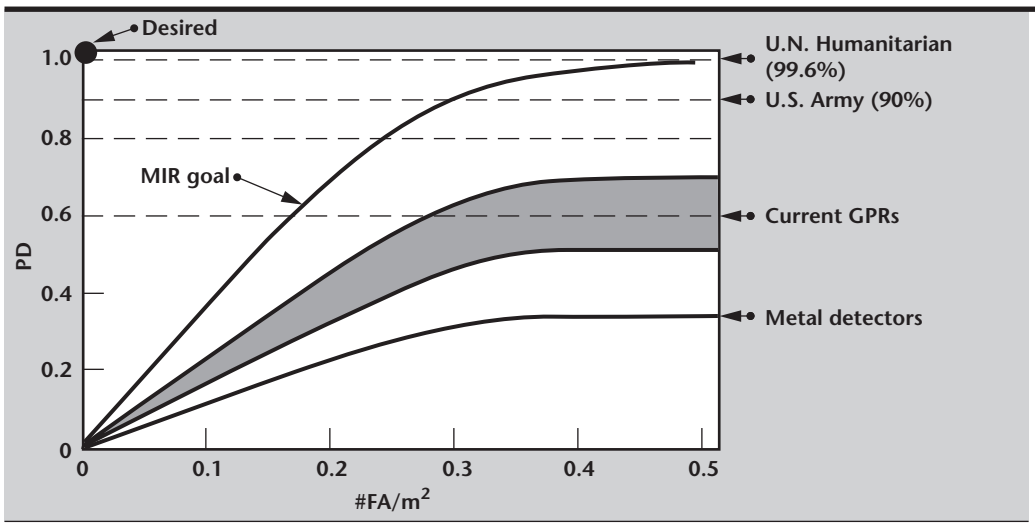

Figure 1. Receiver operating characteristic curves. These curves are indicative of trends only and will differ greatly for varying conditions such as soil type, moisture, mine type, or weather.

radar), to look at temperature differences in disturbed soil (active/passive infrared (IR), airborne LIDAR), and at conductivity differences (GPR). GPR has been attempted by many groups for over 20 years, and MgM identifies three types, as follows:

1. Narrowband GPR (<1 GHz) — suitable for deep objects (up to 100 m); requires large expensive equipment; has depth resolution worse than 1 m.
2. Wideband GPR (FM-CW up to 3 GHz) — resolution up to 10 cm at depths to 2 m (the wide frequency band produces more information); needs excessive computing capacity and small distance to ground; expensive and not mass produced.
3. Interferometric GPR — uses synthetic aperture radar (SAR) principles with the above systems to produce better 3-D resolution; needs expensive and large radar and processing hardware.

Very little work has been done in the higher frequencies (up to 8 or 10 GHz) or with extremely wide bandwidths (many gigahertz). Aside from the expense and size, GPR has always suffered from high false-alarm rates. So, an integrated radar mine-detection system stands the most chance of widespread use if the following problems could be solved:

1. clutter, causing false positives (could try higher 3-D resolution, wider bandwidth);
2. size and weight of the system (currently too big for one person);
3. cost of the sensor; and
4. computer and software complexity.

The LANDMARC mine detection project is directly addressing all of these problems with GPR and is laying the groundwork for a detection system that has the potential to make significant contributions to humanitarian demining.

MIR Mine Detection System

LLNL has technologies and expertise in electromagnetic modeling,[10,11] radar systems,[2,10,12,13] and signal processing[14-18] that can be applied to assess the limits of radar mine detection and improved techniques for clutter reduction. The stated goal is for detection of small AP mines near the surface. LLNL technologies to apply to this problem are the MIR technologies, electromagnetic modeling and simulation expertise, and image processing methodologies.

MIR has optimal radar properties for AP landmine detection, but there is still development to be done to prove its reliability and speed characteristics. Since the sensors are orders of magnitude smaller, lighter, and less expensive than current GPRs, they can be packed together so that, for the first time, radar images of what is below the ground can be made with a portable device. Making images of the routinely sub-surface at optimal radar frequencies reduces the effect of clutter because the operator can now discriminate a mine from a rock based on its shape. The potential for a first-ever fully-3-D, real-time imaging system capable of revealing imagery of volumes beneath the earth's surface would be a dramatic contribution by LLNL. Therefore, the MIR technology can directly improve the two key performance parameters of mine-clearance efforts: reliability and speed of clearance.

The approach taken in this project has been directed toward the following five areas:

1. customizing the MIR technology for the landmine detection problem;
2. developing models of the radar and clutter signatures;
3. incorporating those models into algorithms for optimal processing;
4. performing experiments to validate the theoretical models; and
5. identifying sponsors whose needs are for a radar mine detection system.

Research results are encouraging and have been attracting the attention of mine clearance experts. The goal—which we are convinced is highly likely to be achieved—is to transition MIR technology into fielded systems that save human lives and mitigate the tremendous human suffering (thousands of lost lives and/or limbs) caused by AP land mines.

MIR Technology Overview

MIR technology is an entirely new sensor concept that is based on high-speed pulsed electronics and was developed in LLNL's Inertial Confinement Fusion program.[19-23] The radar exhibits a combination of interesting properties, including wideband operation, very low noise-floor, extremely low power consumption, small size and low cost, array configurability, and noise-encoded pulse generation. An MIR motion sensor circuit is shown in **Fig. 2**.

Of the MIR technology family, the swept range-gate rangefinder with transmit/receive cavity-backed monopole antennas is the sensor used for mine detection. The rangefinder, or variations of it, is used for signal and image processing applications because the return signal is similar to traditional "A-scan" from other radars. From these data, advanced signal processing and detection methods extract information about the soil under inspection.

Variations on the basic rangefinder can change frequency (1 to 4 GHz, nominally), maximum range (0.3 to 10 m possible), and sensitivity. Antenna systems control a number of these parameters and have standard modular connections on more recent MIR implementations. Plots of the radar pulse (reflected from a metal plate) and its spectrum are shown in **Fig. 3**. Notice that the radar response is relatively flat in the passband of 1 to 4 GHz, and also that system noise and jitter are low.

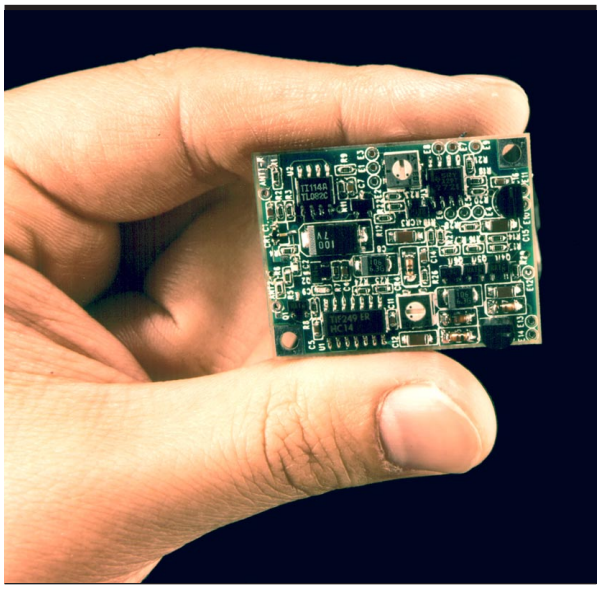

Figure 2. MIR motion sensor—a complete radar system (without antennae or 9V-battery).

Progress

Significant progress has been made in all five areas. It has been clear from the beginning that the clutter problem is of major importance to mine detection. That is, traditional GPR signals are susceptible to false signatures that appear to be mines or, worse, can cause the operator to miss a mine. The design of radar systems and processing algorithms in LANDMARC has been directed toward reducing clutter.

One direction to reduce clutter has been to characterize and optimize the radar signatures for mines. The current radar specifications are given in **Table 2** for a four-element MIR array. Important goals are to have very wide band signatures with low ringing. The MIR signal, reflected from a metal plate, and its spectrum are shown in **Fig. 3**. From this image, the MIR is shown to be stable and very wideband.

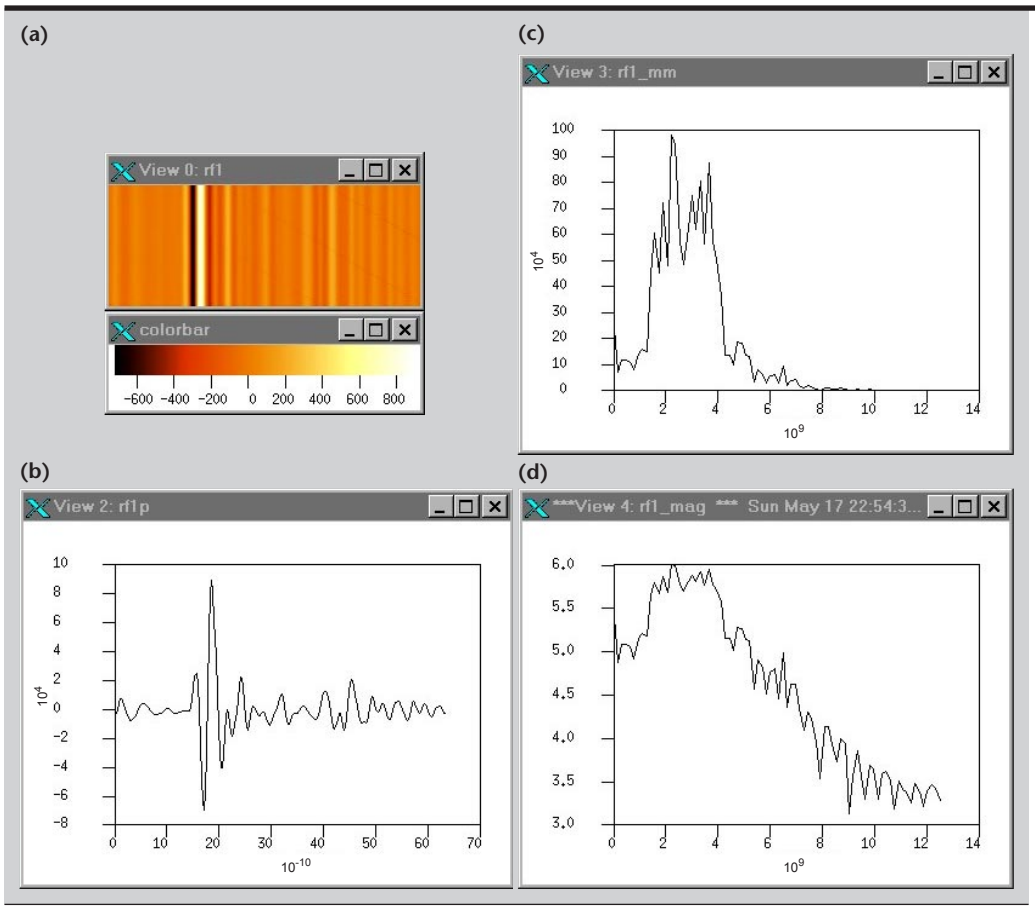

Figure 3. MIR rangefinder pulse echoed from a metal plate at 30 cm. (a) 100 waveforms stacked in an image; (b) the average of all 100 waveforms, (c) and (d) linear and log spectra of (b), respectively. The abscissa values are in seconds and Hertz; the ordinate values are in arbitrary units.

Table 2. MIR mine detection system specifications.

Parameter	Value
Radar Type:	Four-element MIR monostatic rangefinders
Frequency range	1.3 to 4.2 GHz (3dB bandwidth)
Avg. transmitted power	0.1 mW
Peak transmitted power	0.2 W
Pulse repetition frequency	5 MHz
Pulse rise time	80 ps (10 to 90% of peak)
Receiver noise figure	3 to 5 dB
Pulse width	1 ns FWHM
Timing jitter	50 ps p-p
Interface Electronics:	
Timing	Rangefinder ramp, controlled by computer
Ramp frequency	160 Hz (40 Hz for all four)
Number of averages	120
Number of range bins	256
Antenna Type:	Wideband ridged horn
Frequency range	1 to 18 GHz
Gain	3 to 10 dBi , highly-dependent on ground coupling geometry (6 nominal)
VSWR	1:1.8
Computer System:	Dual-processor Pentium, 300 MHz

Besides improving the radar itself, the LANDMARC project has made an initial design of the signal processing performed by the system. A critical issue in this design is a clear understanding of all signal, noise, and clutter sources in the data. We define noise as any contributor to the radar measurement that degrades our capability to detect the targets of interest. With this general definition there are many contributors to the system noise model, from simple to more complex:

1. thermal receiver noise – generally modeled as white, Gaussian additive noise in the radar receiver.
2. inhomogeneity in the soil – any variations in EM properties of the soil, including density variations, moisture changes, buried rocks, or organic matter, will cause radar reflections. These will be modeled as additive non-Gaussian noise with correlations on all lengths.
3. multiplicative noise – antenna sidelobes and quantization will contribute to noise which is signal-dependent.
4. surface artifacts – because the surface is generally the strongest reflector in the returned radar signal, any imperfections in removing it can cause artifacts in the residual measurements.
5. multiple scattering – in an environment with multiple strong scatterers such as mines, rocks, or the surface the radar measurement will contain not only their primary reflections but also multiple reflections caused by the multiple possible paths back to the receiver. These signals will appear as target-like images.

We model the noise in the measurement statistically. The noise model can be most generally described by an N-dimensional joint probability density, where N is the total number of samples in the measurement. We consider only two aspects of this general distribution: the marginal point density function and the correlation of the signal in time (and later in 3-D space).

For the Gaussian case, this provides a complete description; for the non-Gaussian case, we will allow the point distribution to vary but still consider only second-order correlations. This limitation may be relaxed later if analysis of test data shows that higher-order correlations are important.

The development of noise models involves two main activities: the first is the development of a database of measurements from which statistical models can be developed. The noise database must cover the system and environmental parameter space described above for signal models. The second activity is the analysis of the noise data to extract models of point statistics and correlations

followed by the development of noise simulations based on these statistical models.

The signal processing chain, shown in **Fig. 4**, shows the planned steps for reducing clutter based on models of the noise components. The general approach to detection is based on the development of both target and noise models. These models are used to compute a likelihood that the measurement was drawn either from the signal-present (H_1) distribution or from the signal-absent (H_0) distribution. The models will generally be adapted to the measured data and generated in real time.

In the 3-D imaging approach to mine detection, a single-aperture radar can be scanned to form a synthetic 2-D array. An image in x-y-z is formed computationally using the real array in the x direction and by a synthetic aperture in the y direction. This 3-D image is then analyzed to detect the presence or absence of mines.

The general form of the detection model for the 3-D imaging radar is the same as that of the 1-D single-aperture radar. The main difference is the addition of the image formation steps, which gain resolution in x-y and also bring in new noise sources. The detection approaches can be expanded to incorporate x-y information into the template catalogs to supplement the time-frequency information in the 1-D approach.

The image formation step is likened to a refocusing of the data, and thus demonstrates significant performance improvements with this additional information. Our principal approach to clutter rejection requires the use of 3-D radar images to distinguish the shapes of mines from natural subsurface inhomogeneities.

What we have found is that if the target object (the mine) is smaller than one quarter of the highest wavelength, reconstructive imaging provides little improvement in detection. This was verified in field tests as well as simulations. The basic signal model discussed above must include the 3-D point-spread function (PSF) of the imaging formation technique. This PSF will limit the resolution of the imaging system and can be a very complicated function of the radar system, the imaging geometry, and the target itself. For our initial analyses, we have assumed the PSF is position-invariant and consists of a specific 3-D form convolved with the target and clutter distribution.

More complex effects are being analyzed using finite-difference time-domain (FDTD) models and incorporated into the statistical noise models. An EM model of the MIR signal and its response from the ground and various objects (mines) has been developed. The model has been verified by experimental means and used to characterize clutter

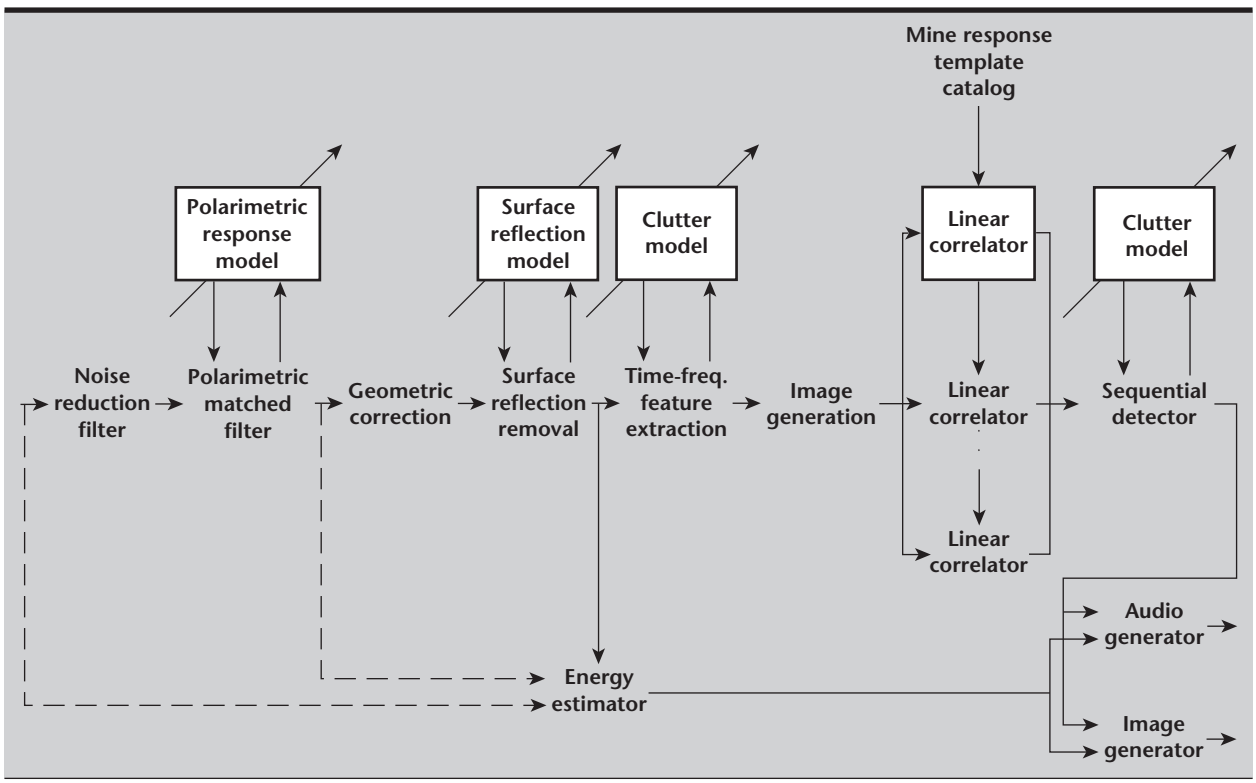

Figure 4. Signal processing block diagram for the LANDMARC mine detection system.

sources in actual data. One of the key results of the modeling effort is that the radar bandwidth for mine detection of near-surface AP mines is 0.5 to 10 GHz. This spectrum is higher than the current MIR (1 to 4 GHz).

On-going development efforts are working toward that end. Further refinements in the radar antennae and electronics have produced mine detection capabilities that are beyond the known state of radar technology. Algorithm refinements, particularly for removal of the first-surface clutter source, have provided step-by-step improvement in the signal-to-clutter ratio.

Another aspect of 3-D radar imaging is the sensitivity of the imaging to motion errors in the radar position estimates. The analysis of radar imaging parameters showed that precise positioning of radar transceivers is necessary to produce clear images that aid in clutter removal. Our initial design of a system that meets this requirement, yet is portable enough to use in the field, is a one-meter-squared array design shown in **Fig. 5**. The sensor array head is cantilevered over the area to be scanned and it produces overhead 3-D images of the sub-surface so that the operator can "see" not only the location of the buried object, but also its depth and shape. After identifying the mines in the image, the system positions its sensors over the mines for marking or removal.

Recent experiments with MIR show promise for improved AP mine detection. The developmental prototype of the mine detection system, with software for noise and clutter reduction, was assembled. A series of tests were performed at LLNL that were intended to challenge the MIR detection capabilities and provide realistic statistics for PD and false alarms.

The experiments involved unknown locations of mines (blind tests), using American-made M14 mines and intentional clutter in three soil types and in generally wet weather. Combined results of 18 independent tests of MIR compared to the Schiebel PSS-12 metal detector (commonly used at this time in most areas of the world) are shown in **Table 3**. From these results we believe that our approach is justified and should be continued.

Using laboratory prototypes and software, MIR has proven itself capable of detecting many plastic AP mine types buried in various soils. From this basic capability we plan to develop full mine detection systems that are based on the MIR concept; that is, radar-based mine detectors that are small, lightweight, low-power (battery-operated), inexpensive to replicate, and reliable.

This means that the laboratory prototypes we now have must be packaged, ruggedized, and made invariant to temperature or environmental effects. Software for control, processing, and display must be optimized and ported to a small (embedded) platform. With industry experts, other sensors must be incorporated into the system to further improve detection probability while minimizing the false alarm rate.

Extensive field testing must be done for various mines, soil conditions, and weather. Once the R&D is completed, we estimate that replication costs of such systems could be below $10,000 when integrated by an industry partner.

Summary

The LANDMARC goals for the second year have been completed and preparations are underway for continuation into FY-99. An array of MIR transceivers has been built, mounted on a portable platform, and shown to detect buried plastic AP land

(a)

(b)

Figure 5. (a) Operational scenario for a proposed MIR mine detection system. (b) Brass-board prototype system for developmental testing.

Table 3. Results of blind experiments of mine detection using a metal detector vs results from MIR.

Average of 18 tests	Detection rate	False alarms (per detected mine)
AN/PSS-12 (metal detector)	44%	7.95
MIR (radar detector)	85%	10.02

mines using imaging software and off-line processing. Results showed this system to out-perform the metal detectors in common use today. The next steps are to further refine the system for field operations and to move toward deployment with industrial participation.

A summary of what MIR currently offers is given below.

1. MIR is the smallest, lightest, lowest power radar system known, and hence cheapest to replicate by factors of perhaps 100; however, its performance in the field under many conditions still needs to be proven.
2. Because it emits a wider frequency band than previous GPR systems, the MIR sensor alone will generally provide greater information. Depth of penetration is enough for most mine detection applications.
3. Unique 3-D imaging software developed for MIR produces underground views not currently used in mine detection. It requires accurate position information and the latest computer technology; both are achievable and could be developed. The imaging provides either horizontal slice planes or a 3-D perspective view as though peering into the ground. The array concept initiated out in this project could provide a rapid acquisition mode for this type of imaging.
4. The miniature properties of MIR make it cost-effective for arrays. MIR imaging arrays for vehicles, robots, and even hand-held systems, should improve discrimination and speed, but this needs to be verified and we are only now starting full field testing.

These characteristics are very appealing to those interested in mine detection. However, there is still much work to be done. For example, Army personnel, and others who evaluate mine detection technologies for deployment, require controlled measures of PD, false alarm rate, and scan rate in technology demonstrations. Evaluation of mine detection systems is performed by the Army in fields of their own design. These demonstrations are intended to be part of Phase 3 experiments to evaluate the system. Modeling, radar and software refinement, and transition to deployment are also planned for the next phase.

Future Work

Recall that the overall objective of the entire project is to transition the successful MIR technology into a prototype land-mine detection system that helps mitigate the tremendous human suffering caused by small plastic AP mines. Attainment of this goal and wide dissemination of this technology will help stabilize local economies and environment, and indirectly enhance global security. Military demining objectives will also be addressed by the same system. Successful completion of this project will demonstrate improved mine detection over current technologies, enhance LLNL technical capabilities in radar imaging for other applications, and also attract cooperative participation from the U. S. Army and other sources.

Specific steps to be taken in the next phase are as follows:

1. Incorporate a higher-frequency radar into the mine detection prototype. The goal is to develop a radar with an expected 9-GHz passband (at 3 dB). A wider bandwidth will significantly improve the radar imaging capability.
2. Refine the noise and clutter models to reflect the wider passband and predict performance in various conditions.
3. Apply the improved models to the algorithms for processing, reconstruction, and detection. In particular, use first-surface echo removal to reduce clutter and study super-resolution methods through the University of California at Davis.
4. Perform the series of experiments necessary to validate the above models and measure the detection performance improvement.
5. Pursue a path toward commercialization.

We also plan to demonstrate the system for various organizations that have already expressed interest in these sensors, including industry, government agencies (DOD, State Department, DARPA), foreign governments and institutions (Japan, Norway), and humanitarian relief organizations (World Bank, U. N.).

The technologies developed for this project will have utility well beyond the life of this project. LLNL and other federal agencies have a need for radar imaging systems that have similar characteristics. Bridge inspection for the Federal Highways Administration (with whom a 64-element array has already been developed) will benefit from the mine detection technologies.

Other imaging for nondestructive evaluation of concrete, wood, and other materials is also underway. The experience and technology gained through the MIR mine detection project will significantly enhance the understanding of radar imaging and will benefit many new areas.

Acknowledgments

The authors acknowledge the contributions of the scientists, engineers and technicians involved with the MIR Project. These include J. Brase, M. Bujak, R. Cavitt, G. Dallum, R. Gilliam, G. Governo, H. Jones, M-L. Liu, J. Mast, S. Nelson, T. Rosenbury, R. Stever, M. Vigars, and P. Welsh. Administrative help from B. Wooton, M. McInnis, and R. Sachau is appreciated. We also acknowledge the continued support from the Laser Programs Directorate (J. Brase, S. Vaidya, and E. M. Campbell) and the Electronics Engineering Department (S. Dimolitsas and R. Twogood). The AN/PSS-12 metal detector was lent to us by P. Harben of LLNL.

References

1. Anderson, C., W. Aimonetti, M. Barth, M. Buhl, N. Bull, M. Carter, G. Clark, D. Fields, S. Fulkerson, R. Kane, C. Lee, F. Lee, B. McKinley, J. Page, F. Roeske, Jr., T. Rossow, P. Sargis, J. Scarafiotti, P. Schaich, S. Sengupta, and R. Sherwood, (1994), "LLNL Electro-optical Mine Detection Program," Lawrence Livermore National Laboratory Internal Report, Livermore, California (UCRL-ID-118672).

2. Azevedo, S. G., D. T. Gavel, J. E. Mast, and J. P. Warhus, (1995), "Statement of Capabilities: Micropower Impulse Radar (MIR) Technology Applied to Mine Detection and Imaging," Lawrence Livermore National Laboratory, Livermore, California (UCRL-ID-5366).

3. Azevedo, S. G., D. T. Gavel, J. E. Mast, E. T. Rosenbury, and J. P. Warhus (1996), "Arrays of Micropower Impulse Radar (MIR) sensors for Subsurface Detection," *Proceedings of the EUREL Conference on the Detection of Abandoned Land Mines, IEE Conf.* Pub. No. 431, Edinburgh, Scotland, UK.

4. Azevedo, S. G., D. T. Gavel, J. E. Mast, and J. P. Warhus (1995), "Land Mine Detection and Imaging Using Micropower Impulse Radar (MIR)," *Proceedings of the Workshop on Anti-personnel Mine Detection and Removal,* Lausanne, Switzerland, pp. 48–51.

5. Clark, G. A., J. E. Hernandez, S. K. Sengupta, R. J. Sherwood, P. C. Schaich, M. R. Buhl, R. J. Kane, M. J. Barth, and N. K. DelGrande (1992), "Computer Vision and Sensor Fusion for Detecting Buried Objects," *IEEE Proceedings of the 26th Asilomar Conference on Signals, Systems and Computers,* Pacific Grove, California, p. 466.

6. Clark, G. A., S. K. Sengupta, W. D. Aimonetti, F. Roeske, J. G. Donetti, D. J. Fields, R. J. Sherwood, and P. C. Schaich (1995), "Computer Vision and Sensor Fusion for Detecting Buried Objects," *Proceedings of the Symposium of Autonomous Systems in Mine Countermeasures,* Monterey, California, April 4-7.

7. Eimerl, D. (1997), "Land-Mine Policy in the Near-Term: A Framework for Technology Analysis and Action," Center for Global Security Research, Lawrence Livermore National Laboratory, Livermore, California (UCRL-ID-130849, CGSR-98-002), August.

8. Gavel, D. T., J. E. Mast, J. Warhus, and S. G. Azevedo (1995), "An Impulse Radar Array for Detecting Land Mines," *Proceedings of the Autonomous Vehicles in Mine Countermeasures Symposium,* Monterey, California, pp. 6–112.

9. Sargis, P.D., F.D. Lee, E. S. Fulkerson, B.J. McKinley, and W.D. Aimonetti (1994), "Ground-Penetrating Radar for Buried Mine Detection," *SPIE* Vol. **2217**, *Aerial Surveillance Sensing, including Obscured and Underground Object Detection,* April, pp. 4-6.

10. Warrick, A. L., S. G. Azevedo, and J. E. Mast, (1998), "Prediction of Buried Mine-like Target Radar Signatures using Wideband Electromagnetic Modeling," *Proceedings of SPIE Conference on Detection and Remediation Technologies for Mines and Mine-Like Targets III*, **3392**. pp. 776-783.

11. Nelson, S. D., (1994), "Electromagnetic Modeling for Target-Rich Embedded Environments," *Engineering Research, Development, and Technology*, Lawrence Livermore National Laboratory, Livermore, California (UCRL-53868-93), March.

12. Azevedo, S. G., J. E. Mast, S. D. Nelson, E. T. Rosenbury, H. E. Jones,T. E. McEwan, D. J. Mullenhoff, R. E. Hugenberger, R. D. Stever, J. P. Warhus, and M. G. Wieting (1996), "HERMES: A high-speed radar imaging system for inspection of bridge decks," *Nondestructive Evaluation Techniques for Aging Infrastructure and Manufacturing, SPIE* Vol. **2946**, pp. 195-204.

13. Warhus, J. P., J. E. Mast, E. M. Johansson, and S. D. Nelson (1994), "Advanced Ground-Penetrating Radar," *Advanced Microwave and Millimeter Wave Detectors*, SPIE Vol. **2275**, pp. 22-24.

14. Mast, J. E. (1993), *Microwave Pulse-Echo Radar Imaging for the Nondestructive Evaluation of Civil Structures*, Ph.D. thesis, University of Illinois at Urbana-Champaign.

15. Mast, J. (1998), "SIGOP Manual," Lawrence Livermore National Laboratory Internal Report, (to be published).

16. Mast, J. (1998), "GPR Manual," Lawrence Livermore National Laboratory Internal Report, (to be published).

17. Mast, J. E., and S. G. Azevedo (1995), "Applications of Micropower Impulse Radar to Nondestructive Evaluation," *Engineering Research, Development, and Technology*, Lawrence Livermore National Laboratory, Livermore, California (UCRL-53868-95), March.

18. Mast, J. E., and E. M. Johansson (1994), "Three-Dimensional Ground-Penetrating Radar Imaging Using Multi-Frequency Diffraction Tomography," *Advanced Microwave and Millimeter Wave Detectors, SPIE* Vol. **2275**, pp. 25-26.

19. Azevedo, S. G., T. E. McEwan, and J. P. Warhus (1996), "Microradar Development," *Engineering Research, Development and Technology: Thrust Area Report*, Lawrence Livermore National Laboratory, Livermore, California (UCRL-53868-95), pp. 6-17.

20. Azevedo, S. G., and T. E. McEwan (1996), "Modular MIR," *Engineering Research, Development, and Technology*, Lawrence Livermore National Laboratory, Livermore, California (UCRL-53868-96).

21. Azevedo, S. G., and T. E. McEwan (1996), "Micropower Impulse Radar," *Science and Technology Review*, Lawrence Livermore National Laboratory, Livermore, California (UCRL-52000-96-1/2), pp. 16-29.

22. "The Pocket Radar Revolution," *New Scientist* (August 1995).

23. "Radar on a Chip: 101 Uses in your Life," *Popular Science* (March 1995).

MAN-3D: A Software Tool-Kit for 3-D Image Analysis

Sailes K. Sengupta
Electronics Engineering Technologies Division
Electronics Engineering

In this project a software tool-kit is written to facilitate 3-D image data analysis. It consists of subroutines written in the commercially available image processing language IDL. The emphasis is on three aspects of image analysis: detection, identification and quantification of regions of interest in image data. All three are important topics in the analysis of 3-D data arising in nondestructive evaluation, including data from x-ray computed tomography and from ultrasonic, infrared, radar, NMR and other scans.

Introduction

Interpretive signal and image analysis plays a key role in nondestructive evaluation (NDE). Especially important are the analyses of 3-D images resulting from the use of such diverse probes as x rays, ultrasound and NMR. Typically, the data consist of a stack of 2-D image slices with each slice representing a certain physical measurement of a horizontal section of the 3-D object under investigation. Researchers are interested in locating, as well as identifying any "anomalies" or "defects" present in the specimen. We are also interested in quantifying (finding the number and size, for example) these anomalies or defects.

As a result, we are led to various questions related to the 3-D images of the objects under study. Some of these questions are negotiable in a straightforward manner akin to those involving 2-D imagery. In a 3-D context however, there are questions that are not directly answered by the methods used for the 2-D images. In some cases, the extensions, when possible, are computationally expensive and must be appropriately modified to be practically applicable.

This is true, for example, for the notion of connectedness that plays a significant role in image segmentation. In the 2-D case, we have 4-, 6- and 8-connectedness. These notions are well defined.[1,2]

But how does one define connectedness in a 3-D image? If k is the number of voxels adjacent to a given voxel, a k-connectedness can be defined for k equaling a number ranging from 6 to 26, and subject perhaps to some 3-D symmetry consideration. Choosing k consistent with a given application is often a nontrivial task.

For another example, second-order statistics (joint distribution of 2 spatially separated pixels) plays a crucial role in texture discrimination of a 2-D image. If we try to extend it in a natural way to the 3-D case we are led to second-, or perhaps "third-order statistics" involving, respectively, the joint distribution of 2 or 3 spatially separated voxels.

Computational complexity, however, precludes the blind use of third-order statistics even when we restrict our consideration to a spatial separation of 1 voxel from one another. Even in the second-order case, one has to be selective in limiting the choice of the direction and magnitude in the choice of the voxel separation.

The examples above point to the need for a 3-D data analysis paradigm that relies on algorithms that are computationally "affordable" and application-specific in scope. The software tool-kit described in this work is based on such a paradigm. As a result, image-processing algorithms that are "global" have been preferred over the "local" ones whenever feasible, often resulting in a faster turn around time.

The software is written in the language IDL[3], which is a C-like language providing access to subroutines that allow many fast and useful image-processing tasks.

In the next section we describe progress in the development of the tool-kit with reference to the specific problems in 3-D image analysis that have been addressed in this work. We also discuss a few applications from projects of recent interest at Lawrence Livermore National Laboratory.

Progress

A NDE procedure frequently results in 3-D digitized images to be analyzed and interpreted. Among the basic tasks related to such analyses are detection, identification and quantification of anomalies or defects, or more generally "regions of interest" (ROI) in the item probed. The detection of a ROI typically involves the detection of a pattern of pixels/voxels with characteristics that may be either known or unknown.

For example, the detection of regions of a given shape (rectangles, circles, or spheroids in 3-D), or known dynamic range of gray levels, or known textural characteristics in an image, is a detection of the first kind. On the other hand, the detection of all anomalous regions in an image where the pixels/voxels differ significantly from those in the background (regional or global) is a detection of the second kind.

In the subsection on detection we have concentrated on detection of unknown or partially known ROIs, relegating the treatment of the first kind to the subsection on identification. We will see there that this task is handled by some traditional methods of classification/pattern recognition where classifiers are trained to learn the image characteristics of the ROIs based on training samples of known categories. Later, an unknown sample is presented to the trained classifier for classification.

Once the ROIs are detected and identified, we need to study them quantitatively.

For example, say we have localized and identified the types of grains of certain known textural characteristics in an image. The questions include: What is the size distribution of this particular grain type in the image? Is this correlated with the size distribution of another grain type in the image? What is the extent of this correlation, if any? Questions of this type have been addressed in the subsection on quantification.

A summary of the main subroutines developed in this project is given in **Table 1**.

Detection

As indicated above, detection usually involves localization of the ROIs when they exist. There are various means of achieving this. We have dealt with some of these methods, described briefly in the following paragraphs.

Table 1. Partial listing of main subroutines in the tool-kit for 3-D image analysis.

Detection:		
Thresholding:	histo_analyze.pro threshold.pro	histo_seg.pro
Clustering and Neighborhood Statistics:	clust_wts.pro* nabor2.pro nabor3.pro nabor3new.pro nabor_stat.pro	cluster.pro* nabor2d.pro nabor3d.pro nabor_mean_range.pro
CFAR Algorithm:	cfar_1d.pro	cfar3d.pro
Segmentation by Region Merging:	reg_merge.pro	reg_merge3d.pro
Connected Component Analysis:	conn_comp.pro	conn_comp3d.pro
Segmentation by Watershed (Meyer):	ws_meyer.pro	ws_marker.pro
Identification:		
Neighborhood Statistics:	See *Detection*	
Shape and Size Features:	See *Granulometry*	
Feature Subset:	See directory "Classify"	
Classification Routine:	See directory "Classify"	
Granulometry:		
Linear Granulometry:	lin_gran.pro	granulo_linear.pro
Granulometry by Opening:	granulo_open.pro granulo_open_line.pro	granulo_open_general.pro

* Indicates IDL subroutines

Global Thresholding. When the intensity level in the ROI is known to have a threshold value (upper or lower), or known to fall in an interval, global thresholding is a powerful way of localizing it. The threshold limits and the interval boundaries can sometimes be provided by the physical properties related to the gray-level/intensity.

For example, in x-ray radiography, tomography, ultrasound, and infrared imagery, the property could be intensity, x-ray attenuation coefficient, sound attenuation, or surface temperature, respectively. Very often however, the limits have to be inferred from the statistical distribution of the gray levels of pixels/voxels in the image. Specifically, these limits are determined from the "peaks" (or modes) and "valleys" (separating two consecutive modes) of the histogram of the distribution when they are prominent.

Global Clustering. Frequently, intensity of the image pixels/voxels alone does not provide the desirable separation between the ROIs, the background, and other objects. In such cases, one may want to pursue this separation in a higher-dimensional space in a multivariate setting. In addition to the intensity, one might include other "features" of the pixels/voxels in the image, such as some statistical parameters associated with a suitably defined neighborhood of them.

More generally, elements of the feature vector could represent gradient magnitude, gradient phase, intensities at multiple spectral bands, or other attributes. It may also be some other measured property of the pixel/voxel. The separation of the ROIs from the background is then sought in the multi-dimensional feature space by an appropriate, unsupervised training procedure such as "clustering." Pixels/voxels that are "close" to one another in the feature space as measured by their Euclidean or some other distance, are considered "similar." In a clustering procedure, these similar objects are clustered together. In this work we have used the K-means clustering algorithm.[4,5]

Constant False Alarm Rate (CFAR) Algorithm. When the intensities in an image vary systematically, with a possible trend, the standard thresholding technique is unlikely to work. In such cases, detection can sometimes be implemented satisfactorily by means of the CFAR algorithm. This is particularly effective when the local variance of the intensity changes at a smaller rate than the local mean.

In this algorithm, one first subtracts the "local" mean from each pixel/voxel. Then a statistical test is applied to each pixel/voxel to determine if it is different "significantly" from its background pixels/voxels. Although computationally intensive, the algorithm allows for a pre-assigned false alarm rate in the detection of ROIs.[6]

Region-Merging-Based Segmentation and 3-D Connected Component Analysis. In this method, each 2-D slice is segmented by a region-growing/merging method with a label attached to each segment by means of a connected component labeling algorithm. Adjacent connected components in consecutive slices are then put together and re-labeled to complete the 3-D connected component analysis.[7,8]

Segmentation by Watershed and 3-D Connected Component Analysis. This is the same as above, except the 2-D segmentation is done by the watershed algorithm.[9]

Identification

As indicated in an earlier paragraph, identification is frequently achieved by a "supervised learning" procedure based on "ground truth" and is outlined in the following steps. The "ground truth" here refers to the known classification categories of the training pixels/voxels.

Feature Computation. Various features are computed for "training" samples of known object types. The nature of features varies widely from one application to another. In this work we have provided routines to compute 2- and 3-D neighborhood statistics and extraction of first- and second-order statistics from these neighborhood statistics.

Feature Subset Selection. If the number of features is large, a smaller subset of these features containing most, if not all, class discriminatory information is often desirable. Frequently, due to resource constraints, the experimenter has a small sample to work with, and as a result is not able to estimate accurately the distribution parameters in a higher-dimensional feature space.

In a subset selection procedure, feature subsets are selected based on their "separability measure," which provides an index of how well the object types in the feature space consisting of a given subset of features are separated.[10]

The simplest possible separability measure in a multi-dimensional feature space is based on the Euclidean distance between pairs of points representing the selected features of samples from two populations. This applies when features may be assumed independent. The minimum of such pairwise distances after appropriate normalization gives the separability measure of the subset of features under consideration. When the features

are correlated, one can replace the Euclidean distance by other distances, such as Bhattacharya or Matusita.

Training and Classification. A suitably chosen "classifier" is then trained, based on the features of the training sample. A classifier is a system that creates class partitions in the feature space based on labeled (known) samples. Based on the features computed from a new sample, the trained classifier checks which cell of the partition the new sample belongs to and labels it accordingly. We have chosen a non-parametric Bayes classifier for the present work. It is also termed the "Probabilistic Neural Network" (PNN). The trained classifier is then used to classify a sample as needed.[11]

Quantification

Having localized and identified the ROIs in the image, the researcher would like to quantify the ROIs in an appropriate manner. We have used the technique of morphological granulometry[12,13] to implement this capability. Traditional granulometry is an essential tool of quantitative morphological image analysis. It consists of sequential application of openings (closings) with structuring elements that are monotonic.

The principle of granulometry can be expressed in simple terms as follows. Imagine a large collection of "grains" of different sizes, filtered through sieves of progressively increasing mesh sizes Numerical characteristics of the residues at each stage are measured until nothing remains. The successive residues provide us with a quantitative measure of the grain size distribution.

In fact, by varying the shapes and orientations of the mesh elements in the sieves, it is possible to get a complete quantitative morphological characterization of the grains. The method was first conceived by Matheron who called it "morphological granulometry."

As a practical application, this method provides a direct computation of the size distribution of "grains"/"pores" in a binary image in one, two, or three dimensions without having to do a connected component analysis first. An interesting feature in this implementation is that one can detect the size distribution of the image grains along any specific direction, or more generally, those fitting specifically shaped objects with a given spatial orientation.

Applications

In this section we provide four typical applications of the subroutines in our tool-kit. This will include 3-D images from computed tomography using x-ray and ultrasonic imagery.

1. Asphalt sample. The Federal Highway Commission provided us with an asphalt sample of approximate diameter 102 mm. The objective was to quantify such components as tar, aggregate, and porosity in the sample. A linear-array detector CT scanner (LCAT) operating at a maximum tube potential of 160 keV (1.9 mA) was used, with the data filtered intentionally to reduce beam-hardening to acquire a 3-D CT image. The image (**Fig. 1**) shows a cross-section measuring 102 mm with a pixel size of 225 μm and a slice plane thickness of 500 μm. **Figure 2** shows the attenuation histogram of the slice.

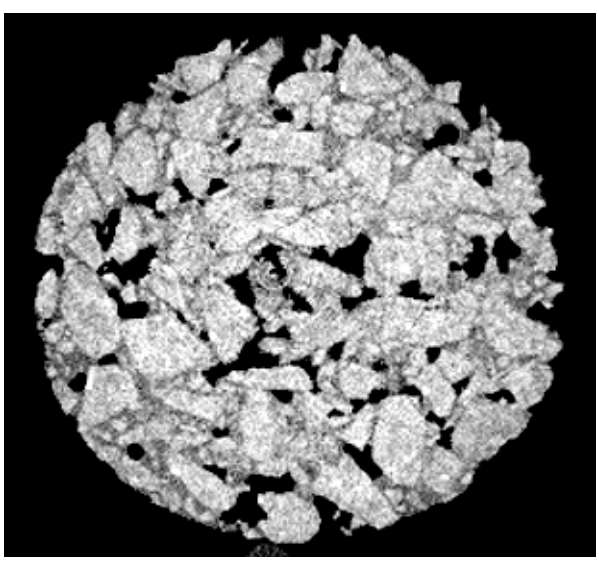

Figure 1. Representative slice of the CT scan of an asphalt sample containing asphalt, rocks and air bubbles.

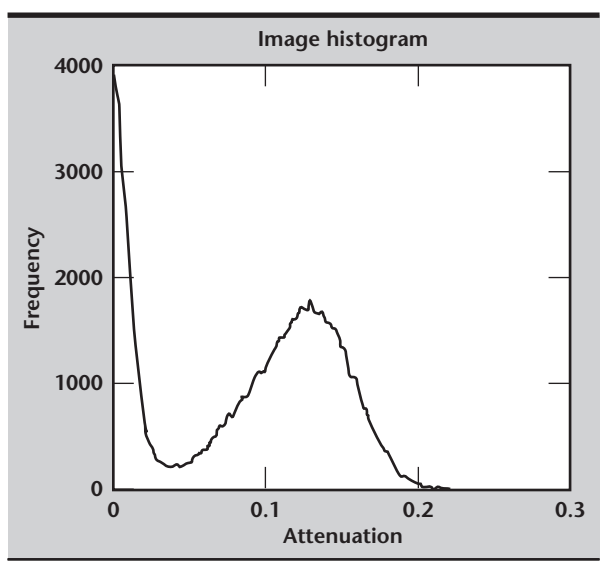

Figure 2. Histogram of the pixel attenuation in the CT image shown in Figure 1.

The image is thresholded using the "valley" points v = [0.04, 0.2], resulting in the three "segments" shown in **Figs. 3**, **4**, and **5**. In **Fig. 3**, attenuation less than 0.04, represents the voids and background; attenuation between 0.04 and 0.2, represents the asphalt; and the high attenuation voxels represent the inclusions. Pixels that are near zero represent air both inside and outside the sample. Thus this simple method has separated air from the rest of the sample.

The first segment (**Fig. 3a**), shows that the background (in white) and the air pockets (also in white) in the block have been separated. The second segment (**Fig. 4b**) shows the rest, including a water droplet at the bottom but excluding the speckled bright spots evident in **Fig. 1**. The third segment (**Fig. 4c**) shows the speckles.

The histogram analysis (*histo_analyze*) and segmentation (*histo_seg*) routines used in this example have been used on the 2-D slice but they are equally applicable with similar results to the global 3-D data.

While thresholding separates some of the objects, it fails when there are physically different objects with highly overlapping ranges of intensities. This is the case with the asphalt, rocks, and water vial in this image. To address this problem we try to separate the objects in a higher-dimensional "feature" space consisting of a set of neighborhood statistics of each pixel/voxel. Specifically, we choose a window centered at each pixel/voxel and compute a set of statistics for the pixels/voxels in the window. We then cluster the pixels/voxels (inclusions excepted) of the image into a fixed number, K, of clusters, where K is the number of separable objects known to be present in the image. The results of the clustering using K = 3 are shown **Fig. 4**.

A tabulation of the percentages of pixels representing the four different objects within the aggregate is given in **Table 2**.

2. Aluminum part. A second example demonstrates the use of the CFAR 3-D code for isolating regions suspected to be porous in 3-D imagery obtained using a high-frequency ultrasonic probe on an aluminum part. One of the objectives in the porosity study is to get an estimate of the pore-size distribution. **Figures 5a** to **d** show a representative slice in the middle part of the ultrasonic scan of the aluminum part. **Figure 5a** shows the raw image. **Figure 5b** shows the result of a pre-processing step,

Table 2. Composition of the aggregate sample by percentage.

Rock	49
Asphalt	29
Void	16
Inclusion	6

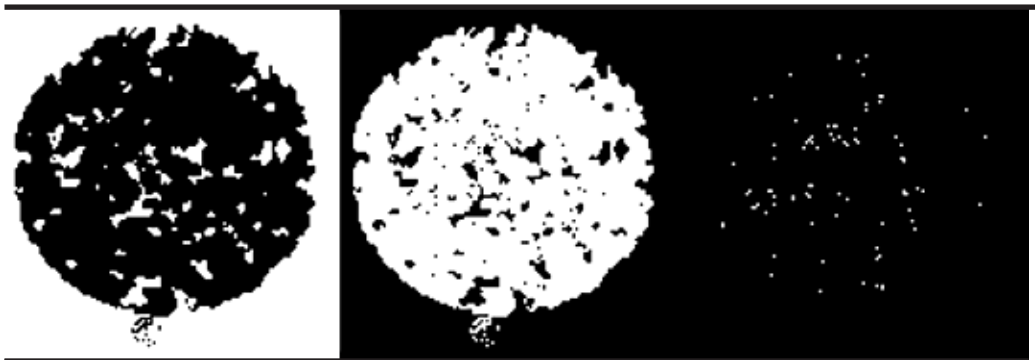

Figure 3. Binary image showing the three segments obtained by using the threshold vector [0.04, 0.2] in the image in Figure 1.

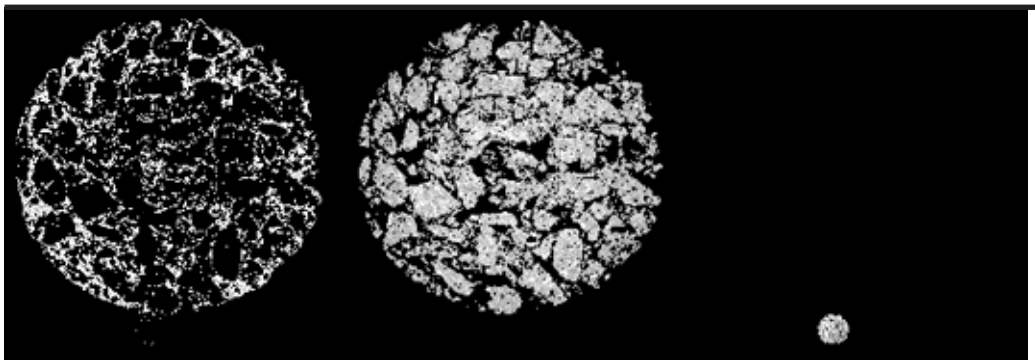

Figure 4. Three segments showing the asphalt, rocks, and the water droplet.

the absolute value of the intensity deviation from the mean image intensity. **Figures 5c** and **d** show the result of applying the CFAR 3-D code to isolate the "anomalies" using a window size of 11 × 11 and 15 × 15, respectively, with the false alarm rate set at the five percent level.

3. A third example illustrates other routines for object detection. We used a combination of the CFAR and a 3-D connected component analysis for a 3-D segmentation. The data used are taken from the Active and Passive Computed Tomography (A&PCT) program for waste drum radioactivity assay. The objective here is to localize the regions of high radioactivity. The frames in **Fig. 6** represent 14 × 14 × 17 slices of A&PCT data acquired at 414 keV. Slices 1 to 15 arranged from top to bottom and left to right in three rows are shown in **Fig. 6**.

The light blobs indicate the presence of high radioactivity. We applied the CFAR_3D algorithm to localize the radioactive objects in the image. The result is shown in **Fig. 7**.

A 3-D connected component analysis led to three distinct segments (not shown) consisting of 6, 16, and 44 voxels, respectively.

4. Our final example is taken from the porosity study of a die-cast pre-stressed aluminum (A-356) tensile bar, to illustrate how methods of morphological granulometry can be used to derive the 1-, 2- and 3-D size distribution of pores (or grains) using 3-D tomographic data. These in turn can be used to model metal composite behavior under different kinds of stress.

Figure 8 shows a single slice of a 3-D CT scan of the aluminum sample using the PCAT system with 80 keV. The CT image has a pixel-resolution

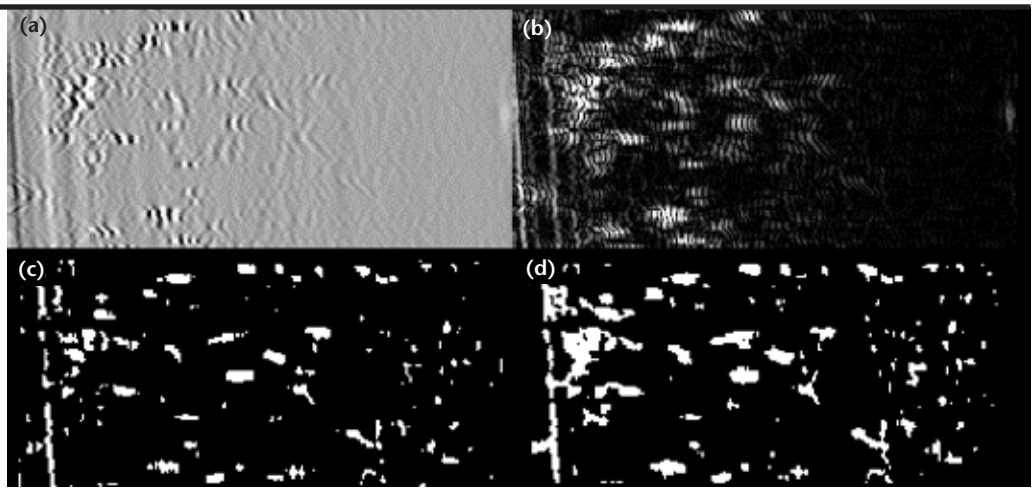

Figure 5. (a) High-frequency ultrasound c-scan image of an aluminum part. Successive steps used to isolate the pores include: (b) absolute deviation from the mean, a preprocessing step; (c) results of the application of CFAR with a 3-D kernel of 11 voxels to (b); and (d) results of the application of CFAR with a 3-D kernel of 15 voxels to (b).

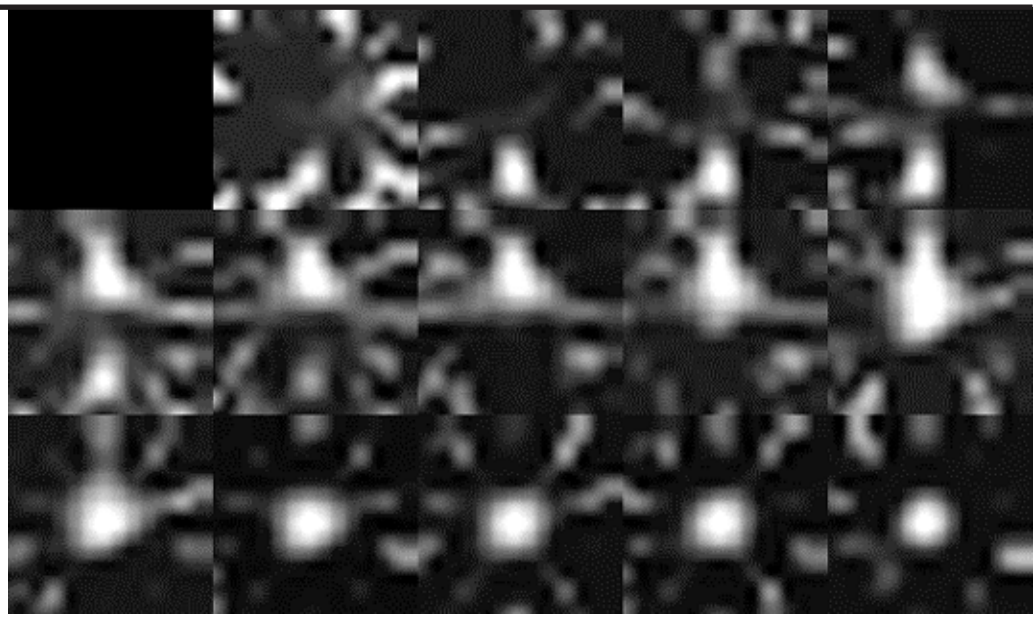

Figure 6. Slices 1 to 15 (top left is blank) of A&PCT data acquired at 414 keV.

of 20.5 μm. It is of interest to find the size distribution of the pores in the matrix along a chosen direction, in particular along the three axes.

One may also be interested in finding the 2- and 3-D size distribution of these pores. The granulometry routines developed in this work have been used to find such distributions applied to the thresholded binary image obtained from the original. **Figures 9** and **10** show the size distributions along the x- and z-axis, and **Fig. 11** the same for the 3-D volume. If needed, a comparison of the two size distributions can be made at this stage.

Future Work

Three-dimensional image analysis resulting from a variety of probes such as x-ray CT, A&PCT, ultrasonic scans, and NMR present a formidable challenge to the data analyst. In this work we have provided a tool-kit based on the commercially available software IDL to address some of the interesting classes of problems that arise in such analyses.

Several possible extensions to improve and extend the capabilities of this tool-kit are being planned. First, like all useful tool-kits, there is the need for a graphical user interface (GUI). The GUI

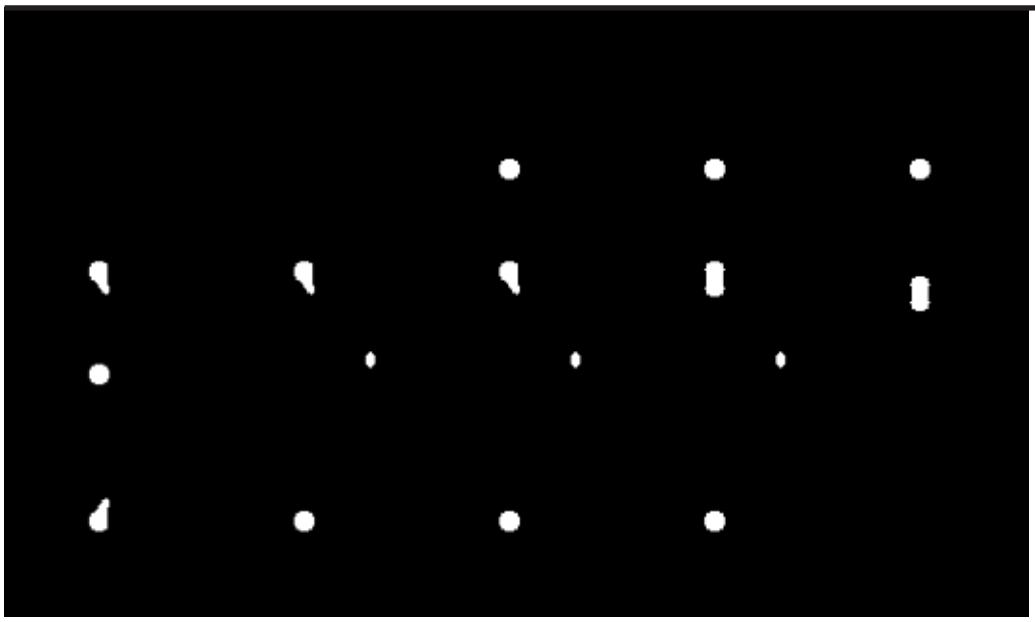

Figure 7. The localized highly radioactive regions in slices 1 to 15.

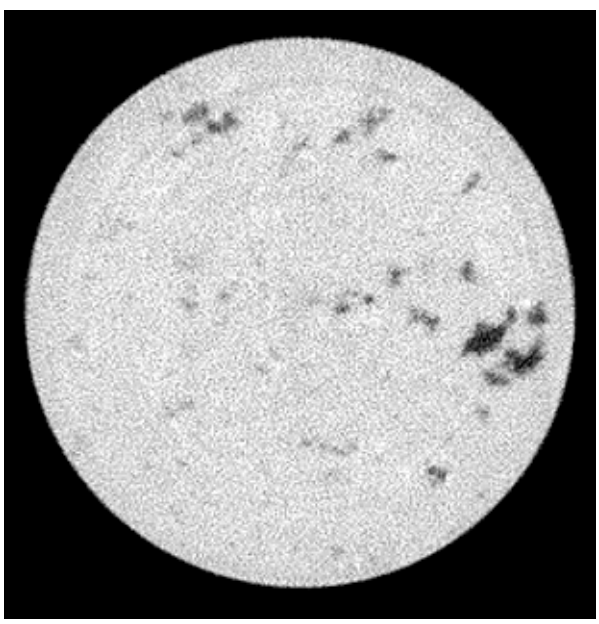

Figure 8. Representative CT slice of a pre-stressed A-356 die-cast aluminum tensile bar with pores showing in dark shade.

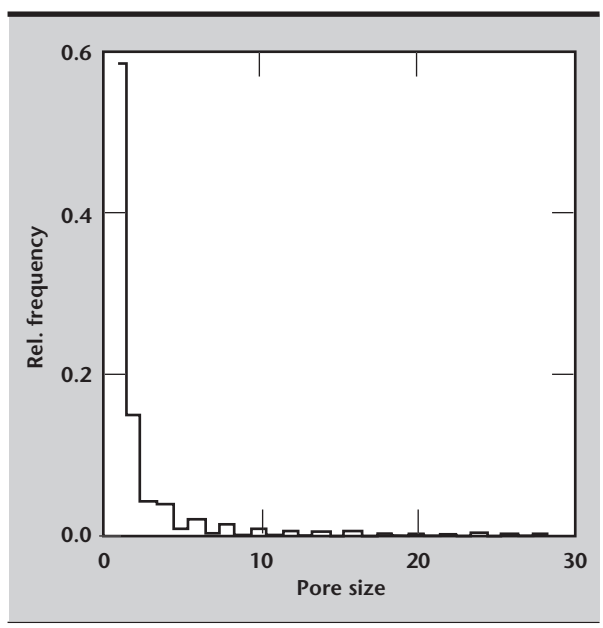

Figure 9. Pore-size distribution along the x-axis in the tensile bar

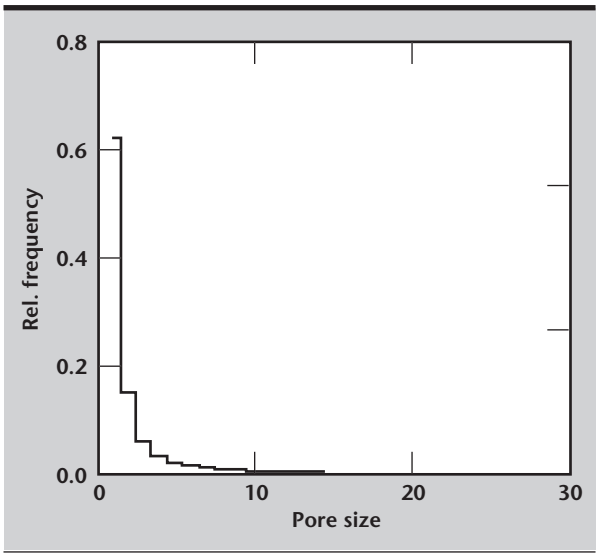

Figure 10. Pore-size distribution along the z-axis in the tensile bar.

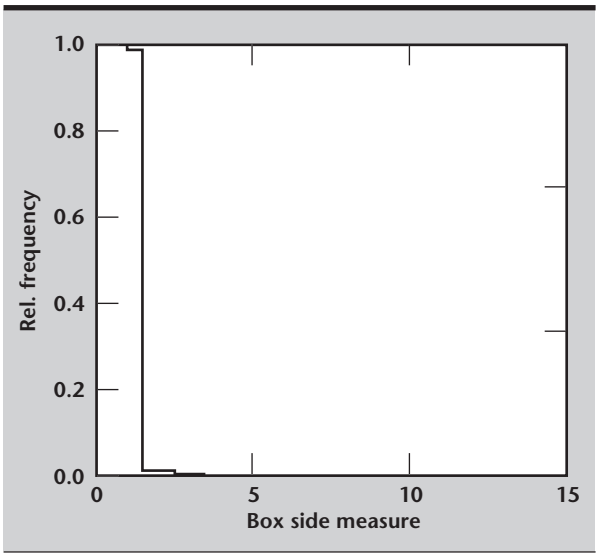

Figure 11. Pore-size distribution using openings by boxes.

allows the investigator to concentrate on the data analysis and inference process without getting bogged down in the image-processing details.

Second, some of the algorithms used for granulometry in this tool-kit are of complexity O(n) or higher, where n is the number of pixels/voxels in the input image. Some recent developments in morphological image processing on "fast" openings[14,15] will allow us to replace these slow executing algorithms by faster ones.

Third, we would extend single granulometry in this work to "multivariate granulometry." A single granulometry yields the size distribution of a single variable where structuring elements grow at the same rate so that their relative sizes are constant. Multivariate granulometry[16] allows each structuring element to grow at its own chosen rate, independent of the scales of other structuring elements enabling better representation of the textural features. A texture classification protocol using multivariate granulometry will capture the morphological characteristics of an image better and allow more accurate image classification.

Acknowledgments

I am grateful to C. Logan, P. Roberson, D. Chinn, and J. Haskins for supplying the data shown in the applications above. I am particularly grateful to H. Martz for carefully reviewing an earlier draft and suggesting numerous improvements.

References

1. Rosenfeld, A., and A. Kak (1982), "Digital Picture Processing," 2nd ed., Vols. **1** and **2**, Academic Press, Orlando, Florida.

2. Serra, J. (1982), "Image Analysis and Mathematical Morphology," Academic Press, New York, New York.

3. IDL Version 5.0 (1997), Research Systems Inc., Boulder, Colorado, March.

4. Ball, G. H., and D. J. Hall (1966), "ISODATA, A Novel Method of Data Analysis and Pattern Classification," *International Communication Conference*, Philadelphia, Pennsylvania, June.

5. Jain, A. K. (1989), "Fundamentals of Digital Image Processing," Prentice Hall, Englewood Cliffs, New Jersey.

6. Reed, I. S., and X. Yu (1990), "Adaptive Multi-Band CFAR Detection of an Optical Pattern with Unknown Spectral Distribution," *IEEE Trans. on Acoustics, Speech and Signal Processing*, June.

7. Levine, M. D. (1985), "Vision in Man and Machine," McGraw-Hill, New York, New York.

8. Haralick, R., and L. Shapiro (1992), "Computer and Robot Vision," Vol. **1**, Addison-Wesley, Reading, Massachusetts.

9. Beucher, S., and F. Meyer (1993), *The Morphological Approach to Segmentation: Watershed transformation* in "Mathematical Morphology in Image Processing," E. Dougherty, ed., Marcel Dekker Inc., New York, New York.

10. Fukunaga, K. (1990), "Introduction to Statistical Pattern Recognition," 2nd. ed., Academic Press, San Diego, California.

11. Specht, D. F. (1990), "Probabilistic Neural Networks," Neural Network, Vol. **3**, No. 1, pp. 109–118.

12. Serra, J. (1982), "Image Analysis and Mathematical Morphology," Academic Press, New York, New York.

13. Dougherty, E., J. Pelz, F. Sand, and A. Lent (1992), "Morphological Image Segmentation by Local Granulometric Size Distributions," *Journal of Electronic Imaging*, Vol. **1**, (1), January.

14. Crespo, J., R. W. Schafer, J. Serra, C. Gratin, and F. Meyer (1997), "The Flat Zone Approach: A General Low-level Region Merging Segmentation Method," *Signal Processing*, Vol. **62**, pp. 37–60.

15. Vincent, L. (1994), "Fast Opening Functions and Morphological Granulometries," *SPIE*, Vol. **2300**, pp. 253–267.

16. Batman, S., and E. Dougherty (1997), "Size Distributions for Multivariate Morphological Granulometries: Texture Classification and Statistical Properties," *Optical Engineering*, Vol. **36**, (5), pp. 1518–29.

Image Recovery Techniques for X-Ray Computed Tomography in Limited-Data Environments

Dennis M. Goodman and Jessie A. Jackson
Laser Engineering Division
Electronics Engineering

Maurice B. Aufderheide
Defense Systems

Erik M. Johansson
Consultant
Tracy, California

There is an increasing requirement throughout Lawrence Livermore National Laboratory (LLNL) for nondestructive evaluation using x-ray computed tomography (CT). Conventional CT methods are non-iterative algorithms that have the advantage of low computational effort, but are not sufficiently adaptable to incorporate prior information or non-Gaussian statistics. In many cases, restrictions on data acquisition time, imaging geometry, and budgets make it infeasible to acquire projection data over enough views to achieve desired spatial resolution using conventional CT methods. Most currently existing iterative tomography algorithms are based on methods that are time-consuming because they converge very slowly, if at all. The goal of our work was to develop a set of limited-data CT reconstruction tools and demonstrate their usefulness by applying them to a variety of problems of interest to LLNL. In the second and final year of this project we continued our development of reconstruction tools and have demonstrated their effectiveness on several important problems.

Introduction

Tomography is used throughout LLNL to investigate the composition and structure of objects noninvasively. Conventional CT algorithms have the advantage that they are noniterative, hence, they are computationally efficient, but they suffer from a lack of flexibility in that they can't incorporate prior information about the solution, nor can they use other than the squared error criterion to fit the data.

Because the image recovery problem associated with most tomography applications is ill-posed, which is particularly true for limited-data situations, all possible prior information about the unknown object must be used to produce high-quality images. Furthermore, although least-squares (that is, minimizing a sum of squares error function that measures the mismatch between the data and the model) is appropriate if the data has a Gaussian distribution with known constant variance, using it when the data has a non-Gaussian distribution can seriously degrade the quality of reconstructed images.

An example is counting problems (such as emission tomography) where the data consists of particle or photon counts that typically have a Poisson distribution. Another example is outlier-corrupted data, in which the distribution function is not known exactly, but it is known that the data pixels are subject to outliers that occur infrequently, but greatly distort those pixels where they occur. These outliers result from a variety of problems including a few bad detectors in a CCD array, improper assumptions about the model, or "hits" from extraneous radiation or particles. Outliers have highly deleterious effects on the reconstructed image when squared error is used.

The problems our techniques have been designed to handle can be described as follows. First there is a linear equation that models the relationship of the unknown to the data:

$$\hat{\mathbf{y}} = \mathbf{A}\hat{\mathbf{x}} , \qquad (1)$$

where the vector $\hat{\mathbf{x}}$ represents the unknown image we wish to reconstruct; and $\mathbf{A}$ is a matrix that

represents such effects as geometry and absorption that lead to the expected data, $\hat{\mathbf{y}}$, if $\hat{\mathbf{x}}$ were the true image.

The actual observed data is **y**, and the estimate of the true image is obtained by using an optimization algorithm to adjust $\hat{\mathbf{x}}$ so that $\hat{\mathbf{y}}$ is a best fit to the actual data according to some criterion function, say

$$f\left(\mathbf{y}, \hat{\mathbf{y}}\right) , \tag{2}$$

where the choice of the criterion function, as we noted earlier, depends on the statistics of **y**. Consequently, our reconstruction problem involves minimizing, with respect to $\hat{\mathbf{x}}$, a function of the form

$$\mathrm{L}\left(\mathbf{y}, \hat{\mathbf{x}}\right) = f\left(\mathbf{y}, \mathbf{A}\hat{\mathbf{x}}\right) . \tag{3}$$

This function is usually a negative log-likelihood function, so the image we recover is the maximum likelihood estimate of the unknown.[1] Because our problems typically are ill-posed, we add penalty parameters and impose prior constraints on **x**. This leads to the minimization problem:

$$\mathbf{x} = \underset{\mathbf{x}\in\mathbf{S}}{\mathrm{Argmin}}\left\{\mathrm{L}\left(\mathbf{y}, \mathbf{x}\right) + \eta\left\|\mathbf{x}\right\|_1 + \lambda\left\|\mathbf{x}\right\|_2\right\} . \tag{4}$$

Here we are recovering a constrained penalized maximum likelihood estimate: the extra Euclidean norm and/or absolute value norm terms penalize large $\hat{\mathbf{x}}$, and the parameters η and λ determine the degree of penalty. It is also possible to include terms that penalize derivatives of **x**, thereby imposing a larger penalty on its higher frequency components.

If outliers are present, we do not use the maximum likelihood approach directly. Instead, we select $f(\mathbf{y}, \hat{\mathbf{y}})$ to make the reconstructed image less sensitive to outliers. We give an example in the next section.

The subset **S** represents upper and lower bounds on the components of the image vector $\hat{\mathbf{x}}$. These bounds provide crucial prior information about the solution, and can greatly improve the quality of the recovered image. Because the unknown image usually represents non-negative quantities such as absorption or energy, the most common constraint is that all the components of $\hat{\mathbf{x}}$ be non-negative. Other constraints on subsets of pixels can result from the known extent of the object and regions of known voids or occlusions.

The optimization problem we have described above is a difficult one for several reasons. The most obvious is its very high dimensionality: both $\hat{\mathbf{x}}$ and **y** frequently have 10^6 or more components. Another reason is that bounds that we have imposed on the solution require a constrained optimization technique. Many iterative nonlinear minimization algorithms require storing an inverse of the matrix of second partials of $\mathrm{L}(\mathbf{y}, \hat{\mathbf{x}})$ with respect to the components of $\hat{\mathbf{x}}$. This is clearly not possible for our problems because a 10^6-×-10^6 matrix is too large to store.

The answer for unconstrained problems is either the conjugate gradient algorithm or the limited memory quasi-Newton algorithm. Both of these algorithms in effect store low-order approximations of the second-order information that is provided by the inverse matrix of second partials.

For bound-constrained problems, conventional optimization techniques[2–4] usually allow only one variable per iteration to attain a bound, so for very large problems these techniques are very slow because they spend too much time finding bounds. Consequently, standard iterative tomography algorithms[5,6] are based on methods that can attain multiple bounds in an iteration. Unfortunately, however, they are essentially steepest descent techniques that use no second-order information about $\mathrm{L}(\mathbf{y}, \hat{\mathbf{x}})$ whatever, so they converge very slowly, if at all.

Progress

Optimization Algorithm Development

Our ability to solve difficult tomography problems is the result of two specialized optimization algorithms that we have developed. The first is an extension of the conjugate gradient algorithm that incorporates bound constraints on the variables.[7] This constrained conjugate gradient (CCG) algorithm is unique in that it incorporates a bending linesearch that permits multiple bounds to be attained during a single iteration. In previous years, the algorithm was applied with great success to a variety of practical problems.[8–15]

The second algorithm is a limited-memory quasi-Newton (QN) algorithm that permits upper and lower bounds on the variables. This year we completed the implementation of our QN algorithm, based on the derivations in Reference 16.

The very large dimensions of **A** typically make calculating the matrix-vector product of **Eq. 1** the most computationally expensive part of finding a solution. Which algorithm is most appropriate depends on the structure of **A**.

In particular, the value of $\mathrm{L}(\mathbf{y}, \hat{\mathbf{x}})$ and a related directional derivative must be calculated at each new sub-iteration within the bending linesearch. Completely recalculating **Eq. 1** each time is very

expensive, but in some cases a different approach is possible. This is because it is necessary to recalculate only that part of **Eq. 1** corresponding to components of $\hat{\mathbf{x}}$ that have either attained or left bounds during a linesearch sub-iteration. For example, if only one component of $\hat{\mathbf{x}}$ has changed its bound status, then it is necessary to compute only one scalar-vector product, the product of that component with its corresponding column of **A**—rather than the entire vector-matrix product shown in **Eq. 1**. If **A** has many columns, this saves considerable effort.

If the columns of **A** are readily available, then CCG appears to be the best choice. However, in many tomography problems, **Eq. 1** is not computed in the usual manner. Often **A** is a discretized version of the forward projection operator; therefore, it represents a set of line integrals, and it is very sparse. Consequently, **Eq. 1** is computed via a rule that calculates only the line integrals and wastes no time on the large portions of **A** that consist of zeros.

Another example is where **A** is the kernel of a shift-invariant blurring function. In this case, using a convolution algorithm based on the fast Fourier transform (FFT) is by far the most efficient method for computing **Eq. 1**.

In some of our future work on the Advanced Hydrotest Facility (AHF)[17] we anticipate that **A** will be of the form **A = BC**, where **C** is a projection matrix and **B** is a blur kernel that represents the effects of detector and source geometries. In this case, both a sparse matrix rule and an FFT convolution algorithm are required. In all the cases discussed in this section, the programming effort required to calculate individual columns of **A** is considerable, and often not worthwhile.

The advantage of the QN method is that bending is used first on a low-order quadratic approximation to $L(\mathbf{y}, \hat{\mathbf{x}})$ to produce a direction for the linesearch. This greatly reduces the need for bending during the linesearch itself, yet it still permits the algorithm to attain multiple bounds during an iteration. In the QN algorithm we have included the options both to perform additional bending in the linesearch if the columns of **A** are available, and to perform no bending in the linesearch if they are not.

Robust Tomography Algorithms

This year we completed work on and demonstrated the usefulness of our robust tomography technique. The squared error function is

$$f\left(\mathbf{y}, \hat{\mathbf{y}}\right) = \sum_{i=1}^{N} r_i^2 = \mathbf{r}'\mathbf{r} , \tag{5}$$

where the residual vector $\mathbf{r} = \mathbf{y} - \hat{\mathbf{y}}$ is one indication of mismatch between the observed data and the model of the data.

If **Eq. 5** is the criterion function in **Eqs. 2** and **3**, then the reconstructed image defined in **Eq. 4** will be very sensitive to outliers. For example, suppose $N = 10{,}000$ in **Eq. 5**, and the magnitude of a typical component of the residual is 1.0, except for one component, r_k, whose value is 100.0. Then r_k contributes roughly as much to the squared error as do all the other components combined, and the minimization algorithm will try very hard to match the outlier, y_k, at the expense of all the other data points.

The solution is to use a robust criterion function[18,19] that reduces the influence of larger residuals. The most common robust criterion is

$$f\left(\mathbf{y}, \hat{\mathbf{y}}\right) = \sum_{i=1}^{N} g\left(r_i\right) , \tag{6a}$$

where

$$g\left(r\right) = \begin{cases} r^2 & \text{if } |r| \le c \\ 2c|r| - c^2 & \text{if } |r| \le c \end{cases} . \tag{6b}$$

The function $g(r)$ transitions smoothly from a squared penalty to a linear penalty, thereby reducing the influence of large residuals. The choice of c is data-dependent.[18,19]

We have demonstrated both that CCG is very effective in minimizing **Eq. 4** when **Eq. 6** is the criterion function, and that this approach greatly improves image quality in the face of outliers. We present a simulated example. The true unknown is shown in **Fig. 1**, and the resulting projection data with noise added is shown in **Fig 2**.

This data is in the form of a sinogram, a 2-D image created by displaying all the ray sums at one angle vs all angles (projections) obtained. The noise is a Gaussian mixture, with probability 0.99 that the noise at a data pixel is Gaussian with standard deviation σ, but with probability 0.01 it is Gaussian with standard deviation 100σ. Consequently, there is an outlier 1% of the time.

These outliers are obvious as speckles in **Fig. 2**. The reconstructed image using **Eq. 5** is shown in **Fig. 3**; the reconstructed image using **Eq. 6** is shown in **Fig. 4**. Outliers caused the streaks in **Fig. 3**. Our robust technique reduced the rms error between reconstruction and true object by a factor of two. Although robust statistical methods have been applied to a variety of problems, to our knowledge this is their first application to tomography. The effectiveness of CCG made this possible.

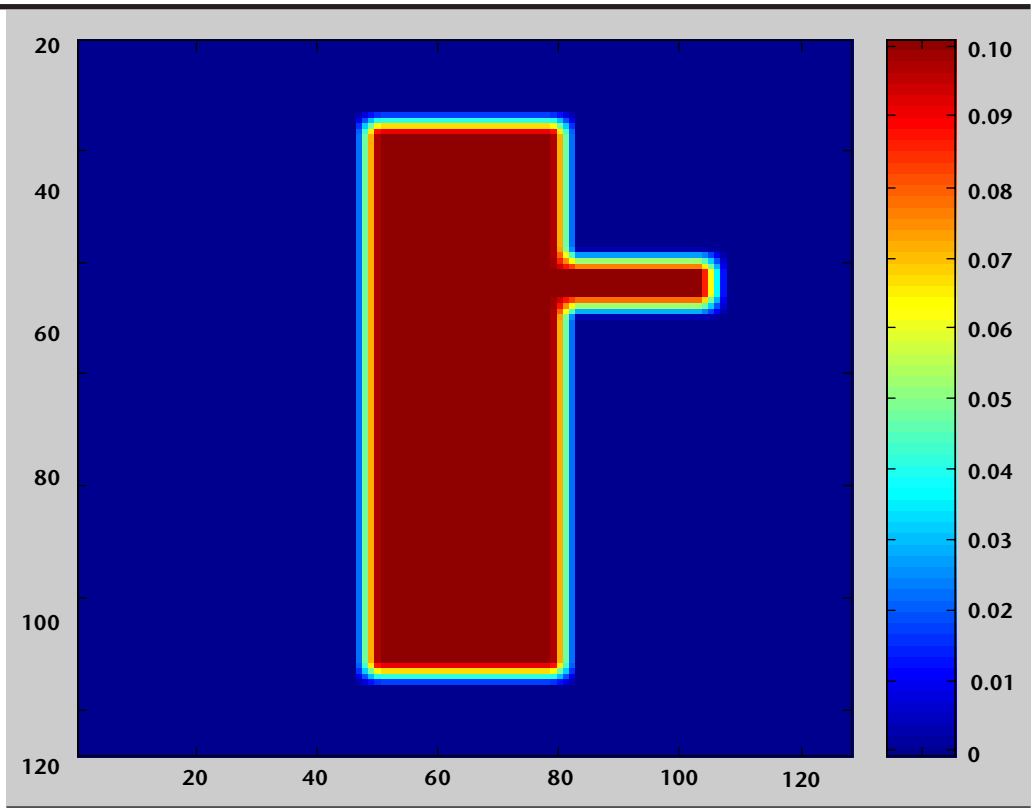

Figure 1. Original object used for CCG simulated example.

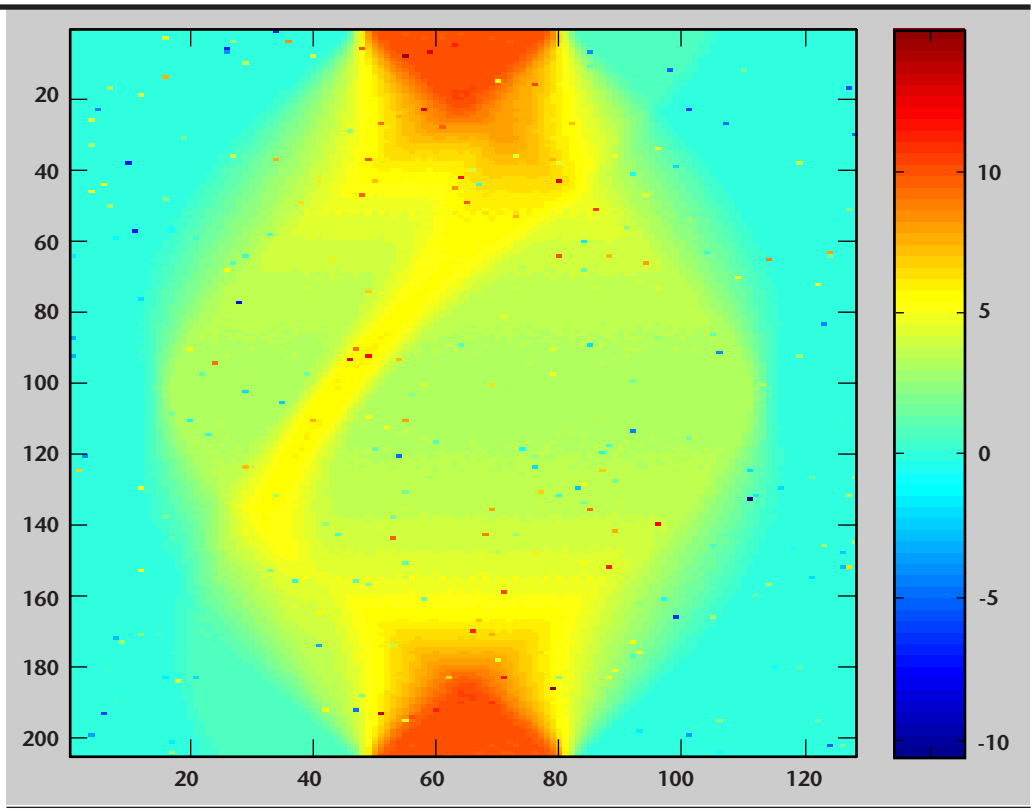

Figure 2. Sinogram of projections of object shown in Figure 1, with Gaussian mixture noise added.

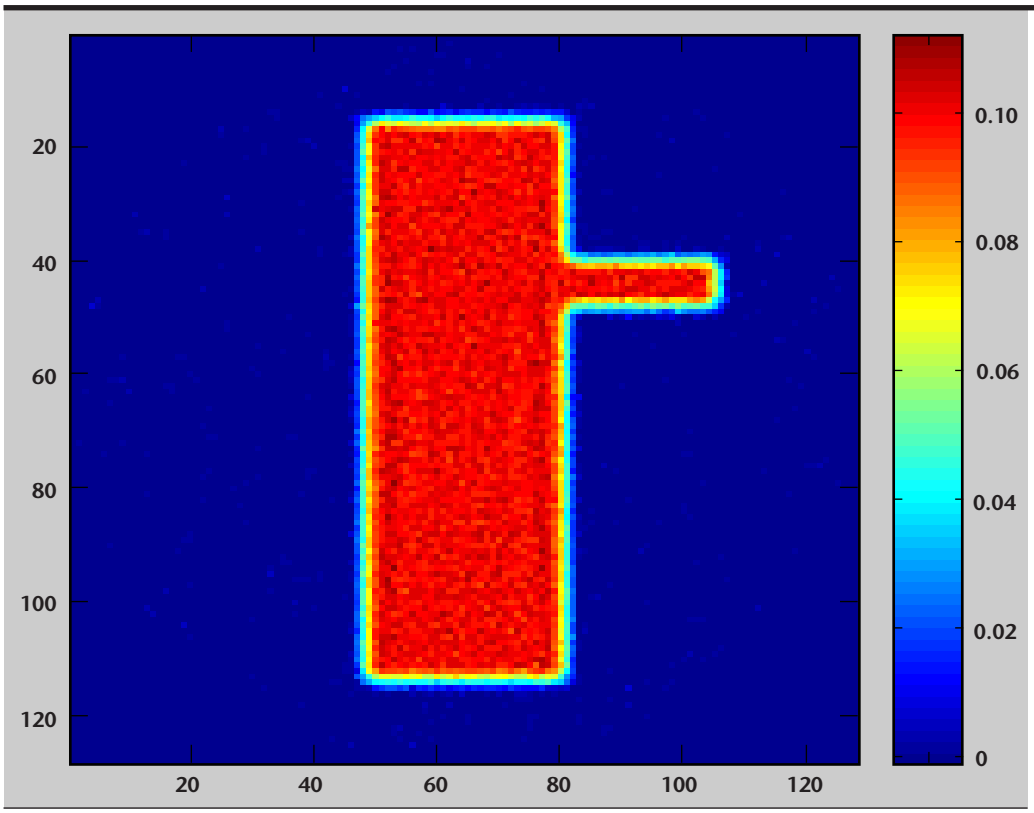

Figure 3. Reconstruction from projection data in Figure 2, using squared error criterion.

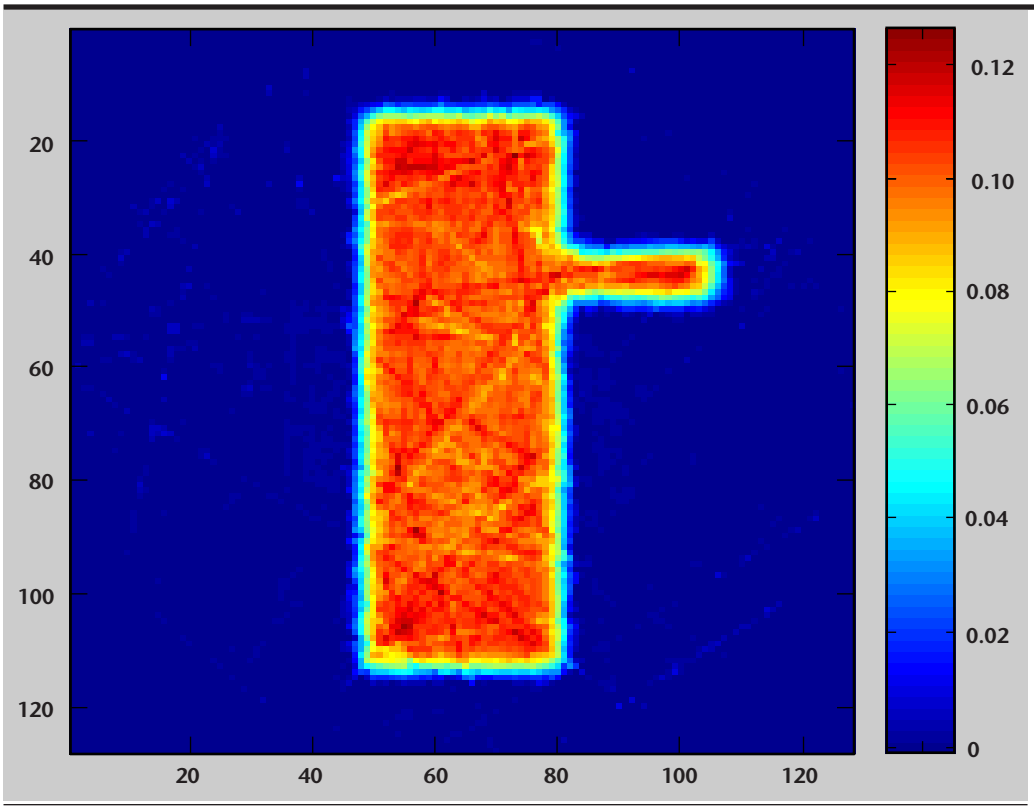

Figure 4. Reconstruction from projection data in Figure 2, using robust technique.

We have also successfully tried other robust criteria. Although we presented only a simulated example, many tomography problems are plagued by outliers, and this method has promise for a variety of real problems.

Waste Drum Assay

Using emission tomography to characterize mixed waste drums has been studied at LLNL for several years.[20] An active and passive computed tomography (A&PCT) technique has been developed that first uses an external radioactive source and active tomography to map the attenuation within a waste barrel. This attenuation map is used to define the matrix **A** for the passive or emission tomography problem that is of interest.

The emission tomography part of the waste drum problem gave us opportunities to demonstrate the effectiveness of our techniques and to develop them for general emission tomography problems.

At each detector position we acquire the entire gamma-ray spectrum, and two counts of gamma-ray emissions are taken. The first count is in the region of a spectral peak of the isotope of interest; the second in a region just outside this spectral peak. The purpose of the second measurement is to determine the level of background radiation and remove its effects on the first measurement.

In previously developed algorithms, the net counts due to the isotope were obtained by subtracting the second measurement from the first. Two maximum likelihood expectation-maximization (MLEM) algorithms were developed, UCSF-MLEM[21] and APCT-MLEM,[22] and applied to the corrected data to obtain a 3-D image of isotope activity. The sum of counts over all the image voxels is related to an estimate of isotope activity within the drum. Unfortunately, subtracting the two counts and then using a maximum likelihood algorithm on the net counts is not a correct application of the likelihood principle. Furthermore, this approach can violate physical reality because there is a non-zero probability that a net count will be negative.

The two MLEM algorithms lack the flexibility to implement the correct log-likelihood function. Last year we derived the correct log-likelihood function;[23] this year we developed a new algorithm, APCT-CCG, for the waste drum problem, and we studied its behavior on both real and simulated data.[24]

The flexibility of CCG made implementing the log-likelihood function relatively simple. It was necessary only to select the appropriate criterion function that accounted for Poisson statistics and incorporated peak and background measurements at each detector location. **Figure 5** compares applying the three algorithms to real data from known Pu-239

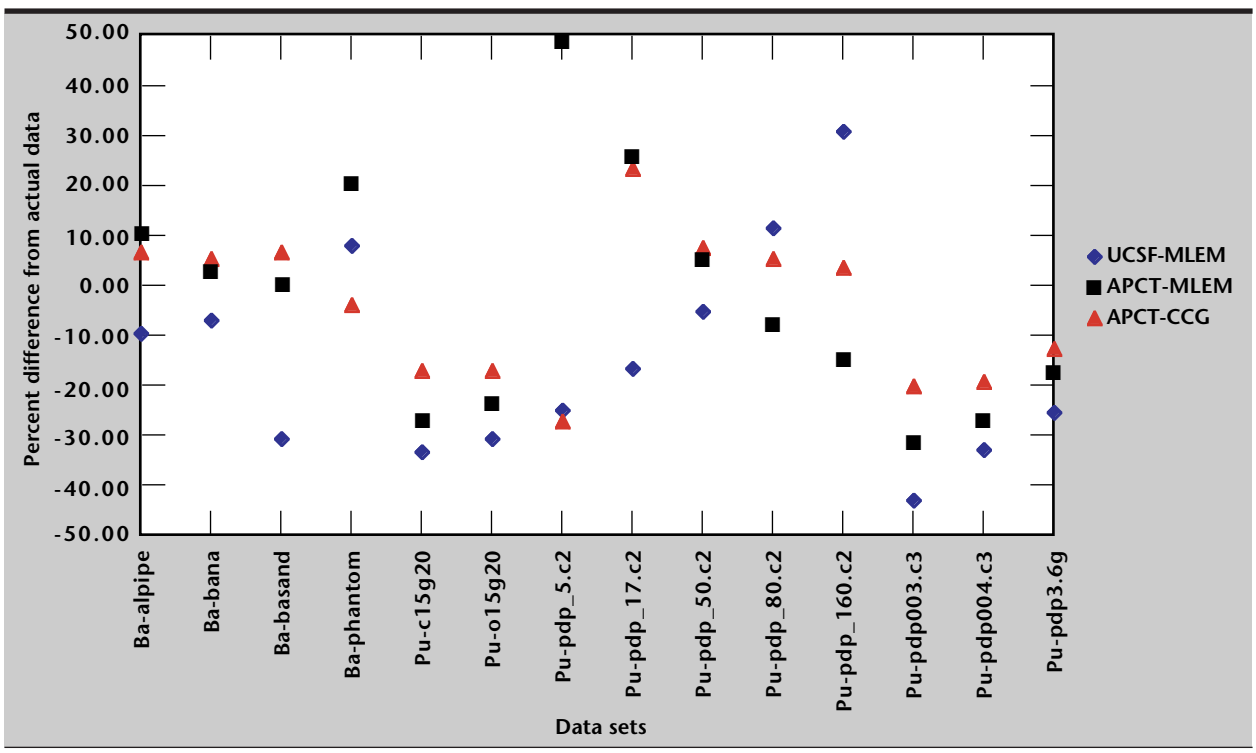

Figure 5. Comparison of assay accuracy for three reconstruction methods.

sources. APCT-CCG was out-performed on only one of the seven sources. Although the voxel sum is the most important parameter for waste drum assay, the reconstructed image is more important for most emission tomography problems. APCT-CCG also did a much better job of reconstructing the image.

A test case was generated using simulated data. A simulated 3-D image was created with three slices. Each slice is 14 × 14 voxels. A point radioactive emission source of 30,350 counts was placed on the center slice at voxel location (5, 5), that is, just off the center of the slice. Using the system matrix, the image was forward projected to create three sinograms. A level background equal to the maximum signal strength was added to these sinograms. The level was carefully chosen to be consistent with and representative of empirical data.

The simulated sinograms were randomized by passing them through a Poisson random generator. Another set of sinograms were created with the same background level. These background sinograms were also randomized. Both the gross and background sinograms were used as input for the APCT-MLEM and APCT-CCG codes. The results are shown in **Fig. 6**.

The APCT-MLEM image is spread out over 3 × 3 voxels within each slice and across all three slices. Its total assay yields 36,710 counts, that is, 121% of the actual value. The APCT-CCG results are more localized and its assay value of 9,936 counts is much closer to the original 30,350 counts, that is, within 1%.

The other important observation is that the APCT-CCG-code-calculated sinograms are more representative of the original source data than the source plus background, which is not the case of the APCT-MLEM sinogram results. We also found this to be the case for real data.[20]

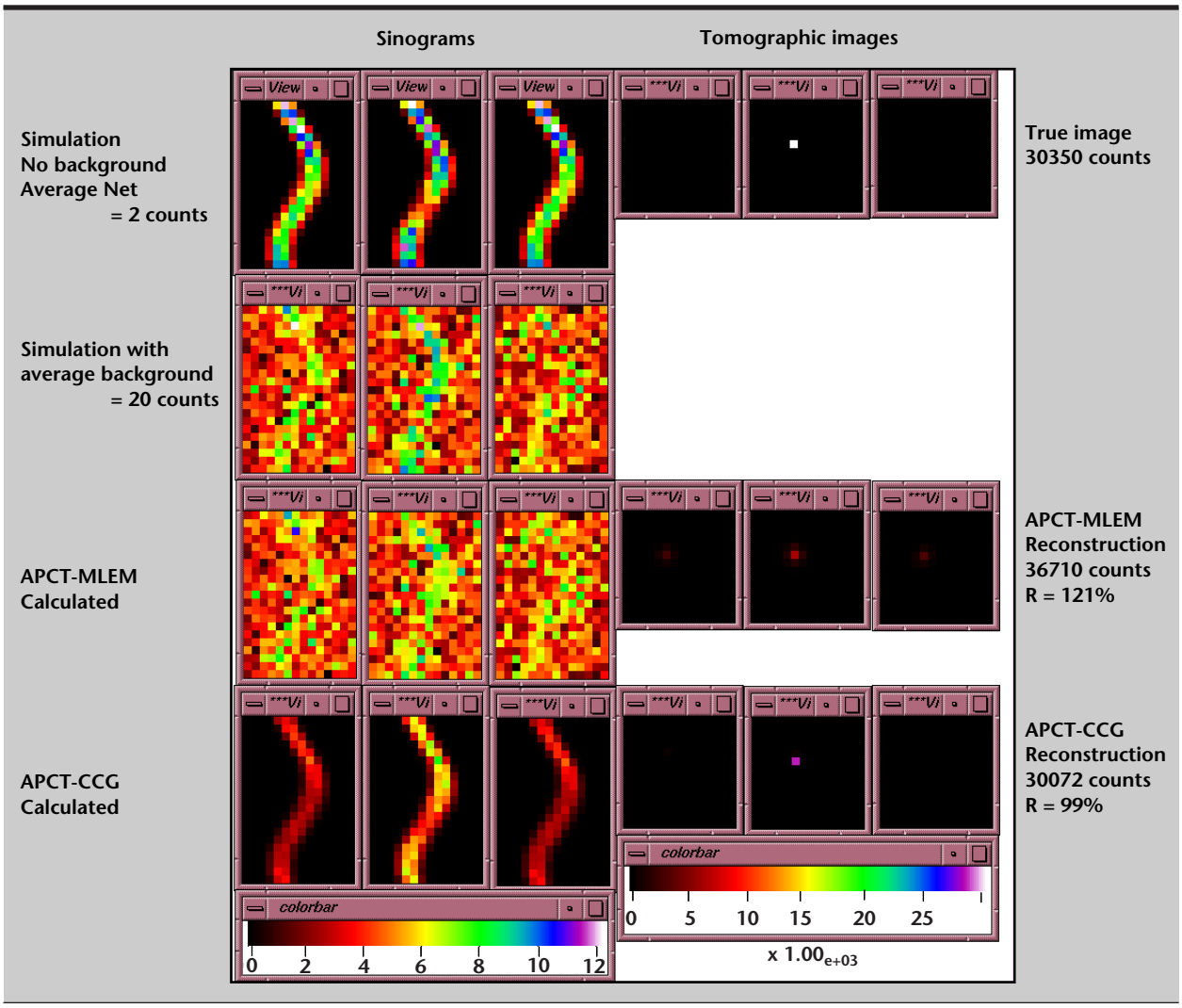

Figure 6. Simulated image and sinogram reconstruction.

For this problem it became obvious to us that model selection and validation are important issues, particularly when accurate estimates of parameters (for example, isotope activity) are as critical as good images. In the case of Gaussian noise problems where the squared error function is used, tomography can be viewed as a linear regression problem, so the usual χ^2 tests can be applied to the squared error to measure goodness of fit and to choose between models. The sinogram of the residuals is a good image to observe the adequacy of a particular model.

However, this is not the case if the noise is not Gaussian. In studying the waste drum problem, we realized that statistically it can be viewed as a generalized linear model in which there is a linear relationship between the unknown and the data, but the statistics are not necessarily Gaussian.[19,25,26] This is basically the model we defined in the Introduction. In this context it is possible to slightly modify $L(\mathbf{y}, \hat{\mathbf{x}})$ so that it becomes a deviance function that has the same minimum with respect to $\hat{\mathbf{x}}$, but exhibits behavior that is approximately χ^2.

Similarly, it is possible to define other sinogram images that behave as the usual residual image does for the squared error case. We have applied these ideas to the waste drum problem, and they will be useful for other tomography problems as well.

Neutron Imaging

LLNL is currently developing a high-energy (10 to 15 MeV) neutron imaging system for use as an NDE tool in support of the Enhanced Surveillance Program (ESP). This approach to tomography promises to be a powerful technique for probing the internal structure of thicker objects that may be opaque to x rays and lower energy neutrons.

Imaging experiments using neutron radiography were conducted at the Ohio University Accelerator Laboratory (OUAL) in FY-98. The object imaged was a right-circular Pb cylinder with an outer diameter of 4 in. and a 2-in.-diameter polyethylene insert, as illustrated in **Fig. 7**. The insert was split into two half-cylinders with one serving as "blank" and the other having a series of 10-, 8-, 6-, 4-, and 2-mm-diameter holes machined to depths of 0.5 in. into its outer (curved) surface. The areal density of the assembly ranged from 62.38 g/cm^2 (along the centerline) to 99.9 g/cm^2 (along the limb of the polyethylene insert).

Reconstructions of this object using both filtered backprojection and our CCG algorithm with nonnegativity constraints are shown in **Fig. 8**. The superiority of the CCG reconstruction is evident. Although we used the squared error criterion with CCG, in fact all the raw data acquired during the OUAL experiments initially bore random sharp spikes rising several hundred to several thousand counts above the local average.

These spikes were due primarily to cosmic ray strikes in the CCD detector used to collect the data. Currently these spikes are removed by preprocessing prior to applying the tomography reconstruction algorithms. However, such data is a perfect candidate

Figure 7. Neutron imaging object.

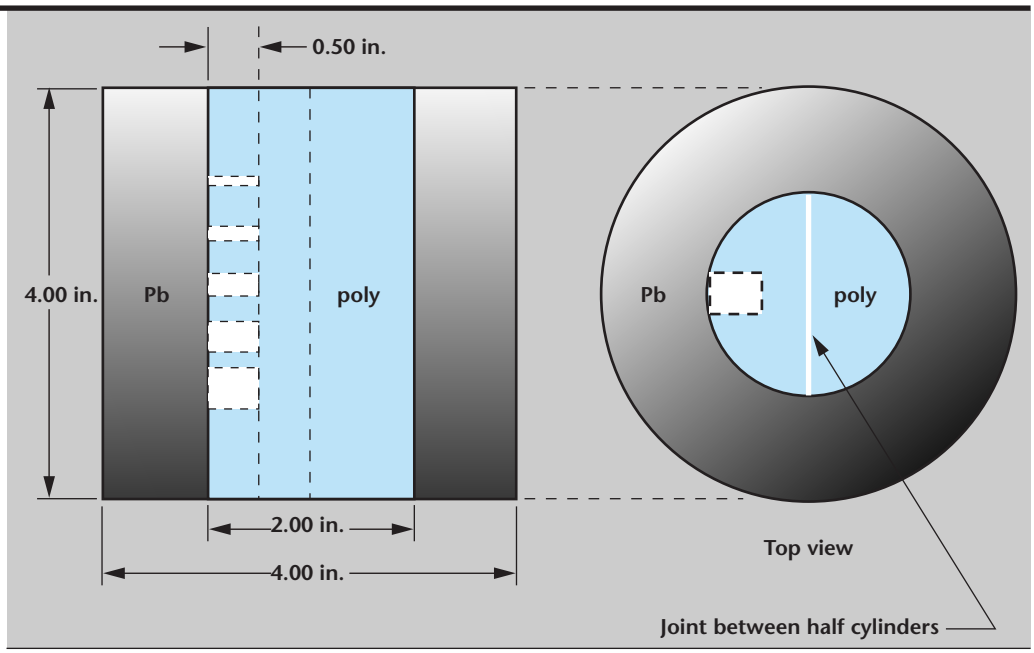

for the robust techniques we developed this year, and we plan to apply them to neutron data in the near future. For a detailed description of the neutron imaging experiments, see Reference 27.

The Advanced Hydrotest Facility

Last year we adapted our CCG algorithm to cone beam tomography problems. This year we used the resulting algorithm, CCG_Cone, extensively, to study limited-view reconstruction for LLNL's AHF. This code has been an indispensable tool in these studies. It has been used to study the efficacy of reconstruction as a function of number of views, as well as how the orientation of views affects the quality of the reconstruction.

These studies have allowed the AHF design group to make recommendations on how many views are needed, as well as where they should be placed. In addition, CCG_Cone has been used to study the effect of constraints on the quality of reconstructions. It has been found that a judicious use of constraints will help the AHF to achieve its objectives. More programmatic work will continue in this area.

Pulsed Photothermal Radiography

In collaboration with researchers at other institutions, we continued to apply our optimization algorithms to the problem of pulsed photothermal radiography (PPTR). This is essentially a tomographic

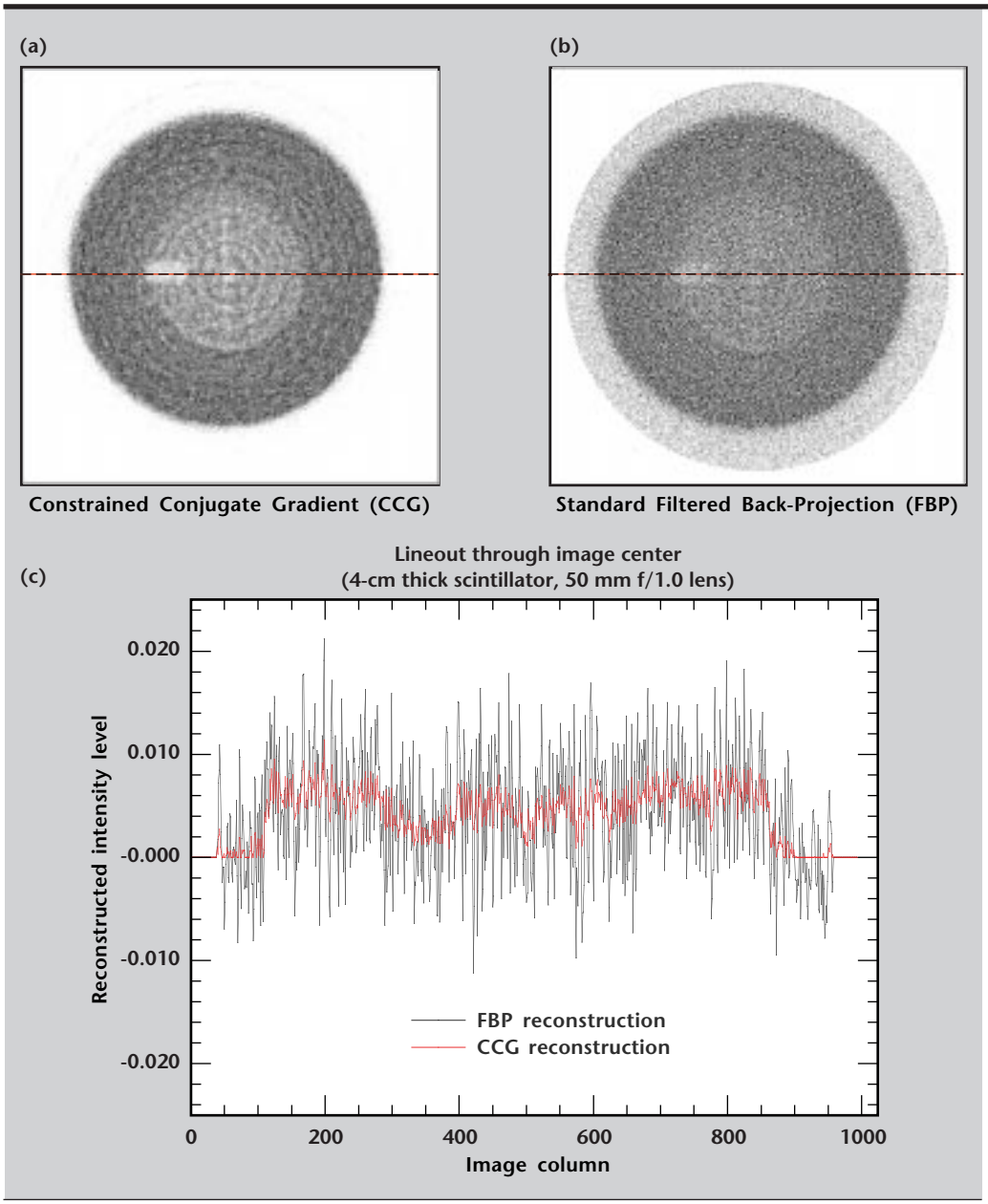

Figure 8. Reconstruction of object from neutron imaging data, using CCG (a) and filtered back-projection (b).

method that inverts data from the time evolution of the heat equation, rather than from x-ray projection data, to see inside an opaque object. This year we obtained the first high-quality 3-D images of port-wine stain blood vessels,[28,29] and we demonstrated the feasiblity of parallelizing our CCG algorithm.[30]

Future Work

In future work we plan to continue refining our algorithms and applying them to practical problems. Immediate plans include parallelizing the algorithms, particularly the implementations of **Eq. 1**; further refinements of the forward projection model, including implementing the AHF blurring model; and further investigations into applying the generalized linear model formalism to tomography.

References

1. Poor, H. V. (1994), *An Introduction to Signal Detection and Estimation*, 2nd ed., Springer-Verlag.

2. Gill, P. E., W. Murray, and M. H. Wright (1981), *Practical Optimization*, Academic Press, New York, New York.

3. Fletcher, R. (1987), *Practical Methods of Optimization*, 2nd ed., John C. Wiley and Sons, New York, New York.

4. Luenberger, D. G. (1984), *Linear and Nonlinear Programming*, 2nd ed., Addison-Wesley, Reading, Massachusetts, pp. 214–220.

5. Stark, H., ed. (1987), *Image Recovery: Theory and Application*, Academic Press, New York, New York.

6. Azevedo, S. G. (1991), Model-Based Computed Tomography for Nondestructive Evaluation, PhD Thesis, Lawrence Livermore National Laboratory, Livermore, California (UCRL-LR-106884), March.

7. Goodman, D. M., E. M. Johansson, and T. W. Lawrence (1993), "On Applying the Conjugate Gradient Algorithm to Image Processing Problems," Chapter 11 in *Multivariate Analysis: Future Directions*, C. R. Rao, ed., Elsevier Science Publishers.

8. Goodman, D. M., T. W. Lawrence, E. M. Johansson, and J. P. Fitch (1993), "Bispectral Speckle Interferometry to Reconstruct Extended Objects from Turbulence-Degraded Telescope Images," Chapter 13 in *Handbook of Statistics, Vol. 10: Signal Processing and its Applications*, N. K. Bose and C. R. Rao, eds., North Holland, Amsterdam.

9. Kolman, J., W. S. Haddad, D. M. Goodman, and K. A. Nugent (1994), "Application of a Constrained Optimization Algorithm to Limited View Tomography," *Proc. SPIE Conf.*, San Diego, California, July.

10. Haddad, W. S., J. E. Trebes, D. M. Goodman, H. R. Lee, I. McNulty, E. H. Anderson, and A. O. Zalensky (1995), "Ultra High Resolution Soft X-Ray Tomography," *Proc. SPIE Conf.*, San Diego, California, July.

11. Somoza, J. R., H. Szöke, D. M. Goodman, P. Beran, D. Truckses, S.-H. Kim, and A. Szöke (1995), "Holographic Methods in X-ray Crystallography IV. A Fast Algorithm and its Application to Macromolecular Crystallography," *Acta Crystallographica*, Vol. **A51**.

12. Milner, T. E., D. M. Goodman, B. S. Tanenbaum, and J. S. Nelson (1995), "Depth Profiling of Laser-Heated Chromophores in Biological Tissues by Pulsed Photothermal Radiometry," *Journal of the Optical Society of America-A*, Vol. **12** No. 7, July.

13. Milner, T. E., D. M. Goodman, B. S. Tanenbaum, B. Anvari, L. O. Svasand, and J. S. Nelson (1996), "Imaging of Laser Heated Subsurface Chromophores in Biological Materials: Determination of Lateral Physical Dimensions," *Physics in Medicine and Biology*, Vol. **41**.

14. Milner, T. E., D. J. Smithies, D. M. Goodman, A. Lau, and J. S. Nelson (1996), "Depth Determination of Chromophores in Human Skin by Pulsed Photothermal Radiometry," *Applied Optics*, June.

15. van Gemert, M. J. C., J. S. Nelson, T. E. Milner, D. J. Smithies, W. Verkruysse, J. F. de Boer, G. W. Lucassen, D. M. Goodman, B. S. Tanenbaum, L. T. Norvang, and L. O. Svaasand (1997), "Non-Invasive Determination of Port Wine Stain Anatomy and Physiology for Optimal Laser Treatment Strategies," *Physics in Medicine and Biology*, Vol. **42**.

16. Byrd, R. H., J. Nocedal, and R. B. Schnabel (1994), "Representations of Quasi-Newton Matrices and Their Use in Limited Memory Methods," *Math. Prog.*, Vol. **63**, No. 2, January.

17. "Advanced Hydrodynamic Radiography Technology Development Plan" (1996), Predecisional Draft, US Department of Energy, Defense Programs, Office of Research and Inertial Fusion, February 16.

18. Huber, P. J. (1981), *Robust Statistics*, John C. Wiley and Sons, New York, New York.

19. Myers, R. H. (1990), *Classical and Modern Regression with Applications*, PWS-Kent, Boston, Massachusetts, Chapter 7.

20. Martz, H. E., G. P. Roberson, D. C. Camp, D. J. Decman, J. A. Jackson, and G. K. Becker (1998), "Active and Passive Computed Tomography Mixed Waste Area Final Report," Lawrence Livermore National Laboratory, Livermore, California, November.

21. Brown, J. K., K. Kalki, J. A. Heanue, and B. H. Hasegawa (1995), "Quantitative SPECT Reconstruction Using Multiray Projection Integrators," *Conference Record 1995 IEEE Nuclear Science Symposium and Medical Imaging Conference*, Vol. **2**, pp. 1272–1276.

22. Keto, E., S. G. Azevedo, G. P. Roberson, D. J. Decman, H. E. Martz, and E. M. Johansson (1995), "Spatial Resolution Versus Signal to Noise in Quantitative Tomography," *Proceedings of the 4th Nondestructive Assay and Nondestructive Examination Waste Characterization Conference*, Salt Lake City, Utah, October 24–26, pp. 405–420.

23. Goodman, D. M. (1997), "Maximum Likelihood Estimation with Poisson (Counting) Statistics for Waste Drum Inspection," Lawrence Livermore National Laboratory, Livermore, California (UCRL-ID-127361), May.

24. Jackson, J. A., D. M. Goodman, G. P. Roberson, and H. E. Martz (1998), "An Active and Passive Computed Tomography Algorithm with a Constrained Conjugate Gradient Solution," *6th Nondestructive Assay Waste Characterization Conference*, Salt Lake City, Utah, November 17–19.

25. McCullagh, P., and J. A. Nelder (1989), *Generalized Linear Models*, 2nd ed., Chapman and Hall, London.

26. Dobson, A. J. (1990), *An Introduction to Generalized Linear Models*, Chapman and Hall, London.

27. Hall, J., F. Dietrich, C. Logan, and G. Schmid (1998), "Development of High-Energy Neutron Imaging in Support of Enhanced Surveillance Program Applications," Lawrence Livermore National Laboratory, Livermore, California, in preparation.

28. Shoari, S., N. Bagherzadeh, D. Goodman, T. E. Milner, D. J. Smithies, and J. S. Nelson (1998), "A Parallel Algorithm for Pulsed Laser Infrared Tomography," *Pattern Recognition Letters*, (**19**)5-6, pp. 521–526, April.

29. Milner, T. E., S. A. Telenkov, B. S. Tanenbaum, J. S. Nelson, and D. M. Goodman (1998), "Non-invasive Evaluation of Biological Materials Using Pulsed Photothermal Tomography," *Proc. Winter Annual Meeting of ASME*, Anaheim, California, November.

30. Telenkov, S. A., D. M. Goodman, B. S. Tanenbaum, J. S. Nelson, and T. E. Milner (1998), "Infrared Imaging of laser-heated port wine stains," *Annual Meeting of the Optical Society of America*, Baltimore, Maryland, October.

Robert T. Langland

The five centers of excellence in the Engineering Directorate at Lawrence Livermore National Laboratory (LLNL) are made up of enabling technologies that are essential for these centers to be world class.

However, in addition to the enabling technologies in each center, the Engineering Directorate also has a broad set of supporting technologies that make up the complete capabilities of engineering at LLNL. These allow engineering projects to accomplish specific tasks and make it possible for a program to meet one or more of its objectives or goals.

When appropriate, the Engineering Directorate sponsors work in these supporting technologies. Many efforts are small and do not require significant funding; however, there are some that demand significant resources. The five articles in this section represent some of these more substantial efforts, which are very broad and diverse.

First, we have sponsored a project in multi-scale material modeling that complements a Strategic Initiative funded by LLNL's Laboratory Directed Research and Development Program. This project, "Modeling of Anistropic Inelastic Behavior," is refining the theory of finite plasticity. It is coordinated with research funded by the National Science Foundation at the University of California at Berkeley. A Ph.D. candidate is using LLNL facilities to develop and carry out very sophisticated testing to map yield surfaces of real materials. The results of this testing will eventually be used in computer codes that have been developed through the leadership of LLNL's Computational Engineering Center.

The second research project, "Modeling Large-Strain, High-Rate Deformation in Metals," has used Hopkinson's bar testing to develop a new model for important materials over a very large range of strain rates, from 10^4 s^{-1} to 10^{-4} s^{-1}. The testing and material models were done for the aluminum alloy 6061-T6 and the titanium alloy Ti-6Al-4V. These plasticity and failure models apply in tension, compression and shear, and are used in the NIKE and DYNA family of computer codes.

The third project, "Uniform Etching of 85-Cm-Diameter Grating," has developed an ion etching process to build 85-cm-diameter optical grating systems of silicon.

The fourth project, "Distributed Sensor Inertial Measurement Unit," has been funded to refine existing theory to develop, build, test and eventually use an accelerometer-based inertial measurement unit (IMU). This project uses six very sensitive accelerometers with special electronic signal conditioning. These accelerometers are arranged in a critical configuration that permits the definition of the full six degrees of freedom demanded by the application. This approach represents a departure from the use of laser-based rate gyro IMUs, which could not be used for our application.

The fifth project, "Fiber-Based Phase-Shifting Diffraction Interferometer for Measurement and Calibration of the Lick Adaptive Optics System," is transforming a new spherical wavefront-based phase-shifting interferometer into a practical optical measurement system. This project and the one on etching represent examples of an underlying and broad expertise in the design and fabrication of optical systems.

All the projects are working at extreme limits of space and/or time. We are attempting to design, fabricate and perform in areas that are pushing the technologies beyond their current limits. In our supporting technologies, we are exploring and creating new boundaries to meet LLNL's programmatic needs and goals for the future.

Supporting Technologies

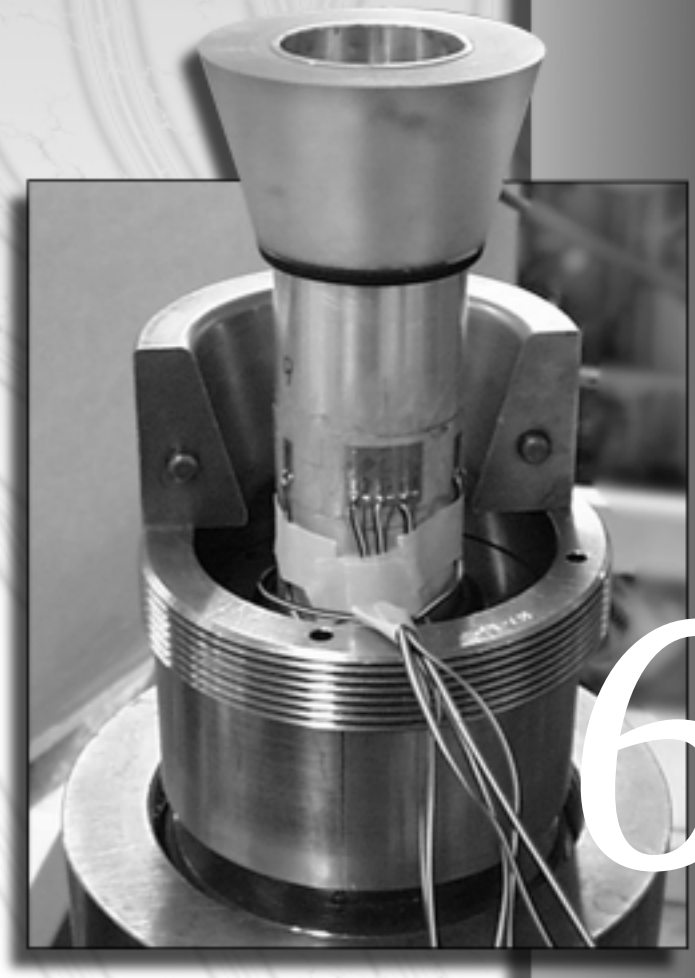

6

6. Supporting Technologies

Overview
Robert T. Langland

Modeling of Anistropic Inelastic Behavior
Daniel J. Nikkel, Jr., Arthur A. Brown, and James Casey *6-1*

Modeling Large-Strain, High-Rate Deformation in Metals
Donald R. Lesuer, Mary M. LeBlanc, and Gregory J. Kay *6-7*

Uniform Etching of 85-Cm-Diameter Grating
Steven R. Bryan, Jr. and David L. Sanders *6-17*

Distributed Sensor Inertial Measurement Unit
Carlos A. Avalle and John I. Castor *6-23*

Fiber-Based Phase-Shifting Diffraction Interferometer for Measurement and Calibration of the Lick Adaptive Optics System
Eugene W. Campbell and Jong R. An *6-27*

Modeling of Anisotropic Inelastic Behavior

Daniel J. Nikkel, Jr.
New Technologies Engineering Division
Mechanical Engineering

Arthur A. Brown and James Casey
University of California
Berkeley, California

We are working to develop better constitutive equations for polycrystalline metals. An experimental capability, developed at Lawrence Livermore National Laboratory (LLNL), is being used to study the yield behavior of elastic-plastic materials. We are directly determining the multi-dimensional yield surface of the material, both in its initial state and as it evolves during large inelastic deformations. These experiments provide a more complete picture of material behavior than can be obtained from traditional uniaxial tests. Experimental results show that actual material response can differ significantly from that predicted by simple idealized models. The yield surface, and its mathematical representation, is an essential component of the constitutive theory for nonlinear anisotropic elastic-plastic materials, and is the main focus of the present project.

Introduction

The ability of numerical simulations to predict the behavior of systems involving materials undergoing large deformations is contingent upon having a realistic model of the behavior of the materials involved. Such models must be accurate in the full range of possible loading conditions that the materials may be subjected to. Use of overly simplified models in regimes where they are not well suited can seriously compromise the validity of a simulation. Many problems of engineering interest involve metal undergoing large deformation under multiaxial states of stress. The need for reliable models for these applications can hardly be overemphasized. As will be seen, simple models for plasticity commonly used in numerical codes do not accurately predict material behavior under these conditions.

From the macroscopic perspective, polycrystalline metals subjected to loads or deformations initially exhibit elastic (reversible) behavior. The material response is path-independent and there is a one-to-one correspondence between stress and strain. However, if the deformation or loads become sufficiently large, the material begins to exhibit plastic behavior (that is, there is no longer a one-to-one correspondence between stress and strain, the response is dependent on the loading path taken to reach a given state of deformation, and residual—plastic—deformations remain after external loads are removed). This gives rise to the theoretical idealization of an elastic-plastic material, and in particular, to the notion of a yield function[1] denoted by

$$f\left(s_{kl},\ e^p_{kl},\ \kappa,\ \ldots\right) = g\left(e_{kl},\ e^p_{kl},\ \kappa,\ \ldots\right). \qquad (1)$$

This function, a key ingredient of the constitutive theory of elastic-plastic materials, describes the boundary between stresses (or strains) that result in only elastic behavior, and those that result in inelastic deformation (**Fig. 1**). In **Eq. 1**, s_{kl} denotes the components of the stress tensor; e_{kl} denotes the components of the strain tensor; e^p_{kl} denotes the components of the plastic strain tensor; κ is a scalar measure of work hardening; and the ellipses represent other inelastic state variables that may be present, depending on the constitutive theory.

Annealed polycrystalline metals typically exhibit isotropic behavior with respect to a reference configuration; that is, at a given point in the material, the material response of a specimen carried out in any direction is the same. This includes the elastic behavior and the initial yield behavior. However, significant processing of materials, or large plastic

deformations, can result in behavior which is anisotropic, where material response in different directions is quite different. Examining the microstructural processes which give rise to inelastic behavior, isotropic behavior can be seen as being due to the random orientation of grains of material, each of which has particular orientations and properties. As a consequence of some types of processing, or due to large inelastic deformations, the initially random grain orientations can become aligned, resulting in anisotropic behavior.

For fixed values of the inelastic variables, the yield condition described by $f = 0$ (or $g = 0$) can be interpreted geometrically from the point of view of stress space (or strain space), the multi-dimensional space whose axes are the components of stress (or strain), as a surface that bounds the region in which only elastic behavior occurs (the elastic region).

As long as the loading of the material is such that the current state is enclosed by the yield surface, the material responds elastically. But, if the loading path intersects the yield surface and tries to cross it, inelastic behavior occurs and plastic deformation results. The current state never moves outside the yield surface, but instead the surface is carried along with it. Typically the yield surface changes shape as the inelastic deformation increases. In addition to the yield function, the constitutive theory includes evolution equations for the inelastic variables during loading ($g = 0$, $\hat{g} > 0$), such as that for the plastic strain:

$$\dot{e}^p_{kl} = \rho_{kl}\left(e_{mn},\ e^p_{mn},\ \kappa,\ \ldots\right)\hat{g},$$

$$\hat{g} \equiv \frac{\partial g}{e_{mn}}\dot{e}_{mn} \qquad (2)$$

Here ρ_{kl} is a constitutive response function which is independent of the rates of stress or strain. For a broad class of materials, under a physically reasonable assumption regarding work in closed cycles in strain space, ρ_{kl} can be replaced with the product of scalar function and the normal to the yield surface in stress space, thus requiring the specification of only one additional scalar response function.[1] For special classes of materials, this scalar function is determined from the yield function and hardening and does not require an independent specification.

Most models for plasticity of metals implemented into numerical codes use a yield criterion that corresponds to a fixed shape of the yield surface (for example, elliptical in the case of the Mises yield criterion). What distinguishes different models is how the yield surface is assumed to evolve. For example, it may translate rigidly, or alternatively change its size while maintaining its shape, or follow some combination of these simple hardening laws.

While the initial yield surface of isotropic materials may be represented reasonably well by an ellipse, subsequent to even moderate plastic deformation, the shape of the yield surface in real materials can change significantly (**Fig. 1**). For this reason, simple representations of the yield function will be satisfactory only under very restrictive loading conditions (for example, monotonic or uniaxial), and are totally inadequate for general multiaxial loading conditions where loads can reverse and change direction during the history of loading.

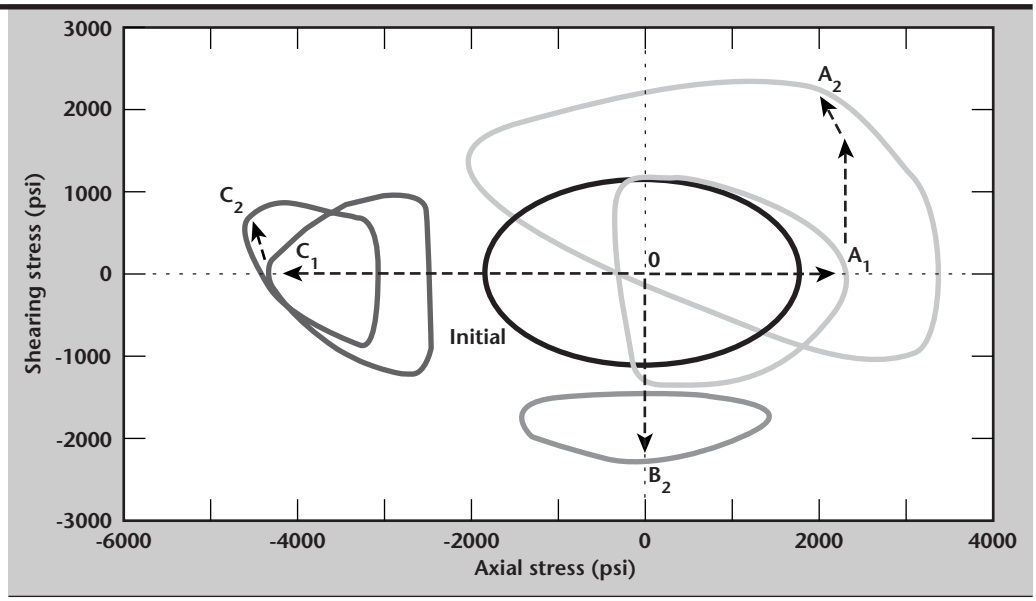

Figure 1. Measured points on yield surfaces in 2-D stress space from three specimens of 1100 aluminum. The subsequent yield surfaces show significant deviation from an idealized ellipse, even though the strains involved are moderately small.

In view of these considerations, and motivated by the fact that the vast majority of experimental data on polycrystalline metals that is available is for uniaxial (and generally monotonic) loading, we developed an experimental capability to map out the yield surface at various fixed states of large inelastic deformation under multiaxial states of loading. By determining the yield surfaces on a single specimen at multiple fixed states, the evolution of the yield surface during plastic deformation can be observed. This data provides the basis for developing improved constitutive equations for polycrystalline metals.

Progress

This project is a combination of a program of novel experiments characterizing inelastic material behavior, together with an effort to develop better material models for implementation into numerical analysis codes. This year, the primary effort has been on the experimental component of the project. Work has also begun examining issues related to numerical implementation of anisotropic plasticity models.

Experiments

The first part of this project involves experiments to directly measure the yield surface. The thin-walled tension-torsion specimen designed for use in a multiaxial MTS hydraulic testing machine is shown in **Fig. 2**. The experimental determination of the yield surface of the material is carried out by loading a specimen under multiaxial conditions and probing until the point of yield is reached, then backing off and probing in a different direction in stress space (and in strain space) until the next yield point is found. This process is repeated until the entire surface is mapped out. The sensitive nature of the measurements being made requires careful attention to the issues of specimen design and preparation, experimental methodology, and interpretation of the data.

The general description of the experiments and the difficulty in carrying out these measurements has been discussed previously.[2] The present discussion will focus on refinements that have been made during FY-98.

The surface that we are trying to map represents the yield surface at an arbitrary fixed inelastic state. Ideally, all points on a given yield surface should be determined without inducing any further plastic deformation to the specimen. In practice, however, a point on the yield surface can only be determined by reaching, and slightly exceeding, the yield point. Each time the yield point is exceeded in this way, the inelastic state, and the yield surface itself, are slightly changed.

For our purposes, it is important to minimize this distortion of the yield surface. To characterize a given surface, a number of points on it must be located (probably a minimum of 10) while changing the inelastic state (hence, the surface itself) as little as possible. The way in which yield is defined experimentally can significantly affect the yield surface which is determined.

A number of alternative definitions have been investigated, and the effects of different definitions on the resulting measured yield surfaces have been studied. The procedure which has been developed can detect yield without producing a plastic strain much greater than 5×10^{-6}. We refined the experimental procedure to reduce a number of sources of error and have demonstrated that the methodology for determining yield surfaces is repeatable.

The importance of rate effects has also been investigated. Even in materials which are not considered highly rate-sensitive, due to the

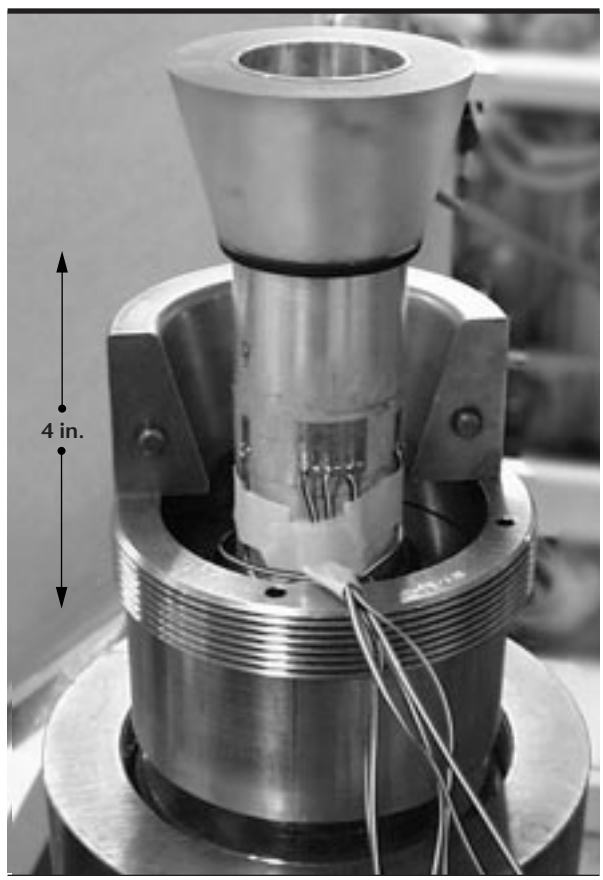

Figure 2. Thin-walled biaxial test specimen that can be subjected to tension, compression and torsion, used to measure points on the yield surface of the material. The yield surface at several different states can be measured from one specimen.

desired accuracy in measuring the yield surface, it was found necessary to run the tests very slowly, increasing the time required to complete each measurement.

In addition to generating data from the measurement of yield surfaces, we are also seeking to address the fundamental question of the proper definition of plastic strain in the context of large inelastic deformations.[3,4] We have successfully measured yield surfaces that have moved so that they no longer enclose the origin in stress space (for example, paths O-B_2 and O-C_1-C_2 in **Fig. 1**).

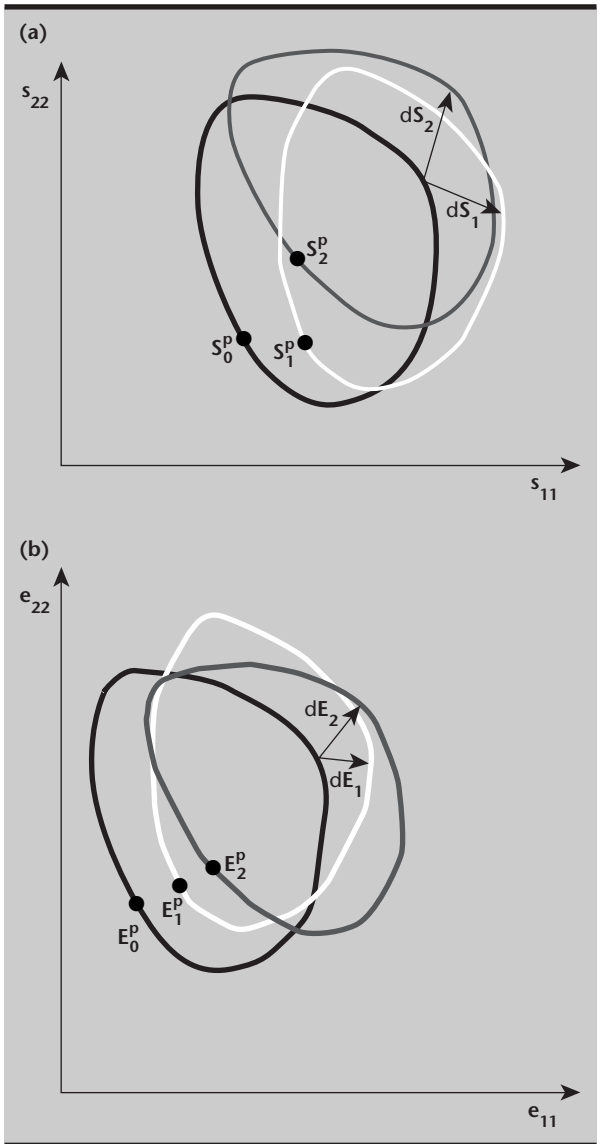

Figure 3. Schematic of the experimental method for verifying the prescription for plastic strain viewed in (a) stress space, and (b) strain space. From a fixed arbitrary state (darkest yield surface), the change due to plastic increments on paths of two differing directions is measured. Colinearity of the points E_0^p, E_1^p, and E_2^p in strain space verifies the proposed prescription.

In this situation, the material cannot be unloaded to zero stress without causing new plastic deformations. The traditional way of defining plastic strain is to identify it with the residual strain remaining when the load is removed. This definition arose intuitively from consideration of uniaxial tests with small deformation, but it is clearly inadequate in the situation of more general states of loading where the yield surface no longer encloses the origin in stress space.

Plastic strain is not among the set of kinematic variables that come from classical continuum mechanics. Since it is a primitive variable in the constitutive theory, one must be able to unambiguously identify it for the theory to be meaningfully predictive and not simply a sophisticated curve-fit.

In view of **Eq. 2**, while the magnitude of the plastic strain increment depends on the strain increment, its direction does not. The direction is the same as the direction of the tensor, ρ_{kl}, which depends only on the current state and not on rates of stress or strain. This fact will be used to verify the validity of the prescription for identifying plastic strain.[3,4]

Two or more specimens will be loaded to an arbitrary inelastic state where the yield surface in stress space does not enclose the origin. The specimens will then be given small plastic load increments starting from the same point on the yield surface, but having different directions in strain space. This is shown schematically in **Fig. 3**, in both (2-D) stress and strain space. The point closest to the origin on a given yield surface in stress space is designated as $\mathbf{S}^p$, and the corresponding state in strain space is identified as the plastic strain tensor, $\mathbf{E}^p$.

The darkest yield surface in **Fig. 3** represents a known arbitrary state. The two lighter surfaces represent two subsequent yield surfaces obtained from the first by loading in two different directions. If the prescription[3,4] is valid, the resulting plastic strain increments for the two cases should have the same direction, although they may vary in magnitude. Thus, colinearity of the points $\mathbf{E}_0^p$, $\mathbf{E}_1^p$, and $\mathbf{E}_2^p$ in **Fig. 3b** would verify the prescription.

Modeling

We have begun efforts to model the anisotropic material behavior exhibited in the experiments, and to explore issues related to numerical implementation of anisotropic models. The Mises yield condition, which is a quadratic polynomial in the

deviatoric stress components, is known to agree well with experimental data on annealed (isotropic) polycrystalline metals, and it also has a physically appealing interpretation in terms of distortion energy.

For anisotropic materials, the most general quadratic yield function representing a smooth initial yield surface that reduces to the Mises yield function in the special case of isotropic materials is of the form[5]

$$f = B_{klmn} s_{kl} s_{mn} - \kappa^2 , \qquad (3)$$

where the coefficient tensor, B_{klmn}, has the obvious symmetries, and hence has 21 independent components. If, as is commonly done, the further assumption is made that the yield behavior is independent of the mean stress (pressure), then the stress in **Eq. 3** can be replaced by the deviatoric stress, and the coefficient tensor can be replaced by a reduced tensor which has 15 independent coefficients.

The yield function (**Eq. 3**) contains as a special case the anisotropic yield condition of Hill which is available in the DYNA code and is sometimes used in sheet metal forming analyses. Even though **Eq. 3** is much more general than the Mises yield function, it still does not adequately represent the kinds of material behavior exhibited in **Fig. 1**. It does, however, provide a reasonable basis to begin exploring some of the issues associated with implementing anisotropic plasticity models into numerical codes.

To evaluate some of these issues, the yield function (**Eq. 3**) was implemented into the parallel version of the ALE3D code. **Figure 4** shows the results of the simulation of a thick-walled anisotropic sphere (initial radius = 10, initial wall thickness = 2) subjected to a uniform external pressure load. With isotropic material properties, the sphere symmetrically compresses as one would expect. By modifying the properties in one direction, the very non-symmetric response in **Fig. 4** is predicted, indicating the significant effect that material anisotropy can have on overall structural response.

For Mises-type yield functions, an efficient numerical procedure for integrating the evolution equations has long been used. This consists of an elastic trial step followed by a radial-return corrector step. This simple and efficient procedure does not work in general for anisotropic yield functions, and one of the challenges ahead will be in developing robust, numerically efficient procedures for integrating the anisotropic evolution equations. In the context of the nonlinear strain-space formulation of the theory of elastic-plastic materials, Papadopoulos and Lu[6] have developed a method for integrating the evolution equations, which for the special case of transversely isotropic materials reduces to computing three separate radial-return steps for three orthogonal parts of the solution.

In addition to this effort to develop a phenomenological continuum model using experimental data, an effort is also underway to develop a homogenization methodology to predict effective macroscopic behavior based on explicit consideration of microstructural features, such as the statistical distribution of grain orientations. To this end, a material model for single crystal plasticity has been implemented into NIKE3D. This model also has the capability to account for polycrystal aggregates at each integration point using Taylor averaging. This model can be used in numerical experiments to predict effective yield surfaces for explicit microstructural configurations.

Future Work

We now have confidence in our ability to measure yield surfaces as accurately as necessary for our purposes. Continued work will involve generating specific data sets to guide the development of better constitutive equations for nonlinear plasticity. The anisotropic yield function (**Eq. 3**), while a useful starting point for evaluating some of the basic numerical issues, is not sufficiently general to represent the behavior we are seeing in the data. We will be focusing on developing a better theoretical model to represent the yield surface and its evolution.

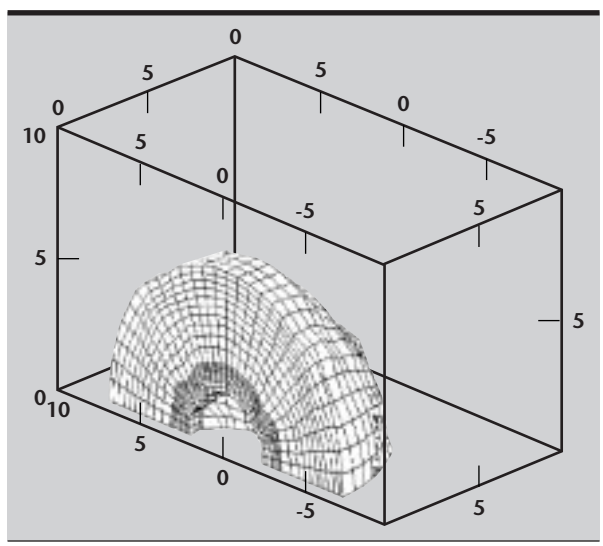

Figure 4. Numerical simulation of a sphere of homogeneous but anisotropic material, subjected to a uniform external pressure. For isotropic material properties, the sphere would compact symmetrically.

We also plan to examine materials of particular relevance to LLNL programs, relevance such as tantalum, which is a target material for the Multiscale Material Modeling effort. We also plan to complete the experiments discussed above to address the question of the correct identification of the plastic strain tensor in the context of general finite deformations.

Acknowledgment

Contributions to this project from Prof. J. Casey result from work supported by a grant from the Solid Mechanics Program of the National Science Foundation. Part of support for A. Brown's work, and material used during the development of the experimental procedure, were also provided through this grant.

References

1. Naghdi, P. M. (1990), "A Critical Review of the State of Finite Plasticity," *J. Appl. Math. and Phys. (ZAMP)*, **41**, pp. 315-394.

2. Nikkel, D. J., A. A. Brown, and J. Casey (1998), "Evolution of Anisotropic Yield Behavior," *Engineering Research, Development and Technology*, Lawrence Livermore National Laboratory, Livermore, California (UCRL-53868-97), pp. 5-1–5-5.

3. Casey, J., and P. M. Naghdi (1992), "A Prescription for the Identification of Finite Plastic Strain," *Int. J. Engng. Sci.*, **30**, pp. 1257-78.

4. Casey, J., and P. M. Naghdi (1992), "On the Identification of Plastic Strain at Finite Deformation," in *Defects and Anelasticity in the Characterization of Crystalline Solids*, L. M. Brock, ed., ASME AMD Vol. **148**, pp. 11-33.

5. Green, A. E., and P. M. Naghdi (1965), "A General Theory of an Elastic-Plastic Continuum," *Arch. Rat. Mech. and Anal.*, **18**, pp. 251-281.

6. Papadopoulos, P. and J. Lu (1998), "A General Framework for the Numerical Solution of Problems in Finite Elasto-Plasticity," *Comp. Meth. in Appl. Mech. and Engng.*, **159**, pp. 1-18.

Modeling Large-Strain High-Rate Deformation in Metals

Donald R. Lesuer and Mary M. LeBlanc
Manufacturing and Materials Engineering Division
Mechanical Engineering

Gregory J. Kay
New Technologies Engineering Division
Mechanical Engineering

The large-strain deformation responses of aluminum alloy 6061-T6 and titanium alloy Ti-6Al-4V have been evaluated over a range in strain rates from 10^{-4} s^{-1} to $>10^4$ s^{-1}. The results have been used to critically evaluate the strength and damage components of the Johnson-Cook (JC) material model. Two new models that address the short-comings of the JC model were then developed and evaluated. One model is derived from the rate equations that represent deformation mechanisms active during moderate- and high-rate loading; the other model accounts for the influence of void formation on yield and flow behavior of a ductile metal (the Gurson model). The characteristics and predictive capabilities of these models are reviewed.

Introduction

Many modeling problems of interest to Lawrence Livermore National Laboratory (LLNL) involve accurate representation of the high-rate deformation response of materials. Examples include the modeling of material processing operations as well as the in-service performance of materials. Typical material processing operations, in which high-rate deformation is observed, include material cutting, numerous forming operations (such as rolling and forging) and material polishing. Typical in-service performance problems include the ballistic penetration and perforation of armor materials, the performance of munitions, and explosive fragmentation.

Many of these problems are difficult to model accurately. Much of this difficulty arises from the large strains and adiabatic heat produced, which, in turn, causes increases in temperature with resulting changes in material microstructure, material properties, and deformation mechanisms. Large changes in strain rate are also produced.

In addition, deformation can produce instabilities in the form of adiabatic shear bands. Voids can also be produced that can influence flow behavior and serve as a precursor to fracture. Thus, accurate material models are necessary for understanding deformation behavior (and strength) as well as failure response.

Objectives

Material models that can adequately represent the deformation response during high-rate loading must account for large strains (and the resulting strain hardening or softening), as well as large changes in strain rate and temperature. Several models have been developed that can represent, to varying degrees, the high-rate deformation response of materials. Examples include models by Johnson and Cook (JC),[1-3] Zerilli and Armstrong (ZA),[4–6] and Follansbee and Kocks (mechanical threshold stress model)[7].

Two of these models (JC and ZA) have been introduced into LLNL's DYNA codes.

Of these two models, the JC model is much more widely used. The JC model was developed during the 1980s to study impact, ballistic penetration, and explosive detonation problems. The model has proven to be very popular and has been used extensively by a number of national laboratories, military laboratories, and private industry to study high-rate, large-strain problems. The reasons for the popularity of this model include the simple form of the constitutive equations and the availability of constants used in the equations for a number of materials. The JC material model also has a cumulative damage law that can be used to assess failure.

In this report, we take a critical look at the JC model and its ability to represent the large-strain deformation behavior of two important structural materials: an α-β titanium alloy (Ti-6Al-4V) and a moderate strength aluminum alloy (6061-T6). The model has been evaluated over a range of strain rates from 10^{-4} s^{-1} to $>10^4$ s^{-1}. The damage law was also evaluated for its ability to predict failure in these materials. Two new models were then developed and evaluated that address some of the shortcomings observed with the JC model. One of the models is derived from the rate equations that represent deformation mechanisms active during moderate- and high-rate loading; the other model accounts for the influence of void formation on yield and flow behavior of a ductile metal (the Gurson model[8]). The characteristics and predictive capabilities of these models are reviewed.

Progress

Materials, Experiments and Results

The materials used in this study were obtained from commercial sources. The 6061 alloy was received as a hot, cross-rolled plate in the T6 temper. The Ti-6Al-4V alloy was obtained according to the AMS 4911 specification, which produced an equiaxed α and transformed β microstructure.

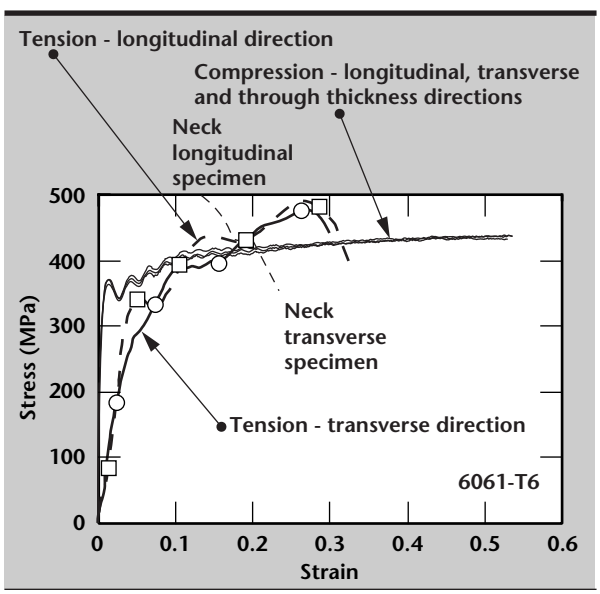

Figure 1. Stress-strain data for aluminum alloy 6061-T6 obtained in tension and compression with the split Hopkinson pressure bar apparatus. The experiments in tension were conducted in two different orientations and at a strain rate of 8000 s^{-1}. The experiments in compression were conducted in three different orientations and at a strain rate of 4000 s^{-1}.

High-rate testing was done in both compression and tension using the split Hopkinson pressure bar technique, and data was obtained at strain rates of 10^3 s^{-1} to 10^4 s^{-1}. In the compression tests, the strain histories for the incident and transmitted waves in the elastic pressure bars were measured and analyzed to determine the nominal stress/strain/strain-rate response of the sample. In the tension tests, the strain history in the elastic pressure bars was used to obtain the stress-time response of the sample. The strain and strain-rate behavior of the sample was obtained from high-speed photographic images derived from a framing camera.

All stress-strain data is provided as "true stress" and "true strain." The stress-strain data for 6061-T6 aluminum obtained in tension and compression is shown in **Fig. 1.** The experiments in tension were conducted at a strain rate of 8000 s^{-1}, and samples were tested with the tensile axis parallel to the longitudinal and transverse orientations in the plate. The experiments in compression were conducted at a strain rate of 4000 s^{-1}, and samples were tested with the compression axis parallel to the longitudinal, transverse, and through-thickness orientations in the plate.

Data for "elastic" loading of the sample can not be obtained in these tests due to wave propagation effects. The stress-strain data shown in **Fig. 1** can be considered valid once the samples have yielded plastically, which is accompanied by stress and strain rate uniformity in the sample. The data for the different orientations of testing show that in both tension and compression, the stress-strain response is highly isotropic. This is especially true in compression, in which the curves for the three orientations fall virtually on top of one another. The compression samples deformed to the limits of the experiment without failure, while the tension samples failed after a strain of 0.26

Johnson-Cook Material Model

The formulation for the JC model is empirically based and represents the flow stress with an equation of the form

$$\sigma = \left[A + B\varepsilon^n\right]\left[1 + C\ln\dot{\varepsilon}^*\right]\left[1 - T^{*m}\right], \qquad (1)$$

where σ is the effective stress, ε is the effective plastic strain, $\dot{\varepsilon}^*$ is the normalized effective plastic strain rate (typically normalized to a strain rate of 1.0 s^{-1}), T^* is the homologous temperature, n is the work hardening exponent and A, B, C, and m are constants.

The values of A, B, C, n, and m are determined from an empirical fit of flow stress data (as a function

Table 1. Johnson-Cook constants for Ti-6Al-4V and 6061-T6.

	A (MPa)	B (MPa)	n	C	m	D_1	D_2	D_3	D_4	D_5
6061-T6	324	114	0.42	0.002	1.34	-0.77	1.45	-0.47	0.0	1.60
Ti-6Al-4V	862	331	0.34	0.012	0.8	-0.09	0.25	-0.5	0.014	3.87

of strain, strain rate and temperature) to **Eq. 1**. For high-rate deformation problems, we can assume that an arbitrary percentage of the plastic work done during deformation produces heat in the deforming material. For many materials, 100% of the plastic work becomes heat in the material. Thus the temperature used in **Eq. 1** can be derived from the increase in temperature according to the following expression

$$\Delta T = \frac{\alpha B}{\rho c(n+1)} \varepsilon^{n+1}, \tag{2}$$

where ΔT is the temperature increase, α is the percentage of plastic work transformed to heat, c is the heat capacity and ρ is the density.

Fracture in the JC material model is derived from the following cumulative damage law:

$$D = \sum \frac{\Delta\varepsilon}{\varepsilon_f}, \tag{3}$$

where

$$\varepsilon_f = \left[D_1 + D_2 \exp\left(D_3 \sigma^*\right)\right]\left[1 + D_4 \ln \dot{\varepsilon}^*\right]\left[1 + D_5 T^*\right], \tag{4}$$

$\Delta\varepsilon$ is the increment of effective plastic strain during an increment in loading and σ^* is the mean stress normalized by the effective stress. The parameters D_1, D_2, D_3, D_4, and D_5 are constants. Failure is assumed to occur when D = 1. The current failure strain (ε_f) is thus a function of mean stress, strain rate, and temperature. The constants for the JC model used in the evaluations in the next section are given in **Table 1**.

Model Evaluation. The adiabatic stress-strain behavior for the 6061-T6 alloy predicted by the JC material model is shown in **Fig. 2** for loading in tension, compression, and shear. The cumulative damage predicted by the failure model is also shown in the figure, and the failure strains for the three stress states are indicated on the stress-strain curve. The three stress states show different damage curves because of the influence of the mean stress term on ε_f in **Eq. 4**.

The stress-strain response predicted by the material model is compared against the experimental data in both tension and compression in **Fig. 3**. The yield strength predicted by the JC model correlates very well with the experimental results. However, the experimental stress-strain curves work harden at a higher rate. This is not a fundamental short-coming of the model, since higher work hardening rates are possible with larger values of B and n in **Eq. 1**. The failure strain in tension as predicted by the JC material model (ε_f = 0.52) is significantly higher than that obtained experimentally (ε_f = 0.26). This is a significant difference and the physical origins of this discrepancy need to be understood. However, detailed studies of failure models are outside the scope of this paper.

The stress-strain rate response for the 6061-T6 alloy is compared against the predictions of the JC model in **Fig. 4**. Data was obtained from the work of Nicholas[9] as well as from this study. Here significant deviations between model predictions and experimental results are evident. The experimental data shows a dramatic increase in strength above a strain rate of 10^3 s^{-1}. This increase in strength has been observed in a number of metals[10] and is generally recognized as resulting from a change in deformation mechanism.

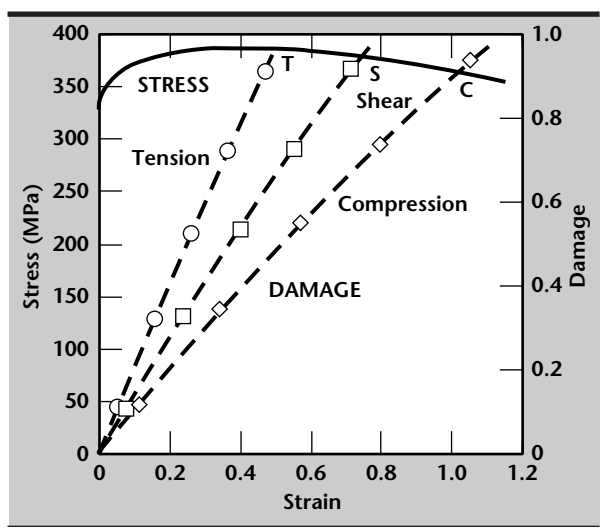

Figure 2. Adiabatic stress-strain behavior for aluminum alloy 6061-T6 at a strain rate of 6000 s,$^{-1}$ predicted by the JC material model. Results are presented for loading in tension, compression, and shear. The cumulative damage predicted by the material model is also shown. The failure point along the stress-strain curve is shown for tension, shear, and compression.

At lower strain rates, the deformation rate is controlled by the cutting or by-passing of discrete obstacles by dislocations. At higher rates, the deformation rate is controlled by phonon or electron drag on moving dislocations. These two mechanisms are represented by different deformation rate equations, which results in the dramatic change in behavior from low strain rates to high strain rates. Such dramatic changes are outside the scope of the JC model. In the next section we present a model that accounts for these mechanism changes.

The predictions of the JC model for the Ti-6Al-4V alloy are shown in **Fig. 5** and compared against experimental data in **Figs. 6** and **7**, obtained from the work of Wulf[11], Meyer[12] and Follansbee and Gray[13]. The same capabilities and limitations of the material model that were observed for the 6061-T6 alloy were noted for the Ti-6Al-4V alloy. The model can adequately represent work-hardening behavior in both materials. The most serious limitation is its ability to predict variations of flow stress with strain rate, as shown in **Fig. 7**. The failure model predicted the correct ductility in tension for the Ti-6Al-4V alloy (ε_f = 0.15) but, in compression, the model predicted a significantly higher ductility than that observed experimentally.

Mechanism-Based Material Model

Rate Equations. We now derive a rate equation representing deformation that can be controlled by two sequential processes: 1) the cutting (or by-passing) of obstacles by dislocations, or 2) the drag on moving dislocations by phonons or electrons. The

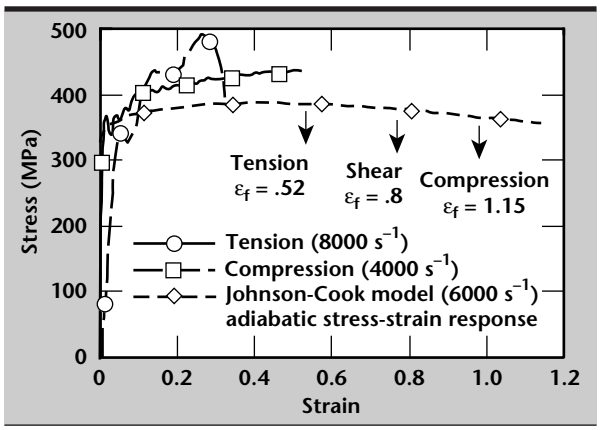

Figure 3. Comparison between the stress-strain behavior predicted by the JC material model and experimental data for aluminum alloy 6061-T6.

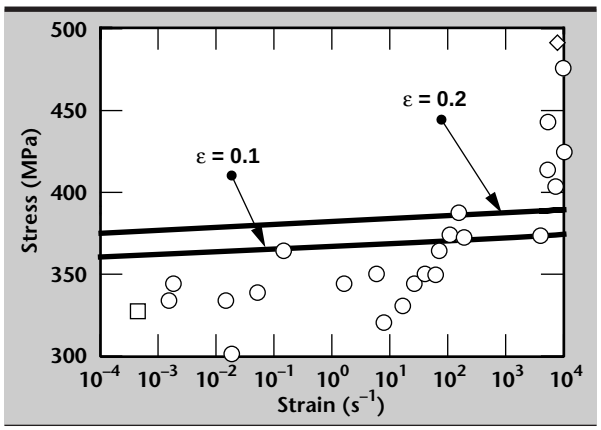

Figure 4. Comparison between the stress-strain rate behavior predicted by the JC material model and experimental data for aluminum alloy 6061-T6. Experimental data is derived from a compilation of LLNL results and data from Reference 9.

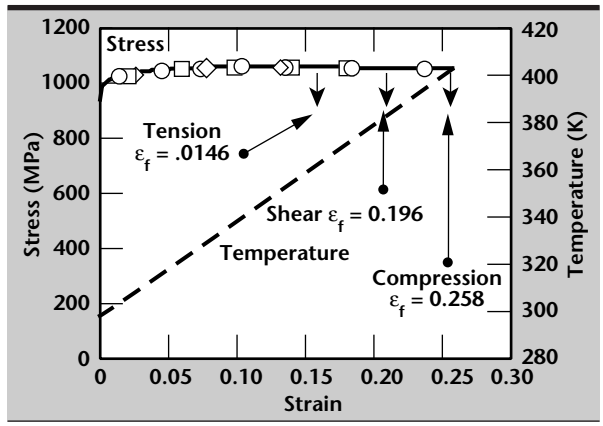

Figure 5. Adiabatic stress-strain behavior for titanium alloy Ti-6Al-4V at a strain rate of 5000 s^{-1}, as predicted by the JC material model. Results are presented for loading in tension, compression, and shear. The adiabatic temperature rise is also shown. The failure point along the stress-strain curve is shown for the three stress states.

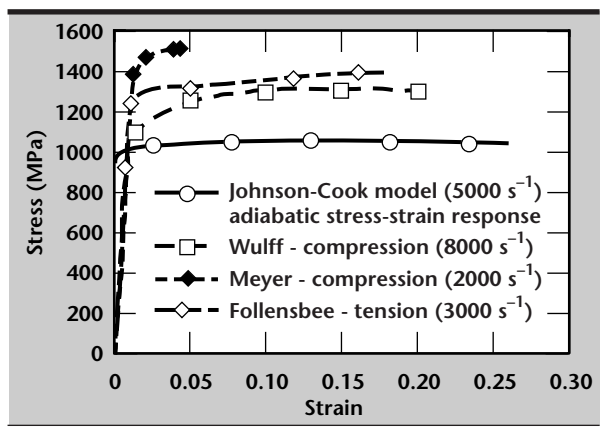

Figure 6. Comparison between the stress-strain behavior predicted by the JC material model and experimental data for titanium alloy Ti-6Al-4V (obtained from References 11 to 13).

problem is illustrated schematically in **Fig. 8**, which shows dislocations in contact with discrete obstacles that have an average spacing, d. After Frost and Ashby[14], the average velocity, v, for a dislocation moving through these obstacles is

$$v = d/(t_1 + t_2), \tag{5}$$

where t_1 is the time required to cut or by-pass the obstacle, and t_2 is the time spent moving to the next obstacle. Different rate equations represent the deformation kinetics associated with discrete obstacles and drag. Let $\dot{\varepsilon}_1$ represent the strain rate when deformation is controlled by the cutting or by-passing of discrete obstacles, and $\dot{\varepsilon}_2$ represent the strain rate when deformation is controlled by drag on moving dislocations. Since

$$\dot{\varepsilon} = \rho b v, \tag{6}$$

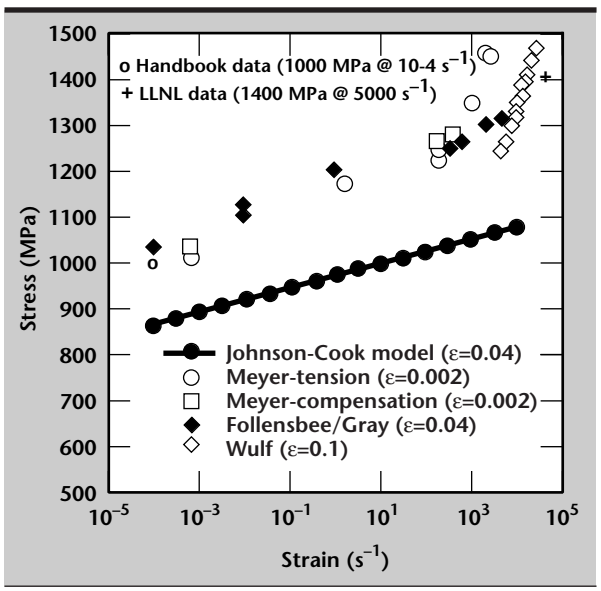

Figure 7. Comparison between the stress-strain rate behavior predicted by the JC material model and experimental data for aluminum alloy 6061-T6.

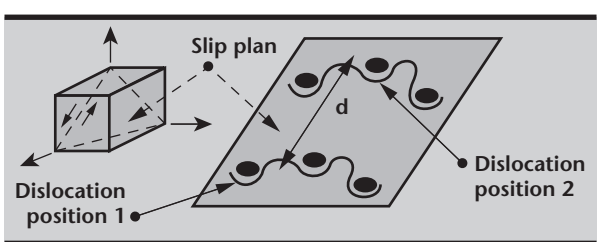

Figure 8. Dislocations on a slip plane in contact with discrete obstacles. The shear stress on the slip plane is σ, and the average spacing between obstacles is d. At high strain rates, the dislocation velocity (and therefore strain rate) is determined by the rate at which the discrete obstacles are by-passed, or the rate at which the dislocation moves from one discrete obstacle to the next.

where $\dot{\varepsilon}$ is the strain rate, b is the Burger's vector and ρ is the mobile dislocation density,

$$\dot{\varepsilon}_{eff} = \frac{d}{\frac{d}{\dot{\varepsilon}_1} + \frac{d}{\dot{\varepsilon}_2}}, \tag{7}$$

where $\dot{\varepsilon}_{eff}$ is the effective strain rate on the slip plane shown in **Fig. 8**. Thus

$$\dot{\varepsilon}_{eff} = \frac{\dot{\varepsilon}_1 \dot{\varepsilon}_2}{\dot{\varepsilon}_1 + \dot{\varepsilon}_2}. \tag{8}$$

The rate equation for discrete obstacle controlled plasticity[15] can be taken as

$$\dot{\varepsilon}_1 = \dot{\varepsilon}_0 \exp\left[-\frac{Q}{kT}\left(1 - \frac{\sigma}{\tau}\right)\right], \tag{9}$$

where $\dot{\varepsilon}_0$ is a constant, Q is an activation energy, k is Boltzmann's constant, σ is the stress and τ is the strength of the obstacle. At constant temperature, the equation can be taken as

$$\dot{\varepsilon}_1 = A \exp(B\sigma), \tag{10}$$

where A and B are constants. The rate equation for phonon- or electron-drag-controlled plasticity can be taken as

$$\dot{\varepsilon}_2 = C\sigma^D, \tag{11}$$

where C and D are constants. Several theoretical treatments have shown that D approaches 1[16,17]. We will use the general form of the rate equation shown in **Eq. 11**. **Equations 8, 10,** and **11** can now be used to calculate the strain rate resulting from the sequential mechanism of discrete-obstacle plasticity and drag-controlled plasticity.

Model Evaluation. The model, as represented by **Eqs. 8**, **10**, and **11**, was evaluated against the stress-strain rate data for the 6061-T6 and Ti-6Al-4V alloys shown in **Figs. 4** and **7**, respectively. The constants for obstacle-controlled plasticity (A and B) were evaluated in the strain-rate range where this mechanism is dominant. Similarly, the constants for drag-controlled plasticity (C and D) were evaluated in the strain-rate range where this mechanism is dominant.

Figure 9 shows a comparison of the stress-strain rate response predicted by the mechanism-based material model and experimental data for the 6061-T6 alloy.

Similarly, **Fig. 10** shows a comparison of the stress-strain rate response predicted by the mechanism-based material model and experimental

data for the Ti-6Al-4V alloy. The figures also show the regions of the stress-strain curves that are dominated by discrete-obstacle plasticity and by drag-controlled plasticity. For both alloys, the agreement between the model predictions and experimental data is excellent.

Gurson Void Growth Model

Observations have been made that ductile fracture in metals is related to the nucleation and growth of voids. Conventional plasticity models, for example, von Mises, are based on the assumption of plastic incompressibility and can not predict the growth of voids during yielding. Studies have indicated[18–20] that void growth during tensile loading is related to the hydrostatic component of stress, and that this porosity increase directly affects material yielding.

In these observations it was assumed that the material surrounding a void was incompressible. Gurson[8] proposed a pressure-sensitive macroscopic yield surface that relates void growth to the evolution of microscopic (pointwise physical quantities of the matrix material) and macroscopic quantities to account for the behavior of void-containing solids. Here, macroscopic refers to the average values of physical quantities, which represent the material aggregate behavior. As defined by Gurson, the yield surface for a ductile material is:

$$\Phi = \left(\frac{q}{\sigma_0}\right)^2 + 2q_1 f \cosh\left(\frac{3p}{2\sigma_0}\right) - \left(1 + q_2 f^2\right) = 0, \tag{12}$$

where σ_0 is the tensile flow stress of the microscopic matrix material, q and p are the equivalent stress and hydrostatic stresses of the macroscopic material, and f is the current void volume fraction which is a function of the initial porosity, the void growth, and nucleation during yielding. The material parameters q_1, q_2 are defined by Gurson.

The Gurson model was added to NIKE2D by B. Engelmann. For the current study, a version of the NIKE2D Gurson model was modified to correctly account for the evolution of plastic strain in the micro (matrix) material and to account for strain rate sensitivity. The model was added to DYNA3D.

The response of a notched bar under uniaxial tensile loading was simulated to demonstrate the DYNA3D application of the Gurson model. Substantial hydrostatic tension is created in the notched regions of the bar for this type of loading. This hydrostatic stress accelerates void growth and leads to the eventual coalescence of voids and ductile failure of the bar. Failure was assumed to correspond to the loss of load-carrying capability in this displacement-controlled simulation.

The bar was assumed to have the following material properties: E = 20.7 GPa, υ = 0.3, yield stress = 690 MPa, with a linear hardening modulus of 1,540 MPa. The initial void fraction was assumed to be equal to 0.050.

The initial and deformed shapes of the tensile specimen are shown in **Fig. 11**, which also depicts the regions of predicted high void growth. The effect of rate-dependence is shown in **Fig. 12**, where an increased loading rate resulted in an increased normalized axial load (actual axial load/initial yield strength), with softening similar to the rate-independent Gurson model results.

Also shown in **Fig. 12** is the conventional plasticity solution, which does not exhibit the

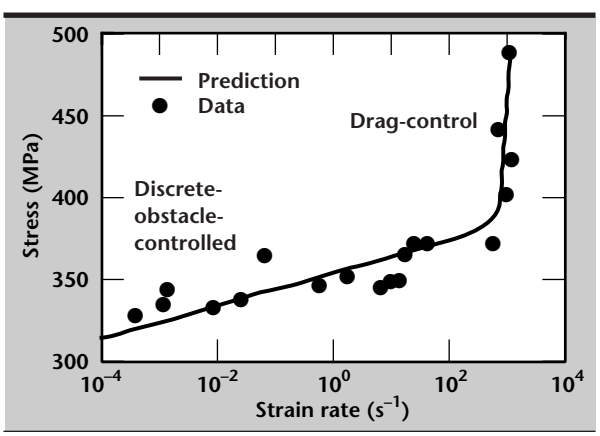

Figure 9. Comparison between the stress-strain rate behavior predicted by the mechanism-based material model and experimental data for aluminum alloy 6061-T6. Regions of the stress-strain rate curve that are dominated by discrete-obstacle plasticity and drag-controlled plasticity are shown.

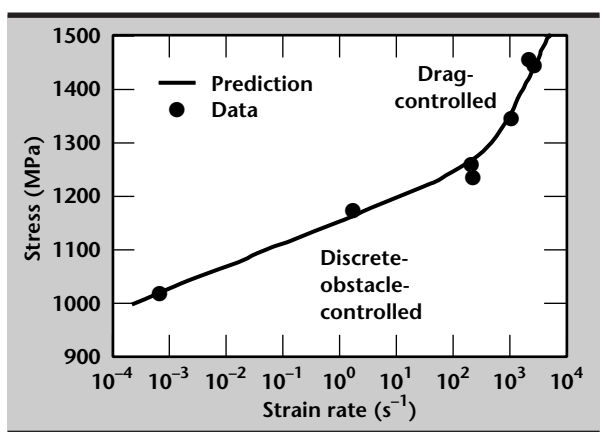

Figure 10. Comparison between the stress-strain rate behavior predicted by the mechanism-based material model and experimental data for titanium alloy Ti-6Al-4V. Regions of the stress-strain rate curve that are dominated by discrete-obstacle plasticity and drag-controlled plasticity are shown.

pronounced softening predicted by the Gurson model. The conventional plasticity yield surface is also shown to be larger, with a higher strain-to-failure, than the porous material, a result confirmed by experimental results.

For this simulation, the final void fraction was 0.70. A calculation was also performed to check the sensitivity of the solution to mesh size. The mesh in this calculation was twice the density of the initial simulation. The results of this calcula-

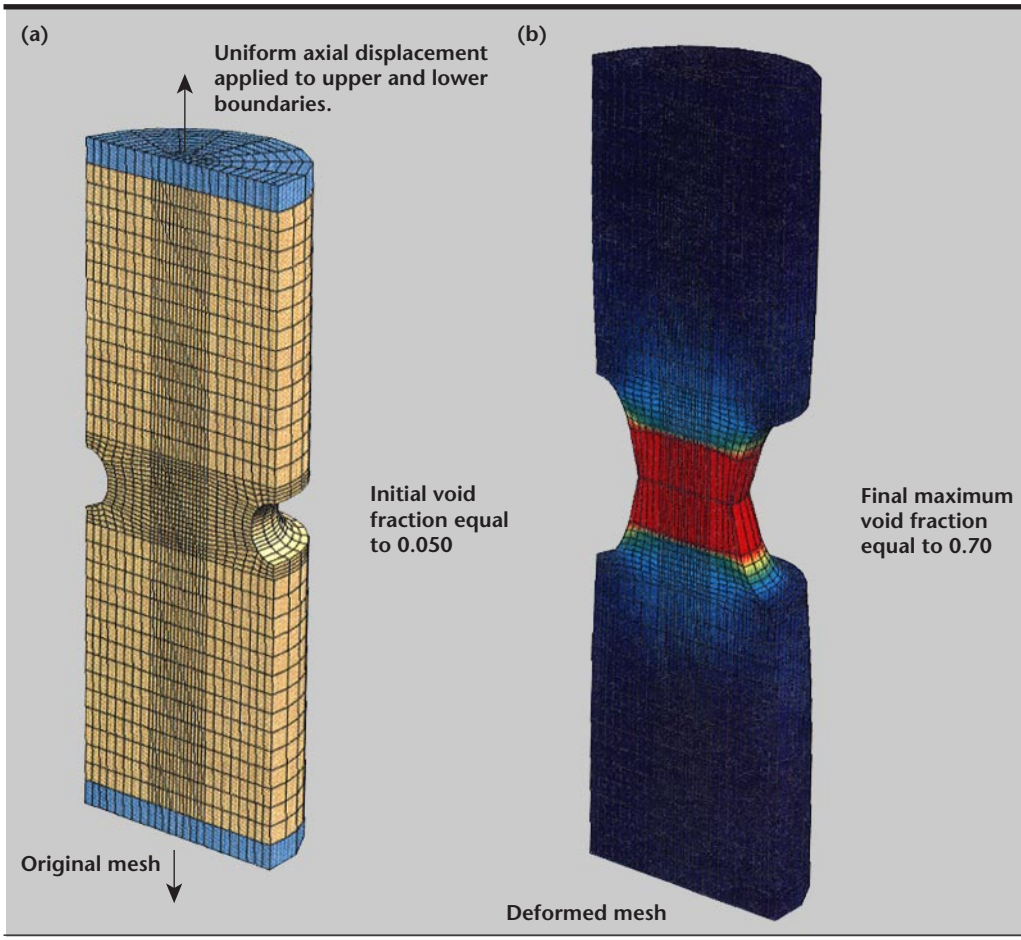

Figure 11. Notched tensile specimen void growth, as predicted by the Gurson model.

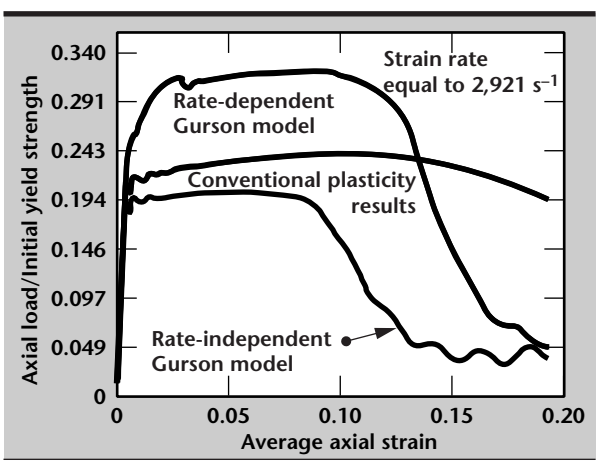

Figure 12. Gurson model rate effects for a notched bar under displacement-controlled axial loading.

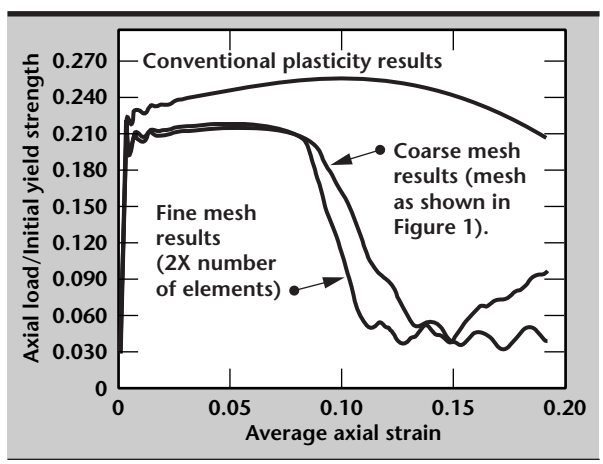

Figure 13. Gurson model mesh sensitivity for a notched bar under displacement-controlled axial loading.

tion, shown in **Fig. 13**, indicate that there is some small mesh sensitivity of the solution, in the post-failure phase, for the rate-independent Gurson solution.

Summary

The primary conclusions and observations relative to the three models studied are as follows:

1. JC model. For the alloys studied, the JC model can accurately represent the yield and work-hardening behavior of the materials. The JC model predicts higher failure strains than those observed experimentally. The most serious short-coming of the JC model is its inability to accurately represent the variation of flow stress with strain rate.
2. Deformation mechanism model. This model accounts for two sequential deformation mechanisms that are active at moderate- and high-deformation rates. The mechanisms are discrete-obstacle plasticity and drag-controlled plasticity. The model has been developed and evaluated against stress-strain rate data for the 6061-T6 alloy and theTi-6Al-4V alloy. Agreement between experimental results and model predictions is excellent.
3. Gurson void growth model. The Gurson void growth model has been introduced into the DYNA3D code. The model was modified to account for the evolution of plastic strain and strain rate sensitivity. The model was used in the DYNA3D code to simulate the response of a notched bar during tensile loading.

References

1. Johnson, G. R., and W. H. Cook (1985), "Fracture Characteristics of Three Metals Subjected to Various Strains, Strain Rates, Temperatures and Pressures," *Engineering Fracture Mechanics*, **21**, No. 1, pp. 31–48.

2. Johnson, G. R., and W. H. Cook (1983), "A Constitutive Model and Data for Metals Subjected to Large Strains, High Rates and High Temperatures," *Proceedings of the Seventh International Symposium on Ballistics,* The Hague, The Netherlands, pp. 541–547.

3. Johnson, G. R., and T. J. Holmquist (1988), "Evaluation of Cylinder-Impact Test Data for Constitutive Model Constants," *Journal of Applied Physics*, **64**, No. 8, pp. 3901–3910.

4. Zerilli, F. J., and R. W. Armstrong (1987), "Dislocation-Mechanics-Based Constitutive Relations for Material Dynamics Calculations," *Journal of Applied Physics*, **61**, No. 5, pp. 1816–1825.

5. Zerilli, F. J., and R. W. Armstrong (1990), "Description of Tantalum Deformation Behavior by Dislocation Mechanics Based Constitutive Equations," *Journal of Applied Physics*, **68**, No. 4, pp. 1580–1591.

6. Zerilli, F. J., and R. W. Armstrong (1992), "The Effect of Dislocation Drag on the Stress-Strain Behavior of FCC Metals," *Acta Metallurgica et Materialia*, **40**, No. 8, pp. 1803–1808.

7. Follansbee, P. S., and U. F. Kocks (1988), "A Constitutive Description of the Deformation of Copper Based on the Use of the Mechanical Threshold Stress as an Internal State Variable," *Acta Metallurgica*, **36**, pp. 81–93.

8. Gurson, A. J. (1977), "Continuum Theory of Ductile Rupture by Void Nucleation and Growth, Part I - Yield Criteria and Flow Rules for Porous Ductile Media," *Journal of Engineering Materials Technology*, **99**, pp. 2–15.

9. Nicholas, T. (1981), "Tensile Testing of Material at High Rates of Strain," *Experimental Mechanics*, May, pp. 177–185.

10. Follansbee, P. S. (1986), "High-Strain-Rate Deformation of FCC Metals and Alloys," in *Metallurgical Applications of Shock-Wave and High-Strain-Rate Phenomena,* L. E. Murr, K. P. Staudhammer, and M. A. Meyers, eds. New York: Marcel Dekker, Inc., pp. 451–479.

11. Wulf, G. L. (1979), "High Strain Rate Compression of Titanium and Some Titanium Alloys," *International Journal of Mechanical Sciences*, **21**, pp. 713–718.

12. Meyer, L. W. (1984), "Strength and Ductility of a Titanium-Alloy Ti-6Al-4V in Tensile and Compressive Loading Under Low, Medium and High Rates of Strain," in *Titanium Science and Technology*, G. Lutjering, U. Zwicker, and W. Bunk, eds., Deutsche Gessellschaft fur Metallkunde .

13. Follansbee, P. S., and I. G.T. Gray (1989), "An Analysis of the Low Temperature, Low and High Strain-Rate Deformation of Ti-6Al-4V," *Metallurgical Transactions A*, **20A**, pp. 863–874.

14. Frost, H. J., and M. F. Ashby (1971), "Motion of a Dislocation Acted on by a Viscous Drag Through an Array of Discrete Obstacles," *Journal of Applied Physics*, **42**, No. 13, pp. 5273–5279.

15. Frost, H. J., and M. F. Ashby (1982), *Deformation Mechanism Maps,* Pergamon Press, Oxford.

16. Granato, A. V. (1973), "Microscopic Mechanisms of Dislocation Drag," *Metallurgical Effects at High Strain Rates,* Plenum Press, New York, New York, pp. 255–275.

17. Kumar, A., F. E. Hauser, and J. E. Dorn (1968), "Viscous Drag on Dislocations in Aluminum at High Strain Rates," *Acta Metallurgica*, **16**, pp. 1189–1197.

18. McClintock, F. A. (1968), "A Criterion for Ductile Fracture by the Growth of Holes," *Journal of Applied Mechanics*, **35**, pp. 363–371.

19. Rice, J. R., and D. M. Tracy (1969), "On the Ductile Enlargement of Voids in Triaxial Stress Fields," *Journal of the Mechanics and Physics of Solids*, **17**, pp. 201–217.

20. Kahlow, K. J., and B. Avitzur (1969), "Void Behavior as Influenced by Deformation and Pressure," American Iron and Steel Institute, Lehigh University.

Uniform Etching of 85-Cm-Diameter Grating

Steven R. Bryan, Jr. and David L. Sanders
Manufacturing Materials Engineering Division
Mechanical Engineering

The purpose of this project was to extend the capability of an existing gridded, broad-beam (Kaufman-style) ion beam system to permit the uniform etching of a fused silica optic 85 cm in diameter with an etch depth uniformity within 5%. Since we hoped to demonstrate that we would be able to fabricate large size diffractive optics (for example, transmission gratings), a secondary requirement was to establish the etching conditions that allow such grating structures to have adequate efficiencies over this same large area.

We had hoped, during the course of this project, to fabricate a full size 85-cm diameter part. Since the substrate blanks for such gratings cost $50,000 each and most of that cost would be sacrificed during an unsuccessful etch, we considered it important to demonstrate a reproducible and predictable process prior to risking such a blank. At this time, we believe we have demonstrated that we can etch such a part with minimal risk of failure. This was accomplished by etching a series of small gratings and fused silica etch witnesses mounted across this diameter, the data from which are presented in this report.

Introduction

During a joint effort between laser and engineering personnel at Lawrence Livermore National Laboratory (LLNL), an ion beam etching system having a 40-cm diameter gridded, broad-beam ion source was established. At the beginning of this project, this system was capable of etching a 30-cm part with an etch depth uniformity of better than ±5%. Our goal was to extend our etching technology base to allow us to etch larger parts in the same system, with the ultimate goal of producing 85-cm-diameter transmission gratings with high efficiency across this full diameter. To accomplish this, we needed to develop a shadow mask allowing us to exactly cancel the inherent non-uniformity in the ion beam. We also needed to determine the etching parameters that are most critical for generating the desired grating profiles to minimize the risk of an unsuccessful etch on a large part.

Progress

Ion Source Modification

To make possible the uniform etching of such large parts, we needed to modify the existing ion source to broaden the ion beam beyond the range for which it was designed. We first removed the original equipment internal baffle to permit use of the entire ion beam. We next removed the acceleration grids and re-installed them in a convex configuration to provide a de-focussed beam with a larger effective diameter. The result of these two modifications can be seen in **Fig. 1**. While the beam intensity is diminished, its diameter is increased. We needed this additional beam diameter to make it possible to etch our large part uniformly.

Substrate Holder and Etching Geometry

In addition to the ion source modifications, the substrate stage was modified to accept a single 85-cm-diameter substrate in place of the existing four 30-cm substrates. This was done while maintaining the ability to control substrate temperature.

Etch geometry, pictured in **Fig. 2**, was dictated by existing hardware: ion source and substrate stage horizontally opposed, with centers offset by 22 cm. The large disk which holds the 85-cm substrate is rotated with the ion source mounted off-center so that the entire surface is exposed to the ion beam during some portion its rotation about its center axis.

Model to Define Shadow Mask

To improve etch uniformity, a beam-shaping baffle was placed between the ion source and the substrate, as near to the substrate as possible. The determination of the shape of this baffle, which ultimately determines the etch uniformity, was critical to meet the goals of this project.

Dependable representation of the actual etch uniformity by a model is dependent upon consistent, reproducible operation of the ion source. Concerns about ion source repeatability were alleviated by periodically mapping the ion current density along a radius of the ion beam. As seen in **Fig. 3**, the current density profile of the ion source was found to correlate quite well to fused silica removal (etch) rates made at the same distances from the source. Ion source parameters, such as beam voltage, beam current, accelerator voltage, discharge voltage, and flow rates for various reactive gases were defined previously and held constant throughout this project.

The etch model was established by:

1. establishing the relationship between etch rate and position relative to the ion source;
2. identifying a second equation that describes the motion of any point on the substrate (relative to the ion source) as a function of time; and
3. substituting the position equation into the etch rate equation to yield etch rate as a function of time for any given point on the substrate.

By performing a numerical integration of etch rate over the period of time that the point on the substrate is in the ion beam, one can compute the etch depth at that point.

Initially, etch rates were measured by positioning fused silica samples in the ion beam, etching the sample for a period of time, then computing the etch rate by dividing the measured etch depth on the sample by the etch time. After the relationship between etch rates and beam current density measurements was established, a more economical method became available: ion current density measurements could be used to accurately predict etch rates. When confined to a plane that contains the surface of the substrate (27.5 cm from the ion source) and the perimeter of the ion beam, the radially symmetric beam yielded a fused silica etch rate that was found to conform well to the polynomial relation:

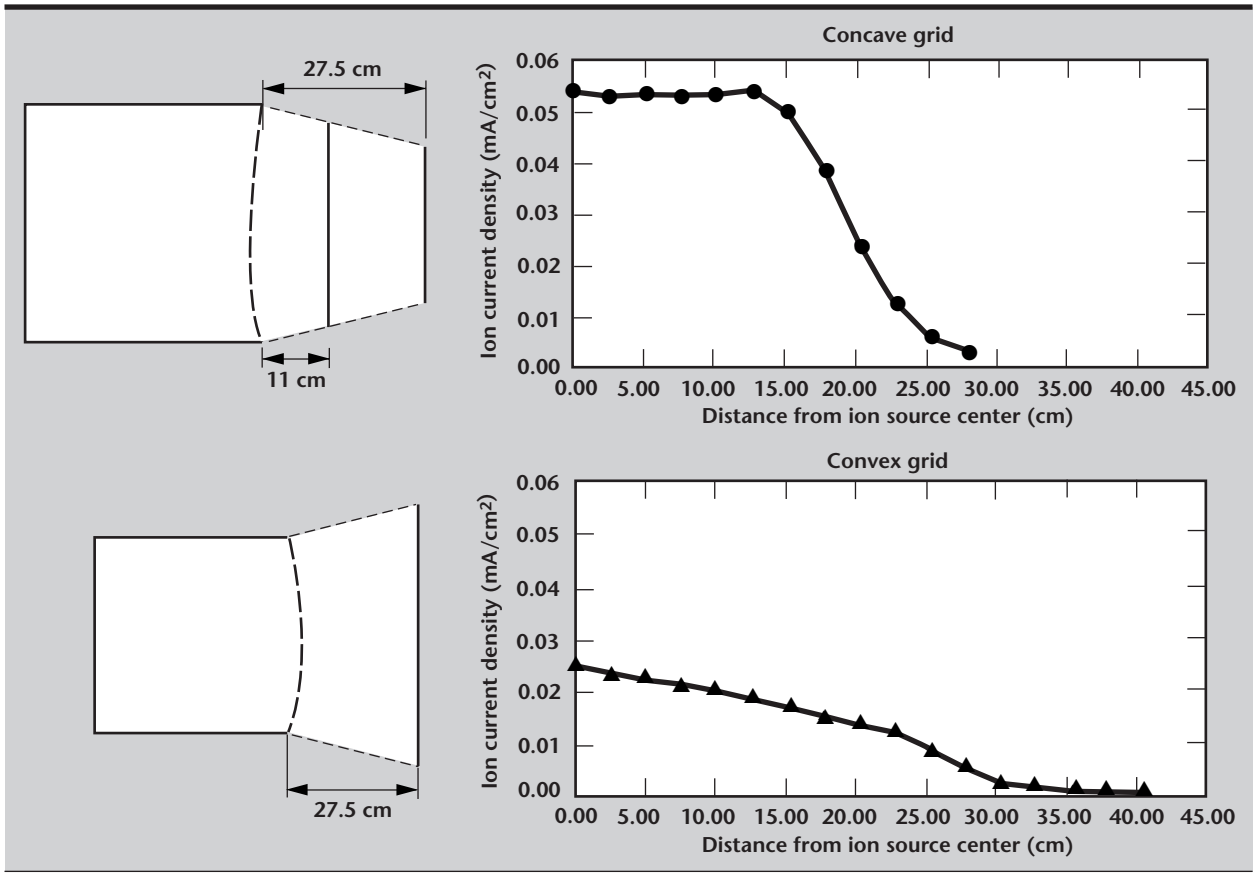

Figure 1. Effect on ion source beam diameter resulting from the source modification described in the text.

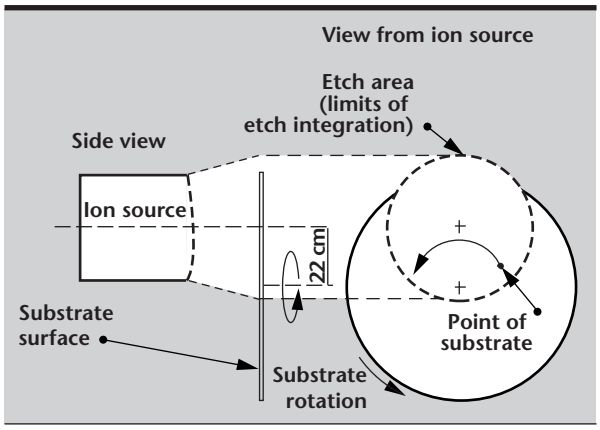

Figure 2. Etch geometry. The geometry was defined by existing hardware with the ion source and substrate horizontally opposed and the axes offset by 22 cm. The source-to-substrate distance was set to 27.5 cm.

$$E(r) = 1.42 - 4.41 \cdot 10^{-4} r + 3.06 \cdot 10^{-3} r^2 - 1.79 \cdot 10^{-4} r^3 + 2.72 \cdot 10^{-6} r^4 \quad , \qquad (1)$$

where E(r) is etch rate (µm/h) as a function of radial distance, r (cm), from the center of the ion source. From this equation, one can immediately see that the etch rate in the center of the ion source, at a distance of 27.5 cm is 1.42 µm/h (**Eq. 1** and **Fig. 3**).

The distance between a point on the substrate and the ion source center at any given time is dependent upon two variables: the location of the point on the substrate and the angle of substrate rotation at the time the distance is measured. Applying the Pythagorean theorem to the etch geometry in **Fig. 4** yields the simple relation: $r^2 = x^2 + y^2$ (where r is distance from the center of the ion source). Substituting for variables x and y, the equivalent in terms of substrate rotation angle, θ, and distance between substrate center and the point of interest, r_s (**Fig. 4**), yields:

$$r^2 = \left(22 - r_s \cos\theta\right)^2 + \left(r_s \sin\theta\right)^2 .$$

Since the rotational angle is a linear function of time (t), one may substitute time for angle (θ), simplify the equation, and solve for only the positive root to produce a usable function:

$$r\left(r_s, t\right) = \sqrt{484 - 44 r_s \cos(t) + r_s^2} . \qquad (2)$$

Note that points on the substrate have been defined only by their distance from the center of the substrate. This is acceptable because all points on a

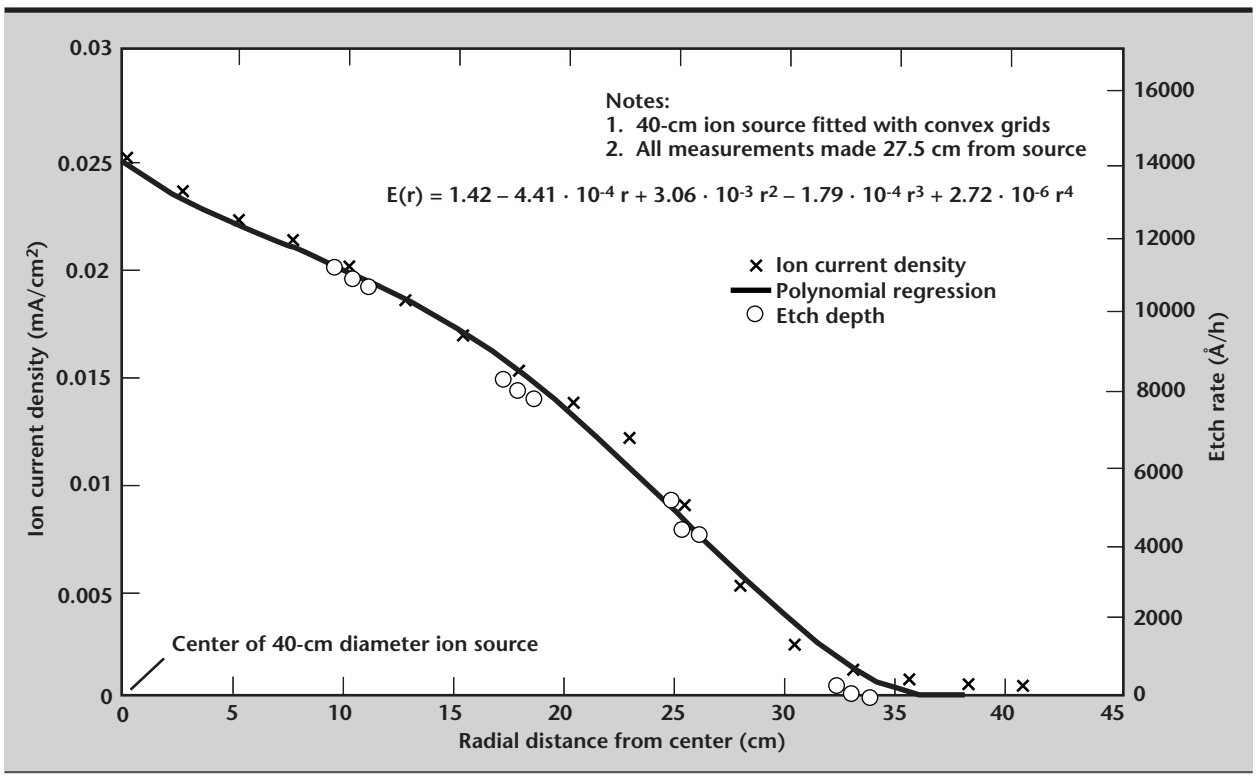

Figure 3. Ion beam profile comparison. Satisfactory correlation between Faraday cup measurements and fused silica etch rates were observed.

given circle of radius, r_s, on the substrate will be exposed to the same ion flux profile from the ion source, and will etch the same amount.

Substituting the equation defining radial distance from the source (**Eq. 2**) into the equation of etch rate (**Eq. 1**) above yields etch rate as a function of time for any point on the substrate. Integration of this etch rate over a period of time will provide a very close approximation of the total etch depth:

$$D\left(r_s, \theta_{\text{limit}}\right) = \int_0^{\theta_{\text{limit}}} E \times \left(\sqrt{484 - 44 r_s \cos(t) + r_s^2}\right) dt, \quad (3)$$

where r_s is the location of any point on the substrate and θ_{limit} is a new variable; the upper limit of integration. This upper limit of integration, defined by the shape of a shadow-mask placed directly in front of the substrate (refer to **Fig. 5**), controls etch uniformity over the surface of the substrate. Increasing the value of θ_{limit} increases the amount of etch time on a revolution of the substrate, thus increasing etch depth on a particular circle of points on the substrate. Similarly, reducing the value of θ_{limit} will reduce etch depth for the same circle of points. As one can imagine, solving the resulting equation is tedious if not particularly complex, but is well suited to numerical integration by computer.

Figure 6 shows the effect of the shadow mask on the uniformity of the etching. In the case without the mask, the etching rate varies by almost a factor of 7 over the part. With a properly designed mask this variation is seen to be within the goal of ±5% over most of the part. (There remains a small area less than 2 cm at the center of the part that is slightly out of tolerance, but we are confident that this can be corrected with a minor adjustment of the position of the mask if such an adjustment is deemed necessary).

Grating Structures

As mentioned in the introduction, in addition to the necessary uniformity in etching rate, it will be necessary to etch steep walled grating structures to achieve the required diffraction efficiency. **Figure 7** shows a scanning electron microscope photograph of a fracture surface of such a grating structure. Similar profiles were observed across the entire width of the grating, indicating that the desired etching behavior can be obtained with our current etching parameters.

Other Important Process Parameters

Initially, based on the experience of others, we assumed that it would be necessary to cool the part being etched to avoid overheating the photoresist. (Such overheating can make the photoresist difficult to remove after the completion of the etching process). To accomplish this cooling, we designed the substrate holder around a thermally conductive dry-chuck material normally used for cooling substrates during ion-etching operations in the semiconductor industry. For our particular application, however, we

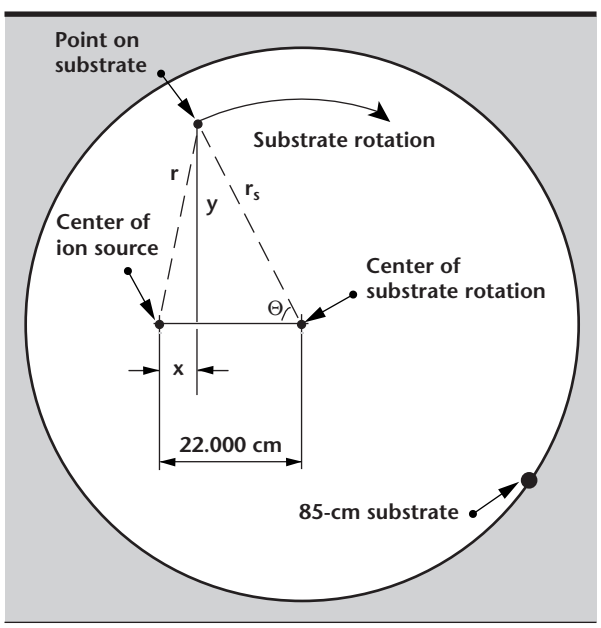

Figure 4. Location of point on substrate. Note that all points can be defined in terms of radial position on substrate. θ is a linear function of time.

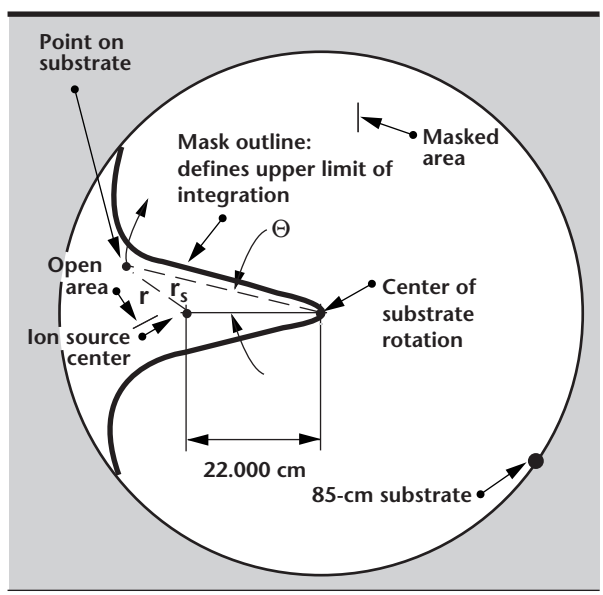

Figure 5. Approximate position and shape of limit-defining shadow mask.

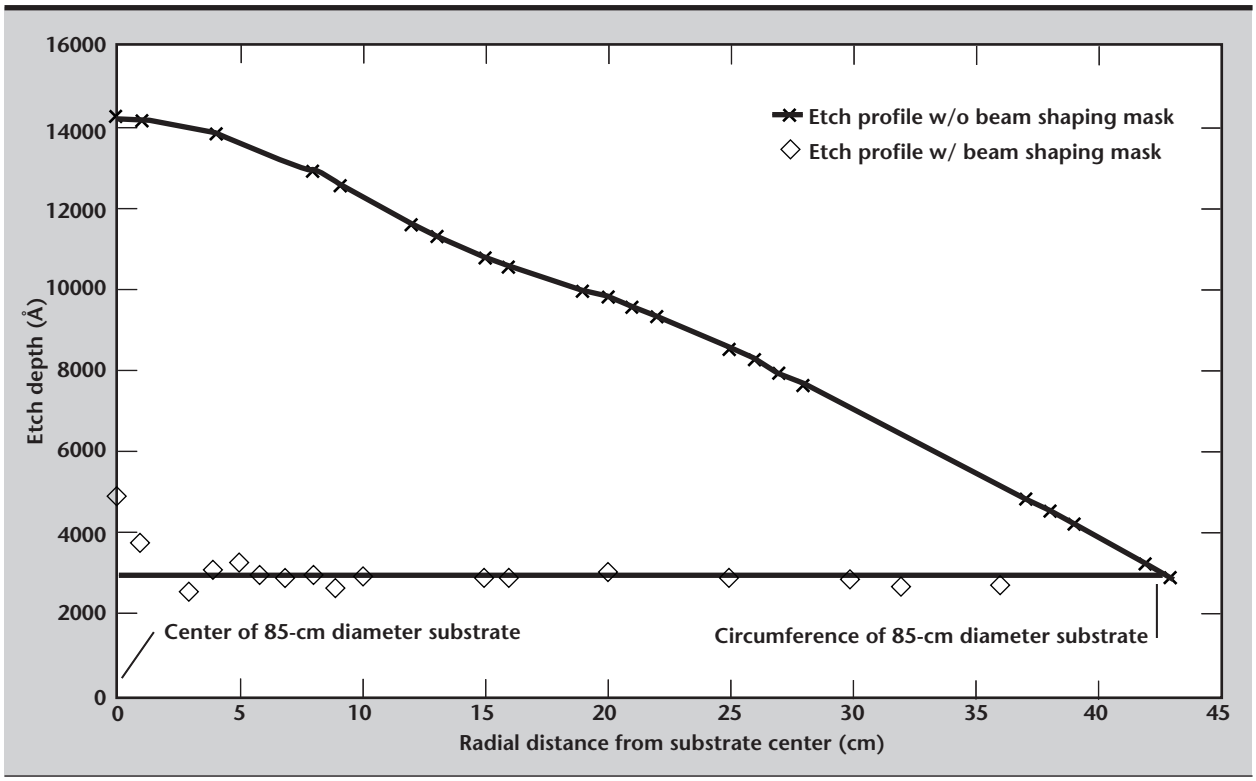

Figure 6. Effect of the shadow mask pictured in Figure 5 on the etch uniformity across an 85-cm-diameter part. Since the part is rotated, this figure represents half of the full diameter.

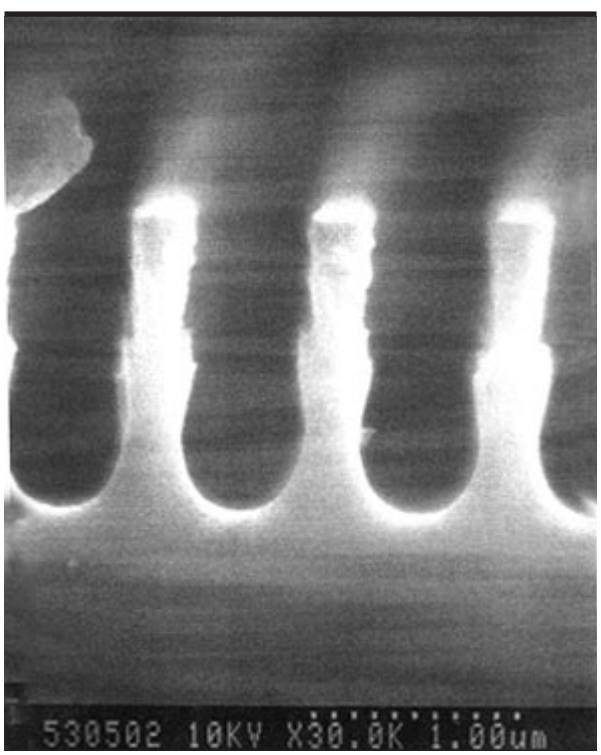

Figure 7. SEM micrograph of a grating structure etched using the current system.

discovered that cooling to temperatures below room temperature was not desirable because it contributed to the build-up of a hydrocarbon deposit in the trenches of the grating. In fact, we found it necessary to allow the substrate to be heated by the ion beam to prevent such buildup. In the future, we will need to investigate this temperature effect in more detail to determine the optimal etch temperature.

A second somewhat unexpected effect was the effect of buildup of a slightly conductive film on the ion gun insulators during the etching process. This buildup was found to lead to a reduction of the ion (etching) current during the etching run by as much as 20%. Recognizing this effect allowed us to compensate by adjusting the ion source to maintain a constant ion etching current throughout the course of the run.

Future Work

As funding and time permit, we plan to etch an 85-cm fused silica grating optic using the parameters we have established during this project. Based on our measurements, we expect the resulting grating will have the required etch depth uniformity and grating profile over the full diameter.

Distributed Sensor Inertial Measurement Unit

Carlos A. Avalle
Defense Sciences Engineering Division
Electronics Engineering

John I. Castor
Defense and Nuclear Technologies

We have developed a new type of Inertial Measurement Unit (IMU) in support of flight tests, based on a set of linear accelerometers distributed inside the flight vehicle. This novel, gyroscope-free design overcomes the restriction for sensors at or near the body's center of gravity (CG). The IMU is capable of determining the kinematics of a rigid body with six degrees of freedom. We have developed the mathematical model and are currently building the hardware for tests.

Introduction

Spacecraft motions are typically measured by IMUs capable of six degrees of freedom (that is, linear and angular motions about three orthogonal axes). Typically, these units consist of integral packages or sensors which are located at, or in the vicinity of, the CG. Our project addresses the need to keep the vicinity of the CG free from IMU equipment, and to avoid the excessive weight of gyroscopes. Thus, we have developed an IMU system that uses only accelerometers, none of which are at the CG.

The theory of accelerometer-only IMU systems is based on the relation

$$\boldsymbol{a} = n \cdot A_{cm} + n \cdot \dot{\omega} \times R + n \cdot \omega \times \omega \times R \qquad (1)$$

where $\boldsymbol{a}$ is the accelerometer response; A_{cm} is the acceleration of the CG; $\boldsymbol{R}$ is the accelerometer location relative to the CG; $\boldsymbol{n}$ is its sensing direction; ω is the angular velocity vector of the body; and $\dot{\omega}$ is the angular acceleration vector.

All the vectors are in the rotating frame of the body. For conventional IMUs, three gyroscopes are used to give the three components of ω directly. Then three accelerometers, with mutually perpendicular sensing directions, give the information needed to find A_{cm}, since the angular acceleration and centripetal acceleration terms in the equation for $\boldsymbol{a}$ (the second and third terms) can be estimated from the gyroscopic data and subtracted.

The rest of the navigation problem, as discussed by Regan and Anandakrishnan,[1] is to integrate the angular rates over time and find the true orientation of the body in space at each instant. The body-frame acceleration can then be transformed to the inertial-frame acceleration, which is then itself integrated to give the true velocity and location of the body.

It is possible to determine the complete motion of a body from acceleration measurements only. Using nine or more accelerometers in different locations with different sensing directions, A_{cm}, ω, and $\dot{\omega}$ can be determined simultaneously. Various methods have been proposed.[2] The number of accelerometers is reduced to six if ω is found by integrating $\dot{\omega}$. This procedure can be numerically unstable.[2]

Our design, based on the paper by Chen, Lee and De Bra,[3] chooses a special set of locations and orientations for six accelerometers, for which $\dot{\omega}$ is obtained independently of the current value of ω, avoiding numerical instability. In this design, the six accelerometers are placed at the centers of the six faces of a cube, with the center of the cube at the CG (**Fig. 1**). The sensing axis of each accelerometer is along one of the diagonals of the cube face on which it lies, with opposing sensors using diagonals that are crossed. (The diagonals will form a regular tetrahedron.)

We have found that a much more general geometry is possible, with most of the advantages of the one in Reference 3. We found that the cube can be replaced by an arbitrary parallelopiped. That means

that the six sensor locations can be any six points that form a figure—a general octahedron—with a center of symmetry. The center of symmetry does not have to be the CG. The six sensors would be placed at the six vertices of the octahedron. The sensing directions are parallel to the diagonals of the parallelogram faces on which the sensors lie. Diametrically opposed sensors choose alternate diagonals of their respective parallel faces.

The only simplicity of the cubical layout of Reference 3 that is not preserved is the ease of solving the six equations for the components of $\dot{\omega}$ and the components of A_{cm}. With the more general arrangement a non-trivial system of six linear equations in six unknowns must be solved at each time. Since the matrix does not vary, most of the work can be done in advance.

The system of linear equations to be solved is the following:

$$[S \;\; T] \begin{bmatrix} \dot{\omega} \\ A_{cm} \end{bmatrix} = \left[\boldsymbol{a}_i - n_i \cdot \omega \times \omega \times R_i \right], \qquad (2)$$

where the right-hand side is a column vector formed by letting the index i run from 1 to 6, that is, over the six sensors, and S and T are 6x3 matrices defined by

$$S = \left[R_i \times n_i \right],$$
$$T = \left[n_i \right] \qquad . \qquad (3)$$

The solution may be written

$$\dot{\omega} = M\left[\boldsymbol{a}_i\right],$$
$$A_{cm} = N\left[\boldsymbol{a}_i - n_i \cdot \omega \times \omega \times R_i\right] \qquad (4)$$

in terms of matrices M and N obtained by inverting $[S \;\; T]$. The special geometry is responsible for the centripetal acceleration term not entering the result for $\dot{\omega}$ After $\dot{\omega}$ is obtained from the first equation, it is integrated forward in time to give the current ω, which is used in the second equation to find the acceleration of the CG. The other aspects of the navigation problem are carried out exactly as described above for the case of gyroscopes.

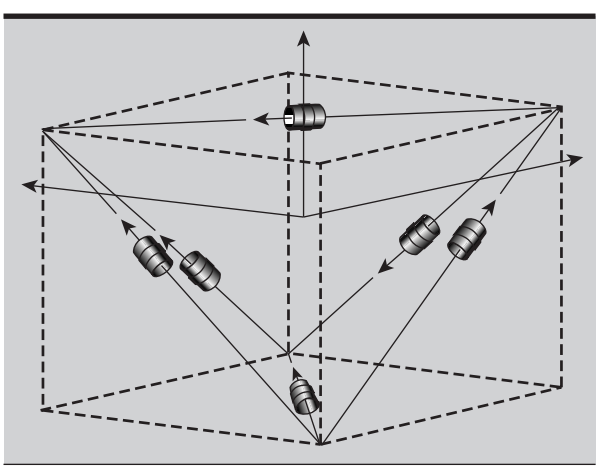

Figure 1. Six-accelerometer IMU configuration.

Progress

To evaluate the performance of the six-accelerometer design, we initially developed a computer model of the system. In the model, the test object is defined in terms of its mass and inertia. Input linear and angular forces on the test object can be defined at multiple locations, and these forces can be time varying. To evaluate the performance of the system, the model takes into account sensor locations and orientations, sensitivity, accuracy, integration times, and sampling periods. The model predicts velocities and acceleration time histories relative to inertial space, at any number of body-fixed points, in any body-fixed direction.

Currently, we are completing hardware development and fabrication for a test flight. Our system is based on Allied Signal QA-3100 inertial-grade accelerometers. These ultra-sensitive sensors are capable of resolution down to <1 x 10^{-7} g, with frequency response DC < f < 1 kHz.

Special signal conditioning was developed for our application. The accelerometer and signal conditioning hardware are shown in **Figs. 2** and **3**, in a photo, and a block diagram, respectively. One application required dynamic scale ranging to prevent high-frequency vibration and shock signals due to launch and flight vibration from saturating

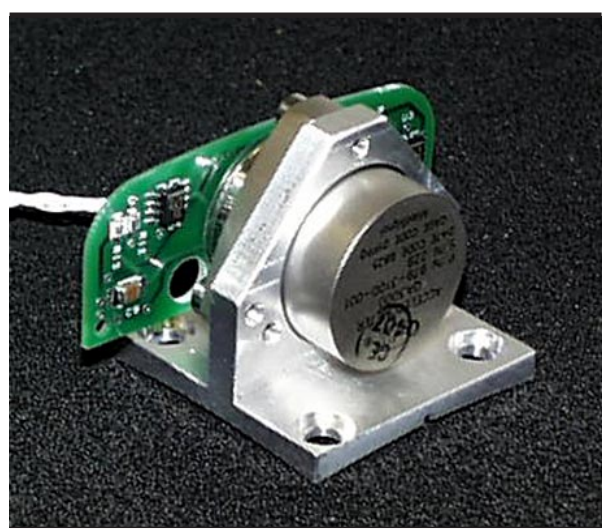

Figure 2. Photo of the accelerometer and signal conditioning hardware.

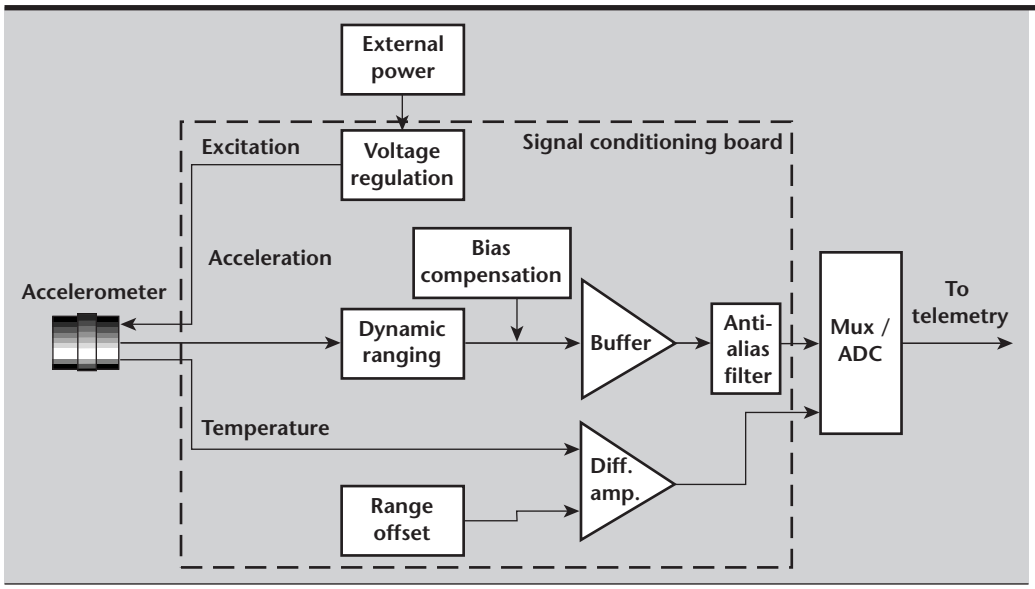

Figure 3. Block diagram of the accelerometer and signal conditioning electronics.

the sensor's output. These shock levels were unknown, thus requiring laboratory and field experiments to characterize and verify the response of sensors in these environments.

Initial attempts were made to isolate the sensors mechanically. However, ultimately that approach was supplanted by the electronic technique. These are true DC servo accelerometers, and as such, they exhibit a small output bias that is nulled prior to buffering and low-pass filtering. The accelerometers are also equipped with internal temperature sensors. Acceleration and temperature signals are digitized simultaneously, and a fourth-order temperature model is applied off-board for correction.

As presently configured for our flight test, the unit is set for a full scale range of ±0.5 g. A standard 12-bit A/D converter provides a resolution of <±0.000250 g, which translates to differential velocities on the order of 0.1 in./s and angular rates down to 0.25°/s for a duration on the order of 1 s.

In our flight test, acceleration and temperature data will be telemetered to ground stations and signals processed off-board. Control or closed-loop navigation applications could be realizable by on-board signal processing, the algorithms based on equations presented earlier.

Future Work

In the period of one year we have completed the development and are currently building the hardware for flight tests. The system has been optimized to work in a zero-g environment, which would be difficult to test in the laboratory. We are taking advantage of an opportunity to test the unit in an upcoming flight test and are presently completing integration of the system into the flight vehicle. Results of the test will not be known for several months, at which time a determination will be made regarding further development.

References

1. Regan, F. J., and S. M. Anandakrishnan (1993), *Dynamics of Atmospheric Re-Entry*, AIAA, Washington, D.C., Ch. 14.

2. Padgaonkar, A. J., K. W. Krieger, and A. I. King (1975), "Measurement of Angular Acceleration of a Rigid Body Using Linear Accelerometers," *ASME Journal of Applied Mechanics*, **42**, pp. 552-556.

3. Chen, J.-H., S.-C. Lee, and D. B. De Bra (1994), "Gyroscope Free Strapdown Inertial Measurement Unit by Six Linear Accelerometers," *Journal of Guidance and Control*, **17**, pp. 286-290.

Fiber-Based Phase-Shifting Diffraction Interferometer for Measurement and Calibration of the Lick Adaptive Optics System

Eugene W. Campbell
Advanced Microtechnology Program
Laser Programs

Jong R. An
Laser Engineering Division
Electronics Engineering

An all-fiber based phase-shifting diffraction interferometer (PSDI) has been developed and integrated into the Lick Observatory adaptive optics system. Preliminary testing shows that the interferometer has a single measurement accuracy of 18 nm RMS, and can achieve better than 6 nm RMS with nine averages. The PSDI now needs to be incorporated into the control loop for the deformable mirror. The system then can be tested during an actual run on the Shane telescope. There are a few engineering difficulties to be overcome, but their solutions are straight forward.

Introduction

This project was initiated to integrate a PSDI into the adaptive optics (AO) system developed by Lawrence Livermore National Laboratory (LLNL) for use on the Shane telescope at Lick Observatory. Adding an interferometer to the AO system is useful for calibrating the control sensors, measuring the aberrations of the entire AO optical train, and measuring the influence functions of the individual actuators on the deformable mirror. A PSDI is particularly well suited for this application. A PSDI operates by using diffraction from a point-like aperture to generate a highly spherical wave that is compared interferometrically to an aberrated spherical wavefront.[1]

Since the Lick AO system can be considered a black box that relays an aberrated point imaged to a corrected, diffraction-limited point image, the reference wave output by the PSDI can be fed without modification into the AO system. Likewise, the corrected output of the AO system can be fed without modification into the input of the PSDI. Thus, the only aberrations measured by the PSDI will be those of the AO system. This provides an extremely accurate measurement of the optical properties of the AO system.

Usually, the input to the AO system is the image created by the 3-m Shane telescope.[2] Because of atmospheric turbulence, this image is distorted and blurred. The AO system uses a fast moving tip-tilt mirror, which corrects for the blurring due to image movement, and a deformable mirror, which corrects for the image distortion.

The tip-tilt mirror is placed in the expanding beam, and the deformable mirror is placed in collimated light between two parabolic mirrors. The first parabola collimates the input point image, and the second parabola focuses the corrected planar wavefront to create a corrected point image. This image is then re-imaged by a scientific camera operating in the infrared.

There are also six auxiliary optics in the system: two are dichroic mirrors, used for splitting off light for the sensors that control the tip-tilt and deformable mirrors, and four are beam-steering mirrors (**Fig. 1**).

All totalled, the image created by the AO system passes through or reflects off of 11 optical elements. For this reason, it is not sufficient to simply replace the deformable mirror with a flat mirror and measure the aberrations right after the flat, as is currently done. This procedure accounts for all the aberrations up to the flat, but leaves out the aberrations introduced beyond it. Using the PSDI to measure the

system aberrations allows the wavefront sensor to be calibrated so that it corrects the image in a way that accounts for the aberrations of the entire optical train.

Progress

Design of the PSDI System

A difficulty in integrating a PSDI into the Lick AO system is that limited space is available for adding hardware. The PSDI systems developed at LLNL have a footprint of approximately 3 ft × 3 ft. To make a system with a much smaller footprint, an entirely fiber optic system was developed. This system occupies a footprint of 9 in. × 12 in., approximately 1/12 the size of the discrete systems. The vertical dimension also has been reduced, from 12 in. to 8 in. A CAD drawing of the system is shown in **Fig. 2**.

The all-fiber PSDI uses a 690-nm laser diode to provide 10 mW of optical power with a coherence length of approximately 3 m. This light is separated into two fibers by a variable beam-splitter that is set so that the beam intensities of each arm of the interferometer are equal. One fiber goes to the phase-shifter in the reference wave arm of the interferometer, and the other fiber goes to a fiber spool that is used to equalize the optical path lengths between the reference and test arms.

From there, the fibers go to polarization controllers (PLC) that are set so that the polarizations of the test and reference waves are identical at the camera. Upon leaving the PLCs, the fibers run to opposite ends of the AO system. The test fiber runs to the input point of the AO system, and the reference fiber runs to the output point of the AO system.

The phase-shifter is a commercially available device that consists of 25 windings of fiber around an oval spool. The spool has piezoelectric (PZT) plates along the two long sides. The fiber is epoxied to the PZT plates so that when a voltage is applied to the plates, the fiber is stretched as the plates grow in length. The fiber-based variable beam-splitter is also a commercial device, and is used to balance the beam powers at the CCD camera to achieve maximum fringe contrast.

Once the test wave passes through the AO system, it converges onto the end of the reference fiber. It then reflects off the reference fiber to combine with the diverging reference wavefront diffracting out of the end of the fiber. The end face of the reference optical fiber is super-polished (RMS roughness < 1 Å) to ensure that the reflected light is not distorted by the shape of the fiber end face.

These two beams are then steered by a knife-edge mirror through an imaging lens and onto a CCD camera. The knife-edge mirror passes half of the cone

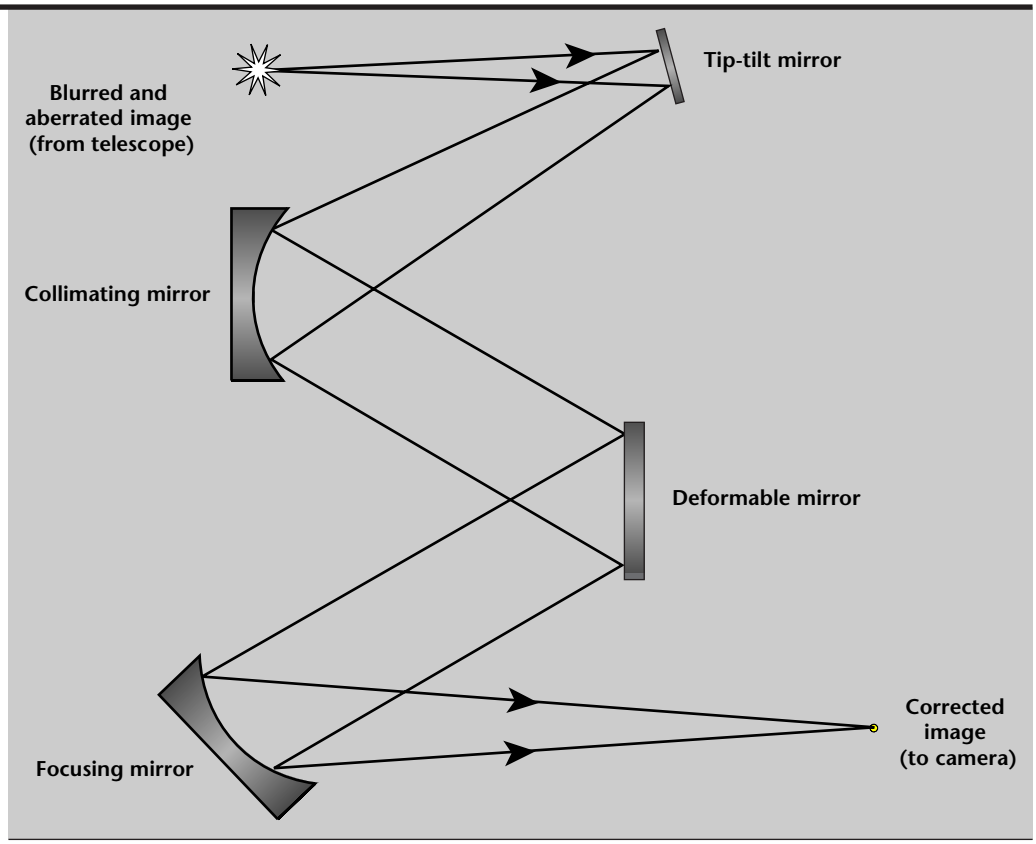

Figure 1. Simplified representation of the Lick Observatory AO system.

of light diffracting from the reference fiber, and reflects half towards the camera. Since the numerical aperture of the beam exiting the AO system is very small ($f^{\#} \approx 27$), it is not clipped by the knife-edge as it focuses onto the reference fiber. This optical system that allows for the interference of the beams' test and reference waves is shown in **Fig. 3**.

Accuracy of the Initial System Test

The PSDI was mounted on the AO system breadboard and initial repeatability tests were performed. It was expected that air currents in the 5.8-m optical path and vibrations of the eight reflective optics would lead to noise in the measurement. However, since

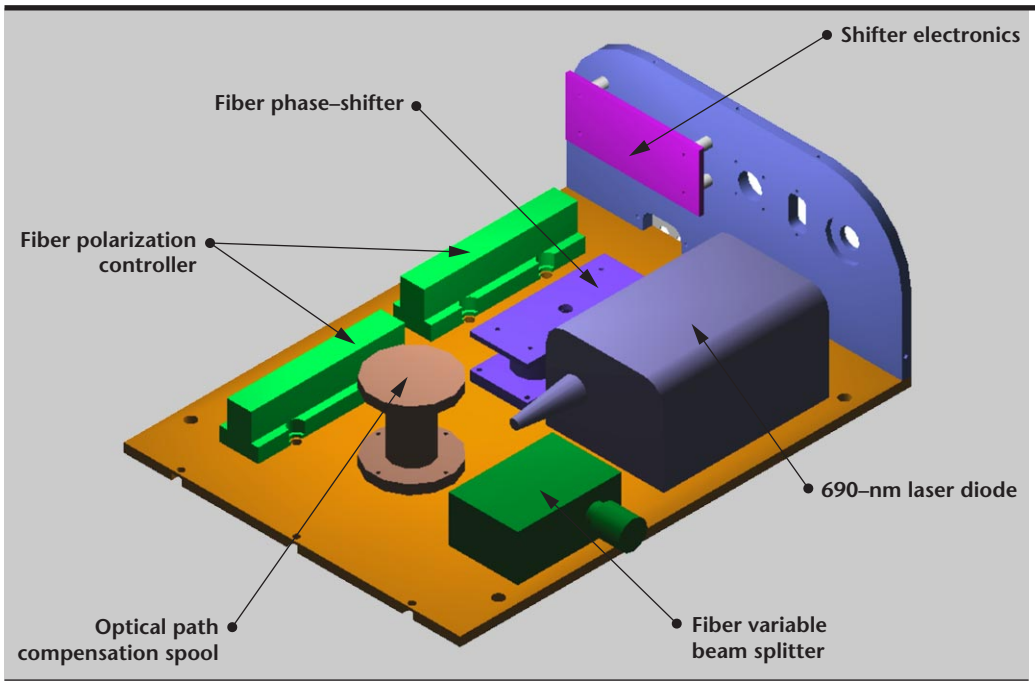

Figure 2. Front-end design of the PSDI system.

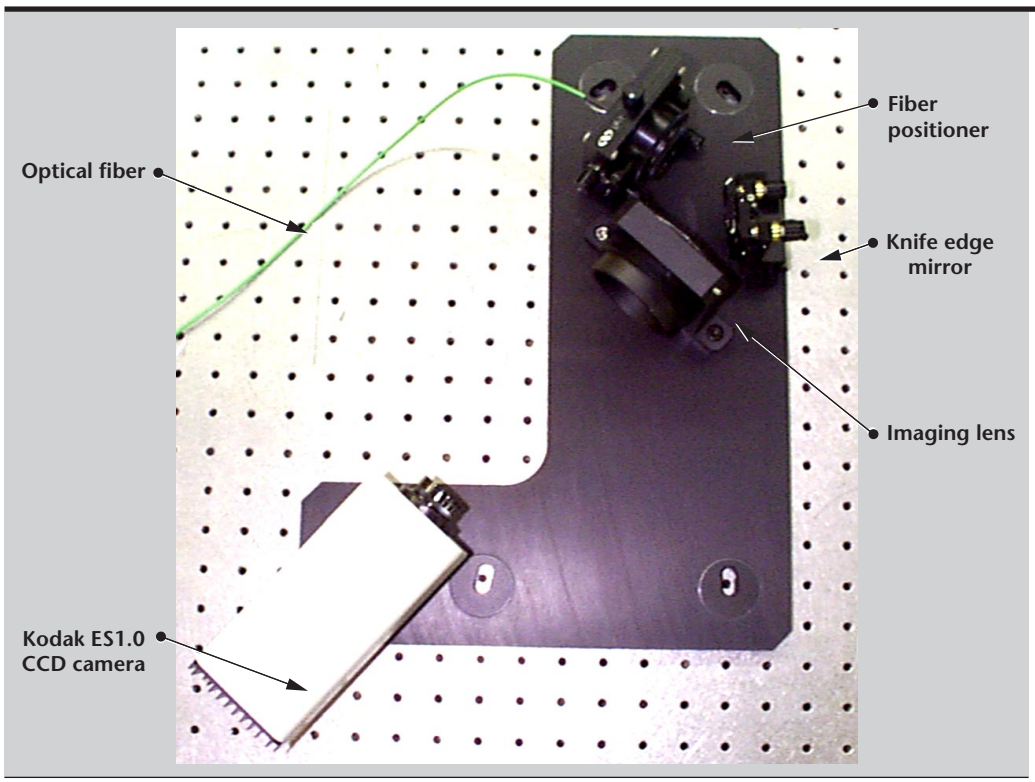

Figure 3. Optical system. The reference wavefront diffracting from optical fiber combines with test wavefront from the AO system and interferes at the camera.

Table 1. Data from repeatability tests.

Number of averages	Average RMS error (nm)	Standard deviation
1	18.6	9.08
4	9.66	3.91
9	5.23	—
16	3.58	—

such noise is typically random, it is possible to make multiple measurements and average them to reduce the noise. Unfortunately, feedback into the laser caused instabilities in the source coherence, and it was necessary to take measurements one at a time. Each measurement was analyzed on the spot, and approximately one quarter of the measurements were rejected due to laser instability. A total of 25 measurements were kept. In the future, a Faraday-type optical isolator will be used to prevent laser feedback.

The complete set of 25 measurements was averaged together to form a baseline measurement. Then each measurement was individually compared to the baseline. The typical difference between a single measurement and the baseline was 18.6 nm RMS, with a standard deviation of 9.1 nm RMS. Averaging groups of four measurements, and comparing them to the baseline yielded an error of 9.7 nm RMS, with a standard deviation of 3.9 nm RMS.

As expected for N measurements of a system with random noise, the RMS error dropped as $1/\sqrt{N}$. As groups of nine and 16 were compared to the total set, the noise dropped more quickly. This is because these groupings no longer appear like independent measurements when compared to a baseline formed with only 25 measurements. The various groupings are given in **Table 1**.

A histogram for the single measurement results is shown in **Fig. 4**, where each bin is 5 nm wide. The minimum difference was 7.8 nm RMS, and the maximum was 48 nm RMS. As can be seen, it is reasonable to treat the noise as random, and nine or more averages should yield a measurement with an RMS error of less than 10 nm. To achieve an accuracy of better than 1/100 of a wave in the visible region, approximately 16 averages would be required. At a processing time of 8 s/average, it will take approximately 2 min to make a measurement accurate to better than 1/100 of a wave.

Wavefront Measurement at the Deformable Mirror

In all the measurements, the imaging lens was focused on the deformable mirror, which forms the pupil of the AO system. Therefore, the optimal deformations of the mirror needed to improve the wavefront can be calculated if the influence functions of the individual actuators are known.

A measurement of the wavefront at the deformable mirror is shown in **Fig. 5**. The peak-to-valley deviation of this wavefront is 1.65 µm, and the RMS deviation is 133 nm. This wavefront is flat to within 1/6 of the 632.8 nm measurement wavelength, which corresponds to a Strehl ratio of 0.36. The accuracy of this measurement is approximately 4 nm RMS. When the

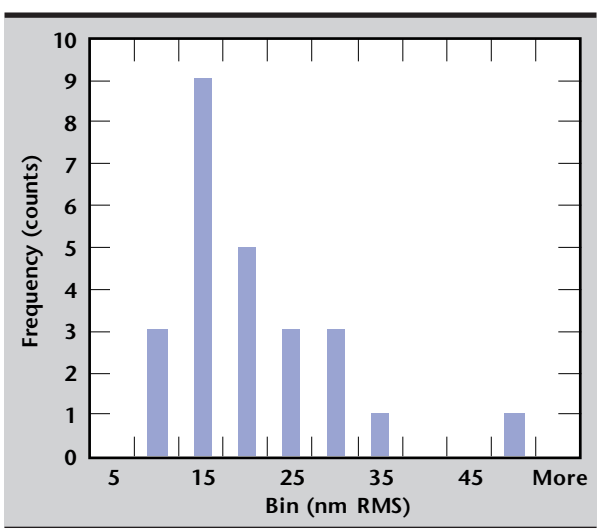

Figure 4. Histogram of the single measurement errors.

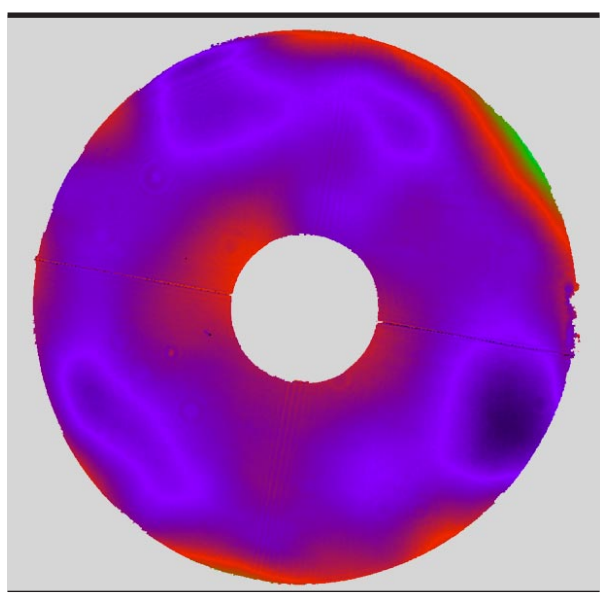

Figure 5. Wavefront of the AO system imaged at the deformable mirror.

wavefront has been freshly flattened using the phase diversity method, Strehl ratios of 0.45 have been obtained. Interactive manipulations of the actuators have yielded Strehl ratios as high as 0.6.

It is expected that the PSDI can be used to flatten the wavefront to obtain Strehl ratios better than 0.8. It should be noted that improving the Strehl ratio from 0.36 to 0.8 at 0.532 μm, only improves the Strehl ratio at 2.2 μm from 0.92 to 0.98. The real advantage in using the PSDI to calibrate the system is that it takes much less time than the current method and is more reliable.

Influence Function of a Single Actuator

A measurement can also be made when a single actuator is either pushed or pulled. The baseline measurement can then be subtracted from this measurement, and the difference yields the influence function for the particular actuator. **Figure 6** shows two measurements of the influence function of mirror actuator #14 as it is pushed and pulled. As can be seen in both measurements, the influence function of the actuator is roughly Gaussian in nature. However, there is a slight hexagonal shape to the deflection because of the hexagonal layout of the actuators. Lineouts through the centers of the deflections better display the magnitude of the wavefront change and are also shown in **Fig. 6**.

Note that this is not equal to the actual mirror deformation. The wavefront deformation is doubled relative to the mirror deformation because of the reflection, and there is also an obliquity factor due to the light not being normally incident. The "pull" data is for a D/A voltage of –4.569 V on the actuator, and the "push" data is for D/A voltage of 4.781 V. An image of the fringes in the pushing and pulling modes is shown in **Fig. 7**. Note that ~30 to 60 tilt fringes have been introduced to overcome problem of multiple pass noise.

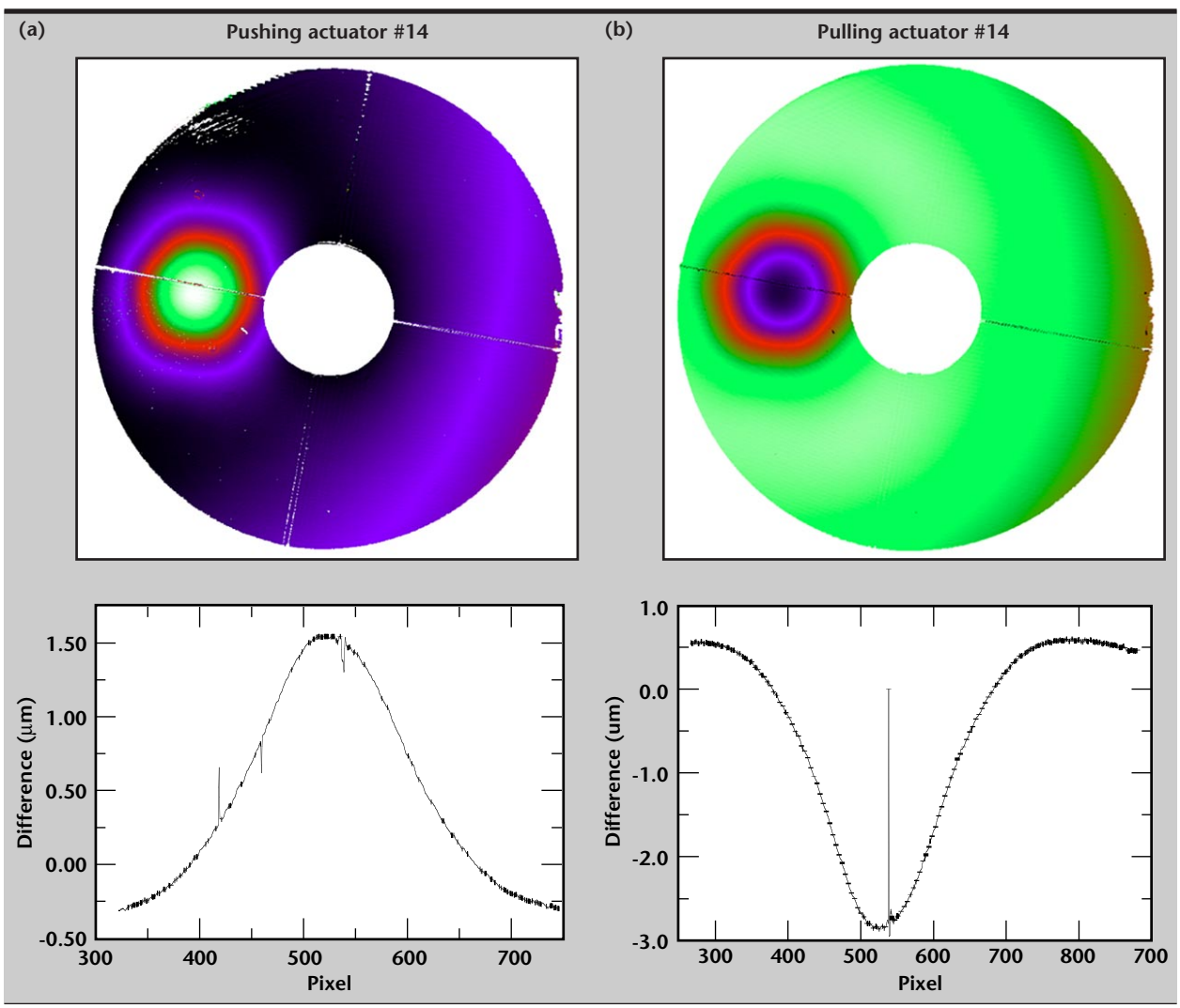

Figure 6. Measurements of influence function of mirror actuator as it is a) pushed and b) pulled.

Actuators at the center of the field and at the edge were also moved to verify the actuator location map. The images in **Fig. 8** show the wavefront difference from the baseline as actuators #02 and #31 were pulled.

During the first year of this experiment, we accomplished the following: 1) developed an all-fiber PSDI system of extremely small size; 2) qualified a fiber-optic phase-shifter to better than 1 nm accuracy; 3) wrote software to control the PSDI and acquire data from a PC running Windows NT; 4) integrated the PSDI system onto the AO bench in a way that least disturbed the existing layout; and 5) used the PSDI system to make preliminary measurements of the AO system.

Future Work

Development of the PSDI system brought to light several problems that remain to be solved:

1. Laser source instability is limiting the accuracy of the PSDI system.
2. Light from the reference fiber is passing through the system, reflecting off the end of the input fiber, passing back through the system, and creating spurious noise fringes.
3. Both dichroics in the AO system must be removed to use the PSDI because the dichroics do not pass sufficient energy at the PSDI laser source wavelength.

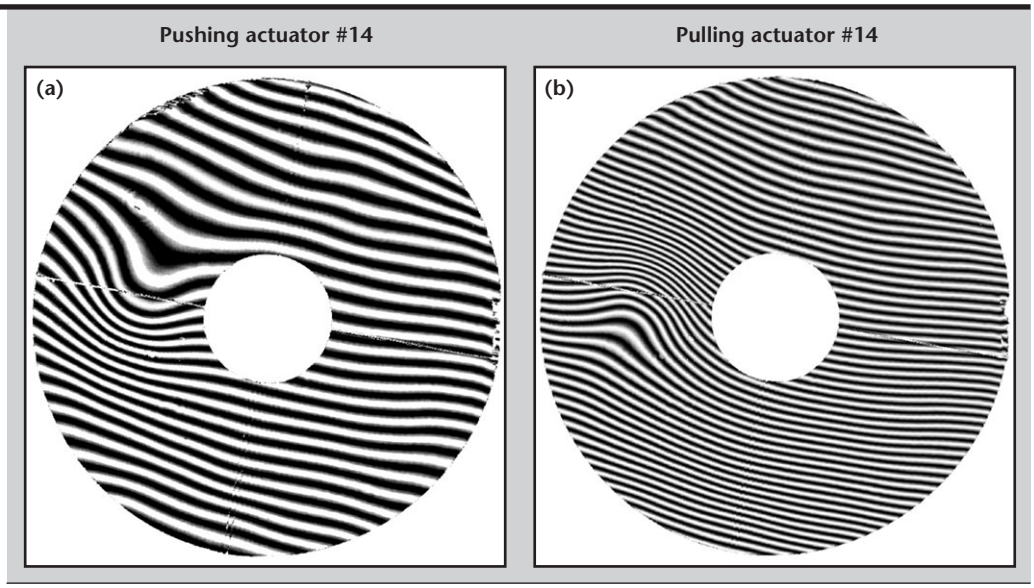

Figure 7. Image of fringes in the a) pushing and b) pulling modes.

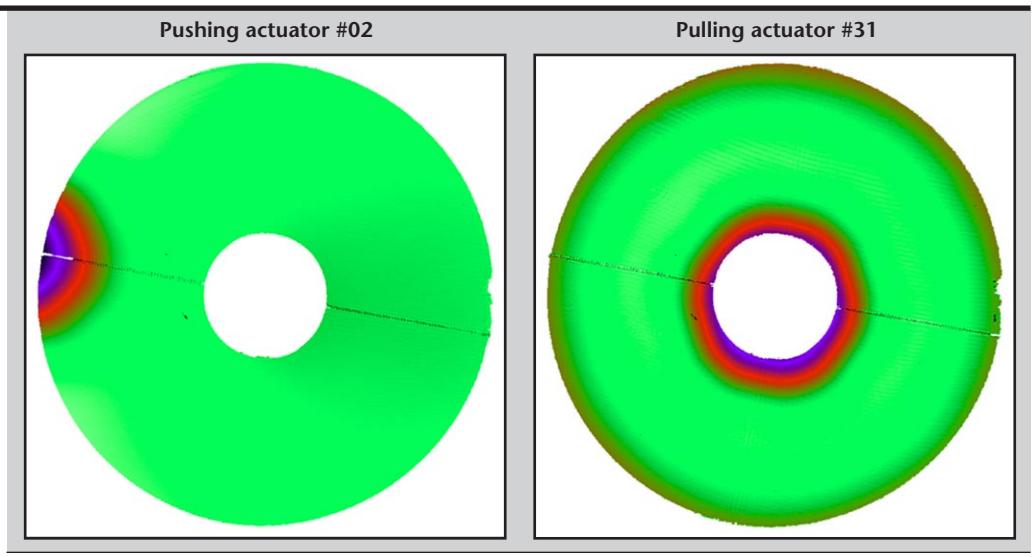

Figure 8. Images showing wavefront difference from baseline as actuators were pulled.

4. The PSDI system has yet to be used while the AO system is mounted on the Shane telescope.
5. Some of the more expensive equipment is on loan from the EUVL program and needs to be replaced.
6. If the system is to become a permanent feature at Lick Observatory, it will have to be converted to use a Sun workstation.

References

1. Sommargren, G. E. (1996), "Diffraction methods raise interferometer accuracy," *Laser Focus World*, pp. 61–71, August.

2. Olivier, S. S., and C. E. Max (1997), "First significant image improvement from a sodium-layer laser guide star adaptive optics system at Lick Observatory," Lawrence Livermore National Laboratory, Livermore, California (UCRL-JC-128088).

Selected Engineering Publications

Selected Engineering Publications

Aceves, S. M., and G. D. Berry (1998), "Onboard Storage Alternatives for Hydrogen Vehicles," *Energy and Fuels*, Vol. **12**, No. 1, pp. 49–55.

Aceves, S. M., and G. D. Berry (1998), "Thermodynamics of Insulated Pressure Vessels for Vehicular Hydrogen Storage," *American Society of Mechanical Engineers Journal of Energy Resources Technology*, Vol. **120**, No. 2.

Aceves, S. M., and J. Martinez (1997), "Effects of Evaporator Frosting on the Performance of Air-to-Air Heat Pump," *Proceedings of the American Society of Mechanical Engineers Advanced Energy Systems Division*, M. L. Ramalingam, J. L. Lage, V. C. Mei, and J. N. Chapman, eds., November, AES-Vol. **37**, pp. 357–363.

Aceves, S. M., and J. R. Smith (1997), "Hybrid and Conventional Hydrogen Engines that Meet EZEV Emissions," Paper 970290, *Society of Automotive Engineers Transactions*.

Aceves, S. M., C. Westbrook, W. Pitz, and J. R. Smith (1997), "Modeling of Homogeneous Charge Compression Ignition (HCCI) of Methane," Paper No. 97-ICE-68, *Proceedings of the 1997 American Society of Mechanical Engineers Internal Combustion Engine Fall Technical Conference*, ICE-Vol. **29-3**, pp. 85–90.

Aceves, S. M., and J. R. Smith (1998), "A Desiccant Dehumidifier for Electric Vehicle Heating," *American Society of Mechanical Engineers Journal of Energy Resources Technology*, Vol. **120**, No. 2.

Aceves, S. M., G. D. Berry, and G. D. Rambach (1998), "Insulated Pressure Vessels for Hydrogen Storage on Vehicles," *International Journal of Hydrogen Energy*, Vol. **23**, No. 7, pp. 583–591.

Aceves, S. M., H. Nakamura, G. M. Reistad, and J. Martinez-Frias (1998), "Optimization of a Class of Latent Thermal Energy Storage Systems With Multiple Phase Change Materials," *American Society of Mechanical Engineers Journal of Solar Energy Engineering*, Vol. **120**, No. 1, pp. 14–19.

Aceves, S. M., and B. T. Kornblum (1997), "Thermal Analysis of Simulated Pantex Pit Storage," *American Society of Mechanical Engineers Proceedings of the Thirty-Second National Heat Transfer Conference*, August, Vol. **10**, pp. 25–30.

Ackler, H. D., and Y.-M. Chiang (1997), "Model Experiment on Thermodynamic Stability of Retained Intergranular Amorphous Films," *Journal of the American Ceramic Society*, July, Vol. **80**, No. 7, pp. 1893–1896.

Alesso, H. P., C. E. Annese, and S. Murty (1997), "On Establishing Benchmark Standards for Parallel Processing Monte Carlo Codes," *American Nuclear Society, Nuclear Criticality Safety Division*, September.

Altenbach, T., and S. Brereton (1997), "Risk Ranking Methodology for Radiological Events," *EFCOG Seventh Annual Safety Analysis Working Group*, Oakland, California, June.

Avicola, K., J. A. Watson, B. V. Beeman, T. C. Kuklo, and J. R. Taylor (1998), "Design and Performance of the Tip-Tilt Subsystem for the Keck II Telescope and Adaptive Optics System," *SPIE International Symposium on Astronomical Telescopes and Instrumentation*, Kona, Hawaii, March, Vol. **3353**.

Blaedel, K. (1998), "Ductile-Regime Grinding of Brittle Materials," *Machining of Ceramics and Composites*, Chapter 6, Marcel Dekker, New York, New York.

Brase, J. M., J. R. An, K. Avicola, B. V. Beeman, G. L. Berry, B. Johnston, C. E. Max, J. A. Watson, and K. E. Waltjen (1998), "Keck Wavefront Control System: Architecture and Initial Laboratory Test Results," *SPIE International Symposium on Astronomical Telescopes and Instrumentation*, Kona, Hawaii, March, Vol. **3353**.

Brereton, S. J., G. Brumburgh, D. Becker, J. Pryatel, R. Wolfe, and J. Yatabe (1998), "Assuring Safety in the National Ignition Facility," *EFCOG Eighth Annual Safety Analysis Working Group Workshop*, April.

Brown, N. W., J. Hassberger, E. Greenspan, and E. Elias (1997), "Proliferation Resistant Fission Energy Systems," *Global '97*, October 5–10.

Brown, S. B., and F. P. Milanovich (1997), Patent Disclosure and Record of Invention: Number IL-10158, "Simple, Inexpensive, Efficient Coupling of Light Emitting Diode (LED) Radiation into an Optical Fiber," May 29.

Brummond, W., and G. Armantrout (1998), "Plutonium Immobilization Project," *American Institute of Chemical Engineers Spring National Meeting*, New Orleans, Louisiana, March.

Bulmer, R. H., and G. H. Neilson (1997), "Alternative Poloidal Field Configurations for ITER," *Proceedings of the Seventeenth IEEE/NPSS Symposium on Fusion Engineering*, San Diego, California, October 6–10.

Burnett, G. C., T. J. Gable, J. F. Holzrichter, and L. C. Ng (1997), "Voiced Excitation Functions Calculated from Micropower Impulse Radar Information," Paper 4aSP4, *One Hundred Thirty-Fourth Meeting of the Acoustic Society of America*, San Diego, California, December 1–5.

Campbell, G. H., S. M. Foiles, H. Huang, D. A. Hughes, W. E. King, D. H. Lassila, D. J. Nikkel, T. D. de la Rubia, J. Y. Shu, and V. P. Smyshlyaev (1998), "Multi-Scale Modeling of Polycrystal Plasticity: A Workshop Report," *Materials Science and Engineering A*, in press.

Canaan, R. E., J. E. Dec, R. M. Green, and D. T. Daly (1998), "The Influence of Fuel Volatility on the Liquid-Phase Fuel Penetration in a Heavy-Duty D. I. Diesel Engine," Paper No. 980510, *Society of Automotive Engineers International Conference and Exposition*, Detroit, Michigan, February.

Carrano, C. J., S. S. Olivier, J. M. Brase, B. A. Macintosh, and J. R. An (1998), "Phase Retrieval Methods for Adaptive Optics," *SPIE International Symposium on Astronomical Telescopes and Instrumentation*, Kona, Hawaii, March 20–28, Vol. **353-111**.

Carter, P. H. (1997), "HyperSoar: A Concept for Global Reach and Space Access," *Strategic Avionics Technology Working Group NASA/Industry National Meeting*, Seattle, Washington, October 21–23.

Carter, P. H., D. J. Pines, and L. vE Rudd (1998), "Approximate Performance of Periodic Hypersonic Cruise Trajectories for Global Reach," accepted by *AIAA Journal of Aircraft*.

Carter, P. H., D. J. Pines, and L. vE Rudd (1998), "Approximate Performance of Periodic Hypersonic Cruise Trajectories for Global Reach," AIAA 98-1644, *Eighth AIAA International Spaceplanes and Hypersonics Systems and Technologies Conference*, Norfolk, Virginia, April 27–30.

Carter, P. H., F. Mitlitsky, A. H. Weisberg, J. C. Whitehead, and R. W. Humble (1998), "Design Trade Space for a Mars Ascent Vehicle for a Mars Sample Return Mission, IAA98-066," *Third IAA International Conference on Low-Cost Planetary Missions*, Pasadena, California, April 27–May 1.

Cartland, H. E., and J. W. Hunter (1997), "The SHARP Light Gas Gun," *Proceedings of the Forty-Third International Instrumentation Symposium*, Orlando, Florida, May 4–8, pp. 501–507.

Chang, J. J., E. P. Dragon, and I. L. Bass (1998), "315 W Pulsed-Green Generation With a Diode-Pumped Nd:YAG Laser," Paper CPD2, *Supplement to Technical Digest, Conference on Lasers and Electro-Optics*, San Francisco, California, May 3–8.

Chang, J. J., E. P. Dragon, C. A. Ebbers, and I. L. Bass (1998), "An Efficient Diode-Pumped Nd:YAG Laser With 451 W of CW IR and 182 W of Pulsed Green Output," Paper PDP-15, *Supplement to Technical Digest, Advanced Solid-State Lasers Conference*, Coeur d'Alene, Idaho, February 2–4.

Chen, Y. J., and G. Caporaso (1997), "Designs for a High Power Superconducting Delay Line," *1997 Pulsed Power Conference*, Baltimore, Maryland, June 29–July 2.

Chen, Y. J., and G. J. Caporaso (1997), "A Novel Design for a High Power Superconducting Delay Line," *1997 Particle Accelerator Conference*, Vancouver, BC, Canada, May 12–16.

Chow, R., J. R. Taylor, Z. L. Wu, Y. Han, and T. Yang (1998), Absorptance Measurements of Transmissive Optical Components by the Surface Thermal Lensing Technique," *Laser-Induced Damage in Optical Materials: 1997*, G. J. Exarhos, A. H. Guenther, M. R. Kozlowski, and M. J. Soileau, eds., *SPIE Proceedings*, Vol. **3244**, pp. 376–385.

Chow, T. S., P. J. Harwood, and S. J. DeTeresa (1997), "Characterization of Cellular Silicone for Weapon System Applications," *Twenty-First Compatibility, Aging, and Stockpile Stewardship Conference*, Kansas City, Kansas, September.

De Groot, A. J., and D. Harris (1998), "Computationally Efficient, Robust Algorithm for Matched Field Processing," *Circuits, Systems, and Signal Processing*, April, Vol. **17**, No. 2, pp. 165–193.

De Groot, A. J., R. J. Sherwood, D. C. Badders, and C. G. Hoover (1997), "Parallel Contact Algorithms for Explicit Finite Element Analysis (DYNA3D)," *Proceedings of the Fourth U. S. National Congress on Computational Mechanics*, San Francisco, California, August 6–8.

De Groot, W. A., L. A. Arrington, J. F. McElroy, F. Mitlitsky, A. H. Weisberg, P. H. Carter II, B. Myers, and B. D. Reed (1997), "Electrolysis Propulsion for Spacecraft," *AIAA Joint Propulsion Conference*, Seattle, Washington.

Dec, J. E., and R. E. Canaan (1998), "PLIF Imaging of NO Formation in a D. I. Diesel Engine," Paper No. 980147, *Society of Automotive Engineers International Conference and Exposition*, Detroit, Michigan, February.

Decker, J. Y., A. Fernandez, and D. W. Sweeney (1997), "Generation of Subquarter-Micron Resist Structures Using Optical Interference Lithography and Image Reversal," *Journal of Vacuum Science Technology*, November/December, B **15** No. 6.

Dehghani, M. (1997), "Numerical Simulation of Conventional Spin Forming," *Fourth U.S. National Congress on Computational Mechanics*, San Francisco, California, August 6–8, p. 250.

DelGrande, N. (1997), "Heat Capacity Mapping for Quality Evaluation of Weapons Materials and Structures," *Twenty-First Compatibility, Aging, and Stockpile Stewardship Conference*, Kansas City, Kansas, August.

Demos, S., M. Yan, B. Woods, M. Staggs, Z. L. Wu, H. B. Radouski, and J. De Yoreo (1998), "Temperature and Spectral Investigation of Bulk KDP Below Damage Using 355 nm Laser Irridiation," *Laser-Induced Damage in Optical Materials: 1997*, G. J. Exarhos, A. H. Guenther, M. R. Kozlowski, and M. J. Soileau, eds., *SPIE Proceedings*, Vol. **3244**, pp. 223–227.

Domansky, K., D. L. Baldwin, J. W. Grate, T. B. Hall, J. Li, M. Josowicz, and J. Janata (1998), "Development and Calibration of Field-Effect Transistor-Based Sensor Array for Measurement of Hydrogen and Ammonia Gas Mixtures in Humid Air," *Analytical Chemistry*, February 1, Vol. **70**, No. 3, pp. 473–481.

Edmunds, T. (1997), *Nondifferentiable and Two-Level Mathematical Programming*, (by Kiyotaka Shimizu, Yo Ishizuka, and Jonathan F. Bard, Kluwer), Section 15.4, pp. 371–380.

Erbert, G., K. Kanz, and I. Bass (1997), "Lamp Pumped Nd:YAG Laser Oscillator With 170 W Green Output" Paper PD2.6, *IEEE Lasers and Electro-Optics Society Annual Conference*, San Francisco, California, November 10–13.

Fabbricator, P., S. Farinon, R. Musenich, C. Priano, T. G. O'Connor, R. A. Bell, W. Burgess, W. Craddock, R. Penco, and P. Valente (1997), "The Superconducting Solenoid for The BABAR Experiment at PEP-II in SLAC," *Fifteenth International Conference on Magnet Technology*, Beijing, China, October.

Feit, M. D., J. Campbell, F. Genin, A. Salleo, D. Faux, A. M. Rubenchik, R. Riddle, M. R. Kozlowski, and J. Yoshiyama (1997), "Analysis Of Laser-Induced Surface Cracks in Silica at 355 nm," *Twenty-Ninth Annual Symposium on Optical Materials for High Power Lasers*, Boulder, Colorado, October 6–8, (to appear in *SPIE*).

Ferguson, J. (1997), "Simultaneous Monitoring of pH, CO_2 and O_2, Using an Optical Imaging Fiber," *Analytica Chimica Acta*, Vol. **340**, pp. 123–131.

Fernandez A., J. Y. Decker, S. M. Herman, D. W. Phillion, and D. W. Sweeney (1997), "Methods for Fabricating Arrays of Holes Using Interference Lithography," *Journal of Vacuum Science Technology*, November/December, B **15** No. 6.

Folta, J. A., C. Yu, W. J. Benett, and D. Ciarlo (1997), "A Miniature DNA Based Analytical Instrument," *Journal of Analytical Chemistry*, May.

Fulkerson, E. S., D. C. Norman, and R. Booth (1997), "Driving Pockel Cells Using Avalanche Transister Pulsers," *Eleventh IEEE International Pulsed Power Conference*, June 29–July 3.

Gable, T. J., G. C. Burnett, J. F. Holzrichter, L. C. Ng, and W. A. Lea (1997), "Comparison of Conventional Acoustic and MIR Radar/Acoustic Processing of Speech Signals," *One Hundred Thirty-Fourth Meeting of the Acoustic Society of America*, December 1–5, San Diego, California, p. 139.

Garcia, M. (1997), "Designing Planar Magnetron Cathodes: Analysis and Experiment," IEEE Conference Record - Abstracts, *IEEE International Conference on Plasma Science*, May 19–22, San Diego, California.

Glosup, J., and M. Axelrod (1997), "Systematic Error Revisited," *Annual Meeting of the American Statistical Association, 1996 Proceedings for the Section on Physical and Engineering Sciences*, pp. 81–86.

Goosman, D., G. Avara, L. Steinmetz, C. Lai, and S. Perry (1997), "Manybeam Velocimeter for Fast Surfaces, *SPIE Proceedings of the Twenty-Second International Congress on High-Speed Photography and Photonics*, Vol. **2869**, pp. 1070–1079.

Groves, S. E., S. J. DeTeresa, and R. J. Sanchez (1998), "Accelerated Durability and Long-Term Testing of High-Temperature Polymer Composites," *ASTM Symposium on Time-Dependent and Nonlinear Effects in Polymers and Composites*, Atlanta, Georgia, May 4–5.

Hakins, J., and W. Jandeska (1998), "Power Flow and Die Filling Studies Using Computed Tomography," *Ninty-Eighth International Conference on Power Metallurgy and Particulate Materials*, Las Vegas, Nevada, May 5–June 4.

Han, Y., Q. Zhao, Z. L. Wu, and K. Mocur (1998), "Near-Field Detection of Laser-Induced Thermal Waves in Optical Materials," *Laser-Induced Damage in Optical Materials: 1997*, G. J. Exarhos, A. H. Guenther, M. R. Kozlowski, and M. J. Soileau, eds., *SPIE Proceedings*, Vol. **3244**, pp. 257–267.

Haney, S. W., L. D. Pearlstein, R. H. Bulmer, and J. P. Freidberg (1997), "Vertical Stability Analysis of Tokamaks Using a Variational Procedure," *Plasma Physics Reports*, September, Michael Ioffe Special Issue #9.

Hartemann, F. V., A. L. Troha, G. P. LeSage, C. V. Bennett, B. H. Kolner, and N. C. Luhmann, Jr. (1997), "Ultrahigh Intensity Compton Scattering Focussed X-Ray Source," *IEEE Conference Record - Abstracts. 1997 IEEE International Conference on Plasma Science*, San Diego, California, May 19–22, p. 271.

Hassberger, J. A., R. N. Schock, and T. H. Isaacs (1997), "Prospects of and Requirements for Nuclear Power as a Contributor Toward Managing Greenhouse Gases," *International Conference on Environment and Nuclear Energy*, October.

Havstad, M. A., and C. Dingus (1997), "Radiant Transmittance of Cerium Doped Quartz from 300 to 1270 K," *Proceedings of the Thirty-Second National Heat Transfer Conference*, Baltimore, Maryland, August 8–12, ASME HTD-Vol. **345**, pp. 73–80.

Holdener, F. R. (1997), "Beam Control and Diagnostic Functions in the NIF Transport Spatial Filter," *Solid-State Lasers for Applications to Inertial Confinement Fusion, Second Annual International Conference*, Paris, France.

Holzrichter, J. F., G. C. Burnett, L. C. Ng, and W. A. Lea (1998), "Speech Articulator Measurements Using Low Power EM-Wave Sensors," *Journal of the Acoustic Society of America*, January, Vol. **103** No. 1, pp. 622–625.

Holzrichter, J. F., W. A. Lea, L. C. Ng, and G. C. Burnett (1997), "New Sensors Offer Breakthroughs in Voice Interfacing," *AVIOS Conference*, San Francisco, California, July.

Honea, E. C., R. J. Beach, S. B. Sutton, J. A. Speth, S. C. Mitchell, J. A. Skidmore, M. A. Emanuel, and S. A. Payne (1997), "115-W Tm:YAG Diode-Pumped Solid-State Laser," *IEEE Journal of Quantum Electronics*, September, Vol. **33**, No. 9, pp. 1592–1600.

Hoover, C. G., A. J. De Groot, D. C. Badders, and R. J. Sherwood (1997), "Parallel Algorithms for Explicit Finite Element Analysis (DYNA3D)," *Proceedings of the Fourth U. S. National Congress on Computational Mechanics*, San Francisco, California, August 6–8.

Hossain, Q. A. (1997), "Why a Performance Goal-Based Seismic Method?" *Proceedings of ASCE Structures Congress XV*, Vol. **1**, April.

Houck, T. L., G. J. Caporaso, C. C. Shang, S. E. Sampayan, N. E. Molau, and M. L. Krogh, (1997), "Measured and Theoretical Characterization of the RF Properties of Stacked, High-Gradient Insulator Material," *1997 Particle Accelerator Conference*, Vancouver, BC, Canada, May 12–16.

Hsiao, M. C., B. M. Penetrante, B. T. Merritt, G. E. Vogtlin, and P. H. Wallman (1997), "Reduction of NO_2 in N_2 by Non-Thermal Plasmas," *Journal of Advanced Oxidation Technologies*, Vol. **2**, pp. 283–285.

Hsiao, M. C., B. T. Merritt, B. M. Penetrante, G. E. Vogtlin, and P. H. Wallman (1997), "Effect of Gas Temperature on Pulsed Corona Discharge Processing of Acetone, Benzene and Ethylene," *Journal of Advanced Oxidation Technologies*, Vol. **2**, pp. 306–311.

Huang, S. T., D. A. Lappa, and T. Chiao (1997), "Use of a Computer-Assisted Administrative Control to Enhance Criticality in LLNL for Fissile Material Disposition Operations," *Nuclear Criticality Technology Safety Project Annual Workshop*, Gaithersburg, Maryland, May 5–9.

Huang, S., D. Lappa, T. Chiao, C. Parrish, R. Carlson, J. Lewis, D. Shikany, and H. Woo (1997), "Real-Time Software Use in Nuclear Materials Handling Criticality Safety Control," *EFCOG Seventh Annual Safety Analysis Working Group*, Oakland, California, June.

Hurst, P. A (1998), "Optic Assembly and Alignment for the National Ignition Faciltiy Project," *Photonics West*, January.

Johnson, Gary W. (1997), "LabVIEW Graphical Programming," 2nd ed., McGraw-Hill, New York, New York.

Kennedy, K., B. Harteneck, G. Millos, M. Benapfl, K. King, and R. Kirby (1997), "TiN Coating of the PEP-II Low-Energy Ring Aluminum Arc Vacuum Chambers," *Twenty-Fifth Annual American Vacuum Symposium and Exhibition*, February 16.

Khanaka, G. H., and J. Yee (1997), "Semiconductors for Room-Temperature, High-Energy Radiation Detection," *Arms Control and Nonproliferation Technologies, U.S. Department of Energy, Office of Nonproliferation and National Security*, pp. 12–13.

Kim, J., J. Simon, S. Saffer, and C.-J. Kim (1998), "Mercury Contact Micromechanical Relays," *Proceedings of the Fourty-Sixth Annual International Relay Conference*, Oak Brook, Illinois, April, pp. 19-1–19-8.

Kondow, M. , T. Kitatani, S. Nakatsuka, M. C. Larson, K. Nakahara, Y. Yazawa, M. Okai, and K. Uomi (1997), "GaInNAs: A Novel Material for Long-Wavelength Semiconductor Lasers," *IEEE Journal of Selected Topics in Quantum Electronics*, June, Vol. **3**, No. 3, pp. 719–730.

Kuzmenko, P. J., and D. Ciarlo (1998), "Improving the Optical Performance of Etched Silicon Gratings," *SPIE International Symposium on Astronomical Telescopes and Instrumentation, Infrared Astronomical Instrumentation*, March.

Kyle, K. R., and S. B. Brown (1997), "Fiber Optic Raman Probe for In Situ Chemical Characterization of the Hanford Underground Storage Tanks," *Proceedings of the Electrochemical Society, Chemical and Biological Sensors and Analytical Electrochemical Methods*, Vol. **97-17**.

Kyle, K. R., and S. B. Brown (1997), "Fiber Optic Raman Probe for the In Situ Cone Penetrometer Chemical Characterization of the Hanford Underground Storage Tanks," *American Chemical Society National Meeting*, Las Vegas, Nevada, September 7–11.

Kyle, K. R., and S. B. Brown (1997), "Fiber Optic Raman Spectroscopy for In Situ Waste Tank Characterization," *Thirty-Seventh ORNL-DOE Conference on Analytical Chemistry in Energy Technology*, Gatlinburg, Tennessee, October 8.

Kyle, K. R., and S. B. Brown (1998), "Fiber Optic Raman Spectroscopy Probe," *Department of Chemistry Inorganic Seminar*, University of California, Santa Barbara, California, March 11.

Larson, M. C., M. Kondow, T. Kitatani, K. Tamura, Y. Yazawa, and M. Okai (1997), "Photopumped Lasing at 1.25 mm of GaInNAs/GaAs Multiple Quantum Well Vertical-Cavity Surface-Emitting Lasers," *IEEE Photonics Technology Letters*, December, Vol. **9**, No. 12, pp. 1549–1551.

Larson, M. C., M. Kondow, T. Kitatani, K. Nakahara, K. Tamura, H. Inoue, and K. Uomi (1998), "GaInNAs/GaAs Long-Wavelength Vertical-Cavity Surface-Emitting Laser Diodes," *IEEE Photonics Technology Letters*, February, Vol. **10**, No. 2, pp. 188–190.

Larson, M. C., M. Kondow, T. Kitatani, Y. Yazawa, and M. Okai (1997), "Room Temperature Continuous-Wave Photopumped Operation of 1.22-mm GaInNAs/GaAs Single Quantum Well Vertical-Cavity Surface-Emitting Laser," *Electronics Letters*, May, Vol. **33**, No. 11, pp. 959–960.

Lavietes, A. D., J. H. McQuaid, and T. J. Paulus (1997), "Cadmium Zinc Telluride Detector System for Nuclear Material Assay," *Proceedings of the Thirty-Eighth Annual Meeting, Institute of Nuclear Material Management*, July.

Lee, C. L., and Lee, C. T. (1997), "A Higher Order Method of Multiple Scales," *Journal of Sound and Vibration*, Vol. **202**, No. 2, pp. 284–287.

Lee, J. D. (1997), "Criticality Safety Challenges in the Next Decade," *Proceedings of the American Nuclear Society*, September 7–11.

LeSage, G. P., C. V. Bennett, W. E. White, E. C. Landahl, L. L. Laurent, N. C. Luhmann, Jr., F. V Hartemann, C. H. Ho, W. K. Lau, and T. T. Yang (1998), "A High Brightness, X-Band Photoinjector for the Production of Coherent Synchrotron Radiation," *APS Conference on Physics of Plasmas*, November 15–21, Vol. **5**, No. 5.

LeSage, G. P., C. V. Bennett, L. L. Laurent, J. A. Van Meter, V. Dinh, A. L. Troha, B. H. Kolner, F. V. Hartemann, and N. C. Luhmann, Jr. (1997), "Cold and High-Power Tests of a Multibunch X-Band Photoinjector," *IEEE International Conference on Plasma Science*, San Diego, California, May 19–22, p. 130.

Lesuer, D. R., C. K. Syn, O. D. Sherby, and J. Wadsworth (1998), "Laminated Metal Composites - Fracture and Ballistic Impact Behavior," *Advanced Materials and Processing - PRICM 3*, O. P. Aurora *et al.*, eds.

Lesuer, D. R., C. K. Syn, O. D. Sherby, D. K. Kim, and W. D. Whittenberger (1997), "Mechanical Behavior of Ultrahigh Strength, Ultrahigh Carbon Steel Wire and Rod," *Thermo-Mechanical Processing and Mechanical Properties of Hypereutectoid Steels and Cast Irons*, D. R. Lesuer, C. K. Syn and O. D. Sherby, eds., TMS, Warrendale, Pennsylvania, pp. 175–188.

Lesuer, D. R., R. Glaser, and C. K. Syn (1998), "The Evolution of Grain Size Distribution During Deformation of Superplastic Materials," *Superplasticity and Superplastic Forming - 1998*, A. K. Ghosh and T. Biehler, eds., TMS, Warrendale, Pennsylvania, pp. 33–42.

Lesuer, D. R., R. Glaser, and C. Syn (1998), "The Evolution of Grain Size Distribution and Its Influence on the Behavior of Superplastic Materials," *One Hundred Twenty-Seventh Annual TMS Meeting*, February.

Li, E., and M. Dehghani (1997), "Constitutive Model Development for U-6 Niobium Using Modified Tensile and Torsional Test Data," *Fourth U.S. National Congress on Computational Mechanics*, San Francisco, California, August 6–8, p. 315.

Liberman, V., V. Malba, and A. F. Bernhardt (1997), "Integration of Vapor Deposited Polyimide into a Multichip Module Packaging Process," *IEEE Transactions Composites, Hybrids, Manufacturing Technology*, Vol. **20**, pp. 13–16.

Liberman, V., V. Malba, and A. F. Bernhardt (1997), "Vapor Deposition of Polyimide: Monomer Segregation at the Polyimide/Si (100) Interface," *Thin Solid Films*, Vol. **305**, pp. 26–29.

Logan, C. (1997), "Advancing Technologies and Applications in Nondestructive Evaluation," *Science and Technology*, December, pp. 4–11.

Malba, V., A. Conder, and A. F. Bernhardt (1997), "A Stacked-DRAM Solid State Recorder Using a Novel Laser 3-D Interconnect Process," *Proceedings of the Third International 3-D Packaging Workshop*, Philadelphia, Pennsylvania, October.

Malba, V., V. Liberman, and A. F. Bernhardt (1997), "Fabrication of DRAM Stacks Using 3-D Laser Direct Write Patterning of Positive Electrophoretic Photoresist," *International Journal of Microcircuits and Electronic Packaging*, Vol. **20**, pp. 371–375.

Martz, H. (1997), "Gamma-Ray Scanner Systems for ND Assay of Heterogeneous Materials," *Symposium on International Safeguards*, Vienna, Austria, October.

Martz, H. (1997), "The Role of NDE in Life Cycle Management," *Third Annual Symposium on Frontiers of Engineering*, August.

Matthews, S. M., T. E. Cowan, and H. S. Peters (1997), "Irradiation of Potting Compound from Fluorescent Light Ballasts for Treatment of PCB, EPRI Municipal Water and Wastewater Program," *Environmental Applications of Advanced Oxidation Technologies, Electric Power Research Institute Industrial and Agricultural Technologies and Services*, September.

McCallen, R. C., B. T. Kornblum, and W. Kollman (1997), "Large-Eddy Simulation in Complex Domains Using the Finite Element Method, FEDSM97-3496," *Proceedings of the American Society of Mechanical Engineers Fluids Engineering Summer Meeting*, Vancouver, Canada, BC, June 22–26.

McCallen, R. C., F. Browand, A. Leonard, and W. Rutledge (1997), "Systematic Approach to Analyzing and Reducing Aerodynamic Drag of Heavy Vehicles," *Annual Automotive Technology Development Customers' Coordination Meeting*, Dearborn, Michigan, October 27–30.

McKoon, R. H. (1997), "Characterization of Electron Beam Melted Uranium - 6% Niobium Ingots," *Proceedings of the Conference on Electron Beam Melting and Refining - State of the Art*, October 5–7, pp. 182–195.

Mill, T., M. Su, C. C. D. Yoa, S. M. Matthews, and F. T. S. Wang. (1997), "E-Beam Treatment of Trichloroethylene-Air Mixtures: Products and Rates," *Radiation Physics and Chemistry*, September, Vol. **50**, No. 3.

Miller, W. (1977), "Improved Axisymmetric View Factor Calculations for FACET," *Tri-Lab Engineering Conference on Modeling and Simulation*, November.

Miller, W., and L. Parietti (1997), "Thermal Analysis of the NIF Final Optics Assembly - Part 2," *Tri-Lab Engineering Conference on Modeling and Simulation*, November.

Murphy, K. D., and C. L. Lee (1998), "The 1:1 Internally Resonant Response of a Cantilever Beam Attached to a Rotating Body," *Journal of Sound and Vibration*, Vol. **211**, No. 2, pp. 179–194.

Nakahara, K., M. Kondow, T. Kitatani, M. C. Larson, and K. Uomi (1998), "1.3-mm Continuous-Wave Lasing Operation in GaInNAs Quantum-Well Lasers," *IEEE Photonics Technology Letters*, April, Vol. **10**, No. 4, pp. 487–488.

Nieh, T. G., R. O. Kaibyshev, and D. R. Lesuer (1998), "Superplasticity in a Conventional Coarse-Grained 6061 Al and the Liquid Phase Effect," *Superplasticity and Superplastic Forming - 1998*, A. K. Ghosh and T. Biehler, eds., TMS, Warrendale, Pennsylvania, pp. 137–144.

Northrup, M. A., B. Benett, D. Hadley, P. Landre, S. Lehew, J. Richards, and P. Stratton (1998), "A Miniature Analytical Instrument for Nucleic Acids Based on Micromachined Silicon Reaction Chambers," *Analytical Chemistry*, March, Vol. **70**, No. 5, pp. 918–922.

Northrup, M. A., B. Benett, D. Hadley, P. Landre, S. Lehew, J. Richards, and P. Stratton (1997), "Aligned Wafer Bonding for Microfluidic Devices," *Proceedings of the Electrochemical Society International Conference*, Paris, France, September.

Page, R. H., R. A. Bartels, R. J. Beach, S. B. Sutton, L. H. Furu, and J. E. LaSala (1997), "1-Watt Composite-Slab Er:YAG Laser," *OSA TOPS - Advanced Solid State Lasers*, Vol. **10**.

Papados, P. P., R. R. Namburu, C. G. Hoover and A. J. De Groot (1997), "Scalability Studies for Soil-Structure Interaction Problems," *Proceedings of the Fourth U. S. National Congress on Computational Mechanics*, San Francisco, California, August 6–8.

Parietti, L., and W. Miller (1997), "Thermal Analysis of the NIF Final Optics Assembly - Part 1," *Tri-Lab Engineering Conference on Modeling and Simulation*, November.

Penetrante, B. M., G. E. Vogtlin, B. T. Merritt, and R. M. Brusasco (1997), "Plasma Technology for Tail Pipe Reduction of NO_x in Diesel Exhaust," *Proceedings of the 1997 South Coast Air Quality Management District Symposium on Air Pollution Health Impacts: Recent Findings, Implications, Dieselization and Policy Initiatives*, Diamond Bar, California, November.

Penetrante, B. M., M. C. Hsiao, B. T. Merritt, and G. E. Vogtlin (1997), "Fundamental Limits on Gas-Phase Chemical Reduction of NO_x in a Plasma," *Proceedings of the 1997 Diesel Engine Emissions Reduction Workshop*, San Diego, California, July.

Penetrante, B. M., M. C. Hsiao, B. T. Merritt, and G. E. Vogtlin (1997), "Multi-Stage Selective Catalytic Reduction of NO_x in Lean-Burn Engine Exhaust," *Proceedings of the 1997 Diesel Engine Emissions Reduction Workshop*, San Diego, California, July.

Penetrante, B. M., M. C. Hsiao, B. T. Merritt, and G. E. Vogtlin (1997), "Fundamental Limits on NOx Reduction by Plasma," *Proceedings of the 1997 Society of Automotive Engineers International Spring Fuels and Lubricants Meeting and Exposition*, Detroit, Michigan, May 5–8.

Penetrante, B. M., M. C. Hsiao, B. T. Merritt, G. E. Vogtlin, C. Z. Wan, G. W. Rice, and K. E. Voss (1997), "Plasma-Assisted Heterogeneous Catalysis for NO_x Reduction in Lean-Burn Engine Exhaust," *Proceedings of the 1997 Diesel Engine Emissions Reduction Workshop*, San Diego, California, July.

Penetrante, B. M., M. C. Hsiao, J. N. Bardsley, B. T. Merritt, G. E. Vogtlin, A. Kuthi, C. P. Burkhart, and J. R. Bayless (1997), "Identification of Mechanisms for Decomposition of Air Pollutants by Non-Thermal Plasma Processing," *Plasma Sources Science and Technology*, Vol. **6**, pp. 251–259.

Penetrante, B. M., M. C. Hsiao, J. N. Bardsley, B. T. Merritt, G. E. Vogtlin, A. Kuthi, C. P. Burkhart, and J. R. Bayless (1997), "Decomposition of Methylene Chloride by Electron Beam and Pulsed Corona Processing," *Physics Letters A* **235**, pp. 76–82.

Penetrante, B. M., M. C. Hsiao, J. N. Bardsley, B. T. Merritt, G. E. Vogtlin, A. Kuthi, C. P. Burkhart, and J. R. Bayless (1997), "Comparison of Pulsed Corona and Electron Beam Processing of Hazardous Air Pollutants," *Journal of Advanced Oxidation Technologies*, Vol. **2**, pp. 299–305.

Penetrante, B. M., W. J. Pitz, M. C. Hsiao, B. T. Merritt, and G. E. Vogtlin (1997), "Effect of Hydrocarbons on Plasma Treatment of NO_x," *Proceedings of the 1997 Diesel Engine Emissions Reduction Workshop*, San Diego, California, July.

Piscotty, M. (1997), "In-Process EDM Truing to Generate Complex Contours on Metal-Bond, Superabrasive Grinding Wheels for Precision Grinding Structural Ceramics," *International Conference on Precision Engineering*, November.

Piscotty, M., T. Saito, and P. Davis (1997), "In-Process EDM Truing to Generate Complex Contours on Metal-Bond, Super-Abrasive Grinding Wheels for Precision Grinding Structural Ceramics" *Amercian Society for Precision Engineering, Twelvth Annual Meeting*, October 5.

Piscotty, M., T. Saito, and P. Davis (1997), "Use of In-Process EDM Truing to Generate Complex Contours on Metal-Bond, Super-Abrasive Grinding Wheels for Precision Grinding Structural Ceramics," *International Conference on Precision Engineering*, Taipei, Taiwan November 18–20.

Poole, B. R., G. J. Caporaso, and W. C. Ng (1997), "Wake Properties of a Stripline Beam Kicker," *1997 Particle Accelerator Conference*, Vancouver, BC, Canada, May 12–16.

Rainer, F. (1998), "Mapping and Inspection of Damage and Artifacts in Large-Scale Optics, *Laser-Induced Damage in Optical Materials: 1997*, G. J. Exarhos, A. H. Guenther, M. R. Kozlowski, and M. J. Soileau, eds., *SPIE Proceedings*, Vol. **3244**, pp. 272–281.

Rasty, J., N. Dutta, M. Dehghani, and M. Rassaian (1997), "Residual Stresses Induced by Co-Drawing of Circular Rods," *Proceedings of the Fourth U.S. National Congress on Computational Mechanics*, San Francisco, California, August, p. 312.

Ratowsky, R. P., L. Yang, R. J. Deri, J. S. Kallman, and G. Trott (1997), "Laser Diode to Single-Mode Fiber Ball Lens Coupling Efficiency: Full-Wave Calculation and Measurements," *Applied Optics 2005*, pp. 3435–3438.

Ratowsky, R. P., S. Dijaili, J. S. Kallman, M. D. Feit, J. Walker, W. Goward, and B. B. Afeyan (1998), "Modeling a Distributed Spatial Filter Low-Noise Semiconductor Optical Amplifier," *Integrated Photonics Research, Optical Society of America Technical Digest Series*, Vol. **4**, pp. 152–154.

Rudd, L. vE., D. J. Pines, and P. H. Carter (1998), "Improved Performance of Sub-Optimal Periodic Hypersonic Cruise Trajectories for Long Range," *AIAA Journal of Aircraft*, May.

Rudd, L. vE., D. J. Pines, and P. H. Carter (1998), "Improved Performance of Sub-Optimal Periodic Hypersonic Cruise Trajectories for Long Range," *Eighth AIAA International Spaceplanes and Hypersonics Systems and Technologies Conference*, Norfolk, Virginia, April 27–30.

Rudd, L. vE., D. J. Pines, and P. H. Carter (1998), "Optimal Parameterized Damped Periodic Hypersonic Cruise Trajectories," *AIAA Journal of Aircraft*, in press.

Ruiz, R., and W. McNab (1998), "Engineering Design and Testing of a Ground Water Remediation System Using Electrolytically Generated Hydrogen with a Palladium Catalyst for Dehalogenating Chlorinated Hydrocarbons," *Proceedings Part A-Technical/Professional Papers, 1998 Mexican American Engineering Society National Symposium*, San Diego, California, January 14–17.

Runkel, M., J. DeYoreo, W. Sell, and D. Milam (1998), "Laser Conditioning Study of KDP on the Optical Sciences Laser Using Large Area Beams," *Laser-Induced Damage in Optical Materials: 1997*, G. J. Exarhos, A. H. Guenther, M. R. Kozlowski, and M. J. Soileau, eds., *SPIE Proceedings*, Vol. **3244**, pp. 51–63.

Runkel, M., M. Yan, J. DeYoreo, and N. Zaitseva (1998), "The Effect of Impurities and Stress on the Damage Distributions of Rapidly Grown KDP Crystals," *Laser-Induced Damage in Optical Materials: 1997*, G. J. Exarhos, A. H. Guenther, M. R. Kozlowski, and M. J. Soileau, eds., *SPIE Proceedings*, Vol. **3244**, pp. 211–223.

Russell, E. W., and D. A. Lappa (1997), "Validation and Verification of Finite Element Method Codes Used for Analyses of Pit Storage/Transport Packages," *Second Biennial Tri-Laboratory Engineering Conference on Modeling and Simulation*, Santa Fe, New Mexico, November 12–14.

Sahai, V. (1997), "Influence of Bulk Convection on Freckle Formation in Castings," *Proceedings of the Fourth International Special Emphasis Symposium on Superalloys 718, 625, 706, and Derivatives*, TMS, June.

Saito, T. (1997), "Policy and the Photon: A Federal Balancing Act," *Optical Engineering Reports*, July, Vol. **163**, p. 2.

Saito, T. (1997), "Policy and the Photon: Time for Attention at the National Level," *Optical Engineering Reports*, May, Vol. **161**, p. 2.

Salleo, A., F. Y. Genin, J. Yoshiyama, C. J. Stolz, and M. R. Kozlowski (1998), "Laser-Induced Damage of Fused Silica at 355 nm Initiated at Scratches," *Laser-Induced Damage in Optical Materials: 1997*, G. J. Exarhos, A. H. Guenther, M. R. Kozlowski, and M. J. Soileau, eds., *SPIE Proceedings*, Vol. **3244**, pp. 341–347.

Sargis, P. D., B. D. Henderer, and M. E. Lowry (1997), "10-Gb/s Subcarrier Multiplexed Transmission Over 490 km of Ordinary Single-Mode Fiber Without Dispersion Compensation," *IEEE Photonics Technology Letters*, December, Vol. **9**, No. 12, pp. 1658–1660.

Schwartz, A. J., D. H. Lassila, and M. M. LeBlanc (1998), "The Effects of Tungsten Addition on the Microtexture and Mechanical Behavior of Tantalum Plate," *Materials Science and Engineering A*, **A244**, pp. 178–190.

Scott, R. P., C. V. Bennett, and B. H. Kolner (1997), "AM and High-Harmonic FM Laser Mode Locking," *Applied Optics*, August, Vol. **36**, No. 24, pp. 5908–5912.

Shang, C. C., Y.-J. Chen, T. L. Houck, G. J. Caporaso, W. C. Ng, N. E. Molau, J. Fockler, and S. Gregory, (1997), "BBU Design of Linear Induction Accelerator Cells for Radiography Application," *1997 Particle Accelerator Conference*, Vancouver, BC, Canada, May 12–16.

Sheaffer, M. K., S. C. Keeton, M. E. Wangler, L. E. Fischer, and Y. Y. Liu (1997), "Recent Developments in Fissile Material Exemptions for Shipping Packages," *Proceedings of the American Nuclear Society Topical Meeting on Criticality Safety Challenges in the Next Decade*, September.

Simon, J., S. Saffer, and C.-J. Kim (1997), "A Liquid-filled Microrelay with a Moving Mercury Microdrop," *Journal of Microelectromechanical Systems*, September, Vol. **6**, No. 3, pp. 208–216.

Simon, J., L.-S. Huang, B. Sridharan, and C.-J. Kim (1997), "Microgasketing and Room Temperature Wafer Joining for Liquid-Filled MEMS Devices," *Proceedings of the American Society of Mechanical Engineers International Mechanical Engineering Congress and Exposition*, Dallas, Texas, November, DSC-Vol. **62**/HTD-Vol. **354**, pp. 29–34.

Souza, P., and D. Chinn (1998), "Ultrasonic Measurement of KDP Solution Concentration," *ASNT 1998 Fall Conference*, Nashville, Tennessee, October 19–23.

Spellman, G. P., R. Jayakumar, and R. P. Reed (1998), "Thermo-Mechanical Properties of ITER Buffer Zone Candidate Materials," *Cryogenics*, January, Vol. **38**, No. 1, p. 33.

Stolz C. J., J. M. Yoshiyama, Z. L. Wu, A. Salleo, J. Green, and R. Krupka (1998), "Characterization of Nodular and Thermal Defects in Hafnia/Silica Multilayer Coatings Using Optical, Photothermal, and Atomic Force Microscopy," *Laser-Induced Damage in Optical Materials: 1997*, G. J. Exarhos, A. H. Guenther, M. R. Kozlowski, and M. J. Soileau, eds., *SPIE Proceedings*, Vol. **3244**, pp. 475–483.

Sugihwo, F. M., C. Larson, and J. S. Harris, Jr. (1998), "Micromachined Widely Tunable Vertical Cavity Laser Diodes," *Journal of Microelectromechanical Systems*, March, Vol. **7**, No. 1, pp. 48–55.

Sugihwo, F., M. C. Larson, and J. S. Harris, Jr. (1997), "Whispering Gallery Mode Operation in Airgap Vertical Cavity Laser Structure," *Electronics Letters*, August, Vol. **33**, No. 17, pp. 1467–1468.

Sugihwo, F., M. C. Larson, and J. S. Harris, Jr. (1998), "Simultaneous Optimization of Membrane Reflectance and Tuning Voltage for Tunable Vertical Cavity Lasers," *Applied Physics Letters*, January, Vol. **72**, No. 1, pp. 10–12.

Swan, J., D. Behne, C. M. Kendall, R. Yamamoto, T. Yokota, and J. Tanabe (1997), "Design and Performance of the PEP-II B-Factory HER QD4 Quadrupole Magnet," *Proceedings of the Fifteenth International Conference on Magnet Technology*, Science Press, China, October.

Syn, C. K., D. R. Lesuer, and O. D. Sherby (1997), "Thermo-Mechanical Processing and Properties of a Ductile Iron," *Thermo-Mechanical Processing and Mechanical Properties of Hypereutectoid Steels and Cast Irons*, D. R. Lesuer, C. K. Syn and O. D. Sherby, eds., TMS, Warrendale, Pennsylvania, pp. 117–125.

Syn, C. K., D. R. Lesuer, T. G. Nieh, H. S. Yang, K. R. Brown, R. O. Kaibyshev, and E. N. Petrov (1998), "Roll Forming Technology for Manufacturing Axisymetric Automotive Components," *Automotive Alloys II*, S. Das, ed., TMS, Warrendale, Pennsylvania, pp. 173–183.

Taleff, E. M., B. L. Bramfitt, C. K. Syn, D. R. Lesuer, and O. D. Sherby (1997), "Mechanical Behavior of an Ultrahigh-Carbon Steel Exhibiting a Damask Pattern," *Thermo-Mechanical Processing and Mechanical Properties of Hypereutectoid Steels and Cast Irons*, D. R. Lesuer, C. K. Syn and O. D. Sherby, eds., TMS, Warrendale, Pennsylvania, pp. 189–198.

Taleff, E. M., C. K. Syn, D. R. Lesuer, and O. D. Sherby (1997), "A Comparison of Mechanical Behavior in Pearlitic and Spheroidized Hypereutectoid Steels," *Thermo-Mechanical Processing and Mechanical Properties of Hypereutectoid Steels and Cast Irons*," D. R. Lesuer, C. K. Syn and O. D. Sherby, eds., TMS, Warrendale, Pennsylvania, pp. 127–142.

Thomas, G. (1998), "Ultrasonic Evaluation of Flood Gate Tendons," *International Syposium on NDE Techniques for Aging Infrastructure and Manufacturing*, San Antonio, Texas, January.

Thomas, N., J. Wolfe, and J. Farmer (1998), "Protected Silver Coating for Astronomical Mirrors," *SPIE International Symposium on Astronomical Telescope and Instrumentation Symposium*, Kona, Hawaii, Vol. **3553**, March.

Tietbohl, G. L., P. M. Bell, R. M. Hamilton, J. B. Horner, R. L. Horton, A. P. Ludwigsen, J. L. Miller, W. H. Olson, C. S. Patel, D. M. Pennington, M. D. Vergino, and T. L. Weiland (1998), "Engineering the Petawatt Laser into Nova," *SPIE Photonics West Conference*, San Jose, California, January 24–30.

Tripathi, B. P., and Q. A. Hossain (1997), "A Critical Review of Methods to Evaluate Response of Structures Subjected to Aircraft Impact," *Proceedings of the Fourteenth Conference on Structural Mechanics in Reactor Technology*, August 27, Vol. **6**, Division J.

Watkins, B. E., R. S. Upadhye, and C. O. Pruneda (1997), "Recent Advances in the Molten Salt Technology for the Destruction of Energetic Materials," *Proceedings of the Air and Waste Management Association Ninetieth Annual Meeting and Exposition*, Toronto, Canada, June 8–13.

Watson, J. (1997), "Tip Tilt Correction System for Astronomical Telescopes Using Adaptive Control," *1997 IEEE WESCON/97 Conference*, November, Record Catalog Number 97CH36148.

Westerberg, K. W., T. C. Meier, M. A. McClelland, D. G. Braun, L. V. Berzins, T. M. Anklam, and J. Storer (1997), "Analysis of the E-Beam Evaporation of Titanium and Ti-6Al-4V," *Electron Beam Melting and Refining State of the Art 1997*, R. Bakish, ed., Bakish Materials Corp., Englewood, New Jersey, pp. 208–221.

Witte, M. C., J. Hovingh, G. C. Mok, S. S. Murty, T. F. Chen, and L. E. Fischer (1997), "Summary and Evaluation of Low-Velocity Impact Tests of Solid Steel Billet Onto Concrete Pads," NUREG/CR-6608, U.S. Nuclear Regulatory Commission.

Woods, B., M. Yan, J. DeYoreo, M. Kozlowski, H. Radousky, and Z. L. Wu (1998), "Photothermal Mapping of Defects in the Study of Bulk Damage in KDP," *Laser-Induced Damage in Optical Materials: 1997*, G. J. Exarhos, A. H. Guenther, M. R. Kozlowski, and M. J. Soileau, eds., *SPIE Proceedings*, Vol. **3244**, pp. 242–248.

Wu, Z. L. (1998), "Photothermal Sensing Techniques for Thin Film Characterization," in *Materials Characterization and Optical Probe Techniques, Critical Review of Optical Science and Technology*, CR 69, pp. 326–356.

Wu, Z. L., J. Green, T. Yang, and R. Krupka (1997), "Non-Destructive Evaluation of Large Aperture Optics With Ultra-Low Optical Absorption," *Thirteenth Symposium on Thermophysical Properties*, Boulder, Colorado, June 22–27.

Young, D. J., V. Malba, J. J. Ou, B. E. Boser, and A. F. Bernhardt (1997), "Monolithic High-Performance Three-Dimensional Coil Inductors For Wireless Communication Applications," *Proceedings of the IEEE International Electron Devices Meeting*, Washington, DC, December 7–10.

Zhao, Q., Z. L. Wu, M. Thomsen, and Y. Han (1998), "Interfacial Effects on the Transient Temperature Rise of Multilayer Coatings Induced by a Short-Pulse Laser Irradiation," *Laser-Induced Damage in Optical Materials: 1997*, G. J. Exarhos, A. H. Guenther, M. R. Kozlowski, and M. J. Soileau, eds., *SPIE Proceedings*, Vol. **3244**, pp. 491–498.

Zocher, M. A., D. H. Allen, and S. E. Groves (1997), "A Three-Dimensional Finite Element Formulation for Thermoviscoelastic Orthotropic Media," *International Journal for Numerical Methods in Engineering*, June, Vol. **40**.

Zocher, M. A., D. H. Allen, and S. E. Groves (1997), "Stress Analysis of a Matrix-Cracked Viscoelastic Laminate," *International Journal of Solids and Structures*, Vol. **34** No. 25.

Author Index

Author Index

Ackler, H. *2-37*
Afeyan, B. B. *4-1*
Allen, K. A. *2-1*
An, J. R. *6-27*
Ashby, E. *4-13*
Aufderheide, M. B. *5-61*
Avalle, C. A. *6-23*
Azevedo, S. *5-39*

Balooch, M. *2-23*
Bettencourt, K. A. *2-1*
Blaedel, K. L. *3-9*
Bland, M. F. *4-29*
Brase, J. M. *5-39*
Brown, A. A. *6-1*
Brugger, S. T. *4-7*
Bryan, Jr., S. R. *6-17*
Burke, G. *4-7*
Butler, J. A. *2-1*

Campbell, E. W. *6-27*
Candy, J. V. *1-3, 5-1*
Caporaso, G. J. *4-85*
Casey, J. *6-1*
Castor, J. I. *6-23*
Chen, Y.-J. *4-85*
Chien, C. *2-11*
Chinn, D. *2-23, 5-1, 5-19, 5-23*
Ciarlo, D. R. *2-5, 2-23, 4-13*
Clague, D. S. *2-19*
Clark, G. A. *1-3*
Cooper, G. A. *2-31*

Darrow, C. B. *2-45*
Davis, P. J. *3-9*
De Groot, A. J. *1-1, 4-47*
DenBaars, S. *2-31*
Deng, C. *2-11*
Deri, R. J. *1-1, 2-49*
Dunlap, J. E. *4-71*
Dupuy, P. C. *3-9*

Erlandson, A. C. *4-37*
Elgorria, I. *2-11*

Feit, M. D. *4-1*
Ferencz, R. M. *4-47*
Fugina, J. M. *5-27*

Garcia, M. *4-33*
Gilman, A. *2-45*
Goodman, D. M. *5-61*
Graff, R. T. *2-27*
Gresho, P. M. *4-81*
Groves, S. E. *2-23, 5-23*

Hagans, K. G. *2-17*
Haigh, R. E. *2-13, 2-17*
Haskins, J. J. *5-23, 5-27*
Haupt, D. L. *5-23*
Hayes, J. P. *2-27*
Hernandez, M. A. *4-7*
Hoehler, M. *1-3*
Hoover, C. G. *4-47*
Huber, R. D. *5-1*

Jackson, J. A. *5-61*
Jancaitis, K. S. *4-37*
Jankowski, A. F. *2-27*
Jensen, S. A. *3-1*
Johansson, E. M. *5-61*
Johnson, R. R. *1-11*
Jones, L. M. *2-7*

Kallman, J. S. *4-1, 4-7, 4-13*
Kay, G. J. *6-7*
Kinney, J. *5-23*
Krulewich, D. A. *3-3*

LaChappel, M. J. *2-23*
Lane, S. M. *2-45*
Larson, M.C. *2-49*
Lavietes, A. D. *5-27*
Law, B. P. *2-5*
LeBlanc, M. *6-7*
Lee, A. P. *2-7, 2-11, 2-45*
Lee, Y. L. *4-47*
Lehew, S. L. *2-31*
Le Sage, G. P. *4-19*
Lesuer, D. R. *6-7*
LeTouze, G. *4-37*
Lin, J. I. *4-55*
Logan, C. M. *5-23, 5-27*
Lowry, M. E. *2-13, 2-49*

Marshall, C. D. *4-37*
Mast, J. E. *4-23, 5-39*
Mayhall, D. J. *4-29*
McCallen, D. B. *1-3*
McConaghy, C. F. *2-7, 2-11, 2-13, 2-45*
Meyer, G. A. *2-31*
Miles, R. R. *2-1*
Mishra, U. *2-31*
Molau, N. E. *4-77*
Morales, K. E. *5-27*
Morse, J. D. *2-23, 2-27*

Nelson, S. D. *4-23, 4-71*
Nikkel, D. J., Jr *6-1*
Nukala, P. K. V. V. *4-65*

Perry, R. L. 5-13
Piscotty, M. A......3-9
Pocha, M. D......2-41, 2-49
Poole, B. R......4-85
Puso, M. A. 4-59

Ratowsky, R. P......4-1
Richardson, R. A. 4-19
Roberts, R. S......5-9, 5-13
Robey, H. F......5-19
Rosenbury, E. T......5-39
Rotter, M. D. 4-37

Sanders, D. L......6-17
Sargis, P. D. 4-77
Satcher, Jr., J. H. 2-45
Schmid, G. J......5-27
Schneberk, D. J. 5-27
Schumann, D. L. 2-1
Sengupta, S. K. 5-51
Seznec, S. 4-37
Shapiro, A. B......4-81
Sherwood, R. J......4-47
Sigmon, T. W. 2-31
Simon, J......2-7
Smart, J. C......1-15
Soltani, P. 5-27
Souza, P. R......5-19
Speck, D. E. 4-47
Spicer, J......5-1
Springer, K......5-27
Steich, D......4-7
Stuart, B. C......3-1
Swartz, K. 5-27
Sweider, D. 4-77
Swierkowski, S. P......2-37

Thomas, G. H......4-13, 5-1
Toet, D. 2-31
Trevino, J. C......2-7

Updike, E. O......5-27

Wang, A. W......2-45
Wang, L. 4-23, 4-85
Warrick, A. L......4-23
Waters, A. 5-23
White, D. A. 4-7

Zapata, L. E......4-37
Zywicz, E. 4-47

Technical Information Department
Lawrence Livermore National Laboratory
University of California
Livermore, California 94551